R-05-85

System and safety studies of accelerator driven transmutation

Annual Report 2004

Waclaw Gudowski, Jan Wallenius, Vasily Arzhanov,
Mikael Jolkkonen, Kamil Tucek, Marcus Eriksson,
Per Seltborg, Daniel Westlén, Christina Lagerstedt,
Patrick Isaksson, Alexandra Åhlander and Christoffer Gottlieb

Department of Nuclear and Reactor Physics
Royal Institute of Technology, Stockholm

December 2005

Svensk Kärnbränslehantering AB
Swedish Nuclear Fuel
and Waste Management Co
Box 5864
SE-102 40 Stockholm Sweden
Tel 08-459 84 00
+46 8 459 84 00
Fax 08-661 57 19
+46 8 661 57 19

ISSN 1402-3091
SKB Rapport R-05-85

System and safety studies of accelerator driven transmutation

Annual Report 2004

Waclaw Gudowski, Jan Wallenius, Vasily Arzhanov,
Mikael Jolkkonen, Kamil Tucek, Marcus Eriksson,
Per Seltborg, Daniel Westlén, Christina Lagerstedt,
Patrick Isaksson, Alexandra Åhlander and Christoffer Gottlieb

Department of Nuclear and Reactor Physics
Royal Institute of Technology, Stockholm

December 2005

The full report including all Appendices is available as a .pdf-file on the enclosed CD-ROM-disc. The printed version contains only the main text and a list of the Appendices.

PREFACE

The research on safety of Accelerator-Driven Transmutation Systems (ADS) at the Department of Nuclear and Reactor Physics at KTH reported here has been focused on different aspects of safety of the Accelerator-Driven Transmutation Systems and on Transmutation research in more general terms. An overview of the topics of our research is given in the Summary which is followed by detailed reports as separate chapters or subchapters.

Some of the research topics reported in this report are referred to appendices, which have been published in the open literature. Topics, which are not yet published, are described with more details in the main part of this report. The main report is also included in a PDF-format on a CD-ROM attached to this report. The Appendices are only included in the CD-ROM disc.

Blue text color in a PDF version of this report implies links which can take a reader by a mouse click to the referred part of the report or to a referred Appendix. The appendices are submitted with the printed report on a CD-ROM.

A summary in Swedish is given in the very early chapter called “SAMMAN-FATTNING”.

SUMMARY

The results of the research activities on System and Safety of Accelerator-Driven Transmutation (ADS) at the Department of Nuclear and Reactor Physics are described in this report followed by the Appendices of the relevant scientific papers published in 2004. In particular a PhD dissertation of Kamil Tuček "Neutronic and Burnup Studies of Accelerator-driven Systems Dedicated to Nuclear Waste Transmutation" (Appendix 1) reflects research mainstream of 2004.
Research activities of 2004 have been focused on several areas:

- Simulation of subcritical experiments in preparation of international ADS experiments
- System studies of ADS
- Dynamics and kinetics of ADS
- Reactor based transmutation
- Nuclear fuel development for transmutation
- Material studies for ADS
- Fuel cycle studies
- Code and methods development

Large part of the research activities has been well integrated with the European projects of the 5th and 6th Framework Programmes of the European Commission in which KTH is actively participating. In particular European projects: PDS-XADS, MUSE, CONFIRM, FUTURE and RED-IMPACT.

Most important results and conclusions from our studies are
Sub-critical experiments:

- *MUSE experiment:*
  - A novel approach of characterizing ADS through proton importance function has been developed and implemented in the MUSE experiment. Proton importance monitoring has been identified as one of the methods for subcriticality monitoring.
  - k_{eff} for the lead-cooled configuration increases with about 1600 pcm compared to the sodium cooled configuration. In order to maintain the same reactivity for the two configurations, which is particularly important for the comparison of the neutron source response, some of the peripheral fuel sub-assemblies were removed. k_{eff} was approximately 0.974 in both cases.
- *SAD experiment*:
  - The reactivity worth of different fuel assemblies in SAD has been determined by Monte Carlo simulations. Fuel assemblies at different radial distances have been replaced with air and the influence on k_{eff} has been investigated
  - The importance of the created neutrons is higher if there are fuel assemblies in all directions. The reactivity worth is around 550 pcm for

all fuel assemblies in the three innermost layers, and a little bit lower, ~450 pcm, for the outermost layer.

- The empty slots correspond to approximately 200-300 pcm each. The core is still subcritical with all fuel assemblies inserted using data from JEF2.2.
- The temperature feedback of SAD is negative both when considering pure Doppler effect and when taking fuel expansion into account. The temperature feedback coefficient should be approximately -0.9 pcm/K at 300 K.

- Yalina:
  - Subcriticality measurements methods were tested:
    - the Source Jerk method
    - the Pulsed Source methods
      - Area method
      - The Slope Fit method.
    - The Pulsed Source experiment has also been simulated using the Monte Carlo code MCNP.
  - The Area method overestimates the subcriticality and the other two methods give reasonable results with larger uncertainties. MCNP provides reliable results considering neutron distributions in space and time but fails in predicting neutron time parameters.
  - The Area method overestimates the subcriticality, but gives low statistical error. Can not be used for online reactivity measurement.
  - The Slope fit method is difficult to use, but seems to give reliable results when the correct slope is found. Can not be used for online reactivity measurement.
  - Source Jerk method has problems with large uncertainties, but can easier be implemented in a continuously running facility.
  - Reactivity monitoring seems to be a difficult task without control rods. None of the methods are able to measure the reactivity without disturbing a running system. The methods can be used to estimate the subcriticality during load and for calibration of eventual indirect measure techniques.
  - The experiments show that the Point Kinetic approximation seems to describe the Yalina system well.

ADS system studies:

- To complete Pb-Bi cooled ADS burner design work, an optimisation of fuel concept and core design has been performed, to achieve favourable neutronic, burnup and safety characteristics. Key thermal hydraulic and material-related constraints were respected.
- Helium cooling of sub-critical cores dedicated to minor actinide transmutation is an interesting alternative to liquid metal cooled cores once the fuel is designed to withstand high temperatures during accident transients. This is possible with TiN-particle fuel.

Dynamics and kinetics of ADS

- Transient safety studies of different minor actinide fuel systems show
  - The better thermal conductivity, higher melting point, and lower coolant void worth of the CerMet fuel combine to contribute to better inherent safety features
  - The swelling behavior and hardness of the molybdenum metal raise safety concerns regarding fuel-cladding mechanical interactions.
  - The CerCer fuel suffers from low thermal conductivity and uncertain melting behavior, which limits both the achievable power density and predicted performance during overpower conditions. In addition, the reactivity void worth of this fuel is relatively high in comparison with the other fuels, which is a safety dilemma.
  - The principal problem with the nitride fuel, with regards to the safety performance, is its tendency to dissociate at low temperatures. A steam generator tube rupture event was identified as a potential threat, which could lead to extensive voiding in current accelerator-driven design proposals.
  - It is important to have a low coolant void reactivity value in a lead/bismuth system, despite of its high boiling temperatures.
- The Doppler feedback in the typical minor actinide fueled ADS is too small to influence the development of a prompt critical accident. For slower reactivity insertions, subcriticality could possibly facilitate faster shutdown, but may be less effective for fast insertions. To some degree axial expansion of the fuel can compensate for a small Doppler coefficient, but it cannot be considered as reliable as the Doppler effect in the general case.
- Seismic analysis of reactor vessel shows an allowable vessel height in the range 10-12 m. A wall thickness of 250 mm should admit a vessel height around 15-16 m, which indicates a rather high sensitivity of the stress level on the vessel height. The dependence on the vessel diameter is not strong, however. Results depend on seismic load conditions, which are site dependent. Use of bottom horizontal structure support and/or base isolation could enhance seismic performance, which may lead to significant reduction of building accelerations in an earthquake.

The Deep Burn - Modular Helium Reactor (DB-MHR)

- Further detail studies performed with the MCB code show that DB-MHR can effectively and safely burn LWRs Pu. The benefits of the helium-cooled graphite-moderated reactors are several: passive safety mechanism, low cost, flexibility in the choice of fuel, high conversion energy efficiency, high burnup, resistant TRISO fuel cladding and low power density. Neutronic parameters of this reactor are also very favorable. Accuracy studies performed on DB-MHR confirm that the methodology, tools and nuclear data for detail simulations of this reactor are reliable.

Nuclear fuel development for transmutation

Safety studies of nuclear fuels

- The major safety concern of the cores investigated is coolant voiding resulting from gas bubble introduction into the core. The source term could be fission/helium gas leakage from ruptured fuel pins, or steam

bubbles from a broken heat exchanger. Fuel types with lower void worths will allow for operation with smaller sub-criticality margin. Hence the molybdenum based cermet fuel appears to provide the best performance with respect to the accident scenarios here investigated – more detailed results are reported in the chapter on **Dynamics and kinetics of ADS**

Thermal stability of nitride fuels

- The dissociation of the actinide nitrides is not a mechanical problem, as the contribution to the overall pressure is minute and rather insignificant in terms of cladding stress. The maximum permissible overheating, in terms of both temperature and duration, is more likely to be dependent on transport effects that may be expected to take place in a real system. In case of a partial dissociation of the fuel, the products, if released from the fuel pellets, would rapidly recombine on any colder surface, presumably the inside of the cladding. The possible issue of a minute but continuous dissociation of nitride in hot zones and recombination on colder surfaces might be possible to investigate by a theoretical approach, but PIE of the experimental fuel pins destined for testing will no doubt provide us with a far more reliable estimate of the extent of such redistribution.

Material studies for ADS and modeling of irradiation effects

- Improved potential for iron and iron based alloys
  - Existing empirical models for pure elements like Fe and Cr have been extended to the Fe-Cr-C system.
  - The Embedded Atom Method potentials for pure iron and chromium developed in 2003 were further improved during 2004, in order to provide interstitial formation energies in better agreement with electronic structure calculations.
  - There are some ambiguity in interpreting the simulations results and more detailed studies are required

Fuel cycle studies and impact of transmutation on nuclear waste repositories

- European Red-Impact project coordinated by KTH has started
- Six fuel cycle scenarios have been selected
- Simulation tools have been benchmarked

Method and code development

- Monte Carlo method of calculating steady state conditions (Xe oscillation convergence) has been developed and preliminary tested
- In-Core fuel management methodology for MCB code has been designed
- Some validation of the MCB code on the existing power reactor data has been performed

SAMMANFATTNING

Denna rapport sammanfattar forskningen av system och säkerhet kring acceleratordrivna system (ADS) på avdelningen för Kärn- och Reaktorfysik (KTH) under 2004. I appendix som följer i slutet av rapporten återfinns relevanta artiklar och avhandlingar som avdelningen publicerat under året. En av doktorsavhandlingarna, "Neutronic and Burnup Studies of Accelerator-driven Systems Dedicated to Nuclear Waste Transmutation" (Appendix 1) av disputerade Kamil Tuček, återspeglar riktningen för avdelningens forskning år 2004.

Forskningen under 2004 har fokuserat på följande områden:

- Simulering av framtida internationella underkritiska experiment
- ADS system
- ADS dynamik och kinetik
- ADS material
- Reaktorbaserad transmutation
- Utveckling av kärnbränsle till transmutation
- Bränslecykelanalys
- Kod- och metodutveckling

En stor del av forskningen har varit förankrad i europeiska projekt knutna till femte och sjätte ramprogrammen inom EU. Framförallt handlar det om projekten PDS- XADS, MUSE, CONFIRM, FUTURE and RED-IMPACT.

De viktigaste resultaten och slutsatserna från avdelningens forskning är:

Underkritiska experiment:

- *MUSE:*
  - Ett nytt sätt att karaktärisera ADS genom "proton importance function" har utvecklats och genomförts i experimentet MUSE. "Proton importance" har identifierats som en metod att kontrollera underkriticitet.
  - k_{eff} för blykylda system ökar med runt 1600 pcm jämfört med natriumkylda system. För att hålla samma nivå på reaktiviteten för de två systemen, vilket är viktigt vid jämförelser av systemens respons på källneutroner, har några av perifera bränsleknippen avlägsnats. k_{eff} var ungefär 0.974 i båda fallen.
- *SAD*:
  - Reaktiviteten hos olika bränsleknippen i SAD har bestämts med Monte Carlo simuleringar. Bränsleknippen på olika radiellt avstånd har ersatts med luft och dess påverkan på k_{eff} undersökts.
  - Fissionsneutronerna har större betydelse för reaktiviteten om bränsleknippena ligger symmetriskt i alla riktningar. Reaktiviteten är

runt 550 pcm för alla bränlseknippen i de tre raderna närmast centrum av härden och 450 pcm i de yttersta raderna.

- Hålrummen motsvarar 200-300 pcm var. Härden är fortfarande underkritisk med alla bränsleknippen laddade (data från JEF2.2).
- Temperaturåterkopplingen i SAD är negativ både när hänsyn tas enbart till dopplereffekten och då även bränsleexpansion beaktas. Temperatur-koefficienten är ungefär -0.9 pcm/K vid 300 K.

- Yalina:
  - Underkritiska mätmetoder undersöktes:
    - ◊ "Source Jerk"-metoden
    - ◊ "Pulsed Source"-metoden
      - Areametoden
      - "Slope Fit"-metoden
    - ◊ Experiment med Pulsed Source-metoden har även simulerats med koden MCNP
  - Areametoden överskattar underkriticiteten men ger till skillnad från de andra metoderna ett lågt statistiskt fel. Areametoden kan inte användas till att mäta reaktiviteten "on-line" under drift. MCNP ger tillförlitliga data gällande neutronernas rums- och tidsfördelning, men misslyckas i att förutse neutronernas tidsparametrar.
  - Slope fit-metoden är svår att använda men verkar ge tillförlitliga resultat om en korrekt lutning går att finna. Denna metod kan inte heller användas att mäta reaktiviteten on-line.
  - Source Jerk-metoden har stora osäkerheter men kan lättare anpassas till mätningar i verkliga anläggningar.
  - Att utföra reaktivitetsmätningar utan kontrollstavar verkar svårt. Inte med någon av dessa metoder ovan kan man mäta reaktiviteten utan att störa systemet man utför mätningen på. Metoderna kan användas för att uppskatta underkriticitet under laddning av härden och för kalibrering av eventuella indirekta mätmetoder.
  - Experimenten visar att punktkinetikapproximationen verkar beskriva Yalina på ett tillfredställande sätt.

ADS-system:

- Ett koncept av en bly-vismutkyld ADS har utvecklats på avdelningen. För att uppnå en gynnsam neutronik och utbränning, samt med hänsyn till de säkerhetskrav som ställs, har bränslekoncept och härddesign optimerats vid fullföljandet av designen. Även termohydrauliska och materiella begränsningar har beaktats.
- Heliumkylning av underkritiska härdar ämnade åt transmutation av mindre aktinider, är ett intressant alternativ till härdar kylda med flytande metall. Men, det kräver ett bränsle designat att klara höga temperaturer vid transienter som

skulle kunna uppstå under ett olycksscenario. Ett bränsle som verkar lämpligt är ett såkallat TiN-partikelbränsle.

ADS dynamik och kinetik:

- Säkerhetsanalys av transienter hos olika system baserade på bränsle innehållande mindre aktinider visar:
  - Hög termisk konduktivitet och hög smältpunkt hos CerMet-bränslet, tillsammans med lågt voidvärde hos kylmedlet, bidrar till bättre säkerhetsegenskaper i systemet.
  - Svällning och ”hardening” av metallen molybdenum påverkar vissa säkerhetsaspekter gällande bränslekapslingens mekaniska egenskaper.
  - CerCer-bränsle har låg termisk konduktivitet och osäkra smältegenskaper vilket begränsar nåbar effekttäthet och försvårar att förutse dess beteende vid effektexkursion. Dessutom är CerCer-bränslets voidkoefficient relativt hög jämfört med andra bränslen, vilket påverkar säkerhetsaspekten.
  - Nitridbränsle har en benägenhet att upplösas vid höga temperaturer vilket är ett problem. Ett brott i ånggeneratorn skulle kunna leda till en omfattande voidbildning i föreslagna ADS-designer.
  - I ett bly-vismutsystem är det av stor vikt att kylmedlet har en låg voidkoefficient trots att bly-vismut har hög kokpunkt.
- Doppleråterkopplingen i en typisk ADS laddad med aktinidbränsle är så låg att den inte kan förhindra prompt kriticitet. Vid långsam reaktivitetsökning kan den underkritiska härden underlätta snabb nedstängning, men vid snabb reaktivitetsökning är den mindre effektiv. Till viss del kan den axiella utvidgningen av bränslet kompensera för en låg dopplerkoefficient, men den har inte samma effekt som dopplereffekten i traditionella fall.
- Seismiska analyser av en reaktortank visade på en tillåten tankhöjd av 10-12 meter. Med en väggtjocklek på 250 mm skulle man kunna öka höjden till 15-16 meter. Tankens diameter är däremot inte av lika stor betydelse vid dimensionering av tankhöjden. Resultaten av dessa analyser är till stor del beroende på de seismiska förutsättningar som gäller vid platsen för reaktorn. Användandet av bottenhorisontell struktur och/eller isolering av botten kan öka hållbarheten vid eventuell jordbävning.

The Deep Burn - Modular Helium Reactor (DB-MHR)

- Studier utförda med koden MCB visar att DB-MHR effektivt och säkert kan bränna LWR-producerat plutonium. Fördelarna med den heliumkylda och grafitmodererade reaktorn är bl a dess inherenta säkerhetsmekanism, låga kostnader, olika valmöjligheter av bränsle, hög verkningsgrad, hög utbränning,

hållbar TRISO bränslekapsling, låg effekttäthet och fördelaktig neutronik. Beräkningarna bekräftar trovärdigheten i metod, program och kärndata för detaljsimulering av denna reaktor.

Utveckling och säkerhetsanalys av kärnbränsle för transmutation

- Det största säkerhetsproblemet hos analyserade reaktorhärdar är voidbildning i kylmedel som kan uppstå då gasbubblor uppträder i härden. Källan till dessa kan vara antingen fission, heliumläckage från sprickor i bränslet eller ånga från en trasig värmeväxlare. Bränsletyper med lägre voidvärde tillåter lägre marginal till kriticitet och det studerade molybdenum-baserade Cermet-bränslet har visat på bra uppträdande vid de olycksscenarios som har undersökt (mer detaljerade resultat återfinns i kapitel "Dynamics and kinetics of ADS").

Termisk stabilitet hos nitridbränslen

- Upplösning av aktinidnitrid är inte ett mekaniskt problem då trycket är förhållandevis obetydligt och därmed inte bidrar till materialspänningar i kapslingen. Tillåten gräns för överhettning, både när det gäller temperatur och varaktighet, är troligtvis mer beroende av transporteffekter som kan uppstå i ett verkligt system. Om några produkter lokalt skulle frigöras ifrån en bränslepellets kommer dessa snabbt att rekombinera vid kontakt med en kallare yta, mest sannolikt på insidan av kapslingen. Upplösning av nitrider i heta zoner som följs av rekombinering vid kallare ytor kan möjligen undersökas teoretiskt, men kommande undersökningar av bestrålade bränslepellets, sk PIE (post-irradiation examination), kommer att bidra till än bättre uppskattningar av dessa fenomen.

ADS materialstudier och modellering av strålningspåverkan

- Ökad potential för järn och järnlegeringar
    - Befintliga empiriska modeller för rena ämnen som järn och krom har utvidgats till system bestående av Fe-Cr-C.
    - *"The Embedded Atom Method potential"* för rent järn och krom, utvecklat under 2003, förbättrades under 2004 för att tillhandahålla *"interstitial formation energies"* som bättre stämmer överens med beräkningar som innefattar elektronstukturer.
    - Viss oklarhet råder vid tolkningen av resultaten och mer detaljerade studier krävs.

Bränslecykelstudier och effekten av transmutation av använt kärnbränsle med avseende på slutförvaret

- Europeiska projektet Red-Impact, koordinerat av KTH har startat.
- Sex bränslecykler har valts ut.
- Simuleringsverktyg har undersökts.

Utveckling av metod och koder

- En metod för att beräkna jämviktstillstånd (konvergering av Xenon-oscilleringar) baserad på Monte Carlo har utvecklats och testats.
- En metod för härdberäkning i koden MCB har designats.
- Viss validering av koden MCB på existerande reaktordata har utförts.

TABLE OF CONTENT

LIST OF APPENDICES

(click on authors or title to go to the selected appendix)

	of radiation damage in Fe–Cr alloys, Journal of Nuclear Materials 329–333 (2004) 1175–1179
11. L. Malerba , D. Terentyev, P. Olsson, R. Chakarova, J. Wallenius	*Molecular dynamics simulation of displacement cascades in Fe–Cr alloys, Journal of Nuclear Mat. 329–333 (2004) 1156–1160*
12. M. Eriksson, J. Wallenius, M. Jolkkonen and J. E. Cahalan	*Inherent Safety of Fuels for Accelerator-Driven Systems, Nuclear Technology, October 2004 (submitted)*
13. K.Tuček J. Wallenius, W. Gudowski	*Coolant void worth in fast breeder reactors and accelerator-driven transuranium and minor-actinide burners, Annals of Nuclear Energy 31 (2004) 1783–1801*
14. W. Gudowski	*"Nuclear waste management. Status, prospects and hopes", International Nuclear Physics Conference - INPC2004,*

ABBREVIATIONS AND ACRONYMS

EUROPEAN PROJECTS:

ADOPT	“Thematic Network on Advanced Options for Partitioning and Transmutation.”
CONFIRM	"Collaboration On Nitride Fuel Irradiation and Modeling"– shared cost project
FUETRA	“Fuel for Transmutation” – cluster of nuclear fuel related EU-projects
FUTURE	“Fuels for transmutation of long lived radiotoxic elements"– shared cost project
ITEM	“Network - Development of multiscale modeling for simulation of radiation effects for Virtual Test Reactors (VTR).
MOST	“Network - Review and revaluation of Molten Salt Reactor technology and previous realizations or projects.”
MUSE	"Multiplication avec Source Externe”- Experiment for Subcritical Neutronics Validation shared cost project
PDS-XADS	“Preliminary Design Studies of an eXperimental Accelerator Driven System” – shared cost project
RED-IMPACT	Impact of Partitioning, Transmutation and Waste Reduction Technologies on the Final Nuclear Waste Disposal
SPIRE	SPallation and IRradiation Effects - "Irradiation Effects in Martensitic Steels under Neutron and Proton Mixed Spectrum" – shared cost project
TECLA	“Technologies, Materials and Thermal-hydraulics and Safety for Lead”
TETRA	Technology for Transmutation – cluster of EU-projects

OTHER ABBERVIATIONS AND ACRONYMS

ADS	Accelerator Driven (Transmutation) System
ALMR	Advanced Liquid Metal Reactor
ANSALDO	Italian electromechanical company, Ansaldo Nucleare is a part of this company
BA	Burnable Absorber
BCC	Body Centered Cubic - type of a crystallographic lattice
BOC	Beginning of Cycle
BOL	Beginning of Life
BR	Breeder Reactor
CAPRA	Consommation Accrue de Plutonium dans les Rapides – Enhanced Burning of Plutonium in Fast Reactors
CERCER	CERamic-CERamic – type of nuclear fuel
CERMET	CERamic-METallic – type of nuclear fuel
CFD	Computational Fluid Dynamics
CR	Control Rods
DB-MHR	Deep Burn Modular Helium Reactor
DF	Driver Fuel (for the high temperature gas cooled reactors)
DIF3D	The multigroup steady state neutron diffusion and transport code
DLC200	Nuclear Data Library release following the standard version of the MCNP-code
DPA	Displacement Per Atom
EAF99	European Activation File, version 99. Nuclear data file containing neutron activation cross-sections
EAM	Embedded Atom Method
EBR	Experimental Breeder Reactor
EFPD	Effective Full Power Days
EM10	type of ferritic steel
ENDFB	Evaluated Nuclear Data File, suffix indicates a version of the file e.g.ENDFB6.8
EOC	End of Cycle
EOL	End of Life
ERMT	European Research on Materials for Transmutation Workshops
FAE	Fuel Adjacency Effect
FBR	Fast Breeder Reactor
FCC	Face Centered Cubic - type of a crystallographic lattice
FCTT	Fuel Cladding Transient Test
FFTF	Fast Flux Test Facility
FTF	Flat-to-Flat, a core design strategy
FZK	Forschungszentrum Karlsruhe
GENEPI	Generateur de Neutrons Pulsés Intenses (High intensity neutron generator) -external neutron source for MUSE experiments
GeV	Giga-electron-Volt, energy unit
GWd	GigaWatt day, energy unit
HfN	Hafnium Nitride
HTGR	High Temperature Gas Cooled Reactors

HM	Heavy Metal
HT-9	High quality stainless steel
H451	Symbol of the nuclear-grade graphite
ISOTX	A format of string/representing of multigroup data neutron cross-sections
ITU	Institute of Transuranium Elements, Karlsruhe
JEF	Joint Evaluated (Nuclear Data) File, suffix indicates a version of the file e.g. JEF2.2
JENDL	Japanese Evaluated nuclear Data Library, suffix indicates a version of the file e.g. JENDL3.2
JNC	Japan nuclear cycle development institute
keV	kilo-electron-Volt – energy unit
KCODE	A MCNP module for k_{eff} (eigenvalue) calculations
KMC	Kinetic Monte Carlo
LA150	Nuclear data cross section library up to 150 MeV for the MCNPX-code, standard release of the Los Alamos (LA) National Laboratory
LBE	Lead Bismuth Eutectic
LOCA	Loss of Coolant Accident
LOF	Loss of Flow
LOHS	Loss of Heat Sink
LWR	Light Water Reactor
MA	Minor Actinides
MASURCA	Maquette SURgénératrice de CAdarache -Fast reactor at Cadarache, hosting MUSE-experiments
MCB	Monte Carlo based computer program for burnup calculations
MCNP	Monte Carlo Neutron Photon transport code
MCNPX	Monte Carlo Neutron Photon and Light Ion transport code
MeV	Mega-electron-Volt, energy unit
MHTGR	Modular High Temperature Gas Cooled Reactor
MOX	Mixed Oxide (fuel)
NEA	Nuclear Energy Agency
NJOY	A computer program for processing evaluated nuclear data files
NNC	NNC Holdings Limited, an international engineering support company, participant of the PDS-XADS Project
P/D	Pitch to Diameter ratio
pcm	pro cent mille, a reactivity unit equal to 10^{-5}
PPS	Plant Protection System
PRISM	Advanced fast reactor concept
P0, P1	Approximation symbols of the nodal transport theory
RSC	Reserve Shutdown Control Rods
SA, S/A	SubAssembly (of the nuclear fuel)
SAS4	Reactor kinetic calculation code
SAS/DIFF-K	Reactor kinetic calculation code system

SNR300	SNR, Schneller Natriumgekühlter Reaktor - fast sodium-cooled reactor, the German fast breeder reactor prototype of 300 MW power
SS	Stainless Steel
SSC	Sing-Sing Core, an accelerator driven system concept of KTH
STAR-CD	Computer program for fluid dynamics problems
TF	Transmutation Fuel (for the high temperature gas cooled reactors)
TiN	Titanium nitride
TOP	Transient Overpower
TRADE	Triga Accelerator Driven Experiment, ADS-related experiment in Italy
TRISO	Triple isotropic coated fuel particles, fuel particles for gas cooled high temperature reactor
TRU	TRansUranium elements
TWODANT	A deterministic neutron transport code
UREX	URanium and fission products Extraction, nuclear fuel reprocessing technology
UTOP	Unprotected Transient Overpower
VARIANT-K	A Nodal transport and diffusion module for the DIF3D
WP	Workpackage

1 SIMULATION OF SUBCRITICAL EXPERIMENTS

1.1 NEUTRON ENERGY SPECTRA

One of the objectives of the studies presented in this section was to compare the effects from the GENEPI-generated (d,d)- and (d,t)-neutron sources with the effects from a spallation source, representative of a future ADS. All of the sources were coupled to the same sub-critical MUSE-4 core. MCNP was used for all calculations with the (d,d)- and the (d,t)-sources, while MCNPX was used to simulate the configurations involving the 1000 MeV proton-induced spallation source.

1.1.1 Neutron Leakage Spectra from the Lead Buffer

One way to investigate the neutron source effects is to first study the sources without the multiplicative medium present and to compare the different neutron leakage spectra. For this purpose, the surrounding fuel and shielding were temporarily removed, as shown in Figure 1.1. For the simulation of the spallation source, the lead buffer/target in the model was extended by one extra sub-assembly towards the proton beam, replacing part of the accelerator tube. Using MCNPX, 1000 MeV protons were directed towards the lead target, generating the spallation source.
The energy spectra of the neutrons exiting the lead buffer are plotted in Figure 1.2 and it is seen that the spectrum from the (d,d)-source has a large peak between 2 and 3 MeV, which is the energy range with which the neutrons are emitted by the

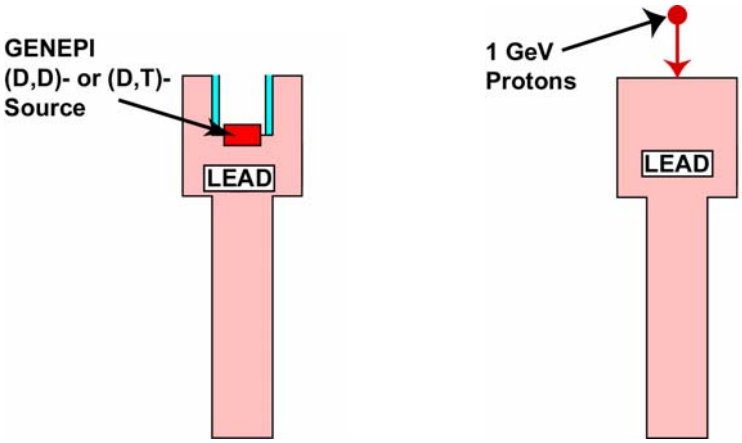

Figure 1.1 Configuration of only the lead buffer region. To the left: (d,d)- or (d,t)-source neutrons emitted at the center of the core. To the right: 1000 MeV protons accelerated towards the extended lead buffer creating a large number of spallation source neutrons.

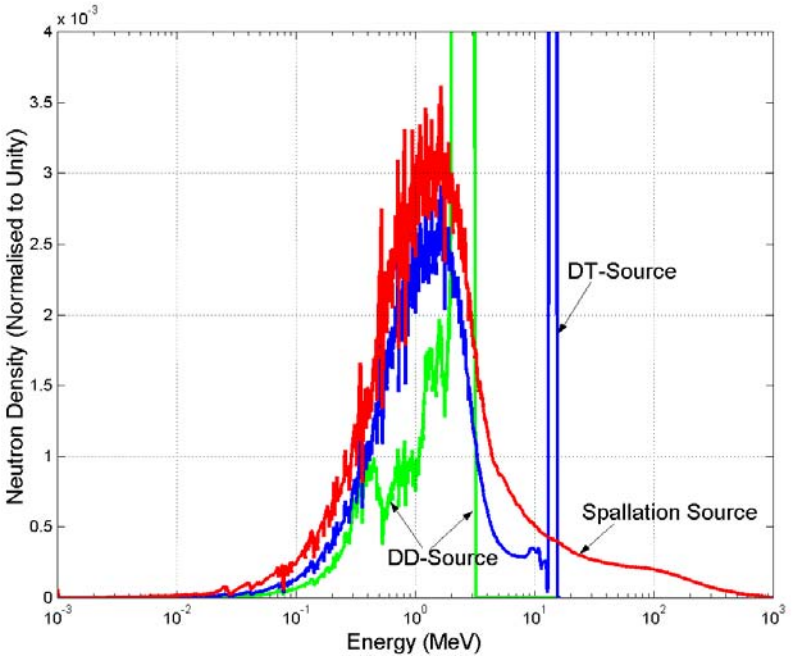

Figure 1.2 Neutron leakage spectrum from the lead buffer/target for a (d,d)-source, a (d,t)-source and a spallation source (1000 MeV protons).

GENEPI generator. Hence, only a small fraction of the source neutrons have lost their initial energy. This is an expected result, since the energy loss by elastic scattering of neutrons in lead is quite small. However, for the (d,t)-source, the energy of the neutron spectrum has decreased significantly, which is explained by the (n,2n)-reactions in the lead buffer, induced by the 14 MeV neutrons. The (n,2n)-reaction in lead has a threshold at about 7 MeV (Figure 1.3), explaining why there is no such effect for the (d,d)-source. However, about 35 % of the neutrons exiting the lead buffer have not interacted with the lead and are still in the 14-MeV peak. For the spallation source, most of the source neutrons have rather low energy compared to the initial proton energy, with the maximum density at a little less than 2 MeV. This is a typical neutron leakage spectrum for 1000 MeV protons impinging on a lead target of this size. About 7 % of the spallation neutrons, however, still have energy higher than 20 MeV.

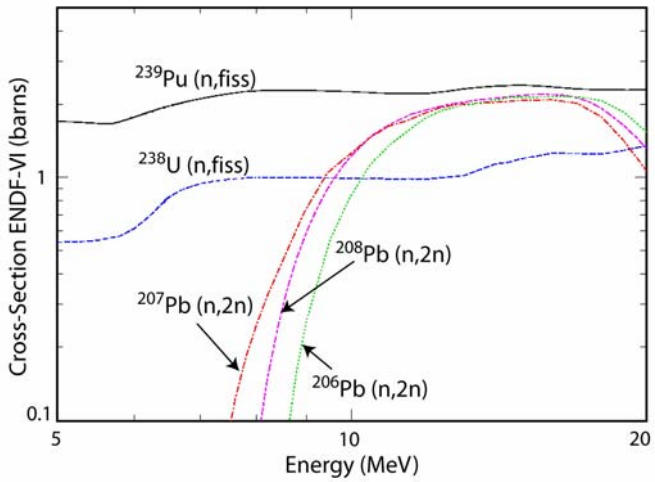

Figure 1.3 Neutron microscopic cross-sections for ^{239}Pu fission, ^{238}U fission and (n,2n)-reactions in ^{206}Pb, ^{207}Pb and ^{208}Pb (ENDF/B-VI).

The GENEPI-generated neutron sources in the MUSE experiments were surrounded by a lead buffer with the purpose to simulate the neutron diffusion of an actual lead (or lead-bismuth) target in an ADS. The comparison of the neutron leakage spectra shows that the neutrons from the (d,t)-source in MUSE-4 have a rather similar energy spectrum as the neutrons from the spallation source have, and can from this point of view be considered more representative for a spallation-driven system than the (d,d)-source.

1.1.2 Neutron Spectra in the Core

The neutron energy spectra for the three different sources have been computed with the entire core present (including fuel, reflector and shields), according to Figure 1.4. As in the case of the neutron leakage calculations in the previous section, the target/buffer was extended by one extra sub-assembly for the calculations with the spallation source (Figure 1.1). The spectra were calculated in two different positions; one in the lead buffer and one in the fuel (marked with black dots in Figure 1.4). The calculations were performed for the second sub-critical state of MUSE-4 (SC2, k_{eff} ~0.97). The spectra for the other sub-critical states (SC0, k_{eff} ~0.994 and SC3, k_{eff} ~0.95) are not shown here, since they are rather similar to the spectra of SC2. However, as there is less fission multiplication for larger sub-criticalities, the origin of the sources becomes a little more pronounced in SC3 and vice versa in SC0.

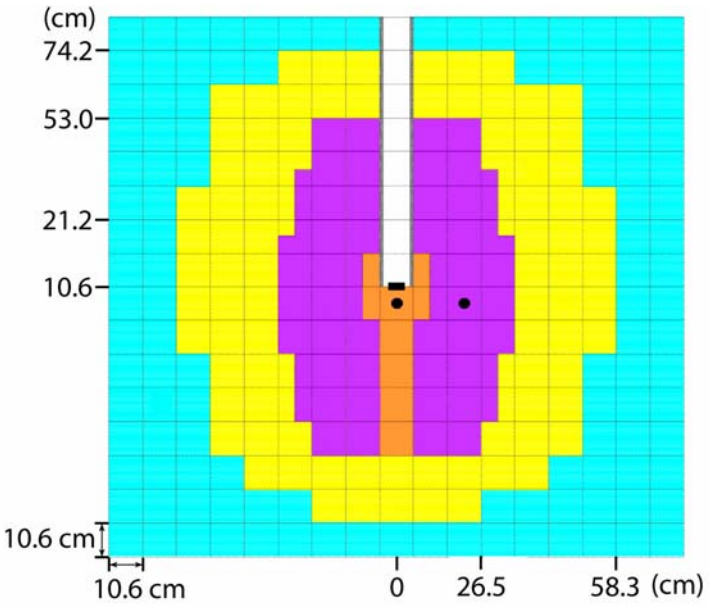

Figure 1.4 The two positions (marked with the black dots) where the neutron energy spectra have been calculated.

In Figure 1.5, the neutron energy spectra for the three different sources calculated in the lead buffer are plotted. The spectra are very similar to each other, the energy density being maximal at about 500 keV. Several spectrum characteristics of the multiplying fuel can be recognized, for example the two dips in the neutron fluxes caused by the scattering resonances in sodium (~3 keV) and oxygen (~0.4 MeV). This indicates that the neutron spectrum in this position is rather dominated by the fission multiplication in the fuel and that many of the neutrons from the fuel enter into the lead buffer. However, a smaller fraction of the neutrons have energies different from the average behavior and the two peaks representing the origins of the GENEPI-generated neutron sources and the high-energy tail of the spallation source are very clear in this position. It should be

noted that the position in the lead buffer where the energy spectra have been calculated is only about 5 cm from the position where the GENEPI source neutrons are emitted.

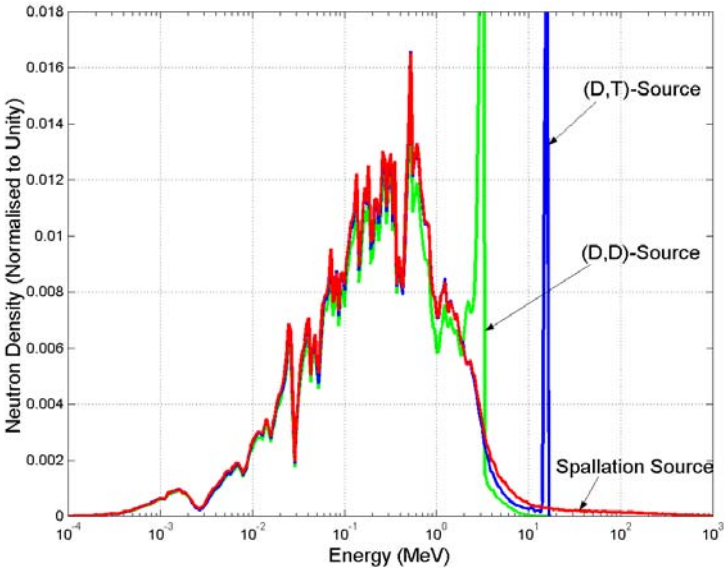

Figure 1.5 Neutron energy spectra in the lead buffer.

In Figure 1.6, the neutron spectra in the fuel at a point located 21 cm from the center of the core and about 10 cm into the fuel are depicted. Naturally, the fuel spectrum characteristics in this case are even more pronounced than in the lead buffer. The three different curves are very similar and almost no traces from the origins of the external neutron sources can be observed. Only about 0.15 % of the (d,t)-source neutrons are still in the 14 MeV peak and about 0.04 % of the neutrons in the spallation-driven system have energies higher than 20 MeV.

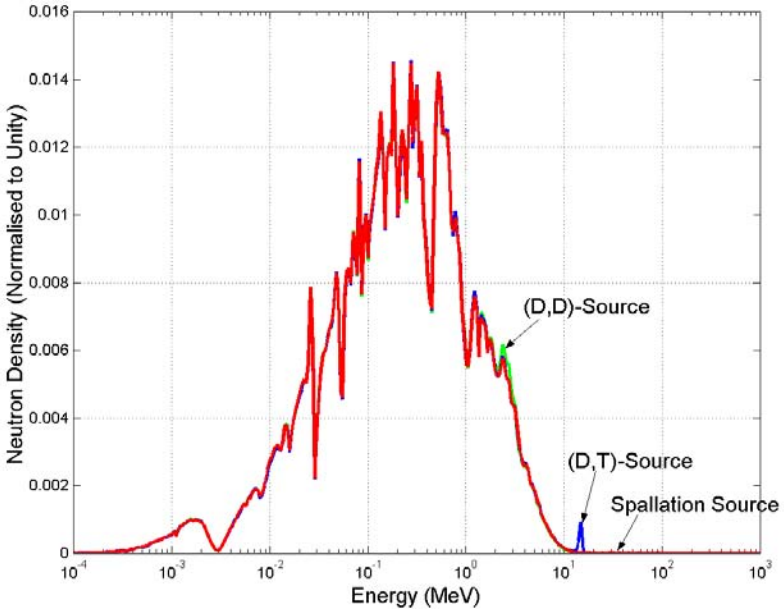

Figure 1.6 Neutron energy spectra in the fuel.

The computed neutron spectra show that the energy spectra in the core, originating from the three different external sources are very similar to each other. These results indicate the validity of one of the basic hypothesis of the experiments, namely that the choice of using a spallation source or the source neutrons produced by the (d,d)- or the (d,t)-

reactions, will affect very little the neutron spectrum in the fuel. Only inside the lead buffer and at the buffer/core interface some differences are observed. We therefore conclude that, for the purpose of computing neutron spectrum-weighted quantities, the presence of the external source can be neglected beyond a few centimeters into the fuel, whatever the neutron source energy distribution.

1.1.3 Distribution of the Spallation Neutrons

The distribution of the neutrons produced in the spallation target was calculated for 1000 MeV protons impinging on the extended MUSE-4 target. The properties, in terms of energy and space, of the neutrons emerging from the proton-induced spallation reactions were recorded. These emitted neutrons have been called “primary neutrons”, as they include only the first neutron in each neutron chain reaction. No neutrons generated in reactions induced by other neutrons (secondary neutrons) are included. The definition of primary neutrons is further treated in and in Section 1.2.
The spatial distribution of the positions where the primary neutrons were created was found to be rather limited. Axially, most of the neutrons were created in the upper part of the lead target (77% within the first 20 cm), as shown in Figure 1.7. It is also seen that the neutron density, which in addition to the primary neutrons include

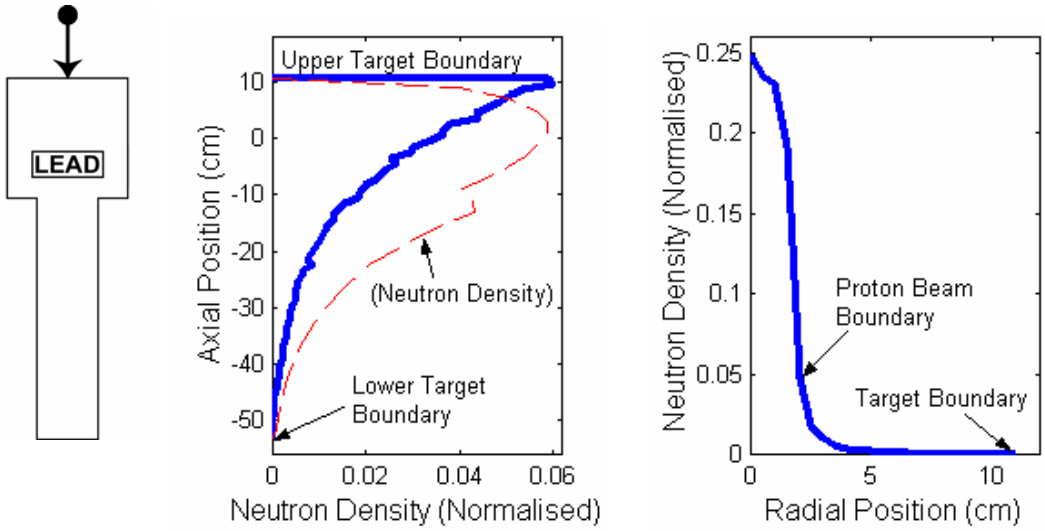

Figure 1.7 To the left: 1000 MeV protons impinging on the extended MUSE-4 lead buffer/target. In the middle: Axial distribution of the primary spallation neutrons. To the right: Radial distribution of the primary spallation neutrons.

also secondary neutrons, has a different shape with its maximum about 10 cm below the top of the target. The radial distribution was found to be very peaked around the axis of the incident proton beam, about 98% of the neutrons were created within a 3 cm radius. In this case, the radius of the uniformly distributed proton beam was 2 cm. The energy distribution of the primary neutrons produced by the 1000 MeV protons is displayed in Figure 1.8. We note that 16.8% of the neutrons have energies higher than 20 MeV and 3.3% of them higher than 150 MeV. The neutrons with very high energy were mainly emitted in the forward direction of the proton beam.

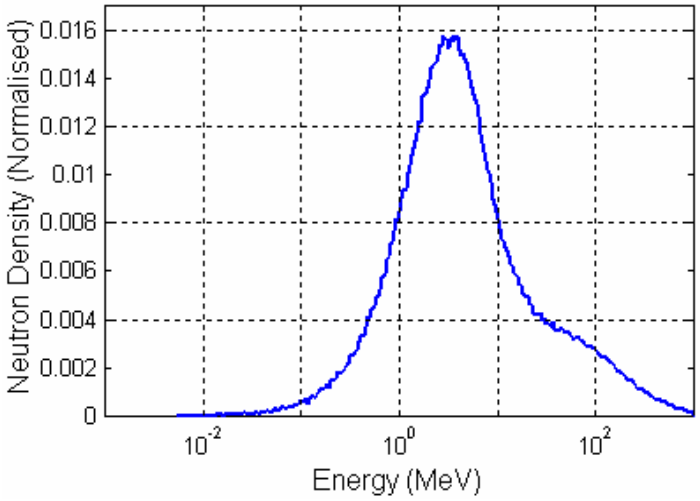

Figure 1.8 Energy spectrum of the primary spallation neutrons created by the 1000 MeV protons.

On average, there were about 14.5 primary neutrons produced in each proton-induced spallation reaction. This value may be compared with the total number of neutrons produced in the lead target, i.e. about 21 neutrons per incident proton. Thus, almost a third of the neutrons that exit the lead target and enter into the fuel are secondary neutrons, most of them created in neutron-induced spallation reactions and (n,xn)-reactions. In a large cylindrical target (r≥30 cm), this fraction is about 50%, the total number of neutrons created per proton being as large as 30, while the number of primary spallation neutrons are the same, independently of the target size.

1.2 NEUTRON SOURCE EFFICIENCY

The neutron source efficiency φ* was determined for the GENEPI-generated neutron sources and for the spallation source, all of them coupled to the second sub-critical state (SC2) of the MUSE-4 experiments.

1.2.1 Definition of φ*

The neutron flux distribution ϕ_s in a sub-critical core is the solution to the inhomogeneous steady-state neutron transport equation

$$\boldsymbol{A}\phi_s = \boldsymbol{F}\phi_s + S \ , \tag{1}$$

where

$$\boldsymbol{A}\phi_s = \boldsymbol{\Omega}\cdot\nabla\phi_s + \sigma\phi_s - \sum_{x\neq f}\iint \sigma'_x f_x \phi'_s d\boldsymbol{\Omega}' dE' \tag{2}$$

$$\boldsymbol{F}\phi_s = \iint \frac{1}{4\pi}\sigma_f \nu(\boldsymbol{r};E'\to E)\cdot\phi'_s d\boldsymbol{\Omega}' dE' \tag{3}$$

$\boldsymbol{F}$ is the fission production operator, $\boldsymbol{A}$ is the net neutron loss operator and S is the external source. The neutron source efficiency, usually denoted φ*, represents the

relative efficiency of the external source neutrons and can be expressed according to the following equation;

$$\varphi^* = \left(\frac{1}{k_{eff}} - 1 \right) \cdot \frac{< \boldsymbol{F}\phi_s >}{< S_n >} \ , \tag{4}$$

which is valid in the range $0 < k_{eff} < 1.0$. $<\boldsymbol{F}\phi_s>$ is the total production of neutrons by fission and $<S_n>$ is the total production of neutrons by the external source. In the above formula, the brackets imply integration over space, angle and energy. Eq. (*4*) relates the total fission neutron production $<\boldsymbol{F}\phi_s>$ to the external neutron source, φ* and the reactivity ($1 - 1/ k_{eff}$). It shows that, for given values of k_{eff} and $<S_n>$, the larger φ* the larger the fission power produced in the system. The quantities on the right hand side of Eq. (*4*) are standard outputs from MCNP and MCNPX.

1.2.2 Estimation of the Statistical Error in φ*

In order to estimate the statistical uncertainty in φ*, the formula for "propagation of error" was applied (Eq. (*5*)), assuming that the errors of $<\boldsymbol{F}\phi_s>$ and $<S_n>$ (labeled *F* and *S* in this sub-section) are ΔF and ΔS.

$$\Delta f(x_1, x_2, ...) = \sqrt{\left(\frac{\partial f}{\partial x_1} \Delta x_1 \right)^2 + \left(\frac{\partial f}{\partial x_2} \Delta x_2 \right)^2 + ... + \rho_{12} \cdot \frac{\partial f}{\partial x_1} \Delta x_1 \cdot \frac{\partial f}{\partial x_2} \Delta x_2 + ...} \ . \tag{5}$$

The correlation constant ρ could be either positive or negative; negative if k_{eff} and *F* are correlated and positive if they are anti-correlated. However, as a first approximation, ρ was assumed to be zero. With the derivatives $\frac{\partial \varphi^*}{\partial k_{eff}}$, $\frac{\partial \varphi^*}{\partial F}$ and $\frac{\partial \varphi^*}{\partial S}$ inserted in Eq. (*5*), an expression for the relative error in φ^* can be obtained,

$$\left(\frac{\Delta \varphi^*}{\varphi^*} \right)^2 \approx \left(\frac{1}{1 - k_{eff}} \cdot \frac{\Delta k_{eff}}{k_{eff}} \right)^2 + \left(\frac{\Delta F}{F} \right)^2 + \left(\frac{\Delta S}{S} \right)^2 \ . \tag{6}$$

Eq. (*6*) was used in all simulations to estimate the statistical uncertainty in φ*.

1.2.3 Definition of the External Neutron Source in Spallation-driven Systems

Since the actual source particles in a system coupled to a proton-induced spallation source are protons and not neutrons, it is not obvious which is the best way to define the external neutron source. The procedure to calculate φ* is usually divided into two steps, the first generating the source neutrons produced from the proton beam interacting with the target and the second step determining the efficiency of these source neutrons. Different source definitions are possible and they will result in different values and meanings of φ*. Among these, the two most frequently used definitions, the target neutron leakage source and the energy cut-off source, as well as the primary neutron source, are described in the following. The fourth definition is the fission source, consisting of the first generation of fission neutrons.

1.2.4 The Target Neutron Leakage Source

The approach of the target neutron leakage source uses the neutrons that leak out radially from the target as source neutrons. The method consists of, in the first step, transporting the high-energy protons and the secondary particles that they produce in the target. The neutrons that leak out from the target are defined as the source and their properties, in terms of position, direction and energy are written to a source file. Only the target is present in the first simulation, so no once-leaked neutrons re-entering the target are included in the source definition. In the second step, the leakage neutrons are reemitted as fixed source neutrons in a separate run and the efficiency (φ*) of them is determined. Since the target neutron leakage spectrum includes a high-energy tail, both step 1 and 2 needs to be simulated with a high-energy transport code (which can simulate neutrons with energy up to the incident proton energy).

1.2.5 The Energy Cut-off Neutron Source

The other way to define the neutron source is to collect the neutrons that fall below a certain cut-off energy (usually 20 or 150 MeV). In the first step, a high-energy code is used to transport the accelerated protons and the secondary high-energy particles. The neutrons that are produced are either killed if they are born below the cut-off energy or transported until they fall below this energy. The properties of the killed neutrons are written to a source file, which is followed by their reemission in the second-step run and the calculation of φ*. An advantage of this approach is that the second step can be simulated with a low-energy transport code. The cut-off energy is set to the upper energy limit of the cross-section library that will be used in the second-step calculation. This is desirable since many reactor code systems are limited to the energy range covered by the cross-section data library (generally 20 or 150 MeV).

1.2.6 The Primary Neutron Source

The source neutrons produced from spallation are here defined as the neutrons produced directly in a spallation reaction induced by a proton (or by any other particle, except neutrons). They are called “primary neutrons”, in contrast to “secondary” neutrons, which are the neutrons created by the primary neutrons (e.g. via neutron-induced spallation or (n,xn)-reactions). In this approach, the starting point for the chain of neutron multiplication is the moment when a neutron is born in a non-neutron-induced spallation reaction. The primary neutron might be multiplied by secondary spallation (if its energy is very high) and/or (n,xn)-reactions in the lead target, followed by fission reactions in the fuel, the end point of the neutron multiplication chain being the absorption or escape of the last neutron originating from the initial primary source neutron.

1.2.7 Calculations of φ* for the MUSE-4 Model

The multiplication factor k_{eff} and the total number of neutrons produced by fission ($<\boldsymbol{F}\phi_s>$) were calculated for the three different sources. Knowing these two parameters φ* can be determined according to Eq. (4). $<\boldsymbol{F}\phi_s>$ is automatically normalized per source neutron in MCNP (and in MCNPX if the source particles are neutrons), so $<S_n>$ was always equal to 1 in the calculations. The corresponding statistical errors (±1 standard deviation) were calculated using Eq. (6). The results, including error estimates, are listed in Table 1.1.

For the calculations of the spallation source, the primary neutron source definition was used and the MCNPX simulations calculating φ* were divided into two steps. In the

first simulation, a large number of protons were accelerated (to 1000 MeV) towards the lead target. The protons were uniformly distributed across the beam of radius 2 cm. The angular, energy and spatial distributions of all neutrons that were created directly in the spallation interactions (primary spallation neutrons) were recorded. After that, the neutron trajectories were immediately terminated. This procedure produces a spectrum of primary spallation neutrons, i.e. no secondary neutrons are included. In the second step, these primary spallation neutrons were supplied to the MCNPX code as fixed source neutrons for separate simulations and φ* was determined.

Table 1.1 Source Efficiency for the MUSE-4 SC2 Configuration

Source	k_{eff}	$< \boldsymbol{F}\phi_s >$	φ*
(D,D)-Source		48.8 (± 0.4 %)	1.36 (± 0.010)
(D,T)-Source	.97285	77.6 (± 0.5 %)	2.17 (± 0.020)
Spallation Source	(± 18 pcm)	80.6 (± 1.0 %)	2.25 (± 0.030)

The energy of the emitted (d,d)-source neutrons (2-3 MeV) is only slightly larger than the average energy of a neutron produced by fission. Since φ* is 1.0 for an average fission neutron, the value for the (d,d)-source is therefore expected to be equal or slightly larger than 1, which is indeed the case. For the (d,t)-source, the reason for the higher values of φ* is the larger fission rate, part of which coming from fissions induced by the neutrons multiplied by (n,2n)-reactions in the lead buffer. It is seen in Table 1.1 that the number of fission neutrons per source neutron is large, approximately 59 % larger than for the (d,d)-source. The (n,2n)-multiplication of the 14 MeV neutrons increases the number of neutrons leaking out into the fuel and inducing fission chain reactions, thus enhancing the neutron source efficiency. In average, about 1.5 neutrons leave the lead buffer per initial 14 MeV neutron, compared to 1 neutron for each 2.7 MeV (d,d)-source neutron.

Concerning the spallation source neutrons, the values of φ* obtained in the simulations are somewhat higher than for the (d,t)-source. This is due to the fraction of primary neutrons having very high energy. Most of the neutrons from the spallation process are born with an energy lower than the (n,2n)-cross-section threshold in lead (i.e. no (n,2n)-multiplication occurs), but the neutrons with very high energy contribute significantly to φ*. Additional calculations investigating the contribution to φ* by the high-energy fraction of the spallation source show that the primary source neutrons with energies higher than 20 MeV (16.8 % of all source neutrons) contribute for about 50% to the total φ*. The explanation for this is that most of the high-energy neutrons from the spallation source have already been multiplied in the lead (most of them via secondary neutron spallation and (n,xn)-reactions) *before* they enter into the fuel. Each of them gives birth to a number of lower-energy neutrons, which then leak out of the lead and induce fission chain reactions in the fuel.

1.3 DYNAMIC NEUTRON SOURCE RESPONSE

Techniques to monitor the sub-criticality level during operation in ADS are under development within the MUSE-4 program. With the introduction of GENEPI into MASURCA, it is now possible to perform accurate dynamic measurements, allowing for experimental reactivity determination of the sub-critical multiplying medium. The dynamic measurements are based on the pulsed mode operation of GENEPI.

In the experiments, after the reactivity calibration by the rod drop technique, the sub-critical level of the different configurations will first be precisely determined by the

well-known static Modified Source Method (MSM). In the next step, based on reactor kinetics and neutron noise theory, different dynamic techniques are applied, in order to determine the reactivity level. The methods being studied are the pulsed neutron source method, the inverse kinetics method, the Rossi-α method and the Feynman-α method. These methods, as well as results and interpretations from the dynamic experiments have been presented in several documents.

1.3.1 The Pulsed Neutron Source Method

When a multiplying medium is sub-critical, the neutron density will decay exponentially and the pulse will quickly disappear, according to basic point-kinetic theory. The decay process after a neutron pulse in a sub-critical medium is governed by the following relation;

$$N(t) = N_0 e^{-\alpha t} \ , \qquad (7)$$

where $\alpha = \dfrac{1 - k_{prompt}}{\Lambda}$ and Λ = neutron generation time. Hence, α is the slope of the decaying curve and it is directly related to the reactivity. Eq. (7) is derived from the reactor kinetics equation, not taking the delayed neutrons into account. Within this time scale there is no contribution from delayed neutrons, which is the reason why α is directly proportional to k_{prompt} and not to k_{eff}.

The "Pulsed Neutron Source Method" is one of the most promising techniques for the experimental reactivity determination of the sub-critical core in a future ADS. The procedure consists of, after having registered the neutron intensity decay after a neutron pulse, determining the slope of the curve (α) and then determine $k_{prompt,}$ according to

$$k_{prompt} = 1 - \alpha \cdot \Lambda \qquad (8)$$

The neutron generation time, Λ first has to be calculated and does not change much with reactivity. In order to obtain the effective reactivity, you also need to determine the effective delayed neutron fraction ($k_{eff} = k_{prompt} + \beta_{eff}$).

The time response in one of the detectors in MASURCA has been simulated for a GENEPI-generated (d,t)-neutron source pulse for the three sub-critical states, SC0, SC2 and SC3 of the MUSE-4 experiments. The generation time Λ was approximately 0.60 microseconds. The results computed by MCNP are plotted in Figure 1.9. It is clear from the figure that the more sub-critical the core is, the faster is the prompt decay rate. The α-values corresponding to the sub-critical states (determined graphically from the plotted curves) are for SC0; $\alpha_0 \approx 1 \cdot 10^4$ ($k_{prompt} \approx 0.995$), for SC2; $\alpha_2 \approx 5 \cdot 10^4$ ($k_{prompt} \approx 0.97$) and for SC3; $\alpha_3 \approx 8 \cdot 10^4$ ($k_{prompt} \approx 0.95$). The results are in good agreement with Eq. (7).

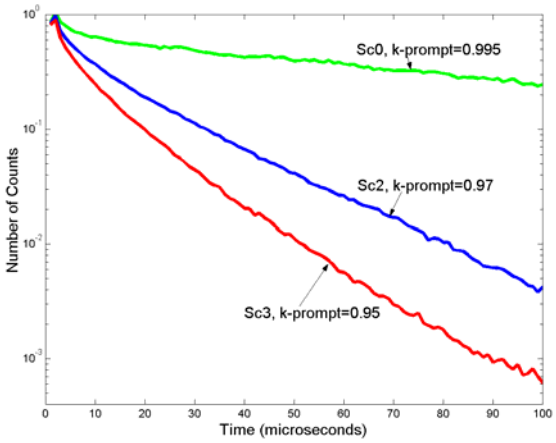

Figure 1.9 Neutron source response after a (d,t)-source pulse for the three different sub-critical configurations in MUSE-4, SC0, SC2 and SC3.

1.4 REPLACEMENT OF SODIUM COOLANT BY LEAD COOLANT

It was decided within the MUSE community to include, in an extended phase of the MUSE-4 experiments, a new configuration, in which 22 of the central sodium-cooled fuel sub-assemblies were replaced by lead-cooled sub-assemblies (the limit of the lead-cooled region being marked by the black line in Figure 1.10). Three parameters; k_{eff}, the source efficiency φ* and the dynamic neutron source response were studied for this centrally lead-cooled configuration. The neutron source used in the study comparing this configuration with the original sodium-cooled configuration was the GENEPI-generated (d,t)-source.

When calculating k_{eff} for the new lead-cooled configuration, it was found that it increases with about 1600 pcm. The reason for this is that there is less absorption in lead and that the energy spectrum is different. In order to maintain the same reactivity for the two configurations, which is particularly important for the comparison of the neutron source response, some of the peripheral fuel sub-assemblies were removed. k_{eff} was approximately 0.974 in both cases.

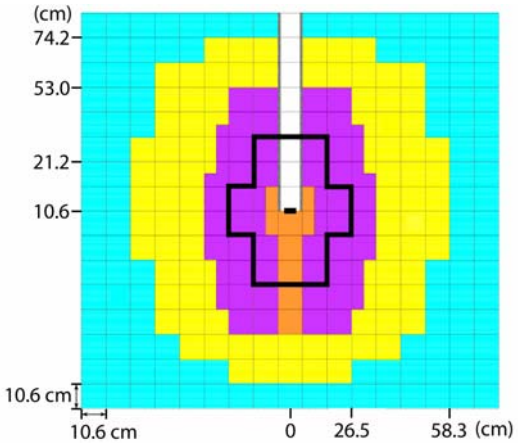

Figure 1.10 Configuration where 22 of the sodium-cooled sub-assemblies were replaced by lead-cooled sub-assemblies (the limit of the lead-cooled sub-assemblies is marked by the black line).

1.4.1 Source Efficiency

The results from the comparison of φ*, for the two configurations, are listed in Table 1.2. As is shown, the value for the lead-cooled configuration is significantly higher than for the sodium-cooled configuration, 2.39 compared to 2.13. The reason for this difference is again the (n,2n)-multiplicative effect in lead, the same effect that caused the large difference in φ* between the (d,d)- and the (d,t)-source. Since there is more lead in the central part of the core in the lead-cooled configuration, where there are still many neutrons with energy higher than about 7 MeV, there is more (n,2n)-reactions. These circumstances enhance the neutron multiplication as well as φ*. Since the source efficiency relates the source intensity to the power produced in the system, we conclude that the replacement of sodium coolant by lead coolant in the 22 central fuel sub-assemblies increases the power by approximately 12%.

Table 1.2 Source Efficiency φ* for the Sodium-cooled and the Centrally Lead-cooled MUSE-4 Configurations

Configuration	k_{eff}	φ*
Sodium-cooled	0.97428 (± 20 pcm)	2.13 (± 0.02)
Centrally lead-cooled	0.97382 (± 27 pcm)	2.39 (± 0.03)

1.4.2 Dynamic Neutron Source Response

Finally, the neutron source response from a pulse insertion from the (d,t)-source, registered by a detector in the core, was calculated and it is seen in Figure 1.11 that the intensity is somewhat higher (on average ~15%) for the lead-cooled configuration. The explanation for this is the same as for the difference in source efficiency, namely the multiplicative effect of the (n,2n)-reactions in the lead. Since the neutron multiplication is higher in the second case, the intensity registered by the detector will also be higher. We also observe that the prompt decay rate is more or less the same for the two systems. The neutron generation time Λ, calculated by MCNP, changes very little and since k_{eff} is the same, the α-value and the decay rate must also be the same.

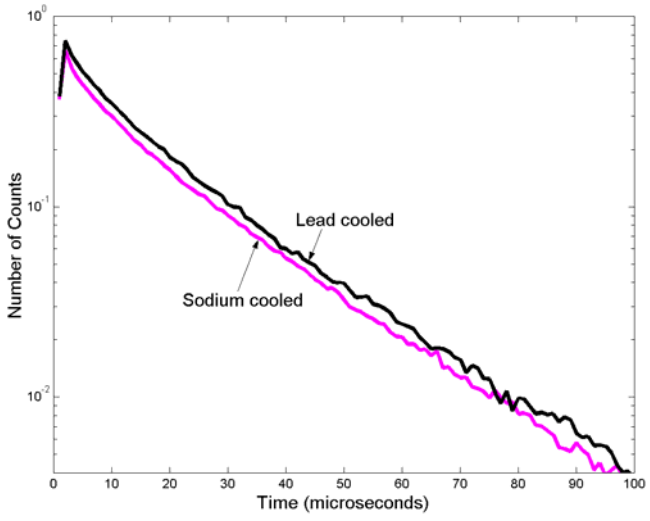

Figure 1.11 Neutron source response in one of the detectors from a neutron source pulse

1.5 INVESTIGATION OF REACTIVITY WORTH OF THE FUEL ASSEMBLIES IN THE SUBCRITICAL ASSEMBLY IN DUBNA (SAD)

1.5.1 Summary

The reactivity worth of different fuel assemblies in SAD has been determined by Monte Carlo simulations. Fuel assemblies at different radial distances have been replaced with air and the influence on keff has been investigated.

1.5.2 SAD

The Subcritical Assembly in Dubna, SAD, is an accelerator driven fast spectrum reactor which is under construction in Russia. The subcriticality and the fast spectrum of the reactor enable use of new kinds of fuel types, which cannot be used in critical reactors due to safety aspects. This is interesting when investigating the possibilities to transmute plutonium and minor actinides found in the nuclear waste. The SAD-experiment will be the first prototype accelerator driven system, consisting of the main components proton accelerator, spallation target and a subcritical core.

1.5.3 The Design of SAD

Accelerator

In this experiment an existing accelerator is used, Phasotron at JINR, Dubna (Figure 1.12). The accelerator is of cyclotron type and gives protons with energy of 660 MeV. The maximum proton current is 3.2 μA, which corresponds to $2 \cdot 10^{13}$ protons/s. The protons are guided to the spallation target by the beam transport system, consisting of the main components bending magnets, quadrupole lenses, cooling system and target window. Since the beam power is only 1 kW there is no problem with destruction of the window. Aluminum foils with a thickness of 200 μm is used. In order to avoid water ingress accidents the proton beam hits the target from the bottom, otherwise cooling water from the bending magnets can leak into the core. Beam current losses do not exceed 3%.

Spallation Target

The target will be replaceable, and it will be possible to chose between lead and tungsten (in the following model of the reactor lead is chosen as a reference material). The proton beam hits the central rod of 19 hexagonal rods in a lattice. Since the power of SAD is just a few kW the target is just air cooled. The temperature increase in the target is not sufficient to melt the material.

Core

The fuel is a MOX fuel consisting of 29.5% PuO2 and 70.5% UO2 with the average density 10.2 g/cm2. Using a cylindrical core with a radius of about 25 cm and a height of 58 cm, an effective multiplication constant k_{eff} of approximately 0.95 and a thermal power of 20 kW are achieved. The core consists of 133 hexagonal fuel assemblies in a lattice, each containing 18 fuel elements. Around the core there will be a thick layer of protecting concrete.

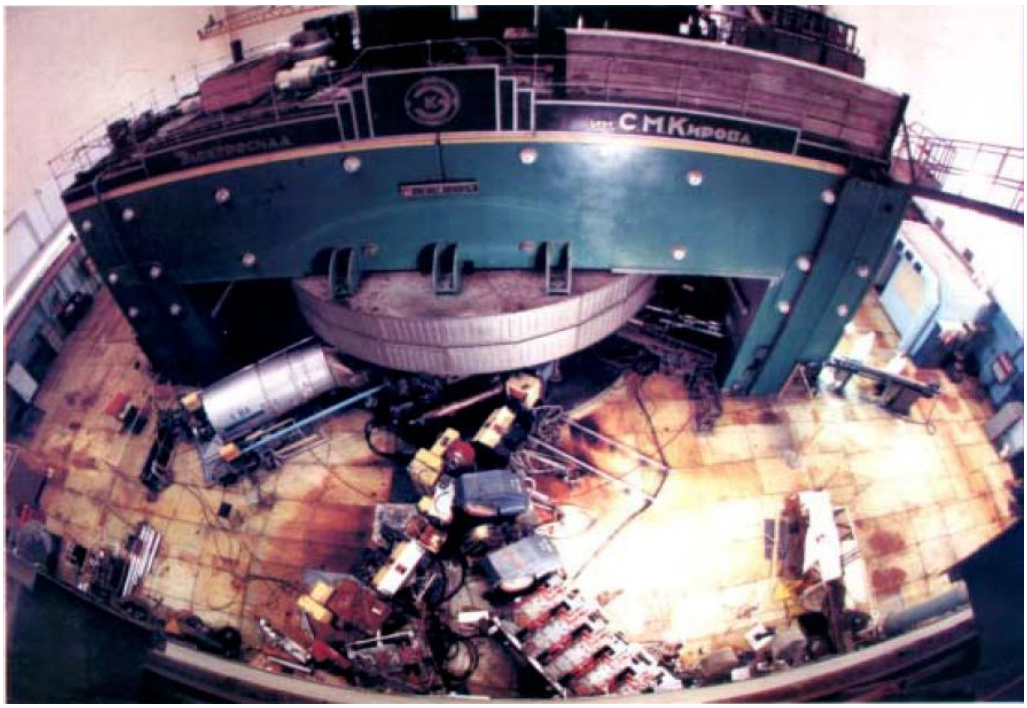

Figure 1.12 The 660 MeV Phasotron at JINR in Dubna.

1.5.4 Theoretical Background

The reactivity is defined as

$$\rho = \frac{k_{eff} - 1}{k_{eff}} \tag{9}$$

Since the core is subcritical, some negative reactivity, ρ_0, is inherent in the system. From an earlier simulation the effective multiplication constant at 300 K is found to be k_0 = 0.96697 with standard deviation σ_{k_0} = 0.014 %. The reactivity worth of the removed (or inserted) fuel assembly is given by the reactivity change

$$\Delta\rho = \left|\rho - \rho_0\right| = \left|\frac{k_{eff} - 1}{k_{eff}} - \frac{k_0 - 1}{k_0}\right| \tag{10}$$

The standard deviation is given by the propagation of error:

$$\sigma_{\Delta\rho} = \sqrt{\left(\frac{\partial\Delta\rho}{\partial k_{eff}}\sigma_{k_{eff}}\right)^2 + \left(\frac{\partial\Delta\rho}{\partial k_0}\sigma_{k_0}\right)^2} = \sqrt{\frac{\sigma_{k_{eff}}^2}{k_{eff}^4} + \frac{\sigma_{k_0}^2}{k_0^4}} \tag{11}$$

1.5.5 Methodology

The effective multiplication constant, k_{eff}, is achieved by simulating the core with MCNPX 2.2.3 using SAD input file version 1 28.04.04 and library based on JEF2.2. The fuel assemblies is removed and replaced one by one and the code gives an

estimation of k_{eff} and its standard deviation for each case. The fuel is replaced by air, and when investigating the empty slots, steel is replaced by fuel. It is also possible to add up to eight more fuel assemblies to the outer part of the core. The configuration of the core can be found in Figure 1.13. The study also covers the libraries JEF3.0, JENDL3.3 and ENDFB-6.8 for the fuel rod positions 5 to 9.

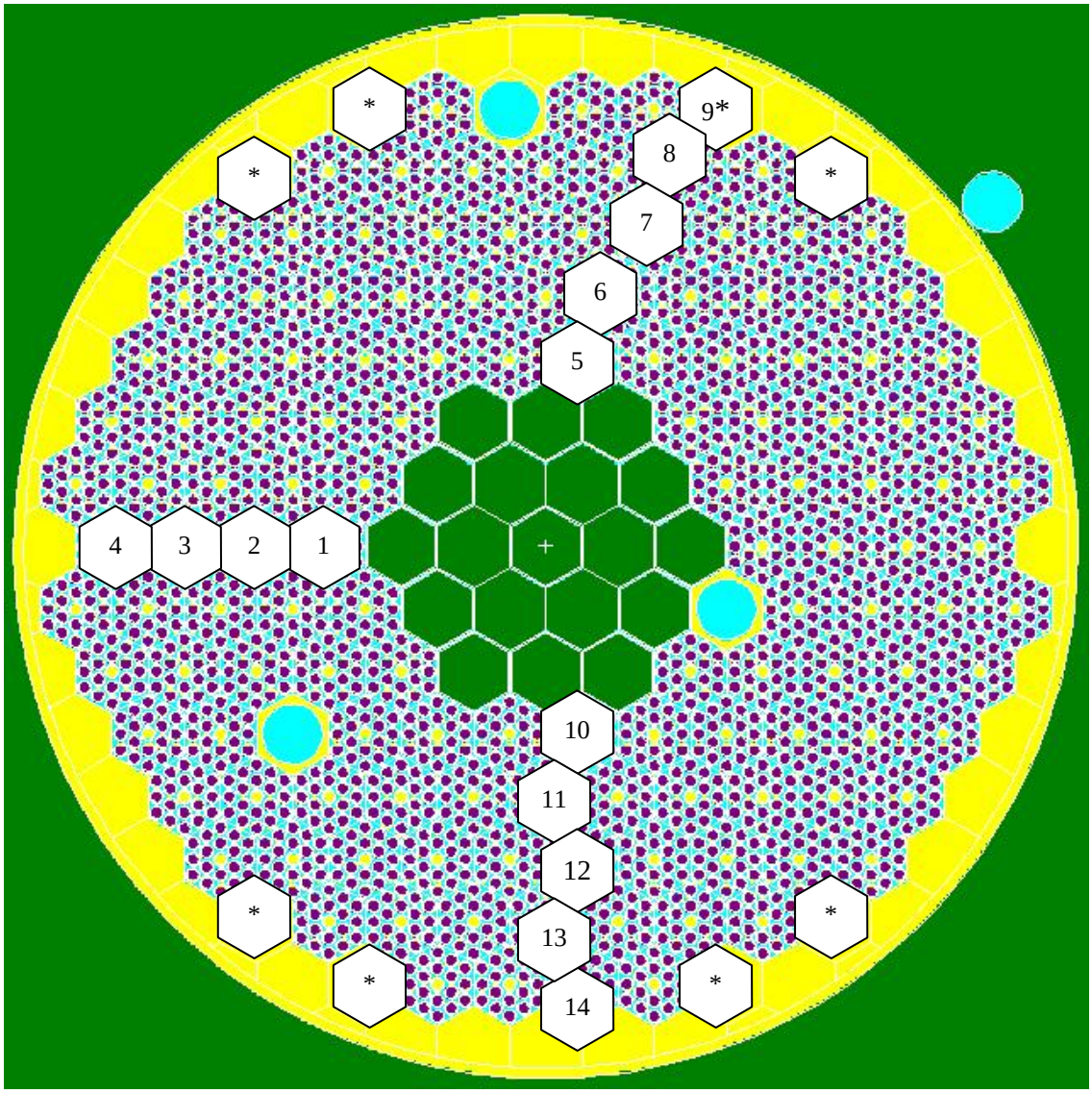

*Figure 1.13 Layout of SAD core, * = empty slot.*

1.5.6 Results

The simulation gave the data in the following table and diagram.

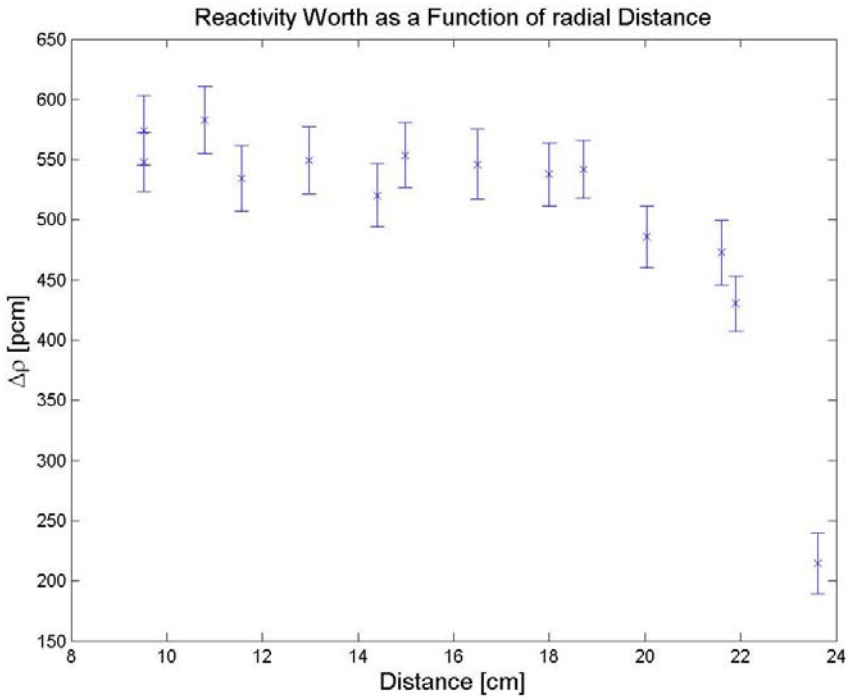

Figure 1.14 Reactivity worth for fuel assemblies at different distances from the centre of the core (JEF2.2).

Table 1.3 Results from simulations (JEF2.2).

r [cm]	Pos.	k_{eff}	$\sigma_{k_{eff}}$ [%]	$\Delta\rho$ [pcm]	$\sigma_{\Delta\rho}$ [%]
9.5	5	0.96163	0.02	574	5.1
9.5	10	0.96187	0.02	548	4.5
10.8	1	0.96155	0.02	583	4.8
11.6	11	0.96200	0.02	534	5.1
13.0	6	0.96186	0.02	549	5.1
14.4	2	0.96213	0.02	520	5.1
15.0	12	0.96182	0.02	554	4.9
16.5	7	0.96189	0.02	546	5.3
18.0	3	0.96197	0.02	538	4.9
18.7	13	0.96193	0.02	542	4.4
20.0	8	0.96245	0.02	486	5.2
21.6	4	0.96257	0.02	473	5.7
21.9	14	0.96296	0.02	431	5.3
23.6	9	0.96898	0.02	215	11.7

When all eight empty slots are filled with fuel following values are obtained (JEF2.2):

k_{eff} = 0.98626
$\sigma_{k_{eff}}$ = 0.02 %
$\Delta\rho$ = 2023 pcm
$\sigma_{\Delta\rho}$ = 1.4 %

Reactivity changes for different libraries are found in Figure 1.15 .

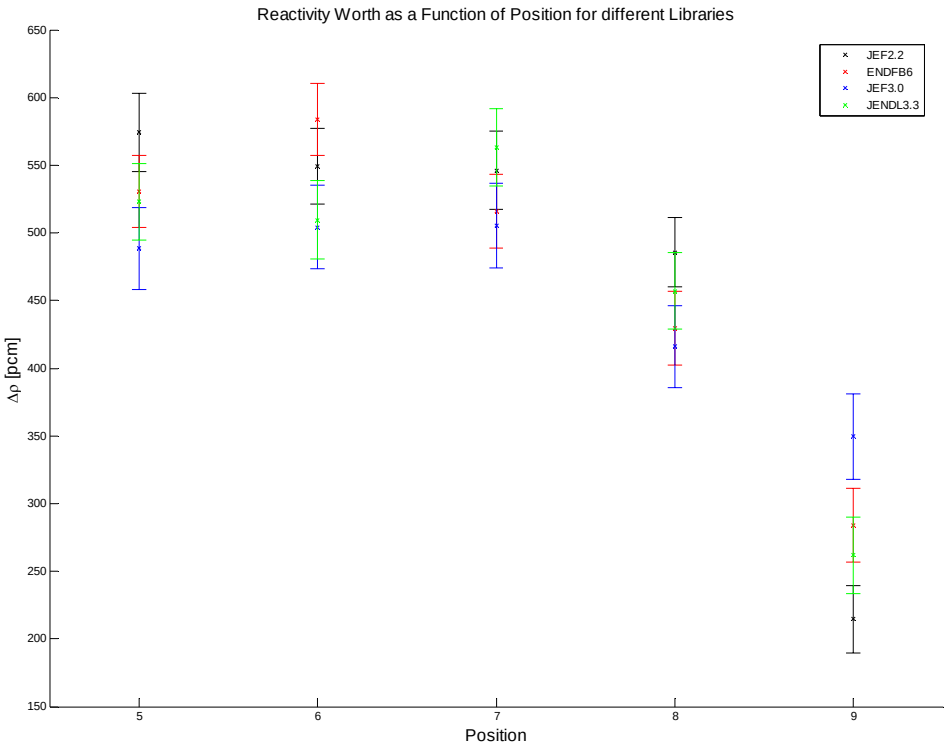

Figure 1.15 Reactivity worth for different libraries for positions 5 to 9.

1.5.7 Conclusion

The importance of the created neutrons is higher if there are fuel assemblies in all directions. This implies that the reactivity worth of the assemblies closest to the measuring channels and at the boundary of the core is expected to be somewhat lower. By symmetry we can assume that the reactivity worth is around 550 pcm for all fuel assemblies in the three innermost layers, and a little bit lower, ~450 pcm, for the outermost layer.

The empty slots correspond to approximately 200-300 pcm each. The core is still subcritical with all fuel assemblies inserted according to JEF2.2.

Different libraries give slightly different results, particularly for the outermost layer. There is no obvious pattern showing that some library always gives higher or lower values that some other library.

1.6 INVESTIGATION OF TEMPERATURE FEEDBACKS IN THE SUB-CRITICAL ASSEMBLY IN DUBNA (SAD)

1.6.1 Summary

The influence of a temperature increase in the SAD has been investigated. The effective multiplication constant, k_{eff}, has been plotted as a function of the temperature of the fuel.

1.6.2 Methodology

The fuel in SAD is a MOX-fuel consisting of 70.5% UO_2 and 29.5% PuO_2. The density of the fuel is 10200 kgm^{-3} at 300 K. Monte Carlo simulations have been performed with different fuel temperatures and fuel densities. Adjustments in the geometry have been performed in order to conserve the fissile mass. Cross section libraries for 300, 600, 900, 1200, 1500 and 1800 K have been used. The density of the fuel has been calculated for the different temperatures according to ref. [4].

D(300) = 10200 kgm^{-3}
D(600) = 10111 kgm^{-3}
D(900) = 10019 kgm^{-3}
D(1200) = 9924 kgm^{-3}
D(1500) = 9819 kgm^{-3}
D(1800) = 9700 kgm^{-3}

The volume of the fuel elements was adjusted to compensate for the density decrease. Both the radius and the height of the cylindrical elements were increased. SAD Input file version 1 28.04.04 was used. First six simulations were performed without taking the density decrease into account. This gave the pure Doppler effect. Then another five simulations were performed with consideration of the fuel expansion.

1.6.3 Results

First the density is kept constant and the temperature is varying, Figure 1.16. The error bars corresponds to one standard deviation in each direction. The simulation with fuel expansion gives the plot in Figure 1.17.

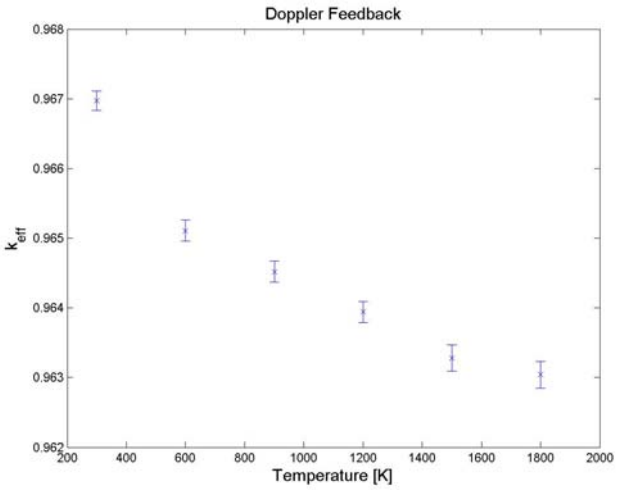

Figure 1.16 k_{eff} as a function of temperature, density = D(300).

Table 1.4 Doppler feedback of SAD

T [K]	k_{eff}	σ [%]	$\Delta k_{eff}/\Delta T$ [pcm/K]
300	0.96697	0.015	-0.62
600	0.96511	0.016	-0.20
900	0.96452	0.016	-0.19
1200	0.96394	0.016	-0.22
1500	0.96328	0.020	-0.08
1800	0.96304	0.020	

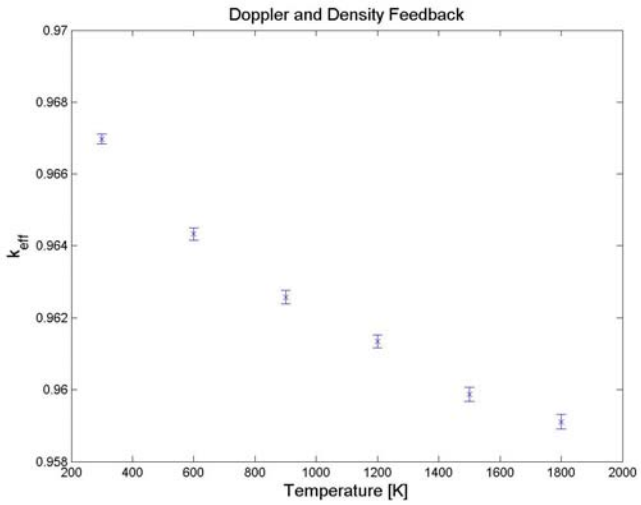

Figure 1.17 k_{eff} as a function of temperature (fuel expansion allowed).

Table 1.5 Doppler and density feedback of SAD

T [K]	k_{eff}	σ [%]	$\Delta k_{eff}/\Delta T$ [pcm/K]
300	0.96697	0.015	-0.88
600	0.96432	0.018	-0.58
900	0.96258	0.020	-0.41
1200	0.96135	0.019	-0.49
1500	0.95987	0.021	-0.25
1800	0.95911	0.021	

1.6.4 Conclusions

The temperature feedback of SAD is negative both when considering pure Doppler effect and when taking fuel expansion into account. The temperature feedback constant should be approximately -0.9 pcm/K at 300 K.

1.7 REACTIVITY DETERMINATION AND MONTE CARLO SIMULATIONS OF THE SUBCRITICAL EXPERIMENT YALINA.

1.7.1 Abstract

In this study experiments concerning determination of subcriticality have been performed at a research facility in Minsk, Belarus. The methods investigated are the Source Jerk method and the Pulsed Source methods Area method and Slope Fit method. The Pulsed Source experiment has also been simulated using the Monte Carlo code MCNP.
The measurements show that the Area method overestimates the subcriticality and the other two methods give reasonable results with larger uncertainties. MCNP seems to provide reliable results considering neutron distributions in space and time but fails in predicting neutron time parameters.

1.7.2 Theoretical background

The Point Kinetic Equations

Assuming that all neutrons have the same energy, the time dependence of the neutron flux can be derived using the neutron diffusion equation. The time dependent neutron flux is given by

$$\begin{aligned} \frac{dn(t)}{dt} &= \frac{\rho(t)-\beta_{eff}}{\Lambda} n(t) + \sum_{i=1}^{6} \lambda_i C_i(t) \\ \frac{dC_i(t)}{dt} &= \frac{\beta_i}{\Lambda} n(t) - \lambda_i C_i(t), \qquad i = 1,...,6 \end{aligned} \tag{12}$$

which are the Point Kinetic equations. In this equation n is the neutron density, ρ is the reactivity, β_{eff} is the effective delayed neutron fraction, Λ is the mean generation time, λ is the decay rate of the delayed neutron precursors C. These equations describe the kinetic behavior of the reactor and are the most fundamental relations from which all following theory in this work is derived. When using the Point Kinetic equations the assumptions made in the derivation must be kept in mind. The relations are valid if the spatial flux distribution is constant in time and if a one energy group model is sufficient to describe the system. [9] [21]

1.7.3 Reactivity Determination Methods

Area Method

The approach in the Area method, or Sjöstrands method, is the same as in the Slope Fit method. The reactivity is achieved by investigation of the neutron flux during repeated injections of neutron pulses at constant frequency. After a large number of pulses an equilibrium level of delayed neutron precursors is obtained. These precursors decay and cause an equilibrium level of delayed neutrons, whereas the prompt neutrons constitute a time dependent behavior. This is clarified in Figure 1.18

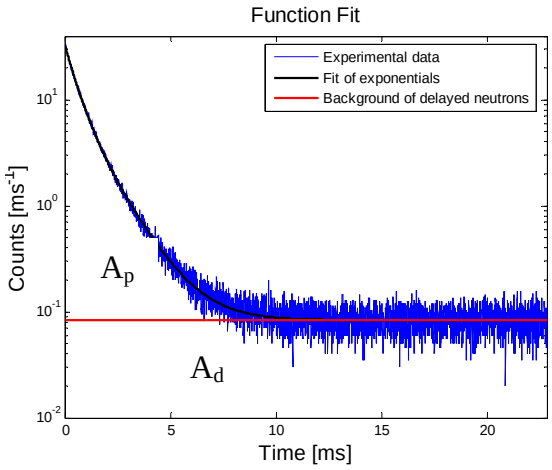

Figure 1.18 Neutron flux after a pulse injection (40000 cycles).

The delayed neutrons are represented by the "delayed area", A_d, and the prompt neutrons by the "prompt area", A_p. If the total amount of neutrons present at the same time in the reactor is divided into prompt and delayed neutrons according to

$$n(t) = n_p(t) + n_d(t) \tag{13}$$

the point kinetic equations, Eq. (12), yields

$$\frac{\rho}{\beta_{eff}} = -\frac{A_p}{A_d}. \tag{14}$$

This method has the advantage that the involved parameters are integrals, which reduces the statistical errors [7][8].

Slope Fit Method

When injecting a neutron pulse into a subcritical core the neutrons will multiply in the fuel, but every neutron chain will die out. The Point Kinetic equations, Eq. (12) give the neutron flux after a neutron pulse as [6]

$$n(t) = \left(\beta_{eff}\lambda' e^{-\lambda' t} - \rho\alpha e^{\alpha t}\right) \tag{15}$$

where $\lambda' = \rho\lambda/(\rho - \beta_{eff})$, λ is the one-group delayed neutron precursor decay constant and α is the prompt neutron decay constant given by

$$\alpha = \frac{\rho - \beta_{eff}}{\Lambda}. \tag{16}$$

Assuming that $\lambda' t \ll 1$, Eq. (15) can be written as a constant and one term with time dependence:

$$n(t) = \left(\beta_{eff}\lambda' + \rho\alpha e^{\alpha t}\right). \tag{17}$$

By measuring the neutron flux after a pulse injection it is therefore possible to find the reactivity of the system by finding the slope of the logarithmic decay constant α.
Note that the Slope fit method only is useful if both the effective delayed neutron fraction and the neutron generation time is known. These quantities can be found either by other experiments or simulations. [27]

Source Jerk Method

The idea behind the Source Jerk method is to run the subcritical reactor at steady state, at flux level n_0, and then suddenly remove the neutron source. At this point the system will make a prompt jump to a lower level, n_1, described by the delayed neutron background. This level is only quasistatic and will decay according to the decay rate of the delayed neutron groups [5]. The Point Kinetic equations, Eq. (12), gives the reactivity in dollars:

$$\frac{\rho}{\beta} = \frac{n_1 - n_0}{n_1}. \tag{18}$$

The neutron levels n_1 and n_0 can easily be obtained by experiment. [5]

1.7.4 Experiments

The Yalina Facility

The Yalina facility is located at the *Joint Institute of Power and Nuclear Research* in Sosny outside Minsk, Belarus. Yalina is the Belarusian word for spruce. And that is exactly what you will see if you visit Sosny, lots of spruces, since this place is situated in the forest approximately 10 km south-east of Minsk.
As already mentioned the facility consists of two main components, a neutron generator and a subcritical core. Yalina does not fulfill the conceptual design of a future ADS, but the neutronics of the subcritical core is anyway an interesting feature since the methods described is applicable in both fast and thermal systems independent of the type of neutron source.

The Neutron Generator

Since the neutrons have no charge they can not be accelerated into the core. They must come from some kind of reaction. As a matter of fact fusion is one way to solve the problem. Have a look on the following reactions [12].

$$^{3}\mathrm{H} + \mathrm{d} \rightarrow {}^{4}\mathrm{He} + \mathrm{n} \qquad Q = 17.6 \text{ MeV}$$
$$^{2}\mathrm{H} + \mathrm{d} \rightarrow {}^{3}\mathrm{He} + \mathrm{n} \qquad Q = 3.3 \text{ MeV}$$

The concept is obviously to accelerate deuterons and let them impinge a target with tritium, (d,t), or deuterium, (d,d). The neutron generator at the Yalina facility is practically a deuteron accelerator and a target consisting of deuterium or tritium, both alternatives are available. The generator can operate in continuous mode, producing a constant current of deuterons, or in pulsed mode sending short deuteron beams at a constant frequency.

Table 1.6 Main parameters of the neutron generator (NG-12-1) [13]

Deuteron energy		100 – 250 keV
Beam current		1 – 12 mA
Pulse duration		0.5 – 100 μs
Pulse repetition frequency		1 – 10000 Hz
Spot size		20 – 30 mm
(d,t)-target	Maximum neutron yield	$1.5 – 2.0 \cdot 10^{12}$ ns^{-1}
	Reaction Q-value	17.6 MeV
(d,d)-target	Maximum neutron yield	$2.0 – 3.0 \cdot 10^{10}$ ns^{-1}
	Reaction Q-value	3.3 MeV

The Subcritical Core

The target is surrounded by the fuel which consists of uranium dioxide with 10% enrichment of ^{235}U. The fuel pins are situated in a lattice of quadratic geometry, Figure 1.19 . The region closest to target is filled with lead in order to study (n,xn)-reactions and the neutron spectrum in presence of lead. Outside the lead zone is the moderating area filled with polyethylene (C_2H_4). This is a rather efficient moderator with moderating ratio ($\xi\Sigma_s\Sigma_a^{-1}$) 122 (compared to 71 for light water). The reflector is made of graphite with a thickness of about 50 cm. Five experimental channels (EC) are distributed at different radial distances, situated in order to minimize their influence on each other. As can be seen in Figure 1.19, EC1 is close to the source, EC2 is in the lead zone, EC3 is in the moderating thermal zone and EC5 and EC6 is situated in the reflector. There are totally 180 fuel elements with diameter 11 mm and spacing 20 mm. The length of the active fuel is 500 mm.

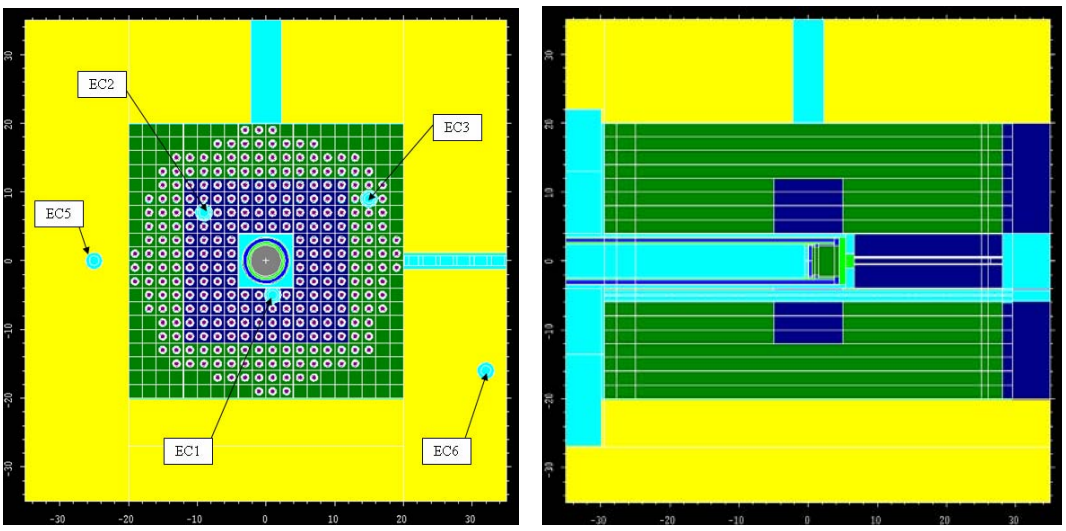

Figure 1.19 Radial and axial cross section of Yalina. Dark blue – lead zone, green – polyethylene zone, yellow – graphite reflector, light blue – experimental channels.

Detectors

In the experiments we used different fission chambers and a ^{3}He-detector. The principle is the same in each detector, a neutron induces charged particles inside the detector and these particles constitute a current in an electric field. The size of the current is proportional to the neutron flux.

In a fission chamber the charged particles are fission products from fissions induced by the incoming neutrons. Since different fissile isotopes are sensitive to different neutron energies, the detectors are sensitive to the energies characteristic of its fissile component. The materials used is ^{232}Th, ^{235}U and ^{Nat}U (natural uranium). The ^{235}U-chamber is sensible mostly to thermal neutrons, the ^{Nat}U-chamber is sensible to both thermal and fast neutrons and the ^{232}Th-chamber is sensible to neutrons with energy higher than 1 MeV [14].

The charged particles in the ^{3}He-counter are protons from (n,p)-reactions. From Figure 1.20 it is obvious that the detector is sensitive to thermal neutrons. The dead time of the detector is 0.8 μs.

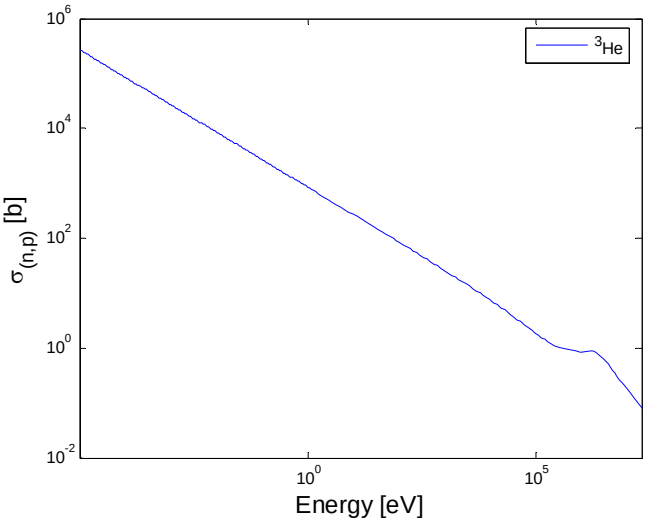

Figure 1.20 Cross section for (n,p)-reaction in ^{3}He [14].

1.7.5 Procedure

Fission Rate Distributions

The axial fission rate distribution was determined by using the different fission chambers in EC1, EC2 and EC3. The detector is connected with a time analyzer (Turbo MCS) with 16 384 channels. The time gate of each channel can be in the interval 5 ns to 65 535 s. The time analyzer collects all counts from the detector at each detector position until sufficient statistics is achieved. During this measurement the neutron generator is working in continuous mode. The measurements performed were

1. ^{235}U-fission chamber in EC2, (d,d)-source.
2. ^{235}U-fission chamber in EC1, EC2 and EC3, (d,t)-source.
3. ^{Nat}U-fission chamber in EC1, EC2 and EC3, (d,t)-source.
4. ^{232}Th-fission chamber in EC1, EC2 and EC3, (d,t)-source.

Kinetic Experiments

The Area- and Slope Fit method was performed with the neutron generator operating in pulsed mode with a constant frequency of approximately 43 Hz and the neutron flux was measured by the ^{3}He-counter in each experimental channel. Every neutron pulse is registered by the time analyzer and all pulses are added to each other. The final diagram is therefore a sum of 40 000 cycles.

The Source Jerk method requires the neutron generator to operate in continuous mode. A sudden source jerk was achieved simply by turning of the neutron generator. During this operation the neutron flux was measured by the ^{3}He-counter in EC2.

1.7.6 Data Analysis

Fission Rate Distributions

The results from the fission rate measurement are shown in Figure 1.21. The first measurement was performed with the (d,d)-source. By comparing the count rates in the different plots it can be seen that this source is much weaker than the (d,t)-source. The double peaks come from the high thermal flux in the moderating material outside the lead zone. In the last plot fission in ^{232}Th is drawn, which shows a fast neutron peak in the middle of the core in EC1. In the middle are most of the neutrons fast, since they are born fast, and bad moderated in lead. Outside the lead zone the neutrons are efficient thermalized causing a large thermal flux. That is why thermal neutron flux maximum is outside the lead zone and fast neutron maximum in the centre. In the reflector are almost all neutrons thermalized.

When using ^{Nat}U both thermal and fast neutrons are detected. This is why there is a triple peak in the third plot. The middle top comes from fast fission, like for ^{232}Th, and the two other tops come from thermal fissions, like for ^{235}U. Of the two thermal tops one is a little big higher, which is explained by the anisotropy of the neutron source. The energy of the incident deuteron causes a displacement of the source geometry in the forward direction.

Area Method

The dead time corrected data from the experiment is shown in Figure 1.22. In order to analyze this information with the Area Method the area under each curve and the equilibrium level must be calculated. If the background is neglected Eq. (14) can be written as

$$\frac{\rho}{\beta_{eff}} = 1 - \frac{A_{tot}}{L_d T} \tag{19}$$

where A_{tot} is the total area under the curve, L_d is the equilibrium level of delayed neutrons and T is the period of the measurement (22.81 ms).

The area is calculated by trapezoidal numerical integration and is given by

$$A_{tot} = \sum_{i=1}^{N-1} \frac{c_i + c_{i+1}}{2} \Delta t = \frac{\Delta t}{2} \left(c_1 + 2 \sum_{i=2}^{N-1} c_i + c_N \right) \tag{20}$$

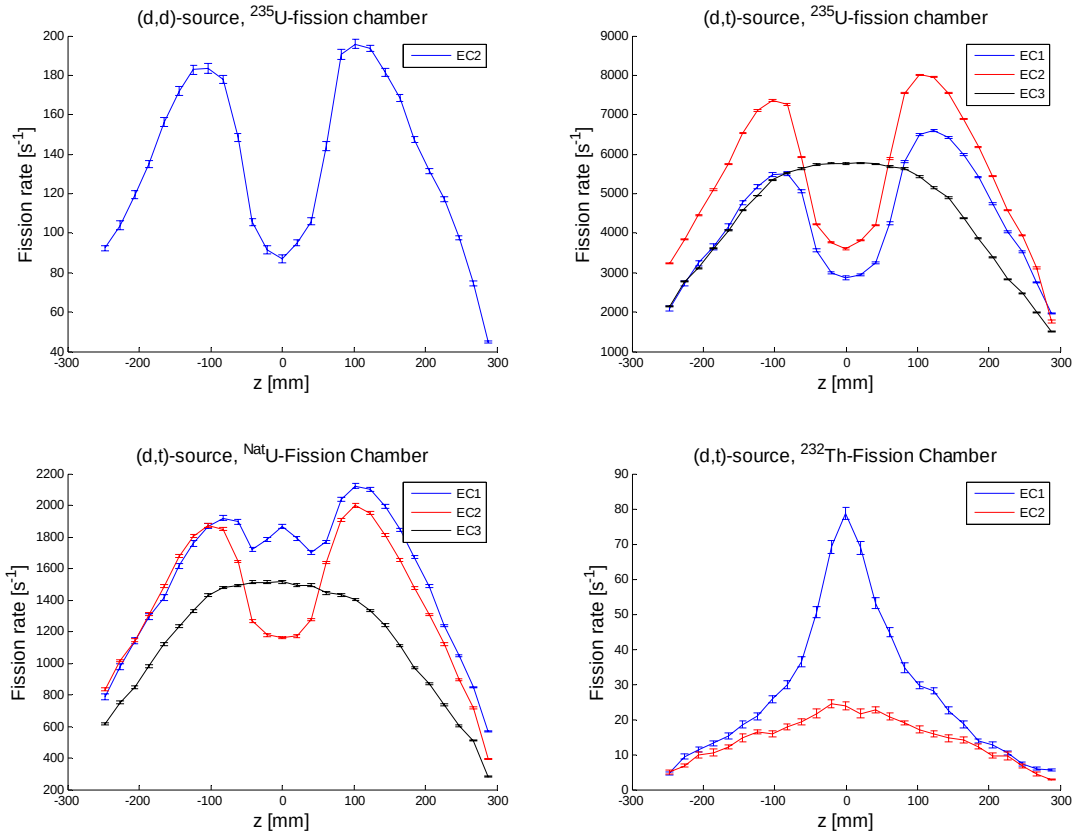

Figure 1.21 Axial fission rate distributions from experiment. The points are connected with lines just to make the shapes clear.

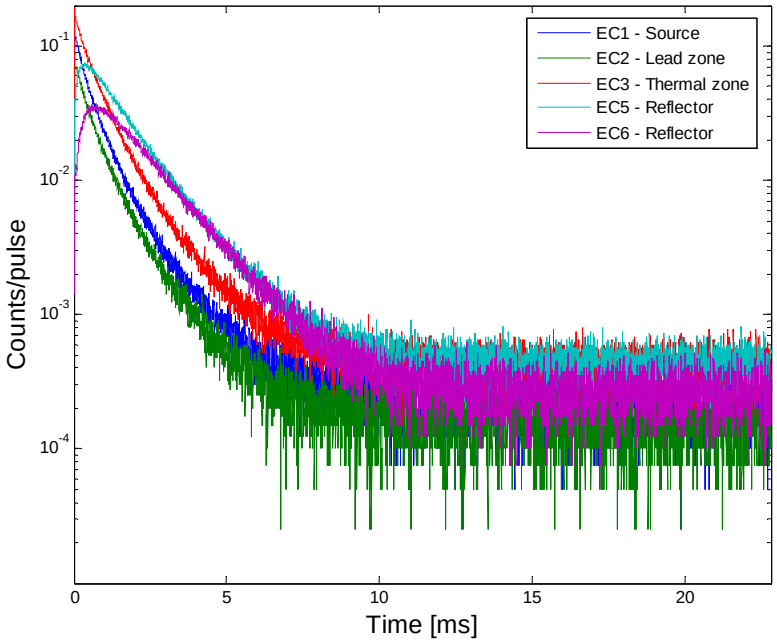

Figure 1.22 Neutron pulse responses from pulsed source experiment.

where c_i is the counts in time bin i, Δt is the width of the time gate and N is the number of time bins (channels). The number of counts in each time bin is assumed to be Poisson distributed with the standard deviation

$$\sigma(c_i) = \sqrt{c_i} \ . \tag{21}$$

The standard deviation of the total area is

$$\sigma(A_{tot}) = \sqrt{\sum_{i=1}^{N}\left(\frac{\partial A_{tot}}{\partial c_i}\sigma(c_i)\right)^2} = \frac{\Delta t}{2}\sqrt{c_1 + 4\sum_{i=2}^{N-1} c_i + c_N} \ . \tag{22}$$

The equilibrium level is calculated as a mean value of the counts from 15 ms to the end.

$$L_d = \frac{1}{N - 3000}\sum_{i=3000}^{N} c_i \tag{23}$$

Now it is possible to calculate the reactivity in dollar with the standard deviation

$$\begin{aligned}\sigma\left(\rho/\beta_{eff}\right) &= \sqrt{\left(\frac{\partial\left(\rho/\beta_{eff}\right)}{\partial A_{tot}}\sigma(A_{tot})\right)^2 + \left(\frac{\partial\left(\rho/\beta_{eff}\right)}{\partial L_d}\sigma(L_d)\right)^2} \\ &= \frac{1}{T}\sqrt{\left(\frac{\sigma(A_{tot})}{L_d}\right)^2 + \left(\frac{A_{tot}\sigma(L_d)}{L_d^2}\right)^2} \ .\end{aligned} \tag{24}$$

The results are presented in Table 1.7. Note that only statistical error is taken under consideration.

Table 1.7 Results from Area Method

Experimental channel	ρ/β_{eff} (Reactivity in \$) ± 1σ
EC1	-13.9 ± 0.1
EC2	-13.7 ± 0.1
EC3	-12.9 ± 0.1
EC5	-13.0 ± 0.1
EC6	-13.5 ± 0.1

The reactivity and effective multiplication constant, k_{eff}, can be calculated if the effective delayed neutron fraction, β_{eff} , is known. This parameter and the delayed neutron fraction, β, were calculated by Monte Carlo simulations using a modified version of MCNP [22], see Table 1.8. The effective multiplication constant calculated using the effective delayed neutron fraction for the different libraries is found in Table

1.9. All values are close to each other, within each library the differences are not more than 0.7%

Table 1.8 Delayed neutron fraction and effective delayed neutron fraction for different libraries calculated by Monte Carlo technique.

Library	$\beta \pm 1\sigma$ [pcm]	$\beta_{eff} \pm 1\sigma$ [pcm]
ENDFB6.8	699.0 ± 5.9	788.4 ± 9.3
JEFF3.0	700.7 ± 5.9	792.5 ±9.4
JENDL3.3	665.3 ± 5.8	742.1 ± 9.0

Table 1.9 k_{eff} calculated from β_{eff} (different libraries) and reactivity (from Area Method).

Experimental channel	Library		
	ENDFB6.8	JEFF3.0	JENDL3.3
EC1	0.9011 ± 0.0013	0.9006 ± 0.0013	0.9063 ± 0.0013
EC2	0.9025 ± 0.0014	0.9021 ± 0.0014	0.9077 ± 0.0014
EC3	0.9077 ± 0.0011	0.9073 ± 0.0011	0.9126 ± 0.0011
EC5	0.9069 ± 0.0011	0.9065 ± 0.0012	0.9119 ± 0.0011
EC6	0.9041 ± 0.0013	0.9036 ± 0.0013	0.9092 ± 0.0012

Slope Fit Method

As described earlier, α is the logarithmic slope of the response function, Figure 1.22. But the task is not so easy since the slope in each channel is time dependent. During the first 2 ms there is a very fast decay in the channels in the core. These are the source dependent neutrons which enters the fuel first. At the same time the neutron population builds up from zero in the non-multiplicative reflector. After a few ms the neutron population is established in the core and in the reflector, and a fundamental decay mode is achieved. This decay mode should be visible in all detectors at the same time, but it might be difficult due to the time dependent slope and the disturbing delayed neutron background. However, a first guess, just by looking at Figure 1.22, tells us that the slope should be found after approximately 4 ms.

To calculate the reactivity from Eq. (16) the effective delayed neutron fraction and the neutron generation time is needed. The effective delayed neutron fraction is found in Table 1.8 as before, but the generation time is still unknown since MCNP fails to simulate it. Therefore we can not use the α-measurement to find the reactivity but we can use it to obtain an experimental value of the mean generation time. By rewriting Eq. (16) Λ/β_{eff} can be found by combining the Area method measurement and the α-measurement:

$$\frac{\Lambda}{\beta_{eff}} = \frac{1}{\alpha}\left(\frac{\rho}{\beta_{eff}} - 1\right). \tag{25}$$

The problem is now how to find α. As discussed above the response behavior is varying in time, giving rise to different harmonics. The idea is to find these harmonics and the

fundamental mode by fitting a series of exponentials. This is done by using Minuit from CERN [16] to fit a function of the form

$$f(t) = \sum_{i=1}^{4} A_i e^{\alpha_i t} \,. \tag{26}$$

This method finds two fast harmonics, one slow harmonic representing the fundamental decay mode, and finally a constant term. The fitted functions are shown in Figure 1.23 and the values in Table 1.10.

Table 1.10 Fitted slope parameters - values from Minuit.

EC	A_1	α_1 [s^{-1}]	A_2	α_2 [s^{-1}]	A_3	α_3 [s^{-1}]	A_4	α_4 [s^{-1}]	χ^2
EC1	1958	-5344	2964	-1612	612	-672±13	8.6	0	1.13
EC2	925	-5760	2020	-1709	533	-720±25	5.7	4	1.17
EC3	1269	-6397	4609	-1664	146	-711±11	16.9	3	1.03
EC5	-3442	-5480	2274	-965	220	-639±22	16.4	0	1.01
EC6	-2818	-2455	0	0	2952	-655±1.2	9.7	0	1.09

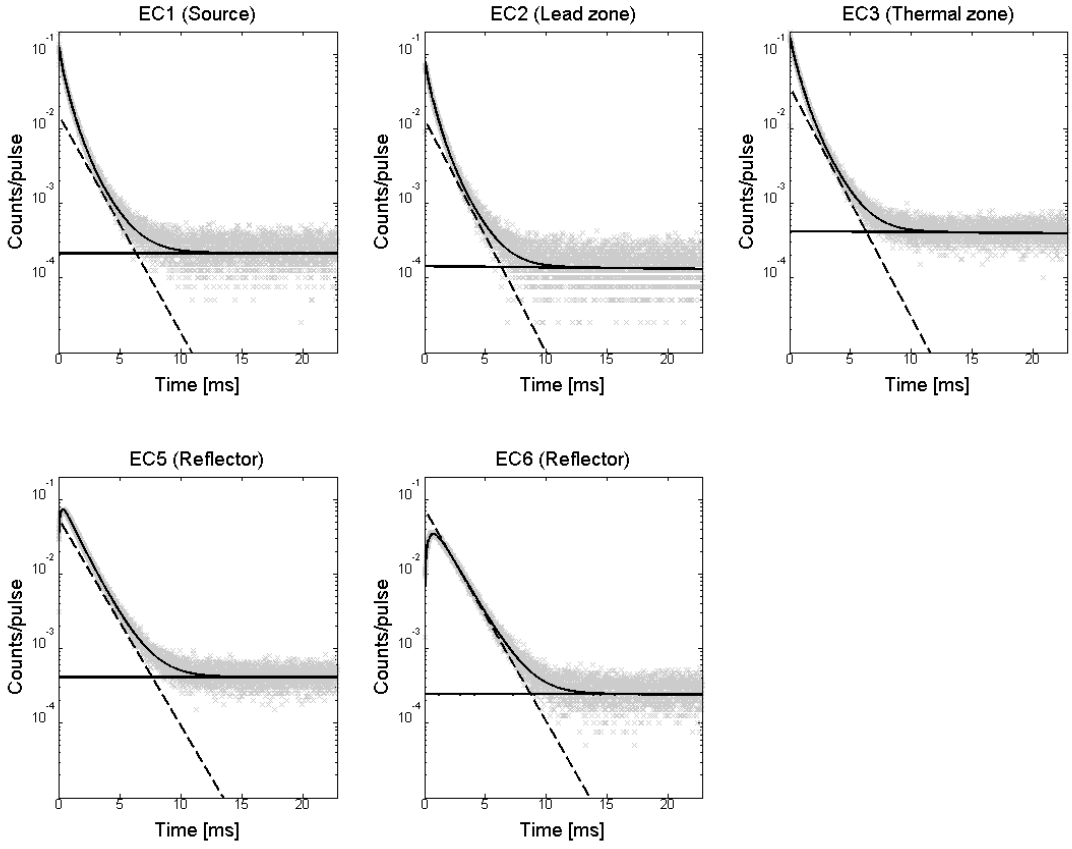

Figure 1.23 Functions fitted by Minuit. The straight lines represent the function and the constant level of the delayed neutron background. The dashed line represents the fundamental decay mode.

The values α_3 are chosen as the fundamental decay constants. It could also be α_2 since they also describe a negative exponential decrease. But α_2 is missing in EC6 and the

values are different in the reflector and in the core, therefore α_3 is more probable since it is present in all channels with similar values. When these values are inserted in Eq. (25) we can calculate the mean generation time, Table 1.11.

Table 1.11 Experimental values of Λ. Effective delayed neutron fraction from different libraries.

EC	Λ/β_{eff} [10^3]	Λ [μs] ENDFB6.8	Λ [μs] JEFF3.0	Λ [μs] JENDL3.3
EC1	22.2±0.4	175.2±3.9	176.1±4.0	164.9±3.7
EC2	20.4±0.7	160.8±5.9	161.7±5.9	151.4±5.6
EC3	19.6±0.3	154.1±3.1	154.9±3.1	145.0±2.9
EC5	22.0±0.8	173.1±6.4	174.0±6.5	163.0±6.1
EC6	22.1±0.04	173.9±2.1	174.8±2.1	163.7±2.0

Source Jerk Method

According to Eq. (18) the Source Jerk method requires determination of two neutron levels. These levels are evaluated as the end values of two functions fitted to the detector counts before and after the source jerk. Before the jerk the source is expected to be constant, therefore a linear function is used. But immediately after the shutdown of the source there will be a fast decay due to the two last delayed neutron groups. This decay is better described by an exponential, Figure 1.24. This procedure gives the values in Table 1.12 neglecting the background. In Table 1.13 are the effective multiplication factor and the generation time presented, calculated from Eq. (25) and the values in Table 1.8. The error bars are very big due to bad statistics in the lower level n_1. Uncertainties are calculated according to ref. [17].
The sensitivity of fitting interval for n_1 was investigated. Choosing a short interval will give a large uncertainty, but with a long interval the validity of the exponential model will fail. The chosen interval of 1.2 s gives relatively good statistics without eliminating the assumption of an one-group exponential decrease.

Table 1.12 Results from Source Jerk Method**.**

Parameter	Value ± 1σ
n_0 [ms^{-1}]	100.0 ± 0.5
n_1 [ms^{-1}]	9.0 ± 1.7
ρ/β_{eff}	-10.1 ± 2.1

Table 1.13 k_{eff} and generation time calculated from Source Jerk results.

Parameter	ENDFB6.8	JEFF3.0	JENDL3.3
k_{eff}	0.926±0.014	0.926±0.014	0.930±0.013
Λ [μs]	129±24	129±24	121±23

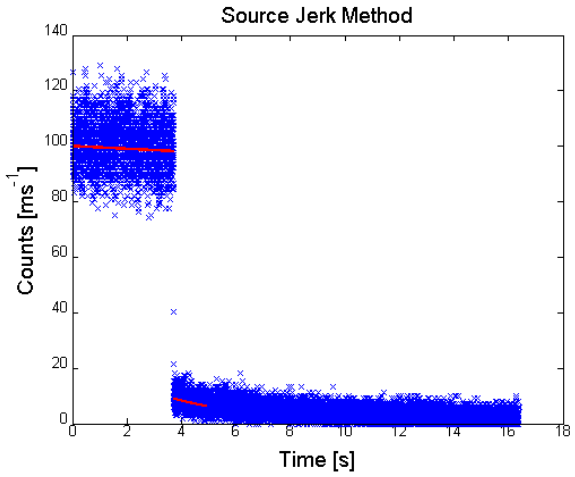

Figure 1.24 . Data from Source Jerk experiment.

1.7.7 Monte Carlo Simulations

The fission rate distribution experiments and the pulsed source experiment was implemented in MCNP. The MCNP input file used is from the institute in Sosny.

Fission Rate Simulation

The fission rate with ^{235}U, ^{Nat}U and ^{232}Th has been calculated by MCNP using data library ENDFB6.8. Results are shown in Figure 1.25.

Pulsed Source Simulation

Pulse responses similar to Figure 1.22 can be obtained by simulation, but without the delayed neutron background. The constant background of delayed neutrons appears in the experiment because a big number of pulses are measured cumulatively. In MCNP only one pulse can be simulated and this is done without delayed neutrons.
As we have already seen, the decay constant of the fundamental decay mode, α, is difficult to find because of its time dependence. It is therefore of interest to perform this experiment for different reactivity levels approaching criticality, to see if this effect also occurs in near-critical cases. This was not possible to do in the Yalina facility, but in

Table 1.14 Different reactivity levels of Yalina investigated by MCNP.

Configuration #	Enrichment (%)	k_{eff} ± 1σ (KCODE using ENDFB6.8)
1	9.9	0.91803±0.00005
2	11.2	0.95164±0.00005
3	12.2	0.97254±0.00005
4	13.6	0.99764±0.00005

MCNP it is an easy task to do by changing the ^{235}U concentration on the material card. Four different configurations have been investigated with four different enrichments. The first configuration is the original Yalina configuration and the fourth is a close-to-criticality configuration. The other two lie between, see Table 1.14. All these configurations have been simulated in exactly the same manner. A neutron pulse with a

duration of 2 μs is injected at time $t = 0$. The reaction rate with ^{3}He, (n,p)-reaction, is then tracked during the following 20 ms in the experimental channels at $z = 0$. The output data can then be analyzed in the same way as in the real experimental case using Minuit, but this time it is simpler because there will be no background of delayed neutrons and only two exponentials are enough to describe the decay.

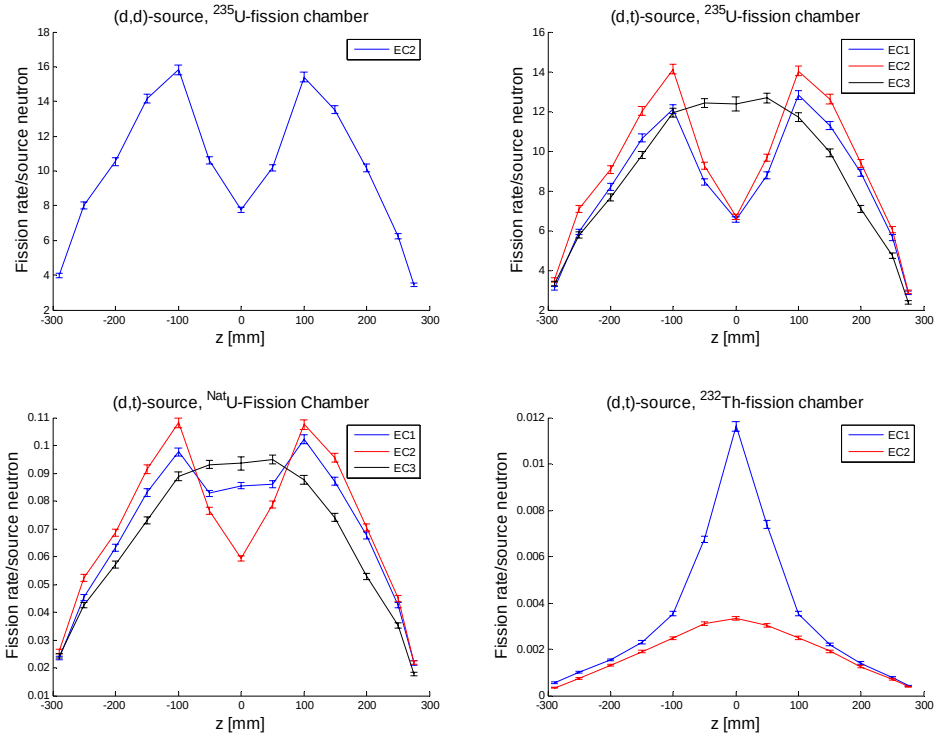

Figure 1.25 Axial fission rate distributions obtained by MCNP simulation. The points are connected with lines just to make the shapes clear.

Results from the MCNP runs are plotted in Figure 1.25. It is easy to see how the slope varies with reactivity as predicted by theory. In the close-to-criticality configuration the time for establishment of a stabilized neutron flux decay is faster than in the most subcritical state and it is much more clear how to find the decay mode. The core channels have stabilized after only 2 ms. In the most subcritical case at least twice as long time is needed. In the real experiment the delayed neutron background starts to influence the decay rate after approximately 5-6 ms, so the fundamental mode gets drowned between the not stabilized part and the background part. This effect can be seen in the first three channels in Figure 1.22

From the plots in Figure 1.26 it is possible to determine α, and the MCNP code also deliver the non-adjoint weighted neutron generation time. Since the effective delayed neutron fraction is known it should be possible to calculate the reactivity and the effective multiplication factor according to Eq. (16). k_{eff} is already calculated with a kcode run so this would be a good way to test if the method works well. But this does not work at all because of the problem with the non-adjoint weighted mean generation time mentioned earlier. Instead the mean generation time can be calculated from Eq. (16), and the effective multiplication constants in Table 1.15.

$$\Lambda = \frac{1}{\alpha}\left(1 - \frac{1}{k_{eff}} - \beta_{eff}\right) \tag{27}$$

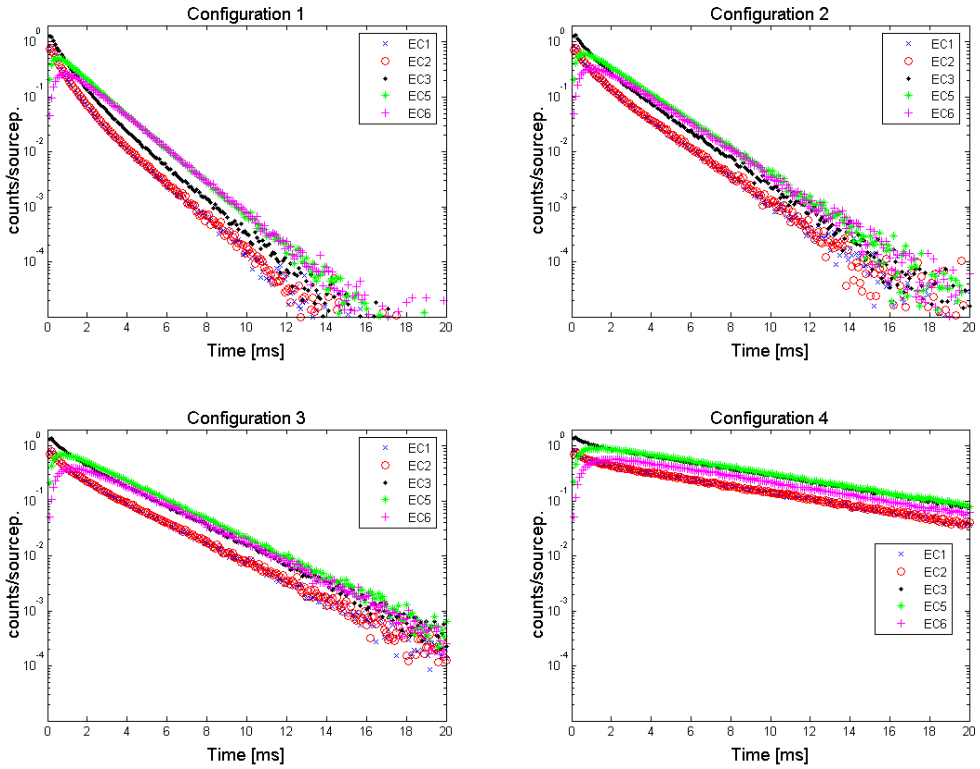

Figure 1.26 Neutron pulses simulated by MCNP for different levels of enrichment (ENDFB-VI).

These values of the mean generation time, originating indirectly from MCNP, are compared with the mean generation time calculated directly from MCNP in Table 1.15. From the table the difference between the calculated mean generation time and the non-adjoint weighted mean generation time can be seen. Assuming that the point kinetics is applicable this value should give an estimation of the *adjoint-weighted* mean generation time. An arithmetic mean value of the mean generation time for the real configuration is 136.05 ± 0.07 μs (statistical error).

1.7.8 Comparison between Experiments and Simulations

Fission Rate Distributions

When the fission rate distributions from the experiment, Figure 1.22, and simulation, Figure 1.26, are plotted in the same diagram it is obvious how well they fit each other, Figure 1.27. This is a good indicator that using MCNP at least with library ENDFB6.8 describes the reality very well. The discrepancies are mostly due to low resolution in *z*-direction.

Table 1.15 Results from MCNP simulation of PNS-experiment with statistical errors. Comparison of mean generation time calculated from data below and given by MCNP. ENDFB6.8 is used overall.

Conf.	k_{eff} (KCODE)	β_{eff} * [pcm]	Experimental channel	α [s^{-1}]	$\Lambda_{MCNP}^{Indirect}$ [μs]	Λ_{MCNP} [μs]
1	0.91803± 0.00005	788±9.3	EC1	-742 ± 11	131.2 ± 0.1	372.2 ± 0.1
			EC2	-718 ± 3	135.3 ± 0.2	
			EC3	-723 ± 6	134.5 ± 0.2	
			EC5	-737 ± 1	131.9 ± 0.1	
			EC6	-686 ± 2	141.7 ± 0.2	
2	0.95164± 0.00005	750±100	EC1	-574 ± 5	102 ± 2	353.0 ± 0.1
			EC2	-570 ± 4	102 ± 2	
			EC3	-573 ± 5	102 ± 2	
			EC5	-561 ± 1	104 ± 2	
			EC6	-551 ± 3	105 ± 2	
3	0.97254± 0.00005	750±100	EC1	-409 ± 2	87 ± 3	341.8 ± 0.1
			EC2	-407 ± 2	88 ± 3	
			EC3	-404 ± 2	88 ± 3	
			EC5	-404 ± 1	89 ± 3	
			EC6	-403 ± 2	89 ± 3	
4	0.99764± 0.00005	750±100	EC1	-136.4 ± 0.6	72 ± 7	329.0 ± 0.1
			EC2	-135.3 ± 2.2	73 ± 7	
			EC3	-135.4 ± 1.8	73 ± 7	
			EC5	-136.1 ± 2.3	73 ± 7	
			EC6	-135.0 ± 0.6	73 ± 7	

*Rough estimations for configuration 2, 3 and 4.

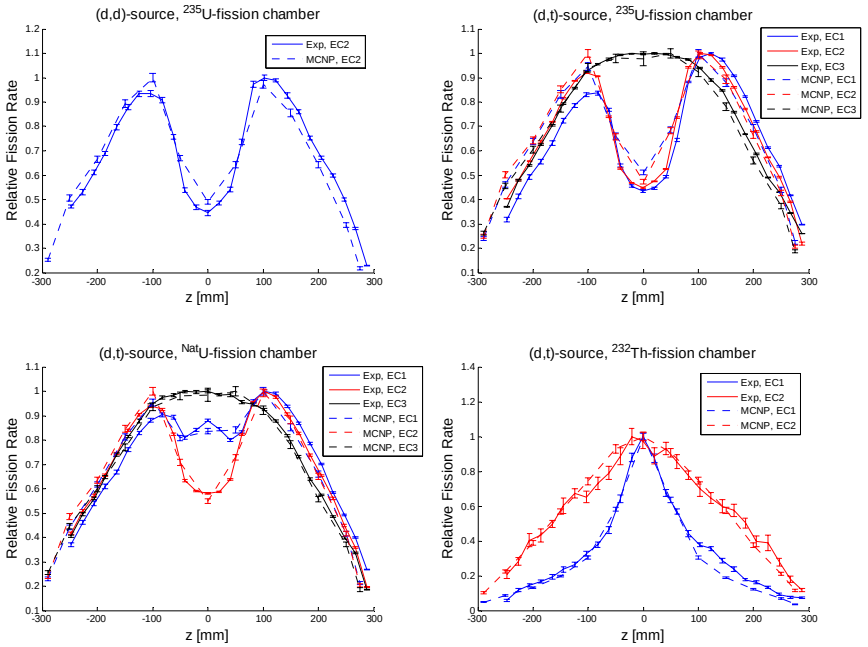

Figure 1.27 Axial fission rate distributions normalized per channel from experiment and simulation. The points are connected with lines just to make the shapes clear.

Kinetic Experiments

As mentioned before no delayed neutron background is achieved when simulating the pulsed source experiment in MCNP. In order to compare the simulation with the experiment this background must be subtracted from the experimental data. The results are found in Figure 1.28. Because of good agreement one can conclude that the α-values found in the experiment should be similar to the α-values found from simulations. This also indicates that the mean generation time calculated by MCNP (ENDFB6.8) through the Slope Fit method should give an accurate value of the adjoint-weighted mean generation time.

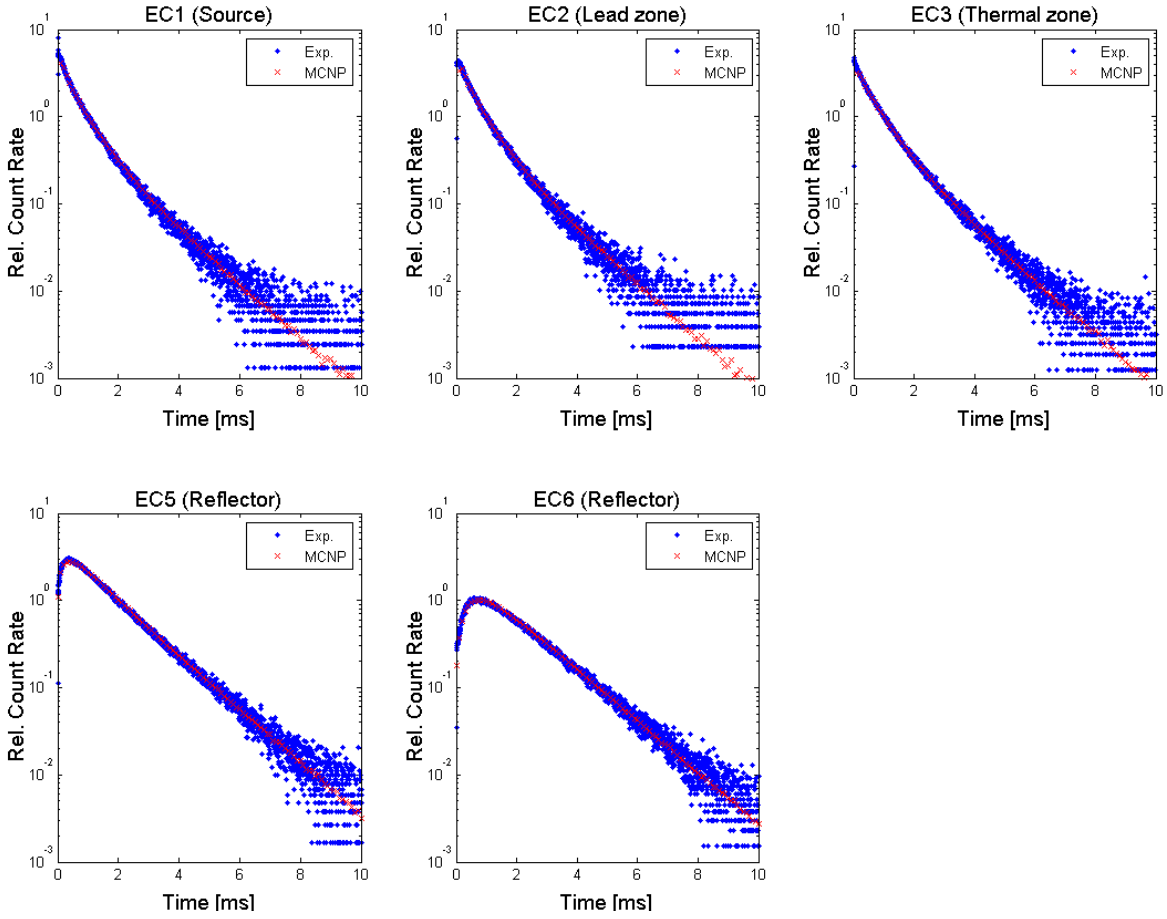

Figure 1.28 Comparison between data from experiment and MCNP (arbitrary units). The delayed neutron background is removed from the experimental data.

1.7.9 Comparison between the Different Reactivity Determination Methods

Knowing that the simulation describes both the static and kinetic behavior of the reactor well, we can assume that the adjoint-weighted mean generation time from MCNP is a good estimation of the real mean generation time. By using the estimations of the adjoint-weighted mean generation time calculated by MCNP, the effective multiplication can be obtained from the experimental α-fitting method. Solving for k_{eff} in Eq. (27) yields the values in Table 1.16 (after "Slope Fit") using ENDFB6.8 values of β_{eff} and Λ.

Table 1.16 Comparison of all effective multiplication constants calculated.

Experimental channel			EC1	EC2	EC3	EC5	EC6
Method	Area	ENDFB6.8	0.9011± 0.0013	0.9025± 0.0014	0.9077± 0.0011	0.9069± 0.0011	0.9041± 0.0013
		JEFF3.0	0.9006± 0.0013	0.9021± 0.0014	0.9073± 0.0011	0.9065± 0.0012	0.9036± 0.0013
		JENDL3.3	0.9063± 0.0013	0.9077± 0.0014	0.9126± 0.0011	0.9119± 0.0011	0.9092± 0.0012
	Slope Fit	ENDFB6.8	0.9248± 0.0015	0.9180± 0.0028	0.9184± 0.0013	0.9279± 0.0028-	0.9213± 0.0001
	Source Jerk	ENDFB6.8	-	0.926± 0.014	-	-	-
		JEFF3.0	-	0.926± 0.014	-	-	-
		JENDL3.3	-	0.930± 0.013	-	-	-
	KCODE	ENDFB6.8	0.91803±0.00005				
		JEFF3.0	0.92010±0.00007				
		JENDL3.3	0.92114±0.00006				

The Monte Carlo based KCODE is very well validated and benchmarked and is supposed to give proper approximations of the effective multiplication factor. According to the KCODE values in Table 1.16, k_{eff} = 0.92 is chosen as a reference value. When the experimental values are compared with this reference level it can be concluded that the Area method gives a lower value and the Slope Fit method and Source Jerk method gives values fairly close but with larger errors (Source Jerk method). Remember that the standard deviations given are only due to statistical errors. Error in model, systematic measurement errors and so on, are not taken under consideration. These errors are expected to be large for the Slope Fit method due to uncertainties in determination of α.

At this moment it is important to remember what exactly the different methods measure. In the derivation of the Area method it was assumed that the prompt and delayed neutrons multiply equally in the system. Since the delayed neutrons have a softer spectrum the Area method should give a result deviating from the point kinetics. When deriving the other two methods no such cruel approximations were made so the results correspond better to the reference. The large subcriticality measured by the Area method leads to a biased value of the experimental value of the mean generation time.

The Slope Fit method and Source Jerk method have other drawbacks. The Slope fit method is difficult to use for large subcriticalities, like in this case, due to the time dependent slope. According to the MCNP-simulations this methods is easier to apply for not so subcritical systems when the fundamental decay mode is achieved faster.

The Source Jerk method has the problem with bad statistics in the lower neutron level, and in some cases it can also be difficult to know where to find this level. A possible strength of this method is that it can be used during operation of the ADS, since it does not require the source to operate in pulsed mode, but unfortunately it requires a short operation break.

1.7.10 Conclusions

From the measurements we can conclude:

- The Area method overestimates the subcriticality, but gives low statistical error. Can not be used for online reactivity measurement.
- The Slope fit method is difficult to use, but seems to give reliable results when the correct slope is found. Can not be used for online reactivity measurement.
- Source Jerk method has problems with large uncertainties, but can easier be implemented in a continuously running facility.

Reactivity monitoring seems to be a difficult task without control rods. None of these methods are able to measure the reactivity without disturbing a running system. However the methods can be used to estimate the subcriticality during load and for calibration of eventual indirect measure techniques.
In this study reactivity changes were not included. Even if the methods do not predict the absolute value of the reactivity absolutely correct they may be able to predict reactivity changes well.
It can also be concluded that MCNP gives reliable results, which was shown by both the static and the kinetic simulations. But big care must be taken when analyzing the time parameters.
Finally, the experiments show that the Point Kinetic approximation seems to describe this system well.

2 SYSTEM STUDIES OF ADS

2.1 SYSTEM STUDIES OF ADS

Partitioning and transmutation of plutonium, americium, *and* curium is inevitable if the radiotoxic inventory of spent nuclear fuel is to be reduced by more than a factor of 100. But, admixing minor actinides into the fuel severely degrades system safety parameters, particularly coolant void reactivity, Doppler effect, and (effective) delayed neutron fractions. The incineration process is therefore envisioned to be carried out in dedicated, accelerator-driven sub-critical reactors (ADS). However, ADS cores operating in concert with light-water reactors (two-component scenario) also exhibit high burnup reactivity swing with penalty on the system performance/economy.

2.1.1 DESIGN STUDIES OF TRANSURANIUM ACCELERATOR-DRIVEN BURNER

In the frame of our design work, presented in a concise manner in [28], we attempted, by choice of coolant and optimisation of fuel concept and core design, to achieve favourable neutronic, burnup and safety characteristics of the transuranium ADS burner. Key thermal hydraulic and material-related constraints were respected.

Core design

A novel fuel matrix material, hafnium nitride, was identified as an attractive diluent option for highly reactive transuranics. (TRU,Hf)N fuels appeared to have a good combination of neutronic, burnup and thermal characteristics: maintaining hard neutron spectra, yielding acceptable values of coolant void reactivity and source efficiency, and providing small burnup reactivity loss. A conceptual design of a (TRU,Hf)N fuelled, lead/bismuth eutectic cooled ADS was developed, see Figure 2.1.

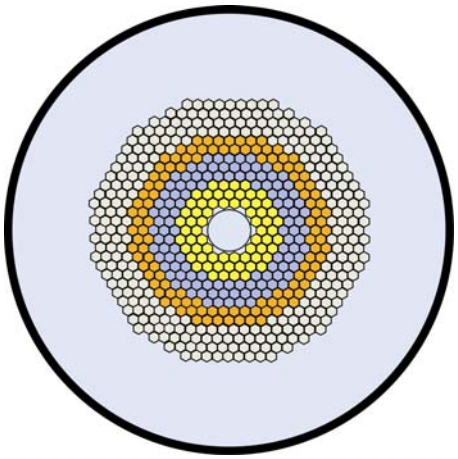

Figure 2.1 Cross section of the conceptual core design of Pb/Bi-cooled ADS employing (TRU,Hf)N. The core consists of three enrichment zones with the different matrix fractions. Radial steel reflector sub-assemblies are depicted in grey. Pitch-to-diameter ratio is 1.75.

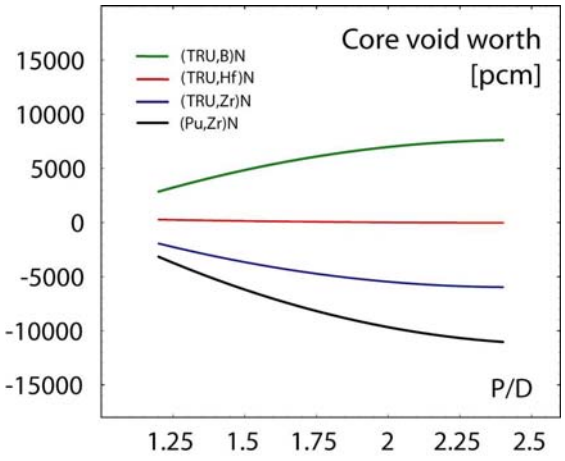

Figure 2.2 Coolant core void worth in Pb/Bi-cooled TRU ADS burner as a function of pitch-to-diameter ratio.

The average discharge burnup of 20% fissions per initial metal atom could be reached even without fuel reshuffling. The fission fraction ratios of even-neutron number americium nuclides are increased by a factor of two in comparison to burners with inert matrix based fuels. Hence, thanks to the reduced production of higher actinides and helium, fuel cycle economy is improved.

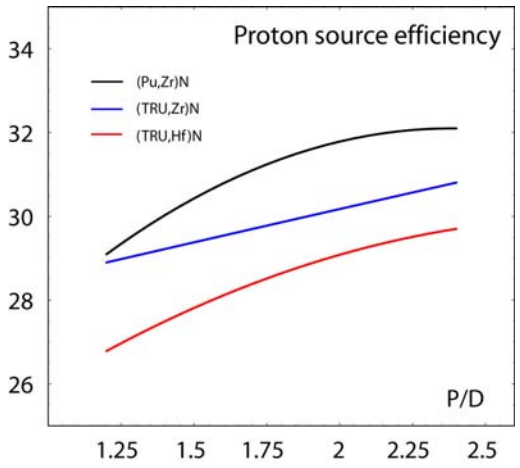

Figure 2.3 Proton source efficiency in Pb/Bi-cooled TRU ADS burner as a function of pitch-to-diameter ratio.

Coolant void worth and source efficiency

The coolant void worth proved to be a strong function of the fuel composition - reactor cores with high content of fertile material or minor actinides in fuel exhibit larger void reactivities than systems with plutonium-rich, inert matrix fuels. In reactor systems cooled by lead/bismuth eutectic, a radial steel pin reflector significantly lowered coolant void reactivity. For transuranic fuel, fertile and strongly absorbing matrices exhibited increasing void worth with increasing pitch, while the opposite was valid for the coolant void worth of inert matrix fuels, see Figure 2.2. Large pitches also appeared to be beneficial for limiting the reactivity worth of the cladding material and improving source efficiency, see Figure 2.3.

Sensitivity of coolant void worth

A sensitivity of the coolant void worth on the choice of cross-section library was investigated using a model Pb/Bi-cooled $(U,Pu)O_2$ fuelled fast reactor. Three neutron cross-section libraries, JEF2.2, JENDL3.2, and ENDF/B-VI, were used in the analyses, which results are displayed in Figure 2.4. Note that JENDL3.2 library provides the most conservative estimate of the coolant void worth for all P/D ratios investigated.

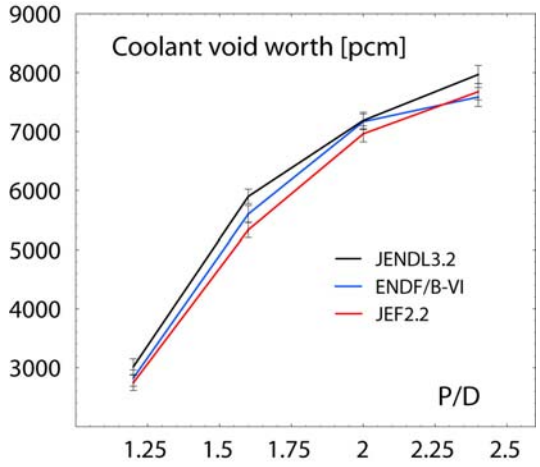

Figure 2.4 Core void worth in a model Pb/Bi-cooled (U,Pu)O2 fuelled FBR without radial steel reflector. 2-σ standard deviation is shown.

2.2 STUDIES ON GAS COOLED TRANSMUTATION SYSTEMS

Over the years, a lot of effort has been invested in lead-bismuth cooled transmutation systems at the department. A design called the Sing-sing core was worked out and also other work addressing safety, fuel and material issues have been performed. These efforts are mainly motivated by the promising transmutation performance shown by lead-bismuth cooled sub-critical cores.

Efficient transmutation of curium and even heavier exotic elements require a hard neutron spectrum. The fission over absorption cross-section rise towards higher incident neutron energies for the nuclides of interest. In suggested transmutation cores [29] several recycles are often required for the heaviest of the nuclides in the spent fuel to reach an equilibrium where the amounts stop level out. The harder the neutron spectrum, the lower the equilibrium levels are.

Gas-cooling of transmutation cores make very hard neutron spectra achievable. Among the possible choices of gas-coolants, helium is the most promising, mainly due to its low neutron interaction cross-sections, its chemical inertness and high heat capacity. This was examined in detail in early design projects aiming at the construction of gas cooled fast reactors [30]. Carbon dioxide has been used extensively in, mainly, thermal reactors. However, helium is the better choice, especially in fast reactors.

In a helium cooled transmutation core, it is possible to achieve a reduction of spent MOX curium inventory already in the first cycle. This is normally not achievable in lead-bismuth cooled cores, where the somewhat softer spectrum results in a build-up of heavy nuclide in the first cycles. Keeping the curium inventory is desirable mainly from a materials handling perspective. Curium is a source of neutron radiation which is

cumbersome in all steps of the fuel cycle including transporting, recycling and fuel manufacturing.
Gas-cooling require high pressure operation. Gases have low densities compared to other coolants – liquid metals in particular. Helium may be treated as an ideal gas and consequently the density of helium has a linear pressure dependence. Sufficient mass flow over the core is thus achieved by increasing the gas pressure or the gas velocity. Since the pressure loss in the core goes as the square of the velocity of the medium, but linearly with the pressure, the incentive for increasing gas pressure rather than gas velocity is strong. For the pumping power required the velocity has an even greater impact, as the work grows with the cube of the velocity. Typically, this has led to high operational pressures in suggested fast gas cooled designs. In the GCFR study undertaken by General Atomics during the end of the sixties, the seventies and early eighties, the operating pressure was in the 8 – 12 MPa range [31].
With mass flow following pressure linearly, so does the heat removal capability. A severe scenario for any gas-cooled system is thus a loss of pressure. In the GCFR-case, a complete pressure loss, from operating to ambient pressure, would lead a reduction in core cooling by about a factor one hundred. Even in the case of immediate scram of the core, stopping the fission process promptly and completely, the decay heat remain. The heat generated by radioactive decay amount for a few percent of full power during the first hours after scram. In a situation where only one percent of the cooling capability remains, this situation potentially lead to increasing core temperatures.
Even though a high coolant velocity implies large pressure losses, it is normally significant. In the GA-GCFR, the design velocity was 70 m/s [31]. In a situation where the main circulators stop and the secondary systems fail to start, the coolant velocity drops to the much lower rate given by the natural circulation of coolant driven by the heat differences in the coolant loop.
In the annual report for 2003 [32], we described extensively how the very good neutron economy of the actinide fuel may be utilized to ease the demand on core pressure at normal operation, thus lowering the potential pressure loss, easing the decay heat removal issue. The most important conclusion of that study was that even though the core design proposed can safely handle both a loss of pressure and a loss of flow accident, the combination of the two results in core damage. Further these kind of accidents in a situation where the operation at full power continues would also cause core damage.

2.2.1 Coated particles in a gas-cooled design

If helium cooling is to be an option for future transmutation cores, or fast breeder reactors, the decay heat issue discussed above needs a more convincing solution. The way out lies in constructing a core that can withstand extremely high temperatures, at least in the case of an accident. The japanese have been working along this track for sometime within their fast reactor programme [41]. The path chosen is to utilize coated particle fuels for the fast reactor. Coated particles are main option for thermal high temperature cores. These are triso-particles consisting of three layers of carbon covering a nucleus of fissile material.
In a fast reactor carbon coated particles is not an option due to the moderating properties of carbon. Instead, titanium nitride (TiN) is suggested as the coating material. Within the japanese fast reactor programme it was shown how a core fuelled with nitride fuel in the form of TiN-coated particles can withstand unprotected loss of pressure transients without release of radioactive material [41].

2.2.1.1 Core design

Plutonium bearing uranium free fuels pose an excellent neutron economy. We have previously shown how the neutron surplus may be used to increase the coolant fraction in the, thus easening the loss of pressure issue in a gas cooled reactor as described above. That work shows how it is possible to assure decay heat removal in a conventional pin-type core design. In such a design, the rapid burst temperature limit of the cladding is the limiting parameter. The upper temperature allowed is typically just over 1300 K [40]. Even though decay heat removal has been shown achievable, fission heat removal is unlikely to be shown possible in a pin-type core design during a severe loss of pressure accident. A different approach is needed.

The upper temperature limit should be as high as possible to avoid fuel or structure damage in the case of an increase in temperature following the loss of coolant pressure. High temperature operation leads to thinking of coated particle fuels. Classically coated particles have meant covering small fuel spheres in carbide [36],[37], [38]. Carbide particles show low failure rates and withstand high temperatures without releasing fission products, but they moderate the neutron spectrum and are thus not possible to use in an efficient transmutation system, where a fast spectrum is mandatory.

An alternative to carbide coating is to coat the fuel spheres with titanium nitride (TiN). This idea is being developed in the japanese fast reactor programme [41]. The fuel is in the form of actinide nitrides. Two TiN-layers keep fission products and fuel inside the particle. The inner layer is a low density buffer layer, the outer layer is a high density pressure vessel layer. JNC have suggested fuel particles with a diameter of 1.94 mm [39]. We have decided to keep their design for this initial analysis.

Two helium cooled core designs have been suggested based on the titanium nitride particles [41]. One is based on blocks formed by pressing the coated particles. The other is based on an original design by Gratton et al [33]. Gratton proposes a porous fuel assembly consisting of two silicon carbide tubes. In the original design helium rises outside the assembly, flows through the porous SiC-layer, through the fuel, and eventually rises out of the core within the inner SiC-tube. In the japanese design, the flow has been turned so that the helium enters inside the assembly, as shown in Figure 3.5. The reverse flow gives a somewhat better temperature distribution [42].

Our design is based on the tube type assemblies. These give a larger fuel to coolant intersection area. This is beneficial for heat transfer, but it implies a larger risk of fission gas contamination of the coolant. The core we are suggesting contains 156 fuel assemblies in total, arranged in a triangular lattice. The seven innermost positions are reserved for the spallation target. Each assembly is filled both with spheres containing the actinide fuel and spheres consisting TiN only. By adjusting the mixing of these sphere types for assemblies in different positions in the core, the radial power profile may be altered. Seven rows of fuel assemblies give enough freedom to achieve a flat radial power profile. It shows however that it is hard to operate such a core in a sub-critical mode, as the source-efficiency becomes rather low for a core with a flat power profile. The beam power needed would be unreasonably high when the source neutrons induce significantly less fission reactions in average than the fission neutrons themselves. By tilting the power profile somewhat a fair compromise may be reached between power peaking and burnup. Figure II shows the power profile chosen. Raising the relative power in the middle fuel assemblies, those in rows three and four, might at first glance seem like an efficient way of increasing burnup. However, this would mean lowering the power in the innermost assemblies, deteriorating the source efficiency.

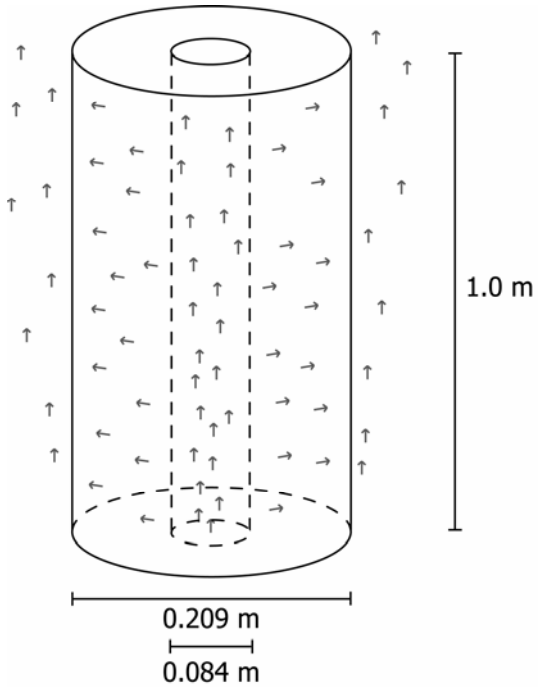

Figure 3.5 The fuel assembly consists of two cylinders. Between the cylinders, TiN-particle fuel is packed. Helium rises inside the inner cylinder, flows through the cylinder wall, though the fuel and eventually out through the outer cylinder and upwards out of the core.

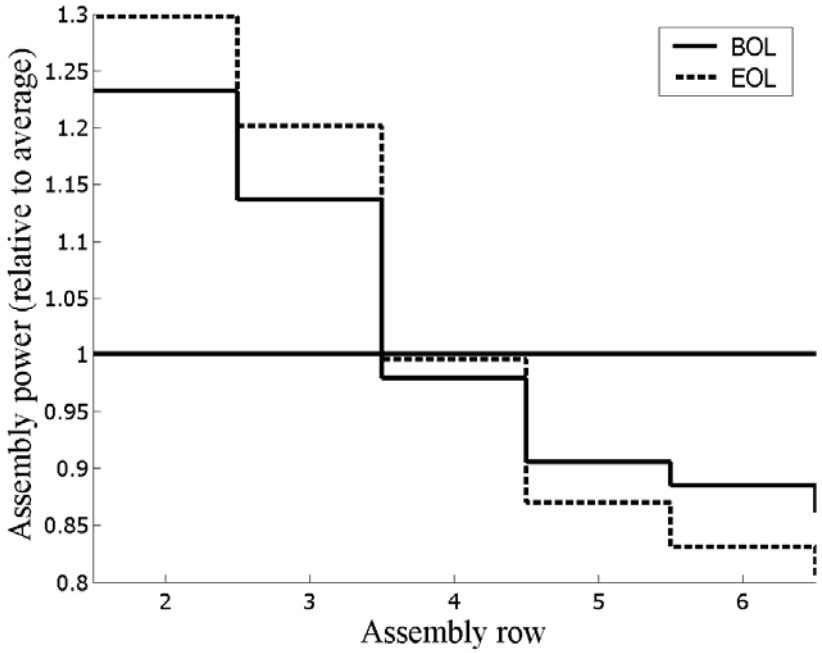

Figure 3.6 An attempt to achieve high burnup by utilizing a flat power profile had to be abandoned since such a profile deteriorates source efficiency to much. The power peaking in the chosen fuel design is 1.29 at BOL and 1.39 at EOL.

With the radial power profile shown in Figure 3.6, the highest peak power at any time in the fuel cycle for a single assembly is 7.1 MW. This results from the core thermal power being limited to 800 MWth by the upper limit in spallation source size. The highest power peaking occurs in the end of the fuel cycle, where the fuel assembly producing the highest power produces 1.39 times the power of the average fuel element. At beginning of life (BOL), the corresponding figure is 1.29, leading to a peak assembly power of 6.6 MW. The average power density in the fuel region is 72 MW at BOL, falling slightly as the accelerator power is increased towards (EOL).

2.2.1.2 Thermal hydraulics

By the end of 2004, the thermal hydraulics analysis for the TiN-assemblies was still under way. The analysis presented here is based on the similar analysis performed by JNC [39][40][41]. The japanese analysis shows that for their very similar design, core melt is avoided even during an unprotected depressurization accident, using only passive components and natural circulation. We expect similar results from our ongoing analysis.

2.2.1.3 Methods used for the neutronics calculations

The core simulation and burn-up calculations were performed using the Monte Carlo continuous energy burn-up code – MCB [35].
Temperature dependent cross section libraries were used with MCB. For most calculations, the neutron transport cross-sections in JEF2.2 were used. For the delayed neutron calculations ENDF/B-6.8 has been used. The transport calculation was performed on a fully heterogeneous geometry model on the level of fuel assemblies, the coated particles were treated as a homogenous material.

2.2.1.4 Fuel composition and core geometry

The 156 fuel assemblies are filled with titanium nitride coated fuel spheres. The spheres have a diameter of 1.94 mm [39]. The outer layer is a gas tight TiN-layer. Inside of the sealing layer, there is a porous layer to lower the pressure produced by emerging gaseous fission products. Within the assemblies, the fuel particles are mixed with particles consisting of pure TiN. By altering the amount of fuel containing spheres, the reactivity of each assembly may be controlled rather precisely. The spheres are assumed to fill out 60 percent of the volume in-between the SiC-tubes of the assemblies [33].
The neutronics calculations have been performed assuming an initial loading of the core consisting of spent MOX-fuel, left to cool for seven years (Table 2.1) [32].

Table 2.1 TRU-composition of the spent MOX fuel (7 year cooling)

^{238}Pu	5.1%	^{241}Am	66.6%
^{239}Pu	37.9%	^{243}Am	33.4%
^{240} Pu	30.3%		
^{241} Pu	13.2%	^{244}Cm	87.3%
^{242} Pu	13.5%	^{245}Cm	12.7%

The excellent neutron economy of the actinide fuel allows for the plutonium fraction in the fuel to be as low as 25 percent.

2.2.1.5 Neutronic parameters

Some neutronic parameters have been calculated for the core. In comparison to other cores (Table 2.2 and Table 2.3) the design we present here show a convincing performance. The GCR below represents data for the pin type core design we previously suggested [34]. ATW [44] and EFR [43] are other fast cores proposed.

Table 2.2 Fission and capture cross-sections for this design, the pin type design we studied earlier – GCR, the American ATW and the Europan Fast Reactor – EFR

	TiN (BOL)		GCR		ATW		EFR	
Nuclide	σ_c	σ_f	σ_c	σ_f	σ_c	σ_f	σ_c	σ_f
^{237}Np	1.13	0.53	0.74	0.61	0.85	0.39	1.58	0.31
^{238}Pu	0.40	1.38	0.26	1.36	0.29	1.15	0.66	1.03
^{239}Pu	0.36	1.76	0.21	1.68	0.23	1.61	0.51	1.85
^{240}Pu	0.38	0.57	0.26	0.66	0.29	0.44	0.41	0.37
^{241}Pu	0.37	2.23	0.37	1.90	0.40	1.92	0.59	2.63
^{242}Pu	0.35	0.46	0.22	0.51	0.24	0.32	0.57	0.26
^{241}Am	1.44	0.46	1.06	0.53	1.23	0.30	1.84	0.28
^{243}Am	1.24	0.37	0.85	0.43	0.97	0.23	1.50	0.24
^{244}Cm	0.38	0.67	0.30	0.77	0.35	0.51	0.67	0.43
^{245}Cm	0.27	2.34	0.16	2.06	0.17	2.01	-	-

Table 2.3 Fission over absorption cross-sections

Nuclide	TiN	GCR	ATW	EFR
^{237}Np	0.32	0.45	0.31	0.16
^{238}Pu	0.78	0.84	0.80	0.61
^{239}Pu	0.83	0.89	0.88	0.78
^{240}Pu	0.60	0.71	0.60	0.47
^{241}Pu	0.86	0.84	0.83	0.82
^{242}Pu	0.56	0.70	0.57	0.31
^{241}Am	0.24	0.33	0.20	0.13
^{243}Am	0.23	0.33	0.19	0.14
^{244}Cm	0.64	0.72	0.59	0.39
^{245}Cm	0.90	0.93	0.92	-

2.2.1.6 Irradiation cycle

The rather high power density together with the hard neutron spectrum gives a burnup of the actinides of 22.8 percent during cycle, where the core has been fueled with spent MOX-fuel, left to cool for seven years before reloading. Table 2.4 gives the figures for individual nuclides. It should be noted that already in the first recycle, the curium

inventory is almost in equilibrium, ^{244}Cm and ^{245}Cm increasing only 16.8 and 8.6 percent respectively. In a softer neutron spectrum a larger increase would be expected in the first cycle, the curium equilibrium inventory being reached after several recycles.

Table 2.4 Burnup performance in 700 days

	BOC	700 d	Δ
^{238}Pu	3.45E+04	1.44E+05	354.6%
^{239}Pu	2.60E+05	1.46E+05	-48.0%
^{240}Pu	2.09E+05	1.97E+05	-6.9%
^{241}Pu	9.16E+04	5.40E+04	-44.7%
^{242}Pu	9.40E+04	1.25E+05	35.7%
^{241}Am	1.15E+06	6.50E+05	-48.5%
^{243}Am	5.83E+05	3.70E+05	-40.8%
^{244}Cm	3.06E+05	3.54E+05	16.3%
^{245}Cm	4.47E+04	4.78E+04	8.6%
Tot	2.78E+06	2.22E+06	-22.8%

2.2.1.7 Conclusions

Helium cooling of sub-critical cores dedicated to minor actinide transmutation is an interesting alternative to liquid metal cooled cores once the fuel is designed to withstand high temperatures during accident transients. This is possible with TiN-particle fuel.

2.3 XADS

The European 5th framework programme came to an end during the last year. Our work within the project led to three published reports.

1. Jerzy Cetnar, Waclaw Gudowski “Assessment of the Possibility to Adopt Special Assemblies with MA and LLFP in the Gas-Cooled XADS Core” Deliverable 36 Work Package 4.2 PDS-XADS issued by KTH, Rev. 0 June 2004
2. Daniel Westlén, Jerzy Cetnar, Waclaw Gudowski, "Monte Carlo Simulation of Transmutation Performance in Special Assemblies with MA and LLFP placed in the Gas-Cooled XADS Core” PDS-XADS, Appendix A Deliverable 36 issued by KTH, Rev. 0 June 2004
3. Jerzy Cetnar, Waclaw Gudowski, “LBE Purification Requirements due to Radiotoxicity” PDS-XADS, Appendix 2 Deliverable 60.3 “Definition of Requirements for Purification Systems for Impurities and Spallation Products” issued by CEA, DTN/SRPA/LPC 2004/037 June 2004

They are all based on calculations performed with the code MCB developed at the department. The first to mentioned above concern the gas-cooled (helium) design studied within the XADS-project. They deal with the possibility of performing transmutation experiment in specially designed core sub-assemblies in this core.
The third work is a calculation of the production of activation products in the coolant of the lead-bismuth eutectic cooled core designed as part of XADS.

3 DYNAMICS AND KINETICS OF ADS

In this chapter issues related to the safety and operation of accelerator-driven reactors are investigated. Included is a transient safety study of minor actinide fuel systems of current interest for application to ADS. Computational studies are used to quantify the performance of cores employing these fuels under transient operating conditions and to develop conclusions regarding their safety features. This work has been treated in detail in a separate paper [68]; the results are presented here in a condensed form. The next topic is superprompt critical reactivity excursions. Application is made to accelerator-driven reactors employing minor actinide fuels. Results are compared with a conventional fast reactor. Further, two technology studies were performed related to the application of lead-bismuth cooling to ADS. The first study evaluates the seismic performance of the reactor vessel containing the high density liquid. The final topic discusses some basic features of lead/bismuth systems with regards to the attainable thermal efficiency of the steam cycle. Although production of power has never been the principal object of an ADS, enough attention has been given to the matter to mention a few important trademarks.

3.1 TRANSIENT SAFETY STUDIES OF FUELS FOR ADS

Studies of ADS neutronics and thermal hydraulics have been accomplished, leading to the selection of lead-bismuth as main choice for the coolant. Concerning the selection of a suitable fuel material, investigations are made in connection with the joint European research programs. While some of the originally suggested fuels did not fulfill basic safety and/or design criteria, three fuels have been selected for detailed examination, namely: a molybdenum-based Ceramic-Metal (CerMet) fuel, a magnesia-based Ceramic-Ceramic (CerCer) fuel, and a zirconium-nitride based fuel. These materials are listed in Table 3.1. A more involved description of these fuels is given in [68, 69] along with neutronics performance data. Here, we focus on the transient safety aspects. Accident analyses are carried out for the response to unprotected loss-of-flow and accelerator beam-overpower transients, and coolant voiding scenarios. Maximum temperatures during transients are determined and compared with design limits. Preliminary design limits are listed in Table 3.2, with further motivation given in [68]. Si-modified 15-15Ti austenitic stainless steel (Phénix type) is the selected cladding material at this stage [70, 71].

Table 3.1 Comparison minor actinide fuels investigated in this study

Fuel*	Composition	Form
AnO_{2-x}-MgO	Oxide	CerCer
AnO_{2-x}-Mo	Oxide	CerMet
(An,Zr)N	Nitride	Solid solution

*"An" denotes a mixture of actinides (Pu, Am, and Cm). The oxide fuels are hypostoichiometric and the chemical formula is referred to as AnO_{2-x}, where x is the deviation from stoichiometry.

Table 3.2 Summary of thermal limits for fuel and cladding.

Component	Failure temp. (K)	Failure mechanism
Fuel		
CerCer	2200-2300	Eutectic melt
CerMet	2640	Oxide melting
Nitride	2400	AmN dissociation
Cladding (type 15-15Ti)		
Surface (steady-state)	840	Corrosive thinning
Midwall (steady-state)	920	Creep rupture
Midwall (transient)	1330	Mech. burst limit

3.1.1 Computational models

The SAS4A/SASSYS-1 computer code [72] is used for thermal- and hydraulic calculations at steady-state and transient conditions. The primary system includes models of the core, primary pumps, shell side of the steam generators, connecting piping, and compressible pool volumes with cover-gas surfaces. Major plant specifications are presented in Table 3.3. Reactivity feedbacks are calculated for coolant expansion, fuel elongation, radial core expansion, and Doppler effect. Changes in power level are computed with point kinetics theory. The performance of the point kinetics approximation for transient analysis of ADS's was considered in a previous assessment [73] and found adequate for similar problems. The pitch-to-diameter (P/D) ratio and the pin diameter are design parameters. The reference configuration uses a P/D equal 1.50 and a pin diameter of 5.72 mm. In a second configuration, the P/D value is increased to 1.75 by changing the pin pitch. In a third modification, the pin diameter is increased to 6.8 mm while holding the P/D ratio at 1.50. Matrix fractions are adjusted to obtain an initial k_{eff} equal 0.97 and a radial peak-to-average power ratio factor of 1.3. The β_{eff} is around 180 pcm for all three fuels. The plutonium fraction is fixed at 40% Pu and 50% MA. Because of lower thermal conductivity, the CerCer fuel is required to operate at lower linear powers; 25 kW/m compared to 35 kW/m for the CerMet and the nitride fuel. The initial gap thickness is chosen so that direct solid-to-solid contact is prevented during transients (assuming unirradiated geometry). These specifications are given Table 3.4. The steady-state temperature profile for the fuels are illustrated in Figure 3.1. The plot reproduces the profile for the hottest pin at core midplane and for the configuration using a pin diameter of 5.7 mm. Because of the low thermal conductivity, the CerCer fuel suffers from a steep temperature gradient (more than 300 K/mm). Despite the lower specific power, the CerCer fuel is the hottest of the three. The CerMet fuel remains relatively cold, reaching a maximum temperature of 1690 K. The margin to melting at operating conditions is 950 K. The larger gap size for the CerMet eliminates some of the advantage of its high conductivity. Maximum cladding temperatures occur at the outlet where coolant temperatures are highest. It is found that the reference case, with a tighter pin lattice and thin pin diameter, is not consistent with a permissible cladding surface temperature of 840 K as dictated by long-term cladding corrosion damage. To maintain the cladding temperature within the given limit, a higher coolant mass flow rate is desirable. This may be achieved by increasing the P/D ratio.

Table 3.3 ADS plant specifications

General	
Type of plant	Pool type
Reactor power	800 MWth
Coolant	LBE (44.5%Pb+55.5%Bi)
Reactor inlet temperature	573 K
Coolant inlet velocity	2.5 m/s
Reactor vessel	
Height	10 m
Diameter	6 m
Wall thickness	13 cm
Weight (incl. coolant)	~2500 ton
Primary system	
Steam generators	4 (integrated)
No. of pumps	4
Pump mass of inertia	400 kg·m^2
Distance between thermal centers of core and SG's	5.5 m

Table 3.4 Fuel pin description (at operating condition).

Fuel	CerCer	CerMet	Nitride
Average linear power, kW/m	25	35	35
Smeared density (%)	91	88	82
Fuel-clad gap width, μm	50	100	50

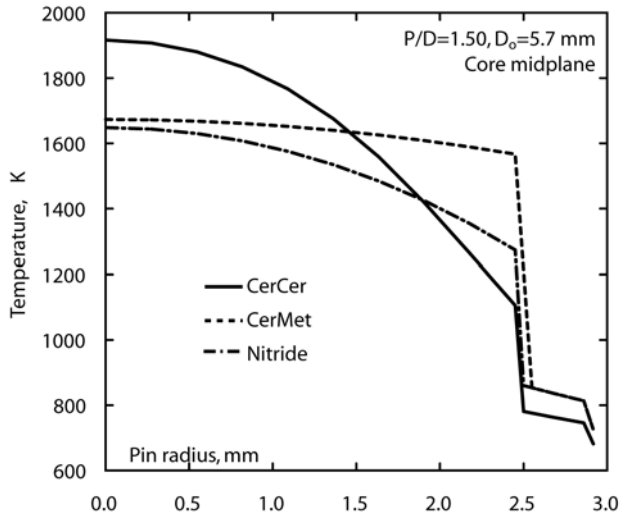

Figure 3.1 Steady-state temperature profile at core midplane

3.1.2 Unprotected loss-of-flow

It is assumed that all primary pumps are tripped in conjunction with failure of the shutdown system, i.e., the proton beam remains on. It is further assumed that the heat rejection system maintains core inlet temperature at the pre-transient value. The pump

moment of inertia has been optimized to soften the cladding-heating rate following pump trip. Figure 3.2 a) shows the coolant flow rate and the power history for a core configuration with pitch-to-diameter ratio equal 1.75. It is seen that the natural circulation flow reaches a quasi-steady value of 23-27% of initial flow at 50-60 seconds after the pump trip. The power decreases steadily during the entire transition to natural circulation conditions. Reactivity feedbacks are illustrated in Figure 3.2 b. For simplicity only the conditions for the CerCer fuel is shown. All three cores feature overall negative temperature-induced reactivity feedbacks. Reactivity feedback from radial expansion of the core (due to expansion of the grid support structure and heating of the duct walls at the above-core load pads) is the dominant negative feedback mechanism – it contributes about minus one dollar at quasi-equilibrium conditions. Axial fuel expansion reactivity differs somewhat between the fuels. As the coolant temperature increases it produces a positive reactivity effect. The resulting reactivity increment due to coolant expansion amounts to +0.5$ for the CerCer core and +0.4$ for the nitride. The coolant reactivity is however exceeded by the reactivity losses due to radial expansion and fuel elongation. The positive coolant expansion effect is largely compensated by the negative feedback from fuel elongation. The Doppler effect is insignificant. The overall effect of the reactivity feedbacks is not great, however. The power falls to approximately 95% of the initial value of 800 MWth when equilibrium is reached. The power response behaviour is similar among the cores.

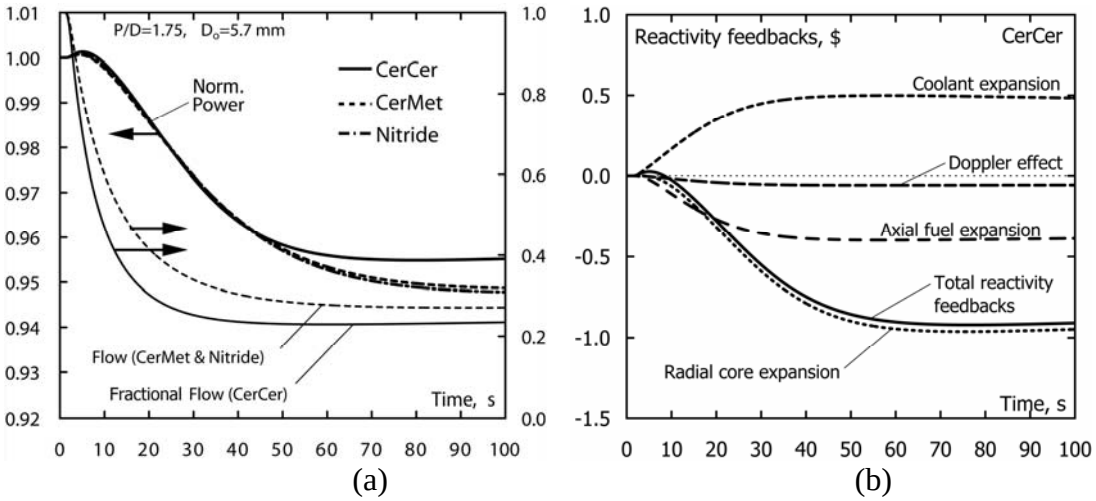

(a) (b)

Figure 3.2 Transient results for an ADS subject to unprotect loss-of-flow. (a) transient power and flow (b) associated reactivity feedbacks for the CerCer fuel.

Coolant boilout is not an issue with lead/bismuth. The primary concern under reduced flow conditions is whether the cladding exceeds design limits. Maximum fuel and cladding temperatures as function of pitch-to-diameter ratio and pin diameter are presented in Table 3.5. Lower cladding temperatures are promoted by higher coolant volume fractions. Larger distance between the fuel pins reduces the core pressure drop and in turn increases contribution from natural circulation. As a result, less forced flow is lost in a pump failure event. Cladding temperature is highest for the CerMet and nitride cores because of their higher power rating. The burst temperature for the cladding is 1330 K, listed in Table 3.2. For the smaller pitch design, the cladding exceeds the failure point within 30-40 seconds after pump failure, which leaves small safety margins. On the other hand, increasing the P/D ratio to 1.75 reduces cladding temperatures by more than 200 degrees. In that case, early cladding failure can be avoided. It is noted however, that damage prevention will eventually require the need

for shutdown and restored cooling capability since thermal creep rates increase rapidly at high temperatures. Since the fuel temperature increases along with the coolant temperature, the potential for fuel damage must also be considered. The temperature of the CerMet fuel reaches 2120 K for the reference configuration (P/D=1.50 and D_0=5.7 mm), which corresponds to a margin to melting of 500 degrees. The nitride fuel, which has lower thermal conductivity than the CerMet fuel but smaller gap size, is slightly colder (2080 K) leaving a margin to dissociation of 320 degrees. The CerCer temperature reaches close to the damage limit for the same configuration. Increasing the pin diameter should be considered in this case.

Table 3.5 Peak fuel and cladding temperatures at a time t=100 seconds during unprotected loss-of-flow transient as function of P/D and pin diameter.

Fuel	P/D=1.50 D_o=5.7 mm		P/D=1.75 D_o=5.7 mm		P/D=1.50 D_o=6.8 mm	
	Fuel	Clad	Fuel	Clad	Fuel	Clad
CerCer	2160	1330	2130	1160	1970	1200
CerMet	2120	1490	2030	1280	1920	1340
Nitride	2080	1490	1980	1280	1920	1340

3.1.3 Accelerator beam overpower

In accelerator-driven system designs, the neutron source is the controller of the chain reaction. Thus, it is appropriate to consider transients in which the accelerator beam intensity suddenly changes. This could for example happen due to a control system failure, accelerator malfunction, or operator error. Since the prompt adjustment time in an ADS is very short (tens of Λ), the power will respond instantaneously to source variation. In the study, it is assumed that the source intensity increases by a factor of 1.5 times the initial strength, which corresponds to the beam output capability at end-of-cycle. The ramp is initiated at t=1 second and halted at 1.001 seconds. The source is held constant thereafter. The transient is depicted in 0 along with fuel hot-channel temperatures. It shows the case with a pin diameter of D=6.8 mm. The primary concern in the overpower transient is fuel melting/dissociation. As indicated in **Error! Reference source not found.**, the configuration with the smaller P/D and smaller pin diameter is unacceptable for the CerCer fuel. The melting point is reached at 3 seconds after the beam insertion, which leaves little room for control action. Transient temperatures drop when a larger pin diameter is used because steady-state temperatures are lower with this configuration. It seems that the CerCer fuel needs to employ a larger pin diameter to avoid premature fuel failure. The temperature of the CerMet fuel reaches 2130 K for the same configuration, which corresponds to a margin to melting of 500 degrees – see Figure 3.3. The nitride fuel, which has lower thermal conductivity than the CerMet fuel but smaller gap size, is slightly colder (2080 K) leaving a margin to dissociation of 320 degrees. As seen in Table 3.6, the cladding remains well below the damage limit for all three fuel-systems and core configurations.

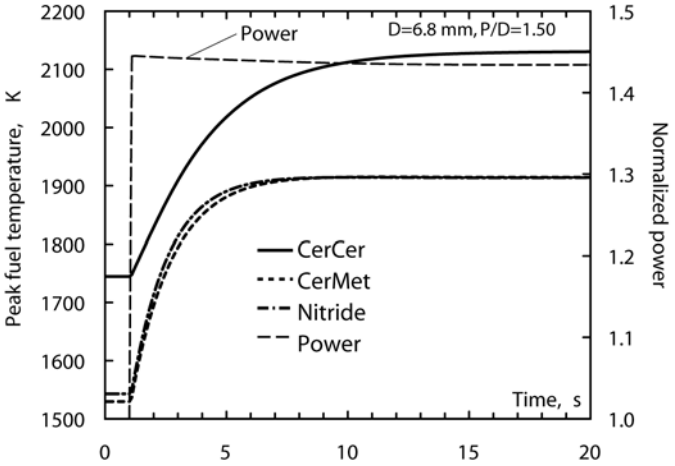

Figure 3.3 Transient power and fuel temperatures for beam overpower transient.

Table 3.6 Peak fuel and cladding temperatures at a time t=20 seconds during beam overpower accident.

Fuel	P/D=1.50 D_o=5.7 mm		P/D=1.75 D_o=5.7 mm		P/D=1.50 D_o=6.8 mm	
	Fuel	Clad	Fuel	Clad	Fuel	Clad
CerCer	2290	950	2300	850	2130	860
CerMet	2130	1090	2130	950	1920	970
Nitride	2080	1090	2070	950	1910	970

3.1.4 Coolant voiding

Major consideration is given to the potential threat of coolant voiding. Extensive voiding in a liquid-metal reactor (LMR) may be caused by a leak in the primary system, sudden release of fission gases, failure in the heat-transport system that causes gas bubbles to enter the coolant, or coolant overheating and vaporization. Usually, LMR plant designs are arranged with backup protection to mitigate the impact of vessel leakage or rupture, to the degree that large-scale loss-of-coolant accidents (LOCA) are extremely unlikely. Pool systems typically have a second guard vessel, and loop systems are normally double pipe and tank designs. Since the liquid-metal coolant is not pressurized under normal operation, a leak in the primary system will not automatically result in coolant boiling, as opposed to the situation in LWR's. In a sodium-cooled reactor, voiding may arise due to boiling out of coolant. This is prevented in a lead-bismuth system. In order for the lead-bismuth to get hot enough to boil (T_b=1940 K), temperatures have to be above the melting point of steel (T_m=1700 K). In that case, much larger reactivity changes may become available due to fuel or cladding relocation. Coolant can be expelled by the rapid escape of fission gases from ruptured fuel pins. Fission gas release is of concern for unvented and high burnup ADS fuels. Another possible mechanism for coolant voiding, without the precondition of steel melting, is the possibility of entrainment of air into the core from the cover gas region or steam/water during a failure in the steam generator, i.e., a so-called steam generator tube rupture (SGTR) event. In sodium plants, intermediate sodium-loops are introduced as a second physical barrier to minimize the consequences of SGTRs and to avoid violent chemical reactions between water and sodium in the primary system. Because lead/bismuth is chemically inert with water/steam, two-circuit designs are suggested,

with the steam generators located in the primary system. In such designs, there will only be one barrier to fail in order to get high-pressure steam into the primary system. It is noted that the pressure on the steam side can be as high as 100-150 bars and low pressure on the metal side, about 1 bar. Thus, a significant head is available to push steam into the primary system or cause overpressurization in the circuit, which could open further leakage paths. Normally, steam generator tube failures have a high enough probability occurrence to be considered in the licensing procedure. It is noteworthy that a steam-generator failure was the cause of a LOCA and radioactive contamination in a Russian lead/bismuth-cooled nuclear submarine in 1982 [74].

Here a transient test case study of a postulated steam generator tube rupture event leading to extensive cooling voiding is investigated. The core model and fuels are the same as in the previous unprotected accidents. In the following analysis, it is assumed that that the coolant is swept upwards through the core, beginning at the lower cold-leg region, and the void front moves at the average coolant velocity through the core (2.5 m/s). Since the total height of the core plus plenum regions is 2.5 m, the passage occurs in 1 second. The transient calculation uses a reactivity history based on progressive axial voiding of the core. It is assumed that the void spreads axially and simultaneously in all subassemblies. The reactivity effect, as function of axial void level, is illustrated in 0a. Note that the reactivity effect is strongest for the CerCer fuel and most positive when the core has been voided up to slightly below the top of the active fuel region. The reactivity insertion rate is highest at core midlevel. As a coincidence, the maximum reactivity insertion due to coolant void corresponded to the initial subcritical reactivity of the CerCer core.

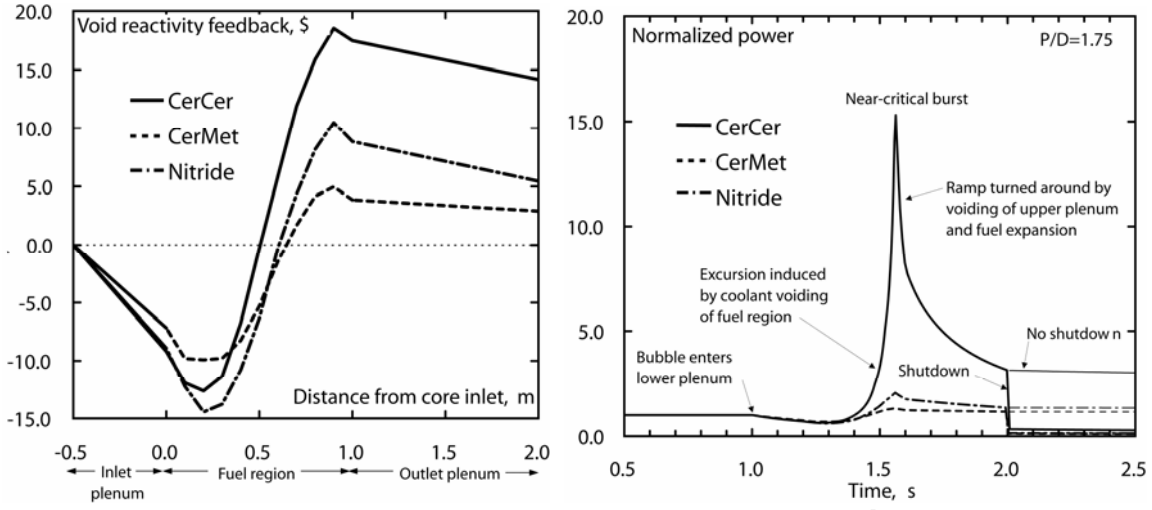

Figure 3.4 Transient results for a postulated steam generator tube rupture accident. (a) shows the reactivity effect ($) following progressive axial voiding of coolant beginning at the lower plenum.transient power. (b) Illustrates the transient power for the same accident.

The resulting power transient is presented in Figure 3.4 b. The steam bubble reaches the lower plenum at 1 second after the steam generator failure. Initially, the bubble passage produces a negative reactivity effect due to increased neutron leakage, as the lower plenum is voided first. The power will find its peak as the reactivity reaches its maximum. The reactivity at peak power, is –0.2$, -12.3$, and –6.8$, respectively for the CerCer, CerMet, and nitride cores, the corresponding peak power is 15.3, 1.3, and 2.1,

times the initial power. The power rise in the nitride and CerMet fueled cores is quite modest. The CerCer core, on the other hand, suffers from a sharp power peak. Except from coolant void, axial fuel expansion is the only feedback effect that has some impact on the transient. At peak conditions, the contribution from axial expansion provided an extra reactivity margin, which was sufficient to maintain the reactor in the subcritical state, thereby limiting the magnitude of the peak. Radial core expansion is too slow to be of any significance. It was found that the flux shape in the voided state was similar to the initial shape, and power peaking factors were even lower. The power rise is halted when the void has extended to the top of the core and begins to void the upper plenum region. Judging from Figure 3.4 b), voiding of the upper plenum plays a vital role in reversing the accident. It is assumed that the beam is shutdown after 2 seconds.
Due to the strong positive reactivity effect, the CerCer system is subject to a sharp power peak, while the power rise in the nitride and CerMet fueled cores is quite modest, which simply confirms the importance of a having a low coolant void reactivity value in a lead/bismuth system, despite of its high boiling temperatures.

3.1.5 Conclusions

In summary, the better thermal conductivity, higher melting point, and lower coolant void worth of the CerMet fuel combine to contribute to better inherent safety features. In none of the studied transients was the CerMet fuel close to melting. The swelling behavior and hardness of the molybdenum metal raise safety concerns regarding fuel-cladding mechanical interactions. The approach so far has been to increase the initial fuel-cladding gap to accommodate fuel swelling. The CerCer fuel suffers from low thermal conductivity and uncertain melting behavior, which limits both the achievable power density and predicted performance during overpower conditions. In addition, the reactivity void worth of this fuel is relatively high in comparison with the other fuels, which is a safety dilemma. Even though the fuel is set to operate at a lower linear power, hot channel fuel temperatures are fairly high, leaving a limited margin to melting. This margin is easily exceeded in an overpower accident and the fuel reaches close to melting during unprotected loss-of-flow conditions. The principal problem with the nitride fuel, with regards to the safety performance, is its tendency to dissociate at low temperatures. A steam generator tube rupture event was identified as a potential threat, which could lead to extensive voiding in current accelerator-driven design proposals. Which confirms the importance of a having a low coolant void reactivity value in a lead/bismuth system, despite of its high boiling temperatures.

3.2 PERFORMANCE OF ADS IN SUPER-PROMPT CRITICAL TRANSIENTS

Even if the probability for prompt critical transients can be made very low, the safety analyses usually require them to be investigated. Considering the high reactivity potentials available by core compaction in a fast neutron spectrum reactor it is always possible to postulate an accident that will proceed into a prompt critical state. The resolution for the large FBR's was to demonstrate a low energetic potential (within the capabilities of the containment) of such accidents [75]. The large oxide cores relied on the presence of a strong Doppler effect to limit the energy yield (and pressure buildup) in a prompt critical reactivity transient. In such cores, the negative reactivity is provided by the Doppler broadening of resonances in primarily ^{238}U resulting in a relative increase in resonance capture over resonance fission. Since the Doppler effect is inherent in the fuel, the feedback mechanism is completely passive. The resulting

reactivity effect is applied immediately since the Doppler broadening occurs simultaneously with the temperature change. As is well-known, the Doppler effect is small for fuels dominated by MA. Hence, the prompt negative effects, might be insufficient to stop an excursion before energetic disassembly occurs. Here we treat a classical problem of reactor excursions, induced by a rapid reactivity ramp in systems with different prompt negative feedbacks. It may be postulated that the accident is caused by a loss-of-coolant (e.g. as a result of a major break in the primary system) and that some fuel is melted and the core collapses by gravity forming a supercritical configuration (traditional Bethe-Tait scenario).

Figure 3.5 illustrates the essential characteristics of the transient in a MA-fueled ADS. The results are compared with calculations for a conventional sodium-cooled and MOX-fueled fast reactor ($U_{0.8}Pu_{0.2}$) presented in the same graph. Consider at first the ADS with initial k_{eff}=0.97. The transient is driven by a linear reactivity insertion, 100 \$/s (0.167 Δk/s), a value which is frequently related to core compaction/meltdown phenomena. It is further assumed that this reactivity ramp continues unterminated. The value for the Doppler constant (T*dk/dT) as well as the effective delayed neutron fraction are chosen to simulate the conditions in the respective cores. The Doppler constant in the fast spectrum MA core ($Pu_{0.4}Am_{0.6}$) is taken as $2.0 \cdot 10^{-4}$ with a β_{eff}=0.167 %. The Doppler constant for the oxide fast reactor is $8.1 \cdot 10^{-3}$ [69], which is about 40 times larger than the MA core. The corresponding ramp rate for the fast reactor is 50 \$/s since the effective delayed neutron fraction (β_{eff}=0.34 %) is about two times larger than the MA core. The Doppler effect contribution is assumed proportional to 1/T, as in the case of large oxide-fueled fast reactor, where T is the average fuel temperature in the core. The fuel heat-up is treated for the simple case of adiabatic boundary conditions for any additional heating above steady-state levels. This is a reasonable approximation considering the overall speed of the transient. The steady-state operational power density is ~1.3 W/mm^3, which is fairly typical for the FBR as well an ADS employing oxide fuel. During the transient, around 86% of the additionally produced fission energy is deposited in the fuel (~8% of the heat is deposited outside the fuel and 6% appears as decay heat which is not immediately affected by the transient). For simplicity, equal prompt neutron generations times (Λ=0.81 μs) are applied for both cores. Reactivity contributions from core disassembly are not treated. The reactor behavior is described by the standard point kinetics equations with six delayed neutron groups coupled with a temperature dependent Doppler feedback.

In the fast reactor the reactivity quickly reaches a prompt critical state. Prompt criticality is established around 20 ms after the onset of the transient. It follows that the power increases rapidly at first. However, as the temperature in the fuel increases, the negative Doppler feedback compensates the ramp-induced reactivity; this causes a decrease in reactivity and a corresponding power reduction. In the example given, the fast reactor is superprompt critical for 6 ms in connection with the first pulse. After the power is reduced, the rate of reactivity reduction by Doppler feedback slows down while the ramp drives the reactor to prompt criticality again, allowing for a second power surge. This causes the familiar damped oscillation in reactor power, where the maxima and minima occur when the reactivity passes through β. As the oscillations die-away, in the given example, the reactivity finds a balance at a level slightly below β. Since the Doppler effect contribution decreases with temperature (1/T dependence), the power tends to increase with time, but at a much slower rate than if the Doppler effect had not been present. It should be noted that progression with ever increasing power is physically unrealistic. At some point the ramp is terminated and the excursion is turned around by fuel displacement, possibly involving some vaporization. As first discussed

by Bethe and Tait [76], rapid fuel motion is resisted by inertial effects and this may prolong the shutdown process, in which additional energy can be produced to enhance the very fast excursion. Under these conditions the Doppler effect is very effective [77], by reactivity reduction to subprompt critical values resulting in substantially lower energy releases.

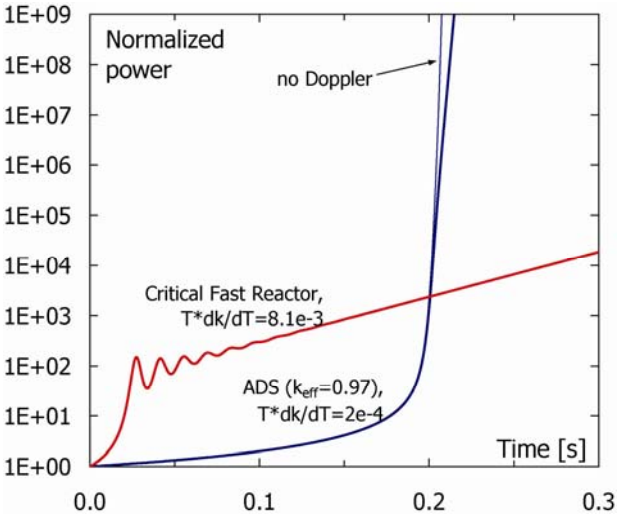

Figure 3.5 Effect of Doppler feedback on prompt critical transients induced by a reactivity ramp insertion. Transients initiated from operating conditions in a conventional fast reactor with a large Doppler constant ($T^*dk/dT=8.1\cdot10^{-3}$) and an ADS ($k_{eff}=0.97$) with a small Doppler feedback ($T^*dk/dT=2.0\cdot10^{-4}$). Core disassembly is neglected.

The transient in the ADS is quite different according to the magnitude of the Doppler reactivity effect and the level of subcriticality. Since the reactivity in the ADS starts at a low value (-\$18.5), the power increases slowly initially. Prompt criticality is reached at 195 ms. Because of the weak Doppler feedback the reactor settles on a fast period above prompt critical (\$1.4). As can been seen from the figure, the Doppler effect has an overall small effect on the transient. While no attempt has been made to calculate the disassembly process in this study, it is well-known [77] that a small Doppler can pose a serious threat to the containment structure in the event of a hypothetical core disruptive accident in a large fast reactor. At this point, it may be added that core disassembly generally starts when fuel boiling begins. The energy released during core disassembly is sensitive to the fuel boiling point [78], which may differ between the investigated fuels, but depends also on the fuel temperature at the start of the excursion. Higher starting temperature together with a low Doppler coefficient generally causes a reduction in the energy release as less reactivity is inserted [77]. One may realize that, starting from a highly subcritical state, the additionally produced heating during the subcritical reactivity insertion phase will cause higher fuel temperatures at the start of the excursion. Thus, subcriticality may in principle advance the shutdown process and limit the energy release. Nevertheless, it was found that for the rapid reactivity ramp (100 \$/s) the fuel temperature rise prior to approaching prompt criticality was rather small ($\Delta\bar{T}_f \sim 170$ K). Hence, the majority of the temperature rise occured in the prompt critical burst which suggests that the potential benefit may be small for rapid reactivity ramps (~100 \$/s). The subsequent fuel displacement would then mainly occur during the excursion phase and hence differences in the Doppler feedback plays a crucial role.

It was found that the subcriticality is more effective in raising the starting temperature for slower reactivity ramps. For example, a reduction of the ramp rate from 100 \$/s to 10 \$/s increases the average fuel temperature by ~2700 K at the onset of prompt criticality.

Longitudinal thermal expansion of the fuel column is a second feedback effect that may contribute with negative reactivity in a fast power excursion. This was not taken into account in the examples presented above. In most cases, fuel expansion may be considered as a prompt reactivity effect, although it is subject to certain time delay conceivably of some importance under disassembly conditions. It is a neutron leakage effect caused by a change in fuel density. Expansion coefficients for a standard MOX-fueled fast reactor and MA oxide-fueled ADS were calculated in [69]. It was found to be similar for both cores and equal to $-0.2 \cdot 10^{-5}$ $\Delta k/T$. This number refers to uniform temperature increase and axial expansion throughout the reactor. It is calculated for the intact core. Hence, it is well-defined during the startup period of the accident, but could be very misleading during the excursion phase involving partial melting. A partly melted core cannot be expected to possess the usual negative reactivity feedbacks from solid fuel expansion, so direct application to the meltdown problem may not be applicable. It is still of some interest to investigate the basic influence, partly due to its traditional usage in fast reactors. It may be noted that, thermal expansion effects were frequently included in the prompt excursion analyses of the early fast reactors (GODIVA, Fermi, EBR-I and EBR-II). These small and highly-enriched reactors essentially relied on this mechanism for early shutdown. Its effect on the present cores is illustrated in Figure 3.6. Apparently, when axial expansion is included in the feedback description the characteristics of the transient are quite similar in the fast reactor core and the ADS. The essential difference is then the timing of the prompt critical burst. The results indicate that axial fuel expansion can stabilize a prompt critical accident in the ADS. But, a word of caution is added as the results are based on the simplified assumption of axial expansion reactivity feedback calculated for an intact core and as being proportional to the temperature rise during the entire accident.

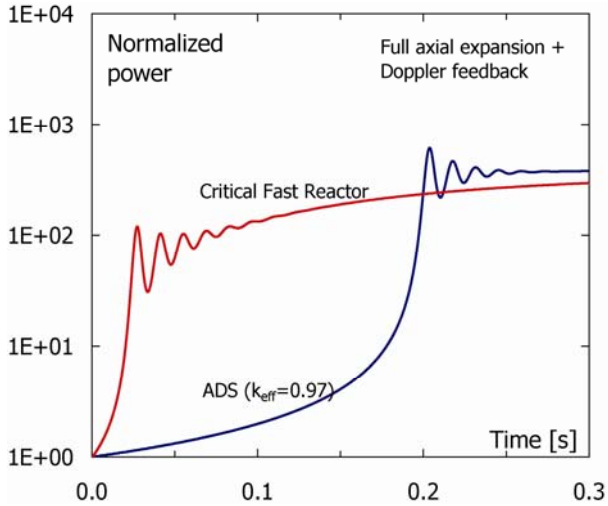

Figure 3.6 Prompt critical transients in a conventional fast reactor and ADS (k_{eff}=0.97) with axial expansion reactivity feedback included from the beginning through the entire transient.

To summarize, the analyses add to the statement that Doppler feedback in the typical minor actinide fueled ADS is too small to influence the development of a prompt critical accident. For slower reactivity insertions, subcriticality could possibly facilitate

faster shutdown, but may be less effective for fast insertions. To some degree axial expansion of the fuel can compensate for a small Doppler coefficient, but it cannot be considered as reliable as the Doppler effect in the general case. It depends on the engineering design and is subject to uncertainties in the thermo-mechanical behaviour of the fuel and overall conditions in the core.

3.3 SEISMIC ANALYSIS OF REACTOR VESSEL

A reactor pool layout is used to take advantage of a simple tank design and to avoid any nozzles and pipes of a loop system. The benefits are reduced probability for pipe rupture (LOCA), large heat capacity, and reliable natural circulation. However, pool designs have drawbacks associated with the fabrication of a large vessel. Safety concerns are related to the use of a large vessel containing heavy liquid metal. Heavy liquid metal increases the mechanical loading on the vessel as a result of earthquake excitation. While a tall vessel is desirable to promote natural circulation it increases the cost and decreases seismic stability. The required vessel thickness increases with the vessel size and weight of the contained liquid. According to one report [79], wall thickness for type 316SS is limited to 130 mm by manufacturing capability. Thus, to ensure acceptable stress levels under a seismic event, it is necessary to limit the size of the vessel. A rough estimate of the allowable vessel height was calculated based on a seismic model suggested by Buongiorno, et al., [80]. It is assumed that the vessel has an outer diameter of 6 m and contains lead-bismuth with an average density of 10.2 g/cm^3. The vessel is made of grade 316 stainless steel with a steady-state operating temperature of 693 K. The vessel is subject to an earthquake with a peak ground acceleration of 0.5g (horizontal motion). This criterion is adequate for licensing purposes of most sites in the U.S. The calculated peak stress intensity is compared with limits specified by the ASME code for 316SS. The preliminary analysis suggests an allowable vessel height in the range 10-12 m, as illustrated in Figure 3.7. It should be noted that this estimate is

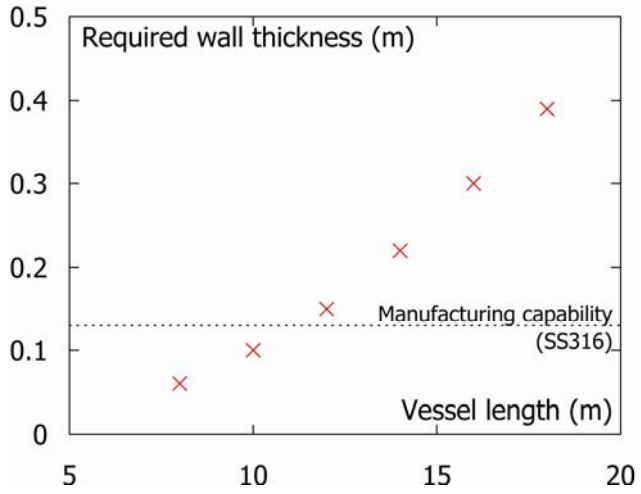

Figure 3.7 Required vessel wall thickness to withstand seismic loading of reactor vessel filled with lead/bismuth

based on a tentative maximum wall thickness of 130 mm for a vessel made of 316SS, as compared to thicknesses around 200-250 mm for PWR systems (utilizing carbon steels). It is found that, a wall thickness of 250 mm should admit a vessel height around 15-16

m, which indicates a rather high sensitivity of the stress level on the vessel height. The dependence on the vessel diameter is not strong, however. The study also depends on seismic load conditions, which are site dependent. Use of bottom horizontal structure support and/or base isolation could enhance seismic performance, which may lead to significant reduction of building accelerations in an earthquake. This was recently shown in the application to an ADS plant [81].

3.4 THERMAL EFFICIENCY OF LBE SYSTEMS

Although production of power has never been the principal object of an ADS, enough attention has been given to the matter to mention an important feature of using LBE as coolant: the attainment of high-temperature operation. According to the 2nd law of thermodynamics (by Lord Kelvin, l824-l907), not all the supplied heat into a heat engine can be used to do work and there is no perfect heat engine. The Carnot cycle (after the Frenchman Sadi Carnot, 1824) is the most effective cycle conceivable, and sets the limiting efficiency of any work-producing cycle. In a nuclear power plant, it determines the maximum fraction of heat produced in the reactor that can be transformed to mechanical power at the turbine shaft. Although not recognizable in practical form, it serves as a standard of comparison for all heat cycles. A basic principle is that the thermal efficiency may be raised by raising the temperature at which energy is received by the cycle, T_H, or lowering the temperature at which energy is rejected, T_C, and it holds for all cycles. It may be expressed as:

$$\eta = 1 - \frac{T_C}{T_H}$$

Apparently, an effective heat engine must not only develop heat, but must develop heat at a high temperature in order to convert the heat generated to useful work with high efficiency. For the LWR the mean temperature of heat addition is close to the evaporation temperature. Recall that the evaporation temperature in the secondary circuit (PWR) and primary circuit (BWR) is around 276-286ºC corresponding to a pressure of about 60-70 bar. In a boiling water reactor, production of superheated steam is restricted because of the problems of adequately cooling the fuel elements (dryout). In the PWR, the primary coolant temperature cannot be raised above the water saturation temperature, which is set by the vessel design pressure (342ºC at 150 bars). The feasibility of raising the evaporation temperature by increasing the boiler pressure (in the steam-generator of a PWR or vessel of a BWR) has not been considered worthwhile so far. The basic principle of the steam-cycle of an LBE-cooled ADS is the same, but the temperature of the primary coolant is significantly higher than in a LWR. Thus, the heat may be injected into the steam-cycle at a much higher temperature, in a way resembling the characteristics a conventional-fueled power plant. The temperature in the primary circuit is essentially limited by material considerations - not by the coolant boiling temperature. With regards to steel corrosion, the LBE temperature during normal operation should not exceed 550-600ºC, depending on the type of steel. A reasonable assumption is that the weighted average temperature of heat addition for all the processes is 100 degrees lower than the LBE outlet temperature[1], which would then correspond to 450ºC (723 K). If we further assume that the heat is removed in the

[1] The temperature of heat addition is the weighted mean temperature of heat injection considering all heating processes (feedwater heating, vaporization, and superheating). Note that the LBE-system must operate with superheated steam. This in turn leads to higher turbine efficiency and reduces blade erosion (as the steam is drier).

condenser at a temperature around 27ºC (300 K), and this is the same, regardless of whether the plant is a LWR or an ADS[2], the efficiencies appears as in Table 3.7. Of course, these are ideal values expressed by the Carnot cycle (assuming isothermal heat addition/rejection and isentropic expansion/compression). In reality, the thermal efficiency of a LWR is around 33%. It nevertheless shows that the LBE-system may offer roughly 25% higher thermal efficiency relative to the LWR.

Table 3.7 Comparison of maximum thermal efficiencies (Carnot cycle) in LWR vs. LBE-cooled ADS. The average temperature of heat addition corresponds to the evaporation temperature (LWR) and the LBE outlet temperature minus 100 degrees (ADS). The condensate temperature is 27ºC (300 K) in all cases.

Reactor type	T_H (ºC)	T_H (K)	η
BWR/PWR	286	559	0.46
LBE-cooled ADS	450	723	0.59

[2] Observe that the feed-water is normally pre-heated in a LWR before it is passed to the steam-generator (PWR) or vessel (BWR) in order to further "Carnotise" the cycle (i.e. to increase the average temperature of heat injection) and such an arrangement is desirable for the LBE-system as well. Apart from the beneficial influence on the thermal efficiency, feed-water preheating is required to reduce the risk of LBE-freezing in the steam-generators.

4 REACTOR BASED TRANSMUTATION

4.1 COMPARATIVE STUDIES OF ENDF/B-6.8, JEF-2.2 AND JENDL-3.2 DATA LIBRARIES BY MONTE CARLO MODELING OF HIGH TEMPERATURE REACTORS ON PLUTONIUM BASED FUEL CYCLES

In the previous studies [45-46] we proposed a scenario in which Light Water Reactors (LWRs) waste fuels the Gas Turbine - Modular Helium Reactor (GT-MHR) [47-54]. Within this scenario the LWRs waste is reprocessed by uranium extraction (UREX) to build two different types of fuels, the Driver Fuel (DF), rich in fissile isotopes (mainly ^{239}Pu and ^{241}Pu) and the Transmutation Fuel (TF), rich in capturing nuclides (^{238}Pu, ^{240}Pu, ^{242}Pu and ^{241}Am). Table 4.1 reports the initial composition of fresh DF. Spent DF is used, with some addition of set-aside Am-Cm from UREX, to manufacture fresh TF; whereas, the spent TF, after a cooling period, is sent to a geological repository. We analyzed a fuel cycle with refueling and shuffling periods of one year and an in-core fuel residency time of three years. With a progressive radial shuffling of fuel from the inner rings to the outer ones, the fuel composition reaches the equilibrium after 12 years of operation since the beginning of life of the reactor [45]. Therefore, we performed all the numerical simulations relevant for this study during the 12th year. The transmutation of: 94% of ^{239}Pu, 61% of Pu and 53% of all actinides[1)], makes the GT-MHR a quite attractive proposal for the destruction of LWRs waste.

Table 4.1 Initial composition of the fresh DF.

Isotope	*Atomic percentage %*	*Mass [kg]*
^{237}Np	1.91	16.49
^{238}Pu	0.56	4.849
^{239}Pu	21.11	184
^{240}Pu	8.5	74.36
^{241}Pu	3.09	27.16
^{242}Pu	1.87	16.49
^{16}O	62.96	36.70

In the present studies we performed a comparative analysis of the burnup results obtained in our previous studies [45-46]; we divided the work into accuracy and precision studies. In the accuracy studies, we equipped the Monte Carlo burnup code with different nuclear data libraries during the 12th year, when the refueling and shuffling schedule set the equilibrium of the fuel composition. In the precision studies, we repeated the simulation of the accuracy studies 20 times with a different pseudorandom number stride and the same nuclear data library.

4.1.1 The Gas Turbine – Modular Helium Reactor

The current design of the GT-MHR is based on four modules of 600 MW_{th}; in the present work, we focused on the performance of a single module. The benefits of the helium-cooled graphite-moderated reactors are several: passive safety mechanism, low

cost, flexibility in the choice of fuel, high conversion energy efficiency, high burnup, resistant TRISO fuel cladding and low power density.
The GT-MHR has been modeled in the numerical calculations as a cylinder, with a radius of 4 m and a height of 10 m, filled by a matrix of hexagonal blocks of graphite and fuel. The fuel is disposed along three concentric rings each of 36 hexagonal blocks (top of Figure 4.1) and it covers just 7.93 m of the height of a hexagonal block; the remaining 2.07 m, 1.035 m at top and at bottom, contain only pure graphite blocks, which act as blankets. The side of the hexagonal blocks is 20.8 cm. In each fuel block there are 108 cooling helium channels, 144 DF pins and 72 TF pins (Figure 4.1); therefore, the ratio between DF pins and TF ones, as well as their volume ratio, is 2:1. The cooling channels have a radius of 0.797 cm, whereas the driver and transmutation pins have a radius of 0.622 cm; the cooling channels surrounding the fuel pins have an external radius of 0.635 cm. Both the driver and transmutation pins consist of a graphite matrix filled with triple isotropic (TRISO) coated layers fuel particles (fig. 1). We set the packing ratio (the fraction of the TRISO particles volume over the total volume of the fuel pin) to 14.41% for DF and to 32.92% for TF. Whereas the packing ratio of the fuel central sphere (kernel) (the fraction of the fuel volume over the total volume of the fuel pin) of TRISO particles is 0.7% both for driver and transmutation fuel; therefore, the volume ratio between DF and TF is 2:1, since the number of DF pins is twice as that one of TF.
TRISO particles are microscopic spheres, with a radius of few hundreds micrometers, of fuel oxide covered by a cladding structured into four different layers: porous carbon layer, inner pyrocarbon, silicon carbide and outer pyrocarbon. The porous carbon layer attenuates fission recoils and provides the volume for the gas fission products; the inner pyrocarbon layer acts as substrate for the silicon carbide; the silicon carbide layer retains fission products and supplies mechanical strength; the outer pyrocarbon covers eventual defects of the silicon carbide layer.
A detailed description of the geometric features and materials composition of the GT-MHR modeled in our numerical simulations has been reported in detail in our previous papers[1-2]. Let us note that in the numerical modeling of the reactor we have done only three major approximations compared to the real system. The first approximation was that we did not consider the axial shuffling in our fuel shuffling strategy. The axial shuffling is important for the GT-MHR optimization and real operation; however, for the aim of this paper the axial shuffling was not essential. In addition, we did not model the control rods, both the 36 operational ones and the 18 reserve shutdown rods; nevertheless, at the year of equilibrium, the reactor is very close to criticality and the breeding of fissile isotopes keeps k_{eff} almost constant and close to criticality. Finally, we did not consider that the real distribution of TRISO particles in the fuel pin might be far away from a square lattice due to manufacture process and this might attach both neutronics and TRISO particles resistance under irradiation.

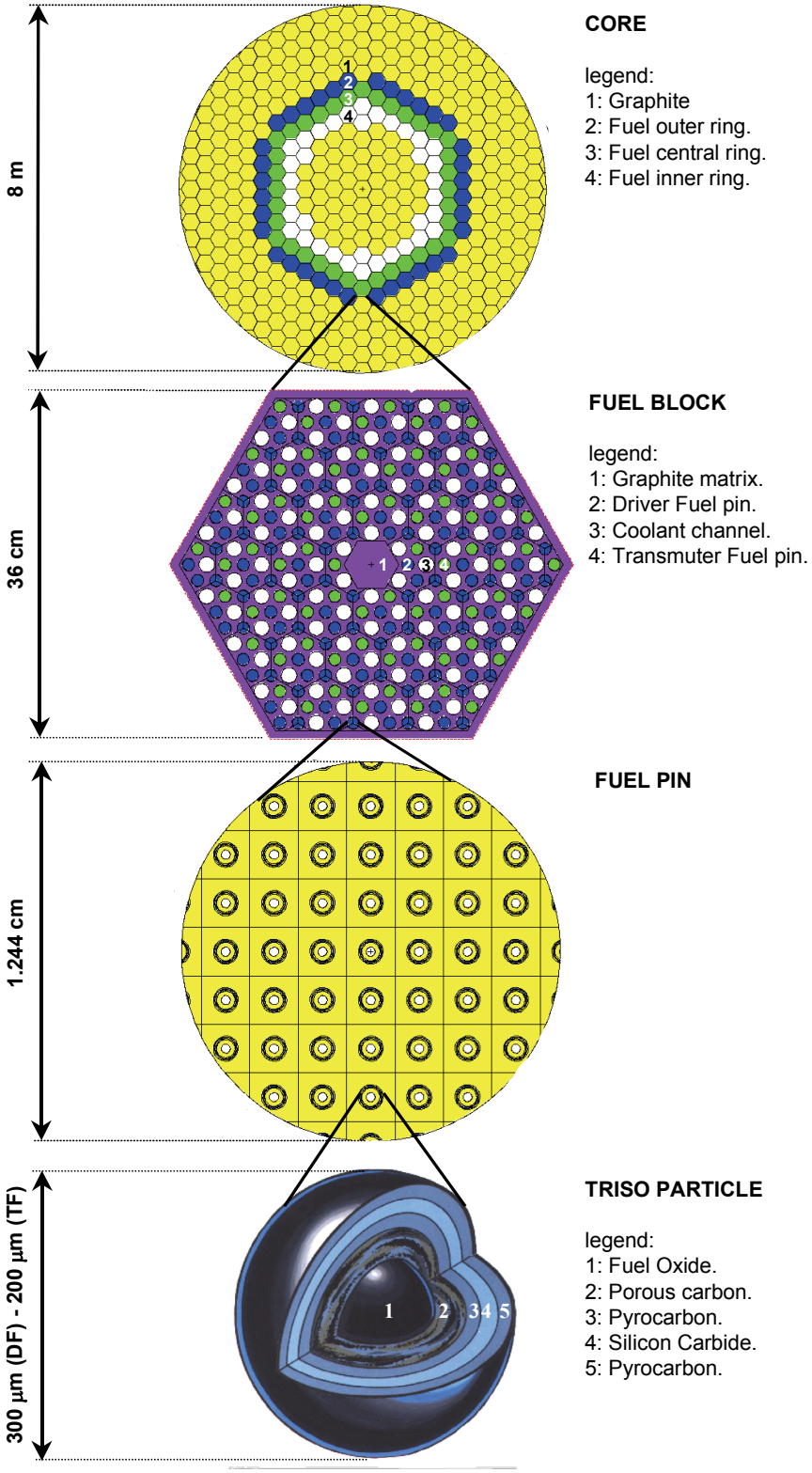

Figure 4.1 The model of the DB-MHR used in simulations.

4.1.2 The Monte Carlo Continuous Energy Burnup Code

We performed all burnup calculations by the Monte Carlo Continuous Energy Burnup (MCB) code [55-57], which has been developed in collaboration of the Royal Institute of Technology of Stockholm and the University of Mining and Metallurgy in Krakow during 1990's. The MCB code merges the MCNP code [22] with a new Transmutation Trajectory Analysis (TTA) code: the MCNP-module performs the transport simulations, whereas the TTA-module does the density and composition evolution ones. At the beginning of each time step, the MCB code calculates all transmutation probabilities for each nuclide by using the MCNP track length estimator of neutron flux, the neutron cross sections and the decay data. The transmutation probability is evaluated for each nuclide, up to a default threshold probability of the transmutation branch equal to 10^{-10}, by solving the Bateman equation. All transmutation probabilities are evaluated using continuous energy cross sections which take into account also energy dependent fission products buildup and isomer formation, e.g. ^{148m}Pm, ^{242m}Am and ^{244m}Am. The decay schemes for over 2400 nuclides are based on the library Table of Isotopes[15] complemented with the data form the ORIGEN code[16]. After evaluating the transmutation probabilities for all isotopes, the MCB code accordingly updates the material density and composition; then, the time step advances and a new MCNP run updates the neutron flux, which is normalized to the required power level. The neutron flux, cross sections, mass and transmutation probabilities are assumed constant within a time step; in addition, all isotopes with a half-life shorter than 1000 s are treated as prompt, though this default value can be changed at expense of computing time. The user can define manually the length of a time step; otherwise, the code automatically calculates it by the change in the k_{eff} or in the heating rate between two consecutive steps.

MCB allows three different types of materials: transport, burnup and residual materials. The transport material data (transport neutron cross-sections) are used in the neutron transport calculation; whereas, the burnup materials are only produced and decaying in the system, unless they accumulate to such a quantity that they can affect the neutron transport (the discrimination is determined by their contribution to the total neutron cross section, the default value is 10^{-10}). Both transport and burnup materials have determined densities; by contrast, residual materials (e.g. very short living isotopes) have no density associated with them because they are used only to calculate the transmutation trajectories. In addition to the above material cards, the MCB code allows also a "MIX" card that allows different materials to be composed into a mixture.

The MCB code normalizes the neutron flux to the total thermal reactor power, in the case of critical calculations, or to a power of an external neutron source, in the case of subcritical calculations. Both the neutron and gamma heating contributions are taken into account. By specifying a zero power, the code performs natural decay calculations.

Monte Carlo methods are by their statistical approach very processor-time consuming. Combining Monte Carlo with burnup calculations increases drastically computing time; therefore, the MCB code uses some speed up procedures. At the beginning of life, MCB starts a *quick run* calculation in order to load into the RAM memory the data of the emerging nuclides. This reduces significantly the computing time because, as general rule, RAM memory access is 10 times faster than a hard disk access. After the *quick run* step calculation MCB starts the *regul*ar burnup calculation.

The current version of MCB calculates (MCB1c2): reaction rates, reaction channel probability, fission product distributions, radiation heating, decay heating, nuclide

density evolution and radiotoxicity. In the present studies, we used the version 1c of MCB.

4.1.3 MCB accuracy studies

The first version of the Japanese Evaluated Nuclear Data Library (JENDL) was released in 1977 and it was mainly addressed for the needs of Fast Breeder Reactors (FBRs); it contained only transport cross sections for 72 isotopes. Data for fission products have been added in 1985 (JENDL-2) and it brought the total number of isotopes up to 181. Further fission products set the number of nuclides to 324 in 1990 (JENDL-3.1). The latest version of the library is JENDL-3.3, which has been released in 2002 and it contains transport data for 337 isotopes and also improved data for medium-heavy and actinides nuclides [61].
The first version of the Joint Evaluated File (JEF) has been completed in 1985 mostly by merging the United Kingdom nuclear libraries and the CEA ones; at that time, the radioactive decay data contained about 700 fission products. The second version of the European nuclear data library came in 1990. JEF-2.2 has been released in 1993: it contains radioactive decay data for 2345 nuclides, including 860 fission products and transport data for 313 nuclides [62]. In 2002, the Nuclear Energy Agency (NEA) released the Joint Evaluated Fission and Fusion nuclear data library (JEFF) version 3.0, which contains 340 isotopes with neutron transport data.
The first Evaluated Nuclear Data File version B (ENDF/B) has been completed in the USA during the 1960's; later, in the 1990's, further improvements produced version 6.8, which is also the latest release [63].
All our numerical simulations have been performed by JENDL-3.2, JEF-2.2 and ENDF/B-6.8. These libraries have temperature dependent cross sections for temperatures of 300, 600, 900, 1200, 1500 and 1800 K.
Table 4.2 shows the number of isotopes with available transport data between different libraries: it reports that all the three libraries contain almost the same number of isotopes. The Japanese library contains the largest number of nuclides with angle-dependent neutron emission spectrum data, about 60; whereas the American and European ones respectively have 53 and 9[20)].

Table 4.2 Comparison of transport data available within different nuclear data libraries.

	JENDL-3.2	**JEF-2.2**	**ENDF/B-6.8**
Number of isotopes	337	313	329

Table 4.3, which reports a comparison of missing data for heavy nuclides (above Th) between the three different nuclear data libraries, shows that some of the Pu isotopes are missing in the Japanese library, even if all of them are of minor importance.

Table 4.3 Comparison of missing isotopes (X) for different nuclear data libraries.

Isotope	JENDL-3.2	JEF-2.2	ENDF/B-6.8
^{227}Th		X	X
^{228}Th		X	X
^{229}Th		X	X
^{232}Pa		X	
^{236}Np		X	
^{237}Pu	X		
^{244}Pu	X		
^{244}Am		X	X
^{250}Cm		X	X
^{250}Bk		X	X
^{253}Cf	X		
^{254}Cf		X	X

To take advantage of all three nuclear data libraries and all available isotope data we combined those libraries into three enlarged libraries:

- JEF+JENDL+ENDF/B+DCL+EAF
- JENDL+ENDF/B+JEF+DCL+EAF
- ENDF/B+JENDL+JEF+DCL+EAF

In each of the three enlarged library, the isotope data are searched in order of appearance, if the isotope is not found in the first library (e.g. JEF), the second library is checked (e.g. JENDL) and so on. The standard MCNP data (the Data Library Collection, DLC-200) and activation data library (the European Activation File, EAF-99) have been appended to all the three enlarged libraries.
In a fuel cycle without burnable poison, the isotopic composition reaches its equilibrium after 12 years of operation. During the approach to equilibrium, the calculations have been performed by using only the enlarged library primary based on the JEF data. We focused on the accuracy and precision studies only after the beginning of the 12th year, at which we separately used the three libraries.
Figure 4.2 plots the monthly evolution of k_{eff} from the beginning of the 12th year up to 330 full power operation days; it can be noted that the difference between libraries diverges with the increase of time. The values obtained by JENDL are in between ENDF/B (bottom curve) and JEF (top curve). In order to produce the data of Figure 4.1, the MCB code has run the MCNP-module 12 times, every 30 days, and each time it simulated 4.5 millions of neutrons distributed over 150 MCNP k-code cycles, including 40 inactive ones. Let us highlight that the statistical errors, which correspond to the standard deviation and are indicated by the vertical bars, do not overlap with the adjacent curves.
Figure 4.3 shows the neutron flux averaged allover the reactor core calculated with the three different libraries. It shows that the flux calculated by the ENDF/B library is higher than those calculated by the other two libraries, which cross each another. In

Figure 4.3, the maximal difference between libraries, during the 11 months, keeps quite constant around the average value of 7%.

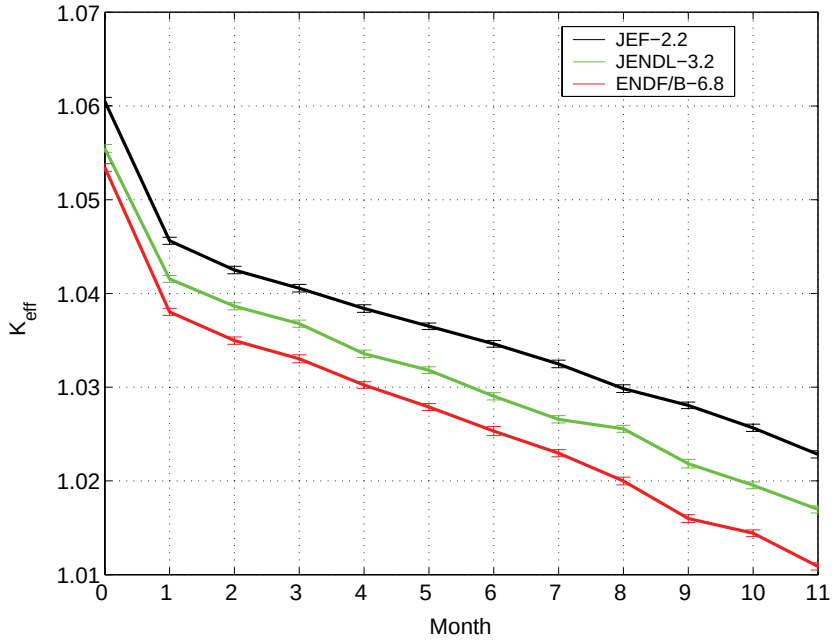

Figure 4.2 Monthly evolution of k_{eff}. Vertical bars on the curves represent the standard deviation. All values have a standard deviation lower than $4.5 \cdot 10^{-4}$.

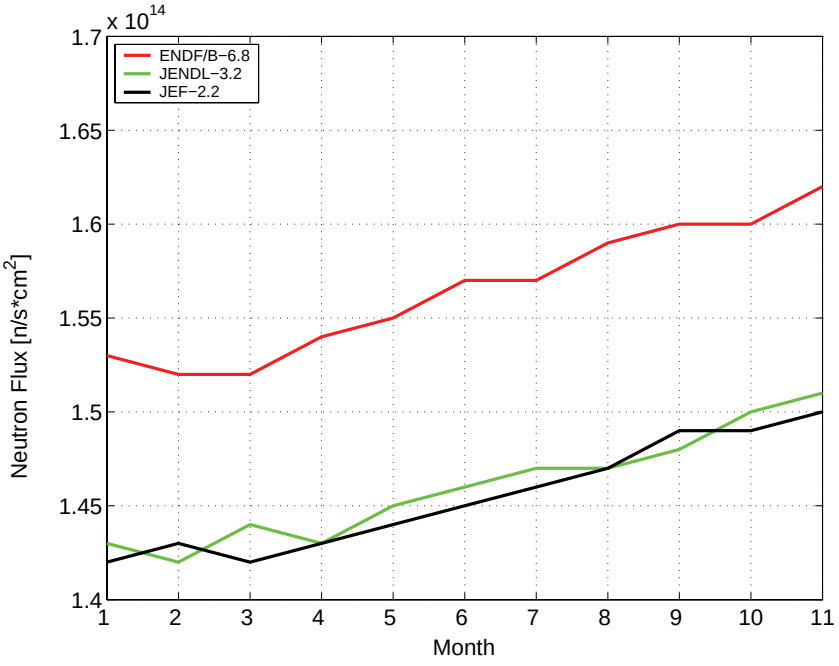

Figure 4.3 Monthly evolution of neutron flux.

Figure 4.4, presents the monthly evolution of the of ^{239}Pu mass in the reactor; the results indicate that there are no significant discrepancies between libraries for this isotope. ENDF/B results slightly diverge in the final months of the cycle but the difference is small; however, it is very difficult to estimate error propagations for mass evolution

calculations. Results of Figure 4.4 are consistent with those ones of Figure 4.3, because ENDF/B exhibits a higher neutron flux, which consequently produces a higher burnup of ^{239}Pu.

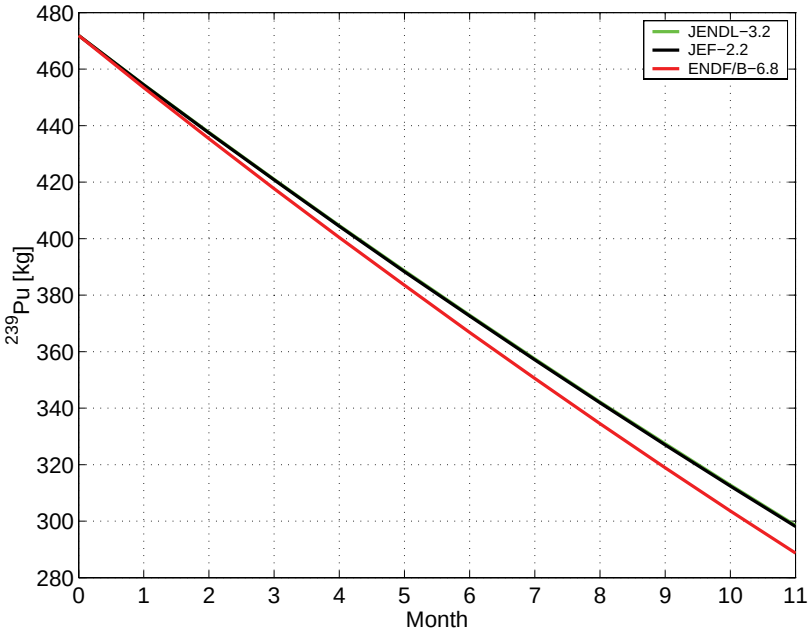

Figure 4.4 Monthly evolution of ^{239}Pu mass.

JEF and JENDL data libraries produce different k_{eff} (Figure 4.2) but almost same flux (Figure 4.3) and ^{239}Pu burnup (Figure 4.4); because of that, we retain that the two libraries have a very close value of the ^{239}Pu cross section data but different data of fission products and other actinides.
Table 4.4 summarizes the inventory of major actinides in the driver and transmutation

Table 4.4 Summary burnup and buildup results obtained by the use of JENDL, JEF and ENDF/B data libraries. Total refers to all actinides.

Actinide	Beginning of the 12th year [kg]	After 330 days – JENDL-3.2 [kg]	After 330 days – JEF-2.2 [kg]	After 330 days – ENDF/B-6.8 [kg]	Max. Difference [%]
^{237}Np	68.46	58.59	58.41	57.84	1.29
^{238}Pu	67.50	85.00	85.68	85.90	1.05
^{239}Pu	471.9	298.5	298.1	288.7	3.32
^{240}Pu	341.9	293.8	294.3	290.3	1.37
^{241}Pu	242.0	251.3	249.7	251.7	0.80
^{242}Pu	123.8	136.2	135.9	135.9	0.22
^{241}Am	77.63	60.61	59.17	58.61	3.36
^{242m}Am	2.769	3.478	3.390	3.304	5.13
^{243}Am	40.41	47.00	47.10	48.57	3.30
^{242}Cm	7.351	11.34	11.79	12.03	5.89
^{244}Cm	18.20	26.40	26.52	27.34	3.51
^{245}Cm	1.993	3.306	3.199	3.934	21.12
Total	14647	12773	12752	12661	0.88

fuel at the beginning of the 12th year and after 11 months. The maximal difference,

reported in the 6th column, has been calculated as the difference between the maximum value between the three libraries and the minimum one divided by the average of the three libraries. We can note in Table 4.4 that the difference between libraries in the burnup and buildup masses never exceeds 3.5%, with the exception of ^{242m}Am, ^{242}Cm and ^{245}Cm. Nevertheless, ^{242m}Am and ^{242}Cm still remain below 6%; by contrast, ^{245}Cm exhibits a 21% difference. This anomalous result for ^{245}Cm might have origin in the ENDF/B library, which produced a quite larger buildup of this isotope. The accumulation of ^{245}Cm is due to the lack of its fission and capture cross sections in the ENDF/B library (since we used an ENDF/B library released in 2001). Moreover, we retain that the lack of ^{245}Cm data may contribute in obtaining the pretty low k_{eff} for the ENDF/B library, because ^{245}Cm has a half life of 8500 years and a fission cross section comparable to that one of ^{239}Pu.

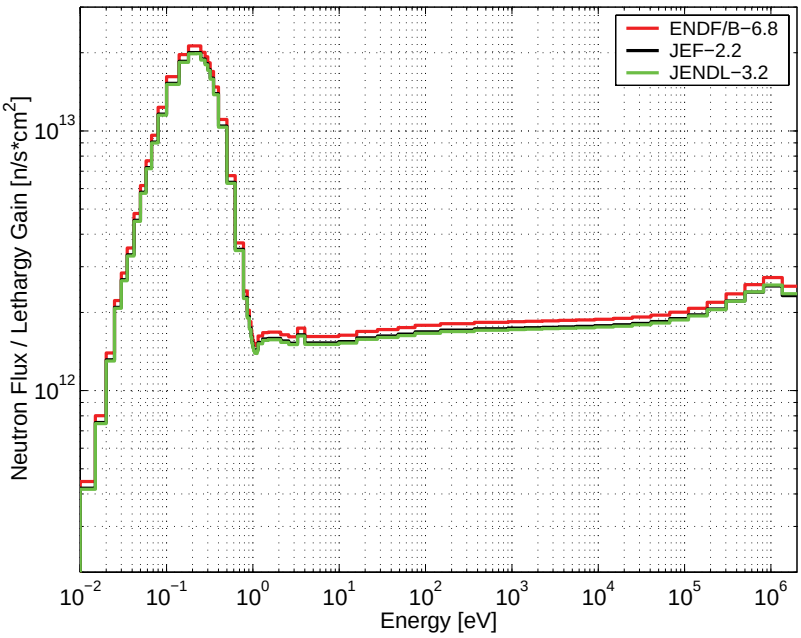

Figure 4.5 Neutron spectrum at the beginning of the 12th year.

Figure 4.5 shows that all the three libraries produce the same neutron spectra at the beginning of the 12th year; the three curves of Figure 4.5 have the same peak at 0.2 eV and a very similar shape. The ENDF/B library data generates a slightly higher flux, as also Figure 4.3 confirms. The neutron spectra have been plotted by using the energy binning corresponding to the 69 energetic groups of the WIMS cross section library for thermal reactors; these groups are approximately composed of 14 fast groups, 12 resonance groups, and 42 thermal groups[21-22]. Let us note that we did not plot the spectra at the end of the 12th year since they do not show a significant difference with those ones at the beginning of the year[2]. In order to produce the data of fig. 5, the MCB code has run the MCNP-module just once and it simulated 15 millions of neutrons distributed over 150 MCNP k-code cycles, including 40 inactive ones.

Table 4.5, which summarizes the one group averaged fission cross sections of DF actinides, shows that ^{239}Pu data are most consistent for all libraries, the differences are below 0.3 %; whereas, the results for other isotopes maintain below 16%, with the exception of ^{242}Cm and ^{244}Cm. The differences for ^{244}Cm are relatively big, since the JEF value is about 30% higher than JENDL value. In addition, the discrepancies are

very large for ^{242}Cm, since the JENDL value is over 4 times higher than that of ENDF/B. The data of Table 4.5 have been obtained by dividing the fission rate of the fresh DF at the beginning of the 12th year by the average neutron flux in the TRISO kernels of the inner ring (both data are available in the BMES file produced by MCB). Let us highlight, in the last row of Table 4.4, the lack of the ^{245}Cm fission cross section for the ENDF/B library, which was not available in the 2001 release. Moreover, the MCB code, while using an enlarged library, performs the check on the nuclide list instead of the available data, that means an incomplete data for one nuclide in one library (e.g. the unavailable ^{245}Cm fission and capture cross sections in ENDF/B) prevents the reading of available data from other libraries (e.g. the available ^{245}Cm fission and capture cross sections in JEF and JENDL). The current version of ENDF/B contains fission and capture cross sections for ^{245}Cm.

Table 4.5 One group averaged fission cross section of the DF actinides in the inner fuel ring at the beginning of the 12th year.

Actinide	σ_f JENDL-3.2 **[b]**	σ_f JEF-2.2 [b]	σ_f ENDF/B-6.8 [b]	Max. difference [%]
^{237}Np	0.34	0.30	0.31	14.48
^{238}Pu	2.00	1.99	1.89	5.85
^{239}Pu	66.09	65.87	65.97	0.33
^{240}Pu	0.38	0.43	0.38	12.74
^{241}Pu	68.04	69.71	68.06	2.44
^{242}Pu	0.26	0.28	0.26	8.56
^{241}Am	0.83	0.97	0.86	15.56
^{242m}Am	296.41	314.56	318.98	7.28
^{243}Am	0.32	0.27	0.31	14.60
^{242}Cm	1.13	0.74	0.27	119.96
^{244}Cm	0.65	0.89	0.84	29.72
^{245}Cm	64.60	68.85	n/a	

Similar comparative studies have been performed by Ridikas et al.[67] In those studies, however, only a limited number of isotopes have been considered: just 80 isotopes for JEF and ENDF/B (tab. 2 of reference 67). In addition, a large statistical error (fig. 2 of reference 67) makes quite difficult a distinction between the results of the different libraries. Moreover, from those studies it appears that the difference in the mass of ^{239}Pu, due to the use of different nuclear data library, is over 21%, a value much greater than our result of 3.3%. Nevertheless, some of the main conclusions of our studies are in agreement with that study: the ENDF/B nuclear data library produces the lowest k_{eff} when the reactor loads fresh fuel, the difference in the neutron flux resulting from the use of different libraries maintains below 7%.

4.1.4 MCB precision studies

It is quite difficult, though not impossible, to estimate properly statistical error propagation throughout a burnup calculation. We approached this problem trying to make a rough estimation of the error propagation by changing the starting random number seed over a set of identical simulations. For each of the three enlarged nuclear data libraries we performed 20 simulations changing the pseudorandom number stride. In these precision studies, the MCB code has invocated the MCNP-module only at the

beginning and at the end of the 12th year, whereas in the accuracy studies it did every month.
We generated, from the set of 20 simulations, one vector containing the k_{eff} values and another one doing the standard deviations (std), both vectors with 20 entries; then, we calculated the average (mean) of the two vectors and their percentage relative standard deviations (prsd) by equation 1:

$$prsd(\vec{v}) = \frac{std(\vec{v})}{mean(\vec{v})\sqrt{20}} \quad (1)$$

Table 4.6 summarizes the average k_{eff} in the 20 simulations, its prsd, the average of the MCB standard deviation in the 20 simulations and its prsd. The results of the 2nd and 3rd rows of table 6 (as well as those of the 8th and 9th) confirm that the standard deviation of k_{eff} decreases according to the square root of the number of neutrons simulated; in fact, the prsd of the vector containing 20 initial (final) values of k_{eff} is very close to the average value of the standard deviation (which may represent the standard deviation of only 1 simulation) divided by the square root of 20. In addition, in this set of 20 calculations, the standard deviation of the MCB standard deviation always maintains lower than 2%, which is a quite low value. Of course, a 20 simulations sampling produces a large difference (from 15% up to 54%) of the standard deviation of the MCB standard deviation; a more precise result would require much more than 20 simulations sampling.

Table 4.6 Precision of MCB. A set of 20 simulations produced two arrays, each of 20 elements, containing respectively the k_{eff} and the standard deviation (std) of the MCB outputs. The average of the two arrays is reported in the italics rows, whereas the percentage relative standard deviation (prsd) of the arrays is reported in the normal rows. sqrt is acronym of square root.

	JENDL-3.2	JEF-2.2	ENDF/B-6.8	Max. Difference [%]
average of initial k_{eff}	1.0581	1.0601	1.0528	0.69
prsd of initial k_{eff} [%]	0.0081	0.0083	0.0094	15.12
average of initial MCB std [%] divided by sqrt(20)	0.0087	0.0086	0.086	1.16
average of initial MCB std [%]	0.0380	0.0385	0.0384	1.31
prsd of initial MCB std [%]	0.9623	1.1227	1.6283	53.81
average of final k_{eff}	1.0240	1.0278	1.0167	1.09
prsd of final k_{eff} [%]	0.0079	0.0107	0.0104	28.97
average of final MCB std [%] divided by sqrt(20)	0.0085	0.0085	0.0085	0
average of initial MCB std [%]	0.0384	0.0382	0.0379	1.31
prsd of final MCB std [%]	1.8312	1.6293	1.5350	17.79

Table 4.7 summarizes the standard deviation of vector, with 20 entries, containing the actinides mass, at the end of the 12th year, obtained by 20 MCB simulations with a different pseudorandom number stride. We can note that the values of heavier actinides, Am and Cm, may be twice as much as the values of Pu isotopes.

Table 4.7 Relative standard deviation (std) of the actinides mass after 11 months operation. Data report the std of a vector containing the nuclide mass obtained in 20 MCB simulations with a different pseudorandom number stride.

Actinide	**std JENDL-3.2 [%]**	**std JEF-2.2 [%]**	**std ENDF/B-6.8 [%]**
^{237}Np	0.0118	0.0102	0.0119
^{238}Pu	0.0156	0.0089	0.0107
^{239}Pu	0.0240	0.0160	0.0171
^{240}Pu	0.0356	0.0288	0.0550
^{241}Pu	0.0269	0.0327	0.0495
^{242}Pu	0.0351	0.0352	0.0377
^{241}Am	0.0267	0.0228	0.0303
^{242m}Am	0.0762	0.0619	0.0383
^{243}Am	0.0784	0.0650	0.0871
^{242}Cm	0.0640	0.0506	0.0576
^{244}Cm	0.0627	0.0552	0.0744
^{245}Cm	0.1858	0.1784	0.1606

In order to complete the precision studies, we evaluated the impact of changing the initial neutron source spatial distribution (the SRCTP file) to the same MCB input and nuclear data library. We obtained almost the same k_{eff} and standard deviation with different initial neutron source spatial distributions. Let us finally remark that, of course, the statistics related to the generation of the pseudorandom numbers (e.g. the stride) is not related to the statistics associated to the spatial neutron source.

5 NUCLEAR FUEL DEVELOPMENT FOR TRANSMUTATION

5.1 NEUTRONIC AND THERMAL-HYDRAULIC ANALYSIS

While the safety performance of a reactor is a complex function of neutronic, thermal-hydraulic and material properties, a first indication of the potential for benign behaviour during a transient can be derived from basic safety parameters like reactivity coefficients and effective delayed neutron fractions.
Wade and Fujita defined the following safety indicators for passive (unprotected) shutdown behavior in sodium-cooled fast reactors [93]:

(1) $A = (\alpha_D + \alpha_l)\Delta T_{fuel}$
(2) $B = (\alpha_D + \alpha_l + \alpha_c + 2\alpha_R)\Delta T_{cool}/2$
(3) $C = \alpha_D + \alpha_l + \alpha_c + \alpha_R$

Where α_D is the Doppler coefficient, α_l is the fuel axial expansion coefficient, α_c is the coolant temperature coefficient and α_R is the radial expansion coefficient. ΔT_{fuel} is the difference between
the average fuel and coolant temperature and ΔT_{cool} is the difference between coolant inlet and outlet temperatures. In the quasi static approximation, the asymptotic rise in coolant outlet temperature during a loss of flow event (LOF) is then given by (neglecting natural circulation):

(4) $\Delta T_{out} = (A/B)\ \Delta T_{cool}$

In the case of a total loss of heat-sink (LOHS), the maximum temperature increase in core inlet temperature is given by (A + B)/C, which may be rewritten as

(5) $\Delta T_{out} = [(1+A/B)/(C\ \Delta T_{cool}/B) - 1]\ \Delta T_{cool}$

To ensure integrity of the clad during these slow transients, T_{out} should remain less than the temperature limit of the clad, which for slow transients is set by the creep rate.
Assuming that the margin to clad failure during normal operation is $M\Delta T_{cool}$, i.e. $\Delta T_{out} < M\Delta T_{cool}$, the following set of conditions sufficient to assure clad integrity may be derived:

(6) $A/B < M$

(7) $C\ \Delta T_{cool}/B > 1$

Provided that A,B and C are all negative, which is the case if the isothermal inlet temperature coefficient C is negative. Condition (6) can be fulfilled by limiting the linear power during normal operation. Equation (7) however requires that a positive void coefficient is compensated for by a prompt negative feedback coefficient (Doppler + axial expansion) of larger magnitude.

When introducing americium into the fuel, the coolant temperature coefficient increases, and the Doppler feedback decreases. With an americium fraction exceeding 10% the sodium inlet temperature coefficient C becomes positive. Hence the fuels investigated in CONFIRM and FUTURE, featuring about 50% americium in the actinide vector, cannot be operated in a critical configuration using sodium as coolant [96]. The re-introduction of ^{238}U into the fuel turns out not be very helpful, as can be seen from Table 5.1, displaying the sodium temperature coefficient and the Doppler constant for different oxide fuels in a pin lattice with P/D=1.2. The reason for this is the high capture cross section of americium, which suppresses the capture rate in ^{238}U resonances.

Table 5.1 Sodium temperature coefficient and Doppler constant KD in an oxide fuel pin cell with P/D = 1.20. $\Delta k/\Delta T$ was calculated as an average between 700 and 900 K, using the ENDFB/VI.8 library. KD = $-T\,\partial k/\partial T$. The inlet temperature coefficient C is calculated assuming $\alpha c + \alpha R = -1.2$ pcm/K

U [%]	Pu [%]	Zr [%]	Am [%]	$\Delta k/\Delta T$ [pcm/K]	K_D [pcm]	C [pcm/K]
80	20	-	-	+1.1	- 820	-0.88
50	20	-	30	+1.8	- 20	+0.38
-	20	80	-	+0.7	- 420	-0.97
-	20	50	30	+2.0	- 20	+0.64

Substituting sodium for lead or lead bismuth eutectic (LBE), the coolant temperature coeffient decreases significantly [95]. Taking the reactivity coefficients calculated for the CONFIRM and FUTURE cores under investigation one arrives at negative inlet temperature coefficients, as shown in Table 5.2.

Table 5.2 Reactivity coefficients and safety indicators of the FUTURE cores. The Doppler coefficient is negligible for all fuels.

Fuel	α_c [pcm/K]	α_l [pcm/K]	α_R [pcm/K]	C [pcm/K]	C $\Delta T/B$
^{92}Mo cermet	+0.37	-0.18	-1.05	-0.86	0.90
MgO cercer	+0.57	-0.27	-0.97	-0.67	0.82
ZrN solsol					

Note however that C $\Delta T/B < 1$, since the magnitude of the void coefficient is larger than the negative sum of axial expansion and Doppler coefficient. Hence, the present cores do not fulfill Wade's criteria for survival of a slow transient under critical operation. The reason for this is the large content of americium, which leads to virtually zero Doppler feedback as well as an increase in coolant temperature coefficient.

Concerning a fast transient, the small effective delayed neutron fraction of the CONFIRM and FUTURE cores, combined with the large void worths, makes critical operation even more unfeasible. Reducing β_{eff} by a factor of two corresponds to doubling of void driven reactivity insertion rates. Given a coolant flow rate of 2 m/s, a steam bubble void worth of 15 dollars may be introduced in half a second. Thus reactivity insertion rates of 30 dollars per second could be conjectured for these cores, which is too large to be compensated for by axial expansion feedback alone.

These are the major motivations for operating minor actinide burners in sub-critical mode. However, sub-criticality is not a sufficient condition for acceptable performance under pressure driven transients.

Deep sub-criticality (i.e. more than several dollars negative reactivity), changes the dynamics of the reactor qualitatively. The system becomes much more insensitive to reactivity insertions, both negative and positive. While this insensitivity is the key for allowing large concentration of americium in the fuel, it also leads to dis-advantages. One example is the difficulty in using scram rods for shut-down of the core [84]. Inserting 5000 pcm (25 dollars) negative reactivity, for instance, only reduces power by a factor of 2-3. In the case of un-protected loss of flow events, the steady state temperature of coolant and clad will mainly be determined by natural circulation flow rates. Figure 5.1 shows the reduction of power and flow rate in earlier versions of the FUTURE and CONFIRM cores where the linear rating was 35 kW/m for cermet and nitride fuels, and 25 kW/m for the cercer fuel. The reduction in power due to thermal feedbacks is less than five percent, the major contributor being radial expansion of the grid. When optimising the natural circulation capability of the core, it was assumed that the total vessel height is limited to 10 meters by seismic constraints [85]. Consequently, the vertical distance between the thermal centers of core and heat exchangers could not be increased beyond 5.5 meters. A pressure drop over the primary circuit of 2.5 bars then leads to steady state flow rates of 23% for the fuel with lower rating, and 27% for the fuels with higher rating. It should be noted that reduction of P/D from 1.75 to 1.50 leads to an increase of the pressure drop by 20%.

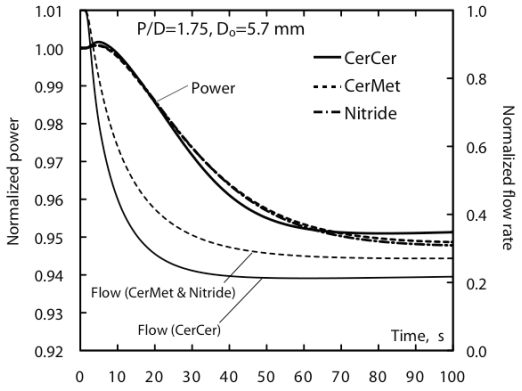

Figure 5.1 Reduction of power and flow rate during an un-protected loss of flow event in early versions of the FUTURE and CONFIRM cores [85].

Figure 5.2 displays the calculated clad temperatures for fuels rated at 35 kW/m. A large pitch is required to maintain the clad temperature below the rapid burst limit of austenitic stainless steels, being 1330 Kelvin for a clad stress of 100 MPa [83]. The use

of ferritic steels would require beam shut-down within 30 seconds, as the mechanical properties of this material is considerably poorer at high temperature. A rapid burst limit of 1140 Kelvin may be derived from data on HT-9, for example [83].

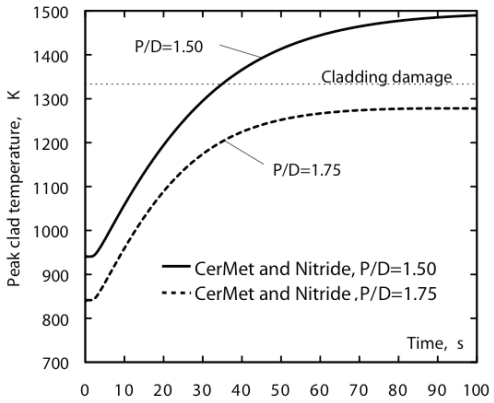

Figure 5.2 Clad temperature evolution during an un-protected loss of flow event [85]

It should be noted that at temperatures exceeding 1200 Kelvin, thermal creep will lead to failure of the clad on the time scale of hours, even when utilizing austenitic steels [91]. For HT-9, creep failure will occur within one hour for T > 1020 Kelvin [82].

The clad performance under loss-of-flow may however be improved by reducing the linear rating, which has been done in the revised version of the FUTURE cores. Transient calculations for the revised core parameters were not made with SAS4A, but results from SIMMER and SITHER calculations are described elsewhere in this report. The reduced rating leads to longer residence time, which probably are incompatible with the life time of oxide film protected ferritic steels at the suggested operating temperature. Aluminisation of the clad surface has however shown to significantly improve the corrosion resistance of both austenitic and ferritic steels in flowing LBE for test times up 7000 hours at T = 820 Kelvin [88].

The fuel itself turns out to be more sensitive to accelerator over-current events. Assuming that the accelerator is designed to allow for a variation of current of 50% to compensate for reactivity losses, one may imagine a case where full accelerator power is inserted at the time of maximum core reactivity [i.e. at BOL]. Figure 5.3 shows the fuel temperature evolution following an increase in accelerator current by 50%. The molybdenum based cermet and the nitride fuel maintain margins to failure of more than 500 Kelvin, while the cercer fuel reaches temperatures where eutectic melting of AmO_{2-x}-MgO might occur.

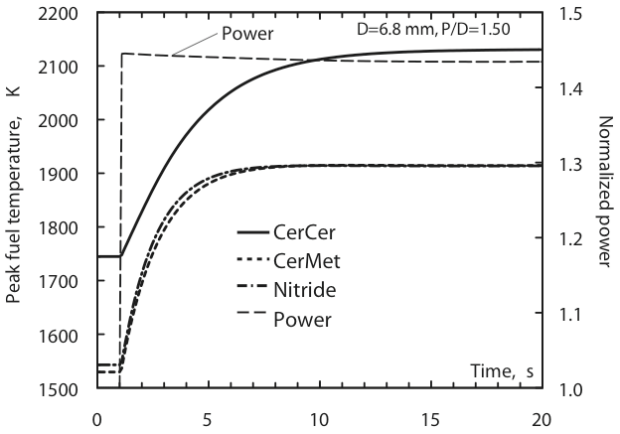

Figure 5.3 Peak fuel temperatures following an un-protected accelerator over-current event [85].

To provide sufficient margin to melt for the magnesia based cercer fuel, the rating would have to be decreased below 25 kW/m, a case that is investigated in the revised cores.

The major safety issue in sub-critical minor actinide burners turns out to be the high void worths pertaining to certain fuel types. The only prompt feedback of significance is axial expansion of the fuel, having a magnitude of less than 0.3 pcm/K. Reactivity insertion rates of the order of 20 $ per second then will lead to fuel failure if sub-criticality is lost. It is however not sufficient to remain sub-critical as will be shown. In Figure 5.4, the reactivity insertion resulting from a steam bubble transport through the FUTURE and CONFIRM cores are shown. A bubble velocity equal to that of the coolant was assumed (2.5 m/s). The maximum positive reactivity insertion occurs after 1.5 seconds when the cercer core reactivity is raised by 18 $, corresponding to a criticality margin of 0.2 $. The other cores maintain criticality margins of several dollars. Figure 5.5 and Figure 5.6 display the corresponding evolution of power and fuel temperature. The cercer fuel is predicted to undergo eutectic melting within half a second after peak reactivity has occurred Melting of the oxide phase would take place within two seconds. From these results it is clear that voiding scenarios leading to significant increase in power should not be allowed. Fuels providing a low void worth hence have a distinct advantage, as they may be operated with smaller margins to criticality, thus improving the economics of the system.

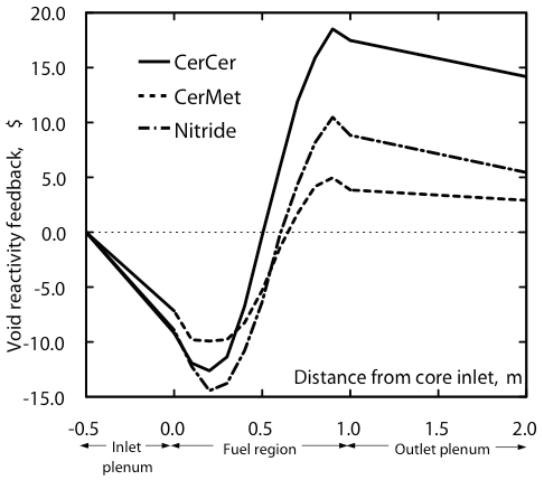

Figure 5.4 Reactivity insertion following progressive axial voiding of the coolant, beginning at the lower plenum [85]

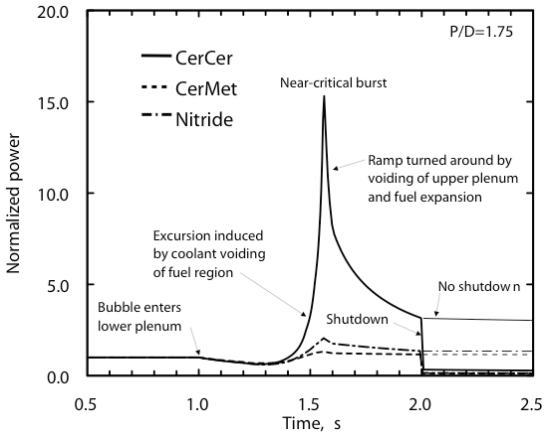

Figure 5.5 Power evolution during bubble transport through the sub-critical cores [85].

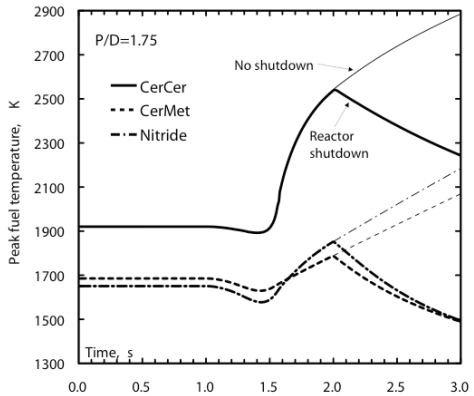

Figure 5.6 Peak fuel temperature during bubble transport through the sub-critical cores [85].

To summarise the results of the transient analysis made with SAS4A, the preliminary linear ratings of the fuels made in the beginning of the project were too high,

considering that the temperature limit of ferritic steels was found to be lower than first estimated. Using ferritic steels (assuming T-91 performs similarly to HT-9 at high temperature) requires shut-down of the accelerator within 20-30 seconds after initiation of a loss of flow event. Applications of austenitic steels could prolong the grace time up to several tens of minutes. Hence there is an incentive for more detailed investigation of an austenitic back-up solution for the cladding material.

The major safety concern of the cores investigated turns out to be coolant voiding resulting from gas bubble introduction into the core. The source term could be fission/helium gas leakage from ruptured fuel pins, or steam bubbles from a broken heat exchanger. Fuel types with lower void worths will allow for operation with smaller sub-criticality margin. Hence the molybdenum based cermet fuel appears to provide the best performance with respect to the accident scenarios here investigated.

5.2 THERMAL STABILITY OF NITRIDE FUELS

The safety discussion of nitride fuels has often focused on the possible dissociation of AmN and PuN into metal and nitrogen gas at elevated temperatures. To investigate this issue, we have performed thermochemical modelling of some actinide nitride (AnN) compounds in various environments, using Thermo-Calc [81] and the ALCHYMY database module originally developed at our department in order to optimise production methods for nitride fuels [86]. ALCHYMY has since then been updated to handle sealed systems (of finite physical volume) and variable pressures. It also has a more accurate description of solid solutions of nitrides and carbides as well as some alloys, and has been expanded to encompass all relevant compounds between Am, Np, Pu, Ce, Y, Hf, Zr, H, C, N and O. Furthermore, the Thermo-Calc software itself has been improved by the developers following some suggestions from our side. These recent studies of the thermal stability have concerned two candidate fuel materials, (Pu0.3Zr0.7)N and (Pu0.2Am0.3Zr0.5)N, whose thermal dissociation was modelled in a constant-volume system mimicking the dimensions and content of the CONFIRM experimental fuel pins, assumed to be at BOL, filled with He of atmospheric pressure (at 25° C). The Gibbs energy of PuN was assumed to follow the function [87]

$$-313295 + 241.168*T - 0.00771*T^2 - 45.002*T*Ln(T)$$

while the corresponding function for AmN was constructed from well-established thermodynamic parameters for the elements combined with the experimental data published in [89], arriving at the estimate

$$-309286.5 + 29075/T + 188.7973T - 0.006238T2 - 5.41E\text{-}07\ T3 - 36.3958TLn(T)$$

As the sealed fuel pin is not an open or even a constant-pressure system, it is not meaningful to speak of a fixed dissociation point for AnN. An initial dissociation of a minute part of the AnN increases the activity (partial pressure) of An(g) and N_2 in the bonding gas, and although the absolute levels remain quite low in the studied temperature interval, the relative increase rapidly halts the dissociation at any given temperature. In other words, AnN is in equilibrium with its dissociation products, typically with the equilibrium shifted strongly towards solid AnN, and the most

convenient way of describing the dissociation is in terms of partial pressures as a function of temperature, which can be easily transformed into the amount of dissociated nitride. That is the method chosen here. When no liquid metal phase appears in the temperature/pressure range studied, as was the case in the following examples, the contribution to the overall pressure is simply 1.5 times the partial pressure of N_2.
The melting of PuN is a poorly defined phenomenon and is not observed at atmospheric pressure. When heated above 2500 K in N2 at atmospheric pressure, PuN eventually forms a liquid, but this "melting" is more properly described as a dissociation, forming a nitrogen-saturated melt of plutonium metal [92]. The nitrogen pressure required for congruent melting of PuN is assumed to be over 24.5 bar N_2 at more than 3000 K (90). In any case, no liquid PuN or AmN phase is implemented in the model we have used. Also, it is commonly agreed that there is no discernible molecular AnN component in the gas phase over PuN and AmN, as the volatilisation proceeds exclusively by dissociation. Thus the reaction is a very simple one:

$$2\ AnN(s) \rightarrow 2\ An + N_2$$

where the metallic actinide may be predominantly solid, liquid or gaseous depending on the element involved, temperature, pressure and the composition of the gas phase. As a rule of thumb, Pu will form as liquid during extensive dissociation of PuN, while Am exhibits a greater tendency towards the gaseous state due to its higher vapour pressure.

In the case of $(Pu_{0.3}Zr_{0.7})N$, we found that up to 2500 K, the increase in pressure arising from PuN dissociation is only 0.05 % of the total pressure and will not be an issue from a purely mechanical point of view. The depletion of Pu from the fuel is very small during uniform heating, less than 0.0002 % at 2500 K, which amount is below the condensation point of the metal in this system. It must, however, be realised that this is the static concentration, not taking dynamical processes into consideration.
As our calculations show, the pressure contribution resulting from dissociation of PuN is three orders of magnitude lower than that following Gay-Lussac's law (the increase in pressure caused by the heating of the bonding gas), and at least from the strictly mechanical viewpoint, the temperature limit for cladding failure will not be different than for any regular fuel pin.

AmN is less stable than PuN, and nitride fuels with a substantial Am content can be expected to perform poorly at extreme temperatures. The reactor design and safety parameters must necessarily be chosen taking this into consideration; however, both manufacture and use of such fuel should be quite feasible. AmN as such must be regarded as a wholly unsuitable fuel for any even remotely conventional reactor concepts, but the tendency towards dissociation is strongly decreased by producing the AmN fuel as a solid solution with appropriate amounts of PuN and inert matrix, such as the eminently thermostable ZrN.
Modelling of $(Pu_{0.3}Zr_{0.7})N$, all other system parameters being the same as above, shows clearly that AmN is the performance-limiting component. The dissociation of PuN is smaller by three orders of magnitude and can be ignored. Yet, up to 2400 K, the increase in pressure arising from AmN dissociation is only a few percent of the total pressure and, again, does not constitute a risk factor as far as cladding rupture is concerned. Likewise, the equilibrium depletion of Am from the fuel is below 0.01%. It may be further diminished by two orders of magnitude by the admixture of 1 % N_2 to the bonding gas [86].

As the model contains some simplifications (uniform heating, congruent vaporisation of AmN at stoichiometric composition, ideal solid solution of nitrides) and the thermodynamical parameters for AmN are based on some reasonable but unverified assumptions, the results should be intrepreted as provisional guidelines in the absence of experimental determination.

In conclusion, the dissociation of the actinide nitrides is not a mechanical problem, as the contribution to the overall pressure is minute and rather insignificant in terms of cladding stress. In our opinion, the maximum permissible overheating, in terms of both temperature and duration, is more likely to be dependent on transport effects that may be expected to take place in a real system. In case of a partial dissociation of the fuel, the products, if released from the fuel pellets, would rapidly recombine on any colder surface, presumably the inside of the cladding. The possible issue of a minute but continuous dissociation of nitride in hot zones and recombination on colder surfaces might be possible to investigate by a theoretical approach, but PIE of the experimental fuel pins destined for testing will no doubt provide us with a far more reliable estimate of the extent of such redistribution.

6 MATERIAL STUDIES FOR ADS

6.1 MODELLING OF RADIATION EFFECTS ON MECHANICAL PROPERTIES OF FERRITIC STEELS.

Irradiation damage of cladding and structural material sets the ultimate limit for burnup in fast reactors, and hence also for transmutation performance. While it is known that ferritic (bcc) steels feature better resistance to swelling and hence allows for higher burnup when used as cladding, they are subject to a dose dependent increase in ductile-to brittle transition temperature (DBTT), which sets a lower temperature limit for their operation at high doses of about 350°C. In addition, the mechanical properties of ferritic steels are inferior to those of austenites at high temperature. Consequently the temperature window for operation of ferritic steels in fast reactors is found between 350 and 550°C. Varying the amount of trace elements in the steel has a profound effect on DBTT and swelling rates. The mechanisms responsible for these variations are not well understood. Hence there is a good incentive for the use of atomistic modelling to understand the basic processes taking place in models of ferritic steels under simulated irradiation.

In the present project, existing empirical models for pure elements like Fe and Cr are extended to the Fe-Cr-C system, which may serve as an idealised model of ferritic steels actually used for reactor components. By the end of the project, a so called ”Embedded atom method”, or EAM model for this system will have been developed, that is able to correctly reproduce elastic, thermo-physical and point defect properties of this material out of pile, as function of Cr and C content. This model will be used for predicting the change of mechanical properties as function of irradiation dose, dose rate and temperature. Comparison with relevant experimental data will then be made, to check the predictive power of the model. Finally, an evaluation of the applicability of the results with respect to real industrial ferritic steels will be attempted.

6.2 IMPROVED POTENTIAL FOR IRON

A good description of interstitial defects arising due to irradiation is one of the major goals of the present study. The Embedded Atom Method potentials for pure iron and chromium developed in 2003 [101] were further improved during 2004, in order to provide interstitial formation energies in better agreement with electronic structure calculations. It was found that the formation energy of the <111> interstitial depends on the magnitude of the model potential at distances of 3.5 Ångström, a region which is not included in the fit of bcc equilibrium properties. With a proper adjustment of the potential it became possible to reproduce the energy difference between <110> and <111> interstitial configurations. As an additional benefit, the fcc energy was raised to a magnitude very close to that found in ab initio calculations made with VASP [102]. The pair potential before and after modification is displayed in Figure 6.1.

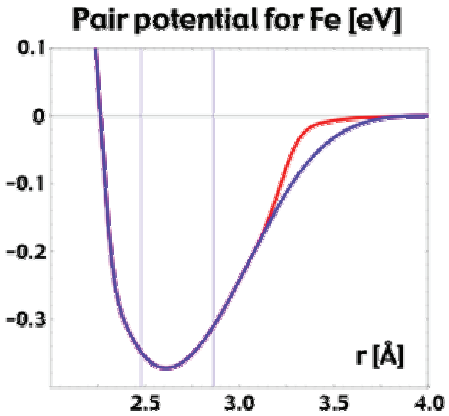

Figure 6.1 Red (blue) line: Fe pair potential yielding 0.67 (0.04) higher energy of the <111> interstitial than the <110> configuration. The positions of 1st and 2nd nearest neighbours are indicated by the vertical lines

6.3 SIMULATION OF RADIATION DAMAGE PRODUCTION IN IRON

This iron potential was used in a comparative study of damage production in recoil cascades, using the molecular dynamics simulation code Dymoka [Becquart00]. By comparing the characteristics of cascades simulated using four recently fitted potentials for α-Fe, each providing different descriptions of point-defects and featuring different threshold displacement energies and stiffness we tried to address the question about the impact of the potential features on the predicted damage state. The comparison is particularly significant because all cascades were simulated following exactly the same procedure and analyzed using the same criteria, so that differences in the results can only be ascribed to the inherent features of the potential used.

The simulations studied in this work were performed using four different potentials [98, 99, 100 and 102]. The potentials were selected for being relatively recent and for providing significantly different descriptions of, in particular, self-interstitial atoms (SIA).

Displacement cascades were performed in the NVE microcanonical statistical ensemble with periodic boundary conditions. Before cascade simulation, a block of atoms was equilibrated for 1 ps at 100 K. The cascade was initiated by giving kinetic energy to a primary knock-on atom (PKA). The PKA was chosen to be at the center of the cubic box and to move in the <135> direction in order to avoid channeling. The cascade energies ranged between 5 and 40 keV with at least 10 cascades 2 performed per energy and potential. The size of the box was chosen depending on the PKA energy to be able to fully contain the cascade. The cascade evolution was monitored visually during the collisional and post-collisional stages to make sure that there was no selfinteraction at boundary crossing. In order to correctly perform the collisions between high energy particles a variable time step adapted to the stage of the cascade is used. During the ballistic stage, the time step was set to Δt=10-17 s while during post-collisional stage it was taken to be Δt=10-16 s. After the recombination stage of the cascade, the cascades were followed for 23 ps, using a larger time step of Δt=10-15 s for the last 10 ps, until the block of atoms was in near thermal equilibrium.

Defects were found and counted using two methods: (1) the Wigner-Seitz cell method and (2) Simple Displacement analysis. The second method is applied for comparison purposes, to make sure that the criterion used to identify point-defects did not influence the result of the analyses, particularly when verifying the absence of cascade self-interaction through periodic boundary conditions. The evolution of the cascades were followed and several stages of the cascades identified; (i) the peak stage, which is the time after cascade initiation where the maximum number of Frenkel pairs is found, (ii) the recombination or relaxation phase and (iii) the number of surviving Frenkel pairs at the end of the cascade. The volume and density of the defects at the peak stage of the cascade were analyzed using the component analysis procedure described in [104,105]. The cascade core is defined by an ellipsoid and the volume distribution can be calculated knowing the eigenvectors and eigenvalues of the ellipsoid. This method may not be completely justified when subcascade formation becomes important but provides nevertheless a good reference. The configurations of the defects remaining after the cascades was analyzed using numeric criteria. The number of vacancy clusters was calculated using second and fourth nearest neighbor criteria and the number of interstitial clusters using first and third nearest neighbor criteria. Visual inspection was also used to estimate SIA clustering since it has been shown that automated procedures give somewhat smaller SIA clustering fractions [106].

The main conclusions obtained in the analysis are:

- The number of Frenkel pairs produced in a cascade during the whole displacement process does not correlate with the threshold displacement energies predicted by the potential.
- A correlation is found with the stiffness and range of the potential in the region of tens of eV interaction. With too stiff potentials damage production cannot reach a full cascade regime, characterized by collective atomic displacements and a pronounced thermal spike, typical of soft potentials. On the contrary, with stiff potentials replacement collision sequences become more frequent and longer and determine an average larger distance between SIA and their vacancies, thereby decreasing the cascade density and partially preventing SIA-vacancy recombination during relaxation. The role of the thermal spike in this process may depend among other things also on the melting point predicted by the potential.
- Nonetheless, with the exception of especially pathological cases, all potentials predict the same final amount of surviving Frenkel pairs. This is likely to be the effect of two mutually offsetting effects of the same cause: namely larger number of defects at peak time, accompanied by longer relaxation time.
- Vacancy and SIA in-cascade clustering are potential dependent, but in a more involved way: differences are the result of a complicated interplay between different features of the potential, from the description of the mobility of point-defects, to the density of the cascade, possibly related to the stiffness, and the extent of the thermal spike, which may depend also on the melting point predicted by the potential. The most worrying conclusion is that the result of cascade simulations using a given potential may be greatly influenced by the partially arbitrary choices made when stiffening it, the TDE being of essentially no use to guide in this operation.

6.4 MODELLING OF ALPHA-PRIME PRECIPITATION IN FE-CR

All Fe-Cr potentials previously published, by us and others, predicted the alloy formation energy to be either strictly positive or negative. Ab initio calculations however show that there is a change in sign of the mixing enthalpy at a Cr concentration of about 6 percent. A major breakthrough in modelling of the mixing enthalpy was accomplished by taking into account the impact of s-band electrons into our model. VASP calculations showed that the concentration of s-electrons in the alloy is higher than expected from a simple linear interpolation. This fact could be modelled by introducing an additional term in the expression for the total energy of the alloy, dependent on s-electron density:

$$E_{tot} = \sum V(r_{ij}) + F(\rho_d) + F(\rho_s)$$

The s-electron density should provide both a cohesive and a repulsive part. The mixing enthalpy fitted to two different Ab Initio calculations using the two band approach is depicted in Figure 6.2.

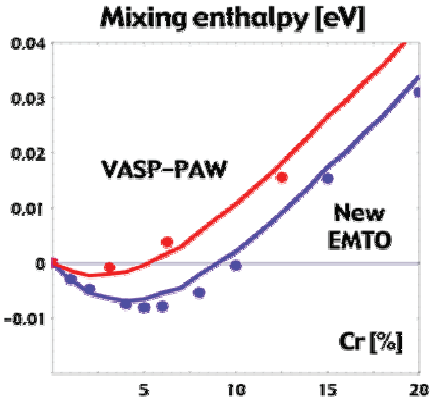

Figure 6.2 Mixing enthalpy of FeCr alloys fitted with the two-band approach to two different sets of ab initio data.

Monte Carlo simulations using the two band approach showed that alloys with a Cr concentration below 7 percent (VASP fitted potential) or 9 percent (EMTO fitted potential) remained perfectly random during simulation of thermal ageing at 750 Kelvin. Above this threshold, precipitation of the alpha-prime phase took place in the simulation. The resulting clusters were Cr rich, containing Fe with a concentration of 10-30 percent, in agreement with experimental facts. Figure 6.3 shows the distribution of Cr atoms in a simulated equilibrium state. One may note the different shapes of the clusters in Fe-10Cr and Fe-32Cr, resulting from the change in second derivative of the free energy in the alloy.

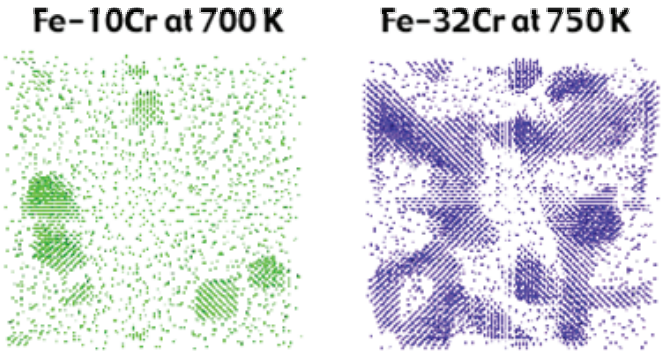

Figure 6.3 Distribution of Cr atoms in originally random alloys, after simulation of thermal ageing.

Using the above described two-band model, we will now be able to do radiation damage simulation in Fe-Cr based on a correct description of alloy thermo-dynamics. Work has also started on construction of potentials for Fe-C and Cr-C.

6.5 EFFECT OF THE INTERATOMIC POTENTIAL ON THE FEATURES OF DISPLACEMENT CASCADES IN α-FE

6.6 INTRODUCTION

Multi-scale modeling is an important tool for understanding material behavior. The success of the modeling rests on how well atomic interactions are reproduced in the material under consideration. Over the years, much effort has been put into the development of iron potentials which correctly describe static and dynamic properties and a number of potentials exist in literature. The potentials are used in the simulation of displacement cascades which are the fundamental process of radiation damage production under neutron and proton irradiation.

The question of determining which characteristics of the interatomic potential are mostly responsible for the result of the simulation arises as an important one. By comparing the characteristics of cascades simulated by molecular dynamics (MD) using four recently fitted potentials for α-Fe, each providing different descriptions of point-defects and featuring different threshold displacement energies and stiffness we try to address this question. The comparison is particularly significant because all cascades were simulated following exactly the same procedure and analyzed using the same criteria, so that differences in the results can only be ascribed to the inherent features of the potential used.

6.7 SIMULATION TECHNIQUE

6.7.1 Interatomic potentials

The simulations studied in this work were performed using four different potentials. The first potential is potential 2 found in [97] and will be denoted AMS. The second potential is the modified Finnis-Sinclair potential described in [98] which will here be called ABC. The two remaining potentials are potentials produced within the EAM

formalism. They will be called CWP and WOL and a description of them is found in [101]. These potentials were selected for being relatively recent and for providing significantly different descriptions of, in particular, self-interstitial atoms (SIA). The fitting and validation of the interatomic potentials used in this work has already been extensively reported and can be found in the references given above.

6.7.2 Displacement cascade simulation

The four potentials chosen for study were used with the molecular dynamics code Dymoka [103] to produce displacement cascades. The cascades were performed in the NVE microcanonical statistical ensemble with periodic boundary conditions. Temperature was not applied as this parameter has been shown to have negligible influence on the results. Before cascade simulation, a block of atoms was equilibrated for 1 ps at 100 K. The cascade was initiated by giving kinetic energy to a primary knock-on atom (PKA). The PKA was chosen to be at the center of the cubic box and to move in the < 135 > direction in order to avoid channeling. The cascade energies ranged between 5 and 40 keV with at least 10 cascades performed per energy and potential. The size of the box was chosen depending on the PKA energy to be able to fully contain the cascade. The cascade evolution was monitored visually during the collisional and post-collisional stages to make sure that there was no self-interaction at boundary crossing.

In order to correctly perform the collisions between high energy particles a variable time step adapted to the stage of the cascade is used. During the ballistic stage, the time step was set to $\Delta t=10^{-17}$ s while during post-collisional stage it was taken to be $\Delta t=10^{-16}$ s. After the recombination stage of the cascade, the cascades were followed for 23 ps, using a larger time step of $\Delta t=10^{-15}$ s for the last 10 ps, until the block of atoms was in near thermal equilibrium.

6.7.3 Cascade analysis

Defects were found and counted using two methods: (1) the Wigner-Seitz cell method (WS) and (2) Simple Displacement analysis (SD). The second method is applied for comparison purposes, to make sure that the criterion used to identify point-defects did not influence the result of the analyses, particularly when verifying the absence of cascade self-interaction through periodic boundary conditions. The evolution of the cascades were followed and several stages of the cascades identified; (i) the peak stage, which is the time after cascade initiation where the maximum number of Frenkel pairs is found, (ii) the recombination or relaxation phase and (iii) the number of surviving Frenkel pairs at the end of the cascade.

The volume and density of the defects at the peak stage of the cascade were analyzed using the component analysis procedure described in [104 and 105]. The cascade core is defined by an ellipsoid and the volume distribution can be calculated knowing the eigenvectors and eigenvalues of the ellipsoid. This method may not be completely justified when subcascade formation becomes important but provides nevertheless a good reference.

The configurations of the defects remaining after the cascades was analyzed using numeric criteria. The number of vacancy clusters was calculated using second and

fourth nearest neighbor criteria and the number of interstitial clusters using first and third nearest neighbor criteria. Visual inspection was also used to estimate SIA clustering since it has been shown that automated procedures give somewhat smaller SIA clustering fractions [106].

6.8 CONCLUSIONS

Detailed results have been submitted for the Proceedings of the Symposium on Microstructural Processes in Irradiated Materials, San Francisco. The manuscript is attached in Appendix 8. For details of the analysis and results, we refer to this document. The conclusions of the work performed are:

- The number of Frenkel pairs produced in a cascade during the whole displacement process does not correlate with the threshold displacement energies predicted by the potential.
- A correlation is found with the stiffness and range of the potential in the region of tens of eV interaction. With too stiff potentials damage production cannot reach a full cascade regime, characterized by collective atomic displacements and pronounced thermal spike, typical of soft potentials. On the contrary, with stiff potentials replacement collision sequences become more frequent and longer and determine an average larger distance between SIA and their vacancies, thereby decreasing the cascade density and partially preventing SIA-vacancy recombination during relaxation. The role of the thermal spike in this process may depend among other things also on the melting point predicted by the potential.
- Nonetheless, with the exception of especially pathological cases, all potentials predict the same final amount of surviving Frenkel pairs. This is likely to be the effect of two mutually offsetting effects of the same cause: namely larger number of defects at peak time, accompanied by longer relaxation time.
- Vacancy and SIA in-cascade clustering are potential dependent, but in a more involved way: differences are the result of a complicated interplay between different features of the potential, from the description of the mobility of point-defects, to the density of the cascade, possibly related to the stiffness, and the extent of the thermal spike, which may depend also on the melting point predicted by the potential.

The most worrying conclusion is that the result of cascade simulations using a given potential may be greatly influenced by the partially arbitrary choices made when stiffening it, the TDE being of essentially no use to guide in this operation. For example, would cascades simulated with the AMS potential, probably the best one available right now for α-Fe, still predict the same large amount of vacancies in clusters after harder stiffening? For the moment, there is no answer to this question.

7 RED-IMPACT ACTIVITIES

7.1 EUROPEAN PROJECT RED-IMPACT

Partitioning, transmutation and conditioning (P&T/C) and waste reduction technologies, if implemented properly and in full consultation with the geological disposal community, are expected to significantly reduce the burden associated with radioactive waste management and disposal. P&T is likely to ease the final repository requirements and it will also contribute to the sustainability of nuclear energy in those countries that pursue this source of energy.
RED-IMPACT is a 3-year, European project under the sixth framework programme with the title *Impact of Partitioning, Transmutation and Waste Reduction Technologies on the Final Nuclear Waste Disposal.* The project is coordinated by the department of Nuclear- and Reactor Physics at KTH.

7.1.1 Objectives of the red-impact

The objectives of the 3-year RED-IMPACT project (Total budget 4 M€ including EC contribution of 2 M€) are:

- Assess the impact of P&T on geological disposal and waste management.
- Assess economic, environmental and societal costs/benefits of P&T.
- Disseminate results of the study to stakeholders (scientific, general public and decision makers) and get feedback during the course of the study.
- Iterate and refine the work based on stake-holders' feedback to achieve full impact of this study on the implementation of the waste management policy of the European Community.

The work of the project is subdivided into six work packages:

WP1: Waste management and transmutation strategies will be reviewed and a number of representative scenarios will be selected for in-depth impact studies.

WP2: Feasibility of the industrial deployment of selected scenarios will be made and their impact on waste management will be studied.

WP3: Assessment of waste streams, waste features, leach resistance, heat generation, reprocessing capability etc will be studied for selected fuel cycles.

WP4: Assessment will be made of the benefits and costs of P&T/C in advanced fuel cycles for waste management and geological disposal.

WP5: Economic, environmental and societal assessment of fuel cycle strategies will be performed.

WP6: Synthesis and dissemination of results of the above studies will be made to stakeholders.

The Consortium of RED-IMPACT project is unique in that it has assembled the most relevant actors in this field and it has a very broad multi-disciplinary scientific and industrial background of partners from 11 countries across Europe:

- Waste Management Agencies/Companies: ENRESA (ES), NIREX (UK), RAWRA (CZ) and SKB (S).
- Nuclear Industries and Utilities: BN (B), BNFL (UK), COGEMA (F), EA (ES), FRAMATOME (F and D) and EnBW (D).
- Research Institutes and Universities: CEA (F), CIEMAT (ES), CITON (Romania), FZJ (D), GRS (D), KTH (S), ITU (EC), NRG (NL), USTUTT (D), SCK.CEN (B), VUJE (Slovakia) and NRI (CZ).

At its completion, the present project is expected to provide a major advance to the P&T research by producing and disseminating a comprehensive and coherent assessment of environmental and societal costs, benefits and difficulties of the deployment of P&T, conditioning and waste reduction technologies for nuclear waste management.

7.2 WORK PACKAGE 1: WASTE MANAGEMENT & TRANSMUTATION STRATEGIES

7.2.1 Objective of Work Package 1

The general objective of the WP1 was to review the waste management and transmutation strategies, proposed worldwide and particularly in the European Union, and to select a number of representative scenarios where the impact of the partitioning (**P**), transmutation (**T**) and conditioning (**C**) technologies on the final high level waste repository and the overall waste management, is to be studied in the other WPs.
The selection of the representative scenarios was based on an overview of previous studies of P&T/C strategies performed in previous EU framework programs, the NEA/OECD and IAEA international organizations and independently by the partners.

7.2.2 Overview by KTH on one of the relevant existing studies

An overview of one of the relevant existing studies, the NEA/OECD report: "Accelerator-Driven Systems (ADS) and Fast Reactors (FR) in Advanced Nuclear Fuel Cycles. A comparative Study" (2002) was the starting point for the identification of possible P&T strategies of interest for the EU member states involved in the Red-Impact project. The report was reviewed by KTH and used as a reference on which the chosen fuel cycle scenarios were based.

7.2.3 Selected Fuel cycle scenarios

- Reference scenario: In this scenario energy is produced in a park of LWR. The spent fuel is then directly disposed to the geological repository.
- Industrial scenario with a PWR/BWR- based reactor park including evolutionary improvements in fuel cycle technology for these types of existing reactors. In this scenario the spent fuel is partitioned and some of its elements are reloaded into the reactors. Pu will be partially or completely recycled.

- Medium term reactor concepts in nuclear power park using a combination of (advanced) LWR's and HTR-deep burn concept, and using (advanced) aqueous partitioning of the LWR fuel.
- Long-term sustainable nuclear energy scenarios with ADS in Double Strata fuel cycle organization. In these scenarios, most of the electricity production is performed in the present or evolutionary LWR with the present U-Pu cycle. The fuel is partitioned with an advanced Purex process and the recuperated Pu is reused in the same LWR. The MA from the original Uranium and the reprocessed fuel is transmuted in fast neutron spectrum ADS, where fuel is continuously recycled after pyrochemical reprocessing. A variant of Double strata with transition will also be considered. In this variant, during the transition period the Pu from the LWR fuel partitioning is used in EPR type reactors and MA are sent to an interim storage. Once the full double strata configuration is reached the park includes a set of EPR type reactors using fresh Uranium and reprocessed Pu and transmuting the Am (and eventually the Np) accumulated in the interim storage. The equilibrium park is completed with fast spectrum ADS where the Am and Cm produced in the EPR reactors and the Cm accumulated in the interim storage are continuously recycle after pyrochemical reprocessing.
- Long-term sustainable nuclear energy scenarios with critical reactors, combining LWR with Fast Reactors. The variant of handling the MA in dedicated fast ADS burners, simplifying the fast critical reactor fuel and reprocessing will also be considered. A combination of aqueous and pyrochemical reprocessing will be required for the different fuel characteristics involved in these fuel cycles.

7.3 WORK PACKAGE 2: INDUSTRIAL DEPLOYMENT SCENARIOS & DATABASE OF PERFORMANCES

7.3.1 Objective of Work Package 2

This work package provided input data to the other work packages involved in the detailed analysis of the overall radiological impact (public, workers, environment), the generation of final waste (main streams and secondary waste), the proliferation resistance features and the estimated cost of various solutions for partitioning and transmutation (**P&T**) or partitioning and conditioning (**P&C**) and waste reduction considered in this study.

7.3.2 Present and future technological options

It was the aim of this task to provide guidance for the choice of relevant waste management options under given political waste management policies.
Detailed data on inventories, capabilities and potential lifetime of existing EU nuclear facilities, which are the available tools for short-term P&T approaches was therefore provided to this WP by each of the countries engaged in the Red-Impact. This data was used as a reference case for judging innovative fuel cycles and waste treatment techniques.
In order to quantify the benefits or disadvantages of P&T in realistic scenarios, the present stockpiles of Pu and minor actinides as already extracted by reprocessing or still stored in spent fuel and their further evolution from continued operation of EU Nuclear Power Plants (NPP) under realistic and improving burn-up targets, was identified. In this respect, overviews on numbers, types, capacities and estimated residual life of

existing EU facilities both reactors and fuel cycle installations including reprocessing, storage and disposal was established.

KTH was responsible in collecting the Swedish data (see part of the data in the Table 7.1 and Table 7.2).

Table 7.1 Swedish Nuclear Power Fleet
PWRs and BWRs loaded with UO_2 fuel, 2003

Reactor	**Type**	**Burn-up (MWd/tU)**	**Enrichment (% ^{235}U)**	**Annual loading 2003 (tU)**
Ringhals-1	BWR	43 000	3,21	14,970* (20,500 2003)
Ringhals-2	PWR	44 000	3,92	20,277
Ringhals-3	PWR	43 000	3,94	18,406
Ringhals-4	PWR	44 000	3,92	22,056* (16,500 2003)
Barsebeck-2	BWR		2,97	0,684
Forsmark-1	BWR	40 000	3,25	24,012
Forsmark-2	BWR	41 000	3,20	22,620
Forsmark-3	BWR	43 000	3,30	27,492
Oskarshamn-1	BWR	40 000	2.8	7,0
Oskarshamn-2	BWR	40 000	3.0	14,0
Oskarshamn-3	BWR	40 000	3.1	22,7

* values 2004

Table 7.2 Swedish nuclear power radioactive waste and storage on site

Reactor	**Annual amount of low level waste generated by the plant (m^3)**		**Spent fuel stored on site 2003-12-31**		
	Solid	**Liquid**	**Storage type (wet/dry)**	**Storage capacity (t Uran)**	**Occupancy (%)**
Forsmark 1	120	8	Wet	233	29
Forsmark 2	105	7	Wet	213	26
Forsmark 3	75	9	Wet	204	19
Oskarshamn-1	160	145	Wet	156,45	29
Oskarshamn-2			Wet	160,83	44
Oskarshamn-3	50	30	Wet	165,20	33
Ringhals-1	105	49200	Wet	254,45	22
Ringhals-2	35	4100	Wet	221,26	46
Ringhals-3	90	4600	Wet	175,26	40
Ringhals-4	80	4200	Wet	167,44	47
Barsebeck-2		22900	Wet	222,25	25

7.4 WORK PACKAGE 3: ASSESSMENT OF WASTE STREAMS

7.4.1 Objectives of Work Package 3

The impact of reduced actinide generation systems and industrialised P&T in general will require an assessment of relevant nuclear fuel cycles especially with regard to the type of fuel, transmuter (reactor), partitioning (reprocessing), waste features, leach resistance, heat generation, etc. The main objective of this WP is to assess every waste stream mass flow, characteristics and physical/chemical form, including secondary waste streams. This evaluation has to be done for the different alternative or complementary systems, separately, but following common criteria and rules for normalization.

Calculation of mass flow and waste streams for each transmutation strategy will be performed. KTH is responsible of calculating the Double Strata Scenario with Pu-burning in LWR and FR followed by a second stratum where minor actinides are burnt in an Accelerator Driven System (ADS) (see Figure 7.1).

Double Strata Strategy

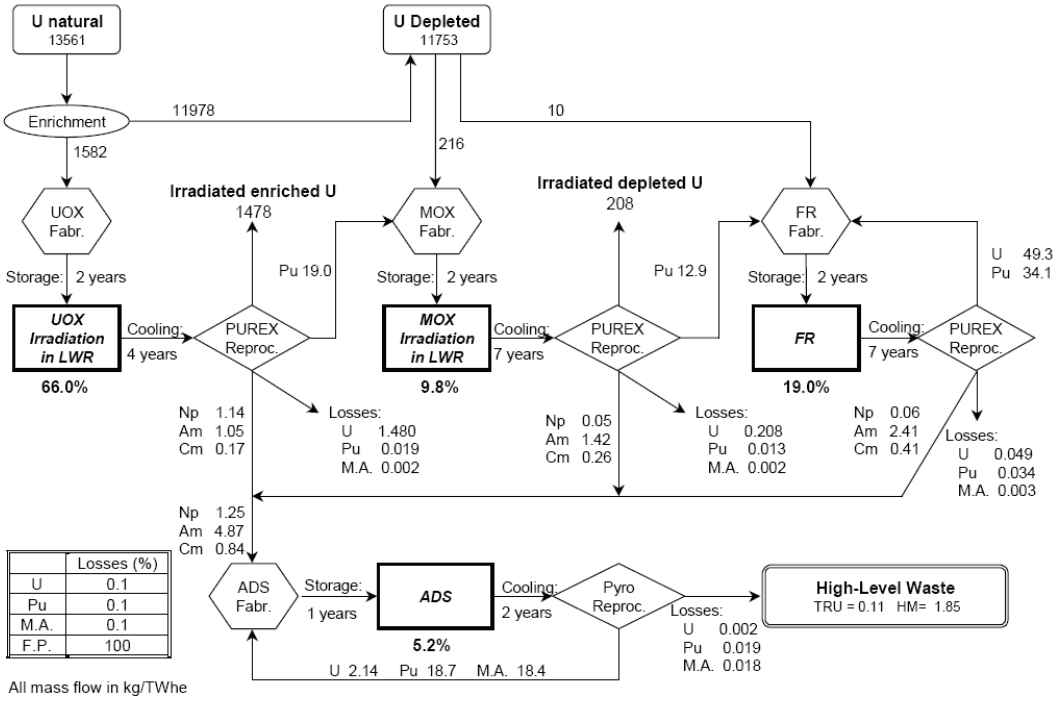

Figure 7.1 Double Strata Scenario for Red Impact

7.4.2 Nuclear Fuel Cycle Simulation

The calculation of mass flow and waste streams for the Double Strata Scenario will be done by KTH using the simulation code Nuclear Fuel Cycle Simulation (NFCSIM). NFCSIM, written in the object-oriented language JAVA and coupled to the burnup code ORIGEN 2.2, tracks mass flow of reactor charges/discharges with arbitrarily fine time resolution and logging its history through a detailed series of processes and facilities. NFCSIM contains a detailed description of nuclear reactors, enrichment plants, reprocessing facilities, fuel fabrication plants, and short and long term storage facilities. The code models life-cycle material balances for an arbitrary number of reactors and includes a cost database. The modeling capabilities include light-water reactor oriented

fuel cycles with the option of actinide recycling and a suite of fast reactors and accelerator driven systems for closure of the nuclear fuel cycle.

Every simulated element of the fuel cycle in NFCSIM is represented as an object. Objects with similar properties and/or functions are grouped into classes in Java. The classes contain fields with the class properties and methods that modify fields or return the results of calculations. Reactors of the same type (same power, enrichment, tons of initial heavy metal etc) permit the formation of a class where each object represents a unique copy of its class. The classes may also be grouped together to form a superclass. For example one superclass, the MineAndMill superclass encompasses all subclasses whose functions are mining and milling. All together there are ten superclasses which are themselves a subclass of a single superclass, Facilities. The Facilities superclass houses the simulation clock and those properties that are common to all subclasses. Examples of common properties are start date for each nuclear facility, days until and type of the next event, and the material list. The implementation of the elemental and isotopic delineation occurs at the lowest class level in which every object receives nuclear material, performs some operation on the material, and/or sends the material to the next object in the nuclear fuel cycle.

With the NFCSIM model it is possible to assess the transient effects of a nuclear growth scenario in which the size and composition of the reactor fleet evolve with time. And as a simulator of the flow of reactor fuel charges through the nuclear fuel cycle, operating in transient and equilibrium mode, NFCSIM is a tool for analysing the impact on repositories concerning mass heat load and radiotoxicity and also in analysing the sustainability and economics.

7.5 RED-IMPACT INDICATORS AND ECONOMIC IMPACT ASSESSMENT

7.5.1 Economical, Environmental and Social Aspects of Partitioning and Transmutation

The department has a main role in the fifth work package of Red Impact, being the main institution there together with BNFL. This work package deal with economical, environmental and societal impacts of the fuel cycles studied. A description of the work within WP5 is given below.

7.5.1.1 Objective

The impact of reduced actinide generation systems and industrialised P&T in general will require an assessment of relevant nuclear fuel cycles especially with regard to the economic, environmental and societal advantages/disadvantages (i.e. the sustainability of the fuel cycles). This assessment can only be fully carried out using the formalism of Life Cycle Assessment. However, due to funding restrictions, this will not be possible and it proposed to perform rather simpler system modeling to carry out the assessment although the assessment of the impact on society will probably require other methods. The inputs to this WP will come primarily from WP2 (Industrial Deployment Scenarios / Data and Methods), WP3 (Assessment of Waste Streams), WP4 (Waste Management & Performance Assessment of Repositories) and WP6 (Sustainability Criteria). The output of the WP will go to the other WPs for reiteration/consistency and to WP6 (Synthesis & Dissemination). The following tasks will be performed in the WP:

7.5.1.2 Task 5.1: Methodology and Criteria for Economical, Environmental and Societal Assessments

This task will prepare the process of defining the methodology through which the work package will deliver its results. This will cover, for example, the assignment of tasks to participants of the work package a selection of the modeling requirements for the tasks on economic impact (5.2) and environmental impact (5.3) taking into account the requirements for sensitivity analyses the development of an agreed methodology to assess societal impact (5.4)

7.5.1.3 Task 5.2: Economic Impact

In this task, an economic assessment of the different fuel cycle scenarios will be performed. For each scenario, these costs will be calculated taking into account all steps of the whole cycle. The outcome of this task will serve as input to the multi-criteria assessment. The most important part of the input from the other work packages is:

- The transmutation/fuel cycle strategies chosen including applied technologies including associated technologies for advanced fuel and reprocessing
- Inventories of wastes with isotopic composition at each part of the fuel cycles
- Waste stream characterisation: waste forms for reprocessing, storage and disposal
- Repository design and capacity or size of repositories needed under different scenarios
- Costs of the LLW and ILW management

Data on the power plants and reprocessing facilities etc. such as:

- Size of nuclear park
- Efficiencies of LWR's, medium-term reactors, ADS and/or advanced reactors
- Load factors
- In house energy consumption for power plants
- Facility life expectancies
- Uncertainties in the models and results

Additional data are:

- O&M costs for different facilities
- Unit costs (euro/kg, euro/Bq, euro/kWe installed etc) for:
- Fuel manufacturing
- Reprocessing
- Repository
- Plant construction costs
- Transports
- Economical data
- Interest rates
- The economies of scale for different facilities

The other work packages are expected to deliver input with uncertainties in line with the additional data. In most cases going in to a very detailed level will not be required by WP5, since other parameters such as the unit cost of future technologies will contain significant uncertainties. In addition the work in this package will be performed in such a way as to enable a sensitivity analysis to be undertaken to indicate which processes of the defined fuel cycles contribute most to the overall costs.

7.5.1.4 Task 5.3: Environmental Impact

The environmental impact of nuclear fuel processing arises from two main areas. The impact of the repository on the ecosystem will be covered by WP4. The other main area

is the environmental impact of the partitioning and transmutation /conditioning and fuel or target fabrication systems which are used to process the nuclear fuel. This area covers all effluents (low level waste, intermediate level waste and secondary waste) which are not destined for the repository. In addition, it is hoped that non-radiological toxic effluent emissions from the processes can also be covered. The impact of these wastes will be generated in two steps:

- system modeling to determine the mass of effluents emitted from all stages of each of the selected fuel cycles
- conversion of the effluent mass into agreed impact types

In addition the work in this package will be performed in such a way as to enable an uncertainty and sensitivity analysis to be undertaken to indicate which processes of the defined fuel cycles contribute most to the overall environmental impact. This task will commence when information is obtained about the fuel cycles and the assessment of waste streams is completed for each fuel cycle.

7.5.1.5 Task 5.4: Societal Impact

On of the most difficult parts of the estimation of the overall impact of P&T is that of its impact on society in general. It is proposed to cover this area in two parts. A stakeholder analysis of existing European initiatives will be carried out to determine the potential decision-makers. This will include stakeholder workshops which have been held to facilitate elicitation of decision-makers preferences with respect to different sustainability criteria. One of the main difficulties associated with decision-making in the context of sustainable development is the multiplicity of the stakeholders and the criteria that must be considered simultaneously. Multi-criteria Decision Analysis (MCDA) is often used as a useful tool in these situations, to help problem and decision structuring. MCDA can be used to support strategic decisions both within organizations and for public-sector decisions. The advantage of MCDA over single-criterion approaches, such as cost-benefit analysis, is to present the relevant information in a disaggregated form where the relevant criteria are considered simultaneously and prioritized according to the decision-makers preferences. MCDA in the context of this project will require input from technical/technological, economic, environmental and social analysis. This task of the WP will be developed based on the input from all the WPs within the project, to develop a decision-support framework which incorporates the relevant decision criteria. These results will be used to inform the final findings of the project in WP6.

7.5.1.6 Deliverables

D5.1. Report specifying the methodology to be used in WP5.
D5.2**.** Preliminary report specifying:

- the economic impact of each of the agreed fuel cycles.
- the environmental impact of each of the agreed fuel cycles
- the societal impact of each of the agreed fuel cycles.

D5.3. Interim report with reiteration (and better specification) of

- the economic impact of each of the agreed fuel cycles.
- the environmental impact of each of the agreed fuel cycles
- the societal impact of each of the agreed fuel cycles.

D5.4. Final report:

- the economic impact of each of the agreed fuel cycles.
- the environmental impact of each of the agreed fuel cycles
- the societal impact of each of the agreed fuel cycles

- uncertainty and sensitivity analysis of the presented results

7.5.1.7 Progress

Most of the WP5 activities are strongly dependent on the deliverables form other workpackages. This applies to i.e. the description of the fuel cycles. The main work during the past year has been related to D5.1, where a detailed discussion on the methodology and focus of the work have been focused on establishing the "performance indicators", that are to be the foundation of the coming analysis.

7.6 WP3 BURNUP CODE BENCHMARK

Within the RED-IMPACT work package 3, which is responsible for Assessment of Waste Streams, a benchmark of burnup codes has been invoked. KTH has participated in the benchmark with both calculation contributions and a report summarizing the benchmark. The involved burnup codes was CASMO-4/FISPIN v10.0.1, CESAR 4.3, EVOLCODE, HELIOS 1.8, MCB1c, MONTEBURNS 5B, ORIGEN2.1 and 2.2, SCALE 4.4a/SAS2H and WIMS8a. The basis for the calculations, on which the codes were compared, was a standard PWR 17x17 fuel assembly loaded with two different fuel configurations; MOX fuel and uranium dioxide. The objective of the benchmark was to confirm that the results of different burnup calculation tools converge with respect to the nuclide density evolution.

7.6.1 Description of the PWR subassembly burnup model

The benchmark was performed for two different fuel cases, a MOX PWR subassembly and a UOX ditto. The conditions for the two cases are described below:

7.6.1.1 MOX

- LWR MOX fuel assembly (17 x 17)
- 8.5 % initial enrichment in Pu
- Pu 238: 3.05%
- Pu 239: 52.25%
- Pu 240: 24.75%
- Pu 241: 11.91%
- Pu 242: 8.04%
- 0.25 % initial enrichment in ^{235}U
- Initial ageing time of 2 years
- 50 GWd/tHM
- 1600 days of irradiation in one step
- 5 years of cooling

7.6.1.2 UOX

- LWR UOX fuel assembly (17 x 17)
- 4.2 % initial enrichment in ^{235}U
- 50 GWd/tHM
- 1600 days of irradiation in one step
- 5 years of cooling

7.6.2 Common model data

Further common geometrical data and material parameters given were:

- 264 fuel rods
- Number of thimble guide: 24
- One instrumentation tube
- No extra water hole
- Length of the network: 1.264916 cm
- Semi diameter of the pellet: 0.41266 cm
- Intern semi diameter of the clad: 0.41266 cm
- Extern semi diameter of the clad: 0.474364 cm
- Density of the cladding: 6.49012 g/cm3
- Density of coolant water: 0.7 g/cm^3
- Thickness of the water between two sub assemblies: 0.10768 cm
- Fuel densities: UO2 = 10.07 g/cm^3, MOX = 10.02 g/cm^3
- Average bore concentration : 456 ppm for UOX, 600 ppm for MOX
- Temperatures :
  UOX : 600°C for the fuel, 306°C for the moderator (choose an approximate clad temperature)
  MOX : 650°C for the fuel, 305°C for the moderator (choose an approximate clad temperature)

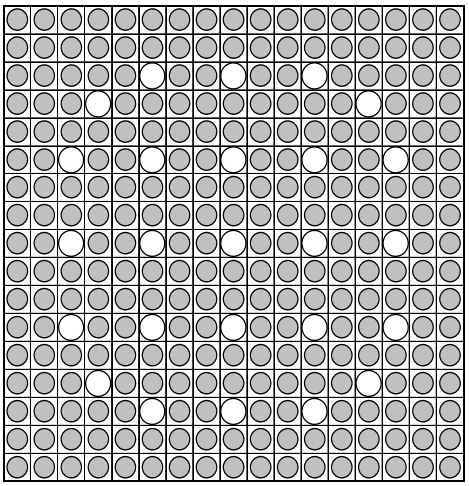

Figure 7.2 Cross section of 17x17 PWR sub assembly model used in benchmark

7.6.3 Involved burnup code tools

The following computer codes have been engaged in the benchmark to perform the burnup calculations:

CASMO is a multigroup, two-dimensional transport theory code for burnup calculations on BWR and PWR fuel assemblies[3]. Two multigroup cross section data libraries are available for CASMO-4 calculations: 70-group E4LBL70 and a condensed 40-group E4LBL40. Both libraries are based mainly on the ENDF/BIV evaluated nuclear data. CASMO-4 is developed at Studsvik Scandpower.

[3] S T U K - Y T O - T R 1 7 0, p 6, Aapo Tanskanen

CESAR (Simplified Evolution Code for Reprocessing Applications) has been developed as a collaboration between CEA and COGEMA[4]. The purpose of CESAR is to provide the required characterization data for burn up fuels from PWRs, BWRs, and FRs. The code calculates the evolution of material balances, activity, decay heat, and neutron source emitted by the irradiated fuel. The neutronics data libraries (cross sections sets) are supplied by the CEA reference calculation codes for neutron physics: APOLLO for thermal spectrum systems and ERANOS for fast spectrum systems. It uses a Runge-Kutta method for calculations during irradiation and a matrix type method for calculations between cycles and during cooling time.
CESAR 4 handles the following types of fuel:
PWR enriched uranium fuel produced from natural uranium or reprocessed uranium from PWR burn up fuel
BWR enriched uranium fuel produced from natural uranium
PWR MOX fuel
UNGG fuel (natural uranium graphite gas type)

EVOLCODE is designed at CIEMAT[5]. EVOLCODE couple different codes and is able to perform a coupled neutronic and isotopic time evolution calculation. Following codes are utilized and combined in EVOLCODE:
NJOY for nuclear data processing
MCNP for the complete 3-D neutron transport simulation. It calculates the neutron multiplication, the energy release by fission, the neutron flux intensity and specific power spatial distributions and the neutron flux energy spectra at different positions.
ORIGEN2.2 for burn-up calculations.

FINSPIN calculates the production and removal of isotopes of three groups; actinides, fission products, and the structural materials[6]. The time-dependent equations are solved by use of a modified form of the Taylor series expansion. In the use of this benchmark the cross sections in the data libraries are partly generated from CASMO-4, but could as well come from a code as WIMS. FINSPIN is developed by Risley Nuclear Power Development Establishment, United Kingdom.

HELIOS is a neutron and gamma transport code for lattice burnup in general two-dimensional geometry. HELIOS performs resonance shielding calculations for nuclides with resolved resonance data. HELIOS uses current coupling collision probability method for neutron transport calculation. The vendor of HELIOS is Studsvik Scandpower.

MCB (Monte Carlo Continuous Energy Burnup Code) is a code for general-purpose use to calculate a nuclide density time evolution with burnup or decay. It includes eigenvalue calculations of critical and subcritical systems as well as neutron transport calculations in fixed source mode or k-code mode to obtain reaction rates and energy deposition that are necessary for burnup calculations. The code has been developed in the form of an f77 patch to MCNP version 4C.

[4] CESAR: A SIMPLIFIED EVOLUTION CODE FOR REPROCESSING APPLICATIONS, M. Samson et al
[5] Comparison Calculations for an Accelerator-driven Minor Actinide Burner, NEA 2001
[6] http://www.nea.fr/abs/html/nea-0706.html

MONTEBURNS is a fully automated tool that links the LANL MCNP Monte Carlo transport code with the radioactive decay and burnup code ORIGEN2. The principle function of MONTEBURNS is to transfer one-group cross-section and flux values from MCNP to ORIGEN2, and then transfer the resulting material compositions (after irradiation and/or decay) from ORIGEN2 back to MCNP. As MCNP, MONTEBURNS is also developed at Los Alamos National Laboratory. The cross-sections have been generated by FZJ for the requested temperatures with NJOY based on ENDF/BVI data.

ORIGEN (The ORNL Isotope Generation and Depletion Code) is a computer code system for calculating the buildup, decay, and processing of radioactive materials. ORIGEN2 is a revised version of ORIGEN and incorporates updates of the reactor models, cross sections, fission product yields, decay data, and decay photon data, as well as the source code. ORIGEN2.1 replaces ORIGEN2 and includes additional libraries for standard and extended-burnup PWR and BWR calculations. ORIGEN2.1 was first released in August 1991 and was replaced with ORIGEN2 Version 2.2 in June 2002. Version 2.2 was the first update to ORIGEN2 in over 10 years and was stimulated by a user discovering a discrepancy in the mass of fission products calculated using ORIGEN2 V2.1.

The **SCALE** system was developed for the Nuclear Regulatory Commission to satisfy a need for a standardized method of analysis for the evaluation of nuclear fuel facility and package designs, and is developed by the Oak Ridge National Laboratory. The SAS2H module uses ORIGEN-S to perform a fuel depletion analysis. SCALE ORIGEN-S uses the matrix exponential method to solve a large system of coupled, linear, first-order ordinary differential equations with constant coefficients. This method is supplemented by a generalized form of the Bateman equations for the concentrations of short-lived nuclides

WIMS is a modular multipurpose neutronics code, presently developed by Serco Assurance, ANSWERS Service and formerly AEA Technology (UK). WIMS8a uses a multigroup library made of 172 energy groups, based upon JEF2.2 data.

Table 7.3 Involved codes and participants

Code used	Benchmark Participant
CASMO-4/FINSPIN	BNFL
CESAR 4.3	CEA
EVOLCODE	CIEMAT
HELIOS 1.8	VUJE
MCB1c2	KTH
MONTEBURNS	KTH (ver 1.0), FZJ (ver 5B)
ORIGEN 2.1 and 2.2	BN, CIEMAT, KTH
SCALE 4.4a	FZJ
WIMS 8a	BN

7.6.4 Data libraries

For the burnup calculations different nuclear data libraries has been in use. See Table 7.4 for further presentations about which code uses which library.

Table 7.4 Cross section data libraries used in benchmark

Code	Cross Section Data Library
CASMO-4/FINSPIN	JEF 2.2
CESAR 4.3	SERMA79
EVOLCODE	ENDF6R4
HELIOS 1.8	ENDF/hy047n18g18a
MCB1c2	JEF 2.2
MONTEBURNS	ENDF/BVI
ORIGEN 2.1	pwru50.lib
ORIGEN 2.2	pwrpupu.lib 5%Pu, pwm0210.lib 10%Pu,
SCALE 4.4a	ENDF/B V
WIMS 8a	JEF 2.2

7.6.5 Results

For the interpretation of the results, the outcomes from CESAR have been chosen as a reference against which the rest of the results are compared. First the results from the MOX calculations will be presented, thereafter the UOx results. The first table in each fuel type refers to the calculated mass of specific actinides normalized to g/tHM, and the second table presents the deviations compared to CESAR. Based on the results and as a mean to measure the difference between CESAR and the other codes, an arithmetic mean and a mass weighted mean has been calculated according to:

1. Arithmetic mean

$$\frac{\sum_{i=1}^{n}(dev_i(\%))}{n}$$

2. Mass weighted mean

$$\frac{\sum_{i=1}^{n}(dev_i(\%)\times mass_i)}{\sum_{i=1}^{n} mass_i}$$

7.6.5.1 MOX

Table 7.5 MOX Mass of actinides [g/tHM]

Actinide Isotope	CESAR 4.3 CEA	WIMS8a BN	WIMS-ORIGEN BN	CASMO-4/FINSPIN BNFL	HELIOS 1.8 VUJE	MCB1c2 JEF 2.2 KTH	ORIGEN 2.2 MONTEBU RNS 1.0 KTH	MONTEBURNS 5B FZJ
^{235}U	1.15E+03	1.15E+03	1.14E+03	1.15E+03	1.11E+03	1.20E+03	1.20E+03	1.13E+03
^{238}U	8.78E+05	8.81E+05	8.81E+05	8.82E+05	8.82E+05	8.84E+05	8.77E+05	8.82E+05
^{237}Np	2.07E+02	1.40E+02	1.95E+02	1.75E+02	1.68E+02	1.86E+02	2.28E+02	
^{238}Pu	2.71E+03	2.72E+03	2.71E+03	2.72E+03	2.63E+03	2.50E+03	2.63E+03	2.33E+03
^{239}Pu	2.55E+04	2.32E+04	2.31E+04	2.26E+04	2.26E+04	2.32E+04	2.79E+04	2.28E+04
^{240}Pu	1.87E+04	1.81E+04	1.80E+04	1.77E+04	1.79E+04	1.89E+04	1.71E+04	1.82E+04
^{241}Pu	8.48E+03	8.25E+03	8.26E+03	8.32E+03	8.18E+03	7.95E+03	8.34E+03	8.56E+03
^{242}Pu	6.98E+03	7.98E+03	7.97E+03	8.03E+03	7.91E+03	7.67E+03	7.66E+03	7.76E+03
^{241}Am	1.88E-01	9.88E-02	1.71E-01	1.74E-01	1.86E-01	2.22E-01	1.37E-01	2.05E-01
^{242m}Am	1.22E+01	9.68E+00	9.46E+00	9.48E+00	8.30E+00	7.30E+00	1.37E+01	6.08E+00
^{242}Cm	1.12E+03	9.16E+02	9.24E+02	8.43E+02	8.97E+02	8.41E+02	1.20E+03	1.61E+03
^{243}Cm	1.97E+02	1.42E+02	1.45E+02	1.32E+02	1.36E+02	1.21E+02	1.36E+02	
^{244}Cm	1.88E-01	9.88E-02	1.71E-01	1.74E-01	1.86E-01	2.22E-01	1.37E-01	2.05E-01
^{245}Cm	1.22E+01	9.68E+00	9.46E+00	9.48E+00	8.30E+00	7.30E+00	1.37E+01	6.08E+00

Actinide Isotope	SCALE 4.4a FZJ	EVOLCODE CIEMAT case1	EVOLCODE CIEMAT case2	EVOLCODE CIEMAT case 3	ORIGEN 2.1 pwru50.li b BN	ORIGEN 2.2 pwrpupu. lib CIEMAT 1	ORIGEN 2.2 pwm0210 .lib CIEMAT 2	ORIGEN 2.2 pwrpupu. lib KTH
^{235}U	1.10E+03	9.87E+02	1.05E+03	1.01E+03	1.08E+03	1.11E+03	1.11E+03	1.19E+03
^{238}U	8.80E+05	8.80E+05	8.78E+05	8.79E+05	8.91E+05	8.99E+05	8.99E+05	8.91E+05
^{237}Np		1.98E+02	2.13E+02	2.00E+02	1.41E+02	1.09E+02	1.05E+02	1.48E+02
^{238}Pu	2.22E+03	2.13E+03	2.20E+03	2.21E+03	2.28E+03	2.31E+03	2.31E+03	2.62E+03
^{239}Pu	2.34E+04	2.05E+04	2.38E+04	2.31E+04	1.43E+04	1.18E+04	1.18E+04	1.43E+04
^{240}Pu	1.75E+04	1.77E+04	1.80E+04	1.72E+04	1.72E+04	1.11E+04	1.11E+04	1.72E+04
^{241}Pu	1.06E+04	7.71E+03	8.08E+03	8.28E+03	7.69E+03	7.53E+03	7.54E+03	7.60E+03
^{242}Pu	8.07E+03	8.19E+03	7.82E+03	8.17E+03	7.57E+03	9.05E+03	9.05E+03	7.52E+03
^{241}Am	1.14E+03	3.03E+03	3.19E+03	3.28E+03	3.06E+03	3.30E+03	3.31E+03	3.18E+03
^{242m}Am	3.72E+01	1.90E+01	2.30E+01	2.59E+01	2.88E+01	9.57E+01	1.66E+02	3.49E+01
^{242}Cm	1.80E+02	1.31E-01	1.38E-01	1.46E-01	1.88E-01	1.60E-01	3.31E-01	5.00E-01
^{243}Cm	9.09E+00	6.99E+00	7.20E+00	6.38E+00	1.22E+01	7.26E+00	7.05E+00	7.70E+00
^{244}Cm	1.21E+03	1.05E+03	1.05E+03	1.04E+03	1.12E+03	1.04E+03	8.84E+02	8.76E+02
^{245}Cm		1.30E+02	1.45E+02	1.51E+02	1.97E+02	9.22E+01	5.33E+01	6.60E+01

Table 7.6 MOX-fuel. Differences in per cent between CESAR and other involved codes [%] ([CESAR – code X]/CESAR x 100)

Actinide Isotope	WIMS8a BN	WIMS-ORIGEN BN	CASMO-4/FINSPIN BNFL	HELIOS 1.8 VUJE	MCB1c2 JEF 2.2 KTH	ORIGEN 2.2 MONTEBURNS 1.0 KTH	MONTEBURNS 5B FZJ	SCALE 4.4a FZJ
^{235}U	-0.04	0.57	-0.34	3.18	-4.24	-4.32	1.42	4.42
^{238}U	-0.31	-0.31	-0.44	-0.49	-0.70	0.10	-0.42	-0.22
^{237}Np	32.47	5.47	15.42	18.93	9.83	-10.35		
^{238}Pu	-0.51	0.05	-0.58	2.95	7.82	2.74	13.82	18.17
^{239}Pu	9.18	9.37	11.31	11.39	8.97	-9.20	10.80	8.10
^{240}Pu	2.95	3.39	5.39	4.07	-1.50	8.59	2.43	6.20
^{241}Pu	2.75	2.64	1.91	3.51	6.30	1.69	-0.93	-25.35
^{242}Pu	-14.42	-14.24	-15.02	-13.33	-9.87	-9.83	-11.27	-15.60
^{241}Am	2.62	3.43	2.44	2.67	4.01	3.58	8.98	68.25
^{242m}Am	28.07	15.92	19.37	1.27	-66.18	53.19	-42.07	-3.52
^{242}Cm	47.30	8.64	7.45	0.67	-18.49	26.78	-9.10	
^{243}Cm	20.84	22.60	22.48	32.09	40.28	-11.90	50.29	25.67
^{244}Cm	18.00	17.26	24.51	19.68	24.71	-7.08	-43.89	-8.70
^{245}Cm	27.98	26.40	33.02	31.19	38.44	31.19		

Actinide Isotope	EVOLCODE CIEMAT case1	EVOLCODE CIEMAT case2	EVOLCODE CIEMAT case 3	ORIGEN 2.1 pwru50.lib BN	ORIGEN 2.2 pwrpupu.lib CIEMAT 1	ORIGEN 2.2 pwm0210.lib CIEMAT 2	ORIGEN 2.2 pwrpupu.lib KTH
^{235}U	14.11	8.91	11.99	6.02	3.86	3.60	-3.80
^{238}U	-0.27	-0.06	-0.11	-1.54	-2.37	-2.35	-1.50
^{237}Np	4.18	-3.22	3.28	31.70	47.39	49.13	28.27
^{238}Pu	21.32	18.68	18.23	15.92	14.60	14.56	3.37
^{239}Pu	19.48	6.74	9.51	43.93	53.79	53.67	43.87
^{240}Pu	5.09	3.29	8.11	7.79	40.42	40.31	7.90
^{241}Pu	9.04	4.72	2.38	9.30	11.25	11.08	10.40
^{242}Pu	-17.36	-12.05	-17.11	-8.45	-29.65	-29.65	-7.78
^{241}Am	15.74	11.09	8.63	14.74	8.09	7.84	11.38
^{242m}Am	47.26	36.11	28.07	19.80	-166.20	-360.3	2.85
^{242}Cm	30.25	26.49	22.27	14.58	-76.51	-166.42	-3.08
^{243}Cm	42.79	41.13	47.85	40.58	42.33	36.99	13.22
^{244}Cm	5.61	5.55	6.52	6.84	20.83	21.57	6.35
^{245}Cm	33.74	26.48	23.32	53.19	72.94	66.47	52.79

Table 7.7 MOX calculations: Comparison with CESAR
Arithmetic mean and mass weighted mean

Calculation tool	Arithmetic Mean [%]	Weighted Mean [%]
CASMO-4/FINSPIN, BNFL	11.7	0.87
EVOLCODE, case 1, CIEMAT	17.8	1.40
EVOLCODE, case 2, CIEMAT	13.8	0.87
EVOLCODE, case 3, CIEMAT	14.8	0.96
HELIOS 1.8, VUJE	10.8	0.94
MCB1c2, JEF 2.2, KTH	17.0	1.31
MONTEBURNS 5B, FZJ	18.8	1.12
MONTEBURNS 1.0, KTH	13.2	0.61
ORIGEN 2.1, pwru50.lib, BN	19.8	2.81
ORIGEN 2.2, pwrpupu.lib 5% Pu, CIEMAT 1	32.4	3.74
ORIGEN 2.2, pwrpupu.lib 5%Pu, KTH	14.6	2.53
ORIGEN 2.2 pwm0210.lib 10%Pu, CIEMAT 2	28.2	3.72
SCALE 4.4a, FZJ	15.5	1.13
WIMS8a, JEF 2.2, BN	14.8	0.75
WIMS-ORIGEN, BN	9.7	0.65

The amount of ^{238}U at EOL calculated by the codes ranges from -2.37% to 0.10% in difference compared to CESAR, where CESAR yields the lowest amount of uranium of all the calculations except for MONTEBURNS KTH. Largest difference with regards to ^{238}U is between CESAR and ORIGEN (ORIGEN CIEMAT -2.37%). The difference in ^{235}U exhibits a greater variety, which is expected due to the tiny initial amounts of ^{235}U. For the plutonium isotope vector the overall discrepancy is larger than for uranium while the total amount of plutonium is an order of magnitude lower than that of uranium, around 40-70 kg plutonium per tHM. For americium and curium the spread in results are even larger, which is anticipated since any deviation in the amount of plutonium will accumulate in the production of heavier elements.
Considering the consumption of ^{239}Pu, there is a significant difference between the ORIGEN calculations and the calculations performed by the other codes. The results can be divided into an ORIGEN group with approximately 60% difference compared to CESAR and a group with the rest of the codes with a deviation of around 10% compared to CESAR. CIEMAT's EVOLCODE case 2 has yield the smallest difference, which is less than 7%.
The WIMS-ORIGEN performed by BN shows the closest correspondence to CESAR according to both the arithmetic and mass weighted mean (see Table 7.7), with values 9.7% and 0.65% respectively.

Table 7.8 UOx Mass of actinides [g/tHM]

Actinide Isotopes	CESAR 4.3 CEA	ORIGEN 2.2 pwrue.lib CIEMAT	ORIGEN2.2 pwrue.lib KTH	ORIGEN2.1 pwru50.lib BN	WIMS8a JEF2.2 BN	WIMS8a-ORIGEN2.1 JEF2.2/ pwru50.lib BN
^{235}U	7.43E+03	6.67E+03	6.67E+03	6.99E+03	7.95E+03	7.83E+03
^{238}U	9.22E+05	9.22E+05	9.22E+05	9.23E+05	9.22E+05	9.22E+05
^{237}Np	7.34E+02	9.40E+02	9.40E+02	7.63E+02	6.06E+02	6.30E+02
^{238}Pu	3.54E+02	4.07E+02	4.07E+02	3.23E+02	3.03E+02	3.10E+02
^{239}Pu	6.06E+03	6.91E+03	6.91E+03	5.85E+03	6.29E+03	6.30E+03
^{240}Pu	2.87E+03	3.25E+03	3.25E+03	2.73E+03	2.89E+03	2.87E+03
^{241}Pu	1.38E+03	1.24E+03	1.24E+03	1.35E+03	1.40E+03	1.42E+03
^{242}Pu	9.32E+02	7.15E+02	7.15E+02	8.45E+02	8.41E+02	8.43E+02
^{241}Am	4.42E+02	4.01E+02	4.01E+02	4.33E+02	4.52E+02	4.55E+02
^{242}Cm	1.39E-02	1.58E-02	1.58E-02	1.44E-02	1.12E-02	1.38E-02
^{243}Cm	1.29E+00	7.97E-01	7.97E-01	9.01E-01	6.84E-01	6.69E-01
^{244}Cm	7.87E+01	8.53E+01	8.53E+01	7.23E+01	6.64E+01	6.80E+01
^{245}Cm	6.08E+00	5.40E+00	5.40E+00	4.22E+00	5.33E+00	5.53E+00

Actinide Isotopes	CASMO-4 / FINSPIN BNFL	HELIOS 1.8 VUJE	MCB1c2 JEF 2.2 KTH	MONTEBURN FZJ	SCALE4.4a FZJ
^{235}U	7.67E+03	7.56E+03	8.62E+03	7.54E+03	7.24E+03
^{238}U	9.22E+05	9.22E+05	9.26E+05	9.22E+05	9.20E+05
^{237}Np	6.96E+02	6.51E+02	6.33E+02		
^{238}Pu	3.32E+02	3.13E+02	2.83E+02	3.36E+02	3.66E+02
^{239}Pu	5.82E+03	5.89E+03	5.83E+03	6.16E+03	6.53E+03
^{240}Pu	2.65E+03	2.74E+03	2.62E+03	2.90E+03	3.01E+03
^{241}Pu	1.33E+03	1.34E+03	1.31E+03	1.42E+03	1.87E+03
^{248}Pu	8.42E+02	8.04E+02	7.64E+02	8.44E+02	9.38E+02
^{241}Am	4.26E+02	4.31E+02	4.23E+02	4.49E+02	7.72E+01
^{242}Cm	1.30E-02	1.34E-02	1.39E-02	1.47E-02	2.55E+01
^{243}Cm	6.49E-01	5.51E-01	5.09E-01	6.42E-01	9.27E-01
^{244}Cm	6.19E+01	7.05E+01	5.92E+01	1.28E+02	1.15E+02
^{245}Cm	4.56E+00	5.25E+00	4.84E+00		

Table 7.9 Uranium dioxide fuel

Differences in per cent between CESAR and other involved codes [%] ([CESAR – code X]/CESAR x 100)

Actinide Isotopes	ORIGEN 2.2 pwrue.lib CIEMAT	ORIGEN2.2 pwrue.lib KTH	ORIGEN2.1 pwru50.lib BN	WIMS8a JEF2.2 BN	WIMS8a-ORIGEN2.1 JEF2.2/ pwru50.lib BN
^{235}U	10.20	10.20	5.88	-7.04	-5.41
^{238}U	0.03	0.03	-0.08	0.05	0.06
^{237}Np	-28.00	-28.00	-3.87	17.42	14.23
^{238}Pu	-15.01	-15.01	8.73	14.36	12.36
^{239}Pu	-13.94	-13.94	3.40	-3.85	-4.03
^{240}Pu	-13.35	-13.35	4.91	-0.74	-0.01
^{241}Pu	9.93	9.93	2.25	-1.54	-3.02
^{242}Pu	23.26	23.26	9.33	9.82	9.56
^{241}Am	9.27	9.27	2.10	-2.19	-2.85
^{242}Cm	-13.44	-13.44	-3.54	19.41	0.80
^{243}Cm	38.20	38.20	30.09	46.98	48.14
^{244}Cm	-8.26	-8.26	8.23	15.73	13.71
^{245}Cm	11.14	11.14	30.51	12.33	8.99

Actinide Isotopes	CASMO-4 / FINSPIN BNFL	HELIOS 1.8 VUJE	MCB1c2 JEF 2.2 KTH	MONTEBURN 5B FZJ	SCALE4.4a FZJ
^{235}U	-3.29	-1.80	-16.13	-1.54	2.51
^{238}U	0.02	0.04	-0.41	0.03	0.25
^{237}Np	5.27	11.31	13.86		
^{238}Pu	6.26	11.64	20.09	5.13	-3.29
^{239}Pu	3.93	2.79	3.87	-1.65	-7.70
^{240}Pu	7.81	4.45	8.84	-0.88	-4.71
^{241}Pu	3.87	3.28	5.16	-2.72	-35.04
^{248}Pu	9.73	13.76	18.03	9.48	-0.61
^{241}Am	3.77	2.65	4.32	-1.40	82.55
^{242}Cm	6.11	3.29	-0.05	-5.77	
^{243}Cm	49.63	57.24	60.55	50.21	28.11
^{244}Cm	21.36	10.51	24.77	-62.80	-46.61
^{245}Cm	24.96	13.55	20.35		

Table 7.10 UOX calculations: Comparison with CESAR
Arithmetic mean and mass weighted mean

Calculation tool		Arithmetic Mean [%]	Weighted Mean [%]
CASMO – 4/FINSPIN	BNFL	16.6	0.13
HELIOS 1.8	VUJE	14.2	0.12
MCB1c2 –JEF 2.2	KTH	30.8	0.67
MONTEBURNS	FZJ	17.6	0.09
ORIGEN 2.2 – pwrue.lib	CIEMAT	18.6	0.34
ORIGEN2.1 –pwru50.lib	BN	11.2	0.18
ORIGEN2.2 – pwrue.lib	KTH	18.6	0.34
SCALE 4.4a	FZJ	34.6	0.42
WIMS8a	BN	11.2	0.17
WIMS8a – ORIGEN2.1	BN	16.3	0.17

The discrepancies in the UOX results are generally less than in the MOX comparison and in general the mean values are lower than the corresponding values for the MOX calculations. The smallest arithmetic mean was shown in the ORIGEN2.1 BN and WIMS8a BN (11.2%) calculations while the smallest weighted mean was manifested in the HELIOS 1.8 VUJE calculation (0.12%). Within the ORIGEN calculations a high degree of congruencies observed.
Except for the ORIGEN calculations CESAR has consumed more ^{235}U than the other codes, but on the other hand burned less ^{239}Pu.

8 METHOD AND CODE DEVELOPMENT

8.1 DEVELOPMENT OF MONTE CARLO METHOD OF CALCULATING THE STEADY-STATE CONDITIONS

8.1.1 Introduction

Our objective is to adapt the Monte Carlo Burnup Code (MCB), developed at KTH in collaboration with the UMM in Krakow for the burnup calculation of thermal reactors. The calculations that we have made by MCB were not stable in the case of thermal reactors; we have observed unnatural spatial xenon oscillations which affected neutron flux and fuel burnup. Therefore we have developed a method of stabilizing the burnup calculation, respecting the Monte Carlo approach. The burnup calculation is usually divided into several rather long time steps (several weeks in the case of the Monte Carlo approach). In general, the burnup calculation of thermal reactors is more complicated than the burnup calculation of fast reactors, since conditions in thermal reactor core (like coolant density distribution, and xenon distribution) very much relate to neutron flux, and neutron flux very much relates to the conditions. Considering the long time steps, the core conditions and the neutron flux are supposed to be steady-state. If the conditions are not kept at the steady-state then one can observe a spatial oscillation of neutron flux and core conditions (see Figure 8.1).

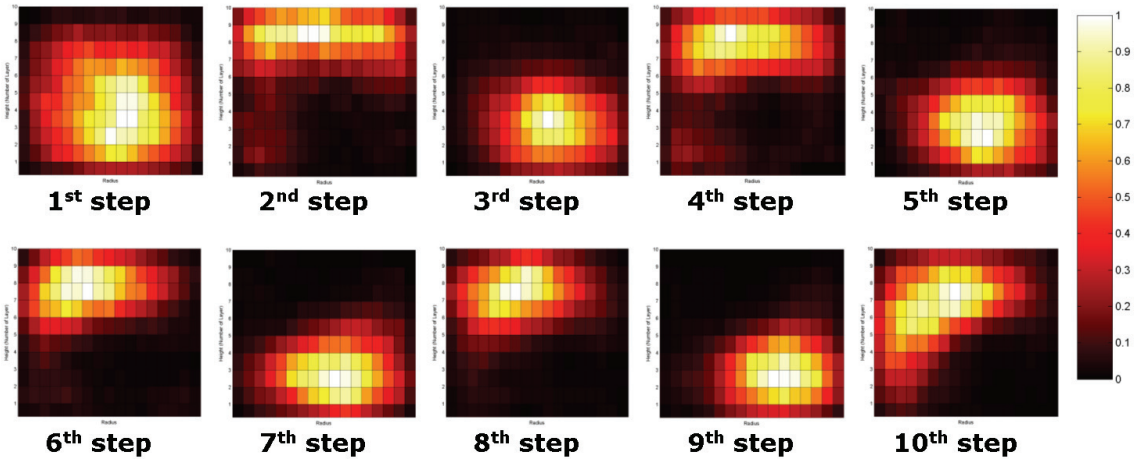

Figure 8.1 Spatial oscillation of the power distribution at the axial cross-section of PWR core

We describe the method for computing the steady-states by Monte Carlo method in detail in [28]. This section provides a simplified description of the method.
The steady-state core conditions (e.g. spatial distribution of coolant density and strongly absorbing fission products) are fully determined by steady-state neutron flux $\phi^*(\mathbf{r}, E)$. For simplicity, we suppose that all conditions can be determined by power distribution, thus, we describe the calculation method on computing the steady-state power distribution $x^*(\mathbf{r})$. The presented method, however, also allows computing the steady-state multigroup neutron flux. The numerical approach involves a discretization of $x^*(\mathbf{r})$ into a number of space nodes.

Let $\mathbf{R}_+^d$ be a set of vectors with d positive real components. Let $\mathbf{\Pi}(\mathbf{x}):\mathbf{R}_+^d \to \mathbf{R}_+^d$ describe an asymptotic spatial mass distribution of ^{135}Xe (in time $t \to \infty$) in the core, corresponding to the spatial power distribution $\mathbf{x} \in \mathbf{R}_+^d$. Next, let $\mathbf{H}(\mathbf{x}):\mathbf{R}_+^d \to \mathbf{R}_+^d$ describe a spatial distribution of coolant density. Finally, let $\mathbf{M}(\mathbf{\Pi},\mathbf{H}):\mathbf{R}_+^{2d} \to \mathbf{R}_+^d$ give an appropriate power distribution at the core with the constant xenon distribution $\mathbf{\Pi}$ and the constant coolant density distribution $\mathbf{H}$. Then, the steady-state power distribution $\mathbf{x}^*$ can be computed as a root of a nonlinear equation

$$\mathbf{x}^* = \mathbf{M}(\mathbf{\Pi}(\mathbf{x}^*), \mathbf{H}(\mathbf{x}^*)) \tag{1.1}$$

which can be reduced to

$$\mathbf{x}^* = \mathbf{G}(\mathbf{x}^*), \tag{1.2}$$

where $\mathbf{G}(\mathbf{x}) \equiv \mathbf{M}(\mathbf{\Pi}(\mathbf{x}), \mathbf{H}(\mathbf{x}))$. The function $\mathbf{G}(\mathbf{x})$ is evaluated in the following way. First, the considered conditions ($\mathbf{\Pi}(\mathbf{x})$ and $\mathbf{H}(\mathbf{x})$) are computed according to $\mathbf{x}$, and implemented into the core model. Then a Monte Carlo code is called to simulate the neutron transport to evaluate the power distribution $\mathbf{G}(\mathbf{x})$ in the model. The Monte Carlo method can not directly compute $\mathbf{G}(\mathbf{x})$, but gives an estimation $\hat{\mathbf{G}}(\mathbf{x})$ which is a stochastic function containing an additive noise term $\boldsymbol{\varepsilon}(\mathbf{x})$:

$$\hat{\mathbf{G}}(\mathbf{x}) = \mathbf{G}(\mathbf{x}) + \boldsymbol{\varepsilon}(\mathbf{x}). \tag{1.3}$$

That turns Eq. (1.2) to

$$\mathbf{x}^* = \hat{\mathbf{G}}(\mathbf{x}^*) \tag{1.4}$$

which is *nonlinear stochastic root-finding problem*. Eq. (1.4) must be solved numerically in the iterative manner. Other steady-state conditions can be computed as

$$\mathbf{\Pi}^* = \mathbf{\Pi}(\mathbf{x}^*), \mathbf{H}^* = \mathbf{H}(\mathbf{x}^*). \tag{1.5}$$

The problem could also be defined as the stochastic root-finding problem for the steady-state neutron flux; however, the calculation method would be the same.

8.1.2 Stochastic Approximation

The nonlinear stochastic root-finding problem is often changed to *stochastic optimization* problem which minimizes a stochastic function of several variables. The stochastic optimization can be described as follows: given stochastic *objective function* $\hat{f}:\mathbf{R}^d \to \mathbf{R}$,

$$\text{minimize } \hat{f}(\mathbf{x}) \text{ in } \mathbf{R}^d.$$

The solution $\mathbf{x}^*$ of Eq. (1.4) can be found as a minimizer of various stochastic functions, e.g. $\hat{f}(\mathbf{x}) = \left\| \mathbf{x} - \hat{\mathbf{G}}(\mathbf{x}) \right\|$. The stochastic optimization method which reaches the best convergence rate is *stochastic approximation* which refers to a class of methods that compute or use an approximation of the gradient of the objective function. The method is usually formulated as follows: given an initial vector $\mathbf{x}^{(1)} \in \mathbf{R}^d$, compute for $n \geq 1$ until convergence

$$\mathbf{x}^{(n+1)} = \mathbf{x}^{(n)} - a_n \hat{\mathbf{g}}^{(n)}, \tag{1.6}$$

where a_n is a positive parameter called *stepsize*, and $\hat{\mathbf{g}}^{(n)}$ is an estimate of the gradient

$$\mathbf{g}^{(n)} = \nabla f(\mathbf{x}^{(n)}) \tag{1.7}$$

of the objective function *f*.

The basic algorithm for the stepsize generation is the *Robbins-Monro algorithm* which is of the form

$$a_n = \frac{a}{n}, \tag{1.8}$$

where a is a positive scalar. Robbins and Monro proved that if $a_n > 0$, $\sum_{n=1}^{\infty} a_n = \infty$, and $\sum_{n=1}^{\infty} a_n^2 < \infty$, then $\mathbf{x}^{(n)} \to \mathbf{x}^*$. The Robbins-Monro algorithm will, under certain conditions, have the fastest possible asymptotic convergence rate $n^{-1/2}$. However, the algorithm strongly depends on the parameter a. The optimal value is $1/\lambda$, where λ is the smallest eigenvalue of the Hessian matrix of the objective function evaluated at $\mathbf{x}^*$.

8.1.3 Description of Stochastic Approximation Approach

The objective is to solve the system of nonlinear stochastic equations

$$\mathbf{x}^* = \hat{\mathbf{G}}(\mathbf{x}^*), \mathbf{x}^* \in \mathbf{R}_+^d, \hat{\mathbf{G}} : \mathbf{R}_+^d \to \mathbf{R}_+^d, \tag{1.9}$$

where $\mathbf{x}^*$ represents the steady-state power distribution in the core. The problem is solved by minimizing the stochastic objective function

$$\hat{f}(\mathbf{x}) = \sum_{i=1}^{d} \left(\hat{G}_i(\mathbf{x}) - x_i \right)^2 . \tag{1.10}$$

The vector $\mathbf{x}^*$ is computed by the stochastic approximation formulated as follows: given an initial vector $\mathbf{x}^{(1)} \in \mathbf{R}_+^d$, compute for $n \geq 1$ until convergence

$$\mathbf{x}^{(n+1)} = \mathbf{x}^{(n)} - a_n \hat{\mathbf{g}}_{s_n}^{(n)} . \tag{1.11}$$

The gradient $\hat{\mathbf{g}}_{s_n}^{(n)}$ is evaluated by a sample of size s_n (number of neutrons simulated by the Monte Carlo method). The efficiency of the calculation depends on a sequence of $\{a_n\}$ and $\{s_n\}$.

The reason to choose a different sample size for each iteration step is very simple. Any MC code has to devote a certain time that does not depend on the sample size to processing the input file, preparing the data libraries, and creating an initial neutron distribution, which can be considered as a lost time t_{lost} since the neutron transport is not simulated. The computer time $t_{simulation}$ during which the neutron transport is simulated is therefore only a part of the total execution time t_{total}. One can require two conditions on s_n (note that $s_n = t_{simulation} / t_{history}$, where $t_{history}$ is the computer time needed to simulate one neutron history). Firstly, s_n should be adequately small so that the precision of $\hat{\mathbf{g}}_{s_n}^{(n)}$ would not be better than the precision of $\mathbf{x}^{(n)}$. Secondly, s_n should be sufficiently large to decrease a ratio of lost time

$$t_{lost} / t_{total} . \tag{1.12}$$

The stochastic approximation can be in the considered case formulated as (derived in [28])

$$\mathbf{x}^{(n+1)} = \mathbf{x}^{(n)} - \alpha_n d(\mathbf{x}^{(n)} - \hat{\mathbf{G}}_{s_n}(\mathbf{x}^{(n)})), \quad d \in <0.5,1> \tag{1.13}$$

where α_n is reduced stepsize which relates to s_n as

$$\alpha_n = \frac{s_n}{\sum_{i=1}^{n} s_i}. \tag{1.14}$$

Apart from Eq. (1.14) one more relation is needed to be able to generate α_n and s_n.

The best convergence rate possible with Monte Carlo algorithms is of order $S^{-1/2}$ in the computational effort S (size of all samples used in the iteration), which is a consequence of the "central limit theorem" behavior. We have performed a lot of calculations to believe that α_n also optimally decays at the rate

$$\alpha_n \propto \frac{1}{\sqrt{S_n}}, \tag{1.15}$$

where

$$S_n = \sum_{i=1}^{n} s_i \tag{1.16}$$

is the total sample size related to the n-th iteration step. Eq. (1.15) is an assumption for all next derivations. Since $\alpha_1 = 1$ (see Eq. (1.14)), one can write

$$\alpha_n = \sqrt{\frac{s_1}{S_n}}. \tag{1.17}$$

Eqs. (1.14) and (1.17) give the quadratic equation

$$s_n^2 - s_1 s_n - s_1 \sum_{i=1}^{n-1} s_i = 0 \tag{1.18}$$

which has a positive root

$$s_n = \frac{s_1 + \sqrt{s_1^2 + 4 s_1 \sum_{i=1}^{n-1} s_i}}{2}. \tag{1.19}$$

The parameter α_n can be consequently computed by Eq. (1.14). Figure 8.2 shows an optimal sequence of α_n and s_n in the case $s_1 = 6 \cdot 10^5$.

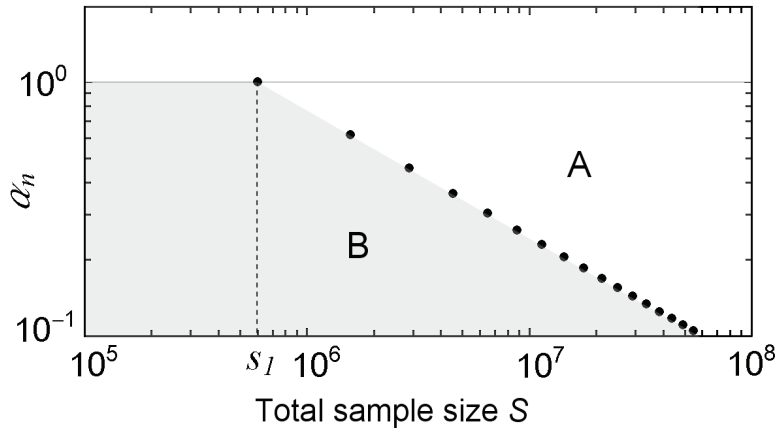

Figure 8.2 The optimal process

In general, the initial sample size s_1 is not known, therefore in [28] we propose an adaptive method which can efficiently handle a wrongly estimated s_1.

8.1.4 Numerical Test Calculation

The adaptive process is demonstrated by a calculation of steady-state conditions in a simplified PWR core model. All neutronic calculations were performed by the MCNP4C2 code running on Linux clusters. The core was modeled in such a way to allow changing of xenon concentration in fuel and coolant density at each node. The whole iteration including thermal-hydraulic calculations and processing the MCNP input and output files was performed by a PERL script. The input data, like total power, water pressure, water mass flow, definition of heat fluxes in the core, local pressure loss coefficients of spacers, were stored in a special file. At each iteration step, the xenon mass distribution was adjusted according to the new power distribution. The xenon concentration was derived from a one-group production and depletion equation for ^{135}Xe and ^{135}I according to the iterated power for each node.

The model of the PWR core contains 241 fuel assemblies of type 17X17-25 (AFA 2G) with a fuel enrichment of 3.1 wt% in ^{235}U. Each fuel assembly has 10 axial nodes. The control rods were not loaded into the core. The power distribution was normalized to 4200 MW after each iteration step. The thermal-hydraulic loop was disabled for PWR test calculation. The initial vector $\mathbf{x}^{(1)}$ was purposely chosen very far from $\mathbf{x}^*$ to test the stability of the calculation. Figure 8.3 shows the power distribution at the axial core cross-section at several iteration steps.

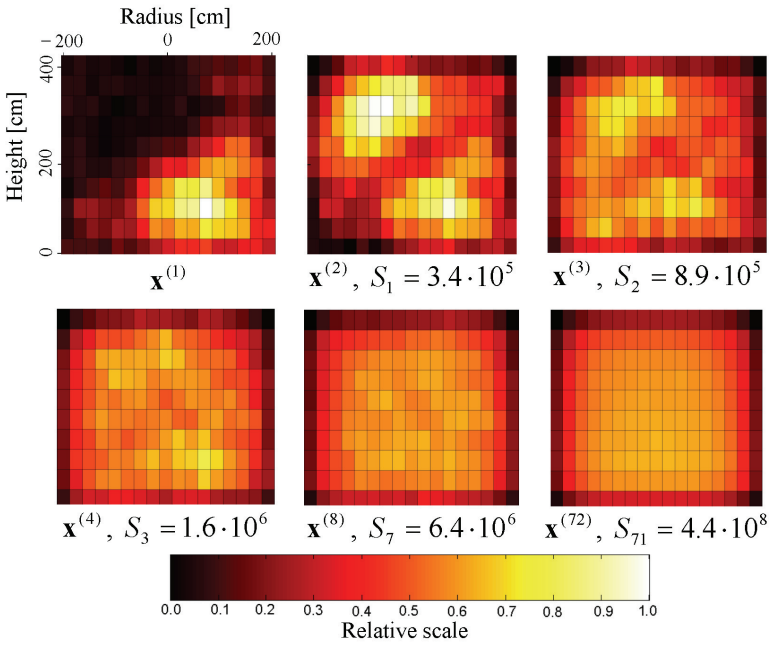

Figure 8.3 Power distribution at the axial cross-section of PWR core model at selected iteration steps

8.1.5 Conclusions

We have derived the process of an efficient Monte Carlo calculation of steady-state conditions in thermal reactors. In general, the stochastic approximation approach that we use requires specifying the stepsize and sample size parameters at each iteration

step. We have introduced the optimal iteration process that can generate those parameters if the optimal value of the initial sample size s_1 is known. In the case that s_1 is not known the adaptive process can be applied to approach the optimal process by monitoring the stability of the calculation. The results show a very good stability and efficiency of the adaptive process which is therefore suitable for computationally demanding Monte Carlo calculations.

The adaptation of MCB for thermal reactors requires a further research. Since the Monte Carlo calculation of steady-state conditions takes considerable time, the steady-state conditions will probably not be computed at all time steps. Thus, there must be developed an algorithm which recognizes at which time step it is necessary to compute the steady-state conditions, and how to treat the conditions at other steps.

8.2 DEVELOPMENT OF IN CORE FUEL MANAGEMENT TOOL (ICM) FOR MCNP/MCB CODE

8.2.1 Introduction

MCB calculation of fuel cycles of large cores is very time-consuming process. Apart from the slow Monte Carlo approach, one has to spend a lot of time by creating and changing a core model. The input file for MCB might have many thousands lines, and is easily understandable usually only for the authors. Indeed, the authors do not write each line manually, but create a very simple program which can generate various parts of the input file, since some parts of the file repeat with systematic changes. The crucial moment comes after the first burnup calculation when one has to change the input file, e.g. it is necessary to shuffle the fuel assemblies (FAs), or to load a fuel assembly with a new geometry. The corrections of such large file are very difficult, and one can possibly make a lot of errors. Therefore we have decided to solve this problem systematically. We have written a new Perl script – In Core Fuel Management Tool for MCNP/MCB Code (ICM) which is able to generate the input file automatically, and can handle basic operations with the fuel assemblies.

8.2.2 Description of ICM

The program is able to create a core model suitable for a burnup calculation (can define independent fuel assemblies), and modify the model (e.g. unloading of irradiated FA, shuffling of FAs in the core, loading of a new FA). The user creates only a relatively simple description of various types of FAs, and specifies the fuel load.

8.2.2.1 Data Flow Chart

Figure 8.4 shows the data flow chart of the fuel cycle burnup calculation when ICM is used to generate the input file for MCB.

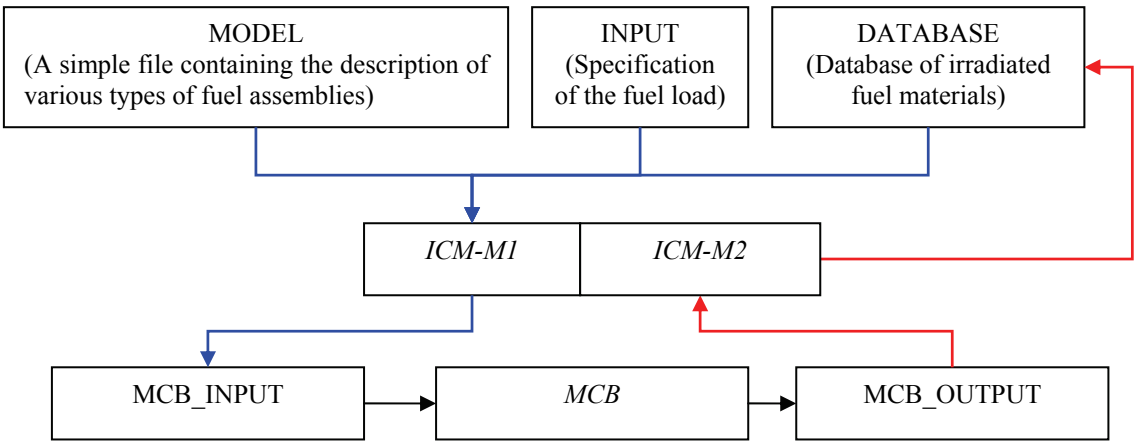

Figure 8.4 ICM data flow chart

ICM can run in two modes. The first mode (ICM-M1) uses the files 'MODEL', 'INPUT', and 'DATABASE', and creates the MCB/MCNP input file. The second mode (ICM-M2) updates the material database (file 'DATABASE') from the output MCB file. The structure of the files is described in detail in the following sections. The file 'MODEL' contains description of the core and various types of fuel assemblies. The file 'INPUT' specifies the fuel load; each position in the core is assigned to a particular fuel assembly. The file 'DATABASE' contains the isotopic composition of fuel of all irradiated assemblies.

ICM-M1 never changes the MCB output file to make a new input file, but always creates a completely new input file, utilizing the material database. The reason for that is to keep the code as simple as possible – it always does the same. ICM–M1 first decrypts the fuel load from the input file. Then it goes through the 'DATABASE' file, and finds occupied universe and material numbers of all irradiated fuel assemblies. When a new fuel assembly is to be created then ICM-M1 generates a new universe and material numbers, and the isotopic composition of fuel is taken from the file 'MODEL'. When an irradiated fuel assembly is to be loaded then ICM-M1 uses the universe and material numbers which are assigned to the assembly in the file 'DATABASE', and also the isotopic composition of all materials is taken from this file.

8.2.2.2 File 'INPUT'

The syntax of file 'INPUT' is simple (see below). First input is the identification of the loaded fuel assembly. The identification consists of two parts separated by a dot, e.g. '`A.11`' denotes a fuel assembly of type '`A`' with a number '`11`'. The identification is followed by the number of the position in the core. The whole first fuel cycle must be described in this way. The second fuel cycle might be described in a simplified way. The assembly identification might be followed by more positions. In the case below a new fuel assembly '`D-6.01`' is loaded into the position 1. The assembly which was in the position 1 before (that is '`A.11`') is moved into the position 5, the assembly which was in the position 5 before is moved into the position 2, and the assembly which was in the position 2 before is unloaded from the core. Some assemblies might be left without shuffling from the previous cycles. Everything what follows after '`C `' typed anywhere in any line is considered as a comment.

Reduced example of the 'MODEL' file:

```
C CYCLE 1
```

```
A.11  1   B.14  2   A.20  3   B.03  4   A.49  5   B.08  6
A.34  7   C.41  8   A.14  9   B.47 10

C CYCLE 2
D-6.01  1  5  2   D-3.01  6  8  7
```

8.2.2.3 File 'MODEL'

The file 'MODEL' contains a comprehensive description of all FA types and the core. This description is based on MCNP programming. The file consists of the following sections:

- TITLE

This section contains only one line – title for the MCB input file

- MAIN

This section contains all the cell cards that are not to be repeated, e.g. the cards describing the core shell, plates, and the reactor vessel. There also must be a lattice card where the numbers of universes of the fuel assemblies are changed to position numbers. The position numbers must be prefixed by the letter 'p' (see below), e.g. 'p41' denotes position 41. These position numbers will be changed automatically into universe numbers of specified FAs by ICM-M1.

- TYPE {I}

where 'I' denotes the type of the fuel assembly (see an example below). Only the cell cards which are to be repeated for each FA can be written here. One separate section must be presented for each FA type. Each material which should be unique for the fuel assembly must have its number prefixed by 'm'. Each universe number which should be unique for the fuel assembly must be prefixed by 'u'. Those numbers will be changed for each particular assembly automatically by ICM-M1. The whole fuel assembly must be composed as one universe which number must be typed in the first line of the section. Descriptions of various types of assemblies may use the same numbers for universes, cell numbers, and materials.

- SURFACES

This section contains all surface cards.

- MATERIALS

This section contains all material cards for the cell cards from the 'MAIN' section.

- MATERIALS {I}

One separate section must be presented for each FA type. This section contains all material cards for the cell cards from the 'TYPE {I}' section.

Reduced example of the 'MODEL' file:

```
[TITLE]
       Ringhals - 4

[MAIN]
320 0     -151 150 152 -153 u=300 imp:n=1 lat=1 fill= 0:8 -8:0 0:0
     1 1 1 1 1 1 1 1 1
   p8 p40 1 1 1 1 1 1
   p7 p37 p38 p39 1 1 1 1
...

[TYPE A] u=11
410 m20 -9.89  -61 105 -106  u=u10 imp:n=1 tmp1=1.0341E-07 vol=40917.92
...

[TYPE B] u=11
410 m20 -9.91  -61 105 -106  u=u10 imp:n=1 tmp1=1.0341E-07 vol=40917.92
...
```

```
[SURFACES]
*800 px 0
*801 py 0
1 pz 0
...

[MATERIALS]
kcode 1000 1.0 10 1000
m1    nlib=06c
      26000. -70.76
      28000. -9.75
      24000. -19.00
      25055. -2.00
...

[MATERIALS A]
m20  nlib=12c  $ 1.8%
     92234.   3.660829E-05
     92235.   6.075346E-03
     92238.   3.272214E-01
      8016.   6.666667E-01
...

[MATERIALS B]
m20  nlib=12c  $ 2.3%
     92234.   4.677425E-05
     92235.   7.762442E-03
     92238.   3.255241E-01
      8016.   6.666667E-01
```

8.2.2.4 File 'DATABASE'

The 'DATABASE' file is created and updated by ICM-M2, and the user does not need to change this file. The structure of the file is very simple. It consists of material cards separated by blank lines. The cards which are delimited by the blank lines belong to one fuel assembly. An example of the first line of the card section follows:

```
c [FA A.05] u=31 20->75 21->76
```

which means that the material cards in the section relate to irradiated fuel assembly 'A.05'. When this assembly was used for the first time, ICM-M1 gave a unique universe number 31 to it, and materials 20 and 21 from the 'MODEL' file were changed to 75 and 76, respectively. Every time this assembly is loaded into the core it has the same universe and material numbers. However, the cells and those universes which are used internally in the FA might have different numbers every time.

8.3 MCB VALIDATION ON RINGHALS 4 EXPERIMENT

8.3.1 Introduction

The Monte Carlo Burnup Code (MCB), developed at KTH in collaboration with the UMM in Krakow is a geometry-dependent burnup simulation tool that can be used to determine the material composition in reactor fuel. Being an extension of Monte Carlo n-Particle (MCNP) code, it solves the Bateman equations for each particular material.

Validation of MCB is an important step in development of the reliable reactor burnup simulation tools based on the Monte Carlo technique.

The experimental burnup data of the pressurized water reactor (PWR) Ringhals4 have been obtained in collaboration with Vattenfall Bränsle. Since the burnup measurements were performed only after the 14^{th} burnup cycle, the amount of calculational work to complete this task is very challenging.

This validation stimulated the development of the ICM tool to be able to handle simply the MCB input file for all fuel cycles. Next work was devoted to solving the stability problem of MCB (described in the following sections). A new simplified core model was created by ICM to speed up the burnup calculation. So far, several fuel cycles have been computed.

8.3.2 Core Model

The core was well described in the previous annual report. The input file was remade by the ICM tool with an accent on the speed of the burnup calculation. The core has quadrant symmetry, thus, the model represents one quarter of the core with reflective surfaces. Each fuel assembly contains at least two independent materials. One fuel material is defined at both ends of each FA (23% of the total fuel volume), and the second fuel material is defined in the middle part.

8.3.3 Stabilizing of ^{135}Xe mass distribution

MCB nowadays fails in burnup calculation of thermal reactors since the conditions are not preserved at the steady-state. In the ideal case the steady-state conditions should be computed at each time step by the method described in Sec. 8.1, however, such approach would slow down the burnup calculation considerably. Therefore we have decided to stabilize the xenon distribution by the 'limit' cards which specify the xenon concentration at certain materials. We have decided to specify the xenon distribution for all time steps in advance. There are several possibilities how to gain the xenon distribution.

One possibility is to specify a uniform distribution of ^{135}Xe depending only on the total power. The xenon concentration depends on the neutron flux ϕ as

$$N_{Xe} = \frac{y_{^{135}I}\Sigma_f\phi + y_{^{135}Xe}\Sigma_f\phi}{\lambda_{^{135}Xe} + \sigma_a^{^{135}Xe}\phi},$$

which is a result of one-group production and depletion equations for ^{135}Xe and ^{135}I, where $y_{^{135}Xe}$ and $y_{^{135}I}$ are production yields of ^{135}Xe and ^{135}I , respectively, in the thermal fission of ^{235}U. However, the fuel load usually contains FAs with various fuel enrichments, and since the xenon concentration depends strongly on the fuel enrichment (Σ_f in the formula), various FAs have also various concentration of xenon. In the case we specify the uniform xenon distribution then the FAs with low enrichment will have too high xenon concentration, and on the contrary the FAs with high fuel enrichment will have too small xenon concentration, which affects the burnup process negatively.

The next possibility is to specify a uniform neutron flux in the core, and to compute the xenon mass distribution according to the fuel enrichment in the fuel assemblies. This approach gives much more precise results, because in reality the neutron flux is more or less uniform in the core. Indeed, the peripheral fuel assemblies are in smaller neutron flux than other assemblies.

Finally, we have decided to specify an approximate steady-state neutron flux in the core in advance, and to compute the xenon concentration according to the fuel enrichment and to the neutron flux. The point is how to specify the approximate steady-state neutron flux in advance. As we said the neutron flux is more or less uniform in the core.

To approach the reality more closely we can e.g. to specify two coefficients c_{ax} and c_{rad} for each core node and to compute the relative neutron flux in certain place as multiple of the two coefficients. The coefficient c_{ax} represents the axial dependency of the neutron flux, and c_{rad} represents the radial dependency of the neutron flux. We have set the coefficients for each node in the core according to our experience from calculations of steady-state core conditions. However, we want to point out that this is a temporary solution, and MCB should automatically handle to stabilize the burnup calculation of thermal cores in the future. The xenon concentration for each material is computed by ORIGEN2. The process is controlled by a PERL script (600 lines). First, the script reads BURN, POWER, and PRIOD cards, and isotopic compositions and volumes of all burnable materials. Then the relative flux is computed for each material by the specified coefficients c_{ax} and c_{rad}. At each time step, one preliminary burnup calculation is performed with the neutron flux normalized to certain value, and the total power is computed. The neutron flux is then adjusted in such a way that the core will give the power specified by the POWER card. Two burnup calculations are performed with different concentration of H_3BO_3 in the water - 0 and 650 ppm, respectively (two ORIGEN2 libraries must be prepared in advance). Finally, the xenon concentration for each material at each time step is interpolated for the real concentration of H_3BO_3 (concentration of H_3BO_3 in water is controlled according to the fuel burnup).

8.3.4 Results

We have successfully finished first two fuel cycles. The following sections describe the results in detail.

8.3.4.1 First Fuel Cycle

The first fuel cycle was divided into 7 time steps. The concentration of H_3BO_3 in the cooling water was decreasing step by step until the zero concentration at the end of the cycle. The credibility of the burnup calculation can be simply checked by the calculated reactivity of the core at the end of the fuel cycle, when the reactivity should by zero in the ideal case. Indeed, even if the reactivity is zero, there is still possibility that the burnup calculation is wrong. However, the calculation is certainly wrong if the reactivity is very different from zero. The calculated reactivity of the core at the end of the cycle was $\rho = 600$ pcm ($k_{eff} = 1.006038$), which is a relatively high value. We think that it could be caused by an inexact specification of a boron glass which was massively used as a burnable absorber. However, the boron glass was removed from the assemblies after the first cycle.

Figure 8.5 shows the fuel enrichment in ^{235}U of all loaded assemblies at the beginning and at the end of the first fuel cycle. Figure 8.6 shows the relative power distribution in the core cross-section at the beginning and at the end of the first fuel cycle. One can see that the power distribution became more uniform during the cycle.

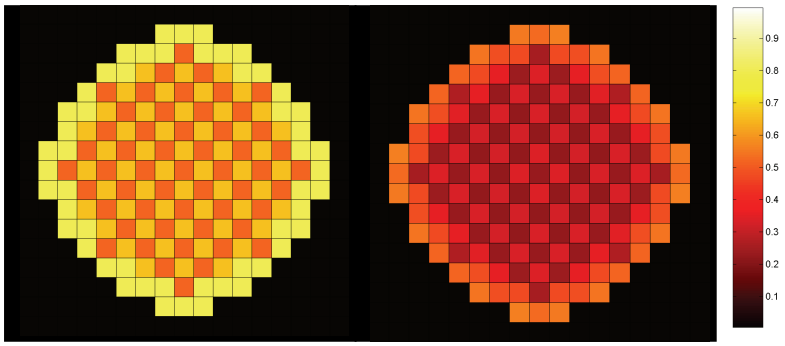

Beginning of the cycle *End of the cycle*

Figure 8.5 Fuel enrichment in ^{235}U (relative value 1 corresponds to 3.5%).

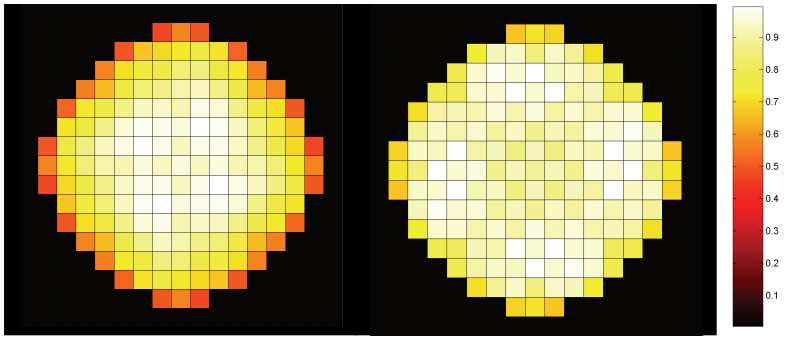

Beginning of the cycle *End of the cycle*

Figure 8.6 Relative power distribution in the core cross-section (normalized to the highest power in the core).

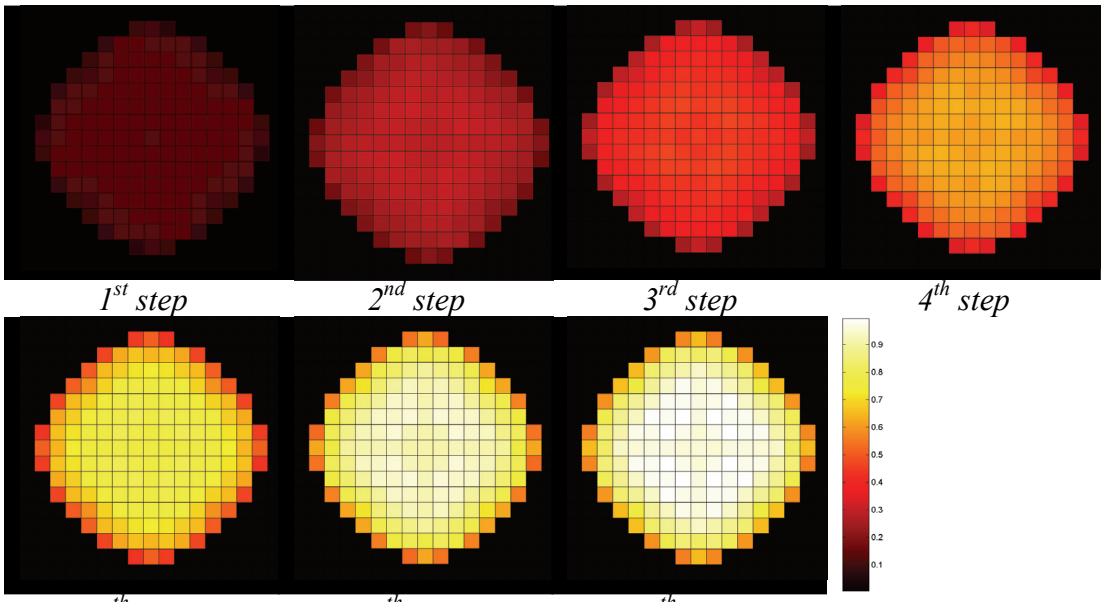

1st step *2nd step* *3rd step* *4th step*

5th step *6th step* *7th step*

Figure 8.7 Burnup distribution (normalized to the highest burnup at the end of the firs cycle)

Figure 8.7 shows the level of burnup at each fuel assembly after each time step. One can see that the burnup process was efficiently stabilized by the pre-computed xenon distribution.

8.3.4.2 Second Fuel Cycle

The second fuel cycle was divided into 11 time steps. The concentration of H_3BO_3 in the cooling water was again decreasing step by step until the zero concentration at the end of the cycle. The calculated reactivity of the core at the end of the cycle was $\rho = 185\,\text{pcm}$ ($k_{eff} = 1.001857$), which is much better result than in the previous case, however, such result can still not be used e.g. to estimate the time of the cycle with a precision of one day.

Figure 8.8 shows the fuel enrichment in ^{235}U of all loaded assemblies at the beginning and at the end of the second fuel cycle. Figure 8.9 shows the relative power distribution in the core cross-section at the beginning and at the end of the second fuel cycle. The power distribution naturally became more uniform again during the cycle.

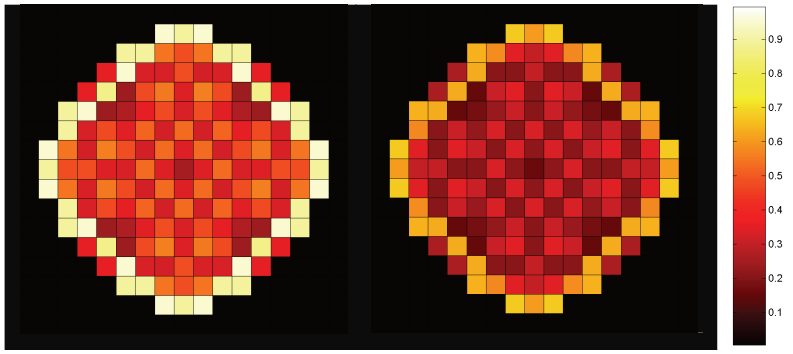

Beginning of the cycle *End of the cycle*

Figure 8.8 Fuel enrichment in ^{235}U (relative value 1 corresponds to 3.5%).

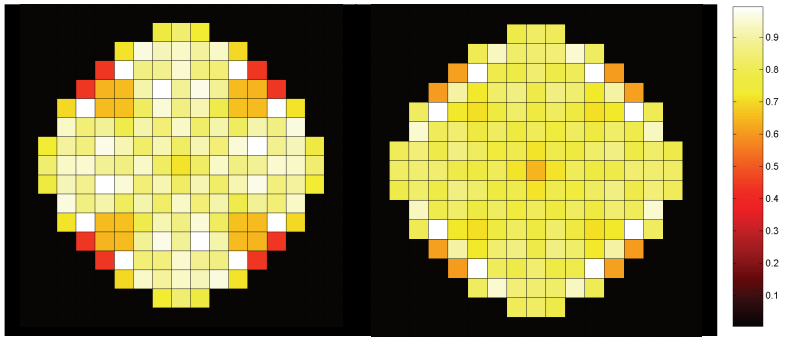

Beginning of the cycle *End of the cycle*

Figure 8.9 Relative power distribution in the core cross-section (normalized to the highest power in the core).

Figure 8.10 shows the level of burnup at each fuel assembly after selected time steps.

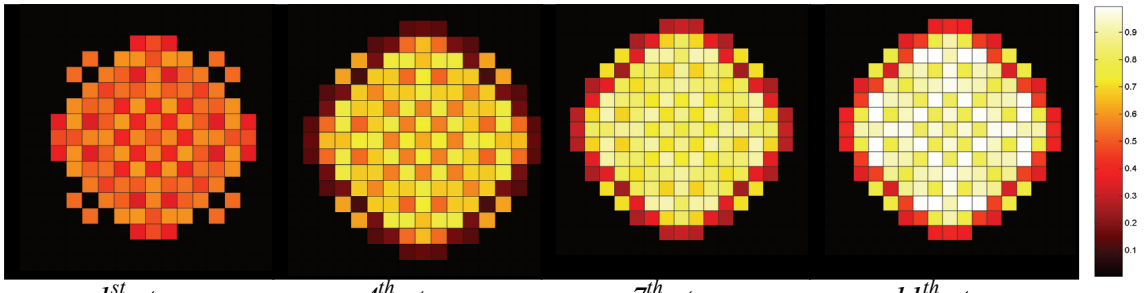

1st step *4th step* *7th step* *11th step*

Figure 8.10 Burnup distribution (normalized to the highest burnup at the end of the second cycle)

9 INTERNATIONAL INTERACTIONS, SEMINARS AND CONFERENCES

9.1 SEMINARS

1. Piero Ravetto (Polito), " Nuclear Technology Education and Research at Poltecnico di Torino", KTH, 2004
2. Francesco Venneri (GA), "Deep burn concept of General Atomics", KTH, 2004
3. V. Arzhanov, "New Developments in Neutron Transport Theory," *Talk given at the Department of Nuclear and Reactor Physics*, Kungliga Tekniska Högskolan, (2004).
4. C. Gottlieb, V. Arzhanov, W. Gudowski, "Transient Identification at Nuclear Power Plants Using Support Vector Machines," *Talk given at the IAEA Technical Meeting on* "Increasing Instrument Calibration Interval through On-line Calibration Technology," Halden, 27th-29th September 2004
5. K. Tucek, Doctoral seminar , KTH, AlbaNova University Centre, Stockholm, December 3, 2004
6. M. Ericsson, Transients in ADS, Westinghouse Electric AB, 2004-01-23
7. M. Ericsson, Transients in ADS, SwedPower AB, 2004-11-19
8. M. Ericsson, Pre-doctoral seminar Department seminar, reactor physics, 2004-11-26
9. D. Westlén, A transmutation seminar for MPs from Folkpartiet, Stockholm, 20041116
10. W. Gudowski and D. Westlén, A transmutation seminar for IVA, Stockholm, 20041118
11. Ch. Lagerstedt, SKC doktorandinternat seminar, Bålsta, Sweden

9.2 INTERNATIONAL CONFERENCES AND TRIPS

1. STNM-11 (11th Symposium on Thermodynamics of Nuclear Materials), followed by "Technical tour at ITU". Karlsruhe, Germany – M. Jolkkonen
2. EU-project SAD meeting in Moscow and Dubna, Russia, January 2004 – W. Gudowski, P. Seltborg
3. Physor 2004 meeting in Chicago, USA, April 21-25, 2004 – W. Gudowski, P. Seltborg, A. Talamo
4. "Nuclear waste management. Status, prospects and hopes", International Nuclear Physics Conference - INPC2004, Gothenburg June 2004 – W. Gudowski, invited talk (see Appendix 14)
5. EU-project MUSE meeting in Krakow, Poland, March 2004 – W. Gudowski
6. EU-project MUSE meeting in Rome, Italy, October 2004 – W. Gudowski, P. Seltborg
7. NEA-OECD – ADS Meeting at Taejon, Maj 2004 - W. Gudowski
8. RedImpact Kick off, Oskarshamn, 20040317 – 20040319 – W. Gudowski, A. Ålander, D. Westlén, P. Isaksson

9. RedImpact, Project meeting, Paris, 20040605 – 20040608 – W. Gudowski, A. Ålander, D. Westlén
10. RedImpact project meeting on the subject performance indicators, Brussels 20040907-20040919 - W. Gudowski, P. Isaksson
11. RedImpact, Project meeting, Madrid, 20041129 – 20041201 – W. Gudowski, A. Ålander, D. Westlén, P. Isaksson
12. EUROTRANS project meeting, Kralsruhe, October 2004 – W. Gudowski, J. Wallenius
13. Fe-Cr workshop SCK-CEN, Mol, Belgium, 2004-05-06 – 2004-05-07 – Ch. Lagerstedt
14. COSIRES, Helsingfors, Finland 2004-06-28 – 2004-0702 - Ch. Lagerstedt
15. 6 Fe-Cr workshop, Paris, France, 2004-11-23 – 2004-11-2 - Ch. Lagerstedt
16. F Juliot and O Hahn Summer school 2004-08-25 – 2004-0903 - Ch. Lagerstedt
17. IAEA Technical Meeting Halden, 27th-29th September 2004 – V. Arzhanov, C. Gottlieb
18. IAEA ADS meeting, Vienna, December 2004 – W. Gudowski, J. Wallenius

10 REFERENCES

1. Shvetsov et al.: *SAD Project at a Glance***,** ISTC Project 2267.
2. Taczanowski, S., Domańska, G., Kopeć, M., Janczyszyn, J.: *Considerations on the Design and Experimental of Accelerator-driven Subcritical Assembly in Dubna* **(SAD*)***, ICRP conference, Funchal, 2004-05-14
3. Smirnov A. V.: SAD MCNP input file vers.1 28.04.04
4. J Carbajo et. al.: *A review of the thermophysical properties of MOX and UO_2 fuels***,** Journal of Nuclear Materials 299 (2001) 181-198.
5. G. R. Keepin, *Physics of Nuclear Kinetics*, Addison-Wesley, 1965.
6. R. Soule et al., "Neutronic Studies in Support of Accelerator-Driven Systems: The MUSE Experiments in the MASURCA Facility," Nucl. Sci. Eng., 148, 124 (2004).
7. N. G. Sjöstrand, "Measurements on a subcritical reactor using a pulsed neutron source", Arkiv för Fysik, 11, 13 (1956).
8. D. Villamarín, "Análisis dinámico del reactor experimental de fisión nuclear MUSE-4"*,* Doctoral Thesis, Universidad Complutense de Madrid, Departamento de Física Atómica, Molecular y Nuclear, 2004.
9. K. O. Ott & R. J. Neuhold, *Introductory Nuclear Reactor Dynamics*, American Nuclear Society, 1985.
10. G. D. Spriggs et al., "On the Definition of Neutron Lifetimes in Multiplying and Non-Multiplying Systems," LA-UR-97-1073, Brazilian Meeting on Reactor Physics and Thermo hydraulics, Pocos de Caldas Springs, MG, Brazil, 1997.
11. R. D. Busch et al., "Definition of Neutron Lifespan and Neutron Lifetime in MCNP4B," LA-UR-97-222, American Nuclear Society Meeting, Orlando, Florida, June 1997.
12. K. S. Krane, *Introductory Nuclear Physics*, Wiley, 1988
13. S. E. Chigrinov and I. G. Serafimovich, "Experimental and Theoretical Research of Long-lived Fission Products and Minor Actinides in Subcritical Assembly Driven by a Neutron Generator", ISTC Project B-070-98, Joint Institute of Power and Nuclear Research, National Academy of Sciences of Belarus, Minsk, Sosny.
14. Janis 2.1. OECD / NEA Data Bank, June 2004.
15. S. C van der Marck & R. Klein Meulekamp, "Calculating the Effective Delayed Neutron Fraction Using Monte Carlo Techniques", PHYSOR 2004, Chicago, Illinois, USA, April 2004.
16. www.cern.ch/minuit.
17. U. Ringström, "Att mäta", Fysik, KTH, 1998.
18. Nifenecker et al. *Accelerator Driven Subcritical Reactors*, Institute of Physics Publishing, 2003.
19. J. Bussac & P. Reuss, *Traité de neutronique – Physique et calcul des réacteurs nucléaires avec application aux réacteurs à eau pressurisée et aux réacteurs à neutrons rapides*, Hermann, 1985.
20. P. Reuss, *Précis de neutronique*, EDP Sciences, 2003.
21. W. M Stacey, *Nuclear Reactor Physics*, Wiley, 2001.
22. J.F Briesmeister, editor, MCNP – A general Monte Carlo N-particle transport code, version 4c, LA-13709-M, Los Alamos National Laboratory, USA, 2000.

23. Table of Nuclides at KAERI, http://atom.kaeri.re.kr/ton/
24. J. Wallenius & M. Eriksson, "Neutronics of minor actinide burning accelerator driven systems with ceramic fuel", Accepted for publication in Nuclear Technology.
25. P. Seltborg, "External Source Effects and Neutronics in Accelerator-driven Systems", Licentiate Thesis, Department of Nuclear and Reactor Physics, Royal Institute of Technology, Stockholm, 2003.
26. K. Tuček, "Neutronic and Burnup Studies of Accelerator-driven Systems Dedicated to Nuclear Waste Transmutation", Doctoral Thesis, Department of Nuclear and Reactor Physics, Royal Institute of Technology, Stockholm, 2004.
27. F. Perdu et al., "Prompt reactivity determination in a subcritical assembly through the response to a Dirac pulse", *Progress in Nuclear Energy*, Vol. 42, No. 1, pp. 107-120, 2003.
28. J. Dufek and W. Gudowski, "Stochastic approximation for Monte Carlo calculation of thermal reactors", submitted to Nuclear Science and Engineering.
29. K. Tuček: Neutronic and Burnup Studies of Accelerator-driven Systems Dedicated to Nuclear Waste Transmutation, Doctoral Thesis, Royal Institute of Technology, Stockholm, 2004
30. J. WALLENIUS et al, *Application of burnable absorbers in an accelerator driven system*, Nucl. Sci. Eng. **137, (**2001)
31. G. B. Melese-d'Hospital, *Rewiev of Gas Cooled Reactors Thermal Hydrualics*, Proc. ANS/ASME/NRC International Topical Meeting on Nuclear Reactor Thermal-Hydrualics, Saratoga Springs, USA, 5-8 October 1980 (1980)
32. P. Fortescue et al, *A developmental gas-cooled fast breeder reactor plant*, Proc. Nuclex 69, Basel 6-11 October 1969 (1969)
33. Systems and safety studies on accelerator driven transmutation – Annual report 2003, Dept. of reactor physics, KTH, 2004
34. C. P. GRATTON et al, *A gas-cooled fast reactor using coated particle fuel,* J Brit. Nucl. Ener. Soc. **7** (1968)
35. D. WESTLÉN and J. WALLENIUS, *Achieving decay heat removal in a sub-critical fast gas cooled reactor,* submitted to Nucl. Technol. (2004)
36. J. CETNAR, J. WALLENIUS and W. GUDOWSKI, *MCB: A continuous energy Monte-Carlo burnup simulation code,* Actinide and fission product partitioning and transmutation, Proc. of the Fifth Int. Information Exchange Meeting Mol, Belgium, 25-27 November 1998, 523, OECD/NEA (1998)
37. J. L. EVERETT, III and E. J. KOHLER, *Peach bottom unit no. 1: A high performance helium cooled nuclear power plant,* Ann. Nucl. Energy, **5**, 321, (1978)
38. A. L. HABUSH and A. M. HARRIS, *330-MW(e) Fort St. Vrain high-temperature gas-cooled reactor,* Nucl. Eng Des, **7**, 312, (1968)
39. C. A. RENNIE, *Achievements of the Dragon project*, Ann. Nucl. Energy, **5**, 305, (1978)
40. M. NAGANUMA et al, *Design study on core and fuel properties of helium gas cooled fast reactors*, in japanese, JNC TN9400 2002-074, (2002)
41. HUNTER, C. W., FISH, R. L., HOLMES, J. J., 1975. Mechanical properties of unirradiated fast reactor cladding during simulated overpower transients. *Nucl. Technol.* 27(3), pp 376-388 (1975)

42. M. KONOMURA et al, *A promising gas-cooled fast reactor and its r&d plan,* Proc. Global 2003, New Orleans (2003)
43. M. SATO et al, Numerical Study on Plant Dynamic Chracteristics of Helium Gas Cooled Fast Reactor, in japanese, JNC TN9400 2003-100, (2003)
44. H.W. WIESE, *Actinide transmutation properties of thermal and fast fission reactors including multiple recycling,* J. Alloys Compd. **271**, 522 (1998)
45. W. S. YANG and H. S. KHALIL, *Blanket design studies of a lead-bismuth eutectic-cooled accelerator transmutation of waste system,* Nucl. Technol. **135** (2001)
46. A. Talamo, W. Gudowski and F. Venneri. The burnup capabilities of the Deep Burn Modular Helium Reactor analyzed by the Monte Carlo Continuous Energy Code MCB. Annals of Nuclear Energy 31/2, pp. 173-196, (2004).
47. A. Talamo, W. Gudowski, J. Cetnar and F. Venneri. Key physical parameters and temperature reactivity coefficients of the Deep Burn Modular Helium Reactor fueled with LWR's waste. Annals of Nuclear Energy, accepted for publication (2004).
48. General Atomic. GT-MHR conceptual design description report. U.S. Nuclear Regulatory Commission, GA/NRC-337-02, (2002).
49. A. Baxter and M. Fikani. Reactor-based transmutation – physics studies of the gas-cooled graphite-moderated deep burn reactor. General Atomic, GA-501-0-TRT-000140, (2002).
50. A. Baxter and C. Rodriguez. The application of gas-cooled reactor technologies to the transmutation of nuclear waste. Progress in Nuclear Energy 38, pp. 81-105, (2001).
51. A. Baxter, C. Rodriguez and F. Venneri. *Deep burn: making nuclear waste transmutation practical.* Nuclear Engineering and Design 222, pp. 299-317, (2003).
52. K. Ohashi, F. Okamoto and H. Hayakawa. Modular High temperature reactor contributing the global environmental protection. Progress in Nuclear Energy 37, pp. 307-312, (2000).
53. Y. Tsuchie. Desirability of small reactors, HTGR in particular. Progress in Nuclear Energy 37, pp. 253-258, (2000).
54. A.I. Kiryushin, N.G. Kodochigov, N.G. Kouzavkov et al. *Project of the GT-MHR high temperature helium reactor with gas turbine.* Nuclear Engineering and Design 173, pp.119-129, (1997).
55. R. Plukiene and D. Ridikas. Modelling of HTRs with Monte Carlo: from a homogeneous to an exact heterogeneous core with microparticles. Annals of Nuclear Energy 30, pp. 1573-1585, (2003).
56. J. Cetnar, W. Gudowski and J. Wallenius. Monte Carlo continuous energy burnup MCB1C – The description, methods and benchmarks. In preparation for NSE.
57. J.Cetnar, W. Gudowski, J. Wallenius and K. Tucek. *Simulation of nuclide transmutation with Monte-Carlo Continuous Energy Burnup Code (MCB1C).* Proc. Accelerator application 2001 and ADTTA 2001 Nuclear application in the new millennium, Reno, (2001).
58. J. Cetnar, W. Gudowski and J. Wallenius. MCB : a continuous energy Monte Carlo burnup simulation code, in actinide and fission product partitioning and transmutation. EUR 18898 EN, OECD/NEA 523, (1999).

59. R.B. Firestone et al. *Table of Isotopes 8th edition.* Willey-Interscience, ISBN: 0471356336, (1999).
60. A. G. Croff, "ORIGEN2: a versatile computer code for calculating the nuclide compositions and characteristic of nuclear materials". Nuclear Technology 62, pp. 335-353, (1983).
61. http://wwwndc.tokai.jaeri.go.jp/jendl/jendl.html.
62. J. Blachot and C. Nordborg. *JEF-2.2 Radioactive Decay Data*. International Symposium on Nuclear Data Evaluation Methodology, BNL, (1992).
63. ENDF/B-VI. *The US Evaluated Nuclear Data Library*. IAEA-NDS-100, Rev.11 (1994).
64. http://www.jaeri.go.jp/english/press/2002/020510/ta02.html.
65. J.J. Kim, J.T. Lee and H.R. Kim. Generation and Benchmarking of a 69 Group Cross Section Library for Thermal Reactor Applications. J. Korean Nucl. Soc., 21, 245, (1989).
66. C.J. Taubman. The WIMS 69-Group Library Tape 166259. Report AEEW-M1324, U.K. Atomic Energy Authority, Winfrith, (1975).
67. D. Ridikas, L. Bletzacker et al. Comparative analysis of ENDF, JEF and JENDL data libraries by modeling high temperature reactors and plutonium based fuel cycles. Journal of Nuclear Science and Technology supplement 2, pp. 1167-1170, (2002).
68. M. Eriksson, J. Wallenius, M. Jolkkonen, and J. E. Cahalan, "Inherent Safety of Fuels for Accelerator-driven Systems," To appear in Nuclear Technology. Accepted January (2005).
69. J. Wallenius and M. Eriksson, "Neutronics of minor actinide burning accelerator driven systems with ceramic fuel," To appear in Nuclear Technology. Accepted January (2005).
70. J. L. Séran, et al., "Behavior under Neutron irradiation of the 15-15Ti and EM10 Steels Used as Standard Materials of the Phénix Fuel Subassembly," Effects of Radiation on Materials: 15th Int. Symposium, ASTM STP 1125, R. E. Stoller, A. S. Kumar, and D. S. Gelles, Eds., American Society for Testing and Materials, p. 1209-1233, Philadelphia (1992).
71. A. Fissolo, "Tensile Properties of Neutron Irradiated 316Ti and 15-15Ti Steels," Effects of Radiation on Materials: 16th Int. Symposium, ASTM STP 1175, A. S. Kumar, D. S. Gelles, R. K. Nanstad, and E. A. Little, Eds., American Society for Testing and Materials, p. 646-663, Philadelphia (1993).
72. J. E. Cahalan, A. M. Tentner, and E. E. Morris, "Advanced LMR Safety Anlaysis Capabilities in the SASSYS-1 and SAS4A Computer Codes," Proc. of the International Topical Meeting on Advanced Reactors Safety, Pittsburgh, April 17-21 (1994)
73. M. Eriksson, J. E. Cahalan, and W. S. Yang, "On the Performance of Point Kinetics for the Analysis Accelerator-driven Systems," Nuclear Science and Engineering, 149, 298-311 (2005)
74. B. F. Gromov, et al., "The Analysis of Operating Experience of Reactor Installations Using Lead-Bismuth Coolant and Accidents Happened," Proc. Heavy Liquid Metal Coolants in Nuclear Technology, Vol. 1, Obninsk, October 5-9, p. 60-

66, State Scientific Center of Russian Federation Institute for Physics and Power Engineering (1998).

75. H. K. Fauske, "The Role of Core-Disruptive Accidents in Design and Licensing of LMFBRs," Nuclear Safety, Vol. 17, No. 5 (1976).
76. H. A. Bethe and J. H. Tait, "An Estimate of the Order of Magnitude of the Explosion when the Core of a Fast Reactor Collapses," British Report UKAEA-RHM (56)/113, 1956.
77. R. A. Meyer, B. Wolfe, and N. F. Friedman, "A Parameter Study of Large Fast Reactor Meltdown Accidents," Proc. Conf. on Safety, Fuels, and Core Design in Large Fast Power Reactors, ANL-7120, Argonne Natl. Lab., Oct. 11-14 (1965).
78. H. K. Fauske, "Assessment of Accident Energetics in LMFBR Core-Disruptive Accidents," Nuclear Engineering and Design 42 (1977) 19-29.
79. H. Takano, et al., "A Design for Inherent Safety Core, Aseismicity and Heat Transport System in Lead-Cooled Nitride-Fuel Fast Reactor," Proc. Int. Topical Meeting on Advanced Reactor Safety, Pittsburgh, April 17-21 (1994).
80. J. Buogiorno and B.D. Hawkes, "Seismic analysis of heavy-liquid-metal-cooled reactor vessels," Nuclear Engineering and Design 228 (2004) 305–317.
81. I. Micheli, et al., "Investigation upon the dynamic structural response of a nuclear plant on aseismic isolating devices," Nuclear Engineering and Design 228 (2004) 319–343.
82. J.-O. Andersson et al., Thermo-Calc and DICTRA, computational tools for materials science, Calphad 26, 273 (2002).
83. T. H. Bauer, G. R. Fenske, and J. M. Kramer, Cladding failure margin for metallic fuel in the integral fast reactor, Transaction of the 9th Int. Conf. on structural mechanics in reactor technology, Vol. C, Lausanne, Aug. 17-21 (1987)
84. N.S. Cannon F.H. Huang and M.L. Hamilton, Transient and static mechanical properties of D9 fuel pin cladding and duct material irradiated to high fluence. Effects of radiation on materials: 15th Int. Symp. ASTM STP 1125, ASTP (1992), page 1071.
85. M. Eriksson and J. Cahalan, Inherent shutdown capabilities in accelerator driven systems, Ann. Nucl. Energy 29(2002) 1689.
86. Eriksson, J. Wallenius, M. Jolkkonen and J. Cahalan, Inherent safety of fuels for accelerator driven systems, Nucl. Techn., accepted for publication (2005).
87. M. Jolkkonen, M. Streit, and J. Wallenius, Thermo-chemical modelling of uranium-free nitride fuels, J. Nucl. Sci. Technol. 41(4), 457 (2004).
88. T. Matsui and R.W. Ohse: Thermodynamic properties of uranium nitride, plutonium nitride and uranium-plutonium mixed nitride, High Temperatures-High Pressures 19 (1987).
89. G. Müller et al, Behaviour of steels in flowing liquid PbBi eutectic alloy at 420-600°C after 4000-7200 h. J. Nucl. Mat. 335 (2004) 163.
90. T. Ogawa, T. Ohmichi, A. Maeda, et al., "Vaporization behaviour of (Pu,Am)N", J. Alloys and Compounds, 224, 55 (1995).

91. W.M. Olson, R.N.R. Mulford, The decomposition pressure of plutonium nitride, J. Phys. Chem., 68, 1048 (1964).
92. R. J. Puigh and M. L. Hamilton, Influence of Radiation on Materials Properties: 13th Int. Symposium (Part II), ASTM STP 956, F. A. Garner, C. H. Henager, N. Igata, Eds., American Society for Testing Materials, p. 22-29 (1987).
93. M.H. Rand, in: O. Kubaschewski (Ed.), Plutonium: physico-chemical properties of its compounds and alloys, Atomic energy review, Special issue 1, Vienna, 1966, p. 36.
94. D.J. Wade and E.K. Fujita, Trends versus reactor size of passive reactivity shutdown and control performance, Nucl. Sci. Eng. 102 (1989) 182.
95. J. Wallenius (Ed.), CONFIRM Project Progress Report 1 (2001)
96. J. Wallenius, Neutronic aspects of inert matrix fuels for application in ADS, J. Nucl. Mat. 320 (2003) 142.
97. J. Wallenius and M. Eriksson, Neutronics of minor actinide burning accelerator driven systems with ceramic fuel, Nucl. Techn., accepted for publication (2005).
98. G. J. Ackland et al., "Development of an interatomic potential for phosphorous impurities in α-iron", J. Phys.: Condens. Matter **16** (2004) S2629–S2642
99. G. J. Ackland et al., "Computer simulation of point defect properties in dilute Fe-Cu alloy using a many-body interatomic potential", Phil. Mag. A 1997, 75, 713
100. R. Chakarova, V. Pontikis and J. Wallenius, Development of FeCr many body potential and cohesion model, Delivery report 6 - SPIRE project, available on http://www.neutron.kth.se/publications/Reports.shtml
101. J. Wallenius et al., "Modeling of chromium precipitation in Fe-Cr alloys", Phys. Rev. B **69**, 094103 (2004)
102. J. Wallenius, P. Olsson and C. Lagerstedt, Relation between thermal expansion and interstitial formation energy in pure Fe and Cr, NIM B 228 (2005) 122.
103. C. S. Becquart et al., "Influence of the interatomic potential on molecular dynamics simulations of displacement cascades", J. Nucl. Mater. 280 (2000) 73
104. M. Hou, "Individual collision cascades in static bcc polycrystals", Phys. Rev. B 31 (7) (1985) 4178
105. A. Souidi et al., "Atomic displacement cascade distributions in iron", J. Nuc. Mater. 295 (2001) 179
106. D. Terentyev et al., "In-cascade interstitial cluster formation in concentrated ferritic alloys with strong solute-interstitial interaction: a molecular dynamics study", Nucl. Instr. And Meth. In Phys. Res. B 228 (2005) 156

91. W.M. Olson, R.N.R. Mulford, The decomposition pressure of plutonium nitride, J. Phys. Chem., 68, 1048 (1964).
92. R. J. Puigh and M. L. Hamilton, Influence of Radiation on Materials Properties: 13th Int. Symposium (Part II), ASTM STP 956, F. A. Garner, C. H. Henager, N. Igata, Eds., American Society for Testing Materials, p. 22-29 (1987).
93. M.H. Rand, in: O. Kubaschewski (Ed.), Plutonium: physico-chemical properties of its compounds and alloys, Atomic energy review, Special issue 1, Vienna, 1966, p. 36.
94. D.J. Wade and E.K. Fujita, Trends versus reactor size of passive reactivity shutdown and control performance, Nucl. Sci. Eng. 102 (1989) 182.
95. J. Wallenius (Ed.), CONFIRM Project Progress Report 1 (2001)
96. J. Wallenius, Neutronic aspects of inert matrix fuels for application in ADS, J. Nucl. Mat. 320 (2003) 142.
97. J. Wallenius and M. Eriksson, Neutronics of minor actinide burning accelerator driven systems with ceramic fuel, Nucl. Techn., accepted for publication (2005).
98. G. J. Ackland et al., “Development of an interatomic potential for phosphorous impurities in α-iron”, J. Phys.: Condens. Matter **16** (2004) S2629–S2642
99. G. J. Ackland et al., ”Computer simulation of point defect properties in dilute Fe-Cu alloy using a many-body interatomic potential”, Phil. Mag. A 1997, 75, 713
100. R. Chakarova, V. Pontikis and J. Wallenius, Development of FeCr many body potential and cohesion model, Delivery report 6 - SPIRE project, available on http://www.neutron.kth.se/publications/Reports.shtml
101. J. Wallenius et al., “Modeling of chromium precipitation in Fe-Cr alloys”, Phys. Rev. B **69**, 094103 (2004)
102. J. Wallenius, P. Olsson and C. Lagerstedt, Relation between thermal expansion and interstitial formation energy in pure Fe and Cr, NIM B 228 (2005) 122.
103. C. S. Becquart et al., “Influence of the interatomic potential on molecular dynamics simulations of displacement cascades”, J. Nucl. Mater. 280 (2000) 73
104. M. Hou, “Individual collision cascades in static bcc polycrystals”, Phys. Rev. B 31 (7) (1985) 4178
105. A. Souidi et al., “Atomic displacement cascade distributions in iron”, J. Nuc. Mater. 295 (2001) 179
106. D. Terentyev et al., “In-cascade interstitial cluster formation in concentrated ferritic alloys with strong solute-interstitial interaction: a molecular dynamics study”, Nucl. Instr. And Meth. In Phys. Res. B 228 (2005) 156

APPENDICES

APPENDIX 1

K. Tuček, “Neutronic and Burnup Studies of Accelerator-driven Systems Dedicated to Nuclear Waste Transmutation”, Doctoral Thesis, Royal Institute of Technology, Stockholm, Dec 2004

Neutronic and Burnup Studies of Accelerator-driven Systems Dedicated to Nuclear Waste Transmutation

Kamil Tuček

Stockholm 2004

Doctoral Thesis
Royal Institute of Technology
Department of Physics

Akademisk avhandling som med tillstånd av Kungl Tekniska Högskolan framlägges till offentlig granskning för avläggande av teknisk doktorsexamen fredagen den 3 december 2004 kl 10.00 i sal FA32, AlbaNova universitetscentrum, Kungl Tekniska Högskolan, Roslagstullsbacken 21, Stockholm.

ISBN 91-7283-890-6
TRITA-FYS 2004:68
ISSN 0280-316X
ISRN KTH/FYS/–04:68–SE

Printed by Universitetsservice US-AB, Stockholm 2004

Abstract

Partitioning and transmutation of plutonium, americium, *and* curium is inevitable if the radiotoxic inventory of spent nuclear fuel is to be reduced by more than a factor of 100. But, admixing minor actinides into the fuel severely degrades system safety parameters, particularly coolant void reactivity, Doppler effect, and (effective) delayed neutron fractions. The incineration process is therefore envisioned to be carried out in dedicated, accelerator-driven sub-critical reactors (ADS). However, ADS cores operating in concert with light-water reactors (two-component scenario) also exhibit high burnup reactivity swing with penalty on the system performance/economy.

In the frame of this design work, we attempted, by choice of coolant and optimisation of fuel concept and core design, to achieve favourable neutronic, burnup and safety characteristics of the transuranium ADS burner. Key thermal hydraulic and material-related constraints were respected.

A novel fuel matrix material, hafnium nitride, was identified as an attractive diluent option for highly reactive transuranics. (TRU,Hf)N fuels appeared to have a good combination of neutronic, burnup and thermal characteristics: maintaining hard neutron spectra, yielding acceptable values of coolant void reactivity and source efficiency, and providing small burnup reactivity loss. A conceptual design of a (TRU,Hf)N fuelled, lead/bismuth eutectic cooled ADS was developed. The average discharge burnup of 20% fissions per initial metal atom could be reached even without fuel reshuffling. The fission fraction ratios of even-neutron number americium nuclides are increased by a factor of two in comparison to burners with inert matrix based fuels. Hence, thanks to the reduced production of higher actinides and helium, fuel cycle economy is improved.

The coolant void worth proved to be a strong function of the fuel composition - reactor cores with high content of fertile material or minor actinides in fuel exhibit larger void reactivities than systems with plutonium-rich, inert matrix fuels. In reactor systems cooled by lead/bismuth eutectic, a radial steel pin reflector significantly lowered coolant void reactivity. For transuranic fuel, fertile and strongly absorbing matrices exhibited increasing void worth with increasing pitch, while the opposite was valid for the coolant void worth of inert matrix fuels. Large pitches also appeared to be beneficial for limiting the reactivity worth of the cladding material and improving source efficiency.

The economy of the source neutrons was investigated as a function of core and target design. An incentive to design the core with as low target radius as allowable by the thermal constraints posed by the ability to dissipate accelerator beam power was identified.

ISBN 91-7283-890-6 • TRITA-FYS 2004:68 • ISSN 0280-316X • ISRN KTH/FYS/–04:68–SE

List of Papers

I. K. Tuček, J. Wallenius, and W. Gudowski
Coolant void worth in fast breeder reactors and accelerator-driven transuranium and minor-actinide burners
Annals of Nuclear Energy, **31**, 1783 (2004)

II. K. Tuček, M. Jolkkonen, J. Wallenius, and W. Gudowski
Neutronic and burnup studies of an accelerator-driven transuranium burner in a start-up mode
Submitted to Nuclear Technology (2004)

III. J. Wallenius, K. Tuček, J. Carlsson, and W. Gudowski
Application of burnable absorbers in an accelerator driven system
Nuclear Science and Engineering, **137**, 96 (2001)

IV. K. Tuček, J. Wallenius, and W. Gudowski
Optimal distribution of fuel, poisons and diluents in sub-critical cores dedicated to waste transmutation
In Proceedings of the International Conference on Emerging Nuclear Energy Systems, ICENES 00, Petten, NRG (2000)

V. P. Seltborg, J. Wallenius, K. Tuček, and W. Gudowski
Definition and application of proton source efficiency in accelerator-driven systems
Nuclear Science and Engineering, **145**, 390 (2003)

Papers which are not included in the thesis:

VI. K. Tuček, J. Wallenius, W. Gudowski and A. Sołtan
IAEA accelerator driven system neutronic benchmark
In Feasibility and Motivation for Hybrid Concepts for Nuclear Energy Generation and Transmutation, IAEA-TC-903.3, CIEMAT (1998)

VII. J. Wallenius, K. Tuček, and W. Gudowski
Technetium-99 neutron absorbers in the reflector of Pb/Bi cooled reactors
In Proceedings of Heavy Liquid Metal Coolants in Nuclear Technology, HLMC 98, IPPE Obninsk, Russia (1998)

VIII. K. Tuček, J. Wallenius, W. Gudowski, and C. Sanders
Burnup in a sub-critical system with flat power density
In Proceedings of the Third International Conference on Accelerator-Driven Transmutation Technologies and Applications, ADTTA 99, Praha (1999)

IX. J. Wallenius, K. Tuček, W. Gudowski, and C. Sanders
Neutronics of a sub-critical system burning non-recycled LWR waste
In Proceedings of the Third International Conference on Accelerator-Driven Transmutation Technologies and Applications, ADTTA 99, Praha (1999)

X. J. Wallenius, K. Tuček, and W. Gudowski
Safety analysis of nitride fuels in cores dedicated to waste transmutation
In Proceedings of the Sixth International Information Exchange Meeting, Actinide and Fission Product Partitioning and Transmutation, Madrid, OECD/NEA (2000)

XI. M. Eriksson, J. Wallenius, K. Tuček, and W. Gudowski
Preliminary safety analysis of a Swedish accelerator driven system employing nitride fuel and burnable absorbers
In Proceedings of the Technical Committee Meeting on Core Physics and Engineering Aspects of Emerging Nuclear Energy Systems for Energy Generation and Transmutation, Argonne National Laboratory (2000)

XII. K. Tuček, J. Wallenius, and W. Gudowski
Source efficiency in an accelerator-driven system with burnable absorbers
In Proceedings of the International Conference on Back-End of the Fuel Cycle: From Research to Solutions, GLOBAL 2001, Paris, ANS (2001)

XIII. D. Westlén, W. Gudowski, J. Wallenius, and K. Tuček
A cost benefit analysis of an accelerator driven transmutation system
In Proceedings of AccApp/ADTTA'01, Reno, USA, ANS (2001)

XIV. J. Cetnar, W. Gudowski, J. Wallenius, and K. Tuček
Simulation of nuclide transmutations with Monte-Carlo continuous energy burnup code (MCB1C)
In Proceedings of AccApp/ADTTA'01, Reno, USA, ANS (2001)

XV. M. Eriksson, J. Wallenius, J.E. Cahalan, K. Tuček, and W. Gudowski
Safety analysis of Na and Pb-Bi coolants in response to beam instabilities
In Proceedings of the Third International Workshop on Utilisation and Reliability of High Power Proton Accelerators, Santa Fe, USA (2002)

Acknowledgments

I would like to express my gratitude to

- Waclaw Gudowski for inviting me to work on transmutations at the Royal Institute Institute of Technology, for his support and encouragement throughout the years.
- František Janouch for bringing me to Sweden, for his constant interest and enthusiasm initiating long discussions on any subject.
- Janne Wallenius for useful suggestions and valuable remarks.
- my colleagues, old and present, from the Department of Nuclear and Reactor Physics for providing a creative, friendly and relaxed atmosphere; particular thanks to Mikael Jolkkonen and Patrick Isaksson for linguistic advice.
- Lvíček and all other friends which made my stay here so enjoyable and cheerful.

Finally, most thanks go to my wonderful parents. Děkuji vám za všechno!

I acknowledge the financial support by the Swedish Nuclear Fuel and Waste Management Co. (SKB AB) and the Swedish Institute.

Stockholm, November 12, 2004

Kamil Tuček

Contents

Nomenclature

ABR	Actinide Burner Reactor
ADS	Accelerator-driven System
AFCI	Advanced Fuel Cycle Initiative
ALMR	Advanced Liquid Metal Reactor
An	Actinide
ATR	Advanced Test Reactor
ATW	Accelerator Transmutation of Waste
BA	Burnable Absorber
BOC	Beginning-Of-Cycle
BOL	Beginning-Of-Life
BWR	Boiling Water Reactor
CERCER	CERamic-CERamic fuel
CERMET	CERamic-METallic fuel
CAPRA	Consommation Accrué de Plutonium en Récteur rApide
CEA	Commissariat à l'Énergi Atomique
CMS	Centre-of-mass system
CNRS	Centre National de la Recherche Scientifique
DIAMEX	DIAMide EXtraction
DIDPA	Di-IsoDecylPhosphoric Acid
dpa-NRT	Displacement per atom (Norgett, Robinson, Torrens)
EdF	Électricité de France
EFR	European Fast Reactor
EFTTRA	Experimental Feasibility of Targets for TRAnsmutation
ENDF	Evaluated Nuclear Data File
EOC	End-Of-Cycle
EOL	End-Of-Life
FBuR	Fast Burner Reactor
FIMA	Fissions per Initial Metal Atom
FTF	Flat-to-Flat
FP	Fission Product
fpd	Full power day
efpy	Effective full power year
FR	Fast Reactor

GEDEPEON	GEstion des DEchets et Production d'Energie par des Options Nouvelles
GWd	Giga-watt day
GW_e	Giga-watt electric
GW_{th}	Giga-watt thermal
HLW	High Level Waste
HLLW	High Level Liquid Waste
ICRP	International Commission on Radiation Protection
IFR	Integral Fast Reactor
ITU	Institute for TransUranium elements
JAERI	Japan Atomic Energy Research Institute
JEF	Joint European File
JENDL	Japanese Evaluated Nuclear Data File
KAERI	Korea Atomic Energy Research Institute
LANL	Los Alamos National Laboratory
LBE	Lead-Bismuth Eutectic
LINAC	LINear ACcelerator
LLFP	Long-lived Fission Product
LWR	Light Water Reactor
MA	Minor Actinide
MCB	Monte Carlo Continuous energy Burnup code
MCNP	Monte Carlo N-Particle code
MCNPX	Monte Carlo N-Particle code eXtended
MOX	Mixed OXide fuel
MW_{th}	Mega-watt thermal
N/A	Not Available
NEA	Nuclear Energy Agency of OECD
OECD	Organisation for Economic Co-operation and Development
OMEGA	Options Making Extra Gain from Actinides and fission products
P/D	Pitch-to-Diameter ratio
P&T	Partitioning and Transmutation
Pb/Bi	Lead-Bismuth Eutectic
PSI	Paul Scherrer Institute
PUREX	Plutonium Uranium Recovery by EXtraction
PWR	Pressurised Water Reactor
S/A	Sub-assembly
SAD	Sub-critical Assembly Dubna
SPIN	SeParation-INcineration
tHM	Metric tonne of Heavy Metal
TRPO	TRialkyl Phosphine Oxide
TRU	TRansUranic element
TRUEX	TRansUranium EXtraction
TWh_e	Tera-watt hour electric
UOX	Uranium OXide fuel

XADS	EXperimental Accelerator-Driven System
XADT	EXperimental Accelerator-Driven Transmutation

We know only a single science, the science of history.

Karl Marx (The German Ideology, 1846)

The History of the Universe in 200 Words or Less

Quantum fluctuation. Inflation. Expansion. Strong nuclear interaction. Particle-antiparticle annihilation. Deuterium and helium production. Density perturbations. Recombination. Blackbody radiation. Local contraction. Cluster formation. Reionisation? Violent relaxation. Virialisation. Biased galaxy formation? Turbulent fragmentation. Contraction. Ionisation. Compression. Opaque hydrogen. Massive star formation. Deuterium ignition. Hydrogen fusion. Hydrogen depletion. Core contraction. Envelope expansion. Helium fusion. Carbon, oxygen, and silicon fusion. Iron production. Implosion. Supernova explosion. Metals injection. Star formation. Supernova explosions. Star formation. Condensation. Planetesimal accretion. Planetary differentiation. Crust solidification. Volatile gas expulsion. Water condensation. Water dissociation. Ozone production. Ultraviolet absorption. Photosynthetic unicellular organisms. Oxidation. Mutation. Natural selection and evolution. Respiration. Cell differentiation. Sexual reproduction. Fossilisation. Land exploration. Dinosaur extinction. Mammal expansion. Glaciation. Homo sapiens manifestation. Animal domestication. Food surplus production. Civilisation! Innovation. Exploration. Religion. Warring nations. Empire creation and destruction. Exploration. Colonisation. Taxation without representation. Revolution. Constitution. Election. Expansion. Industrialisation. Rebellion. Emancipation Proclamation. Invention. Mass production. Urbanisation. Immigration. World conflagration. League of Nations. Suffrage extension. Depression. World conflagration. Fission explosions. United Nations. Space exploration. Assassinations. Lunar excursions. Resignation. Computerisation. World Trade Organisation. Terrorism. Internet expansion. Reunification. Dissolution. World-Wide Web creation. Composition. Extrapolation?

Reprinted from Annals of Improbable Research, **3**, 27 (1997)

Chapter 1

Introduction

1.1 Background

In the present state of scientific knowledge, about 13.7 billions of years ago, some 10^{-33} to 10^{-4} s after the Big Bang, the protons and neutrons were created in baryogenesis process, hence marking the beginning of the **Nuclear Age** [1]. However, it took another $10^{5.5}$ years for first hydrogen atom to be formed, 100-200 million years for stars to be born, and some millions of years for the first supernova to explode spreading heavy elements like carbon, nitrogen, oxygen, and uranium throughout the entire Universe. At least $4.6{\cdot}10^9$ years ago, such a supernova explosion occurred in the vicinity of our present Solar system, providing the primordial material for its formation.

This entire historical prologue was unknown for glassmen around the village of Jáchymov (St. Joachimsthal) in the Bohemian Sudetenland as they, in the middle ages, started to use the shiny black mineral coming as a waste from local silver mines in the production of yellow coloured glass and ceramics products. An exciting mystery has been covered in these rocks, called by German miners *pechblende*, i.e. "bad luck mineral", until they came into the hands of one of the greatest scientists of his time, Henri Becquerel. In 1896, he discovered that the invisible rays emitted by these uranium rocks (a phenomenon he called *radioactivity*) are responsible for exposure of photographic plates [2].

But the major discovery was to come in December 1938. German chemists Otto Hahn and Fritz Strassmann reported that barium, an element lighter than uranium, was found in the neutron irradiated uranium samples [3]. It was Lise Meitner and her nephew Otto Frisch who first interpreted these results as a disintegration of the uranium nucleus and proposed a name for this phenomenon - *fission* [4]. A short time afterwards, Frisch and others demonstrated that the overall energetic balance of the fission reaction is positive, and that the major amount of energy is manifested as kinetic energy of the fission products. In 1939, Kowarski showed that

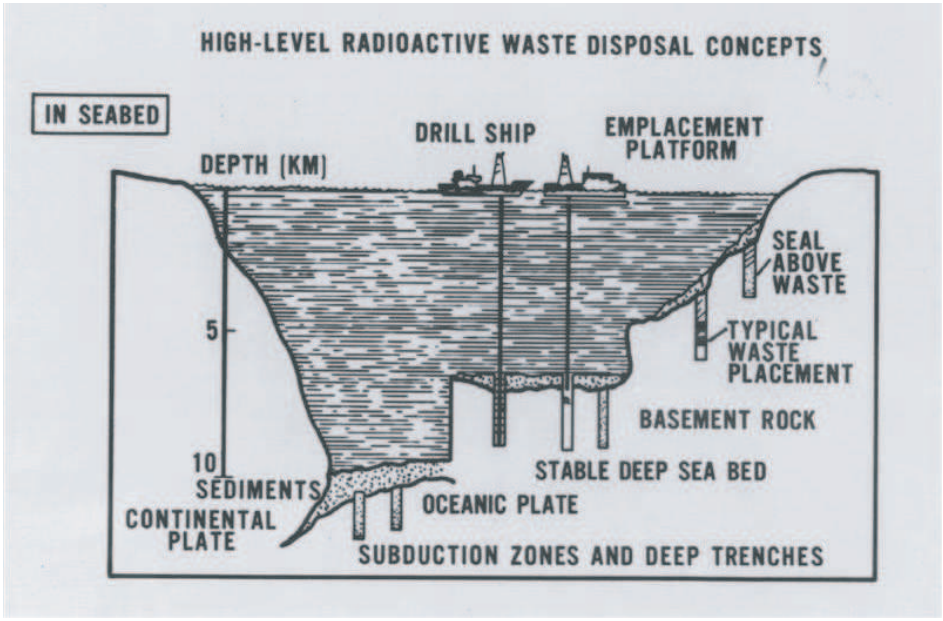

Figure 1.1. Ideas how to manage spent nuclear fuel have reached maturity since the 50s [8].

about three neutrons are liberated in one fission reaction [5, 6], which finally opened the gate for construction of a self-sustainable nuclear energy producing device.

In the shadow of World War Two, the atomic era took off as a race on the track of nuclear weapon development. Americans, being the first to succeed in 1945 and having reached considerable achievements in nuclear weapons (thermonuclear bomb in 1952) and naval reactor designs (the first nuclear driven submarine Nautilus was launched in January 1954), started to refocus their interests into the peaceful utilisation of atomic power. President Eisenhower's "Atoms for Peace" speech on December 8, 1953 and Soviet pledge of help in expanding the nuclear technology in the Eastern Block countries in 1955 had unlocked the doors to a massive and intensive development of nuclear energy on a commercial scale.

And anticipations were quite high - atomic power was supposed to turn rivers and blast valleys as well as drive rail engines and aircrafts [7]. The management of nuclear waste was similarly ambitious - such projects as dumping of nuclear wastes into the sea and launching them out into the space in rockets or depositing the waste in a seabed could be found among the proposals (Figure 1.1).

During the 60s and 70s, the spectrum of nuclear power utilisation narrowed significantly, converging into more realistic projects and focusing on designs of reactors for commercial and military purposes. Waste management strategies had got down to earth, too. Plans for geological repository were put forth proposing to bury spent nuclear fuel in deep geological formations. Such projects are under way in many countries, notably U.S.A., Sweden, and Switzerland. The moral, safety

and economic issues of this waste management option are widely discussed and especially the long-term safety of such repositories has become a major concern of enviromentalists and the general public [9].

Indeed, the safety of an underground repository is a complex function of the endurance of natural and technical barriers as well as of its volume and content of disposed nuclear waste. In the past two decades, several projects aiming to reduce the volume and content of spent nuclear fuel have taken shape and have been gathered under the general banner "partitioning and transmutation technologies" (P&T). The common denominator of all these projects is the use of an external radiation source (nuclear reactor, accelerator, or both) producing particles (neutrons, gammas, protons, etc) which in a controlled manner incinerate (transmute) certain nuclides separated/partitioned from spent fuel. Partitioning techniques are sometimes considered alone as a process of better spent fuel conditioning before final disposal. It is believed that gradual phase-in of P&T technologies into the existing fuel cycle could reduce the risks associated with spent fuel management prior to geological disposal and the long-term radiological and radiotoxic impact of the repository on the environment.

1.2 Thesis overview

This thesis investigates in part the feasibility of deploying accelerator-driven systems (ADS) as a part of a P&T scheme into the existing nuclear fuel cycle and their influence on the long-term safety performance of the geological repository. More explicitly, an attempt is made to achieve, by choice of coolant, fuel concept and core design, favourable neutronic, burnup and safety characteristics of the transuranium ADS burner. In pursuit of this goal, a conceptual design design of an ADS burner employing innovative (TRU,Hf)N fuel was developed in **Paper II**. Preparatory, design scoping studies, with respect to the coolant void worth and source efficiency were performed in **Papers I** and **IV**, respectively. In **Paper V**, a novel theoretical framework to describe the source multiplication in ADS was presented. **Paper III** investigated the feasibility of a massive introduction of a neutron absorber (B_4C) in ADS.

We begin with a presentation of the basic waste parameters of spent nuclear fuel and introduce the reader into the issue of radiotoxic fuel inventory in Chapter 2. Chapter 3 discusses the physical prerequisites for efficient transmutation of transuranics in P&T schemes and provides an overview of existing spent fuel transmutation strategies. A brief description of accelerator-driven systems and projects in this field then follows in Chapter 4. The choice of fuel, diluent matrix, cladding and coolant materials for ADS is discussed in Chapter 5. Chapter 6 accounts for neutronic, safety and burnup characteristics regarding TRU incineration in ADS. Conceptual designs of nitride fuelled lead-bismuth cooled TRU ADS burners with HfN fuel matrix and B_4C absorbers are presented in Chapter 7. Finally, Chapter 8 summarises the results presented in the appended papers.

1.3 Author's contribution

The author of the thesis is the principal author of **Papers I, II** and **IV**. He developed the framework of the study, performed neutronic, burnup and thermal hydraulic calculations, analysed and interpreted results. The author participated in the neutronic and thermal hydraulic design work of **Paper III**, was responsible for transport and burnup calculations and contributed in writing the manuscript. He was involved in the development of the theoretical framework, computational algorithm, analyses, and interpretation of the results of **Paper V**.

Chapter 2

Nuclear waste

Nuclear waste from nuclear power plants encompasses a broad spectrum of categories, inclusive high-level radioactive spent nuclear fuel, intermediate-level active parts, as e.g. water filters, and low-level waste, as protective clothing, scrap, or gaseous and liquid discharges from the plant. The spent nuclear fuel is by far the biggest contributor to the radioactivity of the nuclear waste and poses the highest risk for the environment. Nowadays, most of the countries possesses a growing stock of spent fuel, either non-processed or reprocessed with separated plutonium and vitrified high-level waste.

After the discharge from the reactor, the radioactivity of spent fuel is several orders of magnitude higher than that of the uranium ore used to manufacture the fuel [10]. This excess activity accumulated in the spent fuel is a consequence of nuclear reactions, which took place in the core during fuel burnup. In this respect, the reactions of neutron absorption, i.e., fission and capture, are of a particular importance.

2.1 Fission process

Fission absorption of neutrons in uranium leads to the disintegration of the nucleus into two or three fission fragments, so called *binary* and *ternary* fission, respectively. Fission products (FP) are neutron rich and about 2-3 neutrons are emitted from the fragments at the instant of fission. Most of the recoverable energy is released in the form of kinetic energy of fission products (85%), followed by prompt energy of gamma radiation and fission neutrons. About ten percent of the retrievable energy from fission is liberated with a certain delay as a consequence of successive radioactive decay (β^-) of fission products.

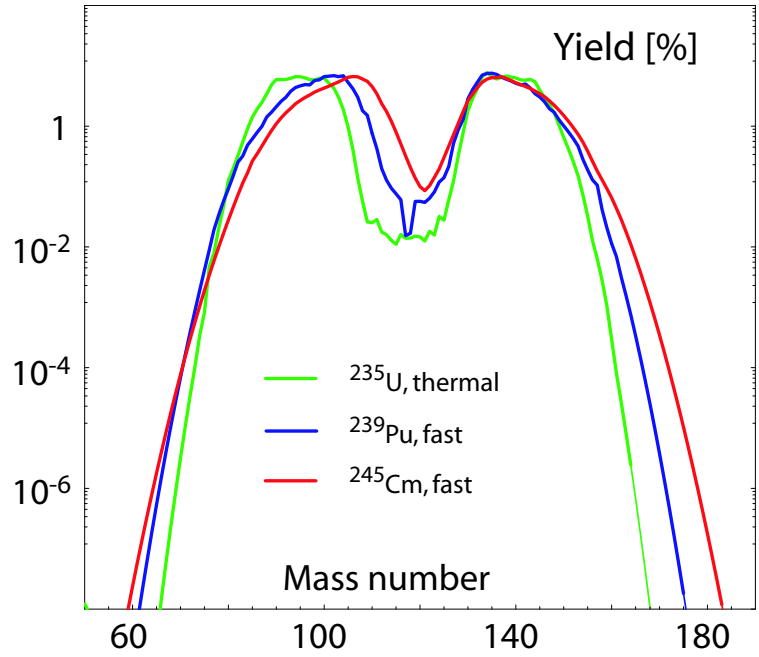

Figure 2.1. Yield of the fission products as a function of mass number given for thermal fission of ^{235}U, fast fission of ^{239}Pu, and fast fission of ^{245}Cm. JEF-2.2 data were used [11].

A typical binary fission process of an actinide, here induced by thermal neutrons on ^{235}U, may look like

$$ {}^{1}_{0}\mathrm{n} + {}^{235}_{92}\mathrm{U} \rightarrow {}^{95}_{37}\mathrm{Rb} + {}^{139}_{55}\mathrm{Cs} + 2\,{}^{1}_{0}\mathrm{n} + \tilde{\nu}_{\mathrm{e}} \qquad (2.1) $$

Fission products (FP) are typically far above the stability line (relating number of protons and neutrons) and are thus decaying by emitting β^-–particles. The mass distribution of fission products depend not only on the nature of the target nucleus, but also the energy of incoming neutron. Giving an example, fission product yields from binary *thermal* ($\overline{E_{\mathrm{n}}} \sim 0.0253$ eV) and *fast* fissions ($\overline{E_{\mathrm{n}}} \simeq$ fission neutron spectrum) of ^{235}U, ^{239}Pu, and ^{245}Cm are displayed in Figure 2.1. We observe that with increasing mass of actinide atoms, the maxima and minima of fission yield curves shift towards higher mass numbers, the difference being most pronounced for the mass range around A$\sim$90.

Transuranic elements (TRU) are produced in a nuclear reactor as a result of neutron captures on actinide nuclei, see Figure 2.2. Consecutive non-fission absorptions are eventually followed by β^- emission as the nucleus compensates for its neutron excess. Such a reaction chain can be exemplified by the production of ^{239}Pu in the fuel - neutron capture in ^{238}U is followed by two successive β^- decays of ^{239}U and ^{239}Np, with half-lifes of 24 min and 2.3 days, respectively. Almost all

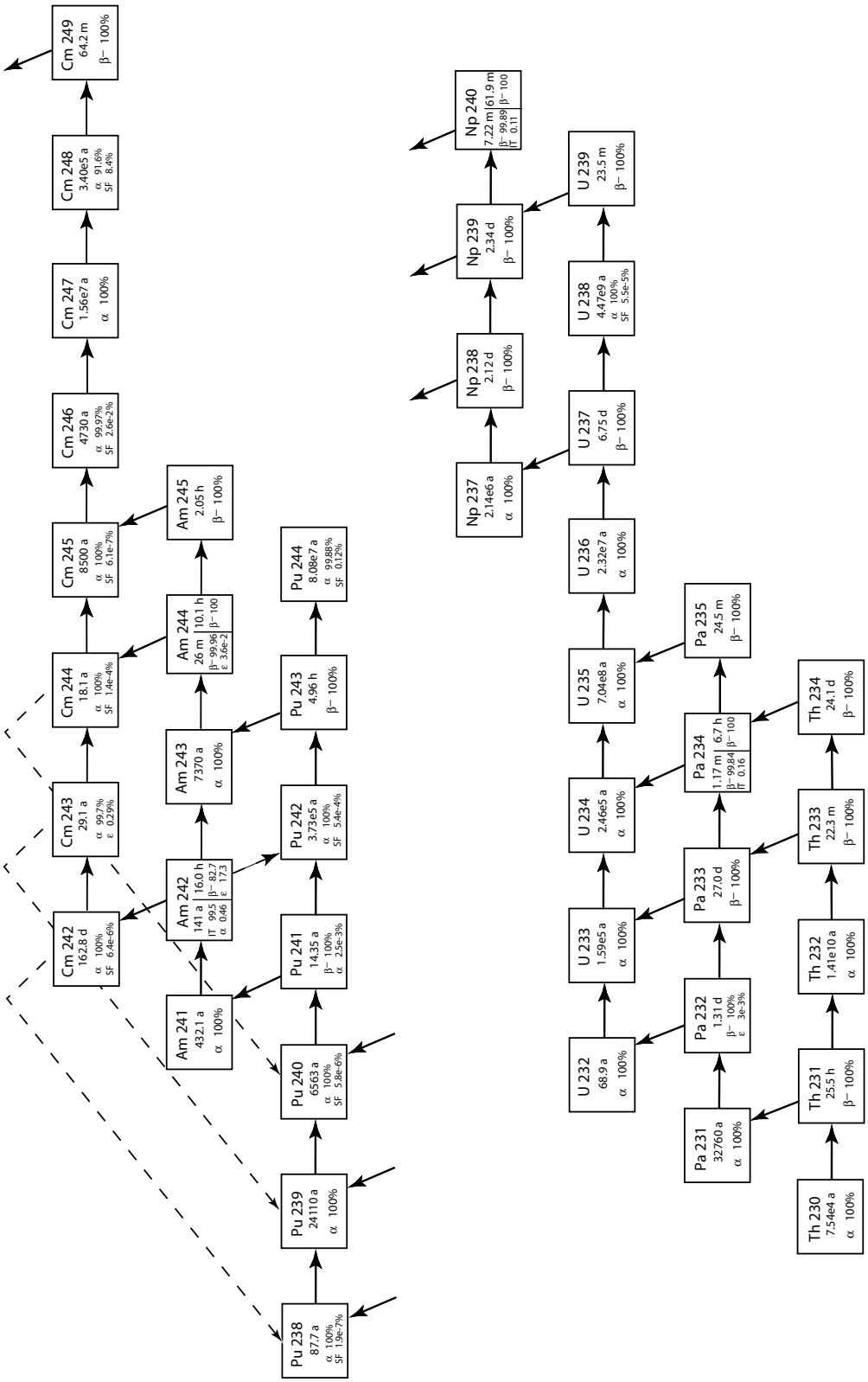

Figure 2.2. Chart of the actinides, marked transmutation paths include (n,γ) reaction, as well as α and β^- decay channels.

Nucl	Half-life [year]	UOX 41.2 GWd/t [kg/tHM]	UOX 50 GWd/t [kg/tHM]	MOX 43 GWd/t [kg/tHM]	e_{50}^{ing} [10^{-8}Sv/Bq] <1 year	adult
^{235}U	$7.04{\cdot}10^{8}$	6.6	6.5	N/A	35	4.7
^{238}U	$4.47{\cdot}10^{9}$	938	929	N/A	34	4.5
^{237}Np	$2.14{\cdot}10^{6}$	0.55	0.71	0.16	200	11
^{238}Pu	87.7	0.27	0.42	2.5	400	23
^{239}Pu	24100	5.9	6.2	21.5	420	25
^{240}Pu	6563	2.6	2.9	17.9	420	25
^{241}Pu	14.4	1.4	1.5	8.3	5.6	0.48
^{242}Pu	$3.73{\cdot}10^{5}$	0.74	0.95	7.2	400	24
^{241}Am	432.1	0.34	0.38	3.0	370	20
^{243}Am	7370	0.19	0.28	1.9	360	20
^{243}Cm	29.1	$<10^{-3}$	$<10^{-3}$	0.014	320	15
^{244}Cm	18.1	0.056	0.098	0.80	290	12
^{245}Cm	8500	0.004	0.007	0.10	370	21
^{246}Cm	4730	$<10^{-3}$	0.002	0.006	370	21

Table 2.1. The basic parameters for most important actinides from LWR-UOX (burnup 41.2 GWd/tHM and 50 GWd/tHM) and LWR-MOX (43 GWd/tHM, initial UOX fuel reprocessed after 4 years) discharges, allowing for four years of decay. Total production of TRU in the LWR-UOX and LWR-MOX is approximately 37 kg/TWh$_e$ and 187 kg/TWh$_e$, respectively. Effective dose coefficients for ingestion e_{50}^{ing} are given for an individual from general public of age under 1 year (column 6) and above 17 year (column 7). Spent fuel data are adopted from OECD/NEA study [10] and effective dose coefficients were taken from an EU directive [13].

accumulated TRU elements in spent fuel release surplus energy first by emission of α-particles and successively transform via four well-known decay chains into stable lead isotopes (^{206}Pb, ^{207}Pb, ^{208}Pb) and extremely long-lived ^{209}Bi ($T_{1/2} = 1.9{\cdot}10^{19}$yr [12]). In the short-term, one very important exception is the β^- decay of ^{241}Pu into ^{241}Am, relatively increasing the amount of minor actinides in the spent fuel by about a factor of 2.5 in a 40 years decay period.

2.2 Spent fuel composition

There are two main parameters, which determine the actual composition of spent fuel - burnup and reactor spectrum. On the other hand, the irradiation history is of a minor importance. A fuel burnup is the amount of recoverable energy obtained as a result of fuel fission and is, in its turn, a function of the power and duration of fuel irradiation, while the reactor spectrum depends primarily of the reactor type (choice of the core materials and lattice design). Moreover, both of these characteristics are dependent on fuel pin positions in the core and thus overall fuel

Isotope	Half-life [year]	Mass UOX 41.2 GWd/t [kg/tHM]	Mass UOX 50 GWd/t [kg/tHM]	e_{50}^{ing} [10^{-8}Sv/Bq] < 1 year	adult	workers
^{93}Zr	$1.5{\cdot}10^6$	0.87	1.05	0.12	0.11	0.028
^{99}Tc	$2.11{\cdot}10^5$	1.00	1.2	1.0	0.064	0.078
^{107}Pd	$6.5{\cdot}10^6$	0.27	0.34	0.044	0.0037	0.0037
^{126}Sn	$\sim 1{\cdot}10^5$	0.03	0.03	5.0	0.47	0.47
^{129}I	$1.57{\cdot}10^7$	0.21	0.26	18	11	11
^{135}Cs	$2.3{\cdot}10^6$	0.46	0.59	0.41	0.20	0.20

Table 2.2. The basic parameters for most important fission products from LWR-UOX fuel with burnup 41.2 GWd/tHM and 50 GWd/tHM, respectively [10]. The effective dose coefficients for occupational exposure (column 7) are age independent and in most of the cases roughly equals the effective dose coefficients assigned for the adult individuals [13]. This is with several important exceptions and e.g. the coefficient for ^{210}Po (not listed in the table) is estimated to be five times higher for general public than for workers exposure.

assembly burnup is in fact an average over local pin burnup rates. The local burnup of LWR fuel can differ as much as ten percent in individual sub-assemblies of one discharged batch corresponding to about five percent difference in the amount of TRU.

In the past 20 years, the average LWR fuel burnup increased from 30 GWd/tHM up to 50 GWd/tHM. Furthermore, it seems feasible that innovative types of fuel with target burnup rates of about 65-70 GWd/tHM could be introduced into LWR cores in the near future [14]. Spent fuel which would be considered as a subject for P&T technologies will thus have a large variety of transuranic and fission product compositions, dependent also on decay time. In order to schematically illustrate spent fuel transuranic content we further consider a typical LWR discharge with burnup of 41.2 GWd/tHM and 50 GWd/tHM after four years of decay, see Tables 2.1 and 2.2 [10]. Generally, the main part (94.5 wt%) of spent nuclear fuel still consists of the original material - uranium, containing about 0.7 wt% of fissile ^{235}U. Approximately one weight percent of spent fuel comprises plutonium and additional 0.1 wt% minor actinides (MA) - neptunium, americium, curium. Fission fragments make up the final four percent of the spent fuel mass. The amount of transuranics and minor actinides is a non-linear function of burnup due to eventual burnup of accumulated plutonium in the reactor.

An important consequence of deep burnup is a steep increase of MA content and thereafter α activity which in a long-term perspective dominates the residual heat of spent fuel and sets limiting parameters for geological repository. Note the strongly increased MA production in MOX fuel sub-assemblies which amounts around 17.5 kg/TWh$_e$ (a factor of four-five higher than for UOX), see Table 2.1.

At the end of year 2002, there were 441 reactors running worldwide with total net installed capacity of 359 GW$_e$. Additionally, 33 reactor units are under construction

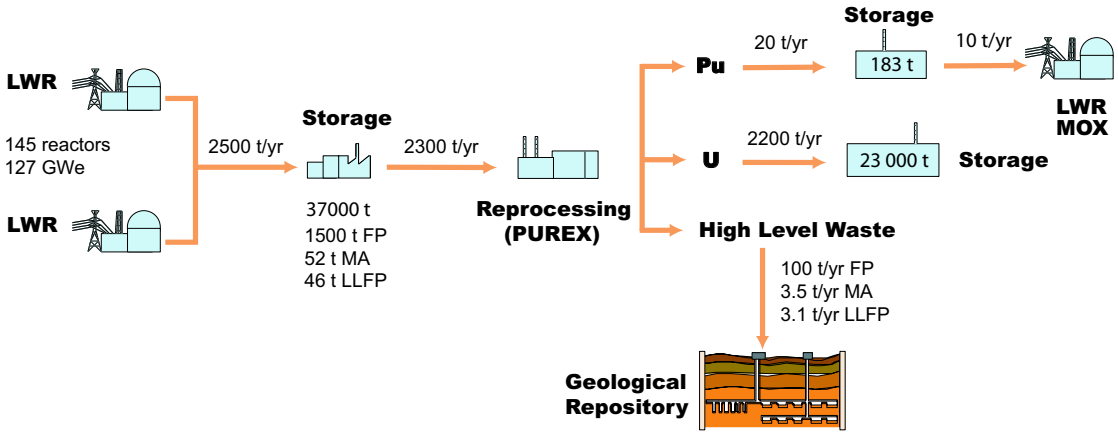

Figure 2.3. Spent and processed fuel flow sheet in the European reactor park (127 GW_e), cumulative amount and annual change as of 2001. Fuel burnup is 50 GWd/tHM. Figure is adopted from an EU roadmap report [18].

with a total capacity of 27 GW_e. The total production of electricity was 2780 TWh, being about 16% of the total world electricity supply. On the global level, about 10 500 tonnes of heavy metal spent fuel are produced annually, which is expected to increase to about 11 500 tHM/yr by 2010. Cumulatively, since the beginning of the nuclear programme, the amount of spent nuclear fuel accumulated by the beginning of 2003 was about 255 000 tHM (containing more than 2500 tonnes of transuranics), which is predicted to increase almost linearly to 340 000 tHM by the year 2010 and 445 000 tHM by the year 2020 [15]. Reprocessing and military stockpiles add approximately 170 tonnes and 100 tonnes of plutonium, respectively [16]. Almost 40% (70 000 t) of the world spent fuel stock has already been reprocessed and plutonium recycled in LWR as MOX fuel.

From the European park of nuclear reactors (Figure 2.3), amounting to 127 GW_e of nominal power, about 2500 t of heavy metal in spent nuclear fuel is produced annually, including 25 t of plutonium and about 3.5 tonnes of minor actinides (fuel burnup is 50 GWd/tHM). Additionally, there is about 100 t of fission products produced each year. We note that the annual output of spent fuel per obtained TWh_e from the European nuclear park is somewhat lower than the worldwide average due to the ongoing partial fuel reprocessing. In Sweden, the total projected amount of fuel generated, allowing for 40 years of the operation of each reactor, is 9500 tonnes [17]. Except for the main part of fuel consisting of UOX fuel sub-assemblies (both of BWR and PWR type), there is 23 t of MOX fuel and 20 t of fuel from the Ågesta reactor, which should be disposed of in geological repository. Swedish annual production of TRU corresponding to the electricity production 70 TWh_e is 2.6 tonnes, including almost 440 kg of minor actinides (around 17 wt% of TRU mass) 40 years after discharge.

2.3 Radiotoxic inventory

In order to quantify the effect of radioactivity of spent fuel on the biological tissues and assess long-term risks of its management strategy, the concept of *radiotoxic inventory* is introduced [10].

The radiotoxic inventory is a measure of the equivalent dose that is imposed to a person following the intake of a given amount of an element. It depends on the physical properties of the nuclides, such as their half-lifes, but also on respiratory deposition, clearance, and post-incorporation biokinetics in the human body (as e.g. uptake into blood). It nowadays refers almost exclusively to ingestion in favour of the earlier used values for inhalation.

Calculations of the radiation risk of a specific radionuclide take into account the type of radiation/particles emitted by the nuclide (neutrons, α, β, γ, X-rays), quantified by quality factors Q (e.g. neutrons in the energy range of 100 keV - 2 MeV and α-particles deposit around twenty times more energy than photons or electrons) as well as the effect of radiation upon the specific tissue or organ, expressed by weight factors w_T. Supposing integral body exposure time equal to 50 years, the committed effective dose intake E_{50} is then defined as

$$E_{50} = \sum_T w_T H_{50}^T, \tag{2.2}$$

where H_{50}^T is committed 50 years equivalent dose to tissue or organ T. Coefficients for committed effective dose intake (alternatively effective dose coefficients e_{50} which correspond to the committed dose E_{50} resulting from the intake of 1 Bq of a specific radionuclide) are then given in several publications, most recently in an EU directive [13] and ICRP recommendations [19, 20]. Annual limits of intake (ALI), used frequently in radiation protection for occupational exposure, can be then estimated as $ALI(Bq) = 0.20\ Sv/e_{50}(Sv/Bq)$ based on the annual average limit of committed dose of 20 mSv (100 mSv over a 5 year period).

As introduced earlier, we will consider the radiotoxic inventory of two types of spent fuel coming from present-day commercial light water reactors - spent uranium-oxide (UOX) and reprocessed mixed-oxide fuel (MOX), see Figures 2.4 and 2.5. In both cases it is assumed that separation of FP and TRU from the uranium matrix has been performed after irradiation. Note that MOX vector in this analysis corresponds to the burnup of 33.5 GWd/tHM (initial Pu content 5.3%) [10].

In the case of spent UOX fuel, the radiotoxic inventory is dominated by fission products for the first 40 years after discharge. It is mainly due to two short-lived nuclides, ^{90}Sr and ^{137}Cs, with half-lifes of around 30 yr. The contribution of plutonium isotopes and their decay daughters start to dominate the radiotoxic inventory at approximately 100 years and remains dominant until it reaches the level of the mined uranium ore used to manufacture the fuel (support factor is $\sim 3.7/0.7 \simeq 5.3$). Thereafter, the radiotoxic inventory is eventually dominated by reprocessed uranium and daughters of its decay chain. Many effective dose coefficients have been

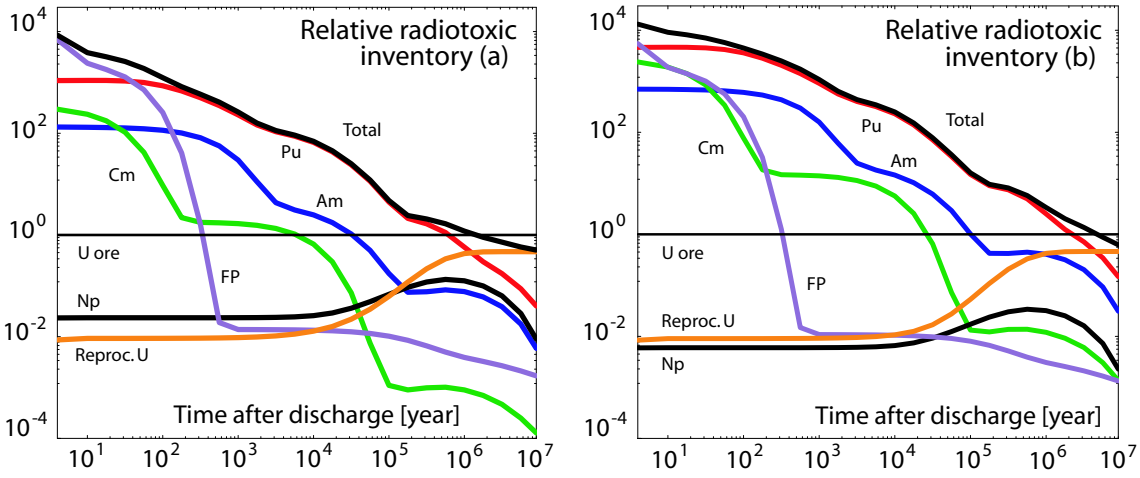

Figure 2.4. The radiotoxic inventory of spent UOX(a) and MOX(b) fuel components and their decay products relative to the radiotoxic inventory of the uranium ore that UOX fuel is manufactured from. The values are shown as a function of time relative to four years after discharge (the likely time delay for fuel reprocessing and further incineration in the P&T scheme); during this time ^{241}Am content was roughly doubled. The radiotoxic inventory of daughter products appearing as a result of decay after 4 years are included in the values of their mother nuclides. Fuel burnup is assumed to be 41.2 GWd/tHM (initial ^{235}U enrichment 3.7%) and 33.5 GWd/tHM (initial Pu content 5.3%, UOX fuel reprocessed after three years) in the case of UOX and MOX, respectively [10]. The values refer to a collective dose of the radiation ingestion intake inducing only stochastic effects. The equilibrium radiotoxic inventory of uranium ore is approximately 20 mSv/g.

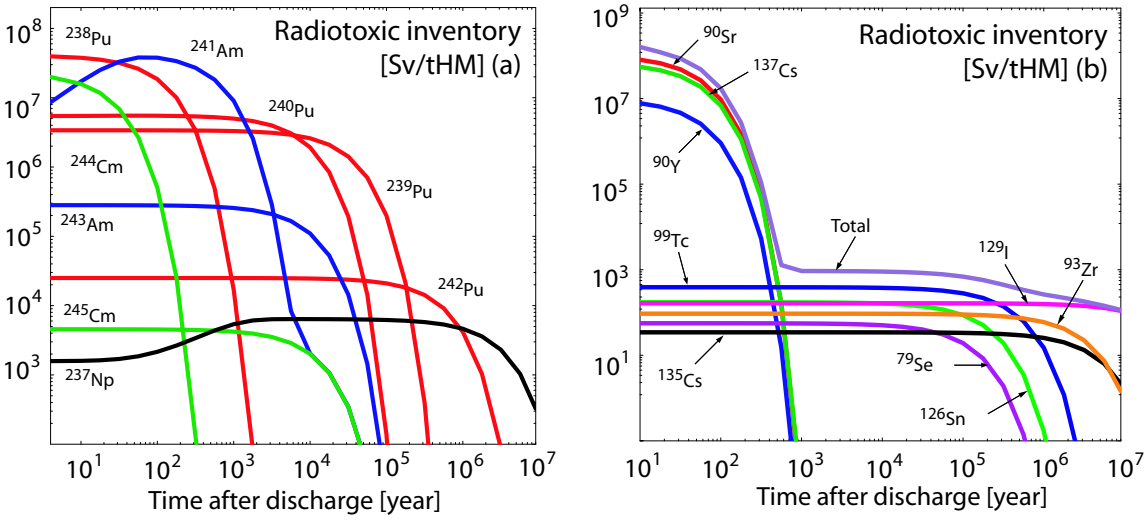

Figure 2.5. The radiotoxic inventory of transuranics (a) and fission products (b) in LWR-UOX discharge fuel, burnup is 41.2 GWd/tHM [10].

adjusted in the past few years, like e.g. those for ^{210}Po and ^{226}Ra (daughter products of ^{238}Pu and ^{238}U decay) which were increased by a factor of about 30 and 180, respectively. At the same time, the effective dose coefficient for ^{229}Th, a mem-

ber of the ^{241}Am, ^{241}Pu, and ^{237}Np family and contributing to long-term (beyond $3{\cdot}10^5$ years) radiotoxic inventory of spent fuel, was raised 25 times. The time until radiotoxic inventory reaches the level of the uranium ore needed for its manufacturing is thus prolonged up to one million years, a factor of five higher than reported in previous works [10, 21]. With respect to the mentioned uncertainties it is obvious that any quantitative estimation of the spent fuel radiotoxic inventory source term, which is an input for long-term risk assessment of repository performance inevitably has to be accompanied by extensive uncertainty analysis of input data and used models.

In the case of MOX spent fuel, the overall radiotoxic inventory is increased after 1000 years by a factor of four (considering only actinide inventory, by a factor of five) in comparison to the UOX discharges. This inventory is determined by plutonium nuclides and its decay daughters (^{241}Am), from a time 50 years after discharge till 1.5 million years when it reaches the level of uranium ore. The radiotoxic inventory of initial Am and Cm does not reach the level of uranium ore until about $2{\cdot}10^4$ years and 10^5 years, respectively, a factor of four longer than for UOX spent fuel. The radiotoxic inventory of curium isotopes is significant, mainly during the first 100 years after a discharge, due to the strong α and neutron emitter ^{244}Cm (half-life 18 year) which in conjunction with an almost doubled heat production significantly increases demands on short-term repository performance.

2.4 Spent fuel management

We see that the issue of spent fuel management spans a time of millions of years, clearly exceeding the anthropological apprehension of mankind. Spent fuel management thus inevitably becomes a question not only for scientists and experts but also for the whole society.

Of course, the most ideal waste management technique would be to reduce the radiotoxic inventories so that controlled manner disposal could be accomplished in predictable - human generation scale-time periods. In terms of spent fuel composition it would mean the complete transformation of all the long-lived actinides by means of fission and long-lived fission products via neutron capture, into stable or short-lived nuclei which would no longer pose a radiological but rather a chemical burden on the environment. However, at the present level of our knowledge, it is not feasible by technical means to reduce the radiotoxic inventory of spent fuel so that geological repository of spent fuel would become redundant [10, 22].

Alpha and Omega of any assessment of spent fuel management scenarios aiming to reduce radiological risk is the consistent consideration of the performance of the entire fuel cycle beginning from uranium mining and milling, through fuel fabrication, reactor operation and final fuel conditioning and disposal. The assessment of P&T technologies is presently a difficult and almost unrealisable task as most of the proposed technologies are still at laboratory and R&D level and e.g. the prediction

of reprocessing loss factors from advanced partitioning technologies achievable on industrial scales are very vague.

2.5 Repository performance

Some studies have been assessing the influence of P&T techniques on the fuel cycle back-end and geological repository performance (leakage resistance) accounting for the relevant exposure time, type and burnup of spent fuel, the strategy and scenario of the repository management. These analyses are very sensitive to the repository characteristics, waste conditions and types of nuclide release scenarios. As basic ones, standard water release pathways and human intrusion scenarios have been studied in different geological formations - crystalline hard rock, salt dome, and clay [23, 24, 25]. Several types of spent fuel source terms were considered, including LWR-UOX and LWR-MOX spent fuels and vitrified high-level waste.

While some nuclides (^{129}I, ^{135}Cs, ^{233}U - a daughter of ^{241}Am and ^{237}Np decay, and decay products of U and Np) have been identified as the routine prime contributors to the individual dose in all cases - there are some nuclides whose significance and contribution to the overall dose is relaxed in some conditions. The prime example of this is the problem with the high solubility of ^{99}Tc in the oxidising environment of proposed repository sites, as Yucca Mountain, U.S.A. [26, 24], which mostly disappears at reducing conditions, see Figure 2.6. The SKB study SR97 [17] assessing the long-term performance of the granite rock repository concludes that only the light mobile nuclides ^{129}I, ^{79}Se, and ^{36}Cl contribute to the geosphere dose, while still being more than four orders of magnitude below the annual limit of 0.15 mSv.

Eventually, in the long-term, the highest dose into the geosphere would be due to fission products. This was, together with non-existence of efficient partitioning techniques for trivalent actinides from lanthanides, the major reason, which made Croff in 1980 [27] and the IAEA expert team in 1982 [28] to wave aside P&T and conclude that there are no long-term safety and cost incentives for partitioning and transmutation of actinides for waste management purposes.

Truly, the water solubility of actinides is very low and their mobility in the geosphere is minimal. But the situation dramatically changes if we consider the scenario of human intrusion into the repository. There, ^{241}Am, Pu isotopes, ^{245}Cm (examination scenario) and ^{99}Tc (site occupation scenario) have been identified as key radionuclides (from clay and hard rock repositories) contributing to the *deterministic* doses for more than 10^5 year (for LWR-UOX spent fuel).

2.6 Defining goals for P&T

Without doubt, the aims of any national P&T strategy have to be merged with risk assessments of every particular repository. But is seems to be clear that *both*

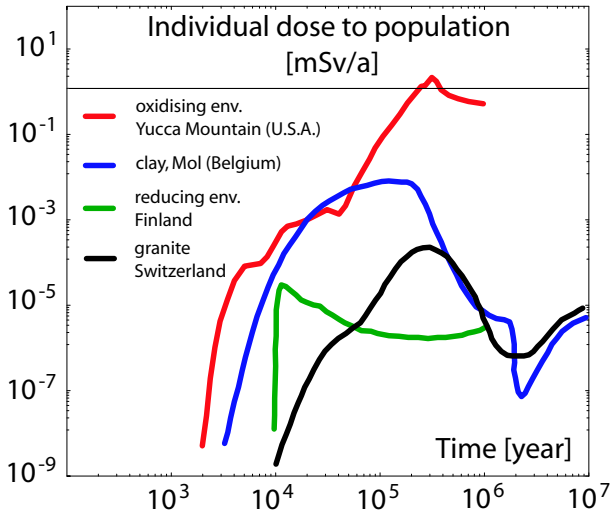

Figure 2.6. Individual doses to population for different repository concepts. In all cases, integrity of the waste canisters is assumed to be lost first after 1000 years. At that moment, the radiotoxic inventory of fuel is dominated by actinides. However, the long-term radiological hazard of spent fuel is associated mainly with fission products as these are highly mobile in ground water. Figure adapted from OECD/NEA report [25].

actinides and long-lived fission products must be considered in P&T schemes. From the viewpoint of the radiotoxic inventory reduction, in the case of the accidental intrusion to the repository, the actinides - plutonium and americium - are of major concern. On the other hand, the long term risks concerning individual doses to population are associated with fission products due to their higher mobility in water. Generally, in this context, the reduction of the radiotoxic inventory by at least a factor of one hundred is desired, thus limiting the radiotoxic risk associated with the fuel within the time when the spent fuel container is supposed to retain its integrity.

Nevertheless, the incentives for spent fuel management strategy might stem not only from the prospect of reducing radiotoxic inventory and assessment of safety and risks but also from completely different factors as e.g. ethical considerations of various management scenarios, which are in their turn influenced by professional, cultural and social factors. An OECD/NEA study [29] emphasises the importance of *inter*generational and *intra*generational equity and fairness in radioactive waste management and concludes that such an approach would minimise the risk of irreversible actions and leave doors open for other options which could be developed in the light of scientific progress and social acceptability in the future. It also cautions whether the society resources could not be used more effectively in other areas where there is a potential for greater reduction of risks to humans or the environment than from a geological repository.

This conclusion can be easily extended onto the introduction of any partitioning and transmutation strategy and thus it might be completely other factors as polit-

ical and/or social ones, which would decide about the fate of P&T technologies in a frame of spent fuel management scenarios. This was admitted also by Croff in 1990 [30] when he reexamined the incentives for actinide transmutation, claiming increased public acceptance of the repository together with higher reliance in technological barriers and predictability of geological conditions. A recent MIT study on future of nuclear power has reached similar conclusions, finding that short-term risks associated with P&T outweigh their long-term benefits [31]. The introduction of P&T technologies would be inevitable, should we give precedence to ethic incentives and the possibility to reduce the radiotoxic inventory of spent fuel at any price and not transferring the burden of its management onto our descendants. On the other hand, should we consider safeguards provided by a geological repository in both short and long terms as satisfactory, the P&T role could be reduced to development of better partitioning techniques for spent fuel conditioning prior to its final disposal.

Chapter 3

Partitioning & Transmutation

Generally speaking *partitioning* means a controlled separation (both in terms of chemical elements and isotopes) of chosen radionuclides from spent fuel. In the vocabulary of P&T technologies, it comprises the break up of inventory into components with high radiotoxic inventory and long-term risks - actinides and long-lived fission products, which are subject for further incineration.

Transmutation is in principle any change of content of nucleons in the atomic nucleus. In the case of actinides it comprises their conversion into fission products. The process can be preceded by consecutive neutron captures, β^- decays and/or isomeric transitions. An comprehensive presentation of an actinide transmutation chain was given in Figure 2.2. Fission product transmutation involves single or multiple neutron captures which are followed by β^- decays until short-lived or stable isotopes are produced.

Re-use (recycling, partitioning and transmutation) of uranium and plutonium from spent nuclear fuel was seen from the beginning of the nuclear era as the axiomatic step complementing uranium burnup and aiming to close the nuclear fuel cycle [32]. From the 50s until 70s, the ultimate goal was to achieve multiple recycling (transmutation) of U/Pu mixture in fast breeder reactors, aiming to reach maximum utilisation of uranium resources (better economy) rather than reduction of the radiotoxic inventory source term of spent fuel. First in 1964 Steinberg [33] drew the attention to the possibility of reduction of radiotoxic inventory of spent fuel focusing on the fission products ^{85}Kr, ^{90}Sr, and ^{137}Cs and their P&T in different reactor systems.

Transmutation itself can be achieved by any suitable beam of particles - neutrons, γ-rays, any reaction - (n,fiss), (n,γ), (n,2n), (γ,n), and both in multiplicative and non-multiplicative devices. However, e.g. the efficiency of γ based transmutation turned out to be unfavourable due to extremely high inventories needed to

compensate for small reaction cross-sections, being in the order of 0.2 barn at γ-energies of 15 MeV for ^{99}Tc [34]. This value is to be compared to the thermal neutron capture cross-section of ^{99}Tc that equals to 20 barn. At the same time, the high flux requirements exclude other sources than devices operating on neutrons. The possibility to directly use spallation neutrons was addressed already by Gregory and Steinberg [35] audaciously proposing a 600-850 MW proton spallation system with liquid uranium alternatively lead/bismuth target for transmutation of ^{137}Cs and ^{90}Sr from a 150 GW_e reactor park. Harada and Takahashi [36] have investigated the issue of fission product transmutation driven by a muon-catalysed neutron source claiming its positive energy balance. This was however based on overestimated deuteron-to-muon conversion factors as concluded by Wallenius [37]. It is obvious that when comparing different transmutation systems, the neutron driven incineration is superior to others due to relatively large reaction cross-sections. It also allows to build self-multiplicative devices which might eventually improve the economy of the transmutation scheme.

We will thus describe spent fuel partitioning techniques and investigate the potential of transmutation of individual spent fuel components (uranium, plutonium, minor actinides and fission products) in various neutron reactor systems (with thermal and fast neutron spectra), based both on the state-of-the-art and advanced, innovative technologies and following different types of incineration scenarios. These will be compared to the strategy of direct fuel disposal in geological formations which serves as a reference, null alternative of spent fuel management.

The strategy of a direct disposal (the fuel cycle is then called "open" or "once-through") is envisioned in some countries mainly due to the unprofitable economic conditions (cheap uranium) and proliferation risks of P&T (U.S.A.) [31]. On the other hand, some studies perceive direct storage of spent fuel as a last resort policy in awaiting a better solution for the back end of the fuel cycle [22].

3.1 Partitioning

3.1.1 Aqueous methods

The PUREX (Plutonium Uranium Recovery by EXtraction) process for separation of uranium and plutonium has been successfully developed on the basis of existing military separation technologies and is applied as a standard on industrial scale in France (La Hague, reprocessing capacity of 1600 tHM/yr) and United Kingdom (Sellafield, 680 tHM/yr) [21]. Japanese Rokkasho Reprocessing Plant (800 tHM/yr) is scheduled to start operation in 2005, Russia and India have pilot scale plants. The total worldwide capacity of reprocessing plants is around 2500 tonnes of LWR-UOX which corresponds to roughly 25% of the world's spent fuel output.

Uranium and Plutonium

In the PUREX process, the spent fuel is dissolved in nitric acid and thereafter uranium and plutonium are recovered by solvent extraction using tri-butyl-phosphate (TBP), reaching recovery efficiencies/yields up to 99.88%. Higher recovery is however obtained on a laboratory scale. At the same time, gaseous fission products as iodine, xenon and krypton are released into the environment (dispersed in sea water).

The uranium and plutonium not recovered (0.12%) are then together with minor actinides, fission products, fuel matrix material (e.g. Zr), and sub-assembly ducts treated as so called high-level liquid waste (HLLW) which is subsequently fixed in glass matrices (vitrification) and incorporated in concrete destined for final disposal. While the recovered Pu is meant to be re-used for MOX fuel fabrication, we should note that annual MOX fuel fabrication capacity is significantly under-dimensioned and amounts to only 400 tonnes worldwide (less than 20% of total reprocessing capacity).

Minor actinides

The neptunium contribution to the spent fuel TRU vector is about 5% and increases with time due to decay of ^{241}Am ($T_{1/2}$=432.6 yr). In a slightly modified PUREX process, neptunium can be treated alone and diverted directly from the U/Pu stream.

A more complex problem is the joint separation of Am/Cm from the main waste streams and, if desired, their mutual partitioning. A major difficulty is the trivalent chemical nature of americium and curium and their similarity to the lanthanide (rare-earth) fission products whose concentration is about a factor of 10-20 higher than for the MAs. As the first step, advanced aqueous methods for separation of residual actinide/lanthanide mixture from PUREX waste streams have been developed - like DIAMEX, TRUEX, TALSPEAK/DIDPA, and TRPO [25]. In order to avoid parasitic absorption of neutrons by lanthanides during transmutation, a high MA purity is required [38]. The separation of Am/Cm from lanthanides is therefore a subject of extensive research and was demonstrated on the laboratory scale for several partitioning processes as e.g. CYANEX 301 and SANEX. The SANEX process showed a 99.9% recovery yield for An/Ln separation. The process for mutual americium and curium separation is recently under investigation in the frame of the SESAME project. For both Am and Cm, a recovery yield of 99.9% was achieved on a laboratory scale.

Fuels containing minor actinides impose higher demands on fabrication and reprocessing technologies due to the increased heat generation as well as γ and neutron dose rates. As an example, reprocessing of irradiated minor actinide targets (20% of Am) has to cope with 32 times as high decay heat as compared to the standard, high burnup fuel of the EFR [39], which makes remote operation and handling of such fuels inevitable.

Fission products

The separation of relevant fission products can be achieved in a slightly modified PUREX process, with efficiencies higher than 99% for iodine and 99.8% for cesium showed on a laboratory scale. The separation of technetium is also technically feasible in the PUREX process, but a technology for recovering of the insoluble part (∼10%) has to be developed.

3.1.2 Pyrochemical methods

A major drawback of water-based reprocessing technologies is their low resistance to radiolysis of organic molecules which, in its turn, limits their capability to handle high minor actinide content fuel. Moreover, the solubility of PuO_2 in nitric acid is limited and in order to assure the reprocessibility of the fuel, the Pu-content in the $(U,Pu)O_2$ is restricted to 25-30%. Dissolution rates for metallic fuels are also very low. These difficulties are, however, relaxed when considering fuel reprocessing in non-aqueous ("dry") pyrochemical processes.

The pyrochemical reprocessing is based on fuel dissolution in molten salts (fluorides, chlorides, T=800-1000 K), from which individual actinides are selectively precipitated by electrorefining. Beside the high radiation stability of molten salts, which allows to shorten cooling times as well as reprocess fuels with high MA content, pyrochemical processes pose a comparative advantage in their relative compactness and proliferation resistance. Most of the fuels are reprocessible with pyroprocessing, which offers a necessary flexibility in P&T with respect to the composition and burnup of the fuel. The unfortunate exception is ZrN, which reprocessing by LiCl-KCl salts is problematic.

Pyrochemical processes have been developed as an option for LWR and FR oxide fuel reprocessing in Russia since 1960s. The molten eutectics salt NaCl-KCl was tested with highly irradiated UO_2 and PuO_2 fuel pins (burnup higher than 20%), reaching recovery yields of 99.8% for Pu and 99.7% for U. The LiCl-KCl eutectics used together with contact metals (Cd or Bi) is envisioned by CRIEPI [40] as a promising route for metallic and nitride fuel reprocessing. In the case of metallic fuels, recovery yields of 95% for U and 99% for mixtures of uranium and minor actinides have been reached on a laboratory scale. Pilot pyro-reprocessing plant at Argonne National Laboratory (ANL) now reprocesses one tonne of sodium-bonded spent fuel from EBR-II annually.

The current disadvantage of reprocessing techniques is the low separation yield together with low throughput of materials. The reagents used in the pyrochemical processes are very corrosive and hostile to the outer environment and steels.

Nitride fuels, on which we elaborate more later on, have been proposed by JAERI as the primary choice in order to accommodate high TRU contents. Their pyrochemical separation procedure appears to be very similar to those for metallic fuels, including molten salt electrorefining. A specific issue of nitride fuels is the necessity of high ^{15}N enrichment (99.9%) in order to avoid the massive production

of ^{14}C in ^{14}N(n,p)^{14}C reactions. While TRU nitrides have, unlike oxides, the property of being reprocessible with standard PUREX methods, pyroprocessing holds a potential of reducing cooling times and allowing efficient ^{15}N recovery. Hence, an effort to reduce the high secondary losses present in pyroprocessing appears to be justified.

3.2 Transmutation

It is customary to describe and compare the effectiveness of transmutation of radiotoxic actinides in the following terms

- burnup (consumption, depletion): $\beta = 1 - M_{\text{out}}/M$,
- specific consumption: $(M - M_{\text{out}})/W$,
- transmutation half-life: $T_{1/2}$= ln $2/(\sigma \cdot \phi)$,
- radiotoxic inventory reduction factor $R(t)$,
- waste mass reduction factor R_{f}.

where M and M_{out} are total masses of nuclides in the fuel cycle before and after the incineration, respectively, W is the energy produced by the reactor, σ is the microscopic cross-section, and ϕ denotes the neutron flux.

3.2.1 Equilibrium fuel cycle

In order to comprehend, compare and easily specify requirements for different components of P&T schemes, the concept of equilibrium cycle (i.e., a cycle with constant composition of the reactor fuel) is additionally introduced.

The actinide mass flow chart in such a cycle is displayed in Figure 3.1. Here an obvious goal is to limit the mass of actinides destined to waste, M_{waste}, in comparison to those fissioned, M_{fiss}, i.e.

$$\frac{M_{\text{waste}}}{M_{\text{fiss}}} = (1-\beta)L\frac{M}{M_{\text{fiss}}} = \delta L \tag{3.1}$$

should be minimised. L is the actinide loss fraction in the reprocessing, and $\delta = (1-\beta)/\beta$ is the burned heavy metal fraction.

Therefore, in order to reduce the amount of the waste destined to the repository, one should aim for

- high discharge burnup in each recycle, β,
- low separation losses, L.

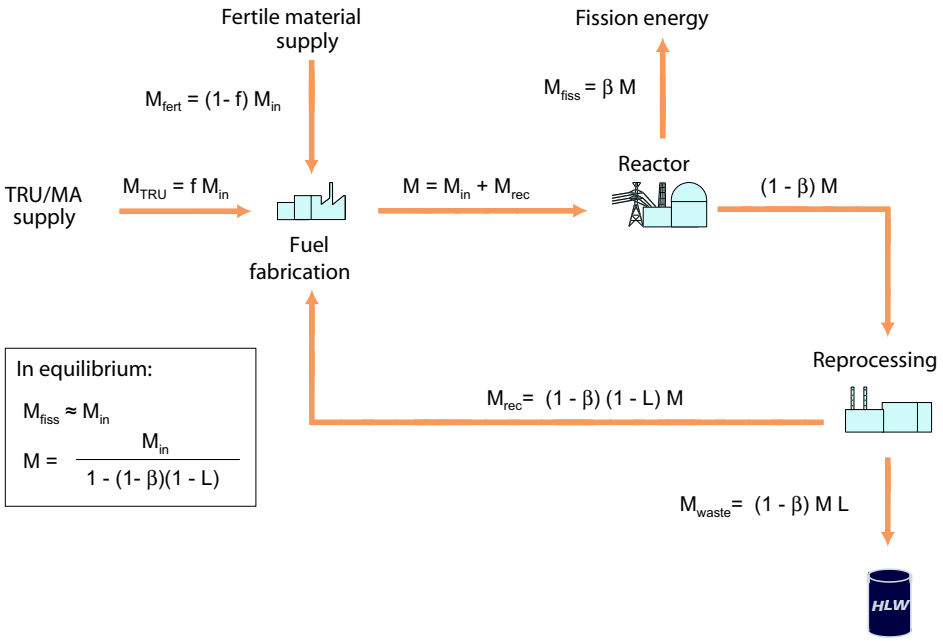

Figure 3.1. Actinide mass flow chart in closed equilibrium fuel cycle.

The amount of the fuel which enters the equilibrium fuel cycle is $M_{\rm in}$, which includes supply of TRU/MA mixture, $M_{\rm TRU}$, and fertile/diluent matrix (^{238}U, ^{232}Th), $M_{\rm fert}$. The fraction of the TRU/MA supply in the load/top-up fuel is then denoted as f.

The amount of fuel in the equilibrium cycle is a function of burnup level β and reprocessing losses L through

$$M = \frac{M_{\rm in}}{1-(1-\beta)(1-L)} \tag{3.2}$$

With the waste mass reduction factor in the fuel cycle defined as $R_{\rm f} = M_{\rm TRU}/M_{\rm waste}$, the losses in the reprocessing are consequently

$$L \approx \frac{f}{\delta R_{\rm f}} \tag{3.3}$$

The radiotoxic inventory reduction factor compares the radiotoxic inventory reduction in the equilibrium cycle to that of the top-up fuel

$$R(t) = R_{\rm neutr}(t)\frac{M_{\rm in}}{M_{\rm waste}} = \frac{R_{\rm neutr}(t)}{\delta L} \tag{3.4}$$

where $R_{\rm neutr}(t)$ is the neutronic toxicity reduction factor, depending on the core characteristics of the reactor and composition of its fuel. The factor $R_{\rm neutr}(t)$ is the radiotoxic inventory for one mole of the feed over one mole of the equilibrium

inventory after a decay time t. Considering that a majority of the transuranics have effective ingestion coefficients e_{50}^{ing} in the range of 10-26·10^{-8} Sv/Bq, we infer that the decisive contribution to the radiotoxic inventory reduction is from the waste *mass* reduction, determined in its turn by burnup level β and reprocessing losses L. In more rigourous analyses, one has shown that the $R_{\mathrm{neutr}}(t)$-factor is in the interval 0.7-2.4 for most of the reactor systems [25]. Hence, the major contribution to the radiotoxic inventory reduction comes from the reduction of actinide mass.

We can therefore directly relate requirements which should be posed on the fuel burnup and recovery yields with respect to the desired radiotoxic inventory reduction factor. Giving the example, we assume a fertile-free top-fuel ($f = 1$) reaching an average burnup of 15%FIMA. In order to attain desired reduction factor of 100 in the radiotoxic inventory of spent fuel, the separation losses have to be under 0.18%. As higher burnups than 15-20%FIMA have not yet been proven, an actinide recovery yield of 99.9% is hence needed in order to accomplish an effective transmutation.

3.2.2 Net consumption

The main purpose of the transmutation reactors operating in radiotoxic inventory reduction schemes is to achieve as high as possible *net consumption* of plutonium and minor actinides. Therefore, in addition to the need for high burnup (and/or low separation losses), the requirement is that

- the reactors' own production of TRU should be minimised, i.e. amount of the fertile material is minimised, limiting TRU breeding ($f \sim 1$),

- the fission fraction ratio of TRU inventory should be as high as possible, i.e. a fast neutron spectrum should be applied in order to take an advantage of higher fission-to-absorption ratios (see Figure 3.2); the cycle transmutation Pu → Am → Cm → Pu is thus avoided with a positive effect on the neutron economy as explained in the next section.

However, removal of ^{238}U together with an increase of mean neutron energy of the reactor system have adverse effects on several core safety parameters, particularly Doppler effect and (effective) delayed neutron fraction. High fractions of even-neutron number (i.e., fertile) plutonium and minor actinide isotopes in the fuel further exacerbate coolant void reactivity. On the other hand, higher minor actinide content somewhat lowers the reactivity loss during burnup in the cycle, allowing to somewhat alleviate the economic penalties associated with higher fuel enrichments otherwise needed. The fuel composition, system's spectrum, and flux level influence the neutron balance in the system. The neutron economy of the TRU fuelled systems is, together with their safety parameters, thoroughly discussed in the next two sections.

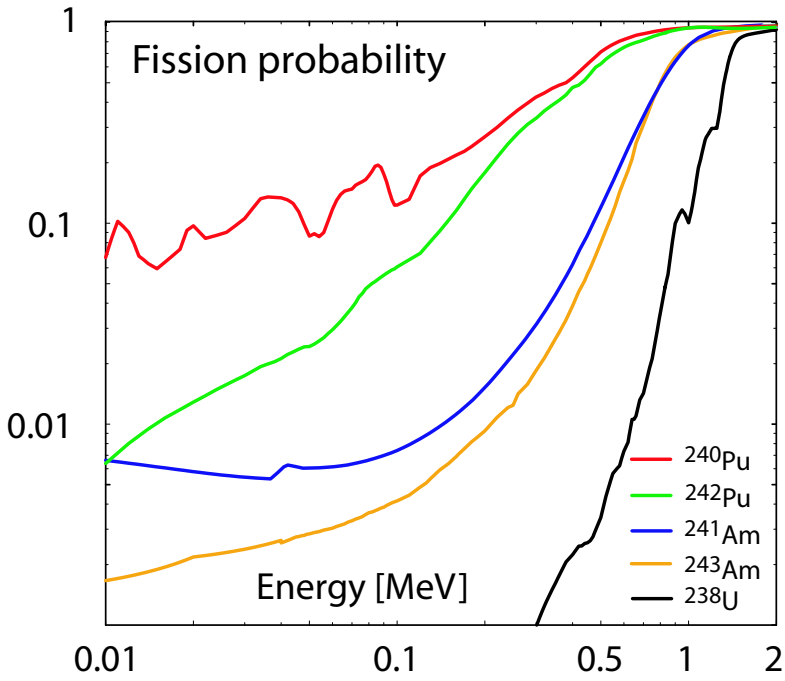

Figure 3.2. Fission probability of the actinide nuclides σ_f/σ_a as a function of neutron energy.

3.2.3 Neutron economy

In order to assess the neutron economy of different types of fuels, and reactor systems with different types of neutron spectra and magnitude of neutron flux, the neutron consumption parameter, D, was introduced for each nucleus in the fuel by Salvatores et al. [41]. The parameter D is defined as the number of neutrons needed to transform the nucleus and its reaction daughters into the required final state, i.e., in the case of actinides, into the fission products. Negative neutron consumption values mean that there is an excess of neutrons in the reactor systems supporting its neutronic needs (i.e. can be used for incineration of e.g. fission products), while neutrons have to be supplied into the reactor if a nuclide with positive D should be transmuted.

The values of D for ^{238}U, plutonium, minor actinide, and TRU vector are given in Table 3.1 for different model reactor systems.

We observe that a pure MA fuel cannot be transmuted in a thermal spectrum, due to the unfavourable neutron balance. However, the spectrum of thermal ADS is not a limiting factor for transmutation of plutonium. Thus, while the whole TRU vector can be incinerated in both thermal and fast spectrum, the fuel with high content of minor actinides is transmutable only in the fast spectrum. The issue of criticality or sub-criticality of the reactor is only the subject of consideration with respect to deteriorated safety characteristics, which we mention in the next section.

Top-up fuel	Thermal TRU ADS	Fast TRU ADS	MA ADS	FR
^{238}U	+0.24	−0.64	−0.64	−0.85
Pu	−0.40	−1.34	−1.28	−1.53
MA	+0.37	−0.86	−0.79	−1.10
TRU	−0.30	−1.29	−1.23	−1.48

Table 3.1. Neutron consumption parameters for different equilibrium cores. Thermal ADS is a graphite-moderated molten salt reactor proposed by LANL [42], fast TRU ADS is a proposal of Pb/Bi-cooled core employing metallic fuel [43], MA ADS is a nitride Pb/Bi burner proposed by JAERI [44], and fast critical reactor (FR) is of an ALMR-type. Pu and TRU vectors correspond to those of discharged LWR-UOX fuel with a burn-up of 50 MWd/tHM; MA vector is the mixture of minor actinides coming from LWRs and FRs of the first stratum reactor park of the double-strata scenario, see Section 3.3.3. Table was adopted from OECD/NEA study [25].

3.2.4 Safety aspects

Inherent stability of a nuclear reactor, as any dynamic system, can be achieved only by *negative* feedbacks acting sufficiently fast that the integrity of the reactor core is not compromised. The feedback mechanisms operating in the nuclear reactors typically constitute of an event chain where an increase in power or change in its distribution leads to decrease in reactivity through temperature dependent microscopic and/or macroscopic cross-sections.

In the sub-critical system, the requirements on the feedback mechanisms are partially relaxed due to the inferred sub-criticality [38]. However, if a substantial reactivity could be introduced into the system, e.g. during coolant voiding, such that the power is significantly increased, absence of negative feedbacks could lead to core damage in spite of the system remaining sub-critical [45]. If a large sub-criticality margin would be required ($k_{\text{eff}} \sim 0.9$) in order to prevent core damage, it would introduce penalties on the total reactor power and discharge burnup. Thus, one might be required to optimise the core sub-criticality level, while, at the same time, provide sufficiently strong negative temperature reactivity feedbacks. The latter could be also stipulated as an *a priory* requirement for successful licensing of any energy producing reactor.

3.2.5 Reactivity temperature coefficients

The total change in the reactivity of the system is given as a sum of

$$\rho_{\text{T}} = \rho_{\text{t}} + \rho_{\text{c}} + \rho_{\text{e}} \tag{3.5}$$

where ρ_{t} is the reactivity due to the temperature changes in the reactor, ρ_{c} is the reactivity introduced by control rods or other absorbing materials as e.g. fission products, and ρ_{e} is the external reactivity introduced from outside.

In the case when no reactivity is introduced from external sources and absorbing materials, ρ_{t} determines the temperature stability of the reactor. The temperature reactivity coefficients are then defined as the change in the reactivity upon temperature change of the i-th component of the reactor core

$$a_{\mathrm{i}} = \frac{\partial \rho}{\partial T_{\mathrm{i}}} \tag{3.6}$$

In a heterogeneous reactor, we usually recognise four distinctive geometrical components: fuel, structural material, moderator and/or coolant.

In the reactor core, the temperature reactivity feedback is mainly due to the following physical events

- neutron spectrum shift affecting effective scattering and absorption cross-sections in the coolant (and moderator),
- widening of the resonance absorption cross-sections, changing the probability for absorption reaction (Doppler effect),
- material density/phase change affecting macroscopic cross-sections,
- changes in the core dimensions due to thermal dilatation of materials (fuel, structure, cladding) and/or bending of the fuel elements.

Therefore, the reactivity changes as function of temperature can be decomposed as

$$\frac{d\rho}{dT} = (\frac{\partial \rho}{\partial T})_{\gamma} + (\frac{\partial \rho}{\partial \gamma})_{\sigma}(\frac{\partial \gamma}{\partial T}) \tag{3.7}$$

where the $(\partial\rho/\partial T)_{\gamma}$ is the nuclear part of the reactivity coefficients (due to the change of the nuclear properties of the material, i.e., cross-sections), and $(\partial\rho/\partial\gamma)_{\sigma}$ is the density reactivity coefficient, describing the temperature changes as a response to the change of the material density.

The total change of reactivity is then given by

$$\rho_{\mathrm{T}} = \sum_{\mathrm{i}} \frac{1}{V_{\mathrm{i}}} \int a_{\mathrm{i}}(\overline{r}) \triangle T_{\mathrm{i}}(\overline{r}) \Omega(\overline{r})\, d\overline{r} \tag{3.8}$$

where $\Omega(\overline{r})$ is the weight/importance function describing the relative spatial influence of the temperature on the reactivity, and $\triangle T_{\mathrm{i}}(\overline{r})$ is the temperature gradient corresponding to the state at which $\rho_{\mathrm{T}} = 0$.

It is important to note that apart from the changes of the reactivity induced by the temperature, one can also have reactivity change due to longer long-term events, such as swelling of cladding material or fuel pellet. Reactivity can be also introduced during a transient, e.g. if the fission gases are released from the pellet to the plenum.

Typical values of temperature coefficients for thermal and fast neutron cores are listed in Table 3.2. While all reactivity coefficients are negative in the thermal

Mechanism $10^6 a$ [K]	EBR II	Fermi	Super Phénix	BREST 1200	PWR UOX fuel
Axial fuel expansion	-3.9	-2.5	N/A	-0.8	≈ 0
Coolant density change	-9.1	-7.1	$+8.0$	$+3.4$	-50 to -8
Structure expansion	-9.7	-6.0	-11.0	-7.7	≈ 0
Doppler coefficient at nominal temperature	N/A	-2.0	-4.0	-5.4	-4 to -1

Table 3.2. Reactivity temperature coefficients for thermal and fast reactor cores [46, 47, 48, 49]. Reactivity coefficients due to the density change of *both* coolant and subassembly material are quoted for EBR-II and Fermi.

reactor, in fast systems the total temperature reactivity coefficient is the sum of positive and negative parts. Moreover, geometrical changes play more significant role in fast spectrum systems than in thermal reactors, where the coolant/moderator temperature coefficient has the major importance.

Prompt, inherent, and negative reactivity feedbacks are needed in order to mitigate positive reactivity transients. Doppler temperature coefficient is a prompt responsive feedback to power changes as it is dominated by the nuclear component involving the broadening of actinide absorption resonances. On the other hand, the coolant and moderator temperature coefficients are somewhat delayed allowing for heat to be distributed from fuel into the coolant. In the next sections, we will treat coolant and fuel temperature reactivity coefficients together with delayed neutron fractions in more detail. The objective is to give as an important theoretical background before advancing into more elaborate studies of safety aspects of transmutation reactors, which will be presented in Chapter 6.

3.2.6 Coolant temperature reactivity coefficient and void worth

The coolant temperature coefficient is not a characteristic of the coolant itself but a collective property of the core lattice and fuel design, fuel composition and coolant/moderator type. In light-water reactors, the negative coolant/moderator reactivity coefficient facilitates an important self-controlling mechanism of the system (core lattice is then so called *undermoderated*). Specifically, in BWR, an increase in steam-to-water ratio leads to a decrease of the reactivity. However, sometimes, reactor cores exhibit positive coolant reactivity coefficients, e.g., D_2O moderated and cooled reactors (CANDU), or H_2O cooled-graphite moderated reactors (RBMK). Operational stability of the reactor with positive coolant reactivity coefficient is then ensured by the strong negative power reactivity coefficients. If that is not present or is weak, one has to rely on actively operated reactor control systems rising serious safety concerns. At the same time, it is impossible to rely on natural circulation in order to cope with the cooling accidents.

Loss of coolant has two distinctive consequences on the reactor operation. First, the ability of the heat removal is lost leading to overheating and possibly also to loss of core integrity. The loss of heat removal capability was one of the main reasons for core melting accidents, e.g. at the Three Mile Island nuclear reactor at Harrisburg, Pennsylvania. Second, it can introduce reactivity into the system. The coolant temperature reactivity is one of the most prominent characteristics of fast reactors and some existing designs of liquid metal cooled reactors have coolant temperature reactivity coefficient positive, e.g. Super Phénix reactor in France (see Table 3.2). The negative temperature reactivity feedback is then ensured by strong contributions from expansion of grid structure and from fuel temperature coefficient.

The coolant density change or occurrence of the void in the core can be a result of the following events

- temperature increase of the coolant due to pump failure, human errors, inadequate instrumentation and prediction of hot-channel factors, crud deposition, and plugging of the coolant channels; ultimately, this leads to a coolant phase change - boiling. Note that accident scenarios assuming coolant boiling are less relevant for systems cooled with lead-alloys due to the high boiling temperature of both Pb and Pb/Bi (Pb: T_{b}= 2023 K; Pb/Bi: T_{b}= 1943 K), while in sodium cooled systems (T_{b}= 1156 K) coolant boiling can occur before any significant damage to the fuel, clad, or structural material would be inflicted.

- blocking of the coolant circulation as a consequence of coolant freezing in the steam generator, i.e. overcooling.

Additionally, void cavities can appear in the core due to

- gas leakage from ruptured pins,

- steam ingress from ruptured steam generator,

- blow-down of bubbles from gas injection system,

- coolant leakage caused by brittle failure of the reactor vessel.

The coolant acts in the reactor not only as a neutron absorber, but also as moderator, affecting the neutron spectra. The reactivity change when decreasing the density of the coolant in fast neutron cores from coolant is mainly due to two effects

- spectral hardening, i.e. reduction of the neutron moderation, with a concurrent increase of actinide fission probabilities,

- reduction of neutron parasitic absorption in fuel, coolant, and cladding.

Coolant	ρ [g·cm^{-3}]	A [u]	N [10^{-22}·cm^{-3}]	T_m [K]	T_b [K]	ξ
Na	0.847	22.99	2.22	371	1156	$8.45{\cdot}10^{-2}$
Pb/Bi	10.15	208.1	2.94	398	1943	$9.59{\cdot}10^{-3}$
Pb	10.48	207.1	3.05	601	2023	$9.63{\cdot}10^{-3}$
He	$4.13{\cdot}10^{-3}$	4.003	0.06	1.05	4.15	$4.25{\cdot}10^{-1}$

Table 3.3. Density (ρ), mass number (A), atomic density (N), melting (T_m) and boiling (T_b) temperatures, and average logarithmic decrement of energy (ξ) of coolants considered in the study. Coolant densities are given at 700 K, helium pressure is 6 MPa [50].

3.2.7 Neutron slowing down

In this section we therefore analyse the neutronic (slowing-down) properties of candidate coolants for the fast reactor systems, see Table 3.3.

With an assumption that the neutron elastic scattering is isotropic in the centre-of-mass system (CMS), we can describe neutron slowing-down process in terms of the averaged logarithmic decrement of energy as

$$\xi = \overline{\ln E_1 - \ln E_2} = 1 + \frac{(A-1)^2}{2A} \ln \frac{A-1}{A+1}, \qquad A > 1 \tag{3.9}$$

where A is the nuclide mass number and E_1 and E_2 are the energies before and after the collision, respectively.

In order to apprehend the nature of the slowing-down process, the moderating power of the respective coolants is usually defined as

$$\xi \Sigma_\mathrm{s} = \Sigma_\mathrm{i} N_\mathrm{i} \xi_\mathrm{i} \sigma_\mathrm{i} \tag{3.10}$$

where N_i is the atomic density of the i-th nuclide and σ_i is its elastic scattering cross-section. However, to include also slowing-down process from the inelastic scattering in the evaluation, the energy-loss cross-section should be studied. It is defined as

$$\overline{\Sigma_{\Delta E}} \equiv \frac{\Sigma_\mathrm{el}\overline{\Delta E_\mathrm{el}} + \Sigma_\mathrm{inel}\overline{\Delta E_\mathrm{inel}}}{E}, \tag{3.11}$$

where

$$\overline{\Delta E_\mathrm{el}} = \frac{1}{2}(1-\alpha)E_\mathrm{n}, \;\; \alpha = (\frac{A-1}{A+1})^2 \tag{3.12}$$

and

$$\overline{\Delta E_\mathrm{inel}} = E_\mathrm{n} - (\frac{A}{A+1})^2[E_\mathrm{n} - Q\frac{A+1}{A}] \tag{3.13}$$

is the average energy loss in elastic scattering and inelastic scattering, respectively; Q denotes the excited energy levels of the target nuclei, E_n is the neutron energy, and A is the target nucleus mass number (see **Paper I**).

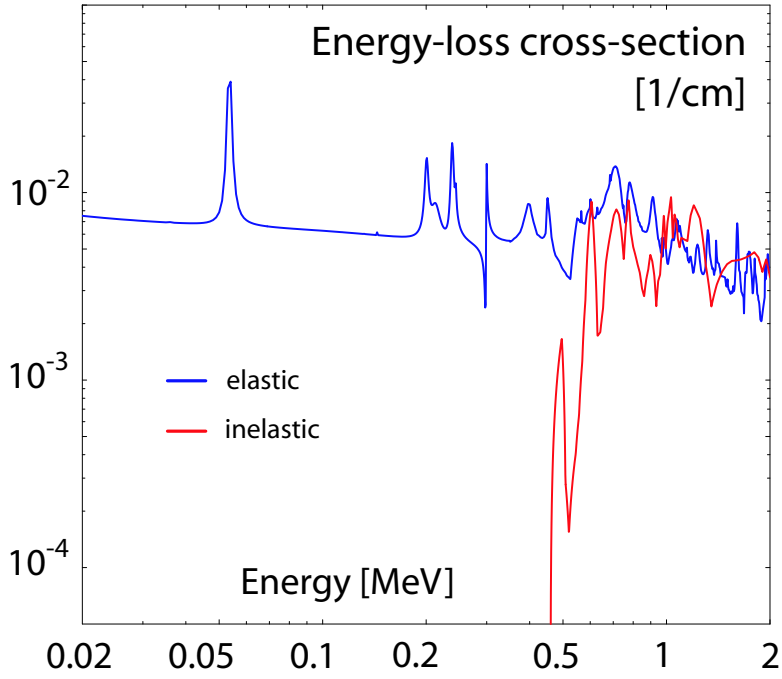

Figure 3.3. Energy-loss cross-section for ^{23}Na. Data from JEF-2.2 library were used. Macroscopic scattering cross-sections were taken at T = 600 K. According to **Paper I**.

Nuclide	Abundance	1st	2nd	3rd
^{23}Na	100%	459.1	2166	2495
^{206}Pb	24.1%	806.9	1171	1347
^{207}Pb	22.1%	572.5	902.1	1641
^{208}Pb	52.4%	2628	3213	3492
^{209}Bi	100%	900.6	1617	2455

Table 3.4. Threshold energies [keV] for inelastic scattering of liquid metal coolants used in this study. ^{206}Pb features additional five excited energy levels yielding threshold energies below or close to 2 MeV limit: 1474, 1692, 1713, 1793, and 2008 keV. Table adapted from **Paper I**.

Threshold energies for the inelastic scattering (i.e., kinetic energies of the neutron in the laboratory system, E_{n}) are higher than excited level energies Q of the system. Considering the kinematics of the inelastic scattering

$$E_{\mathrm{n,CMS}} + E_{\mathrm{N,CMS}} + Q = \frac{A}{A+1} E_{\mathrm{n}} \tag{3.14}$$

$$\text{where} \quad E_{\mathrm{n,CMS}} + E_{\mathrm{N,CMS}} \geq 0 \tag{3.15}$$

we obtain a requirement for the laboratory kinetic energy of the neutron, $E_{\mathrm{n}} \geq \frac{A+1}{A} Q$. $E_{\mathrm{n,CMS}}$ and $E_{\mathrm{N,CMS}}$ are kinetic energies of the neutron and the nucleus in the centre-of-mass system, respectively.

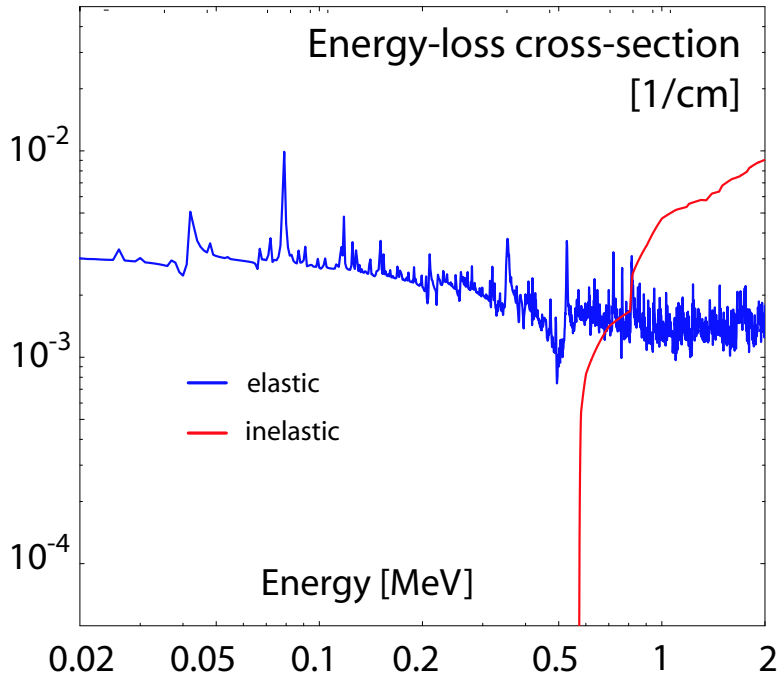

Figure 3.4. Energy-loss cross-section for natural lead. Cross-section data were taken from ENDFB/VI-8 cross-section library. Σ_{el} and Σ_{inel} at T = 600 K were used. Figure adopted from **Paper I**.

The energy-loss cross-section for sodium decomposed into the contributions from elastic and inelastic scattering is displayed in Figure 3.3. The same comparison for natural lead is made in Figure 3.4. In the whole energy range investigated (100 keV - 2 MeV), lead energy-loss cross-section due to the elastic scattering is significantly smaller than for sodium. However, due to the presence of several thresholds for inelastic scattering in the energy interval from 0.57 to 2 MeV, the energy loss in inelastic scattering is notably larger than for sodium. Therefore, neutron spectrum of lead and lead/bismuth cooled reactors will be somewhat suppressed for energies above 1 MeV. On the other hand, the magnitude of neutron flux for sodium-cooled reactor is suppressed in the energy interval of 0.7-1.5 MeV, where contributions to the neutron slowing down from elastic and inelastic scattering reactions are merely equal, see Figure 3.5.

Additionally, the neutron mean free path, (λ=1/Σ_t), in sodium is larger than that of Pb/Bi. Therefore, the leakage of neutrons and their contribution to overall neutron balance in the system is more significant for Na. Further, higher scattering in Pb/Bi without increasing the moderation for neutrons below 0.5 MeV would prevent the neutrons from escaping from the internal parts of the Pb/Bi-cooled cores and, at the same time, provide an excellent reflecting capability for the neutrons which escape the system, see Figure 3.6. Hence, we can also infer that the neutron economy of the Pb/Bi systems would be better than for Na-cooled counterparts and a smaller actinide fraction would be required for Pb/Bi than Na to reach

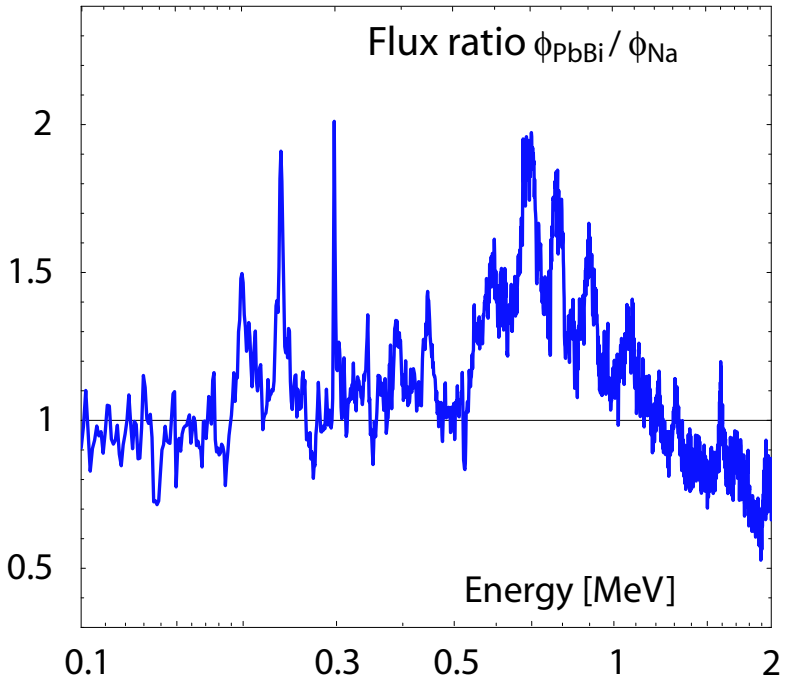

Figure 3.5. Neutron spectrum of the Pb/Bi-cooled system in comparison to the Na-cooled reactor having the same fuel and geometry design parameters. Redrawn from **Paper I**.

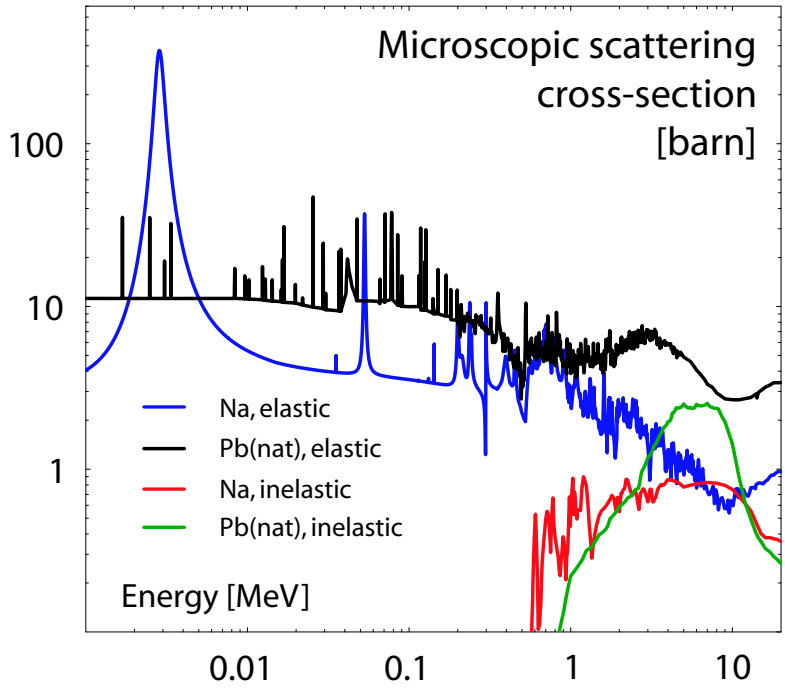

Figure 3.6. Elastic and inelastic scattering cross-sections for Na and Pb. Data were taken from JEF-2.2 library.

criticality/same sub-criticality. On the other hand, e.g. power peaking issues are more relaxed in sodium system as neutrons more easily escape the high reactivity regions. We develop on the subject in Chapter 6.

3.2.8 Feedback through material dilatation

A temperature rise causes expansion of core materials with concomitant changes in geometry. This influences the macroscopic cross-section ($N \cdot \sigma$), affecting the interaction rates ($N \cdot \sigma \cdot \phi$), neutron mean free path, resonance self-shielding effect in the fuel, neutron leakage probability, and consequently changes overall criticality of the system. Moreover, the material dilatation can alter the relative position of core parts, individual fuel pins or whole sub-assemblies. E.g. fuel sub-assembly bowing was the initiator of the accident at the experimental breeder reactor EBR-1 Mark II in November 1955. The subsequent analysis of the core have shown that the transient had resulted in melting of 40%-50% of the fuel elements.

Temperature changes causes a dilatation of all materials in the core. However, the most important reactivity contribution with respect to the geometrical changes appear to be

- axial expansion of fuel column,
- radial expansion of the core lattice grid, changing spacing in-between fuel elements and effective radius of the core,
- thermal bowing of sub-assemblies.

Change in length of the i-th core component per change in temperature is given by the linear expansion coefficient defined as

$$\alpha_{\mathrm{i}} = \frac{1}{l_0} \frac{dl}{dT}_{\mathrm{i}} \tag{3.16}$$

where dl is the change in length, l_0 is the initial length of the material, and dT is the change in temperature. The density of the material then changes as

$$\rho = \frac{\rho_0}{1 + \beta \Delta T} \tag{3.17}$$

where β is the volumetric expansion coefficient ($\beta \approx 3\alpha$), ρ_0 is the initial material density, and $\Delta T = T - T_0$ is the temperature difference.

The linear expansion coefficient is usually itself dependent on the temperature and for actinide nitrides and relevant diluent matrices, ZrN and HfN, it slightly increases with temperature, see Figure 3.7. For comparison, the linear expansion coefficients of uranium, plutonium, uranium dioxide, and structural material are given in Table 3.5. For the mixture of the nuclides, the linear expansion coefficient is obtained by using Vegard's law.

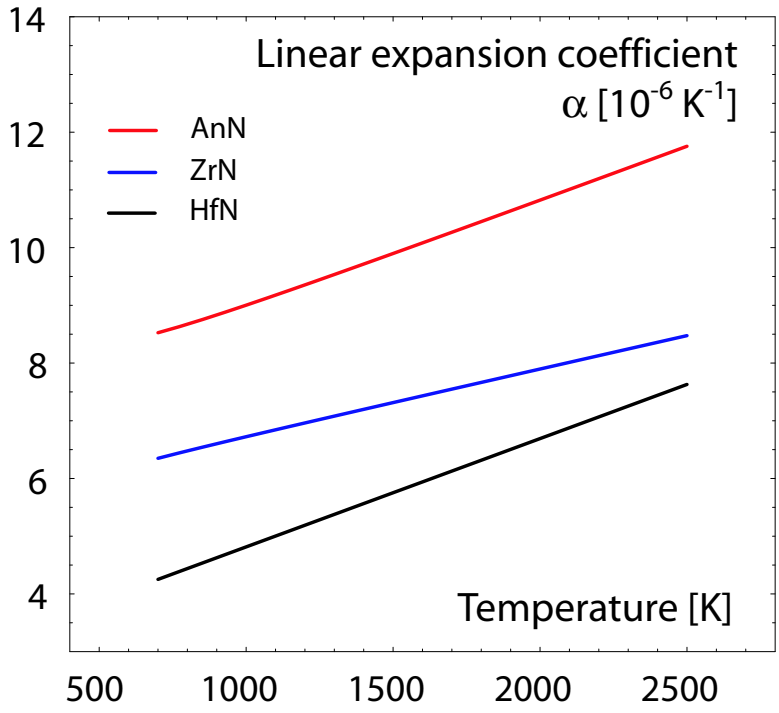

Figure 3.7. Linear expansion coefficient of AnN [51], ZrN [51], and HfN [52] as a function of temperature.

Material	α $[10^{-6}\cdot\mathrm{K}^{-1}]$	Note
U	13.9 (α)	300 K
Pu	55 (α), 35 (β)	300 K
UO_2	11.1 to 13	700−1600 K
AnN	8.5 to 11.8	600−2500 K
SS-316	18.6 to 21.6	300−1300 K

Table 3.5. Linear expansion coefficients of some core materials [53, 32, 50].

The dilatation of the material in the core affects neutron mean free path, which is increased as $\lambda = 1/\Sigma_t = 1/(N \cdot \sigma_t)$. At the same time, the core dimensions increase and the densities of the material in the core decrease, which has positive and negative effect on the system reactivity, respectively.

Increase in the core dimensions, assuming the cylindrical core, decreases the neutron leakage probability as surface-to-volume ratio becomes smaller with larger R and/or H

$$\frac{2\pi r(r+H)}{\pi r^2 H} = 2(\frac{1}{H}+\frac{1}{r}) \tag{3.18}$$

where r and H are the radius and the height of the core, respectively. In the case of the axial expansion of the fuel column, the density of the fuel changes as

$$\frac{\Delta\rho}{\rho_0} \approx -\frac{\Delta l}{l} \tag{3.19}$$

while in the case of the radial displacement of the core grid the density varies with the square of the core radius

$$\frac{\Delta\rho}{\rho_0} \approx \frac{r_0^2 - (r_0 + \Delta r)^2}{r^2} \approx -\frac{2\Delta r}{r} \tag{3.20}$$

Thus, the reactivity change upon the core expansion is actually the result of two components, a positive one due to the core expansion, and a negative one due to smaller densities. In fast reactors, the former effect is usually smaller than the latter, yielding the negative overall expansion coefficient [54]. We also expect that an increase in the core radius is approximately twice as effective in reducing the reactivity than the axial fuel expansion.

3.2.9 Doppler feedback

The Doppler effect involves changes of reactivity due to variation of fuel temperature. This effect has a premium significance in nuclear reactor safety, providing immediate reactivity feedback, which responds to the changes in the fuel temperature. In fact, the absorption cross-section of an actinide is dependent on the relative velocity between the nuclide and neutron. While the area under the resonance integral [55]

$$I^{\mathrm{res}} = \int_{\mathrm{E}}^{\mathrm{E_0}} \sigma_{\mathrm{a}}(E') \frac{dE'}{E'} \tag{3.21}$$

remains constant upon temperature changes, the effective resonance integral is then dependent on temperature through Σ_{a} in the denominator

$$I_{\mathrm{eff}}^{\mathrm{res}} = \int_{\mathrm{E}}^{\mathrm{E_0}} \sigma_{\mathrm{a}}(E') \frac{\Sigma_{\mathrm{s}}}{\Sigma_{\mathrm{s}} + \Sigma_{\mathrm{a}}} \frac{dE'}{E'} \tag{3.22}$$

The probability of neutrons escaping the resonance capture then changes as

$$p = \exp(-\frac{N}{\xi\Sigma_s} I_{\mathrm{eff}}^{\mathrm{res}}). \tag{3.23}$$

The fuel temperature reactivity coefficient can be approximated for most reactor designs by a $1/\mathrm{T}^{\mathrm{a}}$-dependence (a$\sim$1 for oxide-fuelled sodium-cooled fast reactors) and thus the Doppler effect is often in the literature quantified in terms of the Doppler constant

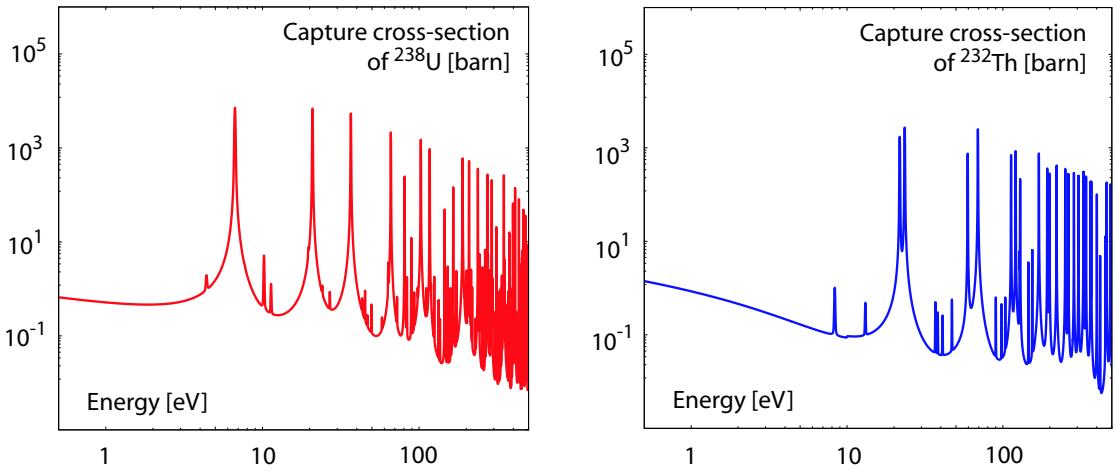

Figure 3.8. The neutron capture cross-section for ^{238}U and ^{232}Th. JEF-2.2 data were used.

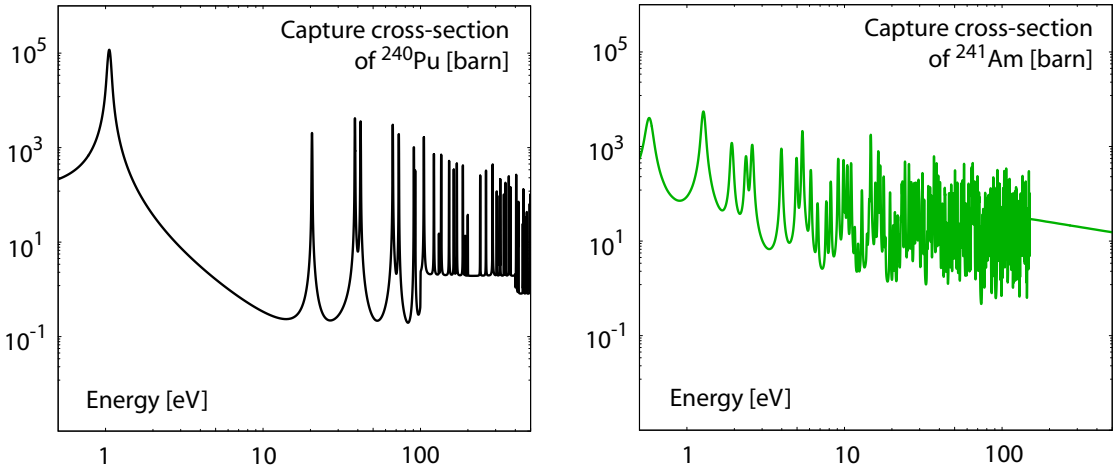

Figure 3.9. The neutron capture cross-section for ^{240}Pu and ^{241}Am. Data were taken from JEF-2.2. Note large ^{240}Pu resonance at ∼1 eV.

$$K_{\mathrm{D}} = T\frac{dk}{dT} \tag{3.24}$$

The Doppler effect itself is prominent in an energy range of well-separated resonances around 1 keV (higher energies cross-section variations with temperature are minimal) and for fertile nuclei it results in a decrease of resonance escape probability [46]. As shown experimentally, mainly fertile materials as ^{238}U, ^{232}Th, and to a minor extent ^{240}Pu, contribute to the Doppler effect, see also Figures 3.8 and 3.9. On the other hand, the Doppler effect of most of the fissile isotopes as ^{239}Pu and ^{235}U appear to be almost zero or even positive [54]. In the thermal spectrum, plutonium fuel can provide positive Doppler feedback due to the huge 0.3 eV resonance of ^{239}Pu.

In the standard FBR design, the major contribution to the negative Doppler effect comes from broadening of ^{238}U resonances. In hard neutron spectra, only small portion of neutrons is moderated down to the region of pronounced resonances (below 100 eV), where the contribution to the Doppler effect is the most profound. At the same time, as uranium content is significantly reduced in transmutation reactors, the Doppler coefficient becomes small. Extensive studies of properties of different fuel carrier material which would help to at least partially regain the Doppler effect were reported e.g. by Lombardi [56] and Conti [57]. It appeared that a certain degree of Doppler could be obtained using materials with significant resonances in the fast energy range - W, Mo, Nb - which, on the other hand, exhibit adverse effect on coolant void worth.

3.2.10 Delayed neutron fractions

The deterioration of kinetic parameters as delayed neutron fraction β and neutron lifetime also imposes constraints on transient behaviour of reactor systems. The delayed neutron fractions are specific characteristics of individual nuclei determined by their distribution of fission yields. In Table 3.6, the values of total delayed neutron yields ν_{d} and average number of neutrons per fission ν_{therm} are listed together with estimated delayed neutron fractions.

Two regularities can be observed from listed data: the total delayed neutron yield increases with the atomic mass of a given element but, on the other hand, decreases with increasing proton number. Furthermore, the delayed neutron yields remain energy independent until 4 MeV when they quickly drop by about a factor of two. For a fast neutron spectrum, the average neutron yields are slightly increased resulting in a further reduction of delayed neutron fractions.

The effective delayed neutron fraction, β_{eff}, is the number of delayed neutrons *inducing* fission in the system $\mathrm{N_{d,i}}$ compared to number of all neutrons *inducing* fission in the reactor $\mathrm{N_i}$. The most rigourous mathematical definition of β_{eff} was given by Keepin [58] as

$$\beta_{\mathrm{eff}} = \frac{\int \Psi(\overline{r}, E', \Omega')\chi_{\mathrm{d}}(E')\nu_{\mathrm{d}}(E')\Sigma_{\mathrm{f}}(\overline{r}, E, \Omega)\phi(\overline{r}, E, \Omega)dEd\Omega dE'd\Omega' d\overline{r}}{\int \Psi(\overline{r}, E', \Omega')\chi(E')\nu(E')\Sigma_{\mathrm{f}}(\overline{r}, E, \Omega)\phi(\overline{r}, E, \Omega)dEd\Omega dE'd\Omega' d\overline{r}} \qquad (3.25)$$

where ϕ is the neutron flux at position $\overline{r}$ with energy E and solid angle Ω, ν is the averaged neutron yield per fission, ν_{d} is the averaged delayed neutron yield, Σ_{f} is the macroscopic fission cross-section, χ_{d}, χ is the energy spectrum function of delayed and all neutrons in the system, respectively, and $\Psi(\overline{r}, E, \Omega)$ is the neutron importance function (i.e. function proportional to the asymptotic power level resulting from introduction of a neutron into the critical system). In sub-critical systems, $\Psi(\overline{r}, E', \Omega')$ is proportional to the probability of neutron to induce fission.

In Monte Carlo code MCNP [59], β and β_{eff} are not given explicitly. Moreover, $\mathrm{N_{d,i}}$ and $\mathrm{N_i}$ cannot be obtained directly. We therefore write

$$\beta_{\mathrm{eff}} = \frac{N_{\mathrm{d,i}}}{N_{\mathrm{i}}} = \frac{P_{\mathrm{d,i}}}{P_{\mathrm{i}}}\frac{N_{\mathrm{d}}}{N} = \frac{P_{\mathrm{d,i}}}{P_{\mathrm{i}}}\beta \qquad (3.26)$$

Isotope	ν_d		ν_{therm}		β [pcm]	
	ENDF	JENDL	ENDF	JENDL	ENDF	JENDL
^{232}Th	0.0527	–	1.949	–	2704	–
^{233}U	0.0074	0.0067	2.495	2.493	297	275
^{235}U	0.0167	0.0160	2.437	2.439	685	656
^{238}U	0.0440	0.0481	2.492	2.489	1766	1933
^{237}Np	0.0108	0.0122	2.636	2.541	410	480
^{238}Pu	0.0042	0.0047	2.895	2.895	145	162
^{239}Pu	0.0065	0.0062	2.881	2.884	226	215
^{240}Pu	0.0090	0.0091	2.803	2.784	321	327
^{241}Pu	0.0162	0.0160	2.945	2.931	550	546
^{242}Pu	0.0197	0.0183	2.810	2.859	701	640
^{241}Am	0.0043	0.0045	3.264	3.224	132	140
^{242m}Am	0.0069	0.0065	3.264	3.275	211	198
^{243}Am	0.0080	0.0095	3.273	3.210	244	296
^{242}Cm	0.0014	0.0021	3.440	3.252	41	65
^{243}Cm	–	0.0030	3.430	3.433	–	87
^{244}Cm	–	0.0044	3.460	3.244	–	137
^{245}Cm	0.0059	0.0063	3.606	3.531	164	178
^{246}Cm	–	0.0092	3.480	3.199	–	288

Table 3.6. Thermal total delayed and average neutron yields per fission together with estimated delayed neutron fractions as obtained from ENDFB-VI, revision 5 and JENDL 3.2 data libraries. Note the large differences in delayed neutron fractions evaluated, which are as high as 50% for some minor actinides.

where $\beta = \mathrm{N_d/N}$ is the number of delayed neutrons compared to number of all neutrons in the reactor, $\mathrm{P_i}$ and $\mathrm{P_{d,i}}$ are the probabilities that the average neutron and delayed neutron induce fission in the reactor, respectively. The values of β, $\mathrm{P_i}$ and $\mathrm{P_{d,i}}$ can be assessed in two separate MCNP calculations.

The probability that the average neutron induce fission is given by

$$P_\mathrm{i} = L_\mathrm{f} = \Sigma_\mathrm{f}\phi \tag{3.27}$$

In the calculation, the transport of both prompt and delayed neutrons is considered, explicitly modelling their respective spectra. Similarly, simulating the transport of prompt neutrons only, we obtain

$$P_\mathrm{p,i} = L_\mathrm{f,p} = \Sigma_\mathrm{f,p}\phi \tag{3.28}$$

In this approach, we assume that the shapes of the ϕ function are same as in both cases, which is almost true as ν_d is two orders of magnitude lower than ν.

The probability that the delayed neutrons induce fission is then determined from

$$\nu L_\mathrm{f} = \nu_\mathrm{p} L_\mathrm{f,p} + \nu_\mathrm{d} L_\mathrm{f,d} \quad \Rightarrow \quad L_\mathrm{f,d} = \frac{\nu L_\mathrm{f} - \nu_\mathrm{p} L_\mathrm{f,p}}{\nu_\mathrm{d}} \tag{3.29}$$

Assembly	Experimental values [pcm]	JEFF-3.0		ENDF/B-VI		JENDL-3.3	
		β	β_{eff}	β	β_{eff}	β	β_{eff}
Godiva	659 ± 10	600	683	633	662	627	635
Jezebel	194 ± 10	191	189	187	176	189	181
^{242}Pu	–	565	–	594	247	545	183

Table 3.7. Effective delayed neutron fractions for Godiva, Jezebel and ^{242}Pu critical configurations. Note that the delayed neutron energy distribution for ^{242}Pu is not given in JEFF-3.0. Experimental values were taken from ref. [60].

where ν_{p} is the prompt neutron yield.

In order to test the reliability of the devised approach, the β_{eff} was calculated for two benchmark configurations, Godiva and Jezebel. Godiva is an unreflected sphere of the highly enriched metallic uranium (^{234}U 1.02 wt%, ^{235}U 93.71 wt%, ^{238}U 5.27 wt%, radius 8.7414 cm, density 18.74 g/cm^3), Jezebel is the similar sphere configuration with weapon grade plutonium (^{239}Pu 95.2 at%, ^{240}Pu 4.5 at%, ^{241}Pu 0.3 at%) enclosed in a thin nickel shell. A critical metallic ^{242}Pu sphere was also modelled. Rather good agreement with the experimental values was obtained, see Table 3.7.

3.3 Transmutation strategies

After defining incentives for P&T of spent nuclear fuel and identifying the basic physical characteristics and constraints which accompany this process, we now give a comprehensive overview of different P&T schemes, involving both thermal and fast nuclear reactors. Most recently, the subject was studied by OECD/NEA [25].

In general, transmutation of transuranics are envisioned to be accomplished in either so called *homogeneous* mode, where TRU nuclei are homogeneously dispersed in the whole reactor core, or *heterogeneous* mode, where the irradiation takes place in dedicated target sub-assemblies or in dedicated reactors operating exclusively TRU fuel.

Transmutation scenarios are considered to be either "once-through", i.e. irradiation takes place until a significant depletion is reached and fuel/targets are directly disposed of, or with multi-recycling when fuel/dedicated targets are discharged from the reactor, reprocessed and again returned to the transmutation process.

In a broad perspective, the different fuel cycle concepts investigated can be categorised as follows

- once-through fuel cycle, without spent fuel recycling, entailing the direct disposal of spent fuel in a geological repository; this strategy is applied in countries without recycling possibilities or with proliferation concerns,

- plutonium burning strategy, where plutonium is first incinerated in light water reactors, and afterwards in critical fast reactors; minor actinides and fission products are concurrently destined into the geological repository,

- closed fuel cycle which, in addition to the preceding scheme, involves burning of MA homogeneously distributed in FRs (BREST [48], EFR [61], IFR [62]) or in dedicated reactor systems, e.g. ADS; such complete recycling entails that secondary waste streams to the repository are limited.

Variations of these basic principle schemes are displayed in Figure 3.10 and will be discussed in detail below. From the system point of view, P&T is proposed to be achieved in two different scenarios: an *evolutionary*, with reactor systems and reprocessing technologies of the present knowledge (aqueous), and *innovative*, where pyrochemistry technologies and advanced reactor systems are used for TRU burning in the closed fuel cycle.

The different fuel cycle/transmutation strategies will be discussed in the next sections with respect to the reactor spectrum. In order to address the safety issues associated with introduction of minor actinides into the fuel, *dedicated* reactor systems operating in both critical and sub-critical mode have been proposed. We will treat these systems in more technological detail in Chapter 4.

3.3.1 Thermal reactors

Thermal neutron spectrum systems encompass both commercial light-water reactors (LWR), i.e., pressurised water reactors (PWR) and boiling water reactors (BWR), and heavy water CANDU type reactors.

Plutonium

The transmutation of Pu from spent LWR-UOX fuel is industrially accomplished in light-water reactors in the form of so called mixed-oxide fuel (MOX). It involves extraction of plutonium and uranium from spent fuel and re-use of plutonium mixed with uranium tailings (^{235}U enrichment of about 0.25%-0.3%) in fabrication of new fuel sub-assemblies. Plutonium reprocessed from about five to eight UOX spent fuel sub-assemblies having a burnup of 40 GWd/tHM is sufficient to produce one MOX sub-assembly with 5% to 8.2% Pu content. Reprocessed uranium has so far been applied in some test MOX sub-assemblies, but its use has not become an industrial praxis also because of the large stocks of depleted uranium (about 7 tonnes is produced per each tonne of enriched uranium). Its usage is also unfavourable due to the presence of a neutron poison (^{236}U), and because of its increased radioactivity due to the strong γ-emitters ^{208}Tl and ^{228}Th, daughter products of ^{232}U (half-life 70 year).

The plutonium fission fraction ratio in the first MOX recycle is only about 25% while additional 10% is transformed into minor actinides [10]. The latter figure highlights the major drawback of plutonium recycling in LWRs, which is the build

up of minor actinides, as even neutron number nuclei have virtually zero fission-to-capture probability ratios in the thermal spectrum. Thus, despite the Pu mass reduction, radiotoxic inventory actually increases.

Indeed, further mass reduction can be achieved by multiple recycling of plutonium. This is, however, accompanied with constraints on core neutronic behaviour and limitation at reprocessing plants as plutonium quality decreases. The quality is defined as a mass fraction of fissile isotopes in the Pu-vector

$$Q_{\mathrm{Pu}} = 100 \cdot \frac{m(^{239}\mathrm{Pu}) + m(^{241}\mathrm{Pu})}{m(\mathrm{Pu_{tot}})}. \tag{3.30}$$

It diminishes in subsequent generations and drops from the value of about 70 for LWR Pu discharge down to about 45 at the fifth recycle generation in standard lattices of LWRs [63]. Due to the lowered plutonium reactivity, its enrichment in the U/Pu mixture has to be increased in further generations which influences several safety characteristics of the reactor - particularly moderator void and temperature reactivity coefficients, the Doppler coefficient and boron reactivity worth. This is due to a spectrum hardening in MOX sub-assemblies which is further pronounced, e.g. in the case of loss-of-coolant accident, when fast fission of fertile Pu isotopes become significant. In order to keep the boron reactivity worth on the same limit, the concentration of the boric acid in the water has to be increased, which however further deteriorate coolant void reactivity. Thus, due to the positive void worth, the plutonium content in standard PWR lattice MOX sub-assemblies cannot exceed 12 wt% [64].

These safety drawbacks may be mitigated by changes of sub-assembly lattice design in order to achieve satisfactory spectrum thermalisation. This is accomplished either by an increase of moderator/fuel ratio (up to 3.5 - 4) - so called high moderation PWR (HM-PWR) [65], or by a radical decrease of the fuel smear density from 9 g·cm^{-3} to 3.5 g·cm^{-3} keeping the same lattice geometry [66]. Another innovative method was presented by CEA, proposing heterogeneous distribution of uranium and plutonium pins in a fuel sub-assembly (Advanced Plutonium Assembly - APA and CORAIL MOX sub-assemblies) allowing to keep also an acceptable power shape [67, 68, 69, 70]. A further possibility to mitigate void problems is to increase the ^{235}U fraction in the fuel keeping plutonium content fixed at 4% (so called MIX approach) which on the other hand result in higher fabrication costs and lower Pu fission fraction ratios [71]. Combining the previous design approaches, an over-moderated ^{235}U-enriched MOX sub-assembly (MOX-UE) was recently developed [72]. In the S/A lattice with slightly increased moderation ratio, the neutron spectrum is sufficiently thermalised such that reasonable value of the void reactivity is maintained also during Pu recycling. In order to compensate for a degradation of the Pu vector (and respect 12% Pu limit), ^{235}U enrichment in the fuel has to be gradually increased (to 3% after 7 recyclings).

An additional major problem with high plutonium content fuels is the small delayed neutron fraction, which entails faster reactor response on reactivity and

power transients. In this respect, the potential of LWRs to recycle stocks of weapon grade Pu (95% ^{239}Pu, 5% ^{240}Pu) seems to be questionable.

Safety of reactor cores is proven up to 30%-50% of MOX fuel assemblies with plutonium enrichment up to 5%. At this level as much plutonium is consumed in MOX sub-assemblies as is produced in UOX. For MOX-UE, stabilising Pu inventory requires that 25-28% of the energy is generated in the MOX sub-assemblies. Maximum plutonium consumption in LWRs would be reached in 100% MOX cores, whose feasibility, however, needs to be further investigated.

Obviously, due to the presence of uranium in the U/Pu matrix, plutonium depletion is somewhat diminished. Use of an inert matrix instead of uranium could gain higher plutonium consumption, which is, however, at the expense of fuel temperature feedback. Some studies have been also done on the use of thorium as a plutonium support in MOX fuel showing improved void characteristics [73, 74].

Nevertheless, recycling of plutonium in LWR does not meet our objectives for P&T technologies as it does not significantly reduce the radiotoxic inventory of spent fuel. The amount of minor actinides produced in a MOX sub-assembly is 3-4 times higher than in corresponding UOX sub-assemblies having increased requirements on interim storage and short-term repository performance as consequence.

Minor actinides

Possible transmutation strategies for minor actinides are with certain limitations determined by the performance and abilities of chemical separation processes. The general problems accompanying addition of minor actinides to the fuel are similar to those already mentioned for plutonium - deterioration of physical characteristics of reactor cores, particularly coolant void temperature coefficient, Doppler feedback, and delayed neutron fractions. An additional serious difficulty is the helium production due to α-decaying ^{242}Cm, ^{244}Cm, and ^{238}Pu which enhances fuel swelling and results in pin over-pressurisation. Thus the content of minor actinides in reactor cores has to be somewhat limited.

Americium and curium Transmutation of *both* americium and curium has to be accomplished if a reduction of radiotoxic inventories higher than a factor of 100 is to be reached [75, 25]. Moreover, incineration of pure curium in a standalone facility can not be considered due to the very high heat production from the α and neutron emitters ^{242}Cm and ^{244}Cm. The only remedy is either its incineration together with americium or transmutation of curium as ^{240}Pu allowing for a decay of ^{244}Cm (half-life 18.1 yr) in a time period of 100 years or so, which still leaves ^{245}Cm untransmuted.

Studies of the homogeneous recycling of americium show a significant deterioration of the coolant void reactivity coefficient. Taking into account limits on uranium enrichment ($< 5\%$) or plutonium content (less than about 12%) in the case of MOX fuels, the maximum concentrations of americium in fuel were identified as 1% for standard PWR and 2% for highly moderated lattices [21]. It results in a

10% decrease of Doppler coefficient while the moderator temperature coefficient is diminished by 25%. The specific consumption of americium in UOX fuel (total inventory of about 1.1 tonne) reaches about 19 kg/TWh$_e$ (annual production of about five 1000 MWe-LWRs). Adding 1% Am into MOX-UE sub-assembly requires that ^{235}U enrichment is increased by about 2% and Pu content decreased to ∼8%. If both plutonium and americium inventory should be stabilised, 40% MOX-UE cores have to be applied [72]. As the fission-to-absorption ratio for ^{241}Am is very low (virtually zero) in thermal spectra, most of the americium (70%) is converted via ^{242}Am into ^{242}Cm which consequently α-decays into ^{238}Pu, resulting in increased fuel swelling rates due to the formation of He bubbles.

Targets A much more attractive option with respect to core neutronic characteristics was thought to be heterogeneous americium recycling in separate sub-assemblies placed at the core periphery, thus having lower influence on core characteristics. As thermophysical properties of AmO_2 are not favourable owing to the low thermal conductivity and melting temperature, several materials have been investigated as suitable matrices for americium incineration. E.g., the EFTTRA-T4 experiments [76] study behaviour of americium incorporated in spinel ($MgAl_2O_4$) matrix (11 wt% of Am) during irradiation in Petten's thermal high flux reactor. Another compound - MgO-AmO_{2-x} - was fabricated and irradiated by ITU [77], having americium particles homogeneously dispersed in the matrix as well as in the macroscopic solution with it.

Due to anticipated significant difficulties with reprocessing of such target fuels, a once-through transmutation scheme is envisaged for thermal americium incineration. Dedicated americium targets are left in the reactor until a significant depletion takes place and are thereafter directly disposed of. The residence time of such assemblies in the reactor is limited by the maximum radiation damage which inert matrix and cladding can withstand and by the maximum capacity of the target pins to accommodate produced helium.

As the preliminary calculations show, consumption of americium in dedicated targets is rather low, reaching about 9 kg/TWh$_e$ in the best case (depletion 74%) having 30 wt% AmO_2 in a mixture with an inert matrix. This corresponds to half the annual LWR americium production (4 years after decay). Furthermore, due to the low reaction rates, the equilibrium incineration of americium in LWRs implies very large fuel inventories - about several hundreds of tons of TRU - much more than waste discharges.

Indeed, the radiotoxic inventory is again increased due to the massive curium production which, together with reactivity and swelling problems, makes LWRs unsuitable for effective MA incineration in a P&T scheme. The fuel swelling problems are only partially relaxed in the fast neutron spectra and need to be addressed in dedicated systems with favourable minor actinide fission-to-absorption ratios and where gasses may be released into the plena, which is not possible in standard LWRs.

Fission products

As discussed in Chapter 2, there are some long-lived fission products (LLFP), which contribute to the long-term geosphere dose, also when considering a human intrusion scenario into the repository. These are hence candidates for partitioning and transmutation schemes - ^{129}I (production rate 5 kg/GW$_e$ ·year), ^{135}Cs (12 kg/GW$_e$·year), and in an oxidising environment ^{99}Tc (21 kg/GW$_e$·year).

The transmutation of fission products is considered to be accomplished in heterogeneous mode fixing individual LLFP nuclides in suitable target forms. The target material/matrix has to be stable upon irradiation and withstand high burnups, the melting point has to be high and compatibility with cladding and coolant must be ensured. Transmutation of selected fission products can be accomplished by single neutron capture, resulting in stable nuclei

$$^{99}\mathrm{Tc} + \mathrm{n} \rightarrow ^{100}\mathrm{Ru} + \beta^- + \tilde{\nu}_\mathrm{e} \tag{3.31}$$

and

$$^{129}\mathrm{I} + \mathrm{n} \rightarrow ^{130}\mathrm{Xe} + \beta^- + \tilde{\nu}_\mathrm{e} \tag{3.32}$$

The superiority of transmutation of these isotopes is that even further double neutron capture would lead to stable nuclei (^{101}Ru, ^{102}Ru, ^{131}Xe, ^{132}Xe). The cross-section for neutron capture is highest at thermal energies with significant resonances in the epithermal region. It is therefore attractive to place LLFP pins in the moderator of thermal reactors. On the other hand, as high fluxes as possible are favourable, which would suggest the placement of LLFP into the specially moderated sub-assemblies of fast reactors. A major drawback of a such approach is a strong self-shielding causing dips in neutron flux at the centre of LLFP pins and, as we will show, the fast neutron induced LLFP transmutation performs at least equally well (see **Paper III**).

The transmutation of long-lived fission products has been studied in the frame of the EFTTRA collaboration since 1992 [76].

In the case of ^{99}Tc, the metallic form was chosen as the most attractive option due to the highest technetium concentration and compatibility with transmutation product (^{100}Ru). The irradiation of sample targets has been done in thermal positions of Petten's high flux reactor reaching burnups from 6% to 16% [78, 79]. Neither swelling nor microstructural changes in the pellets have been observed and it seems that metallic technetium is a good candidate for transmutation. However, its behaviour in fast reactor environments remains to be confirmed. Theoretical predictions of transmutation half-lifes are from 15 to 18 years in fast reactors and 40 to 77 years in LWRs. Due to the limitations posed by radiation damage of cladding materials, the transmutation has to be accomplished in multi-recycling mode in order to achieve a significant reduction of Tc content.

The choice of target material is more complex for iodine. ^{129}I mass proportion is about 80% in a mixture with stable ^{127}I which seems to be rather affable. In elemental form, iodine is rather volatile (melting point 387 K) and thus some binary compounds seem to be more suitable - CeI_3, PbI_2, and NaI. The irradiation

experiments in Petten HFR have revealed incompatibility of PbI_2 with the 15-15Ti stainless steel capsule, which corroded. At the same time, serious difficulties have been encountered while manufacturing CeI_3 and thus NaI seems to be so far the best candidate for iodine incineration. Another important question, limiting iodine transmutation rate, is the accommodation of gaseous ^{130}Xe, which has to be accomplished either by a large gas plenum in the LLFP pin or by special vented design.

In the case of cesium, isotopic separation of ^{133}Cs, ^{135}Cs, and ^{137}Cs has to be accomplished prior to incineration, which makes transmutation of ^{135}Cs economically hardly feasible.

3.3.2 Fast reactors

Plutonium

The development of a self-sustaining U-Pu fuel cycle based on MOX fuelled fast breeder reactors engaged thousands of nuclear scientists during the 60s and 70s. The technical complexity and associated difficulties have together with economical disadvantages (cheap uranium) and political reasons considerably slowed down their introduction into the nuclear reactor parks. Furthermore, in terms of partitioning and transmutation technologies, the incentives for fast reactor deployment changes and are shifting from plutonium/transuranic *breeding* to *burning*.

While incineration of plutonium in thermal neutron spectra is limited due to the deterioration of plutonium vector composition and core neutronic and safety aspects, and the limitation in the PUREX reprocessing technologies, the infinite multiple-recycling of plutonium in fast reactors is theoretically feasible [73]. The superiority of fast spectrum in actinide transmutation and radiotoxic inventory reduction of spent fuel is recognised by most authors [39, 80, 81]. All actinide isotopes are in principle fissionable and in a high flux neutron spectrum of fast reactors act as neutron producers, see also Section 3.2.3 [41, 82].

Special type of fast *burner* reactors (FBuR) without breeding blanket and thus with maximised plutonium consumption are extensively studied. The CAPRA reactor [83] was proposed in 1992 utilising MOX fuel with up to 45% of plutonium enrichment. The CAPRA core can work in symbiosis with about one MOX-LWR and five UOX-LWRs achieving significant reduction of the Pu inventory as only reprocessing losses are treated as a waste. However, due to the massive production of minor actinides, the radiotoxic inventory is reduced only by a factor of three for several thousand years and by five-six afterwards. The plutonium depletion reaches 55% and its concentration in spent CAPRA fuel is reduced to 25% which is the maximum concentration in MOX fuel being compatible with the PUREX process. Obviously, this difficulty could be solved by applying other types of fuel matrices as nitrides or metallic fuels together with pyro-reprocessing.

Minor actinides

The neutron surplus when transmuting minor actinides is positive in fast spectrum for fluxes over 10^{15}n·cm^{-2}s^{-1} [41]. MA incineration is again envisioned in homogeneous and heterogeneous modes considering either a once-through or multi-recycling scheme.

Neptunium As in the case of LWRs, the homogeneous introduction of neptunium in the MOX fuel is the preferred option. Due to the limitations in Doppler feedback and moderator void coefficient (sodium), the content of neptunium in the fuel has to be limited to about 2.5%. However, more strict limitation is posed again by the PUREX reprocessing due to the α and heat emitter ^{238}Pu. Specific consumption rates of Np are not significantly increased when compared to the thermal spectrum and amount to about 10 kg/TWh$_e$ in an EFR-type core.

Extensive calculation studies of MA transmutation in fast reactors have been performed in the frame of European activities on feasibility and cost assessment of P&T [84]. Regarding heterogeneous once-through recycling of neptunium, the targets (40% of Np in an inert matrix material) were placed in the reflector of an EFR-type core and burnup calculations were performed for 4500 effective full power days, after which radiation damage to cladding steels had reached the limit of 200 dpa-NRT. The Np depletion appeared to be rather low, reaching 60% at the very modest fission fraction ratio 24%. Thus, about 60% of the depleted neptunium was converted to non-fissile plutonium isotopes with a high portion of ^{238}Pu.

Americium Due to the limitations on ^{238}Pu concentration, remember

$$^{241}\mathrm{Am} + \mathrm{n} \;\rightarrow\; ^{242}\mathrm{Cm} \;\rightarrow\; ^{238}\mathrm{Pu}, \tag{3.33}$$

the americium content in homogeneous MOX mixtures has to be reduced, as in the case of neptunium homogeneous recycling, to 2.5%. The americium consumption is accordingly very low, only 9 kg/TWh$_e$, and the fast reactor can accommodate the annual production of about 3 LWRs. The fabrication costs of fuel containing americium increase by about 20% compared to standard FBR MOX.

In the case of once-through heterogeneous recycling of americium, targets containing 20%, 40%, and 100% of americium in an Al_2O_3 inert matrix were placed in the reflector of an EFR-type reactor core. It appeared that depletion and fission fraction ratios depend strongly on the americium content. The optimum concentration of americium in the targets was around 40% with respect to power profile characteristics, depletion rates and influence on core performance. The americium consumption was calculated to be comparatively high amounting to 14 kg/TWh$_e$ (which is a factor of 2-3 higher than the internal americium production of the EFR). The irradiation time was, as above, limited to the maximum steel damage of 200 dpa-NRT. In this respect, we note that 200-dpa NRT is probably unrealistic limit considering latest results obtained by Budylkin et al. [85]. For further discussion on this issue, see Chapter 5.

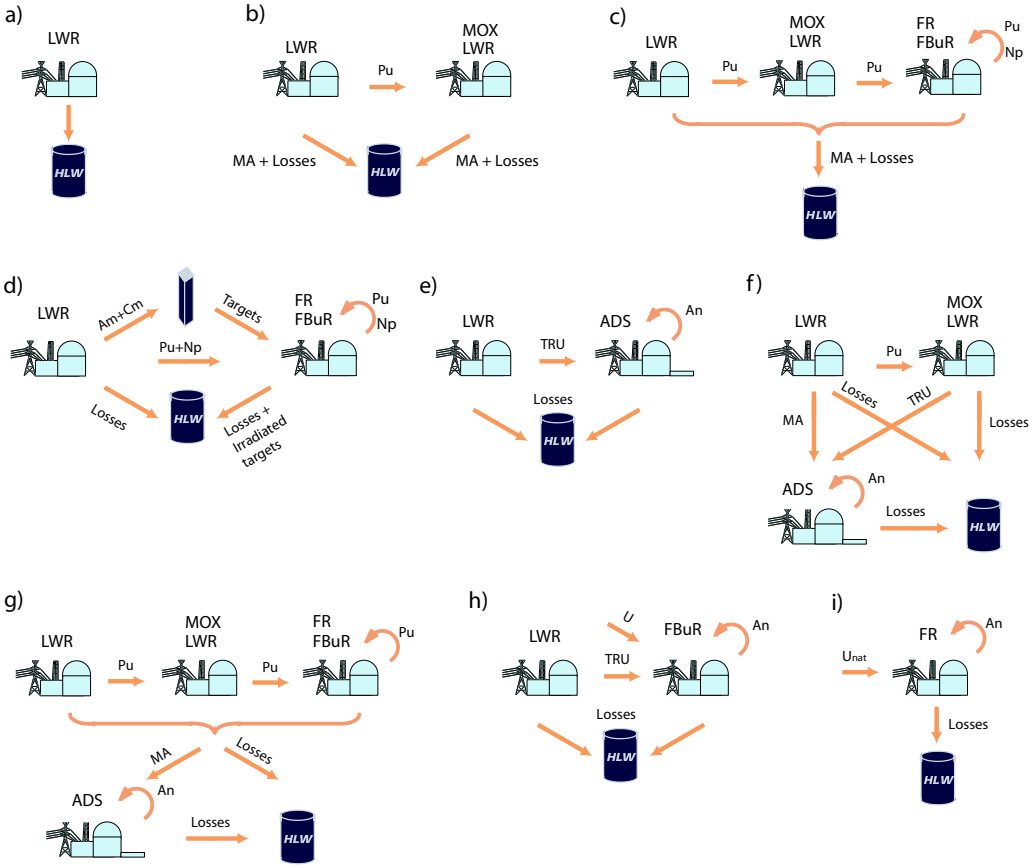

Figure 3.10. Fuel cycle/P&T scenarios: a) open "once-through" cycle; b) Pu MOX burning in LWRs; c) Pu MOX burning in LWRs & fast reactors (∼70% LWR-UOX − ∼10% LWR-MOX − ∼20% FR); d) Pu burning & heterogeneous MA recycling in fast reactors; e) two-component strategy, TRU burning in ADS, ADS support ratio ∼21%; f) two-component strategy, Pu MOX recycling in LWR prior to TRU burning in ADS, fraction of ADS ∼15%; g) double-strata (multi-component, two-tier) scheme, fraction of ADS ∼ 5-10%; h) TRU burning in FBuR, the reactor park consists of 63% LWRs and 37% FBuRs; i) one-component fast reactor cycle.

Neptunium and americium Multiple heterogeneous recycling of neptunium and americium was studied by Baetslé [86] in an admixture with plutonium and depleted uranium (67%U-33%TRU). It was revealed that 1 tonne of Pu+MA mixture from LWR-MOX fuel can be completely transmuted after 15 cycles (255 years) in a CAPRA-like reactor (1 cycle = 5 years of irradiation and 12 years of cooling down) allowing, of course, for reprocessing losses. A fast reactor could thus support 1-2 LWRs of the same power.

Curium Due to the strong α and neutron emission, fabrication of curium target fuels becomes extremely costly and curium is thus preferably diluted with americium. Alternatively, one may, prior to any transmutation, allow ^{244}Cm to undergo α-decay into ^{240}Pu.

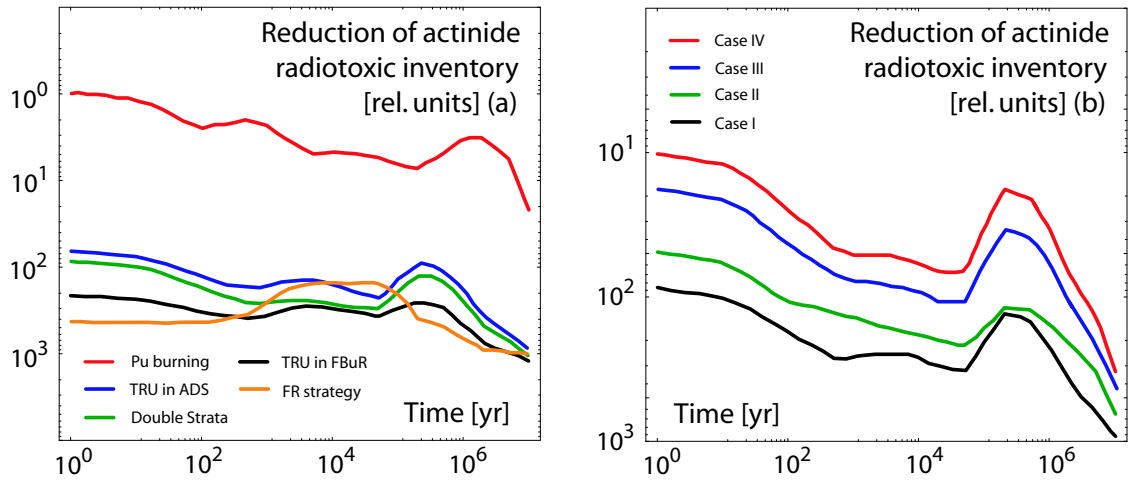

Figure 3.11. Reduction of radiotoxic inventory for different P&T schemes (a) and an impact of fuel losses in separation technologies on a performance of double-strata scenario (b). Reprocessing losses in advanced PUREX of the first stratum were assumed to be either 0.1% for all actinides in Case I, or 0.1% for U&Pu and 1% for MA in Cases II-IV. Losses in pyro-reprocessing are 0.1% (Case I&II), 0.5% (Case III) and 1.0% (Case IV), respectively. Figure courtesy of OECD/NEA [25].

3.3.3 Scenarios

Now, we are ready to discuss the different P&T scenarios involving both evolutionary and innovative reactor system components, recall Figure 3.10, and assess their performance with respect to the reduction of the radiotoxic inventory of spent fuel. A comprehensive analysis of this subject was provided most recently in OECD/NEA study [25]. The results for some principal schemes are given in Figure 3.11(a).

It was shown that multirecycling the *Pu alone* (in either LWRs or in LWRs-FRs schemes, i.e., strategy b) and c)) significantly reduces the losses of TRU to the repository, but its performance with respect to the reduction of the radiotoxic inventory disqualifies it as an effective transmutation strategy. The radiotoxic inventory is reduced by about a factor of two and five for the b) and c) strategy, respectively.

The best strategy for *minor actinide* transmutation in *fast critical reactors* seems to be homogeneous incineration of neptunium in MOX fuel sub-assemblies, while americium together with curium needs to be recycled and irradiated in dedicated sub-assemblies positioned in the core periphery, i.e., scheme d). However, cooling times for the irradiated Am/Cm assemblies become excessive (7-12 years) if aqueous reprocessing is to be used, and the support ratio, i.e. the number of fast neutron cores needed to manage MA production of one LWR, becomes larger than 0.5 with adverse effect on the economy of the P&T fuel cycle. A 90% reduction of TRU would thus be reached in time scales of 100-250 years. As mentioned above, significantly smaller cooling times are possible for pyrochemical technologies, which could reduce the length of an irradiation reprocessing cycle by more than a factor

of two.

But all in all, unfavourable safety characteristics appearing when burning minor actinides in both thermal and fast reactors of the standard design have led to the idea of dedicated actinide and LLFP transmutation in special reactors, conceived originally both as critical and sub-critical. The dedicated systems are envisioned to work either in TRU burning mode - in symbiosis with light-water reactors in a two-component scenario - i.e. strategies e) and f), or in concert with LWRs and FRs - in a so called double-strata (multi-component, two-tier) scheme [87, 82] - strategy g).

The double-strata concept was first proposed by JAERI in 1984 [88]. It comprises dividing the fuel cycle into two rather distinct parts - the first stratum which is based on modestly changed state-of-the-art technologies (reprocessing, fuel fabrication, core design - LWRs and FRs) and the second relying, in all respects, on advanced, innovative processes. The plutonium incineration in the LWRs and FRs of the first stratum is thus seen as an effective way to reduce transuranic mass rather than radiotoxic inventory, which allows to keep the fraction of innovative reactors managing minor actinides at a minimum level.

The impact of the different separation losses on the capability of the double-strata scheme is illustrated in Figure 3.11(b). The losses in the pyroprocessing of the MA burning stratum showed to be decisive with respect to the transmutation performance of the scenario. The actinide radiotoxic inventory can be reduced to 1% of its original value within 100 years after fuel reprocessing, if actinide losses in pyroprocessing are limited to 0.1% - a similar requirement we already imposed on the recovery yields of the separation technologies in the model equilibrium cycle, see Section 3.2.1. In the first stratum, the losses in advanced PUREX were assumed to be limited to 0.1% for U & Pu and 1.0% for minor actinides (Case II).

TRU burning in FBuR and *pure*, one-component fast reactor strategy have been both also identified as promising P&T routes, closing also the fuel cycle for all transuranics. It appeared that if MOX recycling is not pursued in LWR and the whole TRU vector is directed into FBuR, minor actinide fraction in the FBuR fuel can be kept under 2.5% limit (set by deteriorating Doppler feedback and coolant void coefficient). Thus, if whole TRU vector is recycled, the scheme performs equally well or better than scenarios including dedicated systems, see Figure 3.11(a). Therefore, there may be an incentive to re-evaluate the decisions to *continue* with MOX-recycling in LWRs. Fast reactor scenario, strategy i), involves an introduction of a completely new fuel cycle scheme, relevant only for countries not utilising nuclear power today.

Chapter 4

Dedicated reactors

As discussed in the previous chapter, removal of ^{238}U and/or admixture of large amounts of minor actinides into the fuel severally deteriorates the safety parameters of reactor cores, significantly decreasing Doppler temperature feedback and effective delayed neutron fractions. In addition, high content of even-neutron number nuclei in the fuel elevates coolant void worth and/or coolant temperature reactivity coefficient. The possibility to operate dedicated MA burning cores critical hence become doubtful.

Already in 1974, the introduction of slightly sub-critical cores for MA burning was therefore envisioned by Los Alamos scientists [89]. The idea was revived again by Japanese scientists ten years later, proposing a separate management of minor actinides in *dedicated* facilities and adopting fast reactors for recycling of plutonium [88]. Thus, handling of a strong α and neutron emitters is confined only to a very small fraction of the reactor park. Nowadays, another important reason for introduction of dedicated MA burners is the excess of ^{241}Am present in spent fuel due to the long delay in commencing of P&T in most countries. Both critical and sub-critical dedicated MA burners were proposed originally, but in recent years, the focus is naturally on the sub-critical systems. Note that the review provided here is neither complete nor exhaustive.

4.1 Critical actinide burners

In JAERI investigations, two concepts of dedicated critical actinide burner reactors (ABR) have crystallised - lead-cooled pin fuel (L-ABR) and a helium-cooled particle fuel (P-ABR) [80]. For these reactors, JAERI proposed a nitride fuel consisting of 65% of minor actinides (Np,Am,Cm) and 35% of highly enriched uranium. Enriched uranium is mixed into the fuel in order to counterattack problems with extremely low delayed fractions. However, β_{eff} still remained rather low at the level of 260 pcm (about 20% lower than CAPRA reference core). As also neutron lifetimes became

very small (in the order of 0.13 μs), safety margins of the ABRs were significantly deteriorated.

CEA studied a fast modular critical ABR based on the lead-bismuth coolant technology and nitride fuel. The thermal output of these cores was rather modest in the order of 130 MW_{th} with MA consumption rate of about 78 kg/TWh_e. The delayed neutron fraction were again very low on the level of about 170 pcm.

4.2 Accelerator-driven systems

The ADSs couple the technology of high-intensity particle accelerator with spallation targets, which provide neutrons for a multiplicative sub-critical blanket/core. The accelerator is either a linac as proposed by LANL [90] and JAERI [91] or a cyclotron as advertised by CERN [92].

Several types of targets are studied, including a solid one where tungsten is cooled by sodium flowing through holes in the target, and a liquid one - based on lead-bismuth eutectic serving both as a spallation material and coolant. In terms of minor actinide transmutations, ADSs offer much higher flexibility what concerns fuel composition, irradiation times and overall system performance as requirements on safety margins are somewhat relaxed. ADSs can accommodate excess americium and curium and use uranium-free fuel, allowing to reach the theoretical maximum TRU net consumption 360 kg/GW_{th}·year. A majority of the sub-critical cores envisioned for MA transmutation are designed to be operated in a fast or coupled fast/thermal spectrum in order to achieve the most favourable neutronic spectrum for effective MA and LLFP burning. As shown by Salvatores and coworkers [93], the ADSs in comparison to the critical systems supply a higher excess of neutrons which can be used for additional transmutation purposes.

While some of the safety issues of ADSs are common with those considered for critical reactors (e.g. heat removal), there some problems which are ADS specific. They, in particular, occur on the interface and in connection with accelerator and core (blanket) coupling and involve, e.g. irregularities/oscillations in particle beam intensity (e.g. beam-overpower accident) or issues of radiation damage of accelerator beam window and target walls in neutron and proton fields. Reliability and availability of the accelerator beam is another important question. Namely, a frequency of beam trips long enough to cause the shut-down of the system has to be significantly limited.

4.3 Review of ADS related projects

The research on accelerator-driven systems or material/component-related subjects is pursued worldwide. We give a brief overlook and summary of relevant projects.

4.3.1 Japan

In the frame of the OMEGA programme, JAERI studied two types of solid fuel ADSs [94]. The first relied on the established technology of sodium and the second employed lead-bismuth as coolant. The latter option was further developed in recent years [95]. The reactor core 800 MW_{th} is fuelled with minor actinides (60%) mixed with initial plutonium loading, thus mitigating the burnup reactivity swing. The fuel is diluted with ZrN. Ductless fuel sub-assemblies are envisioned in order to avoid crud blockage accidents and enhance self-circulation of Pb/Bi hence improving decay heat removal capabilities. JAERI operates the Pb/Bi material test loop in order to study corrosion stability of structural materials, beam window thermal hydraulics and behaviour of radioactive impurities. Moreover, transmutation experimental facility is planned to be build in the Tokai Research Establishment. The facility would comprise Transmutation Physics Experimental Facility which would be a zero-power sub-critical system coupled with low power proton beam, and ADS Target Test Facility being able to accept 200 keV-600 MeV proton beam in the Pb/Bi spallation target that would be used for material irradiation testing purposes. Studies on fast spectrum molten salt cores were also made, but are given secondary priority due to safety and material compatibility problems. The molten salt chlorides were proposed as a primer choice, having a multifold purpose of fuel carrier ($64PbCl_2$-$36TRUCl_3$), target material and coolant [94].

4.3.2 France

Alluding to the 1991 Law on Nuclear Waste Management, the Separation - Incineration research programme was started in France, investigating the potential of P&T in the spent fuel management scheme [96]. Research in the area of ADS is coordinated in France by the GEDEPEON group, including research organisations (CEA, CNRS) as well as industrial bodies (EdF, Framatome). Development of ADS was considered in a broader frame of advanced nuclear fuel cycles - potentially serving both as dedicated MA burners and being a basis of new, thorium burning reactor generation. Two systems were studied, based on the technology of molten salts [82] and heavy metal (Pb/Bi) cooled, nitride-fuelled blankets [97]. Recently, the activities have refocused from the ADS neutronic and system studies and the priority is given to development of novel sub-assemblies for multi-recycling of Pu in PWRs [71], design of gas-cooled fast neutron reactors [98] (in coherence with Generation IV activities [99]), and development of fuel and targets for FRs and ADSs [100]. R&D concerning spallation target (MEGAPIE), advanced separation technologies for minor actinides and cesium, regarding high energy nuclear data, and development and testing of new materials for ADS (SPIRE) is also pursued. The MUSE experiments at the MASURCA fast critical assembly has been recently concluded gaining an invaluable understanding and experience with physics of sub-critical systems. TRADE (TRIGA Reactor Accelerator Driven Experiment) experiments are planned to be started around 2006-2007 as a follow-up of the MUSE

programme [101]. TRADE will demonstrate the coupling of the spallation target source with a sub-critical reactor at power sufficient to observe reactivity feedback effects. Complementary experiments are also under way in Minsk at YALINA facility coupling the thermal spectrum sub-critical core with a neutron generator. In the frame of SAD project in Dubna, 600 MeV proton accelerator will be connected with a low power MOX core.

4.3.3 U.S.A.

In the past years, a research programme on ADSs in U.S.A. experienced a turbulent development. First, the interest has shifted from thermal spectrum designs [102, 103] to fast spectrum systems [104], based on Pb/Bi coolant technology. The ATW (Accelerator Transmutation of Waste) programme at LANL envisioned incineration of TRU and LLFP coming directly from LWRs in a sub-critical reactor using metallic fuel - an admixture of TRU with zirconium (85%Zr-15%TRU). In 1999, a federal road-mapping activity was performed, defining goals for further transmutation research in the U.S.A. [105]. Rather short-lived AAA (Advanced Accelerator Application) programme was then replaced by Advanced Fuel Cycle Initiative (AFCI) in 2003. AFCI is a common initiative by a team of national laboratories, universities, and industrial bodies aiming at development of advanced fuels and separation technologies. In a broader perspective, it also strives to revitalise U.S. nuclear science and engineering infrastructure.

4.3.4 CERN

The loudest advocate of ADSs was a team at CERN under the leadership of Carlo Rubbia. In 1993, this group presented the so called Energy Amplifier (EA) - a 200 MW_{th} sub-critical reactor core driven by an 800 MeV-6.25 mA cyclotron for "clean" energy production based on the thorium fuel cycle. This concept was originally conceived as thermal, water cooled using thorium metallic fuel [106]. Lately, the design features have shifted to fast spectrum systems driven by a 1 GeV-12.5 mA cyclotron. The Energy Amplifier in energy producing mode was oxide-fuelled with a power output of 1500 MW_{th} [107], while metallic-fuelled in LWR spent fuel incineration mode [108].

4.3.5 EU related projects

The EU 5^{th} Framework Programme on P&T includes significant experimental work on materials (Pb/Bi coolant, ferritic steels and nitride fuels) for accelerator-driven systems. Congruently with these activities, the development of a prototype ADS, eXperimental Accelerator Driven System (PDS-XADS) was started. The project focused on the design of an ADS system based either on heavy metal coolant (Pb/Bi eutectic), so called Ansaldo design (80 MW_{th}), or cooled by gas (He), so called Framatome design.

Within the frame of PDS-XADS, the Belgian MYRRHA project was also envisioned [109]. MYRRHA facility is a multipurpose prototype research fast spectrum sub-critical device driven by a 350 MeV-5 mA proton accelerator. The Pb-(Pb/Bi) spallation target is planned to be windowless in order to avoid problems with the radiation damage.

Considerable effort in ADS research also takes place in several other countries such as Spain (CIEMAT), Italy (ENEA), and Korea (HYPER facility, KAERI).

4.4 Role of ADS in P&T schemes

Obviously, the role of ADSs in the transmutation of the long-lived radiotoxic inventory has to be considered in the symbiosis with existing fuel cycle schemes. As emphasised by Salvatores [39], the minor actinide management is inevitably connected to the plutonium incineration strategy. We already know that a radiotoxic inventory reduction factor higher than ten is achievable only if curium is treated in a P&T process in a special manner. Of course, the easiest way (from the point of view of technology demands) is to let curium decay in the time period of about 100 years and transmute it afterwards as plutonium. This option, however, shifts responsibilities to the future and might not be accepted for ethical reasons. Truly, there is a theoretical possibility of immediate curium transmutation achieving fission fraction ratios as high as 90-95%. As discussed earlier, such incinerations have to be accomplished together with americium in once-through heterogeneous mode placing target dedicated assemblies of fast burners, or in dedicated reactors. This would, however, require very long irradiation times (as high as ten years), posing significant radiation damage to the cladding materials. As studies reported by Beaumont [110] show, MA target residence times in the periphery of the CAPRA high burnup core are limited to five years corresponding to the maximum cladding damage of 180 dpa-NRT. We remind the reader that this figure can be unrealistic considering recent results from low dose rate irradiations of ferritic and austenitic steels in BOR-60 [85]. In addition, the pin plenum length needed to accommodate produced helium (due to ^{242}Cm decay) becomes exceedingly long reaching 3.5 m. In this regime, as high as 80% percent of americium/curium is actually transmuted/fissioned *via* plutonium, with associated constraints on neutron economy.

As we will discuss further in the following chapters, much more favourable fission fraction ratios for *direct* fissioning of even-neutron americium and curium isotopes can be achieved in a novel type of accelerator-driven, sub-critical burner design, presented in **Paper II** and **III**. In the next chapter, we start by by reviewing and motivating the choice of materials for such a system.

Chapter 5

Choice of materials for ADS

The materials which are proposed to be applied in ADS are innovative in many aspects. The fuels should preferably fertile free (without U or Th support) and be able to accommodate large amounts of minor actinides. In order to facilitate efficient transmutation, a hard neutron spectrum should be maintained, imposing demands on the irradiation stability of the construction materials.

General requirements on materials in the ADS can be summarised as follows

- good high-temperature mechanical and irradiation performance,
- chemical stability and inertness to outer environment (air, water, steam), with no hydrogen-forming substances,
- acceptable level of induced activity,
- prolonged in-pile lifetime, achieving high fuel burn-up,
- sufficient abundance in nature.

5.1 Fuel

There are several types of fuel matrices, which could be considered for ADS - oxides, nitrides, and metallic fuels. Sometimes carbide and coated particle fuels are also envisioned. The primary goal for the development of transmutation fuels is to achieve a high burnup, hence fertile-free matrices are preferable in order to maximise TRU consumption and reduce void worths [111]. However, current reactors operate on uranium based fuels. New and innovative fuel types are thus needed. Transmutation fuels have high decay heat and high neutron and gamma emission rates. The decay heat is a factor of 20 higher in the spent fuel than for ordinary LWR fuels, being an incentive for refinement of radiation resistant reprocessing technologies. The irradiation performance of the fuel is also an unanswered question.

5.1.1 Nitride fuel

Already since the 1960s, nitride fuels have been studied in Japan as promising candidates to accommodate high plutonium fractions. The advantages of the nitrides in comparison to the more customary used oxide fuel is higher thermal conductivity (3-4 times), good compatibility with construction and coolant materials, and high solubility in nitric acid in the whole range of Pu compositions.

High thermal conductivities enables low operating temperatures of fuel, limiting fuel swelling and fission gas release. However, the specific feature of nitrides is their susceptibility to decomposition into a liquid or gaseous metal and nitrogen gas at high temperature (e.g. during transient involving power excursion)

$$2\ \mathrm{AnN} \ \rightarrow\ \mathrm{N_2} + 2\ \mathrm{An} \tag{5.1}$$

In this case, the presence of the liquid metallic phase thus precedes the melting of the nitride compound itself and decomposition of the fuel continues until concentrations of An and N_2 reach a level of equilibrium relative to the decomposing nitride.

It was shown that the decomposition behaviour of the AnN fuel is a strong function of the chemical composition of the surrounding gas. Adding nitrogen into the gas effectively lowers actinide vapour pressure, thus delaying the onset of the nitride decomposition by several hundreds of Kelvin. As the thermal conductivity of nitrogen is significantly lower than that for helium, only a small portion of nitrogen (a few per cent) in the gas can be applied. Experiments with UN in frame of the CONFIRM project show that decomposition of UN samples occurred at about 2700 K in inert atmosphere. PuN decomposition values ranges from 2857 to 3103 K in 1 bar N_2, while decomposition occurs at 2200 K in pure He and 1923 K in vacuum at 1 bar [112]. Experimental results indicate that vaporisation of $(U_{0.8},Pu_{0.2})N$ in He atmosphere is small for temperatures below 2150 K [113] and onset of the decomposition can be delayed by at least 400 K in nitrogen atmosphere [112].

The dissociation behaviour of higher actinide nitrides (AmN, CmN) is less well known. Under inert atmosphere, AmN dissociates when temperatures exceed 1600 K [114, 115, 116]. On the other hand, under 1 bar of flowing nitrogen, the dissociation rate decreases by two orders of magnitude [115, 116]. CmN was so far only fabricated in solid solution with PuN and AmN, but appears to feature a vapour pressure similar to that of PuN [117].

Nitrides are obtained from oxide powder by the carbothermic reduction method. The oxides are mixed with an excess of graphite and then heated under flowing nitrogen, resulting in the reaction

$$2\ \mathrm{AnO_2} \ +\ 4\ \mathrm{C} + \ \mathrm{N_2} \ \rightarrow\ 2\ \mathrm{AnN} \ + 4\ \mathrm{CO} \tag{5.2}$$

When oxygen removal is complete, hydrogen is added to the gas flow in order to remove residual carbon by formation of HCN. Limiting both carbon and oxygen impurities is of a crucial importance for the stability and irradiation behaviour of the fuel. E.g. the thermal conductivity has been shown to decrease significantly

Material	Lattice parameter [nm]	k [W/(m·K)]	T_{limit} [K]	T_m [K]
ThN	0.5167	47	–	3098
UN	0.4888	25	2700	3128
PuN	0.4905	13	∼2150	2862
AmN	0.4991	∼9	1570	N/A
CmN	0.5041	∼6	N/A	N/A
ZrN	0.4576	37	–	3250
HfN	0.4520	17	–	3660
β-BN (cub.)	0.3615	29	2550	3270
YN	0.4891	N/A	–	>2970

Table 5.1. Lattice parameters, thermal conductivities, dissociation and melting temperatures for actinide nitrides and nitride inert and absorbing matrices. The thermal conductivity of AnN is a decreasing function of atomic number and the presented values for AmN and CmN were extrapolated from PuN data. The nitride limit(decomposition) temperature is given at p = 1 atm in inert atmosphere; thermal conductivity is given at 1273 K, except for ThN, where a value for 1000 K is used. Table adapted from **Paper II**.

by about 10% for 1% concentration of oxygen. In the present state of technology, the oxygen and carbon content could be reduced to less than 1000 ppm for actinide nitrides.

Mutual solubility of actinide nitrides is desired, as the composition of fuel is going to be very much dependent on the previous history of the sub-assembly in the fuel cycle. It seems that the flexibility of the fuel composition can be achieved with nitride fuels, as the solubility of AnNs has been either successfully demonstrated (in the case of (U,Np,Pu)N, and (Pu,Am,Cm)N) or is expected due to the small differences in the lattice parameters.

Fast reactor irradiation experience includes two full core loads of UN in BR-10. (U,Pu)N pins have been irradiated in Phénix, BOR-60 and JOYO to about 5% FIMA. Irradiation of sodium bonded americium bearing nitride fuels is presently taking place in the Advanced Test Reactor (ATR) in Idaho, as part of the US Advanced Fuel Cycle Initiative (AFCI). Similar fuels are planned to be irradiated in Phénix in the FUTURIX programme.

Japanese and Russian experiments show that the radiation swelling is appreciably small, of the order of 1%/%FIMA, in fuels operated at low temperatures (< 1270 K). Hence, burnup of ∼15%FIMA is attainable [118]. It is assumed that the melting temperature will decrease with burnup similarly as for oxides as, i.e. by 3.4β Kelvin, where β is burnup (see Section 3.2.1). The temperature gradient in the nitride fuel is much lower than in oxides, thus the mobility of the actinide metals and fission products along this gradient is rather reduced.

The thermal conductivity of AnN is a decreasing function of atomic number [119], strongly depending also on the fuel impurities and pellet porosity [120].

Nitrides are also fully compatible with liquid metal coolants (Na, Pb/Bi) and construction materials. The nitrogen reaction with the cladding is less of the problem than the oxidising of the clad is for oxide fuels. In Russian studies, PuN proved compatible with austenitic steels up to 873 K.

As already mentioned, the major economic difficulty associated with nitride fuels is the necessity of nitrogen enrichment by ^{15}N (natural abundance is 0.366% in a mixture with ^{14}N) up to 93-98% in order to avoid the production of radiologically hazardous ^{14}C through the reaction $^{14}N(n,p)^{14}C$ [121].

5.1.2 Diluent for nitride fuel

In order to compensate for the excess reactivity of fertile free ADS fuel, a diluent matrix has to be provided. Its selection process involves a complex assessment of physical and chemical characteristics, irradiation behaviour, as well as compatibility with reprocessing technologies. High conductivity, melting point, and compatibility with cladding and coolant are necessary requirements. Thus, maximum allowable fuel ratings can be increased, fuel has larger margins to damage, and cycle burnup can be prolonged. Higher diluent matrix fraction fuels also feature improved irradiation performance. The matrix provides more space to accommodate fission products, hence allowing for higher discharge burnups.

A number of different nitride matrices have been investigated. It was shown that UN is completely miscible and forms solid solution with YN, LaN, CeN, PrN, NdN, and ZrN, while TiN and BN form a heterogeneous mixture with AnN [51, 122]. Some heterogeneous nitride fuels are also considered, such as PuN-Si_3N_4 and nitride-metallic AnN-Mo. Their major disadvantage is the risk for hot-spot formation, especially for micro-dispersed fuels. At the same time, the dimensional stability of fuel is affected.

In **Paper II**, we investigated a neutronic and burnup performance of some diluent matrix candidates, namely ZrN, YN, HfN and BN. Basic characteristics of the nitride compounds considered in this study are displayed in Table 5.1.

Different fabrication routes for inert matrix nitride fuels are under development. In JAERI, solid solution $(Pu_{0.1},Zr_{0.9})N$ pellets were fabricated by blending of PuN obtained by carbothermic reduction of plutonium with commercial ZrN powder. Sintering yielded densities above 90% of the theoretical density (TD). (Am,Zr)N has been fabricated for two different concentrations of Am. A single phased solid solution of $(Am_{0.1},Zr_{0.9})N$ was obtained without an oxide phase. However, for Am content of 30% in Am+Zr mixture, two solid solutions were present. The reason for formation of these two phases is not known, but one speculates that the cause were high carbon and oxygen impurities. In the CONFIRM project, solid solution $(Pu_{0.20},Zr_{0.80})N$ and $(Pu_{0.30},Zr_{0.70})N$ pellets were produced by carbothermic nitridation of the corresponding oxide powders. In spite of the high affinity for oxygen of zirconium, the residual level of oxygen could be reduced to about 0.2 weight percent, performing the nitridation process under optimised conditions [123]. The

porosity of the pellets could however not be decreased below 18%, even when sintering at 2023 K. For the BORA-BORA experiment in Russia, PuN and ZrN were fabricated by nitridation of metals. The compounds were then mixed and sintered to 85% of the theoretical density. In Los Alamos, (Pu,Zr)N, (Pu,Np,Zr)N and (Pu,Am,Zr)N were fabricated using carbothermic nitridation of oxide powders in argon atmosphere, resulting in high losses of Am during sintering and high levels of residual carbon/oxygen [114].

Inert matrix has a stabilising effect on the fuel, delaying the onset of the fuel decomposition. Experiments have been performed on $(U_{0.2},Zr_{0.8})N$ heated up to 3073 K, with solidus and liquidus temperatures determined to be 2885 and 3038 K, respectively, while dissociation occurred in pure UN at 2700 K [124]. The behaviour of (Pu,Zr)N was assessed in calculations for 49 at% fraction of Zr, showing that melting does not occur below 2804 K. There is an assumption that due to the chemical similarities between actinide compounds, the melting point of (Np,Zr)N system is the same as for (U,Zr)N and (Am,Zr), and that of (Cm,Zr)N same as (Pu,Zr)N. Recent studies have shown that $(Pu_{0.21},MA_{0.09},Zr_{0.7})N$ stability may be expected up to 2400 K in N_2 saturated atmosphere [116]. Some experiments are under way, e.g. irradiation in JMTR and CONFIRM, but the irradiation of minor actinide fuel including inert matrix are pending.

At PSI, $(Zr_{0.75},Hf_{0.25})N$ pellets have been fabricated by carbothermic reduction from mixed oxides and a solid solution was obtained [125, 126]. Due to the similarity of the lattice parameters, actinide nitrides are assumed to form a homogeneous solution also with HfN. Hafnium is a good absorber of neutrons in the thermal and resonance energy regions, effectively hardening the neutron spectrum (see **Paper II**). Moreover, our simulations have shown that the temperature stability of (TRU,Hf)N is maintained at least up to 2400 K. Due to the chemical similarity of Hf and Zr (hafnium and zirconium are both group IV transition metals), the chemical behaviour of the hafnium nitride is thus supposed to be very similar to that of ZrN. Accordingly, we expect that HfN is soluble in HNO_3.

5.1.3 Metallic fuel

Another option considered for advanced TRU burning is their incorporation in metallic fuels. Several reactor concepts as the Integral Fast Reactor (IFR) and Advanced Liquid Metal Reactor (ALMR/PRISM) have been proposed mainly in the U.S.A. [62]. The advantage of metallic fuels is their relatively high thermal conductivity. The ternary compounds, as U-Pu-10wt%Zr, have been envisioned and considerable experience was gained during irradiations in the EBR-II reactor [127]. The fuel burnup of 18%FIMA was reached at linear ratings up to 50 kW/m without pin failure. The metallic fuels allow to reach harder neutron spectra than nitride/oxide fuels, which partially mitigate problems with minor actinide production. However, in order to control swelling for metallic alloys, excessive fuel porosities about 75% are required.

In the dispersion fuels, e.g. TRU-10wt%Zr, the fission products are supposed to be accommodated within the fuel particles mixed in the matrix. It is therefore assumed that these fuels would have much better swelling behaviour than alloy-based counterparts. However, fuel particle volume fraction in the matrix should not exceed 25% [43].

In the frame of Advanced Fuel Cycle Initiative, non-fertile and low-fertile metallic compounds with ∼70 vol%Zr are envisioned. Irradiation of two pairs of samples in Advanced Test Reactor began in 2003 with target burnups of 5-8%FIMA and 15%FIMA, respectively.

5.1.4 Oxide fuel

In comparison to the nitride and metallic fuel, there is a vast experience with in pile operation of oxide fuels. Oxide fuels feature high thermal (melting temperature) and chemical stability, but the thermal conductivity of oxides is significantly lower than that for nitrides, resulting in high temperature gradients in the fuel pellet. The major difficulty is also the plutonium solubility limit in nitric acid (∼25%). Additionally, in order to ensure stability of americium and curium oxides at higher temperatures, the oxygen-to-metal ratio must be considerably less than 2.0, which further lowers their thermal conductivity in comparison with standard oxides. The high MA-content fuels are hence supposed to be stabilised by some inert material (matrix) - either ceramic or metallic.

Ceramic matrices as spinel ($MgAl_2O_4$), zirconium oxide (ZrO_2), and magnesium oxide (MgO) were considered as the promising candidates with respect to their neutronic characteristics (transparent for neutrons) and high thermal conductivities [128, 129, 130, 131, 132, 133]. However, low temperature irradiation experiments of AmO_{2-x} micro-dispersion fuels in spinel showed that this fuel is susceptible to radiation damage. On the other hand, PuO_{2-x}-MgO performed well and high linear power ratings up to 165 kW/m could be achieved. Irradiation tests with AmO_{2-x}-MgO targets are currently under way in Phénix. A candidate matrices for CERMET fuels have to feature both high melting point and low absorption cross-section. The latter condition is posed by the requirement to keep inert matrix volume fraction higher than 50 vol% to ensure fabricability and stability of the fuel. In a recent study, two fuel candidates for MA ADS burner were proposed, a ceramic-ceramic one - $(Pu,Am,Cm)O_{2-x}$-MgO and a ceramic-metallic one - $(Pu,Am,Cm)O_{2-x}$-^{92}Mo [134].

5.2 Coolant

The requirement of a fast neutron spectrum for MA transmutation implies usage of coolants with low moderating power, such as Na, Pb, Pb/Bi and He, see also Section 3.2.7. Basic properties of these coolants are summarised in Table 5.2. Liquid metals allow to operate the system at atmospheric pressures, while gas

Coolant	ρ [g·cm^{-3}]	T_{m} [K]	T_{b} [K]	c_{p} [kJ/(kg·K)]	v [m/s]	k [W/(m·K)]
Na	0.847	371	1156	1.3	∼10	70
Pb/Bi	10.15	398	1943	0.15	2.5	13
Pb	10.48	601	2023	0.15	2.5	16
He	$4.13{\cdot}10^{-3}$	1.05	4.15	5.2	70-120	0.25

Table 5.2. Density (ρ), melting (T_{m}) and boiling (T_{b}) temperatures, specific heat (c_{p}), velocity (v) and thermal conductivity (k) of coolants considered for ADS given at 700 K [50]. Maximum coolant velocities of liquid metals are stated, while typical velocities are given for helium. Helium pressure is 6 MPa.

cooled systems requires high pressures in order to achieve similar heat transfer capability. Problems related to usage of liquid metals include increased corrosion rate and lack of visual inspection possibilities.

The sodium has superior thermal hydraulic capabilities, allowing for small pin pitches. There is a large experience of operation of sodium cooled fast reactors. While several power reactors have been shut down, BOR-60, JOYO, Phénix and BN-600 are still operating, the latter being in quasi-commercial operation since 1982. New reactors are under construction in Russia, China and India. Sodium features reasonably low melting temperature, but the low boiling point (1156 K), which raises safety concerns in connection with transients. Sodium exhibits high chemical activity with water and water vapour, and a sodium fire stopped operation of MONJU in 1998.

Understandably, gas coolants (helium, CO_2) allow to maintain the hardest neutron spectrum. However, high pressurisation (50-70 bars) and special profiling of the cladding is required to ensure appropriate heat removal. Gases do not impose any compatibility issues with the structural material or fuel. On the other hand, a serious safety concerns arise concerning decay heat removal in the case of the accident involving loss of pressure. Thus, the designs with low specific power densites have to be applied in order to allow for a heat removal by a natural circulation of an ambient air.

The choice of lead-alloys as coolants is motivated primarily by their high boiling temperatures, making risks for coolant boiling small. Lead-bismuth eutectic also provides a low melting point (398 K) limiting problems with freezing in the system and features low chemical activity with outer environments (water) excluding the possibility for fire or explosions. In comparison to sodium, lead-alloys also have beneficial effects on coolant void worth in TRU-fuelled systems (for detailed discussion see Chapter 6). On the other hand, Pb/Bi flow rates are limited by erosion concerns to about 2.5 m/s [135]. Typical sodium velocities are around 10 m/s, hence Pb/Bi in practice has a lower heat removal capacity. In addition, poorer heat transfer coefficients and more stringent temperature limits set by corrosion require higher pin P/D to stay below those limits. Using oxygen control the temperature

limit for long term operation of ferritic steels like HT-9 and T91 is roughly 820 K, while silicon modified steels like the Russian EP-823 may operate at temperatures reaching 890 K [136, 137]. Pure lead has a melting temperature of 601 K, which significantly narrows reactor's operational interval to about 680-890 K. A drawback interconnected with Pb/Bi is the accumulated radioactivity in Pb/Bi (mainly due to α-emitter ^{210}Po, $T_{1/2} \simeq 138$ d), which would pose difficulties during fuel reloading or repair work on the primary circuit [138]. A conservative estimation of the bismuth resources on Earth limits the capacity of Pb/Bi-cooled reactors to 280 GW_e [139].

Lead-bismuth eutectic offers a favourable combination of three characteristics. It provides low void worths (see Chapter 6) and features low melting and high boiling temperatures. In this study, we therefore choose Pb/Bi as a primary coolant candidate for a TRU ADS.

5.3 Construction material

The choice of liquid metals as coolant imposes significant challenges with respect to in-pile performance of the structural materials. Ferritic-martensitic steels feature good radiation and corrosion resistance, but are inferior to austenitic when comparing mechanical properties at high temperature. Example given, the rapid burst limit measured for SS-316 (1330 K) is about 200 K higher than that of HT-9 [140].

For high dose rates, certain ferritic-martensitic steels have exhibited very small swelling rates up to doses of 200 dpa-NRT, corresponding to a fast neutron fluence of $4{\cdot}10^{23}$ n/cm^2. Note however that the threshold for swelling appears to be dose dependent. Recent results from irradiations of ferritic as well as austenitic steels indicate that lowering the dose rate (fast neutron flux magnitude) by a factor of three decreases the swelling threshold significantly [85].

Concerning corrosion resistance, nickel has a high solubility in lead alloys, hence ferritic steels generally perform better. Raising the silicon content of the steel improve the corrosion resistance of both austenitic and ferritic steels [141]. The silicon modified Russian steel EP-823 has been shown to withstand temperatures up to 890 K. The price to be paid is however a reduced radiation resistance. Recently it was shown that EP-823 looses ductility and becomes brittle after irradiation at 720 K to relatively modest doses [142].

At the moment it thus appears as there is no obvious choice of cladding material for lead-alloy cooled reactors. In the present thesis, EP-823 was used as reference material, in lack of better options.

5.4 Neutron absorber

Boron carbide is widely used in fast breeder reactors as a control rod absorber material. In this study, the use of B_4C for stationary reactivity compensation was

suggested in **Paper III**. B_4C offers high thermal stability, with melting temperature $T_m = 2720$ K and a thermal conductivity comparable to that of AnN (∼5-10 W/m·K at the operational temperature range 600-900 K). However, the thermodynamical stability of boron carbide is small in reactions with steel materials at temperatures above 970 K, resulting in formation of $(Fe,Cr)_2B$. There is considerable amount of gas released into the fission gas plenum from $^{10}B(n,\alpha)^7Li$ reactions. B_4C is introduced into the fuel sub-assembly in the form of separated absorber pins. The boron carbide is enriched in ^{10}B up to 90%-95% in order to increase its burnup efficiency.

Chapter 6

Neutronic and burnup aspects of TRU incineration

The design and choice of materials for ADS blanket strongly influences its neutronic and burnup performance, and has an impact and imposes demands on other components of the system (spallation target, accelerator, separation technologies). As we mentioned, the fast spectrum is widely established as being favourable with respect to the transmutation performance of the system because of the high fission-to-absorption probabilities, especially for even-neutron numbered nuclides (see Figure 3.2). In the softened spectrum, build-up of the higher actinides adversely affects the neutron balance and influences the neutronic and safety performance of the system. Furthermore, it complicates fuel reprocessing due to the heat and radiation damage caused by high power of americium and curium.

The fast spectrum leads to a positive void worth. Even though the high boiling point of lead and lead-alloys makes coolant boiling a hypothetical event, void cavities may be introduced into the core by, example given, a Steam Generator Tube Rupture (SGTR) event. This type of accident is far from hypothetical, as it actually occurred in one of the Russian Pb/Bi cooled sub-marine reactors [143].

6.1 Design challenges

Our goal is an effective and safe consumption of TRU, i.e. reduction of their mass and thus decreasing the radiotoxic inventory of spent fuel (see Chapter 3). To summarise and develop on this subject, the aim is to

- maximise the discharge burnup,
- minimise the reactivity loss over one irradiation cycle, thus decreasing the accelerator beam power swing and associated power peaking,

- lower coolant void worth in order to reduce the necessary sub-criticality margin at BOC,
- ensure the core integrity at accidental conditions,
- provide efficient multiplication of source neutrons.

We will show that these goals will lead to somewhat contradictory requirements on the system design parameters.

6.1.1 Reactivity loss

The fuel discharge burnup β_{d} (%FIMA) is proportional to the product of total fuel residence time in the reactor T_{res} (fpd) and average power density q_{V} (W/m^3) divided by the mass of actinide inventory m_{act} (kg)

$$\beta_{\mathrm{d}} \propto \frac{T_{\mathrm{res}} q_{\mathrm{V}}}{m_{\mathrm{act}}} \tag{6.1}$$

Hence, in order to maximise β_{d}, one should aim to design the system with high power density and in-pile fuel residence time, while limiting actinide mass in the fuel.

The burnup reactivity loss over an irradiation cycle is given as the product of the reactivity swing rate, $\Delta k^{\mathrm{t}}_{\mathrm{eff}}$ (pcm/fpd), and the cycle duration, T_{i} (fpd), $\Delta k^{\mathrm{c}}_{\mathrm{eff}} = \Delta k^{\mathrm{t}}_{\mathrm{eff}} T_{\mathrm{i}}$. Similarly, discharge burnup is proportional to specific power P_{s} (W/kg) and total fuel irradiation time $T_{\mathrm{res}} = n\ T_{\mathrm{i}}$, where n is the number of the irradiation cycles. For fertile-free fuels, the reactivity loss over one irradiation cycle is, in the first approximation, proportional to the cycle burnup β_{c}. Then,

$$\Delta k^{\mathrm{c}}_{\mathrm{eff}} \propto \beta_{\mathrm{c}} = \frac{\beta_{\mathrm{d}}}{n} \propto P_{\mathrm{s}} T_{\mathrm{i}} \tag{6.2}$$

Thus, intuitively, in order to attain high discharge burnup β_{d} and low reactivity swing over a irradiation cycle, a sufficient number of irradiation batches n is required.

Low reactivity burnup swing can hence be accomplished in designs with low specific power, i.e., low power densities and high TRU inventories, these parameters being, however, in a clear contradiction with aforementioned requirements for high target burnup.

An alternative way is to design the core with high specific power and choose short irradiation periods such that the core's design limits are not exceeded. This option is attractive as it provides for more compact cores facilitating better system economics. However, a very high frequency of outages (every $\sim$ 40-50 days) would negatively influence the system capacity factor. Hence, irradiation cycle has to be sufficiently long ($>$ 100 full power days). The cores with low specific fuel inventories feature high burnup rates, the fraction of transuranics remaining in the discharged fuel thus being low. Additionally, the amount of the untransmuted material at the end of the system operation (the last core) is also minimised.

6.1.2 Power peaking

Reactivity losses exacerbate power peaking behaviour, which effectively limits the cycle length due to thermal hydraulic constraints of the clad/fuel. Design options to explicitly mitigate power peaking are

- enrichment zoning, an excessive number of different zones however complicates fuel fabrication and management,
- fuel shuffling, where high burnup assemblies are placed in the vicinity of the target, the shuffling procedure in liquid metal cooled reactors is however a delicate and time consuming procedure, reducing system availability significantly,
- employment of fewer irradiation cycles for the innermost S/As, which however reduces the discharge burnup.

6.1.3 Burnup reactivity swing & coolant void worth

Options to decrease the burnup reactivity swing and, at the same time, to reduce the coolant void worth, have been extensively studied for fast critical breeder reactor designs with metallic fuel by Khalil & Hill [144]. As the most promising option, an introduction of tightly coupled radially heterogenous pancake-like cores was suggested. However, it appeared that the void worth and burnup reactivity losses can not be reduced *simultaneously* to an acceptably low level, the conclusion, which was confirmed in a subsequent study even for a highly unconventional design, involving BeO moderating layers and movable fuel sub-assemblies [145]. For fast critical burner reactors, strongly heterogenous cores with other solutions like inner B_4C shielding regions [146] or streaming fuel sub-assemblies with double-entry control rod drives [147] have been proposed. These investigations were performed for metallic-fuelled reactors.

Several studies have shown that the coolant void worth is significantly reduced in Pb/Bi-cooled TRU and MA burners in comparison with sodium-cooled systems [148], see also **Paper I**. We note that providing a negative coolant reactivity is not *a priory* a prerequisite for a safe accommodation of coolant voiding transients in accelerator-driven systems since the reactor safety margins can be adjusted by an appropriate choice of initial level of sub-criticality, so that the increase in source multiplication, and thus core power, is not detrimental. On the other hand, if substantial reactivity would be introduced into the system *together with* or as a consequence of an inadvertent increase of the accelerator beam power (unprotected beam overpower transient), this could lead to the loss of core integrity with subsequent potential for core material restructuring and recriticalities. It was shown that providing substantial margin to prevent core damage in the cases with high coolant void reactivity would require very high sub-criticalities, with penalties on the total reactor power, discharge burnup, and/or extensive requirements on the beam power as a result ($\sim$100 MW) [149, 150].

Therefore is appears relevant to find design options that allow to operate the ADS with smaller sub-criticality margins. In order to optimise the core's performance, the choice of materials and the design of the core lattice are most decisive. Therefore, in the next sections we will treat neutronic, safety and burnup characteristics of different core and fuel designs in order to arrive into an optimised core design, as presented in Chapter 7 and **Paper II**. What follows below is a summary of the results presented in the appended papers.

6.2 Source efficiency

The balance of neutrons in a neutron multiplying system without an external source is described by a homogeneous Boltzmann transport equation

$$A\phi = F\phi \tag{6.3}$$

where F is the production operator in matrix form, A is the consumption operator in matrix form, and $\phi \equiv \phi(\vec{r}, \vec{\Omega}, E, t)$ denotes the neutron flux. In a system with an external neutron source, the neutron balance equation reads as

$$A\phi = F\phi + S, \tag{6.4}$$

where $S = S(\vec{r}, \vec{\Omega}, E, t)$ is the spatial distribution of the external neutron source.

In the sub-critical state, the effective multiplication coefficient k_{eff}, which is the largest positive eigenvalue of the homogeneous transport equation

$$A\phi = \frac{1}{k_{\text{eff}}} F\phi \tag{6.5}$$

does not describe the true physical state and actual neutron multiplication in the system.

Rather, the multiplication characteristics of system should be expressed in terms of a number of neutrons released in the multiplication reactions *per source particle*. The multiplication of spallation neutrons exiting target can be evaluated either as

$$M_{\text{ext}}^{\text{n}} = 1 + k_0 + k_0 \cdot k_1 + k_0 \cdot k_1 \cdot k_2 + \cdots \tag{6.6}$$

where k_0 is the external source neutron multiplication factor, and k_i $(i > 0)$ is the generation dependent multiplication factor, or estimated in terms of fission multiplication as

$$M_{\text{ext}}^{\text{f}} = 1 + \bar{\nu} N_{\text{f}} \ , \tag{6.7}$$

where $\bar{\nu}$ is the average number of neutrons emitted per fission, and N_{f} is the number of fissions per source particle.

The resulting difference in neutron multiplication is then often parameterised in terms of the neutron source efficiency ϕ_{i}^{*}, normalising the $M_{\mathrm{ext}}^{\mathrm{f}}$ and $M_{\mathrm{ext}}^{\mathrm{n}}$ per source *neutron* as

$$\phi_{\mathrm{i}}^{*} \equiv \frac{M_{\mathrm{ext}}^{\mathrm{i}} - 1}{M_{\mathrm{fiss}} - 1} \quad \mathrm{i} = \mathrm{f}, \mathrm{n} \tag{6.8}$$

where the fundamental mode multiplication is given by

$$M_{\mathrm{fiss}} = \frac{1}{1 - k_{\mathrm{eff}}} \tag{6.9}$$

The neutron source efficiency is thus a parameter, which describes the difference between the real external source multiplication and the multiplication inherent to the distribution of neutrons corresponding to the fundamental mode.

Then we can, equivalently to $\mathrm{k_{eff}}$, define the source multiplication coefficient as

$$k_s = \frac{\overline{\nu} N_f}{1 + \overline{\nu} N_f} \tag{6.10}$$

The generation dependent multiplication factors k_{i} can be found by running MCNP [59] in KCODE mode, and extracting the track length estimate of k_{i} for individual fission generations. An example of the resulting generation dependence is shown in Figure 6.1 for a model $(\mathrm{U,Th})\mathrm{O_2}$ fuelled lead-cooled ADS [151].

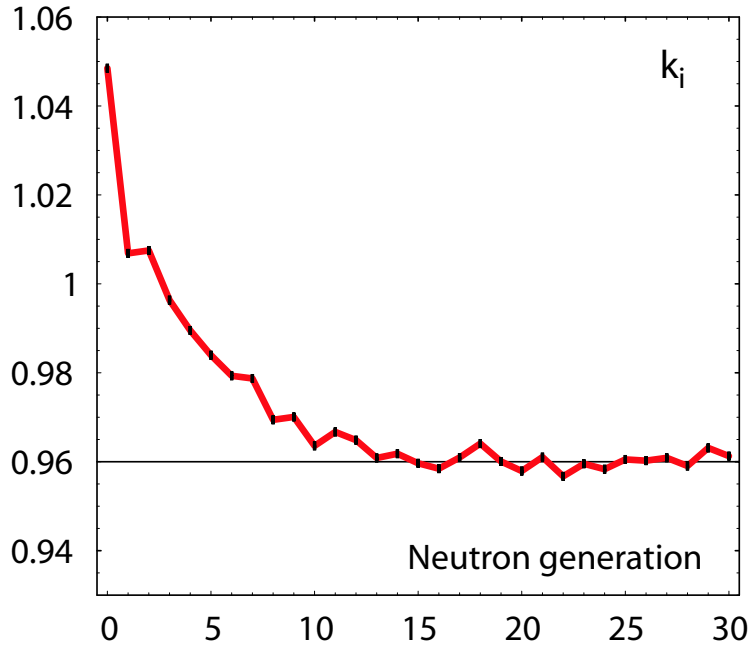

Figure 6.1. Generation dependent multiplication factor $\mathrm{k_i}$.

As can be seen, the first 10-12 generations are subject to significantly lower neutron losses than in the asymptotic limit (fundamental mode). This can be partially attributed to the probability of a fission neutron to enter the spallation

target, where it is allowed to decelerate, avoiding capture in cladding materials and fertile actinides, and then to enter the core again, with a high probability of inducing (epithermal) fission in fuel. Since the first few k_{i}:s may be larger than unity, even for deeply sub-critical systems, this phenomenon enhances the power peaking in the vicinity of the target, and was carefully analysed in design and safety studies of systems with liquid metal coolant/target.

On the other hand, spallation neutrons can also slow down or are absorbed in the target media before entering the core. Thus, *for thick targets*, the probability of spallation neutron induced fission would be smaller than for the average fission neutron and $k_0 < k_{\mathrm{i}}$.

By introducing k_0, the physical model of a neutron chain propagation in the system can be conveniently separated into the *source* and *fission* parts. Such decomposition of a neutron multiplication is a practical tool for scoping calculations while simulations of a whole neutron cascade are inevitable in order to determine the value of the source efficiency.

The neutron source efficiency ϕ^* generally depends on the position of the neutron source and the dimensions and material composition of the reactor core and target. Thus, a comparison of the performance of different ADSs in terms of source efficiency can be done only for systems with the same target/blanket geometry. A novel concept of the proton source efficiency was therefore developed in **Paper V**. The proton source efficiency ψ^* of a sub-critical system may be defined as

$$\psi^* \equiv \frac{M_{\mathrm{ext}}^{\mathrm{p}} - 1}{M_{\mathrm{fiss}} - 1} = \frac{P\overline{\nu}}{\overline{Q}S_{\mathrm{p}}} \frac{1 - k_{\mathrm{eff}}}{k_{\mathrm{eff}}} \tag{6.11}$$

where $M_{\mathrm{ext}}^{\mathrm{p}}$ is the actual multiplication of source spallation neutrons per source *proton*, P is the thermal power of the system, and $\overline{Q}$ is the averaged recoverable energy released in fission.

We have shown that the relationship between neutron source efficiency ϕ^* and proton source efficiency ψ^* is then given by

$$\phi^* = \frac{M_{\mathrm{ext}}^{\mathrm{i}} - 1}{M_{\mathrm{fiss}} - 1} = \psi^* \frac{S_{\mathrm{p}}}{S_{\mathrm{n}}} = \frac{\psi^*}{Z} \quad \mathrm{i} = \mathrm{f}, \mathrm{n} \tag{6.12}$$

where S_{n} is the neutron source intensity [n/s], and $Z = S_{\mathrm{n}}/S_{\mathrm{p}}$ is the number of neutrons per proton (neutron spallation yield).

Consequently, the ADS accelerator current can be determined from

$$I_{\mathrm{p}} = \frac{e\overline{\nu}(1/k_{\mathrm{eff}} - 1)}{\psi^*} \frac{P}{\overline{Q}} \tag{6.13}$$

where $e = 1.609 \cdot 10^{-19}$ C is the elementary charge.

In our parametric, scoping studies, the source efficiency was studied as a function of target radius and axial position of the accelerator beam. We considered a single Pb/Bi target module located in the centre of the core and contained in a 5 mm

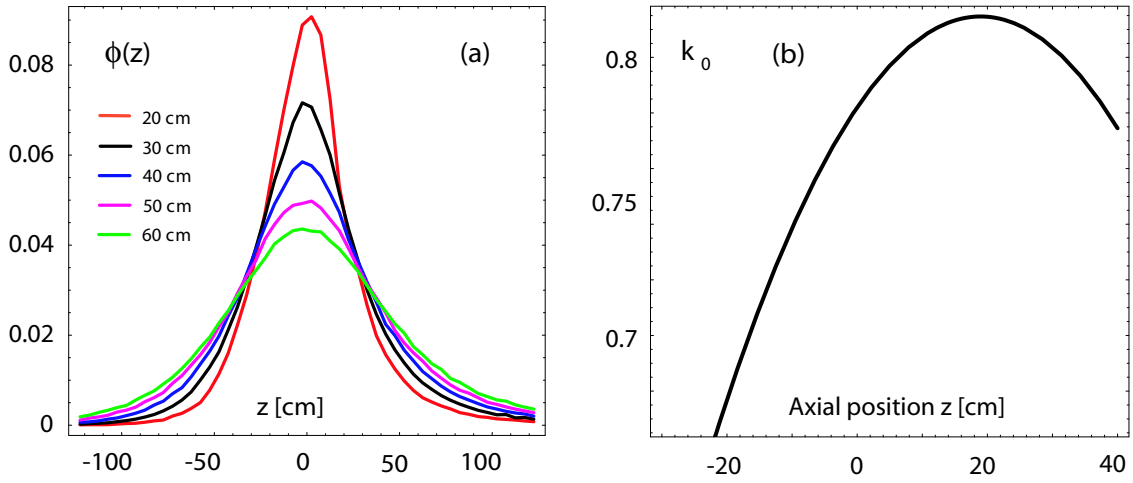

Figure 6.2. The axial distribution of normalised neutron flux exiting target of a given radius (a). The external source multiplication factor k_0 as a function of beam impact relative to the core centre (b).

thick ferritic steel container. Beam tube radius was 15 cm. The incident proton energy was set to 1 GeV, which is approximately the level where increasing the energy does no longer increase the effective neutron yield per energy unit. The simulations were performed with the Monte Carlo code MCNPX [152] using the LA150 cross-section library.

6.2.1 Axial position of beam impact

The optimal relative axial position of the spallation target beam impact was investigated in terms of minimising leakage of neutrons to axial reflectors. Leaked neutrons have lower probability to enter the reactor core and, consequently, induce fission. The neutron leakage is minimised when the target surface was placed 17.6 cm above the core centre for a radius of 20 cm, while for R = 50 cm, the optimal position is z = 19.7 cm, see Figure 6.2(a). The slight shift of the optimal position can be attributed to enhanced diffusion of neutrons in the target material.

In more detailed studies, performed in **Paper V** aiming at maximising the proton source efficiency, the optimal shift of axial position of the target beam impact from the core centre was found to be also ∼20 cm. In Figure 6.2(b), the corresponding external neutron multiplication factor k_0 is shown.

The total number of neutrons leaking out of the target without entering the core is shown in Figure 6.3. Considering a typical active core length of 100 cm, about 8.5% of the neutrons leak outside the core (2.6% in the forward, 5.9% in the backward direction), which is to be compared to the 25.6% in the case of target radius of 50 cm (forward 10.8%, backward 14.8%). More than 95% of the neutrons enters the core when the fuel pin length is larger than 1.3 m, for the 50-cm target the corresponding figure is 2.1 m. This would suggest increasing the height of the fissile column in order to maximise the source efficiency. However, thermal

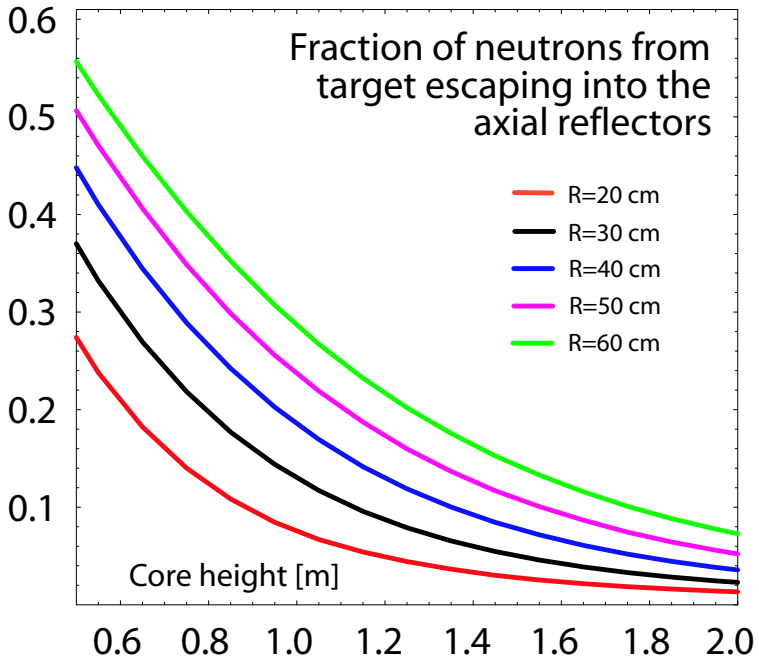

Figure 6.3. The fraction of neutrons not directly entering the reactor core as function of active pin length. R is the radius of the spallation target.

hydraulic constraints and deterioration of the void worth disqualify the choice of extensive core heights [153].

6.2.2 Target radius

The spectrum of neutrons escaping the target has been determined for five different target radii, see Figure 6.4. An increase of target radius implies an increase of probability for axial leakage of neutrons, which diminishes the chances of neutrons to induce fission in the core. At the same time, the absorption of neutrons in the target and core increases as neutrons subsequently slow down. The median energy of neutrons exiting the target thus drops from 1020 keV to 730 keV as target radius is increased from 20 cm to 30 cm. Remembering that fission neutrons are born with a mean energy of about 2 MeV, it is clear that the neutron source efficiency may fall well bellow unity for targets of any reasonable size, i.e., $k_0 < k_\mathrm{i}$. Only 0.4% neutrons are above 20 MeV in the case of the 50 cm target radius and 3.2% in the case of a 20 cm radius.

We conclude that a small target radius is favourable not only from the viewpoint of gaining fast neutron spectra but also for minimising neutron losses to the axial reflector, both effects yielding higher source efficiency.

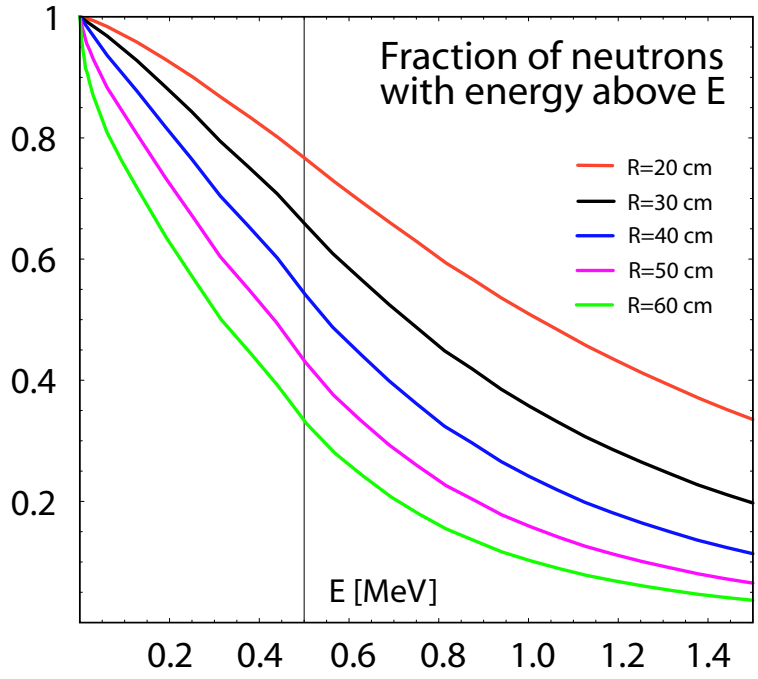

Figure 6.4. Fractions of source neutrons having energies above E when exiting a Pb/Bi target of different radii. With increasing target radius, the probability of source neutrons to induce fission sharply decreases. Figure adapted from **Paper II**.

6.2.3 Coolants

The external neutron multiplication was also estimated for different Pb/Bi-target radii of the Pb/Bi and Na-cooled ADSs. In **Paper IV**, scoping calculations were performed for a radially infinite lattice, see Figure 6.5, while **Paper V** investigated a realistic 3-D configuration of a TRU ADS burner.

Both studies showed that Pb/Bi-cooled systems yield higher source efficiency. The reason is mainly the contribution from (n,xn) reactions which occur in Pb/Bi. For smaller target radii, there is still an appreciable number of neutrons (about 6%) able to induce (n,2n) reactions in lead (threshold energy is ~ 7 MeV). Together with decreased neutron axial leakage in Pb/Bi in comparison to Na, Pb/Bi system yields higher source efficiency than Na-cooled counterpart. However, as the target radius increases, the fraction of the high-energy neutrons entering the core would decrease, and both Pb/Bi and Na-cooled ADS would have similar source efficiencies.

6.3 Neutronic performance

ZrN, HfN, YN, and BN have been investigated in **Paper II** as candidate diluent matrices for TRU ADS burner, see Table 6.1. Performance of fertile matrices (UN,

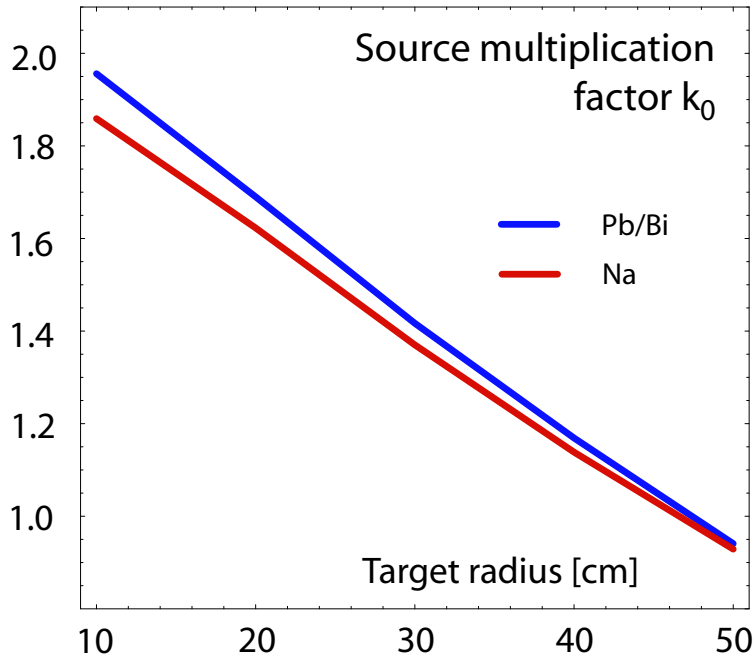

Figure 6.5. The external source multiplication factor k_0 as function of target radius for a model infinite lattice of TRU ADS cooled by lead/bismuth and sodium. Nitride fuel without a diluent matrix was applied. P/D = 1.7. Figure redrawn from **Paper IV**.

Fuel	E_n [keV]	E_ϕ [keV]	ψ^*	^{241}Am σ_f/σ_a
(TRU,Zr)N	87.4	396	29.7	0.104
(TRU,Hf)N	201	524	28.2	0.196
(TRU,Y)N	89.9	398	28.6	0.106
(TRU,B)N	407	811	25.2	0.376
(U,TRU)N	138	438	28.9	0.136
(Th,TRU)N	157	477	28.7	0.161
(U,Pu)N	121	416	28.6	0.121
(Pu,Zr)N	63.7	358	30.8	0.080
(TRUMOX,Zr)N	82.5	384	28.7	0.098
(TRUMOX,Hf)N	195	514	27.7	0.190
(MA,Zr)N	176	515	26.4	0.183

Table 6.1. Number (E_n) and flux (E_ϕ) weighted spectra average energies, proton source efficiencies (ψ^*), and fission probabilities of ^{241}Am in single zone ADS cores with P/D=1.6. Table is adopted from **Paper II**.

ThN) was also evaluated. Different types of TRU vectors were used in the simulations, denoted as TRU (Pu/Am = 4/1) and TRUMOX (Pu/Am = 0.86/0.14). Values for MA ADS burners working in the frame of a double-strata scenario (Pu/Am

ratio equal to 2/3) are also given. One-zone, homogeneous core configurations were used in order to facilitate a systematic comparison of different design options. In each case, the volume fraction of diluent matrix were adjusted to obtain k_{eff}=0.96. The calculations were performed by the Monte Carlo code MCNP [59]. JEF-2.2 nuclear data library was processed with NJOY [154] in order to account for temperature dependence. See **Paper II** for a detail description of the calculation model.

It appeared that the inert diluent matrices as ZrN and YN significantly moderate the neutron spectrum by inelastic neutron scattering, which results in low probabilities for direct fissioning of ^{241}Am. The use of fertile matrices in the fuel yields slightly harder neutron spectrum due to increased absorption in the resonance and thermal regions, which also somewhat improves $\sigma_{\text{f}}/\sigma_{\text{a}}$ for ^{241}Am. Hardening of the neutron spectra due to increased competing absorption in the even-neutron number/fertile actinides is also apparent when comparing values for (U,Pu)N with (U,TRU)N and (Pu,Zr)N with (TRU,Zr)N. BN-based fuels proved to be most efficient in suppressing slow neutron capture in americium, raising the fission probabilities of ^{241}Am to *0.38*. Another absorbing matrix, HfN, increased the ^{241}Am fission-to-absorption probability twice in comparison to ZrN. Hence, understandably, operating the reactor on a fast neutron spectrum is beneficial for limiting MA inventories in the fuel cycle.

In TRUMOX-based fuels, the fraction of strongly absorbing americium isotopes is actually lower than in TRU fuel, due to shorter cooling times than assumed for LWR UOX discharges. TRUMOX gives a slightly softer spectrum and thus also lower ^{241}Am fission probabilities. At the same time, due to the lower quality of the plutonium vector, the fraction of even-neutron number nuclides in TRUMOX fuel is higher, both effects resulting in diminished proton source efficiency.

For fertile matrices (ThN and UN), the source efficiency is slightly lower than for (TRU,Zr)N fuel. The reason is larger probability of parasitic absorption of spallation neutron in fertile matrices than in ZrN (macroscopic absorption cross-section for UN is roughly a factor of eight higher than for ZrN). Absorption of neutrons in BN causes a significant drop of the source efficiency. Interestingly, HfN does not seriously deteriorate the multiplication of source neutrons in the system, keeping ϕ^* well above unity ($\psi^* \sim 28$).

In **Paper IV**, the external source multiplication factor k_0 was investigated as a function of ZrN, UN and B_4C content in the sodium cooled TRU ADS core. Similarly to results obtained in **Paper II**, (TRU,Zr)N fuel provided better multiplication of the source neutrons than (U,TRU)N. B_4C absorbs neutrons very efficiently and gave significantly lower value of the source multiplication factor. The source efficiency of TRUN-fuelled, Pb/Bi-cooled ADS employing B_4C neutron absorber appeared to be very low. **Paper III** reports a value of $\phi^* \sim 0.85$ that corresponds to $\psi^* \sim 22{-}23$.

6.4 Safety performance

In **Papers I** and **II** we have investigated the reactivity changes upon the introduction of the coolant void reactivity into the reactor cores, both critical and sub-critical, fuelled with oxide and nitride fuels and cooled by liquid metals - lead/bismuth eutectic, lead, and sodium.

6.4.1 Coolant void worth

The coolant void worth is given as the difference in the k-eigenvalue between the flooded and voided states

$$W = \quad \Delta k_{\text{eff}} = k_{\text{eff}}^{\text{void}} - k_{\text{eff}}^{\text{flood}} = \overline{\nu}_{\text{void}} L_{\text{f}}^{\text{void}} - \overline{\nu}_{\text{flood}} L_{\text{f}}^{\text{flood}}. \tag{6.14}$$

where L_{f} is neutron loss to fission in one neutron generation for the respective core state - flooded or voided.

The average fission neutron yield can be considered as constant ($\overline{\nu} \equiv \overline{\nu}_{\text{flood}} \simeq \overline{\nu}_{\text{void}}$) in fast neutron systems. Therefore,

$$W = \overline{\nu}\ (L_{\text{f}}^{\text{void}} - L_{\text{f}}^{\text{flood}}), \tag{6.15}$$

which gives $W = \overline{\nu}\Delta L_{\text{f}}$.

Normalising the neutron balance equation in an eigenstate for *one neutron fission generation* we obtain

$$1 + C_{\text{x}} - L_{\text{x}} = L_{\text{c}} + L_{\text{e}} + L_{\text{f}}, \tag{6.16}$$

where L_{x} denotes the neutron loss rate in non-fission multiplication reactions, $C_{\text{x}} = \overline{\nu_{\text{x}}} L_{\text{x}}$ is the neutron creation rate in non-fission multiplication reactions, $\overline{\nu_{\text{x}}}$ is the average neutron yield in non-fission multiplication reactions ($\overline{\nu_{\text{x}}} \simeq 2$), L_{e} denotes the loss rate to leakage, L_{c} the loss rate to capture reactions, and L_{f} is the loss rate to fission.

Upon coolant voiding, $\Delta C_{\text{x}} \leq 10^{-3}$ in most of the cases. The coolant void worth can be subsequently decomposed in the infinite pin lattice 2-D model ($L_{\text{e}} = 0$) as

$$W = \overline{\nu} \cdot \Delta L_{\text{f}} = -\overline{\nu}(\Delta L_{\text{c}}^{\text{fuel}} + \Delta L_{\text{c}}^{\text{coolant}} + \Delta L_{\text{c}}^{\text{clad}}). \tag{6.17}$$

where $L_{\text{c}}^{\text{fuel}}$, $L_{\text{c}}^{\text{coolant}}$, and $L_{\text{c}}^{\text{clad}}$ is neutron capture rates to fuel, coolant, and cladding, respectively.

The neutron balance equation was further evaluated in realistic three dimensional core configurations, where the system geometry also included reflectors and plena. The void worth was then determined as

$$W = \quad -\overline{\nu}(\Delta L_{\text{c,fuel}} + \Delta L_{\text{c,coolant}} + \Delta L_{\text{c,clad}} + \tag{6.18}$$

$$\Delta L_{\text{e}} - \Delta G_{\text{x}}), \tag{6.19}$$

where L_{e} quantifies a rate of neutron leakage from the system, and $G_{\text{x}} = C_{\text{x}}$ - L_{x} is the neutron gain from non-fission multiplication reactions. Note that $G_{\text{x}} < 10^{-3}$.

Fuel − Coolant	ΔL_{f}	$\Delta L_{\mathrm{c,fuel}}$	$\Delta L_{\mathrm{c,cool}}$	$\Delta L_{\mathrm{c,clad}}$	$(\frac{\sigma_{\mathrm{f}}}{\sigma_{\mathrm{a}}})_{\mathrm{voided}}/(\frac{\sigma_{\mathrm{f}}}{\sigma_{\mathrm{a}}})_{\mathrm{flooded}}$
$(U,Pu)O_2$ − Na	+0.078	-0.059	-0.012	-0.007	1.20
(TRU,Zr)N − Na	+0.108	-0.090	-0.011	-0.007	1.22
(MA,Zr)N − Na	+0.119	-0.111	-0.005	-0.003	1.33
(TRU,Zr)N − Pb/Bi	+0.090	-0.039	-0.048	-0.003	1.11

Table 6.2. Infinite pin lattice void worth analyses. Pitch-to-diameter ratio is 2.0. The neutron loss rates are normalised per one fission neutron generation. Table redrawn from **Paper I**.

Infinite lattice analyses

The infinite lattice analysis, the effect of the spectrum hardening and changes in the neutron capture upon the coolant voiding was investigated for three types of fuels: standard FBR fuel $(U,Pu)O_2$, a plutonium based - TRU mononitride fuel (TRU,Zr)N, and minor actinide based ADS double strata fuel (MA,Zr)N, see **Paper I** for details. The results of the study decomposed into individual components are summarised in Table 6.2.

A reduction in fuel capture rate with concurrent increase of fission probability of even-neutron number actinides appeared to be the main contributor to the void worth. While capture reduction in the fuel provides about 76% of the void worth for (TRU,Zr)N fuel, it is more then 93% for the fuel containing 60% of minor actinides, i.e., (MA,Zr)N. The spectral gradient accompanying removal of the coolant from the lattice is also strongest for (MA,Zr)N fuel due to the significant increase of fission probabilities of the even-neutron number nuclides. The capture rate in the cladding is less significant and constitutes less than 10% of the void worth. Comparison of the sodium and Pb/Bi coolant void worths for (TRU,Zr)N fuel shows that Pb/Bi provides *smaller* spectral gradient upon coolant voiding limiting the change in the probability of neutrons being captured in fuel, which gives lower void worth.

3-D system analyses

Investigating the coolant void worth in realistic 3-D system configurations illustrates the influence of leakage effect upon coolant removal. Note that in contrast to the standard notion of the leakage term [32], L_{e} in our case denotes the neutrons leaking out of the *whole reactor system* to the surrounding shielding. The probability of these neutrons to enter the core and induce fission is rather remote and the reason why we list the leakage component separately in our study is merely phenomenological. Such neutrons can hence be effectively perceived as captured in the cladding and structural material of the reflector. The effect of the enhanced neutron leakage *from the core* upon coolant voiding is then exhibited as a change in the capture of neutrons in coolant and structural material of plena and reflectors.

Coolant	ΔL_{f}	$\Delta L_{\mathrm{c,fuel}}$	$\Delta L_{\mathrm{c,cool}}$	$\Delta L_{\mathrm{c,clad}}$	ΔL_{e}
Na	Core void worth, $(U,Pu)O_2$				
	+0.0071	-0.0908	+0.0265	+0.0428	+0.0156
	Core & upper plenum void worth, $(U,Pu)O_2$				
	-0.0166	-0.1282	+0.0471	+0.0397	+0.0598
	Core void worth, (TRU,Zr)N				
	-0.0102	-0.0839	+0.0205	+0.0524	+0.0214
Pb/Bi	Core void worth, radial reflector with steel pins, $(U,Pu)O_2$				
	+0.0114	-0.0709	-0.0129	+0.0677	+0.0039
	Core void worth, Pb/Bi radial reflector, $(U,Pu)O_2$				
	+0.0216	-0.0555	+0.0124	+0.0060	+0.0163
	Core void worth, radial reflector with steel pins, (TRU,Zr)N				
	-0.0226	-0.0650	-0.0104	+0.0903	+0.0060

Table 6.3. Void worth analyses in a model FBR and ADS, employing $(U,Pu)O_2$ and (TRU,Zr)N fuel, respectively. Pitch-to-diameter ratio is 2.0. $\Delta L_{\mathrm{c,clad}}$ includes capture in the structural material of the reflectors. Results according to **Paper I**.

In contrast to the infinite pin lattice analyses the changes in the capture probability in cladding introduces therefore a *negative* reactivity upon coolant voiding. In the case of the Pb/Bi-cooled core, we investigate two different radial reflector configurations

a) similar to the one used for sodium cooled systems, i.e. consisting of steel pins, immersed in the coolant; coolant volume ratio being 20 vol%,

b) with the whole radial reflector region filled by lead/bismuth eutectic only. Such radial reflector configurations have been proposed in a number of studies [108].

In Table 6.3, we display the coolant void worth for a model FBR with $(U,Pu)O_2$ fuel and an ADS employing (TRU,Zr)N fuel cooled by sodium and lead/bismuth (P/D = 2.0). Three (interconnected) results are interesting here. First, the Pb/Bi void worth for $(U,Pu)O_2$ fuel is actually *larger* than that of sodium-cooled system for realistic Pb/Bi pitches ($P/D \gtrsim 1.4$), see also Figure 6.8. Due to the better neutronic characteristics of Pb/Bi, the fraction of uranium in the (U,Pu) vector is higher than that for sodium. Hence, during coolant voiding, the spectral gradient becomes more pronounced in Pb/Bi due to higher content of fast fission thresholds isotopes in fuel, resulting in higher void worths. Second, varying the fraction of whole TRU vector in (TRU,Zr)N fuel leads to the opposite effect for the void worths of the respective coolants, as the inert matrix fraction is larger in the Pb/Bi system than for the Na-counterpart. Third, the negative reactivity feedback is supplied in Pb/Bi systems by the increase of neutron capture in the *structural material of reflector* only, while in the case of sodium, the capture in both reflector

coolant and structure introduces negative reactivity. When the steel pin reflector is replaced by Pb/Bi, the only significant effect on negative reactivity feedback is the increased neutron capture in coolant and surrounding reactor shielding material (manifested in our study as an increased leakage term L_e), resulting in excessive void reactivities. Introducing an absorbing material into the core reflector in order to increase the neutron capture upon coolant voiding would consequently also reduce void worth [155].

An extension of the coolant void worth study for a Pb/Bi-cooled, nitride fuelled ADS with different types of the diluent and fertile matrix fuels was performed in **Paper II**. A brief description of the modelling approach was given in Section 6.3. The high sensitivity of the void worth on the content of americium in the fuel was again shown: compare the core coolant void worths for (TRU,Zr)N and (Pu,Zr)N, which are −4300 and −7000 pcm, respectively. MA-based fuel again yielded very high positive void worth, of the order of +8000 pcm.

6.4.2 Cladding worth

At accidental conditions, melting of cladding may result in flush-out of structural material from the core, inserting a positive reactivity due to the decreased parasitic absorption in steel. The corresponding effect was calculated in **Paper II** by substituting pin cladding with coolant.

Again, the highest positive reactivity increase was observed for absorbing matrices and fuels with large content of even-neutron number actinides. For (MA,Zr)N, the cladding flush-out results in an extensive reactivity insertion larger than 5000 pcm. Thus, optimisation of the cladding (and duct) thickness is the imperative in order to improve the safety of the ADS cores.

Consider that in our heterogenous core designs employing 2.5-mm thick duct, the cladding void worth was elevated by about +2800 pcm when larger amount of the structural material was introduced to the system by decreasing the sub-assembly flat-to-flat from 18.3 cm to 10.8 cm (**Paper II**).

6.4.3 Reactivity temperature feedbacks

Reactivity temperature coefficients were investigated in detail in **Paper II** for the same set of fuel compositions as described in Section 6.3.

Coolant reactivity feedback

The coolant reactivity temperature coefficient was investigated by varying the Pb/Bi density in the reactor core from 10 g·cm^{-3} to 9 g·cm^{-3}, corresponding to a temperature change from 810 to 1540 K. Density of Pb/Bi as a function of temperature is shown in Figure 6.6 [50]. Sodium and lead values are given as a reference.

In summary, a strong negative feedback was understandably exhibited by fertile-free fuels with inert diluent matrices (ZrN and YN). Addition of fertile elements

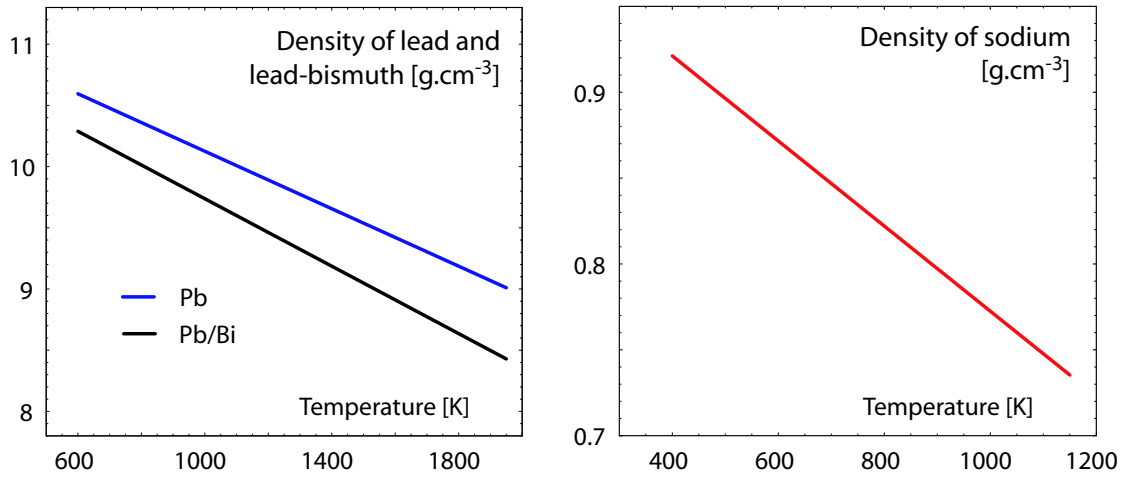

Figure 6.6. Coolant density as a function of temperature for liquid metal coolants - Pb, Pb/Bi and Na.

and/or employment of absorbing matrices elevates the coolant temperature reactivity feedback, which becomes positive. The effect of coolant voiding in high minor actinide content cores is further pronounced by the increased reactivity worth of americium being more significant than that of ^{238}U, see fast fission thresholds in Figure 3.2. Similarly, due to the spectral hardening during coolant temperature increase, the parasitic capture in absorbing materials as BN is significantly diminished, resulting in very large reactivity insertion.

Material dilatation

The system response to material dilatation was calculated for two distinctive events - axial dilatation of the fuel column, providing prompt reactivity feedback, and the expansion of the core lattice grid, providing somewhat delayed response to the fuel temperature changes. We assume that the thermal dilatation of the core components was not restricted.

The system response to the **axial fuel expansion** was calculated by increasing the pin length by 1 cm. In the case of ZrN and HfN-based fuels it corresponds to a temperature change from 1000 to 2070 K and from 1000 to 2050 K, respectively. The resulting reactivity coefficients were then -0.21 pcm/K for (TRU,Zr)N and -0.19 pcm/K for (TRU,Hf)N. For other types of fuels the axial expansion temperature feedback was in the interval from -0.18 to -0.28 pcm/$(10^{-5}\Delta H/H)$.

The reactivity change due to expansion of the **core lattice grid** was calculated by increasing the lattice pitch by 2%. For all fuels investigated, the reactivity change was rather similar, being in the range from -0.35 to -0.47 pcm/$(10^{-5}\Delta P/P)$. As expected, the grid expansion gives about a factor of two larger temperature feedback than axial elongation of the fuel (Chapter 3).

Doppler temperature reactivity

The Doppler reactivity coefficient is considered as "prompt" feedback, almost instantly following changes in the fuel temperature. In fuels with fertile support, the strongest Doppler was provided by fuels with ^{238}U and ^{232}Th matrices. In U/Th-free fuels, the largest contributor was apparently ^{240}Pu. A negative effect of the absorber material or americium on the fuel reactivity feedback was again revealed. As these materials compete with resonant capture on ^{240}Pu, a sharp cut-off in the spectrum below 1 keV may further suppress the Doppler feedback. Substituting Zr with Hf or mixing Am into the fuel thus decreases the Doppler constant by more than a factor of three. In the BN-bearing fuels, Doppler feedback is completely non-existent.

6.4.4 Effective delayed neutron fractions

Comparing individual core design configurations in **Paper II**, the highest effective delayed neutron fractions were observed for (U,TRU)N fuel, where the major contributor to β_{eff} is ^{238}U. When uranium is removed from the fuel, β_{eff} can be partly regained by introduction of ^{232}Th, or in fuels with soft spectrum, by large fractions of ^{242}Pu. Since a significant fraction of delayed neutrons is rather absorbed in ^{10}B than inducing fission, BN-based fuels provide very low β_{eff}. For (TRU,Hf)N fuel, β_{eff} is $\sim$160 pcm, which is 82% of the value observed for (TRU,Zr)N fuel or about one-half of β_{eff} for the CAPRA 04/94 core.

6.5 Burnup performance

Following the static analyses of neutronic and safety performance of different fuels for TRU ADS, we investigated their burnup merits. A summary of the results is presented in Table 6.4.

In the case of (U,Pu)N fuel, breeding of ^{239}Pu from ^{238}U somewhat diminishes the burnup reactivity swing. However, it is interesting to note that an admixture of 20% americium in the TRU vector significantly reduces reactivity burnup loss due to the production of additional plutonium via

$$^{241}\text{Am} + \text{n} \;\rightarrow (\sim 80\%)\; ^{242g}\text{Am} \;\rightarrow\; ^{242}\text{Cm} \;\rightarrow\; ^{238}\text{Pu}$$

channel, compare results for (U,Pu)N with (U,TRU)N. Actual burnability of the absorbing matrices (HfN & BN) showed to be questionable, as the reactivity swing per percent burnup appeared to be *larger* for these fuels than for inert diluents. In the faster spectrum, capture in fertile nuclides is suppressed leading to decreased production of fissile isotopes. A similar observation was also made by Yang & Khalil [43]. The 25% decrease in the reactivity swing as reported in **Paper III** for our TRU ADS design with a neutron absorber (B_4C) is therefore due to the introduction of uranium into the core, rather than due to burnability of boron carbide pins.

Fuel	m_{act}^{BOL} [kg]	Burnup rate [%FIMA/fpd]	$\Delta k_{eff}^{c}/\beta_c$ [pcm/%]	$^{242}Cm/\beta_c$ [%/%]	Doubling of I_p [fpd]
(TRU,Zr)N	942	0.076	-750	0.20	60
(TRU,Hf)N	1751	0.043	-780	0.12	115
(TRU,Y)N	919	0.078	-750	0.18	65
(TRU,B)N	2900	0.027	-780	0.06	190
(U,TRU)N	5513	0.014	-230	0.07	>1000
(Th,TRU)N	4810	0.016	-330	0.08	≈const
(U,Pu)N	5525	0.014	-690	0.001	300
(Pu,Zr)N	631	0.116	-930	0.002	40
(TRUMOX,Zr)N	950	0.078	-930	0.11	55
(TRUMOX,Hf)N	1822	0.042	-870	0.07	105

Table 6.4. Burnup characteristics of different single zone ADS cores with P/D=1.6. $\Delta I_p = I_p^{EOC} - I_p^{BOC}$. The reactivity swing and ^{242}Cm fractions per percent FIMA burnup are given for 5% FIMA. Table is adopted from **Paper II.**

On the other hand, the absorbing matrices perform well when it comes to the task of limiting the amount of minor actinides in the spent fuel. The fraction of ^{242}Cm in the actinide vector is almost halved when ZrN matrix is exchanged for HfN in the case of transuranics fuel. Using BN is even more effective in cutting the thermal parts of the spectra thus promoting *direct* fissioning of americium.

The accelerator power swing is one of the decisive factors limiting the effective length of one irradiation batch. The thermal constraints imposed by the cladding material (power peaking) and target module (ability to dissipate heat from the accelerator beam) play the major role. The accelerator power is doubled in about two full power months for (TRU,Zr)N, while for (TRU,Hf)N fuel it is in approximately 115 full power days. Use of the fertile material can notably prolong the length of the batch, but on the other hand, also effectively destroys the transmutation capability of the reactor, significantly diminishing burnup rates.

6.6 Influence of increased pitch-to-diameter ratio

The effect of large coolant fractions on the neutronics, safety, and burnup performance of the burner was investigated in **Paper I** and **Paper II** by varying reactor lattice pitch-to-diameter ratios between 1.2 and 2.4 corresponding to a change of coolant volume fractions from 37% to 84%. Due to the enhanced heat removal capabilities, the safety margins and grace time to fuel and cladding damage increase at transients (beam overpower, loss-of-flow, and loss-of-heat sink). The obvious drawback of the large volume fractions is, however, an increase in the neutron leakage, adversely affecting neutron economy and higher specific fuel inventories as the

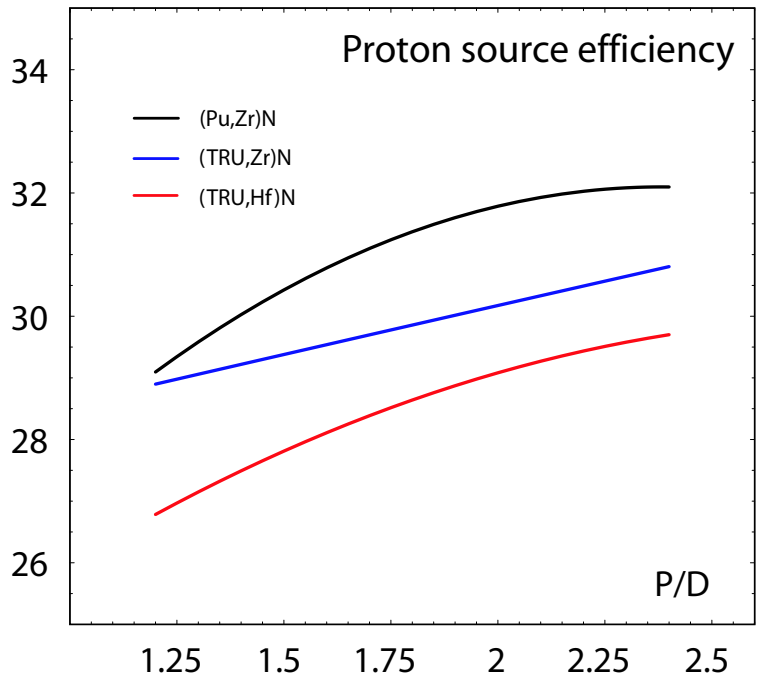

Figure 6.7. The proton source efficiency ψ^* as a function of P/D in Pb/Bi-cooled single zone ADS. Figure is adopted from **Paper II.**

amount of the diluent matrix has to be decreased in order to keep the reactivity constant.

6.6.1 Source efficiency

The proton source efficiency was calculated as a function of P/D in **Paper II**. Non-intuitively, the source efficiency increases as a function of P/D, see Figure 6.7. This phenomenon is a result of the mutual interplay of three processes. First, the actinide fuel fraction in the fuel is larger for increased P/D which elevates the neutron absorption probability in fuel. Second, the probability of the fission chain to be accommodated within the core increases with increasing core dimensions. Third, the difference in the neutron spectra of the source and eigenmode neutrons increases with P/D (remember: $\phi^* > 1$).

In **Paper IV**, we reported a *decrease* of the external source multiplication coefficient k_0 while increasing P/D, for both sodium and Pb/Bi. However, in contrast to the modelling approach applied in **Paper II**, the amount of the inert matrix was **not** adjusted in order to keep constant reactivity. The results presented there hence illustrate the sole effect of the spectrum thermalisation with a consequent decrease in fission-to-absorption probabilities due to the increased pin pitches leading to the gradual decrease of k_0 with increasing P/D. We again remind the reader that the external source multiplication factor k_0 does not describe the real multiplication

in the system and our results are to be seen merely in terms of comparison of the performance of the two coolants, Pb/Bi and sodium.

6.6.2 Coolant void and cladding worth

As the spectral effect (reduced capture in fuel) is a major contributor to the positive reactivity insertion during coolant voiding, the appropriate choice of heavy metal coolants (Pb, Pb/Bi) or low density gas coolants (He, steam) might somewhat alleviate the void worth. Understandably, the void worth is not only a function of coolant, but also of the type of fuel applied in the system and the lattice geometry. While lead-alloy coolants would be a favourable choice to reduce void worth for $(U,Pu)O_2$ fuel for small P/Ds only, see Figure 6.8, the choice of Pb/Bi appeared to be preferable for the transmutation related fuels as (TRU,Zr)N and (MA,Zr)N in the whole range of realistic P/Ds. Details are presented in **Paper II**.

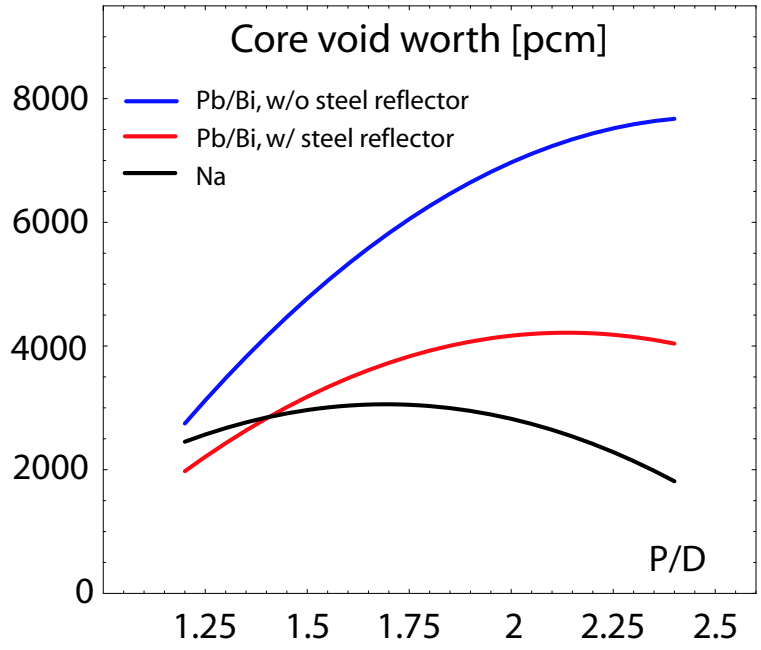

Figure 6.8. Coolant void worth in a critical FBR employing $(U,Pu)O_2$ fuel. The Pu/(U + Pu) ratio was varied with P/D in order obtain $k_{\text{eff}} \sim 1$, for Na in the range between 17% and 33%, for Pb/Bi without steel pin reflector between 16% and 26%, and in the case of Pb/Bi with steel reflector between 17% and 27%. Figure adapted from **Paper I.**

Enlarging the pin lattice in order to reduce the void worth can prove successful only in systems with inert matrix fuel, see Figure 6.9. In cores with a significant amount of fertile isotopes and/or with substantial presence of absorbing materials, the coolant void worth is significantly elevated due to the increased spectral hardening which accompanies larger P/D. The cladding worth appeared to be a decreasing function of the lattice pitch. The parasitic absorption in the structural

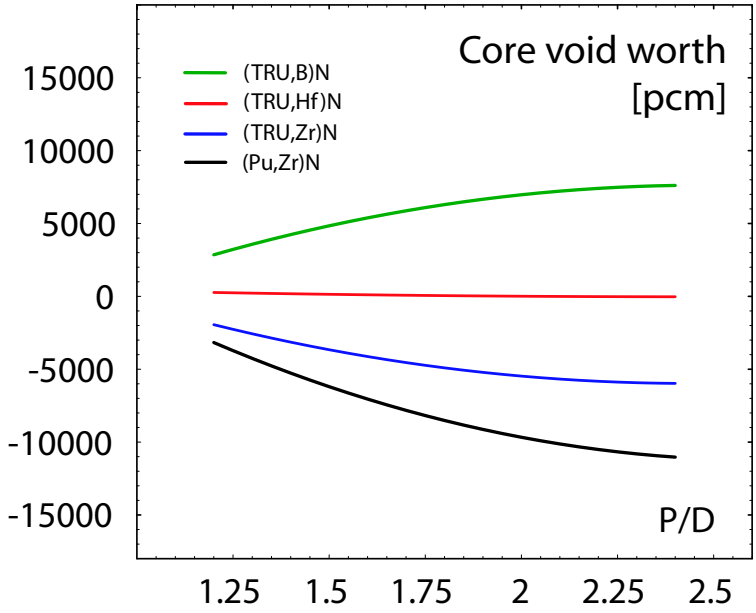

Figure 6.9. Core void worths in Pb/Bi-cooled TRU burners. Introduction of strongly absorbing materials to the fuel has an adverse effect on the coolant void reactivity. Figure redrawn from **Paper II**.

Fuel	P/D	^{241}Am σ_f/σ_a	Clad worth [pcm]	Coolant $\Delta k/\Delta T$ [pcm/K]	m_{act} at BOL [kg]	Burnup rate [%/fpd]	Doubling of I_p [fpd]
(TRU,Zr)N	1.2	0.106	+3700	−0.19	746	0.094	50
	2.0	0.101	+2300	−0.35	1155	0.063	85
	2.4	0.097	+1800	−0.38	1400	0.053	90
(TRU,Hf)N	1.2	0.214	+4300	+0.13	1532	0.048	95
	2.0	0.178	+2900	+0.27	1981	0.038	115
	2.4	0.163	+2400	+0.43	2244	0.034	120
(TRU,B)N	1.2	0.432	+5600	+0.17	2621	0.030	140
	2.0	0.328	+3400	+0.79	3179	0.025	190
	2.4	0.286	+2400	+0.90	3442	0.023	200

Table 6.5. Neutronic and burnup performance of the transuranium ADS Pb/Bi-cooled burner with ZrN, HfN, and BN as a function of pitch-to-diameter ratio. Table adopted from **Paper II**.

material is less and less significant with larger P/D, and likewise the reactivity which is introduced into the system during flush out, see Table 6.5.

6.6.3 Burnup performance

When enlarging pin pitch, the probability of neutrons to induce fission decreases due to the increased leakage and spectrum softening, This, in turn, implicates higher specific fuel inventories and consequently lower burnup rates which are approximately inversely proportional to the actinide masses. Decrease of the burnup rates consequently diminishes the accelerator proton beam swing. For ZrN and HfN matrices, the reactivity swing is approximately independent of P/D, while it decreases slightly for BN (see **Paper II**). With larger pitch, the neutron spectrum becomes softened, which increases the actual burnability of the matrix.

6.7 Homogeneous vs. heterogeneous modelling

In a separate, parametric study we also investigated the sensitivity of our results to the modelling approximation of the system geometry. The self-shielding effects observed in standard fast reactor design can be even more pronounced in reactor cores with heavy presence of heterogeneously distributed neutron absorbers.

A full pin-by-pin core geometry model of a refined TRU ADS core with heterogeneously distributed neutron absorber (B_4C), see **Paper III**, was compared with the homogeneous approximation, where fuel and absorber pins were smeared together with the coolant and cladding material. The structure in axial and radial reflectors were also smeared. A similar comparison was made for a model Pb/Bi-cooled core employing (TRU,Zr)N smearing core fuel, structural and coolant material. The results of these simulations are displayed in Table 6.6.

System	Design	k_{eff}	$M^{\text{f}}_{\text{ext}}$
(TRU,Zr)N	Homogeneous	0.96204 ± 0.00049	29.280 ± 0.0236
	Heterogeneous	0.95963 ± 0.00056	28.195 ± 0.0238
TRUN + B_4C	Homogeneous	0.94079 ± 0.00054	18.463 ± 0.0049
	Heterogeneous	0.96086 ± 0.00053	27.461 ± 0.0055

Table 6.6. Comparison of eigenvalue and source calculations for homogeneous and heterogeneous designs together with corresponding 1-σ relative statistical errors. In the case of eigenvalue calculations, totally 1 million of neutrons have been simulated in 100 active histories, while 5000 protons were used in a source multiplication run. Simulations have been performed on a single 1 GHz Pentium III processor PC running Linux operating system.

In order to dispatch our studies and match realistic calculation times, the homogeneous modelling approach would clearly be preferable as calculation times are increased by more than a factor of five in the case of heterogeneous modelling in order to reach similar 1-σ relative statistical errors. However, the homogeneous approximation implies the strong underestimation of the neutron multiplication in

a system with heterogeneously placed absorber pins. Sub-criticality level is also underestimated by ∼2000 pcm. Note that with respect to uncertainties of our Monte Carlo calculations, the change in the source efficiency is not significant, $\phi^* = 1.162 \pm 0.009$ (for homogeneous model) and $\phi^* = 1.119 \pm 0.014$ (for heterogeneous configuration).

Chapter 7

Design of a TRU ADS burner

The physical characteristics and challenges interconnected with transuranic burning in a nuclear reactor have been reviewed in previous chapters. The neutronic, safety & burnup performance of any incineration system will depend not only on the composition of the reactor's fuel but also on the choice of the core materials and geometry. Different diluent materials, core lattice configurations and coolants have been assessed in order to identify suitable fuel concepts and core design configurations for accelerator-driven transuranium burners. The results of these parametric, scoping studies were summarised in Chapter 6. Here, by appropriate choice of materials and by optimising fuel and core design, we aim at achieving favourable neutronic, burnup and safety characteristics of the transuranium ADS burner while respecting key thermal hydraulic and material-related constraints.

7.1 Core concept

Our concept is based on the introduction of neutron-absorbing materials into the core of accelerator-driven systems incinerating TRU nuclides in the frame of a two-component scenario, see Figure 3.10 - strategy e) and f). The system studies refer to a scenario of ADS-startup and introduction into the nuclear reactor park, assuming therefore a TRU composition being that of spent LWR UOX fuel (burnup 41.2 GWd/tHM) after 30 years of cooling, see Table 2.1.

The use of absorbing material was considered also for the CAPRA design [83] in order to dilute highly reactive plutonium fuel. Due to the severe degradation of Doppler and sodium void reactivity coefficients this option was, however, substituted by the dilution strategy. Requirements on safety margins (concerning reactivity coefficients) are somewhat relaxed in sub-critical reactors and a considerable

amount of neutron absorbers can be introduced. Absorbing materials can accommodate higher TRU inventories, which somewhat alleviate reactivity loss, reduce accelerator power swing and limit production of higher actinides in fuel cycle. Our extensive scoping and feasibility studies identified two candidate absorbing materials, hafnium nitride and boron carbide. Their merits were evaluated in two separate studies - **Paper II** and **Paper III**.

7.2 Down-selections of core materials

7.2.1 Fuel

The nitride fuels have been adopted as the primary option. As discussed in Section 5.1.1, nitrides feature good compatibility with liquid metal coolants and combine high thermal conductivity with acceptable solubility in nitric acid.

7.2.2 Diluent material

Boron carbide was chosen as a heterogenous diluent material in **Paper III** especially for its good thermal and irradiation stability in fast spectrum. Boron carbide features superior neutronic characteristics allowing to cut the thermal parts of the neutron spectra and thus attain high fission-to-absorption probabilities (~ 0.4 for ^{241}Am). The boron (19.82% ^{10}B isotopic abundance) was enriched up to 95% in order to avoid neutron moderation on ^{11}B nuclei and minimise absorber inventory.

In **Paper II**, an innovative absorbing material, HfN, was proposed to be homogeneously mixed with actinide nitrides. HfN has excellent thermophysical properties: very high melting temperature and favourable thermal conductivity. (Hf,Zr)N pellets have been produced by carbothermic reduction from mixed oxides and a solid solution was obtained [126]. Due to the similarity of the lattice parameters, actinide nitrides are assumed to form a homogeneous solution also with HfN. Hafnium is a good absorber of neutrons in the thermal and resonance energy regions, effectively hardening the neutron spectrum. Our scoping studies showed that HfN-based fuels provide a good combination of the neutronic, safety and burnup characteristics: a) maintaining hard neutron spectra and thus minimising the production of higher actinides in the fuel cycle, b) providing acceptable coolant void reactivity, hence reducing necessary sub-criticality margin at BOC, c) attaining a reasonable value of the source efficiency, thus limiting the requirements on the accelerator beam power, d) decreasing the burnup reactivity swing, thus alleviating power peaking.

7.2.3 Coolant

Lead-bismuth eutectic is investigated as a candidate coolant, combining low melting and high boiling temperatures with favourable voiding characteristics (see Section 6.4.1). Pb/Bi also features low chemical activity with outer environments (water, air) excluding the possibility for fire or explosions. However, Pb/Bi flow

rates are limited by erosion to about 2.5 m/s - eventuating in higher pitches than usual for sodium. Liquid lead-bismuth eutectic is also highly corrosive in contact with cladding and structural materials at higher temperatures. Silicon modified ferritic/martensitic steels like Russian EP-823 may reach temperatures up 890 K. However, recent experiments have however shown that these steels feature reduced radiation resistance [142], see Section 5.3 for detailed discussion.

7.3 Design constraints

Design constraints taken into account include

- maximum coolant velocity in order to limit corrosion and erosion of structural materials ($v_{\max} = 2.5$ m/s),
- peak linear power and minimum P/D as limited by requirements to maintain stability of the structural materials at steady state ($T_{\max} \approx 890$ K) and in transients ($T_{\max} \approx 1140$ K) as well as to keep nitride fuel temperature below the decomposition/melting limit,
- peak fluence in the pin cladding (~ 100 dpa-NRT) and maximum internal gas pressure, both effectively limiting the discharge burnup,
- minimum fuel pin diameter (fabricability limit) & maximum fuel column height, attaining reasonable pressure drop and limiting thermal bowing,
- maximum TRU fraction in the fuel (~ 50 vol%), respecting the requirements as posed by stability and fabricability considerations,
- minimum target radius, providing sufficient heat removing capabilities to dissipate heat generated by accelerator beam at steady state and in transients,
- allowing only double-fold increase in the accelerator power beam,
- ensuring acceptable safety characteristics of the core, namely preventing the system from an instantaneous damage.

As we discussed in Chapters 3 and 6, the actinide discharge burnup has to be maximised in order to minimise losses to the waste streams. Simultaneously, the number of recycling steps should be minimised. What follows below is an extended summary of the results presented in **Papers II** and **III**. The reader is advised to consult the respective papers for details.

7.4 Design employing HfN

A cross section of the conceptual core design of (TRU,Hf)N-fuelled Pb/Bi-cooled ADS, as presented in **Paper II**, is displayed in Figure 7.1. The core is subdivided

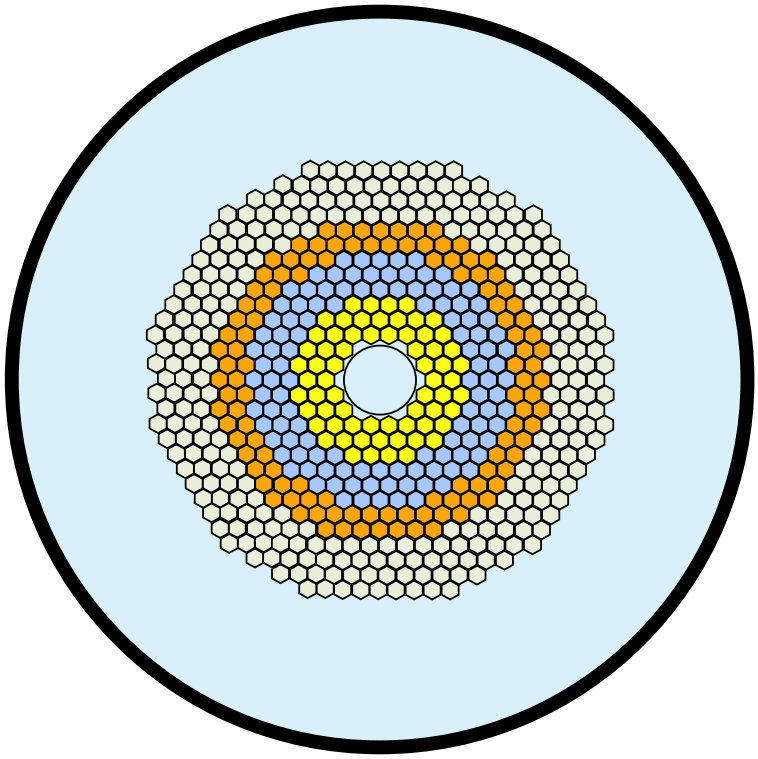

Figure 7.1. Cross section of the conceptual core design of Pb/Bi-cooled ADS employing (TRU,Hf)N. The core consists of three enrichment zones with the different matrix fractions. Radial steel reflector sub-assemblies are depicted in grey. The thickness of the radial reflector is optimised such that the coolant void reactivity is minimised. Pitch-to-diameter ratio is 1.75. Figure adapted from **Paper II**.

Sub-assembly row/zones	1-3	4-6	7-8	9-12
Actinide fraction (vol%)	32	37	45	–
Number S/As	66	114	114	282

Table 7.1. TRU volume fractions in fuel and a number of S/As in each enrichment zone yielding a radial power peaking factor less than 1.3 at BOL. There is 282 sub-assemblies in the radial reflector. Table adapted from **Paper II**.

radially into three enrichment fuel zones surrounded by four S/A rows of steel reflector (the steel volume fraction being 80%). The fraction of the matrix was adjusted so that a radial power peaking factor less than 1.3 is obtained at BOL, see Table 7.1.

The pellet, pin, sub-assembly, and system design parameters can be seen in Table 7.2. The flat-to-flat (FTF) of the S/A is adjusted such that the core fits a ∼20 cm radius target module. In this design, a relatively small sub-assembly FTF of 10.8 cm is chosen, thus allowing finer distribution of fuel in the core and facilitating symmetric reloading patterns. The power of the system was kept constant at the

Pellet density (% TD)	0.85
Pellet outer radius R_{fuel} (mm)	2.4
Cladding inner radius R_{gap} (mm)	2.5
Cladding outer radius R_{pin} (mm)	3.0
Pin bond	Pb/Bi
Active pin length (cm)	100
Length of upper fission gas plenum (cm)	150
Length of lower fission gas plenum (cm)	10
Length of bottom plenum spacer (cm)	10
S/A outer flat-to-flat (cm)	10.8
S/A pitch (cm)	11.0
Thickness of the duct (cm)	0.25
Pins per S/A	91
Pitch-to-diameter ratio	1.75
Number of core S/As	294
Length of radial reflector S/As (cm)	140
Length of upper reflector (cm)	200
Length of lower reflector (cm)	230
Spallation target outer radius (cm)	22.5
Radius of accelerator beam tube (cm)	15
Distance of target window from centreplane (cm)	20

Table 7.2. Pellet, pin, sub-assembly, and system design specifications of the (TRU,Hf)N-fuelled Pb/Bi-cooled ADS. A triangular pin lattice is adopted. The initial level of sub-criticality was set to $k_{\text{eff}} = 0.962$. Table adapted from **Paper II**.

level of 800 MW_{th} as limited by availability of the target coolant to remove the heat evolved by the accelerator beam. The proton beam impact window was placed 20 cm above the midplane of the core in order to minimise the number of neutrons leaking out of the spallation target into the axial reflectors and hence maximise the source efficiency. At the same time, almost axially symmetric power distribution is yielded. The gas plenum is located in the upper part of the core, reducing risks associated with positive reactivity insertion due to gas release from ruptured cladding. The length of the upper plenum was assumed to be relatively large, 150 cm, sufficient to accommodate released fission gases (mainly Xe, Cs, and Sr) and all helium from decayed ^{242}Cm.

Basic characteristics of the conceptual design of (TRU,Hf)N-fuelled Pb/Bi-cooled ADS are given in Table 7.3. Observe that despite the presence of absorbing matrix in the core, a slightly negative void reactivity (-270 pcm) could be obtained

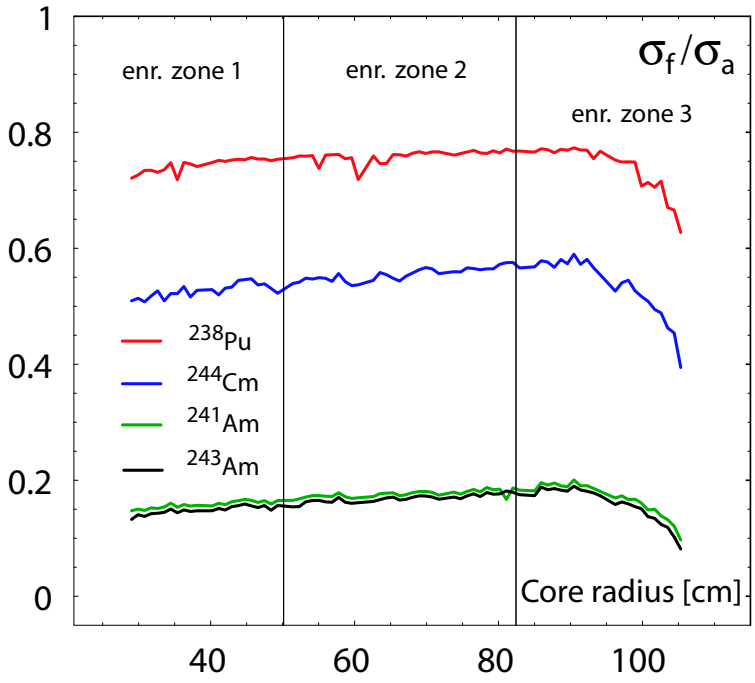

Figure 7.2. Pin-by-pin calculated radial distribution of fission probabilities. Fission-to-absorption fraction of ^{241}Am reaches 20%. Adapted from **Paper II.**

in the present design. Voiding the core together with the upper plenum and radial reflector brings the system additional negative reactivity (−3500 pcm).

Radial distribution of fission-to-absorption probabilities for even-neutron number nuclides is then presented in Figure 7.2. The fission probability is increased by a factor of two in the case of ^{241}Am and ^{243}Am in comparison to the CAPRA and Energy Amplifier figures (see also Table 7.4), resulting in a significant reduction of the He-producing nuclides ^{242}Cm and ^{238}Pu.

Irradiating the fuel for 100 days at the constant thermal power of 800 MW yielded a reactivity swing of 3300 pcm which was compensated for by an increase of accelerator power from 16 to 30 MW. The average cycle burnup reached 3.6%, with local burnups ranging from 5.5% in zone one to 2.5% in zone eight. The burnup calculations were accomplished by the MCB code [156].

The maximum achievable burnup of fuel pin was consequently determined by respecting cladding radiation damage and pin burst limits. The gas pressure in the fuel pin was calculated assuming that all fission gases (elements with boiling temperature lower than 2150 K) together with all helium from ^{242}Cm decay are released from the fuel. The maximum pressure in the most exposed pin in the S/A closest to the target is 3.7 MPa at the end of one irradiation cycle/batch (100 fpd), generating a hoop stress of 18.5 MPa. In order to keep this figure under the limiting value of 100 MPa, measured for irradiated rods at the temperature of 1140 K [140], the maximum residence time of the most exposed sub-assembly is 540 fpd.

Parameters	Unit	Conceptual design
Averaged linear power	kW/m	29.9
Proton efficiency ψ^* (BOC/EOC)		26.9/26.0
Coolant void worth at BOL	pcm	-270
Cladding and duct worth at BOL	pcm	$+6390$
Flooding of the accelerator tube	pcm	$+200$
Doppler T$\Delta k_{\text{eff}}/\Delta T$	pcm	-47
Axial fuel expansion $\Delta k_{\text{eff}}/(\Delta H/H)$	pcm/10^{-5}	-0.21
Grid expansion $\Delta k_{\text{eff}}/(\Delta P/P)$	pcm/10^{-5}	-0.52
Coolant density change $\Delta k_{\text{eff}}/\Delta T$	pcm	$+0.13$
β_{eff} at BOL	pcm	230
m_{act} at BOL	kg	2140
Burnup rate	%FIMA/fpd	0.036
Reactivity loss	pcm/batch	-3300
$\Delta k^{\text{c}}_{\text{eff}}/\beta_{\text{c}}$	pcm/%FIMA	-850
Doubling of the accelerator power I_{p}	fpd	100
^{242}Cm fraction in fuel	%/%FIMA	0.12
Number of batches		5
Batch length	days	100
Average burnup w/o core reshuffle	%FIMA	$\sim$20
Maximum radiation damage at EOL	dpa-NRT	100
Net Pu consumption	kg/efpy	188
Net MA consumption	kg/efpy	21

Table 7.3. Neutronic, safety and burnup performance of the conceptual ADS core design employing (TRU,Hf)N fuel and Pb/Bi coolant. P is the lattice pitch, H is the active core length. A capacity factor of 0.75 was assumed. Table is adapted from **Paper II**.

The radiation damage has been estimated using the formula suggested by Garner [157], relating 200 dpa-NRT damage rate to the damage neutron fluence ($E_{\text{n}} > 0.1$ MeV) of $4{\cdot}10^{23}$ n/cm^2. The highest exposure is found for high-burnup pins placed closest to the spallation target. There, 69% of the neutron flux is above the 100 keV, with a cycle/batch averaged fast flux of $4.2{\cdot}10^{15}$n/cm^2/s. Considering an axial power peaking factor of 1.28, the maximum fast fluence in cladding after 540 fpd is $2{\cdot}10^{23}$ n/cm^2 $\sim$ 100 dpa-NRT, which could be a reasonable estimate of the dose limit of Si-modified ferritic steels like EP-823 [142]. Thus, a sub-assembly burnup of 0.55%FIMA/fpd $\cdot$ 540 fpd $\sim$ 30%FIMA is in principle possible.

The fuel cycle our conceptual TRU ADS design thus consist of five 100-days long irradiation cycles. During the outages a few reflector sub-assemblies in the

core perimeter will be substituted with fuel S/As. Even without fuel reshuffling, an average burnup of the first, BOL core of ∼20% can be reached neutronically. Due to the burnup of TRU fuel and consequently increasing fractions of fission products, proton source efficiency decreases. The k_{eff} in the beginning of each irradiation batch is thus increased from 0.962 at BOL to 0.970 at the fifth irradiation cycle in order to keep the accelerator beam power at approximately 16 MW at BOC. The reactivity drop during one irradiation batch is compensated by an increase in accelerator beam by less than a factor of 2.0.

The linear power ratings are 39 kW/m at the beginning of life (power peaking 1.3 in the first S/A row) and rise up to 54 kW/m at EOC (100 full power days) when the burnup of the core has to be interrupted due to the limitation in maximum cladding temperatures (890 K). In Figure 7.3, the radial power profile is displayed at the beginning and at the end of the irradiation cycle, respectively.

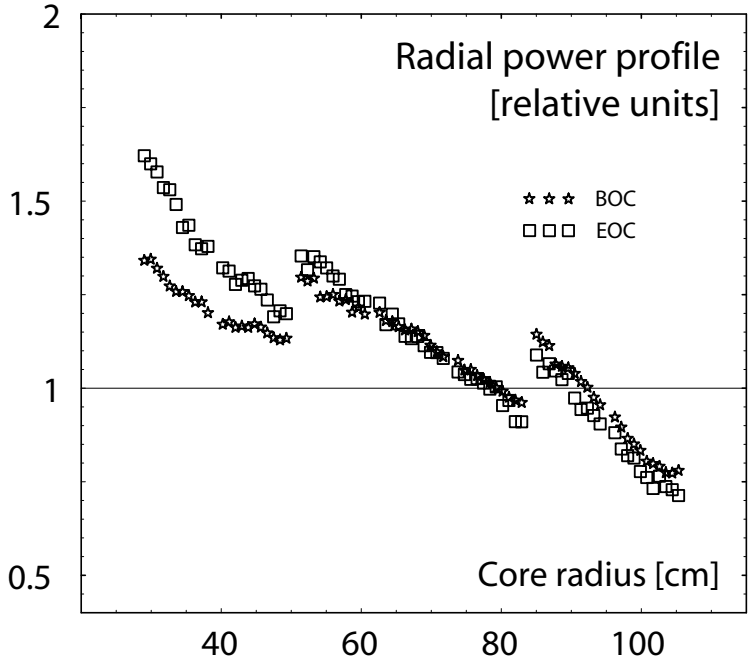

Figure 7.3. Radial power profile at BOC and EOC as reported on in **Paper II**. The maximum steady-state linear power remains bellow 60 kW/m, ensuring thermal stability of the structural material.

The beneficial effect of the HfN matrix in terms of the limitation of higher actinides in the fuel cycle is illustrated by evaluating the concentration of curium in the equilibrium fuel cycle. The qualitative analyses showed that curium inventory in mass-constrained equilibrium is about 1% for the present conceptual design, which is to be compared to more than 4% in a CAPRA type spectrum.

The lattice pitch of the reactor was chosen so that instant decomposition of nitride fuel or cladding damage are prevented under accidental conditions involving unprotected beam overpower transient, unprotected loss-of-flow, and unprotected

loss-of-heat sink. The thermal conductivity of the fuel is enhanced by HfN hence the peak centerline steady state temperature of the fuel remains below 1510 K at the EOC in the most exposed fuel pin. The corresponding coolant temperature difference is 220 K, which is a 60 K increase in comparison to BOC. At accidental conditions, when the accelerator beam is increased by a factor of two at BOC, the peak fuel temperature remains under 2150 K, still leaving a 250 K margin to the fuel decomposition limit.

In summary, our conceptual design of (TRU,Hf)N-fuelled Pb/Bi-cooled ADS features good combination of the neutronic and burnup characteristics - providing slightly negative coolant void worth, low burnup reactivity swing, and reasonable value source efficiency. However, excessive coolant volumes are required in order to guarantee cladding integrity under unprotected loss-of-flow accidents as the burst limit of ferritic steels is low (about 200 K below that for austenitic). Because austenitic steels feature very low (high temperature) corrosion resistance towards lead-alloys, it appears that, at present, there is no obvious choice of cladding material for our system.

Moreover, further studies are required in order to investigate the system transient behaviour in more detail and analyse its characteristics during an approach and in the equilibrium. Safety merits of increased TRU inventories being a consequence of HfN matrix have to be assessed, too. Finally, the high temperature material and irradiation performance of the Hf-based fuels needs to be established.

7.5 Design employing B_4C

In **Paper III**, the feasibility of employing a strong neutron absorber (B_4C) in the TRU ADS was investigated. We showed that one can achieve a significant increase in fission-to-absorption probabilities by a factor of 2.5 in the case of ^{241}Am and by a factor of three for ^{237}Np in comparison to the CAPRA and Energy Amplifier figures, see Table 7.4.

However, the introduction of boron carbide into the core yielded adverse effects on core safety parameters, particularly fuel temperature and coolant void coefficients. Due to the hard neutron spectrum, the Doppler coefficient virtually disappeared as hardly any neutrons reached the resonances. At the same time, spectral hardening upon the coolant voiding diminishes the parasitic capture in absorbing materials, which resulted in very large reactivity insertion, +3500 pcm.

The results of the burnup calculations are presented in Table 7.5. Fuel irradiation time was 300 days.

The reactivity decrease of 5600 pcm had to be compensated by an increase of accelerator power from 20 to 75 MW. Observe that the latter value would not be acceptable with respect to the ability of the 20-cm radius target to dissipate heat generated by proton beam. Hence, shorter irradiation cycle of about 50 full power days should be applied instead. Alternatively, total core power should be decreased, increasing also margins to the fuel/cladding damage. In the original

Nuclide	zone 1	zone 2	zone 3	zone 4	CAPRA	EA
^{237}Np	0.22	0.30	0.47	0.46	0.15	0.15
^{238}Pu	0.72	0.78	0.86	0.85	0.64	0.69
^{240}Pu	0.48	0.58	0.73	0.72	0.37	0.40
^{242}Pu	0.43	0.55	0.72	0.71	0.33	0.32
^{241}Am	0.14	0.20	0.33	0.33	0.12	0.12
^{243}Am	0.13	0.19	0.34	0.33	0.10	0.11
^{244}Cm	0.50	0.59	0.73	0.72	0.40	0.36

Table 7.4. Fission-to-absorption probability ratios for quickly decaying α-emitters and their predecessors in the fuel zones of nitride-fuelled Pb/Bi-cooled TRU ADS employing a B_4C absorber presented in **Paper III**. These values are compared to corresponding values of CAPRA and Energy Amplifier designs. The benefit of introducing neutron absorbers to reduce α activity and helium accumulation in fuel pins is clear.

Property	BOL	100 d	200 d	300 d
k_{eff}	0.972	0.955	0.936	0.916
ϕ_n^*	0.877	0.870	0.850	0.802
ϕ_f^*	0.875	0.867	0.847	0.797
Target power (MW)	20.5	36.9	54.9	75.1
Power peaking in zone 1	1.08	1.29	1.49	1.70
Average flux (10^{19} m^{-2}s^{-1})	3.86	4.14	4.45	4.78
Flux peaking in zone 1	1.97	2.27	2.57	2.88

Table 7.5. Burnup characteristics of nitride-fuelled Pb/Bi-cooled TRU ADS with B_4C neutron absorbers. Thermal power of the system is 1200 MW. Table adapted from **Paper III.**

design, presented in **Paper III**, the total burnup reached 8.7% in one irradiation cycle, local burnups were ranging from 7.3% in zone three to 11.5% in zone one and two. All transuranics were homogeneously dispersed throughout the whole core.

In this study, nitrogen alone was proposed to be used as pin bonding gas in order to suppress the decomposition of the nitride fuel. However, nitrogen has very low thermal conductivity, yielding extensive temperature gradients in the pellet-clad gap, of the order of 1000 K, before the gap is closed. In **Paper III**, the peak fuel temperature was estimated to be kept below 2100 K during the whole irradiation cycle at the steady state conditions. However, if the whole accelerator beam power margin would be accidently inserted into the system at BOL when pellet-clad gap is open, the fuel dissociation limit could be surpassed. Recent studies show that admixing of only small portions of the nitrogen into the inert gas is sufficient to delay the onset of the fuel dissociation by several hundreds Kelvin [116]. Hence, a

remedy would be to exchange nitrogen bonding with He-1%N_2 gas or apply liquid-metal bond, as was proposed for the (TRU,Hf)N burner (**Paper II**).

Chapter 8

Papers

Abstracts of the appended papers are summarised below.

8.1 Paper I

Liquid metal coolant void worths have been calculated as a function of fuel composition and core geometry for several model fast breeder reactors and accelerator-driven systems. The Monte Carlo transport code MCNP with continuous energy cross-section libraries was used for this study. With respect to the core void worth, lead/bismuth cooled FBRs appear to be inferior to those employing sodium for pitch-to-diameter ratios exceeding 1.4. It is shown that in reactor systems cooled with lead/bismuth eutectic, radial steel pin reflectors significantly lower the void worth. The void worth proves to be a strong function of the fuel composition, reactor cores with high content of minor actinides in fuel exhibiting larger void reactivities than systems with plutonium based fuel. Enlarging the lattice pitch in ADS burners operating on Pu rich fuel decreases the void worth while the opposite is true for ADSs employing americium based fuels.

8.2 Paper II

We have studied the neutronic & burnup characteristics of an accelerator-driven transuranium burner in a start-up mode. Different inert and absorbing matrices as well as lattice configurations have been assessed in order to identify suitable fuel and core design configurations. Monte Carlo transport and burnup codes were used in the analyses. The pin pitch was varied in order to optimise the source efficiency and coolant void worth while respecting the fuel and cladding limits during steady-state conditions and at transients. HfN provides a good combination of safety characteristics (negative coolant void worth and prompt reactivity feedback) and reasonable values of source efficiency and burnup reactivity swing. HfN-based fuels

yield twice higher neutron fission-to-absorption probabilities in americium isotopes compared to reactor designs relying on inert matrices, thus limiting the production of higher actinides in the fuel cycle. A safety analysis of the conceptual core design shows that the system withstands an unprotected accelerator overpower transient.

8.3 Paper III

The application of burnable absorbers (BA) for minimisation of power peaking, reactivity loss and capture to fission probabilities in an accelerator driven waste transmutation system (ADS, ATW) has been investigated. ^{10}B enriched B_4C absorber rods were introduced into a lead/bismuth cooled core fuelled with TRU discharges from light water reactors in order to achieve the smallest possible power peakings at a BOL sub-criticality level of 0.97. Detailed Monte Carlo simulations show that a radial power peaking equal to 1.2 at BOL is attainable using a four zone differentiation in BA content. Using a newly written Monte Carlo Burnup code (MCB), reactivity losses were calculated to be 640 pcm per percent transuranium burnup for unrecycled TRU discharges. Compared to corresponding values in BA free cores, BA introduction diminishes reactivity losses in TRU fuelled sub-critical cores by about 20%. Radial power peaking after 300 days of operation at 1200 MW thermal power was less than 1.75 at a sub-criticality level of $\sim$0.92, which appears to be acceptable with respect to limitations in cladding and fuel temperatures. In addition, the use of BA yields significantly higher fission to capture probabilities in even neutron number nuclides. A fission to absorption probability ratio for ^{241}Am equal to 0.33 was achieved in the configuration studied here. Hence, production of the strong α-emitter ^{242}Cm is reduced, leading to lower fuel swelling rates and pin pressurisation. Disadvantages following BA introduction, such as increase of void worth and decrease of Doppler feedback in conjunction with small values of β_{eff}, need to be addressed by detailed studies of sub-critical core dynamics.

8.4 Paper IV

The introduction of accelerator driven systems (ADS) is believed to be of importance for efficient and safe transmutation of americium and curium. Among the problems related to the use of ADS in this context are comparatively high power peakings and high helium accumulation rates in fuel pins. The present study shows that radial power peakings similar to those of critical configurations ($\sim$1.1) can be achieved in sub-critical cores by adequate distribution of fuel, burnable absorbers and diluents. The introduction of strong neutron absorbers in sub-assemblies containing americium increases fission to absorption ratios up to $\sim$0.50, which reduces helium production due to ^{242}Cm decay by a factor of two. In order to maintain a source importance reasonably close to unity, neutron poisons should be placed in

the periphery of the core, and diluent materials with small cross sections for capture and inelastic scattering should be used in the vicinity of the spallation target.

8.5 Paper V

In order to study the beam power amplification of an accelerator driven system (ADS), a new parameter, the proton source efficiency (ψ^*) is introduced. ψ^* represents the average importance of the external proton source, relative to the average importance of the eigenmode production, and is closely related to the neutron source efficiency (ϕ^*), which is frequently used in the ADS field. ϕ^* is commonly used in the physics of sub-critical systems driven by any external source (spallation source, (d,d), (d,t), ^{252}Cf spontaneous fissions etc.). On the contrary, ψ^* has been defined in this paper exclusively for ADS studies, where the system is driven by a spallation source. The main advantage with using ψ^* instead of ϕ^* for ADS is that the way of defining the external source is unique and that it is proportional to the core power divided by the proton beam power, independently of the neutron source distribution.

Numerical simulations have been performed with the Monte Carlo code MCNPX in order to study ψ^* as a function of different design parameters. It was found that, in order to maximise ψ^*, and therefore minimise the proton current needs, a target radius as small as possible should be chosen. For target radii smaller than about 30 cm, lead-bismuth is a better choice of coolant material than sodium, regarding the proton source efficiency, while for larger target radii the two materials are equally good. The optimal axial proton beam impact was found to be located approximately 20 cm above the core centre. Varying the proton energy, ψ^*/E_{p} was found to have a maximum for proton energies between 1200 and 1400 MeV. Increasing the americium content in the fuel decreases ψ^* considerably, in particular when the target radius is large.

Chapter 9

Conclusions

Accelerator-driven systems (ADS) have been proposed to deal with the excess of americium and curium in P&T schemes closed for entire transuranic vector. In countries without developed fast reactor programmes or with politically motivated proliferation concerns, the ADS are envisioned to operate together with light-water reactors in the so called two-component scheme. A major difficulty associated with this scenario is, however, high reactivity losses due to rapid burnout of fissile isotopes, which simultaneously exacerbates power peaking.

In this work, we addressed the issue of extensive burnup reactivity swing in transuranium ADS, while also achieving good neutronic, burnup and safety characteristics of the reactor. Series of parametric, scoping studies were performed in order to identify promising coolant candidates, fuel concepts and core designs.

The economy of the source neutrons was first investigated as a function of core and target design. For these analyses, a novel, generalised framework was presented in order to describe the source multiplication in ADS. This parameter is defined independently of the distribution of the *neutron* source, allowing for a fair mutual intercomparison of different ADS designs. The source efficiency showed to be a strong decreasing function of target radius due to inelastic slowing down of neutrons in the target.

We furthermore focused on the evaluation of the coolant void worth in the model FBR and ADS designs. Most importantly, it appeared that in reactor systems cooled by lead/bismuth eutectic, radial steel pin reflectors have to be applied in order to significantly lower the coolant void reactivity. The void worth proved to be a strong function of the fuel composition - reactor cores with high content of fertile material or minor actinides in fuel exhibiting larger void reactivities than systems with plutonium-based inert matrix fuels.

For transuranic fuel, fertile and strongly absorbing matrices yielded higher void worth when increasing P/D, while the opposite was valid for inert matrices. Moreover, large pitches appeared to be favourable for limiting the reactivity worth of the cladding material and improving the source efficiency.

HfN-based fuels were subsequently identified as an attractive option for transuranium ADS burners. (TRU,Hf)N appeared to have a good combination of neutronic, burnup and thermal characteristics: maintaining hard neutron spectra, yielding acceptable coolant void reactivity and source efficiency, and providing small burnup reactivity swing. HfN appears to have a stabilising effect on the fuel, improving its thermal conductivity and thus its margin to failure.

Considering key material-related and thermal hydraulic design constraints, we presented a conceptual design of a lead/bismuth eutectic cooled ADS burner employing (TRU,Hf)N fuel. The design featured a hard neutron spectrum yielding a factor of two higher ^{241}Am and ^{243}Am fission probabilities than are typical for systems employing inert matrix fuel. Hence, the production of higher actinides in the fuel cycle is minimised. The burnup reactivity swing and associated power peaking were managed by an appropriate choice of cycle length (100 days) and by core enrichment zoning. The average discharge burnup of 20% fissions per initial atom was reached. The conceptual core design features favourable safety characteristics - core coolant void worth being slightly negative. A safety analysis shows that the system is protected from an instant damage during unprotected beam overpower transient.

In conclusion, it seems that the principal merits of accelerator-driven systems in terms of their potential to reduce radiotoxic inventory of spent nuclear fuel are well established. However, several important issues have to be resolved in the near future before they are implemented. The choice of core and target materials - fuel matrix, coolant, and structural material - is still an open question alluding to their long-term mechanical, thermal and irradiation performance. E.g. while the well established oxide fuel seems to be the most natural choice for ADS-demo, the advanced fuel types as e.g. nitrides appear to be a more favourable option for gigawatt-size ADS units. Nevertheless, it might be completely other factors than technological, which would decide about the future fate of ADS and P&T technologies, e.g. political and social one. In this regard, an increase of easily apprehended, short-term risks which are associated with P&T could play an important role.

Bibliography

[1] C. Bennett et al., Astrophysical Journal Supplement Series **148**, 1 (2003).

[2] A. Becquerel, Comptes Rendus de l'Académie des Sciences (Paris) **122**, 501 (1896).

[3] O. Hahn and F. Strassmann, Naturwissenschaften **27**, 11 (1939).

[4] L. Meitner and O. Frisch, Nature **143**, 239 (1939).

[5] F. Joliot et al., Nature **143**, 470 (1939).

[6] F. Joliot et al., Nature **143**, 680 (1939).

[7] J. Lewellen, *The Mighty Atom*, Knopf, 1955.

[8] http://howard.engr.siu.edu/mech/faculty/hippo/lecture16a.htm, September 17, 2004.

[9] L. Brown et al., *State of the World*, W.W. Norton & Company, 1992.

[10] *Actinide and Fission Product Partitioning and Transmutation, Status and Assessment Report*, OECD/NEA, 1999.

[11] JEF-PC, version 2.0, OECD/NEA.

[12] P. de Marcillac et al., Nature **422**, 876 (2003).

[13] *Council directive lying down basic safety standards for the protection of the health*, Number 96/29/EUROATOM, 1996.

[14] B. Gautier, Innovative fuel physics: Reactor core design and high burnup fuel performance, in *Lecture notes: The 1999 Frédéric Joliot/Otto Hahn Summer School*, CEA/FZK, 1999.

[15] K. Fukuda et al., IAEA overview of global spent fuel storage, Technical Report IAEA–CN–102/60, IAEA, 2003.

[16] N. Oi, Plutonium challenges: Changing dimensions of global cooperation, 40/1/1998, IAEA Bulletin, 1998.

[17] Post-closure safety of a deep repository for spent nuclear fuel, Technical Report TR-99-06, Swedish Nuclear Fuel and Waste Management Co., 1999.

[18] A EU roadmap for developing accelerator driven systems (ADS) for nuclear waste incineration, Technical report, The European Technical Working Group on ADS, ENEA, 2001.

[19] *Dose Coefficients for Intakes of Radionuclides by Workers*, ICRP Publication 68, 1994.

[20] *Age Dependent Doses to Members of the Public from Intake of Radionuclides: Part 5 - Compilation of Ingestion and Inhalation Dose Coefficients*, ICRP Publication 76, 1995.

[21] H. Gruppelaar et al., Advanced technologies for the reduction of nuclear waste, Technical Report ECN-R-98-008, ECN, Petten, 1998.

[22] Nuclear waste: technologies for separations and transmutations, Technical report, National Research Council, 1996.

[23] G. Volckaert et al., Long-term environmental impact of underground disposal of P&T waste, in *Proceedings of the Fifth International Information Exchange Meeting on Actinide and Fission Product Partitioning and Transmutation*, page 463, OECD/NEA, Mol, Belgium, November 25-27, 1998.

[24] N. Cadelli et al., *Performance Assessment of Geological Isolation Systems for Radioactive Waste*, Commission of the European Communities, 1988.

[25] *Accelerator-driven Systems (ADS) and Fast Reactors (FR) in Advanced Nuclear Fuel Cycles, A Comparative Study*, OECD/NEA, 2002.

[26] T. Pigford, Reprocessing incentives for waste disposal, in *Transactions of the American Nuclear Society*, volume 62, page 97, ANS, 1990.

[27] A. Croff et al., Actinide partitioning-transmutation program final report, Technical Report ORNL-5566, Oak Ridge National Laboratory, 1980.

[28] Evaluation of actinide partitioning and transmutation, Technical Report 214, IAEA, 1982.

[29] *The Enviromental and Ethical Basis of Geological Disposal of Long-Lived Radioactive Wastes*, OECD/NEA, 1996.

[30] A. Croff, A reexamination of the incentives for actinide burning, in *Transactions of the American Nuclear Society*, volume 62, page 76, 1990.

[31] *The Future of Nuclear Power, An interdisciplinary MIT study*, Massachusetts Institute of Technology, U.S.A., 2003.

[32] A. Waltar and A. Reynolds, *Fast Breeder Reactors*, Pergamon Press, 1981.

[33] M. Steinberg et al., Neutron burning of long-lived fission products for waste disposal, Technical Report BNL-8558, Brookhaven National Laboratory, 1964.

[34] Y. Shubin et al., Evaluations of photoneutron reaction cross sections of radioactive fission product nuclei, Technical Report INDC(CCP)-408, IAEA, 1997.

[35] M. Gregory and M. Steinberg, A nuclear ransmutation system for disposal of long-lived fission product waste in an expanding nuclear power economy, Technical Report BNL-11915, Brookhaven National Laboratory, 1967.

[36] H. Harada et al., Fusion technology **24(2)**, 161 (1993).

[37] J. Wallenius, Fusion technology **33**, 456 (1998).

[38] I. Slessarev et al., On neutron consumption requirements for long-lived fisson products (LLFP) transmutation and lanthanides, in *Proceedings of the International Conference on Future Nuclear Systems, GLOBAL'99*, ANS, 1999.

[39] M. Salvatores, Transmutation and innovative options for the back-end of the fuel cycle, in *Proceedings of the International Conference on Future Nuclear Systems, GLOBAL'99*, ANS, Jackson Hole, USA, August 29 - September 3, 1999.

[40] Y. Sakamura et al., Studies on pyrochemical reprocessing for metallic and nitride fuels: behaviour of transuranium elements in LiCl-KCl/liquid metal systems, in *Proceedings of the International Conference on Future Nuclear Systems, GLOBAL'99*, ANS, Jackson Hole, USA, August 29 - September 3, 1999.

[41] M. Salvatores et al., Nuclear Science and Engineering **116**, 1 (1994).

[42] F. Venneri et al., The physics design of accelerator-driven transmutation system, in *Proceedings of the International Conference on Evaluation of Emerging Nuclear Fuel Cycle Systems, GLOBAL'95*, page 474, ANS, Versailles, France, September 11-14, 1995.

[43] W. Yang and H. Khalil, Neutronics design studies of an LBE cooled ATW blanket, in *Proceedings of the IAEA Technical Committee Meeting on Core Physics and Engineering Aspects of Emerging Nuclear Energy Systems for Energy Generation and Transmutation, IAEA-TECDOC-1356*, Argonne National Laboratory, USA, November 28 - December 1, 2000.

[44] T. Takizuka et al., Dedicted accelerator-driven system for nuclear waste transmutation, in *Proceedings of the Third International Conference on Accelerator-Driven Transmutation Technologies and Applications, ADTTA'99*, Praha, Czech Republic, June 7-11, 1999.

[45] M. Eriksson, J. Wallenius, M. Jolkkonen, and J. Cahalan, Inherent safety of fuels for accelerator-driven systems, Submitted to Nuclear Technology, 2004.

[46] T. Thompson and J. Beckerley, editors, *The Technology of Nuclear Reactor Safety*, volume 1, The M.I.T. Press, 1964.

[47] B. Pershagen et al., *Snabba bridreaktorer*, NE 1982:6, Nämnden för energiproduktionsforskning, Sweden (in Swedish), 1982.

[48] E. Adamov et al., *White book of nuclear energy*, MINATOM, Russia (in Russian), 2001.

[49] W. Satcey, *Nuclear Reactor Physics*, John Wiley & Sons, Inc., 2001.

[50] H. Etherington, editor, *Nuclear Engineering Handbook*, McGraw-Hill Book Company, 1958.

[51] H. Kleykamp, Journal of Nuclear Materials **275**, 1 (1999).

[52] H. Pierson, *Handbook of Refractory Carbides and Nitrides*, William Andrew Publishing/Noyes, 1996.

[53] R. Thetford and M. Mignanelli, Journal of Nuclear Materials **320**, 44 (2003).

[54] H. H. Hummel and D. Okrent, *Reactivity Coefficients in Large Fast Power Reactors*, American Nuclear Society, 1970.

[55] S. Glasstone and A. Sesonske, *Nuclear Reactor Engineering*, volume 1, Chapman and Hill, 1994.

[56] C. Lombardi et al., Journal of Nuclear Materials **274**, 181 (1999).

[57] A. Conti et al., CAPRA exploratory studies of U-free fast Pu burner cores, in *Proceedings of the International Conference on Evaluation of Emerging Nuclear Fuel Cycle Systems, GLOBAL'95*, page 1316, ANS, Versailles, France, September 11-14, 1995.

[58] G. Keepin, *Physics of nuclear kinetics*, Addison-Wesley,Reading,USA, 1965.

[59] J.F. Briesmeister, editor, MCNP – A general Monte Carlo N-Particle transport code, version 4C, Technical Report LA–13709–M, Los Alamos National Laboratory, USA, 2000.

[60] International handbook of evaluated criticality safety benchmark experiments, Technical Report NEA/NSC/DOC(95)03, OECD/NEA, 2003.

[61] M. Asty, A review of the collaborative programme on the European Fast Reactor (EFR) and on the CAPRA activities, in *27. meeting of the International Working Group on Fast Reactors*, IAEA-TECDOC-791, IAEA, Vienna, 1994.

[62] D. Wade and R. Hill, Progress in Nuclear Energy **31**, 13 (1997).

[63] K. Hesketh et al., Multiple recycle of plutonium in PWR - a physics code benchmark study by the OECD/NEA, in *Proceedings of the International Conference on Future Nuclear Systems, GLOBAL'97*, page 287, 1997.

[64] W. Bernnat et al., PWR benchmarks from OECD working party on physics of plutonium recycling, in *Proceedings of the International Conference on Evaluation of Emerging Nuclear Fuel Cycle Systems, GLOBAL'95*, page 627, ANS, Versailles, France, September 11-14, 1995.

[65] J. Kloosterman, Multiple recycling of plutonium in advanced PWRs, in *RECOD'98*, page 266, 1998.

[66] M. Delpech, Innovative fuel physics: Innovative concepts, in *Lecture notes: The 1999 Frédéric Joliot/Otto Hahn Summer School*, CEA/FZK, 1999.

[67] A. Puill and S. Aniel-Buchheit, Full MOX core for PWRs, in *Proceedings of the International Conference on Future Nuclear Systems, GLOBAL'97*, page 274, 1997.

[68] A. Puill et al., Mastery of the plutonium inventory in PWRs: The APA concept, in *Proceedings of the International Conference on Future Nuclear Systems, GLOBAL'99*, ANS, Jackson Hole, USA, August 29 - September 3, 1999.

[69] H. Golfier et al., Plutonium and minor actinide recycling in PWRs with new APA concepts, in *Proceedings of the International Conference on Future nuclear systems, GLOBAL 01*, Paris, France, September 9-13, 2001.

[70] A. Vasile et al., Feasibility studies of the CORAIL subassembly for Pu multi-recycling in PWRs, in *Proceedings of the International Conference on Future Nuclear Systems, GLOBAL 2003*, ANS, New Orleans, USA, November 16-20, 2003.

[71] G. Youinou et al., Plutonium management and multirecycling in LWRs using an enriched uranium support, in *Proceedings of the International Conference on Future Nuclear Systems, GLOBAL'99*, ANS, Jackson Hole, USA, 1999.

[72] G. Youinou et al., Plutonium and americium multirecycling in the European Pressurized Reactor (EPR) using slightly over-moderated U-235 enriched MOX fuel assemblies, in *Proceedings of the International Conference on Future Nuclear Systems, GLOBAL 2003*, ANS, New Orleans, USA, November 16-20, 2003.

[73] M. Delpech et al., Scenarios of plutonium and minor actinide recycling, in *Proceedings of the International Conference on Future Nuclear Systems, GLOBAL'97*, page 731, 1997.

[74] J. Kloosterman and H. Gruppelaar, Multi-recycling of actinides in thorium based fuels, in *Proceedings of the International Conference on Future Nuclear Systems, GLOBAL'99*, ANS, Jackson Hole, USA, August 29 - September 3, 1999.

[75] M. Delpech et al., The Am and Cm transmutation, physics and feasibility, in *Proceedings of the International Conference on Future Nuclear Systems, GLOBAL'99*, ANS, Jackson Hole, USA, August 29 - September 3, 1999.

[76] D. Haas et al., The EFTTRA European collaboration for development of fuels and targets for transmutation: Status of recent developments., in *Proceedings of the International Conference on Future Nuclear Systems, GLOBAL'99*, ANS, Jackson Hole, USA, August 29 - September 3, 1999.

[77] K. Richter et al., Journal of Nuclear Materials **249**, 121 (1997).

[78] R. Konings et al., Nuclear Science and Engineering **128**, 70 (1998).

[79] A. Conti et al., Long-lived fission product transmutation studies, in *Proceedings of the International Conference on Future Nuclear Systems, GLOBAL'99*, ANS, Jackson Hole, USA, August 29 - September 3, 1999.

[80] T. Mukaiyama et al., Minor actinide transmutation in fission reactors and fuel cycle considerations, in *Second international information exchange meeting*, page 320, OECD/NEA, 1992.

[81] L. Baetslé et al., Impact of advanced fuel cycles and irradiation scenarios of final disposal issues, in *Proceedings of the International Conference on Future Nuclear Systems, GLOBAL'99*, ANS, Jackson Hole, USA, August 29 - September 3, 1999.

[82] M. Salvatores et al., Nuclear Instruments and Methods in Physics Research **A414**, 5 (1998).

[83] A. Languille et al., CAPRA core studies - the oxide reference option, in *Proceedings of the International Conference on Evaluation of Emerging Nuclear Fuel Cycle Systems, GLOBAL'95*, page 874, ANS, Versailles, France, September 11-14, 1995.

[84] D. Leliévre, Nuclear science and technology – perspectives and costs of partitioning and transmutation of long-lived radionuclides, Technical Report EUR-17485, European Communities, 1996.

[85] N. Budylkin et al., Journal of Nuclear Materials **329-333**, 621 (2004).

[86] C. D. Raedt and L. Baetslé, Impact of high burnup irradiation and multiple recycling in fast burner reactors on the plutonium and minor actinide inventories, in *Proceedings of the International Conference on Evaluation of Emerging Nuclear Fuel Cycle Systems, GLOBAL'95*, page 922, ANS, Versailles, France, September 11-14, 1995.

[87] T. Mukaiyama, OMEGA program in Japan and ADS development in JAERI, in *Proceedings of the Third International Conference on Accelerator-Driven Transmutation Technologies and Applications, ADTTA'99*, Praha, Czech Republic, June 7-11, 1999.

[88] H. Murata and T. Mukaiyama, Atomkernenergie-Kerntechnik **45**, 23 (1984).

[89] D. Foster et al., Review of PNL study on transmutation processing of high level waste, Technical Report LA–UR–74–74, Los Alamos National Laboratory, USA, 1974.

[90] F. Venneri et al., The Los Alamos accelerator-driven transmutation of nuclear waste (ATW) concept - development of the ATW target/blanket system, in *Proceedings of the Second International Conference on Accelerator-Driven Transmutation Technologies and Applications*, page 758, Uppsala University, 1996.

[91] M. Mizumoto et al., Proton linac development for neutron science project, in *Proceedings of the Third International Conference on Accelerator-Driven Transmutation Technologies and Applications, ADTTA'99*, Praha, Czech Republic, June 7-11, 1999.

[92] C. Rubbia and J. Rubio, A tentative programme towards a full scale Energy Amplifier, Technical Report CERN/LHC/96–11(EET), 1996.

[93] M. Salvatores et al., Nuclear Science and Engineering **124**, 280 (1996).

[94] T. Sasa et al., Conceptual design study and code development for accelerator-driven transmutation system, in *Proceedings of the International Conference on Future Nuclear Systems, GLOBAL'97*, page 435, 1997.

[95] H. Oigawa et al., Research and development program on accelerator driven system in JAERI, in *Proceedings of the International Conference on Future Nuclear Systems, GLOBAL 2003*, ANS, New Orleans, USA, November 16-20, 2003.

[96] M. Viala et al., The SPIN program - assets and prospects, in *Proceedings of the International Conference on Future Nuclear Systems, GLOBAL'97*, page 706, 1997.

[97] M. Salvatores, Advanced options for transmutation strategies, in *Proceedings of the Fifth International Information Exchange Meeting on Actinide and Fission Product Partitioning and Transmutation*, OECD/NEA, Mol, Belgium, November 25-27, 1998.

[98] J. Garnier et al., Feasibility study of an advanced GFR, in *Proceedings of the International Conference on Future Nuclear Systems, GLOBAL 2003*, ANS, New Orleans, USA, November 16-20, 2003.

[99] A technology roadmap for Generation IV nuclear energy systems, Technical report, U.S. DOE Nuclear Energy Research Advisory Committee and the Generation IV International Forum, 2002.

[100] S. Pillon, Design of a moderated target for transmutation of americium, in *Proceedings of the Seventh Information Exchange Meeting on Actinide and Fission Product Partitioning and Transmutation*, OECD/NEA, Jeju, Korea, October 4-16, 2002.

[101] G. Imel et al., The TRADE experiment and progress, in *Proceedings of the International Conference on Future Nuclear Systems, GLOBAL 2003*, ANS, New Orleans, USA, November 16-20, 2003.

[102] C. Bowman et al., Nuclear Instruments and Methods in Physics Research **A320**, 336 (1992).

[103] W. Sailor et al., Progress in Nuclear Energy **28**, 359 (1994).

[104] F. Venneri, Disposition of nuclear waste using sub-critical accelerator driven systems, Technical Report LA-UR-98-985, Los Alamos National Laboratory, 1998.

[105] A roadmap for developing accelerator transmutation of waste (ATW) technology: A report to Congress, 1999.

[106] F. Carminati et al., An Energy Amplifier for cleaner and inexhaustible nuclear energy production driven by a particle beam accelerator, Technical Report CERN/AT/93–47(ET), CERN, 1993.

[107] C. Rubbia et al., Conceptual design of a fast neutron operated high power Energy Amplifier, Technical Report CERN/AT/95–44(ET), CERN, 1995.

[108] C. Rubbia et al., Fast neutron incineration in the Energy Amplifier as alternative to geologic storage: The case of Spain, Technical Report CERN/LHC/97–01(EET), 1997.

[109] H. A. Abderrahim et al., Nuclear Instruments and Methods in Physics Research **A463**, 487 (2001).

[110] H. Beaumont et al., Heterogeneous minor actinide recycling in the CAPRA high burnup core with target sub-assemblies, in *Proceedings of the International Conference on Future Nuclear Systems, GLOBAL'99*, ANS, Jackson Hole, USA, August 29 - September 3, 1999.

[111] J. Wallenius, Journal of Nuclear Materials **320**, 142 (2003).

[112] K. Richter and C. Sari, Journal of Nuclear Materials **184**, 167 (1991).

[113] H. Matzke, *Science of Advanced LMFBR fuels*, North-Holland, 1986.

[114] R. Margevicius, AFC fuels development update: 2003 semi-annual meeting, LA-UR-03-0415, Los Alamos National Laboratory, 2003.

[115] M. Takano et al., Study on the stability of AmN and (Am,Zr)N, in *Proceedings of the International Conference on Future Nuclear Systems, GLOBAL 2003*, ANS, New Orleans, USA, November 16-20, 2003.

[116] M. Jolkkonen, M. Streit, and J. Wallenius, Journal of Nuclear Science and Technology **41**, 457 (2004).

[117] M. Akabori et al., in *International symposium on nitride fuel cycle technology*, JAERI, Tokai-mura, August 2004.

[118] B. Rogozkin, N. Stepennova, and A. Proshkin, Atomnaya Energiya **95**, 208 (2003).

[119] Y. Suzuki and Y.Arai, Journal of Alloys and Compounds **271–273**, 577 (1998).

[120] Y. Arai et al., J. Nucl. Mater. **195**, 37 (1992).

[121] J. Wallenius and S. Pillon, N-15 requirement for 2nd stratum ADS nitride fuels, in *AccApp'01 & ADTTA'01 Nuclear Applications in the New Millennium*, ANS, Reno, USA, November 11-15, 2001.

[122] N. Cocuaud et al., Inert matrices, uranium-free plutonium fuel and americium target. Synthesis of CAPRA, SPIN, EFTTRA studies, in *Proceedings of the International Conference on Future Nuclear Systems, GLOBAL'97*, page 1044, 1997.

[123] J. Wallenius, CONFIRM: status and perspectives, in *Eight international information exchange meeting on P&T*, OECD/NEA, Las Vegas, November 2004.

[124] M. Mignanelli, Stability of U and U,Zr nitrides at high temperatures, in *CONFIRM progress meeting, 27-28 September 2001.*

[125] M. Streit et al., Journal of Nuclear Materials **319**, 51 (2003).

[126] M. Streit, Personal communication, 2004.

[127] G. Hofman et al., Progress in Nuclear Energy **31**, 83 (1997).

[128] C. Degueldre and J. Paratte, Journal of Nuclear Materials **274**, 1 (1999).

[129] N. Chauvin et al., Optimisation of minor actinide fuels for transmutation in conventional reactors (PWR, FR), in *Proceedings of the International Conference on Future Nuclear Systems, GLOBAL'99*, ANS, Jackson Hole, USA, August 29 - September 3, 1999.

[130] H. Matzke et al., Journal of Nuclear Materials **274**, 47 (1999).

[131] R. Konings et al., Journal of Nuclear Materials **274**, 84 (1999).

[132] A. Languille et al., Journal of Alloys and Compounds **271–273**, 517 (1998).

[133] J. Kloosterman and P. Damen, Journal of Nuclear Materials **274**, 112 (1999).

[134] J. Wallenius and M. Eriksson, Neutronic design of sub-critical minor actinide burners, submitted to Nuclear Technology, 2004.

[135] N. Novikova, Y. Pashkin, and V. Chekunov, Some features of sub-critical blankets cooled with lead-bismuth, in *Proceedings of the Third International Conference on Accelerator-Driven Transmutation Technologies and Applications, ADTTA'99*, Praha, Czech Republic, June 7-11, 1999.

[136] A. Rousanov et al., Developing and studying the cladding steels for the fuel elements of the NPIs with heavy coolant, in *Proceedings of the Conference Heavy liquid metal coolants in nuclear technology, HLCM'98*, Institute of Physics and Power Engineering, Obninsk, Russia, October 5-9, 1998.

[137] F. Barbier and A. Rusanov, Journal of Nuclear Materials **296**, 231 (2001).

[138] D. Pankratov et al., Polonium problem in nuclear power plants with lead-bismuth as a coolant, in *Proceedings of the Conference Heavy liquid metal coolants in nuclear technology, HLCM'98*, Institute of Physics and Power Engineering, Obninsk, Russia, October 5-9, 1998.

[139] T. Mihara, Y. Tanaka, and Y. Enuma, Conceptual design studies on various types of HLMC fast reactor plants, in *Power reactors and sub-critical blanket systems with lead and lead-bismuth as coolant and/or target material. Utilization and transmutation of actinides and long lived fission products*, IAEA-TECDOC-1348, 2003.

[140] N. Cannon et al., Transient and static mechanical properties of D9 fuel pin cladding and duct material irradiated to high fluence, in *Effects of Radiation on Materials: 15$^{\text{th}}$ International Symposium, ASTM STP 1125*, edited by R. Stoller, A. Kumar, and D. Gelles, American Society for Testing and Materials, Philadelphia, USA, 1992.

[141] J. Séran et al., Behaviour under neutron irradiation of the 15-15Ti and EM10 steels used as standard materials of the pénix fuel subassembly, in *Effects of Radiation on Materials: 15$^{\text{th}}$ International Symposium, ASTM STP 1125*, edited by R. Stoller, A. Kumar, and D. Gelles, American Society for Testing and Materials, Philadelphia, USA, 1992.

[142] S. Porollo et al., Journal of Nuclear Materials **329-333**, 314 (2004).

[143] B. Gromov et al., The analysis of operating experience of reactor installations using lead-bismuth coolant and accidents happened, in *Proceedings of the Conference Heavy liquid metal coolants in nuclear technology, HLMC'98*, Institute of Physics and Power Engineering, Obninsk, Russia, October 5-9, 1998.

[144] H. Khalil and R. Hill, Nuclear Science and Engineering **109**, 221 (1991).

[145] T. Hamid and K. Ott, Nuclear Science and Engineering **113**, 109 (1993).

[146] H. Choi and T. Downar, Nuclear Science and Engineering **133**, 1 (1999).

[147] P. Hejzlar, M. Driscoll, and M. Kazimi, Nuclear Science and Engineering **139**, 138 (2001).

[148] T. Takizuka et al., Studies on accelerator driven transmutation systems, in *Proceedings of the Fifth international information exchange meeting*, page 383, OECD/NEA, Mol, Belgium, November 25-27, 1998.

[149] W. Maschek et al., Safety analyses for ADS cores with dedicated fuel and proposals for safety improvements, in *Proceedings of the IAEA Technical Committee Meeting on Core Physics and Engineering Aspects of Emerging Nuclear Energy Systems for Energy Generation and Transmutation, IAEA-TECDOC-1356*, Argonne National Laboratory, USA, November 28 - December 1, 2000.

[150] M. Eriksson et al., Safety analysis of Na and Pb-Bi coolants in response to beam instabilities, in *Proceedings of the Third International Workshop on Utilisation and Reliability of High Power Proton Accelerators*, Santa Fe, USA, May 2002.

[151] K. Tuček et al., IAEA accelerator driven system neutronic benchmark, in *Feasibility and motivation for hybrid concepts for nuclear energy generation and transmutation*, IAEA–TC–903.3, 1998.

[152] M. Chadwick et al., Nuclear Science and Engineering **131**, 293 (1999).

[153] Y. Kim, W. S. Park, T. Y. Song, and C. K. Park, Nuclear Science and Engineering **143**, 141 (2003).

[154] R. MacFarlane and D. Muir, *The NJOY nuclear data processing system, version 91*, LA-12740-M, Los Alamos National Laboratory, USA, 1994.

[155] S. Kessler, Nuclear Science and Engineering **117**, 254 (1994).

[156] J. Cetnar et al., Transmutation calculations with Monte Carlo continuous energy burnup system MCB, in *Proceedings of the Third International Conference on Accelerator-Driven Transmutation Technologies and Applications, ADTTA'99*, Praha, Czech Republic, June 7-11, 1999.

[157] R. Cahn, P. Haasen, and E. Kramer, *Materials Science and Technology: a comprehensive treatment*, volume 10A, VCH, 1994.

Paper I

K. Tuček, J. Wallenius, and W. Gudowski
Coolant void worth in fast breeder reactors and accelerator-driven transuranium and minor-actinide burners
Annals of Nuclear Energy, **31**, 1783 (2004)

Coolant Void Worth in Fast Breeder Reactors and Accelerator-Driven Transuranium and Minor-Actinide Burners

Kamil Tuček*, Janne Wallenius, and Waclaw Gudowski

Royal Institute of Technology, Dept of Nuclear & Reactor Physics, SE-106 91 Stockholm, Sweden

Abstract – *Liquid metal coolant void worths have been calculated as a function of fuel composition and core geometry for several model fast breeder reactors and accelerator-driven systems. The Monte Carlo transport code MCNP with continuous energy cross-section libraries was used for this study. With respect to the core void worth, lead/bismuth cooled FBRs appear to be inferior to those employing sodium for pitch-to-diameter ratios exceeding 1.4. It is shown that in reactor systems cooled by lead/bismuth eutectic, radial steel pin reflector significantly lowers the void worth. The void worth proves to be a strong function of the fuel composition, reactor cores with high content of minor actinides in fuel exhibiting larger void reactivities than systems with plutonium based fuel. Enlarging the lattice pitch in ADS burners operating on Pu rich fuel decreases the void worth while the opposite fact is true for ADSs employing americium based fuels.*

I. INTRODUCTION

A number of innovative reactor systems for transmutation of plutonium and minor actinides were proposed in last decades [1, 2]. Fuels utilised in these reactors have low uranium content or are completely U-free, and the systems are usually conceived to operate on fast neutron spectrum. The presence of americium leads to a decrease in Doppler reactivity coefficient and delayed neutron fractions, raising significant safety concerns [3]. It was therefore suggested that sub-critical reactor systems should be implemented in fuel cycles involving recycling of minor actinides. For this purpose, accelerator-spallation [4,5] and deuterium-tritium fusion neutron sources [6–8] were both envisioned. Additional reactivity margin is hence provided in sub-critical systems, limiting the influence of reactivity coefficients and allowing steady-state operation of the system. However, it has appeared that such MA-fuelled ADS have a potential for rapid reactivity excursions following loss of coolant from the core, which may lead to fuel failure and core disruption [9, 10].

Therefore, it is necessary to provide a fuel and core design that minimises conceivable reactivity insertions in the standard set of design basis accidents. In this parametric study, we investigate coolant void worth for series of fast breeder and accelerator-driven system (ADS) configurations with aim to identify suitable core and fuel design parameters.

First, we discuss physical mechanisms involved in coolant voiding. Then, we perform scoping studies of Δk_∞ in two-dimensional pin lattices for several fuel compositions and wide range of pitches. Finally, we investigate the coolant void worth in various types of model critical & ADS transmutation systems, employing nitride and oxide fuel, different types of inert matrices and two types of coolants - lead/bismuth and sodium. Void reactivity is studied as a function of core geometry parameters as e.g. reactor lattice pin pitch and fuel pin design. The optimal pin pitch is then identified for each configuration. Finally, we discuss the implications of our results for ADS core design in general.

II. VOIDING MECHANISM

The occurrence of void in the core can be a result of following events

- fuel pin rupture, releasing fission gases and helium into the core,
- blow-down of steam from ruptured steam generator,
- coolant boiling,
- blow-down of bubbles from gas injection system [11].

We note, that in sodium cooled systems undercooling can result in coolant boiling prior any significant damage to the fuel, clad, or structural material is inflicted. On the other hand, due to the high boiling temperatures of lead and lead/bismuth (Pb: T_b= 2023 K; Pb/Bi: T_b= 1943 K), coolant boiling in these systems occurs first *after* the integrity of reactor core is lost, rendering such events to the realm of beyond-design basis accident analyses.

*E-mail: kamil@neutron.kth.se

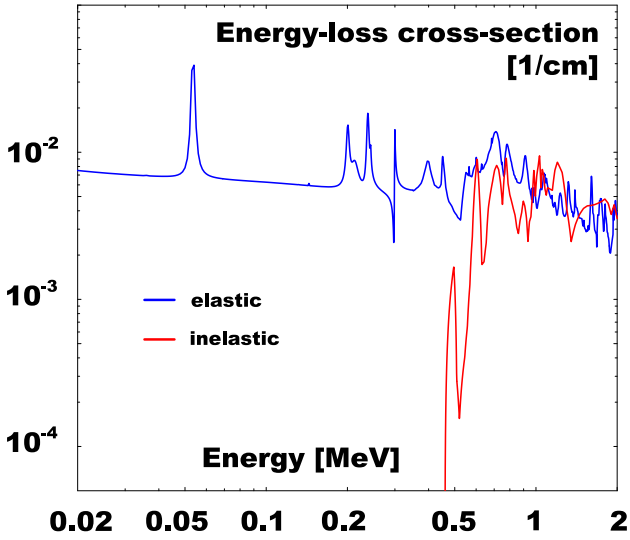

Fig. 1. Energy-loss cross-section for ^{23}Na. Data from JEF2.2 library were used. Macroscopic scattering cross-sections were taken at T = 600 K.

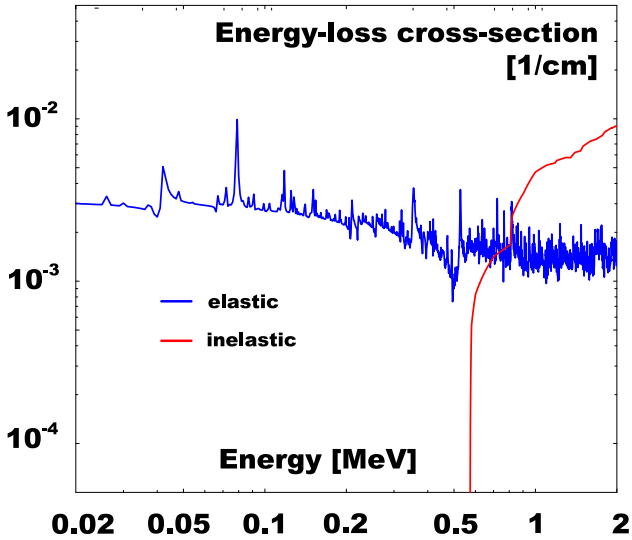

Fig. 2. Energy-loss cross-section for natural lead. Cross-section data were taken from ENDFB/VI-8 cross-section library. Σ_{el} and Σ_{inel} at T = 600 K were used.

The void worth and void reactivity coefficient are the major safety parameters, determining permissive maximum criticality level of the system (k_{eff}).

II.A. Phenomena occurring during the voiding

The physical effects associated with coolant voiding are

- reduction of neutron moderation (spectral hardening), increasing fission probabilities of even neutron number actinides
- reduction of neutron capture in fuel, coolant, and cladding.

The coolant void worth is the difference in the k-eigenvalue between the flooded and voided state

$$W = \Delta k_{\mathrm{eff}} = k_{\mathrm{eff}}^{\mathrm{void}} - k_{\mathrm{eff}}^{\mathrm{flood}} = \quad (1)$$

$$= \overline{\nu}_{\mathrm{void}} L_{\mathrm{f}}^{\mathrm{void}} - \overline{\nu}_{\mathrm{flood}} L_{\mathrm{f}}^{\mathrm{flood}}. \quad (2)$$

where L_{f} is neutron loss to fission in one neutron generation for respective core state - flooded or voided.

In fast neutron systems, the average fission neutron yield can be considered as constant ($\overline{\nu} \equiv \overline{\nu}_{\mathrm{flood}} \simeq \overline{\nu}_{\mathrm{void}}$). Then,

$$W = \overline{\nu}\ (L_{\mathrm{f}}^{\mathrm{void}} - L_{\mathrm{f}}^{\mathrm{flood}}), \quad (3)$$

from which follows that $W = \overline{\nu} \Delta L_{\mathrm{f}}$.

The neutron balance equation for *one neutron fission generation* in an eigenstate can be written as

$$1 + C_{\mathrm{x}} = L_{\mathrm{c}} + L_{\mathrm{e}} + L_{\mathrm{f}} + L_{\mathrm{x}}, \quad (4)$$

where L_{x} denotes the neutron loss rate in non-fission multiplication reactions, $C_{\mathrm{x}} = \overline{\nu_{\mathrm{x}}} L_{\mathrm{x}}$ is the neutron creation rate in non-fission multiplication reactions, $\overline{\nu_{\mathrm{x}}}$ is the average neutron yield in non-fission multiplication reactions ($\overline{\nu_{\mathrm{x}}} \simeq 2$), L_{e} denotes the loss rate to leakage, L_{c} the loss rate to capture reactions, and L_{f} is the loss rate to fission.

Upon coolant voiding, $\Delta C_{\mathrm{x}} \leq 10^{-3}$ in most of the cases yielding $\Delta L_{\mathrm{f}} + \Delta L_{\mathrm{c}} + \Delta L_{\mathrm{e}} \sim 0$. In the infinite pin lattice 2-D model (L_{e} = 0), the coolant void worth can be subsequently decomposed as

$$W = \overline{\nu} \cdot \Delta L_{\mathrm{f}} = -\overline{\nu}(\Delta L_{\mathrm{c}}^{\mathrm{fuel}} + \Delta L_{\mathrm{c}}^{\mathrm{coolant}} + \Delta L_{\mathrm{c}}^{\mathrm{clad}}). \quad (5)$$

where $L_{\mathrm{c}}^{\mathrm{fuel}}$, $L_{\mathrm{c}}^{\mathrm{coolant}}$, and $L_{\mathrm{c}}^{\mathrm{clad}}$ is neutron capture rates to fuel, coolant, and cladding, respectively.

In realistic three dimensional core configurations, the void worth is given by

$$W = -\overline{\nu}(\Delta L_{\mathrm{c,fuel}} + \Delta L_{\mathrm{c,coolant}} + \Delta L_{\mathrm{c,clad}} + \quad (6)$$

$$\Delta L_{\mathrm{e}} - \Delta G_{\mathrm{x}}), \quad (7)$$

where L_{e} quantifies a rate of neutron leakage from the system, and G_{x} = C_{x} - L_{x} is the neutron gain from non-fission multiplication reactions. The neutron balance equation is evaluated for the whole geometry inclusive reflectors and plena.

II.B. Cross-sections

In order to apprehend the nature of neutron slowing-down process in coolant due to the elastic and inelastic scattering,

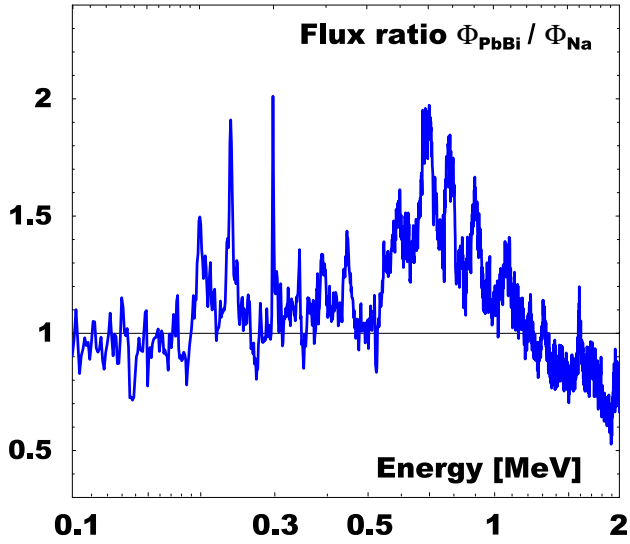

Fig. 3. The neutron spectrum of lead-bismuth cooled system relative to that cooled by sodium with the same geometry and fuel composition.

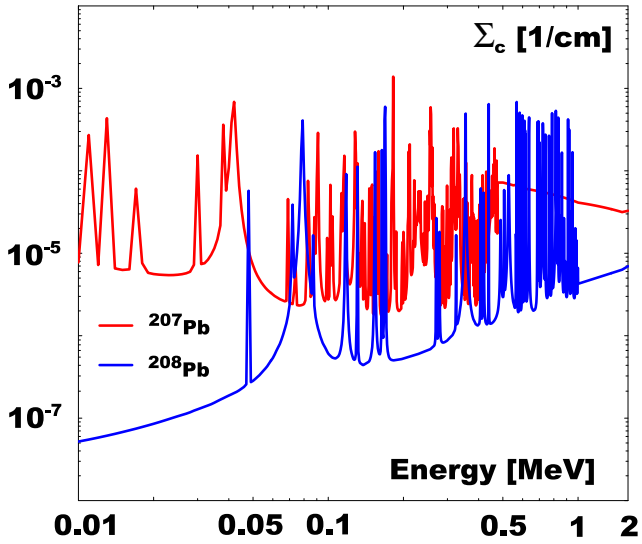

Fig. 4. Macroscopic capture cross-section of ^{207}Pb and ^{208}Pb. ENDFB/VI-8 cross-section library data were used.

we define the energy-loss cross-section as

$$\overline{\Sigma_{\Delta E}} \equiv \frac{\Sigma_{\rm el}\overline{\Delta E_{\rm el}} + \Sigma_{\rm inel}\overline{\Delta E_{\rm inel}}}{E}, \qquad (8)$$

where

$$\overline{\Delta E_{\rm el}} = \frac{1}{2}\left(1-\alpha\right)E_{\rm n}, \;\; \alpha = \left(\frac{A-1}{A+1}\right)^2 \qquad (9)$$

and

$$\overline{\Delta E_{\rm inel}} = E_{\rm n} - \left(\frac{A}{A+1}\right)^2\left[E_{\rm n} - Q\frac{A+1}{A}\right] \qquad (10)$$

is the average energy loss in elastic scattering and inelastic scattering, respectively; Q denotes the excited energy levels of the target nuclei, $E_{\rm n}$ is the neutron energy, and A is the target nucleus mass number.

The energy-loss cross-section for sodium decomposed into the contributions from elastic and inelastic scattering is displayed in Figure 1. We observe that for the energy region below 500 keV, neutron slowing down is dominated by elastic collisions, while in-between 0.7-2 MeV inelastic scattering becomes about equally effective.

In Figure 2, the same comparison is made for natural lead. We note that energy-loss cross-section due to the elastic scattering is significantly smaller than for sodium in whole energy range investigated. However, due to the presence of several thresholds for inelastic scattering in the energy interval from 0.57 to 2 MeV, the energy loss in inelastic scattering is notably larger than for sodium. The neutron spectrum of lead and lead/bismuth cooled reactors will be thus somewhat suppressed for energies above 1 MeV comparing with Na-cooled systems having the same geometry, see Figure 3. For sodium, the magnitude of neutron spectrum relative to lead/bismuth is suppressed in the energy region of 0.7-1.5 MeV where contributions to the neutron slowing down from elastic and inelastic scattering reactions merely equal.

We further note that within the range the ^{206}Pb features a number of threshold levels, while the threshold for inelastic scattering of the doubly magic isotope ^{208}Pb is well above 2 MeV, see Table I.

One could therefore theoretically consider to enrich lead in ^{208}Pb. With energy-loss cross-section remaining below 0.003 cm^{-1}, a very hard neutron spectrum can be attained. As also the capture cross-section of ^{208}Pb is low in comparison to other isotopes, see Figure 4, such a coolant would yield a very small void worth [12].

II.C. Calculation methodology

Our study of void reactivity is performed as a function of core geometry: reactor lattice pin pitch and fuel pin design parameters. Two types of fuel actinide isotopic compositions have been studied: corresponding to an immediate (four years of cooling), and somewhat delayed (30 years of cooling) use of spent LWR UOX fuel. The plutonium and americium vectors applied in our studies are presented in Table II.

The void worth is typically a relatively small difference between two large terms, critically depending on a correct description of geometry as well as transport slowing-down and

TABLE I

Threshold energies for inelastic scattering of heavy metal coolants used in the study. ^{206}Pb has further five excited energy levels yielding threshold energies below or close to 2 MeV limit: 1474, 1692, 1713, 1793, and 2008 keV.

Nuclide	Abundance	Threshold energies [keV]		
		1^{st}	2^{nd}	3^{rd}
^{23}Na	100%	459.1	2166	2495
^{206}Pb	24.1%	806.9	1171	1347
^{207}Pb	22.1%	572.5	902.1	1641
^{208}Pb	52.4%	2628	3213	3492
^{209}Bi	100%	900.6	1617	2455

TABLE II

Pu and Am vectors used in the investigations. The compositions correspond to those found in spent LWR UOX fuel with an averaged burnup of 41.2 GWd/tHM; fuel cooling time is 4 and 30 years, respectively.

Isotope	Cooling time	
	4 years	30 years
^{238}Pu	0.024	0.020
^{239}Pu	0.520	0.521
^{240}Pu	0.226	0.229
^{241}Pu	0.119	0.035
^{242}Pu	0.065	0.064
^{241}Am	0.030	0.114
^{243}Am	0.016	0.017

capture cross-sections properly adjusted for change in self-shielding. Hence, we used the Monte Carlo code MCNP, version 4C3 [13], for the present study. The estimation of neutron creation and loss rates is performed exclusively in the eigenstate as modelled by MCNP KCODE mode. A temperature adjusted version of the JEF2.2 cross-section library is applied.

We start by evaluating the void worth in an infinite triangular fuel pin lattice for three heavy metal coolant candidates - sodium, lead, and lead/bismuth eutectic. Fuels with different fractions of plutonium and minor actinide, relevant for use in accelerator-driven systems, are analysed. The impact of fast fission threshold for even neutron number nuclides is thus assessed.

In the 3-D reactor model, we further evaluate the effect of neutron leakage from the core on the void worth. The reactor core, axial plena, and bottom plenum spacer regions are modelled pin-by-pin, while materials were smeared in axial and radial reflectors, as well as in ADS target region. For simplicity, a ductless fuel assembly design is assumed. The target region consists of Pb/Bi eutectic, steel structures contain 90 at% iron and 10 at% chromium. For individual components

TABLE III

Reference system, pin, and pellet design specifications. A triangular pin lattice is adopted.

Pellet density (% TD)	0.85
Pellet outer radius R_{fuel} (mm)	2.4
Clad inner radius R_{gap} (mm)	2.5
Clad outer radius R_{pin} (mm)	3.0
Active pin length (cm)	100
Length of upper fission gas plenum (cm)	150
Length of lower fission gas plenum (cm)	10
Length of bottom plenum spacer (cm)	10
Length of radial reflector S/As (cm)	140
Thickness of radial reflector (cm)	150
Length of upper reflector (cm)	200
Length of lower reflector (cm)	230
ADS target radius (cm)	20
Radius of accelerator beam tube (cm)	15
Distance of target window from centreplane (cm)	20

TABLE IV

Atomic fractions of metallic elements in fuels investigated in the elementary cell analyses.

Element	$(U,Pu)O_2$	$(TRU,Zr)N$	$(MA,Zr)N$
U	0.750	–	–
Pu	0.250	0.165	0.133
Am	–	0.035	0.267
Zr	–	0.800	0.600

of the heterogeneous design, average stead-state temperatures are assumed: 1500 K for fuel, 900 K for pin clad in the core, and 600 K for coolant and steel structures of plena, spacer, target, and reflectors.

The model parameters as used in the calculations are summarised in Table III. The total core power was set to 800 MW_{th}. The assumed linear power of 30 kW/m then corresponds to cores with $\sim$26700 fuel pins.

A homogeneous, single zone core configuration is assumed in all cases. In this context, we note that core heterogeneity significantly alters the coolant void reactivity [14]. The results of this study should be thus considered rather as qualitative, in terms of a relative intercomparison of the void worths in-between different design options.

III. RESULTS

Three types of fuel are used for our analyses: standard FBR fuel $(U,Pu)O_2$, a plutonium based - TRU mononitride fuel (TRU,Zr)N, and minor actinide based fuel (MA,Zr)N,

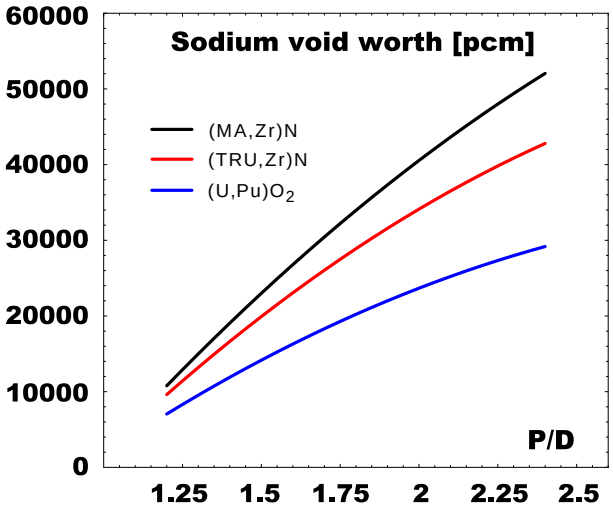

Fig. 5. Sodium void worth in an infinite pin lattice with a pin diameter of 6 mm.

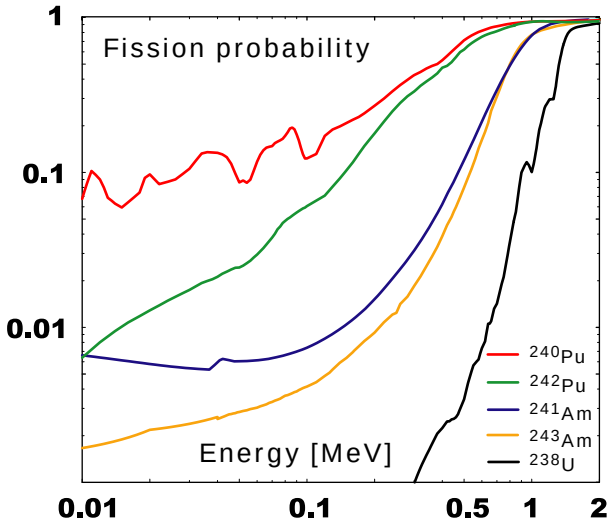

Fig. 6. Fission probability $\sigma_{\rm f}/\sigma_{\rm a}$ of even neutron number actinides.

relevant for ADS minor actinide burners operating in double-strata incineration scheme. An inert matrix has to be added to the fuel in order to compensate for high fuel reactivity and achieve an reasonably good stability at high temperature. In our studies we have chosen ZrN as a representative inert matrix material. In order to reduce production of ^{14}C, the use of nitride fuel with 99% ^{15}N enrichment is foreseen.

III.A. Elementary cell analysis

The void worth was analysed in an infinite pin lattice geometry, examining effects of changes in spectral and capture gradient. The relative fractions of metals in the fuel is given in Table IV. In Figure 5, the void worth for three types of fuel

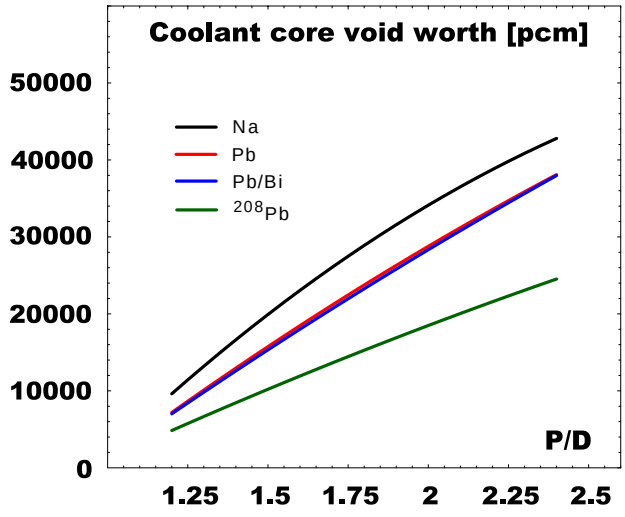

Fig. 7. Void worth in an infinite pin lattice of a system employing (TRU,Zr)N fuel. Four types of coolant were investigated - sodium, lead/bismuth, lead, and ^{208}Pb. ENDFB/VI-8 cross-section library data were used for ^{208}Pb.

are displayed as a function of pitch-to-diameter ratio. We note that, as expected, the void worth increases with increasing fraction of higher actinides in the fuel; the difference being most significant for high pin pitches. Results of pin lattice sodium void worth decomposed into individual components are displayed in Table V. The values given in the table corresponds to P/D = 2.0, in order to emphasise any effect of reduced capture in the coolant, should it be significant.

We observe that the main contribution to the void worth is a reduction in fuel capture rate, with concurrent increase of fission probability of even neutron number actinides, see Figure 6. While capture reduction in the fuel provides about 76% of the void worth in TRUN fuel, it is more then 93% for the fuel containing 60% of minor actinides. We further note that the spectral gradient accompanying removal of the coolant from a lattice is strongest for (MA,Zr)N fuel. The capture rate in the cladding is less significant and constitutes less than 10% of the void worth.

In Table VI, we illustrate the effect of increasing the pin pitch on the void worth. Comparing with Table V, one may note that the contribution of the coolant capture reduction to the void worth is significantly higher for Pb/Bi than for sodium, for same P/D. With increasing P/D ratio, understandably, the relative contribution of coolant capture rate reduction to the void worth increases. Even for P/D=1.2, 41% of the LBE void worth constitutes of $\Delta L_{\rm c,cool}$.

The void worth of lead is very similar to that of lead/bismuth for the whole range of pitches investigated, see Figure 7. Both heavy metals - lead and lead/bismuth - feature

TABLE V

Infinite pin lattice void worth analyses. Sodium void worth was decomposed into the individual constituents. Pitch-to-diameter ratio is 2.0. The neutron loss rates are normalised per one fission neutron generation.

Fuel	$\Delta L_{\rm f}$	$\Delta L_{\rm c,fuel}$	$\Delta L_{\rm c,cool}$	$\Delta L_{\rm c,clad}$	- $\Delta L_{\rm c,fuel}/\Delta L_{\rm f}$	$(\frac{\sigma_{\rm f}}{\sigma_{\rm a}})_{\rm voided}/(\frac{\sigma_{\rm f}}{\sigma_{\rm a}})_{\rm flooded}$
(U,Pu)O_2	+ 0.078	-0.059	-0.012	-0.007	0.76	1.20
(TRU,Zr)N	+ 0.108	-0.090	-0.011	-0.007	0.83	1.22
(MA,Zr)N	+ 0.119	-0.111	-0.005	-0.003	0.93	1.33

TABLE VI

Void worth analyses in an infinite pin lattice employing lead/bismuth coolant, and (TRU,Zr)N fuel; Pu/Am fraction was kept at 4/1. The neutron loss rates are normalised per one fission neutron generation.

P/D	$\Delta L_{\rm f}$	$\Delta L_{\rm c,fuel}$	$\Delta L_{\rm c,cool}$	$\Delta L_{\rm c,clad}$	- $\Delta L_{\rm c,fuel}/\Delta L_{\rm f}$	- $\Delta L_{\rm c,cool}/\Delta L_{\rm f}$
1.2	+ 0.022	-0.012	-0.009	-0.001	0.55	0.41
1.6	+ 0.057	-0.027	-0.028	-0.002	0.47	0.49
2.0	+ 0.090	-0.039	-0.048	-0.003	0.43	0.53
2.4	+ 0.121	-0.047	-0.070	-0.004	0.39	0.59

very similar neutronic characteristics and we therefore further focus in our studies only on systems cooled by sodium and lead/bismuth eutectic.

Due to its low moderating power, lead enriched in double-magic isotope ^{208}Pb displays very low void worths. We note, however, that lead enrichment process is not realistically feasible.

III.B. Critical 3-D systems

The importance of enhanced leakage becomes apparent when observing the void worth in realistic system configurations, see Figure 8. In Table VII and Figure 9, we display the coolant void worth as a function of pitch-to-diameter ratio for a model critical fast reactor employing (U,Pu)O_2 fuel cooled by sodium and lead/bismuth. In the case of the Pb/Bi-cooled core, we investigate two different radial reflector configurations

a) similar to the one used for sodium cooled system, i.e. consisting of steel pins, immersed in the coolant; coolant volume ratio being 20 vol%,

b) with the whole radial reflector region filled by lead/bismuth eutectic only. Such radial reflector configurations have been proposed in a number of studies [15].

In contrast to the standard notion of the leakage term [16], $L_{\rm e}$ in our case denotes those neutrons leaking out of the *whole reactor system* to the surrounding shielding. We note that the probability of these neutrons to enter the core and induce fission is rather remote and these neutrons can be effectively perceived as captured in clad and capture material of reflector. The reason why we list the leakage component separately in our study is thus merely phenomenological.

In our model, the effect of the enhanced neutron leakage *from the core* upon coolant voiding is thus exhibited as a change in the capture of neutrons in coolant and structural material of plena and reflectors. Hence, in contrast to the infinite pin lattice analyses the changes in the capture probability in clad introduces a *negative* reactivity upon coolant voiding.

We note that the spectrum hardening responsible for reduction of neutron parasitic capture in fuel is the only source inserting positive reactivity into the system in the case of sodium. With increasing pitches we observe both reduction of the neutron capture probability in the fuel as well as its gradual increase in coolant and clad material of plena & reflectors. The probability of neutrons to leak out the reactor system increases consequently with increasing pitches too, though not as strongly as the coolant capture term. For P/D > 1.6, the coolant & clad capture and leakage terms together increase faster than the neutron capture probability in fuel is reduced, leading to a subsequent decrease of the void worth.

In comparison to sodium cooled system, the reduction of neutron capture in Pb/Bi during coolant voiding for the core with radial steel pin reflector introduces positive reactivity to the system. The negative reactivity feedback is then supplied mainly due to the increase of neutron capture in the *structural material of reflector*. However, this negative feedback is not able to compensate for the total reduction in fuel & coolant capture rates. Adding smaller leakage, in comparison to sodium, Pb/Bi-cooled FBRs thus yield higher void worths than systems cooled by sodium, for P/D larger than 1.4!

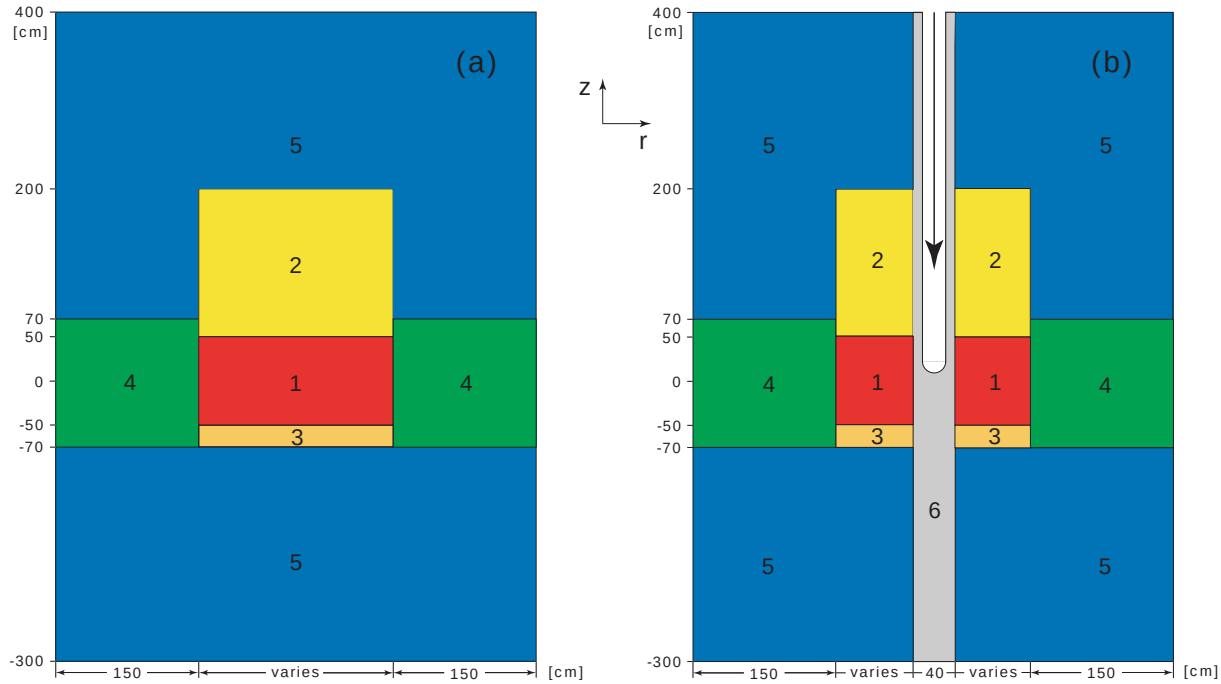

Fig. 8. R-z view of critical (a) and sub-critical (b) reactor model configurations. The regions are 1−core, 2−upper fission gas plenum, 3−lower fission gas plenum & bottom plenum spacer, 4−radial reflector, 5−axial reflector, and 6−target. Axial reflector and bottom plenum spacer regions are filled by their respective core's coolant. The spallation target consists of lead/bismuth eutectic.

When the steel pin reflector is replaced by Pb/Bi, the only significant effect introducing negative reactivity to the systems is the increased neutron capture in coolant and surrounding reactor shielding material (manifested in our study as an increased leakage term L_e). This results in excessive void worths even for large pitch-to-diameter ratios.

One could therefore supply an absorbing material into the core reflector in order to increase the neutron capture upon coolant voiding and consequently reduce void worth.

The leakage effect itself becomes significantly pronounced when the upper plenum is voided together with the reactor core, providing more than 40% of the negative reactivity upon coolant voiding.

III.C. ADS

The void worth was further studied in realistic models of accelerator-driven systems for fuel compositions relevant for transmutation purposes.

Figure 10 shows coolant void worth for TRU fuels having a fixed inert matrix fraction, a condition which might be imposed by reasons of high temperature stability or fabricability [3]. In order to keep k_{eff} constant, the Pu/Am ratio is hence varied as a function of P/D. We note that the absolute value of the core void worth is a factor of 2-3 higher than for FBRs utilising (U,Pu)O_2 fuel. However, on the contrary to the situation in the FBR, lead/bismuth yields *lower* core void worth than sodium for pitch-to-diameter ratios less than 2.3!

A dramatic change in core void worth behaviour with respect to increasing P/D is observed when the Pu/Am ratio in fuel is kept constant at Pu/Am = 2/3, corresponding to the equilibrium fraction of fuel in MA-ADS burner in double-strata scheme [17]. In this case, the enhanced neutron leakage and capture in structural material are not able to compensate for reduction of neutron capture rate in the fuel and coolant, causing core void reactivity to grow with P/D, see Figure 11. A similar behaviour was also observed for solid solution oxide fuels [18].

In Figure 12, the change in reactivity while voiding both core & upper plenum is compared to the core void worth. In this case, neutron leakage is enhanced proportionally to P/D, reducing the void worth by several thousands of pcm (for standard size pitch-to-diameter ratio equal to 1.6, by more than 2000 pcm). W however remains positive, even for P/D=2.4.

Figure 13 displays results of the void worth calculations in a TRU-ADS burner cooled by lead/bismuth eutectics for two pin diameters, 6 and 8 mm. The ratio of Pu/Am is kept at 4/1, corresponding to a case when all Pu from the LWRs is directed to the ADS, a so called two component scenario. The relative fraction of MA in fuel is small and the increase in

TABLE VII

Void worth analyses in a model fast-breeder reactor, for sodium and lead/bismuth coolant with (U,Pu)O_2 fuel. $\Delta L_{\mathrm{c,clad}}$ includes capture in the structural material of the reflectors. Note that $\Delta G_{\mathrm{x}} = \Delta C_{\mathrm{x}} - \Delta L_{\mathrm{x}} < 10^{-3}$.

Coolant	P/D	Atomic fraction Pu/(U + Pu)	ΔL_{f}	$\Delta L_{\mathrm{c,fuel}}$	$\Delta L_{\mathrm{c,cool}}$	$\Delta L_{\mathrm{c,clad}}$	ΔL_{e}	ΔG_{x}
Na	Core void worth							
	1.2	17%	+0.0076	-0.0281	+0.0063	+0.0123	+0.0037	+0.0002
	1.6	22%	+0.0096	-0.0689	+0.0181	+0.0316	+0.0105	+0.0001
	2.0	27.5%	+0.0071	-0.0908	+0.0265	+0.0428	+0.0156	+0.0006
	2.4	33%	+0.0035	-0.1048	+0.0323	+0.0487	+0.0197	+0.0006
	Core & upper plenum void worth							
	2.0	27.5%	-0.0166	-0.1282	+0.0471	+0.0397	+0.0598	+0.0006
Pb/Bi	Core void worth, radial reflector with steel pins							
	1.2	16%	+0.0058	-0.0247	-0.0036	+0.0211	+0.0008	-0.0003
	1.6	19%	+0.0107	-0.0506	-0.0088	+0.0471	+0.0023	-0.0006
	2.0	22.5%	+0.0114	-0.0709	-0.0129	+0.0677	+0.0039	+0.0006
	2.4	26%	+0.0112	-0.0804	-0.0172	+0.0819	+0.0053	-0.0008
	Core void worth, Pb/Bi radial reflector							
	2.0	22%	+0.0216	-0.0555	+0.0124	+0.0060	+0.0163	-0.0006

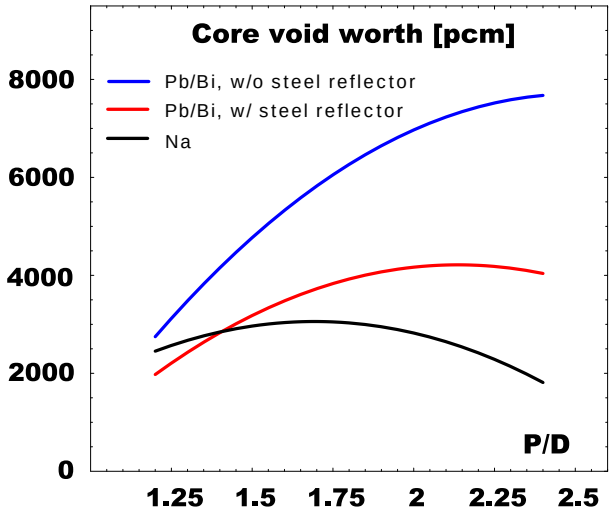

Fig. 9. Coolant void worth in a critical FBR employing (U,Pu)O_2 fuel. The Pu/(U + Pu) ratio was varied with P/D in order obtain $k_{\mathrm{eff}} \sim 1$, for Na in the range between 17% and 33%, for Pb/Bi without steel pin reflector between 16% and 26%, and in the case of Pb/Bi with steel reflector between 17% and 27%.

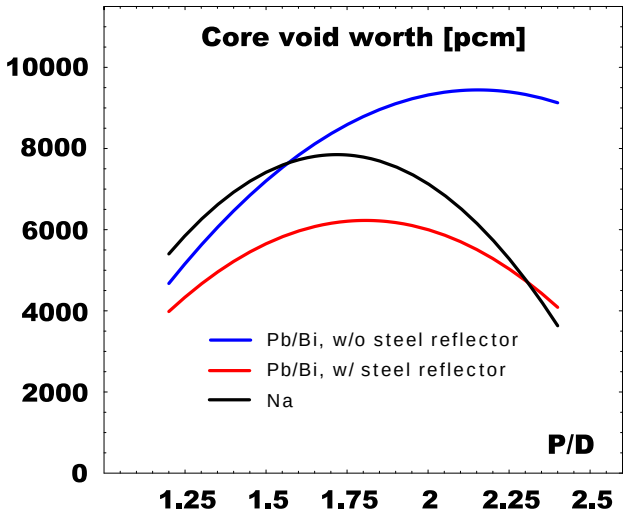

Fig. 10. Core void worth in ADSs cooled by sodium and lead/bismuth. The inert matrix fraction is kept constant at 50 vol%, and Pu/(Pu + Am) ratio is adjusted to obtain $k_{\mathrm{eff}} \sim 0.96$, for Na in the range between 23% and 67%, for Pb/Bi without steel pin reflector between 20% and 49%, and in the case of Pb/Bi with steel reflector between 21% and 51%. The Pu and Am vectors are those of spent LWR UOX fuel after 30 years of cooling.

neutron fission-to-capture ratio upon coolant voiding is thus not as dramatic as in MA-based ADSs, leaving the reduction of neutron capture probability in fuel to be the only significant factor introducing positive reactivity to the system. Generally, the void worth is now found to be decreasing with growing pitch due to increasing neutron leakage.

In order to illustrate an effect of the fissile isotope content in the Pu-vector on the void worth, the same calculation was also made for "fresh", high quality, plutonium, coming from LWR UOX spent fuel after 4 years of cooling. In this case, the minor actinide content in fuel is further decreased, lowering consequently also the void worths.

Fuel pins with smaller pin diameter appeared to be more favourable with respect to the void worth, the difference being most pronounced for larger pitches.

Exchanging ZrN for an absorbing matrix, in our case HfN, increases the void worth, but in the case of TRU-based fuel,

TABLE VIII

Breakdown of coolant void worth into individual components shown for different types of mononitride fuels employed in a model ADS with sodium or lead/bismuth coolant; pitch-to-diameter ratio is 2.0.

Coolant	Atomic fraction Pu/(Pu + Am)	Volume fraction AcN/(AcN + inert matrix)	R_{pin}	ΔL_{f}	$\Delta L_{\mathrm{c,fuel}}$	$\Delta L_{\mathrm{c,cool}}$	$\Delta L_{\mathrm{c,clad}}$	ΔL_{e}
Na	Core void worth							
	80%	29.5%	3 mm	-0.0102	-0.0839	+0.0205	+0.0524	+0.0214
	55%	50%	3 mm	+0.0164	-0.0910	+0.0171	+0.0409	+0.0172
	40%	66%	3 mm	+0.0296	-0.0948	+0.0148	+0.0361	+0.0150
Pb/Bi	Core void worth, radial reflector with steel pins							
	80%	20%	3 mm	-0.0226	-0.0650	-0.0104	+0.0903	+0.0060
	80%	15.5%	4 mm	-0.0156	-0.0690	-0.0138	+0.0908	+0.0059
	42%	50%	3 mm	+0.0109	-0.0794	-0.0019	+0.0649	+0.0048
	40%	52%	3 mm	+0.0127	-0.0803	-0.0019	+0.0646	+0.0046
	40%	36.3%	3 mm	-0.0041	-0.0652	+0.0029	+0.0671	+0.0045

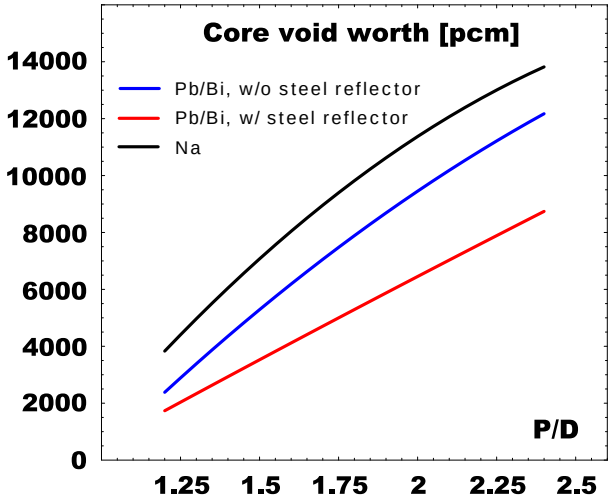

Fig. 11. Core void worth in ADSs cooled by sodium and lead/bismuth. The Pu/Am ratio was kept constant at 2/3, and actinide fraction (AcN) in fuel was adjusted to obtain $k_{\mathrm{eff}} \sim 0.96$, for Na in the range between 35 vol% and 85 vol%, for Pb/Bi without steel reflector between 31 vol% and 59 vol%, and in the case of Pb/Bi with steel pin reflector between 33 vol% and 63 vol%. The Pu & Am vectors are those of spent LWR UOX fuel after 30 years of cooling.

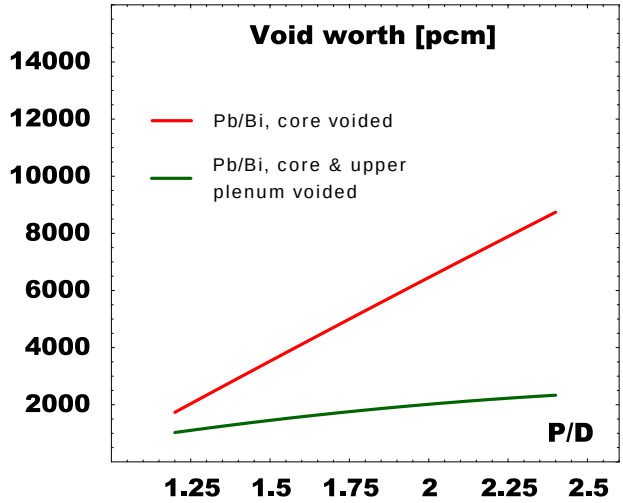

Fig. 12. Core and plenum void worths in ADS employing Pb/Bi coolant and steel pin radial reflector. Pu/Am fraction was kept at 2/3, AcN fraction was varied to obtain $k_{\mathrm{eff}} \sim 0.96$. The Pu & Am vectors are those of spent LWR UOX fuel after 30 years of cooling.

W remains at acceptable levels, see Figure 14. While the core void worth becomes slightly positive, the coupled core & upper plenum void is still strongly negative for all pitches.

In Table VIII, we display the coolant void worth for different types of mononitride fuels employed in a model ADS burner with lattice pitch-to-diameter ratio equal to two and decomposed into the individual terms with respect to capture in fuel, clad, coolant, and to neutron leakage. We note that the statistical error of calculations is of the same order of magnitude as ΔG_{x}, which we therefore do not list.

Similarly to the results obtained for the pin lattice model, the amount of positive reactivity introduced upon coolant voiding by reduction of capture in fuel increases with growing MA fraction in the fuel. Evidently, this is due to the pronounced increase of fuel fission-to-capture ratio. As a common characteristics for all fuels studied, the positive reactivity introduced by the reduction of capture in fuel is lower in sodium cooled systems than for lead/bismuth. We also observe that the reactivity being introduced by a change in coolant capture is lower for high MA content fuel than for fuels dominated by plutonium.

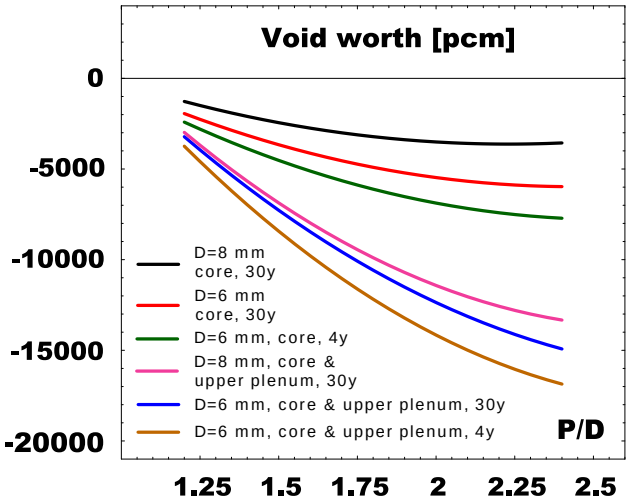

Fig. 13. Coolant void worth in ADS employing (TRU,Zr)N fuel, Pb/Bi coolant and steel pin radial reflector. Pu/Am ratio is 4/1, ZrN fraction is varied with P/D to obtain $k_{\rm eff} \sim 0.96$, for pins with a radius of 3 mm in the range between 13 vol% and 25 vol% (when applying 30-y actinide vector) and between 12% and 23% (for 4-y actinide vector). For 4-mm-radii pins, ZrN volume fraction was adjusted in the range between 10% and 19%.

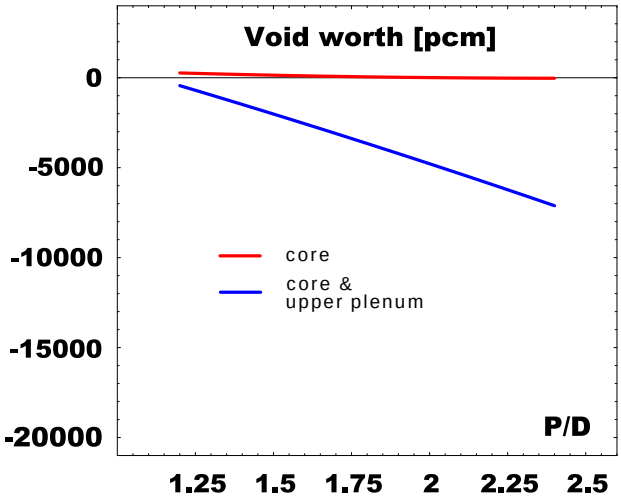

Fig. 14. Coolant void worth in Pb/Bi-cooled ADS employing TRU fuel with an absorbing matrix - (TRU,Hf)N. The steel pin reflector is used. Pu/Am fraction is kept at 4/1, AcN fraction in fuel is varied between 28 vol% and 41 vol% to obtain $k_{\rm eff} \sim 0.96$. Pin diameter is 6 mm, the Pu & Am vectors are those of spent LWR UOX fuel after 30 years of cooling.

IV. CONCLUSIONS

We found that reactor cores with high minor actinide content fuel exhibit generally higher void worths than cores fuelled primarily with plutonium. A disadvantage of sodium versus Pb/Bi in terms of larger positive coolant void worth is apparent for all transmutation type fuels investigated.

For an FBR with (U,Pu)O_2 fuel, on the contrary, Pb/Bi yields larger void worth than sodium when P/D $\gtrsim$ 1.4, which is in contradiction with the results obtained by Yiftah and Okrent [19]. While in sodium cooled FBRs the negative reactivity is introduced upon coolant voiding by both increase of neutron capture in structural material and coolant (in the reflectors and plena), in Pb/Bi-cooled reactors the reactivity contribution is negative only from the former.

In lead/bismuth-cooled systems, a radial steel pin reflector has to be applied, if coolant void worth is to be significantly reduced.

Enlarging the pitch-to-diameter ratio lowers the coolant void worth in ADS burners operating in two-component scenario, while ADS burners with MA based fuel should be designed with minimum allowable P/D.

Pins with small diameters and non-absorbing fuel matrices are preferable with respect to the coolant void worth. However, even an application of strongly absorbing matrix (HfN), does not have to deteriorate the void worth critically; large amount of negative reactivity still being introduced into the reactor upon voiding both core & upper plenum, as e.g. in TRU-fuelled ADS.

ACKNOWLEDGMENTS

Financial support of the Swedish Nuclear Fuel and Waste Management Co (SKB AB) is acknowledged.

REFERENCES

1. T. Takizuka et al., Conceptual design of transmutation plant, in *Proceedings of the Specialist meeting on accelerator driven transmutation technology for radwaste*, page 707, LA–12205–C, Los Alamos National Laboratory, USA, 1991.

2. A. Conti et al., CAPRA exploratory studies of U-free fast Pu burner cores, in *Proceedings of the International Conference on Evaluation of Emerging Nuclear Fuel Cycle Systems, GLOBAL'95*, page 1316, Versailles, France, 1995.

3. J. Wallenius, In: NEA/WPPT status report on fuels for transmutation. Editor T. Ogawa., to be published.

4. D. Foster et al., Review of PNL study on transmutation processing of high level waste, Technical Report LA–UR–74–74, Los Alamos National Laboratory, USA, 1974.

5. H. Murata and T. Mukaiyama, Atomkernenergie-Kerntechnik **45**, 23 (1984).

6. R. Rose et al., Fusion-driven actinide burner design study, Technical report, Electric Power Research Institute, EPRI ER-451, USA, 1977.

7. E. Cheng et al., Actinide transmutation with small tokamak fusion reactors, in *Proceedings of the International Conference on Evaluation of Emerging Nuclear Fuel Cycle Systems, GLOBAL'95*, page 1428, Versailles, France, 1995.

8. W. Stacey et al., Fusion Science and Technology **41**, 116 (2002).

9. W. Maschek et al., Safety analyses for ADS cores with dedicted fuel and proposals for safety improvements, in *Proceedings of the IAEA TCM Meeting*, Argonne National Laboratory, USA, 2000.

10. M. Eriksson et al., Safety analysis of Na and Pb-Bi coolants in response to beam instabilities, in *Proceedings of the Third International Workshop on Utilisation and Reliability of High Power Proton Accelerators*, Santa Fe, USA, 2002.

11. L. Cinotti and G. Gherardi, Journal of Nuclear Materials **301**, 8 (2002).

12. A. Shmelev et al., Atomnaya Ehnergiya **73(6)**, 450 (1992).

13. J. Briesmeister, MCNP – A general Monte Carlo N-Particle transport code, version 4C, Technical Report LA–13709–M, Los Alamos National Laboratory, USA, 2000.

14. H. Khalil and R. Hill, Nuclear Science and Engineering **109**, 221 (1991).

15. C. Rubbia et al., Fast neutron incineration in the energy amplifier as alternative to geologic storage: The case of Spain, Technical Report CERN/LHC/97–01(EET), 1997.

16. A. Waltar and A. Reynolds, *Fast Breeder Reactors*, Pergamon Press, 1981.

17. T. Takizuka et al., Studies on accelerator driven transmutation systems, in *Proceedings of the Fifth international information exchange meeting*, page 383, OECD/NEA, Mol, Belgium, 1998.

18. J. Wallenius, Journal of Nuclear Materials **320**, 142 (2003).

19. S. Yiftah and D. Okrent, Some physical calculations on the performance of large fast breeder power reactors, Technical Report ANL-6212, Argonne National Laboratory, USA, 1960.

Paper II

K. Tuček, M. Jolkkonen, J. Wallenius, and W. Gudowski
Neutronic and burnup studies of an accelerator-driven transuranium burner in a start-up mode
Submitted to Nuclear Technology (2004)

Neutronic and Burnup Studies of an Accelerator-driven Transuranium Burner in a Start-up Mode

Kamil Tuček*, Mikael Jolkkonen, Janne Wallenius, and Waclaw Gudowski

Royal Institute of Technology, Dept of Nuclear & Reactor Physics,
SE-106 91 Stockholm, Sweden

Abstract – *We have studied neutronic & burnup characteristics of an accelerator-driven transuranium burner in a start-up mode. Different inert and absorbing matrices as well as lattice configurations have been assessed in order to identify suitable fuel and core design configurations. Monte Carlo transport and burnup codes were used in the analyses. The lattice pin pitch was varied in order to optimise the source efficiency and coolant void worth while respecting key thermal and material-related design constraints posed by fuel and cladding. HfN matrix appeared to provide a good combination of neutronic, burnup and safety characteristics: maintaining hard neutron spectrum, yielding acceptable coolant void reactivity and source efficiency, and alleviating burnup reactivity swing. A conceptual design of a (TRU,Hf)N fuelled, lead/bismuth eutectic cooled ADS was developed. Twice higher neutron fission-to-absorption probabilities in americium isotopes were achieved compared to reactor designs relying on inert matrices. The production of higher actinides in the fuel cycle is hence limited. The burnup reactivity swing and associated power peaking in the core are managed by an appropriate choice of the cycle length (100 days) and by core enrichment zoning. A safety analysis shows that the system is protected from an instant damage during unprotected beam overpower transient.*

I. INTRODUCTION

Minor actinide transmutation in nuclear reactors was first suggested by Claiborne almost 30 years ago [1]. Two years later, in 1974, Los Alamos scientists proposed the introduction of slightly sub-critical dedicated cores for this purpose [2]. During the last decade, there has appeared a growing consensus that such systems should operate on a fast neutron spectrum in order to limit the accumulation of higher actinides (Am, Cm) in the fuel cycle, and take advantage of its better neutron economy [3–7].

The role of such dedicated systems in transmutation scenarios is intimately interconnected with the selected plutonium management strategy. In the frame of multi-component (double-strata, two-tier) concepts, dedicated MA burners are suggested to work in concert with a fleet of critical reactors (fast and/or thermal). Directing the whole TRU discharge into dedicated burner reactors has been investigated by several authors as an alternative strategy (two component scenario), relevant particularly in the case when fuel with high minor actinide content would turn out to be too difficult to fabricate and reprocess [8]. A major difficulty associated with this strategy is however high reactivity losses due to rapid burnout of fissile isotopes, which simultaneously exacerbates power peaking. Additionally, introduction of minor actinides into the fuel severely degrades system safety parameters - most importantly coolant void reactivity, but also Doppler coefficient and delayed neutron fractions.

In order to keep the total thermal power constant, and consequently attain economically viable operation of the accelerator-driven system, the reactivity loss in the irradiation cycle may be compensated by adjusting the intensity of the external neutron source, thus avoiding the potential for excessive reactivity insertions resulting from the erroneous control rod withdrawal (run out). Typically, in reactor systems with low fertile material support, a beam power margin more than a factor of two-three has to be provided in order to compensate for losses in neutron multiplication during one irradiation cycle [9–11]. Due to the lack of strong favourable temperature feedbacks, the accidental insertion of full available beam power margin into the system thus becomes a major safety concern. The ability of passive devices as those proposed by Wider [12] or Rubbia [4] to shut-off the beam power before any fuel or cladding damage has occurred still remains to be investigated. Thus, one should aim at providing minimum accelerator power swing, but at the same time limit frequency of reactor outages and refuelling, allowing for high discharge burnups.

While sub-criticality may be a *necessary* requirement for safe operation of cores with small delayed neutron fractions and temperature feedbacks, it is not always *sufficient*. In systems with high coolant reactivity worth, coolant voiding may lead to core damage [13–15], if the sub-criticality margin is

*E-mail: kamil@neutron.kth.se

too small. A too large sub-criticality, e.g. $k_{eff} \simeq 0.9$ at EOL, would however have negative consequences for neutronics and system economics (lower total reactor power and discharge burnup, extensive requirements on the beam power).

In this paper, we show that by fuel and core design, it is possible to achieve better safety parameters of the system while also maintaining good neutronics and burnup features. In Section II of the paper, we start by reviewing reference design parameters of this study, presenting a rationale for choice of fuel, coolant, and structural materials. Assessment of fuel production and temperature stability is provided in Section III, followed by the description of our calculation tools and modelling approach in Section IV. Basic design considerations are put forth in Section V. A scoping study investigating several core design options and comparing their neutronic and burnup performances is presented in Section VI. , where we also discuss how safety issues can be addressed. The presentation of a conceptual core design and a review of its characteristics is given in Section VII. We conclude with a safety analysis of the system behaviour in Section VIII.

II. REFERENCE DESIGN

II.A. Geometry

An overview of reference system, pin, and pellet design data is given in Table I and Figure 1.

In this study, pin and pellet design parameters similar to those used for CAPRA 04/94 core design were selected [16]. The pellet diameter is small, on the limit of fabricability, to provide smaller void worths [17]. At the same time, it limits recriticality potential due to core compaction. On the other hand, for a fixed linear power, choosing a small pellet diameter leads to increased burnup rates, thus enlarging reactivity swing in one irradiation cycle. The choice of the active core height is dictated by two contradicting goals. Larger core heights decrease the maximum linear power for a given P/D. In order to keep stability of the clad and fuel, the P/D would have to be increased thus softening neutron spectra. On the other hand, lowering the core height would lead to an unacceptable drop in multiplication of the source neutrons. The value of one metre is thus chosen as a good compromise [10, 11, 18].

The thickness of the cladding and the length of the the plena has to be adjusted so that released helium and fission gases can be safely accommodated for an audaciously assumed target discharge burnup of 30 % FIMA (% FIMA, fissions per initial metal atom, *i.e.*, actinide).

The criteria for target diameter and beam tube radius are imposed by the abilities of the target module coolant to dissipate the beam power and accommodate a given beam profile. A detailed discussion on this issue is provided in Section V. . The axial position of the beam window is offset 20 cm from the core midplane, maximising source neutron multiplication in the core [18].

The core structure is immersed in a pool of lead-bismuth eutectic coolant with heat exchangers and primary pumps well elevated in order to promote natural circulation. Loop design as used in certain sodium cooled reactors is not appropriate due to the high density of the Pb/Bi-coolant. The pool system, which avoids nozzles and pipes, has the further benefits of extremely low probability for loss-of-coolant accidents, a large heat capacity, and reliable natural circulation. Pool designs, on the other hand, use large vessels containing massive amounts of heavy liquid metal. The large volume and high density of the coolant may exert significant impulsive load on the vessel in the event of an earthquake excitation [19].

The system has four identical steam generators with four primary centrifugal pumps located in the cold pool. The vessel is filled with Pb/Bi eutectic to a prescribed level, with the remainder of the vessel being occupied by an inert cover gas. The compressibility of the cover gas permits the coolant to expand with rising temperatures. An auxiliary tank of sufficient volume to contain cover gas may be connected to the reactor vessel to account for nitrogen gas that might be generated by thermal dissociation of the nitride fuel [20]. Because lead-bismuth eutectic is nearly incompressible, and the saturation temperature is high, there is no need to pressurise the primary system.

II.B. Materials

II.B.1. Fuel

Actinide mononitrides, combining high power to melt with high dissolution rates in nitric acid, are chosen as core fuel. In order to reduce the reactivity of Pu rich fuels, a diluent matrix has to be introduced - this can be either inert (e.g. ZrN) or absorbing (e.g. HfN).

Both ceramic and metallic composite (heterogenous) as well as solid solution (homogenous) nitride fuels were proposed [21, 22]. Diluents forming solid solution with fuel enhance the thermal stability of the fuel and improve its thermal conductivity, thus increasing maximum allowable peak power and prolonging burnup in one irradiation cycle (batch). In our study, we consider five types of both fertile and inert matrices forming solid solution type fuels with TRU nitrides: UN, ThN, ZrN, YN, HfN, and one, BN, creating a heterogenous system with AnN.

TABLE I

Reference system, pin, and pellet design specifications. A triangular pin lattice is adopted. Maximum allowed internal gas pressure in the fuel pin is 20 MPa.

Pellet density (% TD)	0.85
Pellet outer radius R_{fuel} (mm)	2.4
Cladding inner radius R_{gap} (mm)	2.5
Cladding outer radius R_{pin} (mm)	3.0
Active pin length (cm)	100
Length of upper fission gas plenum (cm)	150
Length of lower fission gas plenum (cm)	10
Length of bottom plenum spacer (cm)	10
Length of radial reflector S/As (cm)	140
Thickness of radial reflector (cm)	150
Length of upper reflector (cm)	200
Length of lower reflector (cm)	230
Spallation target radius (cm)	20
Radius of accelerator beam tube (cm)	15
Distance of target window from centreplane (cm)	20

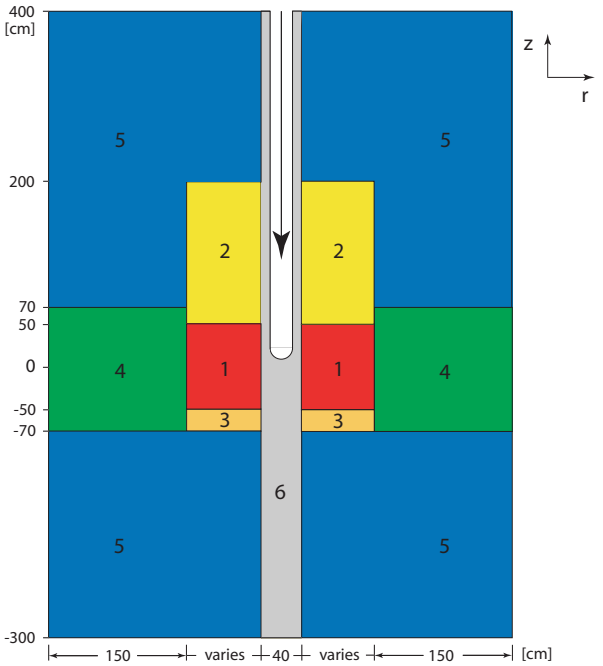

Fig. 1. R-z view of a reference sub-critical reactor model configuration. The regions are 1−core, 2−upper fission gas plenum, 3−lower fission gas plenum & bottom plenum spacer, 4−radial reflector, 5−axial reflector, and 6−target. The spallation target consists of lead/bismuth eutectic.

Actinide mononitrides The basic characteristics of the actinide nitride fuels: lattice parameters, thermal conductivities, dissociation and melting temperatures, are summarised in Table II.

Unlike oxide based fuels, there are large uncertainties associated with the thermophysical properties of the nitride fuel, especially concerning their stability at elevated temperatures. The specific feature of nitrides is their susceptibility to decomposition into a liquid or gaseous metal and nitrogen gas at high temperature.

It was shown that the decomposition behaviour of the AnN fuel is a strong function of the chemical composition of the atmosphere gas. Adding a small part of nitrogen into the gas effectively lowers actinide vapour pressure, thus delaying the onset of the nitride decomposition by several hundreds of Kelvin. E.g., experimental results indicate that decomposition of PuN occurs at about 2150 K in inert atmosphere but between 2850 and 3130 K in 1 bar N_2 [23].

Unlike UN and PuN, the dissociation behaviour of higher actinide nitrides (AmN, CmN) is experimentally not well known up to now. The stability limit of AmN in inert gas atmosphere is conservatively assumed to be the same as its fabrication temperature [24–26]. Recent experimental data and calculations suggest that AmN dissociation occurs somewhere in the temperature range 1600-1800 K [27].

Actinide mononitrides appear to be completely miscible in the full range of compositions. The mutual solubility of actinide mononitrides has been either successfully demonstrated (in the case of (U,Np,Pu)N, and (Pu,Am,Cm)N) or is expected due to the small differences in the lattice parameters. The radiation experience involves the irradiation of both UN and (U,Pu)N fuel in JOYO, JMTR, and BOR-60 to ∼5% FIMA [28].

The thermal conductivity of AnN is a decreasing function of atomic number [24], strongly depending also on the fuel impurities and pellet porosity [29]. In the study, 15% porosity is assumed. The thermal conductivity deteriorates with the irradiation due to the presence of the fission products in the matrix. We assume a 30% decrease in the conductivity for target burnup of 30% FIMA [30].

In order to reduce the (n,p)-production of troublesome (during reprocessing) ^{14}C, the nitrogen should be enriched up to 99% in ^{15}N [31].

The nitride fuels appear to be compatible with the stainless steel; the nitridation of the cladding is less of a problem than is oxidation for oxide fuels.

Diluent matrix As mentioned, the function of the diluent matrix in the fuel is two-fold. Firstly, it reduces the reactivity of the fuel. Secondly, it stabilises the fuel at high temperatures and improves the thermal conductivity. Fuels with high diluent matrix fractions also feature improved irradiation per-

TABLE II

Lattice parameters, thermal conductivities, dissociation and melting temperatures for actinide nitrides, nitride inert and absorbing matrices. The nitride limit (decomposition) temperature is given at p = 1 atm in inert atmosphere; thermal conductivity is given at 1273 K, except for ThN, where a value for 1000 K is used. "N/A" = Not Available.

Material	a [nm]	λ [W/(m·K)]	T_{limit} [K]	T_{melt} [K]
ThN	0.5167	47 [32]	–	3098 [33]
UN	0.4888	25 [21]	2700 [34]	3128 [33]
PuN	0.4905	13 [21]	2150 [23]	2862 [33]
AmN	0.4991	∼9	1570 [25]	N/A
CmN	0.5041	∼6	N/A	N/A
ZrN	0.4576	37 [35]	–	3250 [36]
HfN	0.4520	17 [36]	–	3660 [36]
β-BN (cub.)	0.3615	29 [21]	2550 [21]	3270 [36]
YN	0.4891	N/A	–	>2970 [33]

TABLE III

Limit temperatures for coolant and construction materials.

Material	T_{steady} [K]	T_{limit} [K]
Fe-12Cr steel	890 [37]	1140 [38]
Pb/Bi coolant	–	1943 [39]

formance. The matrix provides more space to accommodate fission products, thus allowing for higher discharge burnups. The fabrication process of the fuel may be easier as well. In this study, we assume that the fraction of the diluent matrix in the fuel should exceed 50 vol%.

ZrN nitride provides a good combination of high melting temperature (3230 K) and thermal conductivity (35-37 kW/m in the temperature range 900-2300 K). ZrN has a tolerable dissolution rate in the nitric acid, it is compatible with cladding material and features good neutronic characteristics (small absorption and slowing down power).

ZrN forms a homogeneous solid solution with uranium and plutonium and the same behaviour is also expected for americium. ZrN has a stabilising effect on the fuel, delaying the onset of fuel decomposition [26]. For (U,Zr)N, experiments have been performed on ($U_{0.2}$,$Zr_{0.8}$)N heated up to 3073 K, with solidus and liquidus temperatures determined to be 2885 and 3038 K, respectively, while dissociation occurred in pure UN at 2700 K [40]. The behaviour of (Pu,Zr)N was assessed in calculations for 49 at% fraction of Zr, showing that melting does not occur below 2804 K. Due to chemical similarities, (Am,Zr)N and (Cm,Zr)N melting temperatures are assumed to be same as (Pu,Zr)N. Recent studies have shown that ($Pu_{0.21}$,$MA_{0.09}$,$Zr_{0.7}$)N stability may be expected up to 2400 K in N_2 saturated atmosphere [27].

The irradiation performance of nitride inert matrix fuel is limited, but several experiments with (Pu,Zr)N pins are underway. ($Pu_{0.1}$,$Zr_{0.9}$)N pellets were fabricated by the classical blending method at JAERI for irradiation tests in the Japanese Material Testing Reactor. In the frame of the CONFIRM project, (Pu,Zr)N with 20 and 30 mol% Pu will be irradiated during 2005. In the BOR-60 reactor, the irradiation of two (Pu,Zr)N pins is currently under way.

Hafnium nitride (HfN) has excellent thermophysical properties: very high melting temperature (3660 K) and favourable thermal conductivity (19 W/m·K at 1773 K) [36]. At PSI, (Hf,Zr)N pellets were produced by carbothermic reduction from mixed oxides and a solid solution was obtained [41, 42]. Due to the similarity of the lattice parameters, actinide nitrides are assumed to form a homogeneous solution also with HfN. Hafnium is a good absorber of neutrons in the thermal and resonance energy regions, effectively hardening the neutron spectrum. Further experimental work is however needed to establish the stability and performance of HfN based compounds. Due to the chemical similarity of Hf and Zr (hafnium and zirconium are both group IV transition metals), the chemical behaviour of the hafnium nitride is supposed to be very similar to that of ZrN. Accordingly, we expect that HfN is soluble in HNO_3.

YN has high melting temperature and is soluble in nitric acid. Solid solutions of (Pu,Y)N and (Am,Y)N was prepared at JAERI [26, 43]. A comparative drawback of YN is, however, its susceptibility to rapid oxidation at room temperature.

Boron mononitride forms a composite (heterogenous) solution with actinide nitrides. It exhibits rather high thermal conductivity (23 W/m·K) but decomposes already at temperatures around 2200 K. In this study, boron nitride is *enriched* in ^{10}B up to 90% in order to attain a hard neutron spectrum in the core. Considerable amounts of gas are released into the fission gas plenum from ^{10}B(n,α)^{7}Li reactions. At the same time, in reactor systems with hard neutron spectrum, tritium production via the ^{10}B(n,t)2α channel becomes significant for energies above 1 MeV.

II.B.2. Coolant and target material

The choice of lead/bismuth as a coolant is motivated primarily by its favourable effect on coolant void worth in TRU-fuelled systems [17]. Lead-bismuth eutectic also has good thermophysical properties: low melting point (398 K) limiting problems with freezing in the system, and high boiling point (1943 K) making risks for coolant boiling and subsequent core voiding rather hypothetical. Lead-bismuth eutectic is also conveniently chosen as a target material. We note

that special measures would to be introduced in order to cope with accumulated radioactivity in Pb/Bi (which is mainly due to ^{210}Po, $T_{1/2} \simeq 138$ d) during fuel reloading or repair work on the primary circuit [44].

II.B.3. Construction material

12%Cr-Si steels have been identified as a suitable cladding and structural material for heavy metal cooled reactors in an extensive Russian experimental and testing programme running since the fifties. It was shown that by controlling the oxygen concentration in the liquid metal, the corrosion stability of the steels can be substantially increased, elevating the permissible operating temperature by about 200 K [45]. However, the steady-state temperature of the oxygen-passivated steel components still has to be kept below 890 K as higher temperatures strongly impair plasticity, mechanical strength, embrittlement susceptibility and creep resistance of the material [37]. Moreover, in order to prevent erosion of corrosion protective oxide films on structural material/cladding, the bulk coolant velocity should not exceed 2.5 m/s [46]. Due to the lack of relevant experimental data, the thermophysical properties of the cladding and structure materials were assumed to be as those for HT-9 ferritic stainless steel. The HT-9 steel has a similar chemical composition to Russian EP-823 steel with exception of silicon concentrations (being 1.1-1.3 wt% for EP-823 and 0.3 wt% for HT-9). Maximum cladding temperature at extended operational conditions (during transient) was estimated according to the results obtained by Cannon [38]. The clad burst temperature corresponding to the hoop stress 100 MPa (internal pin pressure of 20 MPa) is approximately 1140 K, see also Table III.

Recent tests have shown that EP-823 looses ductility and becomes brittle after irradiation at 720 K to relatively modest doses [47]. As the corrosion behaviour of austenitic steels is generally worse due to a high solubility of nickel in lead-alloys, it appears that at present, there is no obvious choice of cladding material for lead-alloy cooled reactors. In the this paper, EP-823 was used as reference material, in lack of better options.

II.B.4. Pin bonding

Filling the fuel pin with a gas containing a certain (~ 1 mol%) amount of N_2 could seem to be an attractive way to increase design fuel power rating while keeping the same safety margins as for pins bonded with an inert atmosphere. However, under accidental conditions when the integrity of the fuel pin is lost, the protective effect of the nitrogen would be lost, with fuel disintegration as a possible outcome. Moreover, due to the low conductivity of the filling gas (He), pins would also exhibit large temperature gradients in the pellet-cladding gap, which effectively decreases maximum allowable fuel ratings.

On the other hand, liquid metals would provide an excellent heat transfer capability due to the high thermal conductivity (14 W/m·K at 800 K in the case of Pb/Bi and 66 W/m·K for Na). There is an substantial experience with sodium bonding which was investigated both in the Great Britain and in the USA (EBR-II). For our purpose, however, introduction of sodium into the core would rise serious compatibility issues [48]. We therefore choose Pb/Bi as a pin bond material. Russian tests has shown compatibility of Pb/Bi with UN and (U,Pu)N and EP-823 steel up to 1073 K for 2000 hours and 1473-1573 K for 5 hours [49, 50]. We note, however, that further testing would be needed to assess the compatibility of Pb/Bi with the fuel and the risk for steel corrosion during irradiation.

II.C. Fuel composition

The transuranium transmutation reactor would work in symbiosis with a park of light-water reactors in the frame of a two component strategy. Here we investigate a start-up scenario (first cycle) assuming the composition of the TRU vector as being that of light-water reactor spent fuel discharges with average burnup of 41 GWd/tHM after a cooling period of 30 years. Such a delay could be a reasonable estimation of an ADS implementation into nuclear reactor parks. During this period, the relative concentration of ^{241}Am in the TRU vector is more than doubled due to the β-decay of ^{241}Pu. A scenario of single plutonium MOX recycling in LWR prior the actinide incineration in ADS is also studied. The composition of transuranic vectors used in the studies is given in Table IV. Neptunium is not assumed to be transmuted due to its low radiotoxic inventory in the spent fuel [51]. For reasons of simplicity, the TRU vector of initial/fresh fuel is assumed to contain only plutonium and americium.

III. FUEL STABILITY

Nitride-based TRU fuels, as solid solution in a ZrN or HfN inert matrix, can be produced by carbothermic nitridation of the corresponding dioxides [41]. For practical purposes an excess of carbon is used to ensure as nearly quantitative reduction as possible, and this excess is removed in a subsequent decarburisation step where HCN is formed [27]. In the case of a zirconium-based matrix, practical experience as well as modelling [27, 41] have shown that temperatures between 1500 and 2000 K are required. Lower temperatures result in slow and incomplete reaction, while higher temperatures lead

TABLE IV

TRU vectors used in the investigations. The average burnup of spent UOX fuel is 41.2 GWd/tHM burnup; fuel cooling time is 30 years. In the case of MOX recycling prior to TRU incineration in ADS (UOX+MOX), the composition of the plutonium vector is assumed to be that of once recycled LWR MOX fuel, initial Pu content 8.2%, burnup 43.5 GWd/tHM and 10 years of cooling time. Americium vector is then that of UOX and MOX spent fuel, MOX/UOX support ratio being $\simeq 7.5$.

Isotope	UOX 30 years	UOX+MOX 10 years
^{238}Pu	0.023	0.044
^{239}Pu	0.599	0.390
^{240}Pu	0.264	0.323
^{241}Pu	0.040	0.112
^{242}Pu	0.074	0.130
^{241}Am	0.871	0.689
^{243}Am	0.129	0.311

to loss of americium by evaporation [22]. A major difficulty resides in the formation of stable zirconium carbide, or rather carbonitride, sometimes leading to an unacceptably high carbon content in the produced material. The possible evaporation of the americium component in nitride-based TRU fuels is also a major concern in the evaluation of in-pile performance and safety margins under overpower conditions [13].

We modelled the stability of two fuels of the compositions ($Hf_{0.663}$,$Pu_{0.270}Am_{0.067}$)N and ($Zr_{0.787}$,$Pu_{0.170}Am_{0.043}$)N, corresponding to a TRU fraction of the composition ($Pu_{0.8}$,$Am_{0.2}$)N in ZrN (25 vol% TRU content) and HfN (40 vol% TRU content). The production of the nitride fuel was modelled using the REACTOR module included with the Thermo-Calc package [52] and an as yet unreleased, enhanced version of the ALCHYMY database module. The modelling was designed to mimic the practically employed production process and was performed essentially in the same way as described in [27]. The stability of these fuels was modelled in a simplified fuel pin of the size and proportions outlined in Section II. In Pb/Bi bonded fuel pins the thermal conductivity of the plenum gas is of little importance, and thus 100 % N_2 can be used, which significantly suppresses nitride evaporation.

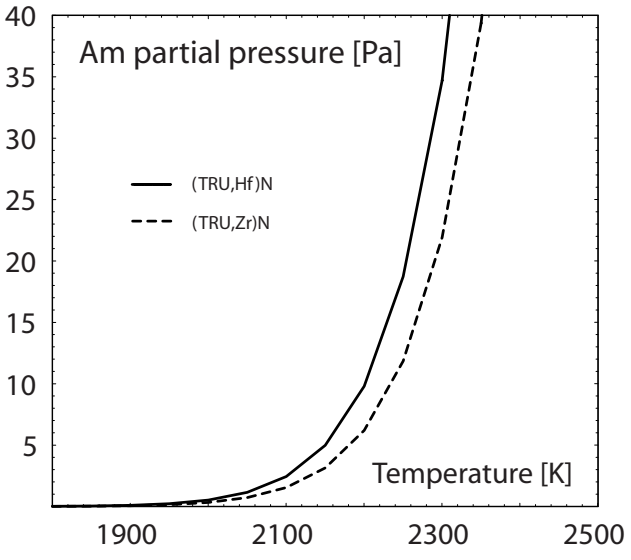

Fig. 2. Americium partial pressure in (TRU,Zr)N and (TRU,Hf)N.

The main simplifications of the model are that the Pb/Bi melt is regarded as an inert material in which the other components have no solubility, and that the system is uniformly heated and in thermodynamic equilibrium (no limiting reaction rates). In reality we would have a temperature gradient present, which, at sufficiently high temperatures, might cause a slow transport of americium nitride by evaporation in hot zones and re-crystallisation on colder surfaces, such as the inside of the cladding. Also, the calculations are made on fresh fuel of nominal composition, with no contribution from fission gasses to the overall pressure.

Thermochemical modelling shows that from a strictly thermodynamic viewpoint, a completely pure product can be obtained by a nitridation process starting at 1500 K and ending at 1700 K, followed by decarburisation at 1950 K. Both fuel compositions showed fairly similar behaviour in this respect. In the same model, 0.8% (ZrN matrix) and 0.9% (HfN matrix) of the americium was lost by evaporation. These losses may not necessarily reflect what is to be expected in actual production. No significant losses of other materials were observed.

Thermodynamic calculations on the HfN-based fuel indicate a somewhat greater predisposition towards the formation of carbide (as opposed to nitride) than for the ZrN-based fuel, but this difference is rather slight. We conclude that the production of a (TRU,Hf) nitride fuel should be feasible with only small modifications of the established process for (TRU,Zr) nitride fuel.

Since the evaporation of AmN produces 1 Am(g) and 0.5 N_2, the contribution to the overall pressure will equal 1.5 times the partial pressure of Am. As can be seen from Figure 2, this pressure increase is negligible at 2100 K ($< 0.001\%$), and the contribution from PuN dissociation is yet two orders of magnitude lower. The observed difference between Hf- and Zr-based fuel is proportional to the molar fraction of AmN in the respective fuels. Even at 2400 K, the stability of both fuels appears to be satisfactory, the contri-

bution from the AmN dissociation to the total pressure being about 0.01%.

IV. MODELLING

Eigenvalue calculations of temperature reactivity feedbacks as well as coolant void and cladding worths, delayed neutron fractions, and neutron lifetimes were performed by the Monte Carlo code MCNP, executed in KCODE mode [53]. In this case, only neutrons under 20 MeV are followed.

Calculation of source efficiencies, neutron fluxes, power densities, and one-group cross sections both at the beginning of the cycle and during fuel depletion were carried out by Monte Carlo code MCB [54] integrating MCNP4C neutron transport with in-flight calculation of reaction rates and nuclide density evolution. For this purpose, the external neutron source was first recorded in MCNPX [55] on the surface of the spallation target and subsequently supplied to MCB. The validity of such a source "decomposition" was shown by Seltborg et al [56].

The LA150 library was used for analyses of the spallation target with MCNPX code, while simulations of the reactor system were based on standard JEF2.2 nuclear data library processed with NJOY [57] in order to account for temperature dependence. For the sake of simplicity, average steady-state operational temperatures were used for individual components of the heterogeneous design - 1500 K for fuel pellets, 1200 K for cladding, and 900 K for coolant and upper plenum and upper reflector structure. The temperature of the lower axial plenum and radial reflector was assumed to be 600 K. Delayed neutron fractions were calculated with JENDL3.3 library.

V. BASIC DESIGN CONSIDERATIONS

We have reviewed and determined thermal properties and limiting characteristics of the fuel, cladding and coolant and fixed the lattice parameters of the fuel pin and pellet. Now, four other important design parameters can be investigated:

- spallation target radius,
- maximum reactor steady-state power,
- minimum lattice pitch-to-diameter ratio in order to ensure the operational stability of the fuel and cladding,
- linear power of the system.

V.A. Target radius, reactor power

The choice of target radius is dictated by the need for reasonably high source efficiency of spallation source neutrons. At the same time, the radius has to be large enough enough to assure sufficient transfer of dissipated heat.

The proton source efficiency ψ^* of a sub-critical system may be defined as

$$\psi^* \equiv \frac{M_{\rm ext}^{\rm p} - 1}{M_{\rm fiss} - 1} = \frac{P\overline{\nu}}{\overline{Q}S_{\rm p}} \frac{1 - k_{\rm eff}}{k_{\rm eff}} \tag{1}$$

where $M_{\rm ext}^{\rm p}$ is the actual multiplication of source spallation neutrons per source *proton*, $M_{\rm fiss} = 1/(1 - k_{\rm eff})$ is the fundamental mode multiplication, P is the thermal power of the system, $\overline{Q}$ is the averaged recoverable energy released in fission, $S_{\rm p}$ is the proton source intensity [p/s], and $\overline{\nu}$ is the average neutron yield.

The neutron source efficiency ϕ^* is then given by

$$\phi^* = \frac{M_{\rm ext} - 1}{M_{\rm fiss} - 1} = \psi^* \frac{S_{\rm p}}{S_{\rm n}} = \frac{\psi^*}{Z} \tag{2}$$

where $M_{\rm ext}$ is the actual multiplication of source spallation neutrons per source *neutron*, $S_{\rm n}$ is the neutron source intensity [n/s], and $Z = S_{\rm n}/S_{\rm p}$ is the number of neutrons per proton (neutron spallation yield). We note that the latter figure is a function of specific design geometry of a target/blanket. Thus, while ψ^* is a general parameter, defined independently of the distribution of the *neutron* source, the neutron source efficiencies can be truly intercompared only for ADSs with the same target/blanket geometry.

The accelerator current can be then determined from

$$I_{\rm p} = \frac{e\overline{\nu}(1/k_{\rm eff} - 1)}{\psi^*} \frac{P}{\overline{Q}} \tag{3}$$

where e is the elementary charge.

The source efficiency describes how well source neutrons are multiplied in comparison with the average fission neutron *in the asymptotic mode*. A high value of source efficiency is desirable in order to diminish the accelerator beam power (source strength) necessary to maintain a given power level of the core.

In Figure 3 we display the cumulative fraction of neutrons above a specified energy emerging from a Pb/Bi target bombarded with protons. We consider a single target module located in the centre of the core and constituted of a liquid lead/bismuth loop contained in a 5 mm thick ferritic steel container. The incident proton energy was set to 1 GeV, which is approximately the level where increasing the energy no longer increases the effective neutron yield per energy unit. A uni-

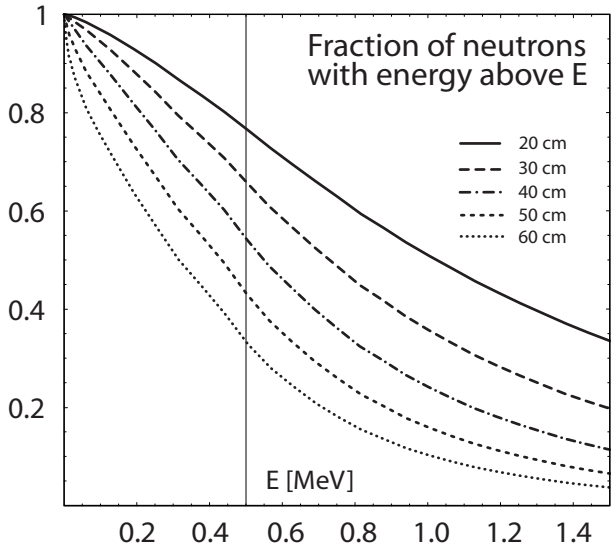

Fig. 3. Fractions of source neutrons having energies above *E* when exiting a Pb/Bi target of given radius. A proton energy of 1 GeV and target length of 700 cm were assumed. With increasing target radius, the probability of source neutrons to induce fission sharply decreases.

form beam profile with a radius of 10 cm was used in the simulations, performed with the Monte Carlo code MCNPX [55] using the LA150 cross-section library.

In spite of a small energy decrement in elastic collisions, the moderation power of lead/bismuth is high due to inelastic scattering at E_n>1 MeV. This yields a spectrum of target neutrons well below fast fission thresholds of even neutron number plutonium isotopes (being in the range of 500-800 keV). The fission probability of source neutrons thus sharply decreases with increasing target radius in the investigated range. Remembering that fission neutrons are born with a mean energy of about 2 MeV, it is clear that the neutron source efficiency may fall well bellow unity for targets of any reasonable sizes.

As a compromise between keeping the source efficiency at reasonable levels and assuring adequate heat removal capabilities, a target radius of 20 cm, with beam tube radius of 15 cm, was adopted.

We also choose so called "windowless design" of the target, which is believed to provide higher heat removal capacity than a target with hot window. A simple, tentative thermal-hydraulic analysis shows that the maximum beam power which can be accommodated by a 20-cm radius windowless target is $P_{\rm b}^{\rm max} = 30$ MW [58], while the corresponding value for the hot window design with the same outer dimensions would be approximately halved [59]. It was assumed that approximately 65% of the beam power is dissipated as heat in the target.

The power level of any accelerator-driven system is limited by the ability of a target module to remove heat produced within the target. It was shown that the optimal level of the initial sub-criticality is somewhere in the range of $k_{\rm eff} \in [0.95 - 0.97]$, considering safety and burnup performance of the ADS TRU burner [18]. Also, the reactivity swing per irradiation batch should be limited to $\Delta k_{\rm eff}$ = 2000-3000 pcm, in order to avoid extensive radial power peakings and relax demands on the available margin in the accelerator power. The later can be estimated simply from Eq. (3) as $I_{\rm p}^{\rm EOC}/I_{\rm p}^{\rm BOC} \sim$ (1-$k_{\rm eff}$(EOC))/(1-$k_{\rm eff}$(BOC)), which, assuming limit values of $k_{\rm eff}$ = 0.97 and $\Delta k_{\rm eff}$ = 3000 pcm, gives $I_{\rm p}^{\rm EOC}/I_{\rm p}^{\rm BOC} \sim 2$. Thus, for our configurations, it is necessary to provide a two-fold accelerator beam margin in order to compensate for the reactivity swing in one irradiation batch. Consequently, the maximum steady state fission power of the system for a 20-cm radius target can be estimated from Eq.(1) as

$$P = \frac{I_{\rm p}^{\rm BOC}}{I_{\rm p}^{\rm EOC}} \frac{P_{\rm b}^{\rm max}}{eE_{\rm p}} \frac{\psi^* \overline{Q}}{\overline{\nu}} \frac{k_{\rm eff}}{1-k_{\rm eff}} \approx 800\,{\rm MW_{th}} \qquad (4)$$

where for realistic ADS designs with radial power peaking management $\phi^* \sim 0.95$. In our heterogeneous target/blanket configuration $Z \approx 27$ n/p, which gives $\psi^* \sim 26$.

Here we note the need for rigourous simulations of different target design options in the beam power range of 20-50 MW with respect to the heat removal capability as well as stress and radiation damage behaviour.

V.B. Linear power, pitch-to-diameter ratio

The above given temperature limits are used in order to determine the maximum linear power rating of fuel pins as a function of coolant fraction in the pin lattice.

The thermal conductivity is a decisive parameter determining the ability of fuel to transfer the heat from the pellet. For actinide nitrides, the conductivity is a decreasing function of the atomic number. Inert and absorbing matrix materials (ZrN, HfN,YN, and BN) usually have higher thermal conductivities than actinide nitrides The margins to fuel failure are hence improved and/or cycle burnup can be prolonged. Thermal conductivities for several actinide and actinide-inert matrix nitride fuels are displayed in Figure 4 as a function of temperature. Thermal conductivity for AmN and CmN was estimated by extrapolation from UN, NpN , and PuN [24].

Consequently, in Figures 5 and 6, the maximum cladding and fuel temperature was calculated as a function of P/D ratio for PuN. The pin average linear power was varied from 20 kW/m to 80 kW/m. The coolant inlet temperature and bulk velocity were 550 K and 2.5 m/s, respectively. Using the

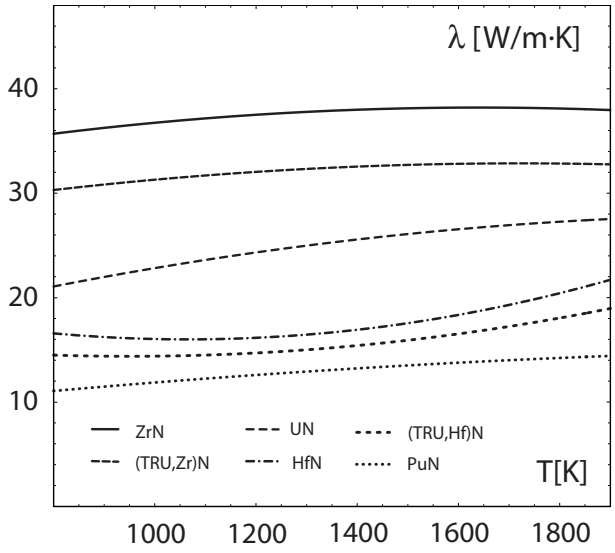

Fig. 4. The thermal conductivity (100% TD) of actinide nitride fuels and matrices as a function of temperature. ZrN, UN and PuN values are taken from [21], and HfN values from Pierson [36]. Conductivities of solid solution ($Zr_{0.787}$,$Pu_{0.170}Am_{0.043}$)N and ($Hf_{0.663}$,$Pu_{0.270}Am_{0.067}$)N fuels were estimated using Vegard's law.

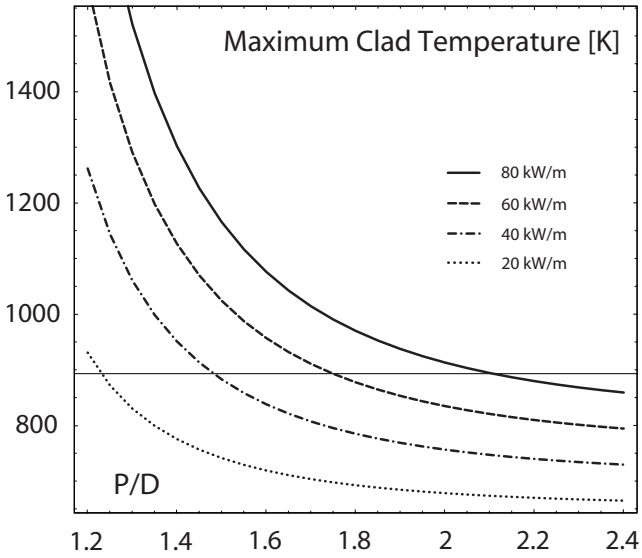

Fig. 5. Peak cladding temperature in Pb/Bi-cooled reactor as a function of P/D. The thermal conductivity was adjusted for the fuel porosity, axial power profile was assumed to be cosine-like. Active pin length is 100 cm.

conductivity values for PuN in the forthcoming analysis will provide *conservative* estimates of maximum linear power ratings and corresponding minimum P/Ds. These values will be updated when a final choice of the fuel is made.

Our choice of the pitch-to-diameter ratio and steady state linear power is guided by the requirement to maintain integrity of the reactor core both during steady state operation and following an instantaneous increase of reactor power. The prerequisite is thus to keep fuel temperatures below the disintegration limit (see Table II), while cladding temperatures should be kept below 890 K as dictated by the need to maintain stability of 12%Cr-Si steels. However, for a short period of time (during a transient), the temperatures of the clad can be elevated up to the burst temperature limit ($\sim$1140 K) [38].

The maximum potential for instantaneous power increase exists at the beginning of each irradiation batch. Considering that the radial power peaking can be managed by varying the diluent matrix fraction in different core zones such that $K_{\rm r} \lesssim 1.3$ at BOL, and that the available beam power margin at the BOC is $I_{\rm p}^{\rm EOC}/\ I_{\rm p}^{\rm BOC} \sim 2$, the pin linear power can be instantaneously increased maximally by a factor of $\chi_{\max}/\overline{\chi}_{\rm steady} \sim 2.6$, where $\overline{\chi}_{\rm steady}$ is the core *averaged* steady-state linear power. In addition, $K_{\rm r}^{\max} \lesssim 2$ is an upper estimate of the maximum radial power peaking in the fuel pins closest to the target at the end of irradiation batch/cycle.

In the case of PuN, we observe that enlarging P/D above 1.7 has little effect on the decreasing of the maximum fuel centerline temperature. For 80 kW/m, fuel temperatures remains below 2100 K and the cladding temperature is kept safely under the cladding burst limit of 1140 K, too. We therefore fix until further the core averaged linear power of the system to 80 kW/m/$(\chi_{\max}/\overline{\chi}_{\rm steady}) \sim 30$ kW/m, thus maintaining also the long term stability of the clad (maximum clad temperature during steady state conditions is at EOC $K_{\rm r}^{\max}\overline{\chi}_{\rm steady} \lesssim$ 60 kW/m.)

We note that the issue of the extensive power peaking, as mentioned in the previous analysis, applies only for the two or three innermost core zones. We could thus set up larger pin pitches P/D $\gtrsim 1.75$ in the innermost core zones close to the target, while pitches as low as 1.5-1.6 could be applied in the zones further from the core's centre.

VI. SCOPING STUDY

An extensive scoping study of different diluent materials and core lattice configurations was performed in order to identify suitable fuel concepts and core designs for an accelerator-driven transuranium burner.

Three different transuranic vectors are considered here: Pu/Am = 4/1 and Pu/Am = 7/3 corresponding to the ADS operating in a two-component scenario, and Pu/Am = 2/3 applying to the MA ADS burners working in the frame of double-strata strategy (see Table V). The latter is used as a reference only.

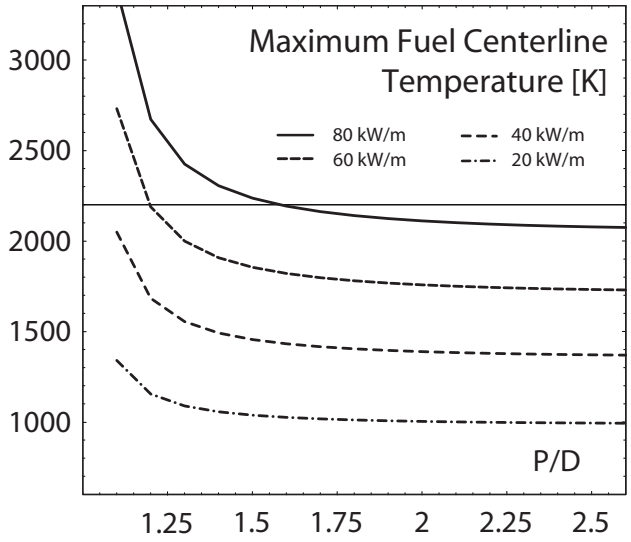

Fig. 6. Peak centreline temperature in Pb/Bi-bonded PuN fuel of Pb/Bi-cooled ADS. Linear power was varied from 20 to 80 kW/m.

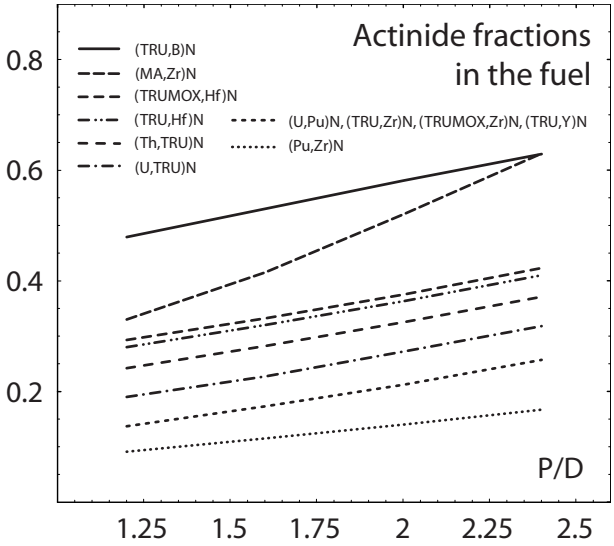

Fig. 7. Volume fractions of actinides in the fuels required to obtain k_{eff}=0.96 as a function of pitch-to-diameter ratio.

TABLE V

Atomic fractions of transuranic elements in fuels investigated in the scoping study. "TRU" and "TRUMOX" denote the compositions of the actinide vector corresponding to unrecycled UOX fuel and once recycled UOX+MOX fuel, respectively.

Element	TRU	TRUMOX	PuMA	MA
Pu	0.8	0.86	0.7	0.4
Am	0.2	0.14	0.3	0.6

VI.A. Homogeneous, 1-zone core

One-zone, homogeneous core configurations were used in order to facilitate a systematic comparison of the different design options. The volume fractions of diluent matrix were adjusted to obtain k_{eff}=0.96. The corresponding actinide fractions are displayed as a function of P/D in Figure 7.

Observe that for all configurations using high quality TRU fuel, the actinide fractions do not exceed a tentative limit of 50 vol% in the whole range of P/Ds, thus ensuring fabricability and irradiation stability of the fuel. However, to fulfill this condition for MA-based fuels, the pitch to-diameter ratio of the core lattice would have to be kept under 2.0.

VI.A.1. Choice of fuel matrix

The design and choice of materials for ADS blanket strongly influences its neutronic and burnup characteristics, and have an impact and impose demands on other components of the system (spallation target, accelerator, separation technologies). In this study, a performance of four candidate diluent matrices, ZrN, HfN, YN, and BN, is investigated in this respect. Values for fertile matrices (UN, ThN) are given as a reference. Here pitch-to-diameter ratio is kept constant, equal to 1.6.

TABLE VI

Average energies [keV], proton source efficiencies, and fission probabilities of ^{241}Am in single zone cores with P/D=1.6.

Fuel	E_n [keV]	E_ϕ [keV]	ψ^*	^{241}Am σ_f/σ_a
(TRU,Zr)N	87.4	396	29.7	0.104
(TRU,Hf)N	201	524	28.2	0.196
(TRU,Y)N	89.9	398	28.6	0.106
(TRU,B)N	407	811	25.2	0.376
(U,TRU)N	138	438	28.9	0.136
(Th,TRU)N	157	477	28.7	0.161
(U,Pu)N	121	416	28.6	0.121
(Pu,Zr)N	63.7	358	30.8	0.080
(TRUMOX,Zr)N	82.5	384	28.7	0.098
(TRUMOX,Hf)N	195	514	27.7	0.190
(PuMA,Hf)N	208	535	26.6	0.202
(MA,Zr)N	176	515	26.4	0.183

Neutronic performance We embark on our study by investigating neutronic performance of different fuels and assessing different design configurations in terms of number and flux weighted neutron spectra, proton source efficiencies, and fission-to-absorption probabilities of ^{241}Am. Results obtained are given in Table VI.

As discussed above, operating the reactor on a fast neutron spectrum is beneficial for limiting MA inventories in the fuel cycle. Therefore, as hard a neutron spectrum as attainable is

desired. In addition, the source efficiency has to be kept at a reasonable level in order to relax requirements on the accelerator beam power.

Note that the neutron spectrum is most thermalised in the fuels with the inert diluent matrices ZrN and YN resulting in low probabilities for direct fissioning of ^{241}Am. The use of fertile matrices in the fuel gives a slightly harder neutron spectrum due to increased absorption in the resonance and thermal regions, which also somewhat improves $\sigma_{\rm f}/\sigma_{\rm a}$ for ^{241}Am. Observe that absorbing matrices are the most efficient in shielding the thermal parts of the neutron spectrum, raising the fission probabilities of ^{241}Am up to 0.38 for BN. E.g., the ^{241}Am fission-to-absorption ratio of (TRU,Hf)N is twice as high as for (TRU,Zr)N.

The content of strongly absorbing americium isotopes in TRUMOX-based fuels is actually *lower* than in TRU fuels, yielding a slightly *softer* spectrum and thus also ^{241}Am fission probabilities. However, at the same time, the fraction of even neutron number nuclides is higher due to the lower quality of the plutonium vector, both resulting in a diminished proton source efficiency.

For inert and fertile matrices, the proton source efficiency is in the range of 29, while absorption of neutrons in BN causes a significant drop of the source efficiency. Note that HfN does not seriously deteriorate the multiplication of source neutrons in the system, keeping ϕ^* well above unity ($\psi^* \sim 28$).

Safety parameters It was shown that providing substantial margin to prevent core damage in the cases with high coolant void reactivity would require very high sub-criticalities, with penalties on the total reactor power, discharge burnup, and/or extensive requirements on the beam power as a result ($\sim$100 MW) [13, 14]. Therefore is appears relevant to find design options that allow to operate the ADS with smaller sub-criticality margins. We therefore studied the impact of different diluent and fertile matrices on the void worth of TRU fuelled ADS, see Table VII. The reactivity worth of the cladding material and temperature reactivity feedbacks were also investigated.

If coolant is voided, positive reactivity is introduced into the system mainly by reduction of parasitic neutron capture in fuel [17]. This effect increases with growing fraction of even-neutron number nuclides in fuel, either fertile (^{238}U and ^{232}Th), or minor actinides. Note a high sensitivity of the void worth on the content of americium in the fuel: compare the core coolant void worths for (TRU,Zr)N and (Pu,Zr)N, which are -4330 and -7000 pcm, respectively. MA-based fuel yielded very high positive void worth, of the order of +8000 pcm. Similarly, void worth is elevated when strongly *absorbing* materials are blended with the fuel. However, (TRU,Hf)N fuel yields acceptable void worth, $+120$ pcm.

Significant amount of positive reactivity can be introduced to the core due to flush-out of structural material from the core. The corresponding worth of the cladding material was calculated by substituting the cladding with coolant. The resulting increase in reactivity is larger than 2000 pcm for all configurations investigated. Again, the highest positive reactivity increase was observed for absorbing matrices and fuels with large content of even-neutron number actinides. For (MA,Zr)N, the cladding flush-out results in an extensive reactivity insertion larger than 5000 pcm. Thus, optimisation of the cladding (and duct) thickness is the imperative in order to improve the safety of the ADS cores.

The Doppler reactivity coefficient is considered as "prompt" feedback, almost instantly following changes in the fuel temperature. In this study, Doppler was calculated in terms of the Doppler constant, $K_{\rm D}$ = T·dk/dT. In practice, $k_{\rm eff}$ was evaluated for six equidistant values of temperature in the interval of $300-1800$ K. Doppler broadening of absorption resonances decreases the probability of neutrons to escape resonance absorption. The effect is thus most significant in the range of profound well-separated resonances, corresponding to energies around 1 keV.

Understandably, the strongest Doppler was provided by fuels with ^{238}U and ^{232}Th matrices. In U/Th-free fuels, the largest contributor was apparently ^{240}Pu. Note a negative effect of the absorber material or americium on the fuel temperature reactivity feedback. As these materials compete with resonant capture on ^{240}Pu, a sharp cut-off in the spectrum below 1 keV may further suppress the Doppler feedback. Substituting Zr with Hf or mixing Am into the fuel thus decreases the Doppler constant by more than a factor of three. In the BN-bearing fuels, Doppler feedback is completely non-existent. Observe note that for fuels without fertile support, with the exception of (Pu,Zr)N, the overall contribution of the Doppler effect to the prompt feedback mechanism is small, and the prompt temperature feedback is rather provided by axial expansion of the fuel column.

The system response to the axial fuel expansion was calculated by increasing the length of the pin by 1 cm, which in the case of the fuel with ZrN and HfN matrix corresponds to a temperature change from 1000 to 2070 K and 1000 to 2050 K, respectively, with the reactivity coefficients -0.21 pcm/K for ZrN and -0.19 pcm/K for HfN. For other types of fuel the axial expansion temperature feedback is in the interval from -0.18 to -0.28 pcm/($10^{-5}\Delta$H/H). The reactivity change due to expansion of the core lattice grid is calculated by increasing the lattice pitch by 2%. For all fuels investigated, the reactiv-

TABLE VII

Safety parameters of single zone cores with P/D=1.6. Coolant void and cladding worths were calculated by voiding the active part of the core only. Note that a temperature change of 1 K approximately corresponds to $\Delta H/H \sim 10^{-5}$.

Fuel	Coolant worth [pcm]	Clad worth [pcm]	Doppler $T\Delta k/\Delta T$ [pcm]	Axial fuel $\Delta k/(\Delta H/H)$ [pcm/10^{-5}]	Grid radial $\Delta k/(\Delta P/P)$ [pcm/10^{-5}]	Coolant $\Delta k/\Delta T$ [pcm/K]	$\beta_{\rm eff}$ [pcm]	τ [μs]
(TRU,Zr)N	-4330	+2900	-121	-0.22	-0.41	-0.32	199	2.3
(TRU,Hf)N	$+120$	+3300	-28	-0.20	-0.36	+0.15	165	0.63
(TRU,Y)N	-4650	+2700	-123	-0.25	-0.42	-0.39	238	2.4
(TRU,B)N	$+5190$	+4300	$\approx$0	-0.19	-0.35	+0.64	109	0.16
(U,TRU)N	$+840$	+3200	-260	-0.22	-0.39	+0.16	359	1.2
(Th,TRU)N	-930	+3100	-241	-0.24	-0.40	+0.09	240	1.2
(U,Pu)N	$\approx$0	+2900	-430	-0.23	-0.37	+0.11	358	1.6
(Pu,Zr)N	-7000	+2100	-360	-0.24	-0.40	-0.59	263	3.8
(TRUMOX,Zr)N	-4390	+2700	-224	-0.21	-0.39	-0.37	346	2.6
(TRUMOX,Hf)N	$+240$	+3400	-35	-0.22	-0.35	+0.16	213	0.67
(PuMA,Hf)N	$+1030$	+3700	-20	-0.18	-0.37	+0.22	171	0.59
(MA,Zr)N	$+8200$	+5400	-20	-0.28	-0.47	+0.59	122	0.72

TABLE VIII

Burnup characteristics of different single zone cores. $\Delta I_{\rm p} = I_{\rm p}^{\rm EOC} - I_{\rm p}^{\rm BOC}$, The reactivity swing and ^{242}Cm fractions per percent FIMA burnup are given for 5% FIMA.

Fuel	$m_{\rm act}$ at BOL [kg]	Burnup rate [%FIMA/fpd]	$\Delta k_{\rm eff}$/% FIMA [pcm/%]	^{242}Cm/% FIMA [%/%]	$\Delta I_{\rm p}$/fpd [mA/fpd]	Doubling of $I_{\rm p}$ [fpd]
(TRU,Zr)N	942	0.076	-750	0.20	0.29	60
(TRU,Hf)N	1751	0.043	-780	0.12	0.14	115
(TRU,Y)N	919	0.078	-750	0.18	0.26	65
(TRU,B)N	2900	0.027	-780	0.06	0.10	190
(U,TRU)N	5513	0.014	-230	0.07	0.01	$>$1000
(Th,TRU)N	4810	0.016	-330	0.08	0	$\approx$const
(U,Pu)N	5525	0.014	-690	0.001	0.04	300
(Pu,Zr)N	631	0.116	-930	0.002	0.48	40
(TRUMOX,Zr)N	950	0.078	-930	0.11	0.27	55
(TRUMOX,Hf)N	1822	0.042	-870	0.07	0.14	105

ity change is rather similar, being in the range from -0.35 to -0.47 pcm/($10^{-5}\Delta$P/P).

The coolant temperature coefficient was evaluated by varying the Pb/Bi density in the reactor core from 10 g·cm^{-3} to 9 g·cm^{-3}, corresponding to a temperature change from 810 to 1540 K. A strong negative feedback is exhibited by fertile-free fuels with inert diluent matrix (ZrN and YN). However, addition of fertile elements, and/or employment of absorbing matrices elevates the coolant reactivity feedback, which becomes positive. In high MA-content cores, coolant reactivity coefficient is pronounced by the increased reactivity worth of americium. Similarly, due to the spectral hardening during coolant temperature increase, the parasitic capture in absorbing materials as BN is significantly diminished, resulting in very large reactivity insertion.

The effective delayed neutron fraction $\beta_{\rm eff}$ is defined as the fraction of delayed neutrons inducing fission relative to the number of all fission-inducing neutrons in the reactor. The figure can be determined in two consecutive MCNP runs. Comparing individual core design configurations, the highest effective delayed neutron fractions are provided by (U,TRU)N fuel, as the major contributor to $\beta_{\rm eff}$ is ^{238}U. When uranium is removed from the fuel, $\beta_{\rm eff}$ can be partly regained by introduction of thorium or, in fuels with soft spectrum, by large fractions of ^{242}Pu. Boron nitride fuel performs badly ($\beta_{\rm eff}$=109 pcm) as a significant fraction of delayed neutrons is rather absorbed in ^{10}B than inducing fission. For (TRU,Hf)N fuel, the delayed neutron fractions are 82% of the values observed for ZrN matrix-based TRU fuel, i.e., $\sim$160 pcm; this value is about one-half of $\beta_{\rm eff}$ for CAPRA 04/94 core.

Burnup performance Reactivity losses exacerbate power peaking behaviour, which effectively limits the cycle length due to thermal hydraulic constraints posed by cladding material. Another limiting factor is the ability of the target module to dissipate heat from the accelerator beam. The irradiation cycle has to be sufficiently long ($>$ 100 full power days) as a very high frequency of outages (every $\sim$ 40-50 days) would negatively influence the capacity factor and overall system economy.

We therefore investigated the burnup performance of different diluent materials and assessed their merits in limiting burnup reactivity swing. The results of the depletion performance studies are given in Table VIII.

The accelerator power is doubled in about two full power months for (TRU,Zr)N, while for (TRU,Hf)N fuel it is in approximately 115 full power days. Use of the fertile material can notably prolong the length of the batch, but on the other hand, also effectively destroys the transmutation capability of the reactor, significantly diminishing burnup rates.

It appeared that the actual burnability of the absorbing matrices (HfN & BN) is questionable, as the reactivity swing per percent burnup is *larger* for these fuels than for inert diluent matrices, a result which also was observed by Yang & Khalil [60]. The reason is apparently the faster spectrum, which suppresses capture in fertile nuclides.

On the other hand, the absorbing matrices perform well when it comes to the goal to limit the amount of minor actinides in the spent fuel. Observe that the produced fraction of ^{242}Cm is almost halved when ZrN is exchanged for HfN. Using BN proves to be even more effective in cutting thermal parts of the spectra and thus promote *direct* fissioning the americium.

Down-selection of the matrices Hence, with respect to the neutronic and burnup performance of different diluent matrices investigated in our scoping study, HfN seems to provide a good combination of the neutronic and burnup characteristics:

a) maintaining hard neutron spectra and therefore minimising the production of higher actinides in the fuel cycle,

b) yielding acceptable coolant void reactivity, thus omitting a need to provide excessive BOC sub-criticalities,

c) attaining reasonable source efficiency, thus limiting the requirements on the accelerator beam power,

d) decreasing the burnup reactivity swing, thus alleviating power peaking and decreasing number of outages.

The material and thermal behaviour of this matrix is also promising and HfN is supposed to form a solid solution with actinide nitrides.

HfN is thus chosen as a candidate diluent material for our conceptual design of transuranium accelerator-driven system.

VI.A.2. Optimising pitch-to-diameter ratio

Before advancing into more elaborate studies, the effect of large coolant fractions on the neutronics, safety, and burnup performance of the burner was investigated. Large volume fractions of coolant enhance the core's potential for heat removal, thus improving safety margins to fuel and cladding damage during reactivity transients (beam overpower, loss-of-flow, and loss-of-heat sink). The obvious drawback is, however, an increase in the neutron leakage, adversely affecting neutron economy and increasing fuel inventories.

The effect of large coolant fractions on the neutronics and burnup performance was investigated by varying the reactor lattice pitch-to-diameter ratio between 1.2 and 2.4, which corresponds to coolant volume fractions of 37%, and 84%, respectively, see Table IX.

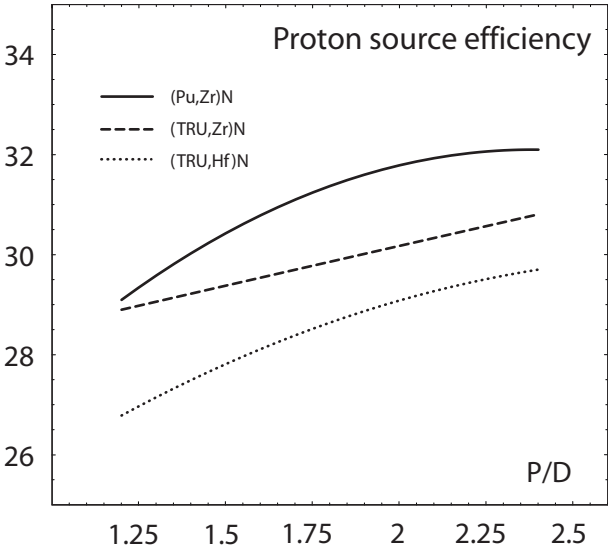

Fig. 8. The proton source efficiency ψ^* as a function of P/D in Pb/Bi-cooled ADS.

Neutronic parameters In summary, we observe that the drop in ^{241}Am fission-to-absorption ratio is rather drastic for absorbing matrices while enlarging P/D has a minor effect on the neutron spectra for (TRU,Zr)N.

Non-intuitively, the source efficiency increases as a function of P/D, see Figure 8. We infer that this phenomenon is a result of the mutual interplay of three processes. First, the actinide fuel fraction in the fuel is larger for increased P/D which elevates the neutron absorption probability in fuel. Second, the probability of the fission chain to be accommo-

TABLE IX

Neutronic and burnup performance of the transuranium burner with ZrN, HfN, and BN as a function of pitch-to-diameter ratio.

Fuel	P/D	^{241}Am $\sigma_{\rm f}/\sigma_{\rm a}$	Clad worth [pcm]	Axial fuel Δk/(ΔH/H) [pcm/10^{-5}]	Grid radial Δk/(ΔP/P) [pcm/10^{-5}]	Coolant Δk/ΔT [pcm/K]	$m_{\rm act}$ at BOL [kg]	Burnup rate [%FIMA/fpd]	$\Delta k_{\rm eff}$/ %FIMA [pcm/%]	Doubling of $I_{\rm p}$ [fpd]
(TRU,Zr)N	1.2	0.106	+3700	-0.27	-0.36	-0.19	746	0.094	-740	50
	2.0	0.101	+2300	-0.24	-0.48	-0.35	1155	0.063	-760	85
	2.4	0.097	+1800	-0.20	-0.51	-0.38	1400	0.053	-760	90
(TRU,Hf)N	1.2	0.214	+4300	-0.20	-0.29	+0.13	1532	0.048	-780	95
	2.0	0.178	+2900	-0.19	-0.44	+0.27	1981	0.038	-800	115
	2.4	0.163	+2400	-0.22	-0.56	+0.43	2244	0.034	-780	120
(TRU,B)N	1.2	0.432	+5600	-0.22	-0.30	+0.17	2621	0.030	-820	140
	2.0	0.328	+3400	-0.21	-0.44	+0.79	3179	0.025	-750	190
	2.4	0.286	+2400	-0.21	-0.47	+0.90	3442	0.023	-700	200

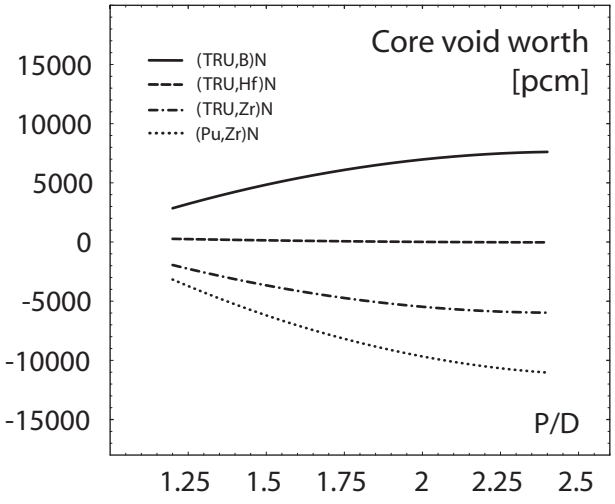

Fig. 9. Core void worths in Pb/Bi-cooled TRU burners. Introduction of strongly absorbing materials to the fuel has an adverse effect on the coolant void reactivity.

dated within the core increases with increasing core dimensions. Third, the difference in the neutron spectra of the source and eigenmode neutrons increases with P/D.

Safety performance Note furthermore that enlarging the pin lattice in order to reduce the void worth can prove successful only in systems with inert matrix fuel, see Figure 9. In a core with a significant amount of fertile isotopes and/or with substantial presence of absorbing materials, the coolant void worth is significantly elevated.

The cladding worth is a decreasing function of the lattice pitch. The parasitic absorption in the construction material is less and less significant with larger P/D and likewise the reactivity, which is introduced into the system during flush out of structural material from the core.

Burnup performance As the volume fractions increases with P/D, the probability of neutrons to leak out the system increases. This, in turn, implicates higher specific fuel inventories and consequently lower burnup rates. Decrease of the burnup rates also diminishes the accelerator beam swing. Observe that for ZrN and HfN matrices, the reactivity swing is approximately independent of P/D, while it decreases slightly for BN. With larger pitch, the neutron spectrum becomes softened with increasing burnability of the matrix as a result.

TABLE X

The four zone heterogeneous design of the (TRU,Hf)N burner, the fraction of the HfN in individual zones was adjusted such that radial power peaking factor is kept under 1.3.

S/A flat-to-flat (cm)	18.2
S/A pitch (cm)	18.4
Thickness of the duct (cm)	0.25
Pins per S/A	331
Pitch-to-diameter ratio	1.6
Number of S/As	80
Averaged linear power (kW/m)	30.2
AnN fractions (vol%)	29/31/35/42
Spallation target radius (cm)	20
Radius of accelerator beam tube (cm)	15
$E_{\rm n}$ (keV)	194/210/221/191
$\sigma_{\rm f}/\sigma_{\rm a}$ for ^{241}Am	0.17/0.19/0.20/0.18
Proton efficiency ψ^* at BOL	24.5
Core void worth (pcm)	+ 880
Cladding and duct worth (pcm)	+ 3660
^{242}Cm/%FIMA (%/%)	0.12
$m_{\rm act}$ at BOL (kg)	1915
Burnup rate (%FIMA/fpd)	0.040
$\Delta k_{\rm eff}$/%FIMA (pcm/%)	-850
Doubling of $I_{\rm p}$ (fpd)	110

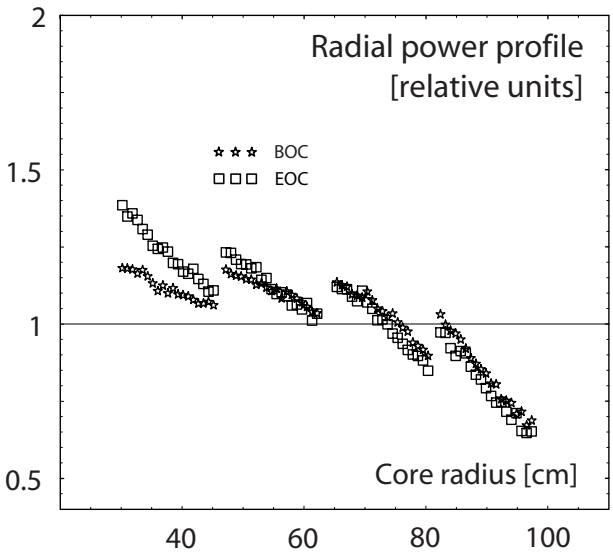

Fig. 10. Radial power profile for four-zone design, pitch-to-diameter ratio was kept at 1.6.

VI.B. Heterogenous, 4 zone core

For our scoping, parametric studies we used one-zone, homogeneous duct-less modelling approach. In order to investigate the influence of the heterogeneous zoning on the ADS performance, the four-zone heterogeneous core was set up. The sub-assembly design was chosen such that a direct intercomparison between homogeneous and heterogenous configurations is possible. Therefore, both pellet and pin geometry is retained as well as pitch-to-diameter ratio and spallation target dimensions. The basic geometry parameters of the heterogenous, a four zone core are summarised in Table X. In the centre of the system, seven sub-assemblies have been removed and replaced by a target module.

The amount of HfN matrix was adjusted in each zone so that the radial power peaking is limited to 1.3 at BOL and k_{eff}=0.96, see Figure 10.

The heterogenous zoning results in an increase of the specific actinide inventory by 8.3% in comparison to the one-zone design. Consequently, the burnup rate and reactivity swing decrease. The accelerator beam is doubled in 110 effective power days, a slight decrease in time in comparison to the homogeneous case. The neutron spectrum is harder in the second and third core zone while neutrons entering the innermost and outermost zones are additionally slowed down in the target and radial reflector, respectively.

VII. CONCEPTUAL CORE DESIGN

In our scoping studies we have identified HfN as a promising candidate diluent material for highly reactive TRU fuel.

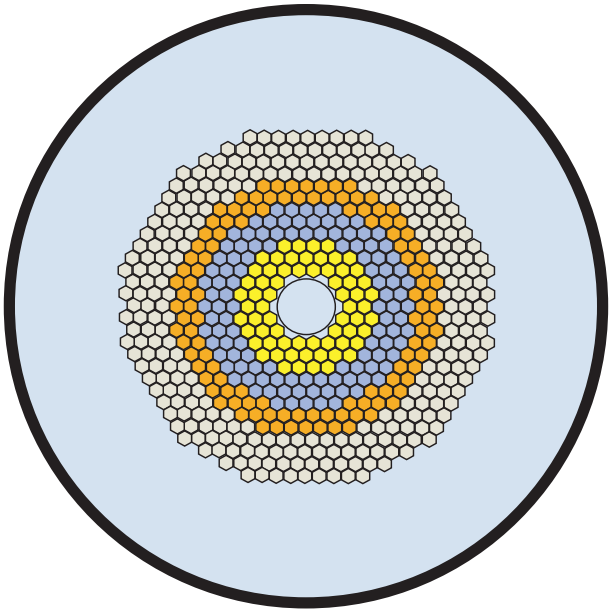

Fig. 11. Cross section of the conceptual core design. The core consists of three enrichment zones with different matrix fractions. Radial steel reflector sub-assemblies are depicted in grey. The thickness of the radial reflector was optimised so that the coolant void reactivity is minimised.

In the next section, we present a conceptual core design of a (TRU,Hf)N-fuelled Pb/Bi-cooled ADS operating in the two-component scenario.

VII.A. Core geometry

For the optimised conceptual core design, the pin-to-diameter ratio is selected as a compromise between the requirements to provide sufficient margin to core damage and reasonable neutronic and burnup characteristics of the core. For the sake of simplicity, the same pin pitch has been chosen throughout, P/D=1.75. The conceptual core design parameters are presented in Table XI.

The flat-to-flat (FTF) of the S/A is then chosen correspondingly in order fit the ∼20-cm radius target module. In this design, the sub-assembly FTF is decreased to 10.8 cm, thus allowing finer distribution of fuel in the core and facilitating symmetric reloading patterns. Further decrease of the duct FTF would not however be meaningful as this would lead to an excessive fraction of construction materials in the core which would cause softening of the neutron spectra. The power of the system was kept constant at the level of 800 $\mathrm{MW_{th}}$ as limited by ability of the target to remove the dissipated heat.

The proton beam impact window was placed 20 cm above

TABLE XI

Design specifications of the conceptual core. Pin and pellet parameters were presented in Table I.

Parameters	Conceptual design
S/A outer flat-to-flat (cm)	10.8
S/A pitch (cm)	11.0
Duct thickness (cm)	0.25
Pins per S/A	91
Pitch-to-diameter ratio	1.75
Number of core S/As	294
Thermal power (MW)	800
Averaged linear power (kW/m)	29.9
Spallation target outer radius (cm)	22.5
Radius of accelerator beam tube (cm)	15

TABLE XII

TRU volume fractions in fuel and a number of S/As in each enrichment zone yielding a radial power peaking factor less than 1.3 at BOL. There is 282 sub-assemblies in the radial reflector.

Sub-assembly row/zone	1-3	4-6	7-8	9-12
TRU fraction in fuel (vol%)	32	37	45	–
Number S/As	66	114	114	282

the midplane of the core in order to minimise the number of neutrons leaking out of the spallation target into the axial reflectors and thus maximising the source efficiency. At the same time, it yields almost axially symmetric power distribution. The gas plenum is located in upper part of the core, reducing risks associated with positive reactivity insertion due to gas release from ruptured cladding. The length of the upper plenum was assumed to be relatively large, 150 cm, sufficient to accommodate released fission gases and all helium from decayed ^{242}Cm.

The outer radius of the spallation target is slightly enlarged to 22.5 cm and the core now consists of three distinctive zones as illustrated in Figure 11. The fraction of the matrix was adjusted so that a radial power peaking factor less than 1.3 is obtained at BOL, see Table XII. The radial reflector consists of four rows of sub-assemblies, steel volume fraction being 80%.

VII.B. Neutronics

The characteristics of the optimised core design are summarised in Table XIII. The presence of an absorbing matrix in the fuel yields hard neutron spectrum thus decreasing neutron capture probability in even-neutron number nuclides. The distribution of fission-to-absorption probabilities of ^{238}Pu, ^{241}Am, ^{243}Am, and ^{244}Cm is displayed in Figure 12. Note that in the present design the fission probability is increased by a factor of two in the case of ^{241}Am and ^{243}Am in comparison to CAPRA cores or other ADS TRU burners with inert matrix fuel, resulting in a significant reduction of the He-producing nuclides ^{242}Cm and ^{238}Pu.

The void worth was calculated by the voiding of coolant from core including spaces inbetween sub-assemblies. Despite the presence of absorbing matrix in the core, a slightly negative void reactivity feedback (-270 pcm) could be obtained in the present design. Voiding the core together with the upper plenum and radial reflector brings the system additional negative reactivity (-3500 pcm).

The presence of americium results in deterioration of prompt fuel temperature feedback. In the very hard spectrum, hardly any neutrons reach resonance region and the Doppler feedback is accordingly rather unreliable. The effective delayed neutron fraction $\beta_{\rm eff}$ is also small.

VII.C. Burnup

Irradiating the fuel for 100 days at the constant thermal power of 800 MW yielded a reactivity swing of 3300 pcm which was compensated for by an increase of accelerator power from 16 to 30 MW. The average cycle burnup reached 3.6%, with local burnups ranging from 5.5% in zone (S/A row) one to 2.5% in zone (S/A row) eight.

The maximum achievable burnup of fuel pin was consequently determined by respecting cladding radiation damage and pin burst limits. The gas pressure in the fuel pin was calculated assuming that all fission gases (elements with boiling temperature lower than 2150 K) together with all helium from

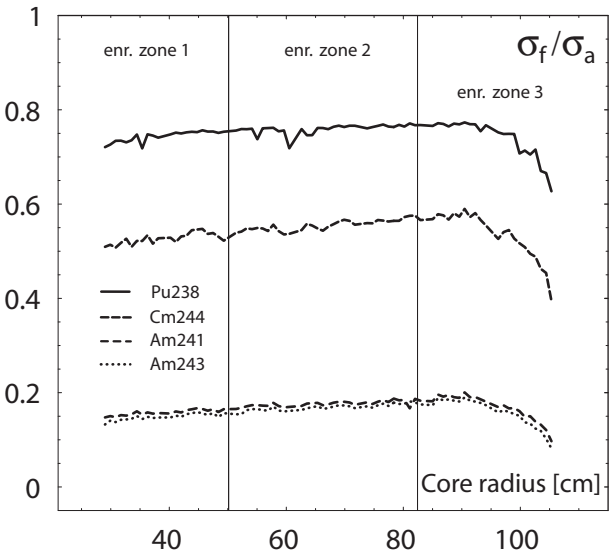

Fig. 12. Pin-by-pin calculated radial distribution of fission probabilities.

TABLE XIII

Neutronic, safety and burnup performance of the conceptual core design. A capacity factor of 0.75 is assumed.

Parameters	Unit	Conceptual design
E_n ($1^{st}/2^{nd}/3^{rd}$ enrichment zone)	keV	164/183/166
Proton efficiency ψ^* (BOC/EOC)		26.9/26.0
Coolant void worth at BOL	pcm	-270
Cladding and duct worth at BOL	pcm	$+6390$
Flooding of the accelerator tube	pcm	$+200$
Doppler $T\Delta k/\Delta T$	pcm	-47
Axial fuel expansion $\Delta k/(\Delta H/H)$	pcm/10^{-5}	-0.21
Grid expansion $\Delta k/(\Delta P/P)$	pcm/10^{-5}	-0.52
Coolant density change $\Delta k/\Delta T$	pcm	$+0.13$
$\beta_{\rm eff}$ at BOL	pcm	230
m_{act} at BOL	kg	2140
Burnup rate	%FIMA/fpd	0.036
Reactivity loss	pcm/batch	-3300
$\Delta k_{\rm eff}$/%FIMA	pcm/%	-850
Doubling of the accelerator power I_p	fpd	100
^{242}Cm fraction in fuel	%/%FIMA	0.12
Number of batches		5
Batch length	days	100
Average burnup without initial core reshuffle	%FIMA	$\sim$20
Maximum radiation damage at EOL	dpa-NRT	100
Net Pu consumption	kg/efpy	188
Net MA consumption	kg/efpy	21

^{242}Cm decay are released from the fuel. The maximum pressure in the most exposed pin in the S/A closest to the target is 3.7 MPa at the end of one irradiation cycle/batch (100 fpd), generating a hoop stress of 18.5 MPa. In order to keep this figure below the limiting value of 100 MPa, measured for irradiated rods at the temperature of 1140 K [38], the maximum residence time of the most exposed sub-assembly is 540 fpd.

The radiation damage was estimated using the formula suggested by Garner [61], relating 200 dpa-NRT damage rate to the damage neutron fluence (E_n>0.1 MeV) of $4{\cdot}10^{23}$ n/cm^2. The highest exposure is found for high-burnup pins placed closest to the spallation target. There, 69% of the neutron flux is above 100 keV, with a cycle/batch averaged fast flux of $4.2{\cdot}10^{15}$n/cm^2/s. Considering an axial power peaking factor of 1.28, the maximum fast fluence in cladding after 540 fpd is $2{\cdot}10^{23}$ n/cm^2 $\sim$ 100 dpa-NRT, which could be a reasonable estimate of the dose limit of Si-modified ferritic steels like EP-823 [47].

Thus, a sub-assembly burnup of 0.55%FIMA/fpd $\cdot$ 540 fpd $\sim$ 30%FIMA is in principle achievable. In our simplified approach, we have neglected pellet-cladding interaction which might somewhat overestimate the value of cladding burst temperature. Recent Russian tests have shown that the swelling of the liquid-metal bonded ($U_{0.2}$,$Pu_{0.8}$)N pins does not exceed 1-1.2%/%FIMA, which allows burnup $\sim$15%FIMA [50].

The fuel cycle our conceptual TRU ADS design thus consist of five 100-days long irradiation cycles. The length of the reactor stops in-between maintenance outages is three days assuming half a day for reactor shut-down and restart. During that period a few reflector sub-assemblies in the core perimeter are substituted with fuel S/As. Thus, even without fuel reshuffling, an average burnup of the first, BOL core $\sim$20%FIMA can be reached neutronically.

Due to the burnup of TRU and consequently increasing fractions of fission products in the fuel, proton source efficiency decreases. The $k_{\rm eff}$ in the beginning of the each irradiation batch is thus increased from 0.962 at BOL to 0.970 at the fifth irradiation cycle, in order to keep the accelerator beam power at approximately 16 MW at BOC. The reactivity drop during one irradiation batch is compensated by an increase in accelerator beam by less than a factor of 2.0.

The radial power profile of the core at BOC is displayed in Figure 13. At the EOC, the pin averaged linear power ratings of the most exposed pins in the first zone reaches 54

kW/m, leaving maximum cladding temperatures below the 890 K limit.

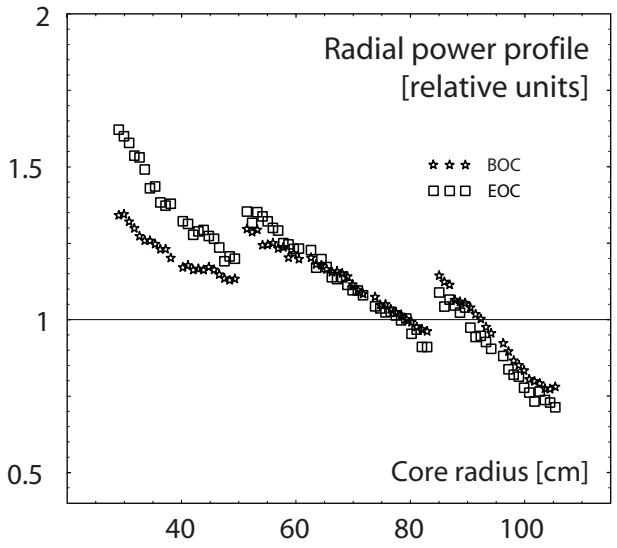

Fig. 13. Radial power profile at BOC and EOC. The maximum steady-state linear power of fuel pin remains under 60 kW/m, ensuring thermal stability of the structural material.

VII.D. Equilibrium

The quality of the transuranium vector decreases when approaching the equilibrium state, which implies higher TRU specific fuel inventories. Mainly, the amount of the fissile isotope ^{239}Pu diminishes, while ^{242}Pu and ^{238}Pu (from ^{242}Cm decay) become more abundant in the fuel. Similarly, the amount of fertile isotopes ^{243}Am and ^{244}Cm increases. The core specific power is consequently lowered, alleviating reactivity loss and power peaking.

The beneficial effect of the HfN matrix in terms of the limitation of higher actinides in the fuel cycle is illustrated by evaluating the concentration of curium in the equilibrium fuel cycle. The qualitative analyses showed that curium inventory in mass-constrained equilibrium is about 1% for the present conceptual design, which is to be compared to more than 4% in a CAPRA type spectrum ($4{\cdot}10^{15}$ n/cm^2/s).

VIII. SAFETY CONSIDERATIONS

The lattice pitch of the conceptual design is chosen so that instant decomposition of nitride fuel or cladding damage are prevented under accidental conditions, involving unprotected beam overpower transient, unprotected loss-of-flow, and unprotected loss-of-heat sink. The thermal hydraulic analyses show that the maximum centerline steady-state temperature of the fuel is about 1510 K at the EOC in the most exposed fuel pin. The corresponding coolant temperature gradient is 220 K, which is a 60 K increase compared to BOC. During an unprotected beam overpower transient when the accelerator beam is increased by a factor of two at BOC, the peak fuel temperature remains under 2150 K, still leaving 250 K margin to the tentative fuel decomposition limit.

For P/D$\sim$1.75 and coolant column height of 5.5 m, about 23% of the flow is maintained during loss-of-flow accident and the cladding temperature reaches the 1140 K burst limit in about 25 s [15]. The preliminary calculations revealed that the separation distance between core midplane and thermal centre of the steam generator would need to be increased to about 20-25 m in order to guarantee the cladding integrity under ULOF. In this respect we note that austenitic steels (e.g. 15-15Ti) provide much higher margins to the pin burst during accidental conditions (1333 K [38]) due to their higher irradiation creep resistance. Their ability to withstand Pb/Bi corrosion is, however, small requiring much lower power ratings and/or excessive coolant volume fractions, both with adverse effect on the burnup performance (burnup rate, softening neutron spectra and thus increasing production of higher actinides). Thus, it appears that, at present, there is no obvious choice of cladding material for our system.

IX. CONCLUSIONS

We investigated the neutronic & burnup characteristics of a lead/bismuth cooled accelerator-driven transuranium burner in a start-up mode scheme. A wide spectrum of inert and absorbing matrices and core lattice configurations was studied in order to select promising fuels and core designs.

HfN-based fuels have been identified as an attractive option for TRU ADS burners. HfN provides a good combination of neutronic, burnup and thermal characteristics: maintaining hard neutron spectra and thus limiting the production of higher actinides in the fuel cycle, providing acceptable coolant void reactivity, hence omitting a need to provide excessive BOC sub-criticalities, yielding a reasonable value of the source efficiency limiting thus the requirements on the accelerator beam power, and allowing for high specific fuel inventories, decreasing the burnup reactivity swing and number of required outages. HfN appears to have a stabilising effect on the fuel in terms of improving its thermal conductivity. Moreover, it is assumed to form a solid solution with actinide nitrides and be reprocessible in aqueous technologies.

Considering key material-related and thermal hydraulic design constraints, we presented a conceptual design of a lead/bismuth eutectic cooled ADS burner employing (TRU,Hf)N fuel. The design featured a hard neutron spec-

trum yielding a factor of two higher ^{241}Am and ^{243}Am fission probabilities than are typical for systems employing inert matrix based fuels. The burnup reactivity swing and associated power peaking in the core were managed by an appropriate choice of the cycle length (100 days) and by core enrichment zoning. In each batch, the accelerator power is allowed to increase by less than a factor of two. Average fuel discharge burnup reached 20%FIMA even without reshuffling of the initial core S/As. The amount of curium in the equilibrium cycle is limited by a factor of four in comparison to the fuel cycle involving CAPRA type burners or any TRU ADS burner employing inert matrix fuel.

The conceptual core design features favourable safety characteristics - core coolant void worth being slightly negative. At the same time, fuel and cladding damage is prevented during unprotected beam overpower transient. However, preliminary studies show that the excessive coolant volumes are required in order to guarantee cladding integrity under unprotected loss-of-flow accidents as the burst limit of ferritic steels is low (about 200 K below that for austenitic). Because austenitic steels feature very low high temperature corrosion resistance towards lead-alloys, it appears that the choice of the cladding material for our system remains to be an open question.

Further studies are required in order to investigate the system transient behaviour in more detail and analyse its characteristics during an approach and in the equilibrium. Especially, safety merits of increased TRU inventories being a consequence of HfN matrix have to be assessed. High temperature material and irradiation performance of the Hf-based fuels needs to be investigated, too.

ACKNOWLEDGEMENTS

The authors would like to thank Marcus Eriksson for clarifying questions concerning transient behaviour of the system. Financial support from Swedish Fuel and Waste Management Board (SKB AB) and European Commission is gratefully acknowledged.

REFERENCES

1. H. Claiborne, Neutron-induced transmutation of high-level radioactive waste, Technical Report ORNL-TM-3964, Oak Ridge National Laboratory, 1972.

2. D. Foster et al., Review of PNL study on transmutation processing of high level waste, Technical Report LA–UR–74–74, Los Alamos National Laboratory, USA, 1974.

3. T. Takizuka et al., Conceptual design of transmutation plant, in *Proceedings of the Specialist meeting on accelerator driven transmutation technology for radwaste*, page 707, LA–12205–C, Los Alamos National Laboratory, USA, 1991.

4. C. Rubbia et al., Conceptual design of a fast neutron operated high power Energy Amplifier, Technical Report CERN/AT/95–44(ET), CERN, 1995.

5. M. Salvatores et al., Nuclear Instruments and Methods in Physics Research **A414**, 5 (1998).

6. T. Takizuka et al., Studies on accelerator driven transmutation systems, in *Proceedings of the Fifth international information exchange meeting*, page 383, OECD/NEA, Mol, Belgium, November 25-27, 1998.

7. B. Carluec and P. Anzieau, Proposal for a gas cooled ADS demonstrator, in *Proceedings of the Third International Conference on Accelerator-Driven Transmutation Technologies and Applications, ADTTA'99*, Praha, Czech Republic, June 7-11, 1999.

8. A roadmap for developing accelerator transmutation of waste (ATW) technology: A report to Congress, 1999.

9. F. Venneri, Disposition of nuclear waste using subcritical accelerator driven systems, Technical Report LA-UR-98-985, Los Alamos National Laboratory, 1998.

10. R. Hill and H. Khalil, Physics studies for sodium cooled ATW blanket, in *Proceedings of the IAEA Technical Committee Meeting on Core Physics and Engineering Aspects of Emerging Nuclear Energy Systems for Energy Generation and Transmutation, IAEA-TECDOC-1356*, Argonne National Laboratory, USA, November 28 - December 1, 2000.

11. K. Tsujimoto et al., Journal of Nuclear Science and Technology **41**, 21 (2004).

12. H. Wider and H. Schönherr, Beam pipe with safety function for accelerator driven nuclear systems, European patent No. 9811339.7, 1998.

13. W. Maschek et al., Safety analyses for ADS cores with dedicated fuel and proposals for safety improvements, in *Proceedings of the IAEA Technical Committee Meeting on Core Physics and Engineering Aspects of Emerging Nuclear Energy Systems for Energy Generation and Transmutation, IAEA-TECDOC-1356*, Argonne National Laboratory, USA, November 28 - December 1, 2000.

14. M. Eriksson et al., Safety analysis of Na and Pb-Bi coolants in response to beam instabilities, in *Proceedings of the Third International Workshop on Utilisation and Reliability of High Power Proton Accelerators*, Santa Fe, USA, May 2002.

15. M. Eriksson, J. Wallenius, M. Jolkkonen, and J. Cahalan, Inherent safety of fuels for accelerator-driven systems, Submitted to Nuclear Technology, 2004.

16. A. Conti et al., CAPRA exploratory studies of U-free fast Pu burner cores, in *Proceedings of the International Conference on Evaluation of Emerging Nuclear Fuel Cycle Systems, GLOBAL'95*, page 1316, ANS, Versailles, France, September 11-14, 1995.

17. K. Tuček, J. Wallenius, and W. Gudowski, Annals of Nuclear Energy **31**, 1783 (2004).

18. K. Tuček et al., Source efficiency in an accelerator-driven system with burnable absorbers, in *Proceedings of the International Conference on Future nuclear systems, GLOBAL 01*, Paris, France, September 9-13, 2001.

19. H. Takano et al., A design of inherent safety core, aseismicity and heat transport system in lead-cooled nitride-fuel fast reactor, in *Proceedings of the International Topical Meeting on Advanced Reactor Safety*, Pittsburgh, USA, April 17-21, 1994.

20. T. Umeoka et al., Study of CDA driven ULOF for nitride fuel core, in *Proceedings of the International Conference on Future Nuclear Systems, GLOBAL'99*, ANS, Jackson Hole, USA, August 29 - September 3, 1999.

21. H. Kleykamp, Journal of Nuclear Materials **275**, 1 (1999).

22. M. Takano et al., Study on the stability of AmN and (Am,Zr)N, in *Proceedings of the International Conference on Future Nuclear Systems, GLOBAL 2003*, ANS, New Orleans, USA, November 16-20, 2003.

23. K. Richter and C. Sari, Journal of Nuclear Materials **184**, 167 (1991).

24. Y.Suzuki and Y.Arai, Journal of Alloys and Compounds **271–273**, 577 (1998).

25. M. Takano et al., Synthesis of americium mononitride by carbothermic reduction method, in *Proceedings of the International Conference on Future Nuclear Systems, GLOBAL'99*, ANS, Jackson Hole, USA, August 29 - September 3, 1999.

26. K. Minato et al., Journal of Nuclear Materials **320**, 18 (2003).

27. M. Jolkkonen, M. Streit, and J. Wallenius, Journal of Nuclear Science and Technology **41**, 457 (2004).

28. Y. Arai and T. Ogawa, Research on nitride fuel and pyrochemical process for MA transmutation, in *Proceedings of the Seventh Information Exchange Meeting on Actinide and Fission Product Partitioning and Transmutation*, OECD/NEA, Jeju, Korea, October 4-16, 2002.

29. Y. Arai et al., J. Nucl. Mater. **195**, 37 (1992).

30. H. Matzke, *Science of Advanced LMFBR fuels*, North-Holland, 1986.

31. J. Wallenius and S. Pillon, N-15 requirement for 2^{nd} stratum ADS nitride fuels, in *AccApp'01 & ADTTA'01 Nuclear Applications in the New Millennium*, ANS, Reno, USA, November 11-15, 2001.

32. Thorium cycle, Status of R&D and evolution, Technical report, Research Committee of Survey of Thorium Cycle, Atomic Energy Society of Japan (in Japanese), 1980.

33. T. Kosolapova, editor, *Handbook of high temperature compounds: Properties, production, applications*, Hemisphere Publishing Corporation, 1990.

34. M. Mignanelli, Stability of U and U,Zr nitrides at high temperatures, in *CONFIRM progress meeting, 27-28 September 2001*, 2001.

35. V. Basini, J. Ottaviani, and J. Richaud, Characterisation of (Pu,Zr)N pellets, Technical Report FIKW-CT-2000-00096, EU project, Collaboration On Nitride Fuel Irradiation and Modelling (CONFIRM), 2004.

36. H. Pierson, *Handbook of Refractory Carbides and Nitrides*, William Andrew Publishing/Noyes, 1996.

37. A. Rousanov et al., Developing and studying the cladding steels for the fuel elements of the NPIs with heavy coolant, in *Proceedings of the Conference Heavy liquid metal coolants in nuclear technology, HLCM'98*, Institute of Physics and Power Engineering, Obninsk, Russia, October 5-9, 1998.

38. N. Cannon et al., Transient and static mechanical properties of D9 fuel pin cladding and duct material irradiated to high fluence, in *Effects of Radiation on Materials: 15$^{\mathrm{th}}$ International Symposium, ASTM STP 1125*,

edited by R. Stoller, A. Kumar, and D. Gelles, American Society for Testing and Materials, Philadelphia, USA, 1992.

39. H. Etherington, editor, *Nuclear Engineering Handbook*, McGraw-Hill Book Company, 1958.

40. R. Thetford and M. Mignanelli, Journal of Nuclear Materials **320**, 44 (2003).

41. M. Streit et al., Journal of Nuclear Materials **319**, 51 (2003).

42. M. Streit, Personal communication, 2004.

43. A. Freeman and C. Keller, editors, *Handbook of the Physics and Chemistry of the Actinides*, volume 4, North-Holland, Amsterdam, 1986.

44. D. Pankratov et al., Polonium problem in nuclear power plants with lead-bismuth as a coolant, in *Proceedings of the Conference Heavy liquid metal coolants in nuclear technology, HLCM'98*, Institute of Physics and Power Engineering, Obninsk, Russia, October 5-9, 1998.

45. G. Yachmenyov et al., Problems of structural materials' corrosion in lead-bismuth coolant, in *Proceedings of the Conference Heavy liquid metal coolants in nuclear technology, HLMC'98*, Institute of Physics and Power Engineering, Obninsk, Russia, October 5-9, 1998.

46. N. Novikova, Y. Pashkin, and V. Chekunov, Some features of sub-critical blankets cooled with lead-bismuth, in *Proceedings of the Third International Conference on Accelerator-Driven Transmutation Technologies and Applications, ADTTA'99*, Praha, Czech Republic, June 7-11, 1999.

47. S. Porollo et al., Journal of Nuclear Materials **329-333**, 314 (2004).

48. AAA Quarterly Report, Apr-Jun 2002, Technical Report LA–UR–02–5515, Los Alamos National Laboratory, USA, 2002.

49. B. Rogozkin et al., Preliminary experimental substantiation of fuel element design with mononitride fuel and lead sublayer for BREST reactor, in *Proceedings of the Conference Heavy liquid metal coolants in nuclear technology, HLCM'98*, Institute of Physics and Power Engineering, Obninsk, Russia, October 5-9, 1998.

50. B. Rogozkin, N. Stepennova, and A. Proshkin, Atomnaya Energiya **95**, 208 (2003).

51. *Actinide and Fission Product Partitioning and Transmutation, Status and Assessment Report*, OECD/NEA, 1999.

52. J.-O. Andersson et al., Calphad **26**, 273 (2002).

53. J.F. Briesmeister, editor, MCNP – A general Monte Carlo N-Particle transport code, version 4C, Technical Report LA–13709–M, Los Alamos National Laboratory, USA, 2000.

54. J. Cetnar et al., MCB - a continuous energy Monte Carlo Burnup code, in *Fifth international information exchange meeting*, page 523, OECD/NEA, Mol, Belgium, November 25-27, 1998.

55. M. Chadwick et al., Nuclear Science and Engineering **131**, 293 (1999).

56. P. Seltborg, J. Wallenius, K. Tuček, and W. Gudowski, Nuclear Science and Engineering **145**, 390 (2003).

57. R. MacFarlane and D. Muir, *The NJOY nuclear data processing system, version 91*, LA-12740-M, Los Alamos National Laboratory, USA, 1994.

58. J. Wallenius and M. Eriksson, Neutronic design of subcritical minor actinide burners, Submitted to Nuclear Technology, 2004.

59. C. Cho, T. Song, and N. Tak, Nuclear Engineering and Design **229**, 317 (2004).

60. W. Yang and H. Khalil, Neutronics design studies of an LBE cooled ATW blanket, in *Proceedings of the IAEA Technical Committee Meeting on Core Physics and Engineering Aspects of Emerging Nuclear Energy Systems for Energy Generation and Transmutation, IAEA-TECDOC-1356*, Argonne National Laboratory, USA, November 28 - December 1, 2000.

61. R. Cahn, P. Haasen, and E. Kramer, *Materials Science and Technology: a comprehensive treatment*, volume 10A, VCH, 1994.

Paper III

J. Wallenius, K. Tuček, J. Carlsson, and W. Gudowski
Application of burnable absorbers in an accelerator driven system
Nuclear Science and Engineering, **137**, 96 (2001)

Application of burnable absorbers in an accelerator driven system

Jan Wallenius, Kamil Tuček, Johan Carlsson, Waclaw Gudowski
Department of Nuclear & Reactor Physics
Royal Institute of Technology
100 44 Stockholm, Sweden
E-mail: janne@neutron.kth.se

Abstract

The application of burnable absorbers (BA) for minimization of power peaking, reactivity loss and capture to fission probabilities in an accelerator driven waste transmutation system (ADS, ATW) has been investigated. ^{10}B enriched B_4C absorber rods were introduced into a lead/bismuth cooled core fuelled with TRU discharges from light water reactors in order to achieve smallest possible power peakings at a BOL sub-criticality level of 0.97. Detailed Monte Carlo simulations show that a radial power peaking equal to 1.2 at BOL is attainable using a four zone differentiation in BA content. Using a newly written Monte Carlo Burnup code (MCB), reactivity losses were calculated to be 640 pcm per percent transuranium burnup, for unrecycled TRU discharges. Comparing to corresponding values in BA free cores, BA introduction diminishes reactivity losses in TRU fuelled sub-critical cores by about 20%. Radial power peaking after 300 days of operation at 1200 MW thermal power was less than 1.75 at a sub-criticality level of $\sim$ 0.92, which appears to be acceptable, with respect to limitations in cladding and fuel temperatures. In addition, the use of BA yields significantly higher fission to capture probabilities in even neutron number nuclides. Fission to absorption probability ratio for ^{241}Am equal to 0.33 was achieved in the configuration here studied. Hence, production of the strong α-emitter ^{242}Cm is reduced, leading to smaller fuel swelling rates and pin pressurization. Disadvantages following BA introduction, such as increase of void worth and decrease of Doppler feedback in conjunction with small values of β_{eff}, need to be addressed by detailed studies of sub-critical core dynamics.

Introduction

As was shown in studies made at CEA, recycling of both plutonium, americium *and* curium is mandatory in order to achieve a substantial reduction factor ($\sim$ 100) of the radiotoxic inventory sent to geological repository from present nuclear parks [1]. The introduction of a major fraction of minor actinides into the nuclear fuel cycle however raises complex issues regarding reprocessing, fuel fabrication, core behaviour during transients and fuel performance during irradiation. In general, it is assumed that americium (and curium) is to be recycled in fast reactors, due to the superior neutron economy of the fast neutron spectrum, which will allow for higher burnups, and hence lower losses to secondary waste streams.

One option being considered for the minor actinide (MA) management is burnout in a second stratum of "dedicated" actinide burner reactors [2, 3]. As the vanishing Doppler feedback in conjunction with a very low β_{eff} would lead to deterioration of safety margins for critical configurations, sub-critical designs have been adopted for these MA-burners by a number of authors [4, 5, 6, 7].

Excess plutonium from light water reactors may be recycled in fast reactors. Homogeneous mixing of Pu with the minor actinides in accelerator driven systems (ADS) has also been proposed [8, 9, 10]. Since requirements on Doppler feedback are relaxed, the ADS core spectrum can be much harder than for corresponding critical configurations [11, 12, 13]. Consequently, americium and curium production in the entire fuel cycle is minimised. A major drawback of this approach is the large reactivity loss appearing due to burnout of ^{239}Pu and ^{241}Pu, with a concomitant increase in power peaking that may not easily be compensated for by a change in accelerator proton current. Consequently, maximum burnup becomes limited by power peaking factors, rather than by radiation damage to cladding and fuel.

The introduction of thorium as a fertile material to keep up reactivity [9] would imply the implementation of an entire new fuel cycle, and must be regarded as a distant future option. The application of burnable absorbers to perform the same task has to the authors' knowledge not received much attention in the published literature, apart from the suggestion to use ^{99}Tc in-core sub-assemblies [10]. Hence we have performed an investigation of advantages and drawbacks resulting from a massive introduction of classical burnable absorbers in sub-critical TRU-fuelled cores. First we show how power peakings can be minimised by use of a differentiated concentration of neutron absorbers in a lead/bismuth cooled core. Then, burnup calculations reveal the impact of the BA introduction on reactivity losses and effective minor actinide destruction rates. Finally we discuss how the design can be further improved.

System concept

The burnable poison option was considered for the CAPRA design [11], in order to cope with the high Pu reactivity. The option was however rejected due to degradation of reactivity coefficients needed for safe operation of a critical reactor. On the other hand, in a sub-critical system, one may have enough criticality margin in order to accommodate a positive void coefficient in conjunction with vanishing Doppler feedback. In addition, the absorber will have a positive influence on transmutation efficiencies in terms of fission to absorption ratios, since they shield slower neutrons from being captured by even neutron number TRU nuclides.

While already having introduced BA into the core, a differentiated concentration could be used for flattening of the core's power density distribution. As it turns out, radial power peakings at BOL can be virtually eliminated by an appropriate distribution of absorber pins among the fuel pins in each sub-assembly. Since the absorbers should be burnable, we have chosen enriched boron carbide as a reference material. Boron carbide is used in FBR control rods due to its high reactivity worth in fast neutron spectra.

Since sub-criticality is assumed, an additional cost is to be paid in terms of spallation neutrons to initiate the fission cascade. In order to maintain a high multiplication of source neutrons during burnup we substitute the absorber matrix in the inner core zones with depleted uranium, which also is more tolerant to increase in power peaking. Obviously, this diminishes effective TRU transmutation rates somewhat.

Even with a successful power flattening strategy implemented at BOL, power peaking will increase with burnup in sub-critical systems, as neutron multiplication decreases. Since power densities are limited by linear ratings, the number of fuel pins and consequently the number of dedicated cores needed to manage the minor actinides will depend on choice of fuel matrix and coolant. In the present study we have adopted nitride fuels, which may enable a doubling of linear ratings, as compared to the corresponding uranium free oxide and metal fuels.

Expected problems with high temperature stability of nitride fuels may be addressed by use of nitrogen bonding, which is known to suppress decomposition of actinide nitrides up to temperatures of 2800 K [14, 15]. Production of ^{14}C may be minimised by usage of 99% ^{15}N enriched nitrogen, today available on a commercial basis.

We have chosen lead/bismuth as a coolant in our present simulations, in order to mitigate the increase in void worth due to massive BA presence in the core. The spallation target was also set to be liquid/lead bismuth, in accordance with European ADS project preferences.

One purpose of our design study is to show how one may avoid americium production during the transmutation of transuranics nuclei. Thus the composition of TRU vector, exhibited in Table 1, was assumed to be that of typical un-recycled PWR spent fuel 30 years after discharge (which may be a reasonable value for the ADS introduction time delay). This vector differs from the one assumed for

Isotope	Mass fraction
^{237}Np	0.049
^{238}Pu	0.019
^{239}Pu	0.494
^{240}Pu	0.217
^{241}Pu	0.033
^{242}Pu	0.062
^{241}Am	0.108
^{243}Am	0.016
^{244}Cm	0.002

Table 1: TRU vector of the fuel used in the present study. The composition represents the TRU discharge of an average PWR after a burnup of 40 GWd/t and 30 years of cooling.

the CAPRA design, i.e. a mixture of Pu from fresh PWR discharges and recycled CAPRA plutonium [16]. The core design is hence to be regarded as a start-up configuration in a two-component scenario [6]. It is true that the Pu vector in a plutonium *only* recycling scheme reaches equilibrium within 25 years, [16]. However, adding the inevitable americium recycling, the appearance of (quasi) equilibrium TRU vectors is delayed by another 50 years [17, 9], and therefore we find it relevant to start by investigating requirements for start-up cores.

Core design

Figure 1 shows the geometry of our preliminary core design. The core is baptized to the "Sing Sing Core" (SSC), alluding to Swedish laws on reactor design. The fuel assembly duct flat to flat distance was taken to be 22.0 cm. The radius of our spallation target then becomes 24.9 cm, with a five mm thick steel container enclosing the target circuit. The active core height is assumed to be 100 cm, with proton beam impact located 18 cm above mid plane.

The choice of lead/bismuth as a coolant leads to certain constraints on sub-assembly designs, required for avoiding problems with corrosion of clad and structural material: Pitch to pin diameter ratios have to be comparatively large, to compensate for limitations in Pb/Bi flow velocities ($v <$ 3.0 m/s) imposed by erosion rates of cladding protective oxide films [18]. Pellet, pin and assembly dimensions were configured to keep outer cladding temperatures below 600 degrees C in the hottest channel at EOL and are displayed in Tables 2 and 3. Technetium and burnable absorber pellets have the same diameter as the the fuel pellets, but come without the central hole.

Modelling tools

We have applied continuous energy Monte Carlo simulation methods to all aspects concerning neutronics and burnup modelling of the Sing Sing Core. The JEF2.2 neutron cross section library was processed with NJOY [19] to create Doppler broadened pointwise cross section files for MCNP [20] in the temperature range 300 K to 1800 K. A three dimensional geometry setup was constructed, where all 84 fuel bundles of the core were modelled separately. Duct walls were explicitly present, while a smeared coolant/cladding/fuel material composition was used for the duct interior in most cases. MCNP4C with explicit delayed neutron transport was used to obtain *k*-eigenvalues and β_{eff}, while MCNPX [21] in proton source mode was applied to all calculations of neutron fluxes, power densities, cross sections, and neutron life times at BOL. A pin by pin model was used to calculate the relative fraction of heat deposition in cladding and coolant.

Burnup calculations were made with MCB, a continuous energy Monte Carlo Burnup code being developed at KTH

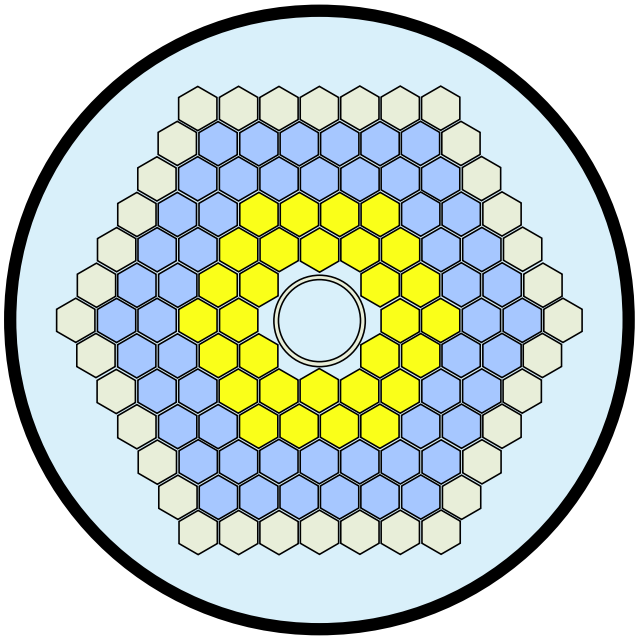

Figure 1: Cross section of the Sing Sing Core. 84 hexagonal fuel assemblies with duct flat to flat distances of 22.0 cm are configured in four fuel zones containing variable concentrations of TRU, depleted uranium (yellow zones) and boron carbide (blue zones). Technetium pins are present in zone two, and grey denotes steel reflector assemblies.

Property	Value
Active pin length	100 cm
Pellet inner radius	1.00 mm
Pellet outer radius	2.40 mm
Clad inner radius	2.49 mm
Clad outer radius	2.94 mm
Fuel density	0.90 TD
Smear density	0.70 TD

Table 2: Pin and pellet design parameters of the lead/bismuth, nitride fuelled Sing Sing Core.

in cooperation with AGH in Cracow [22, 23]. MCB extends MCNP with *internal* modules for reaction rate and heating calculations *in flight*. MCNPX was used to write a low energy (E $<$ 20 MeV) neutron source on the surface of the spallation target, that was employed for the burnup calculations with MCB. The effect of neglecting the high energy tail of spallation neutrons (1.4% of the source flux entering the core) was estimated to be within Monte Carlo error bars for power densities and actinide burnup.

Absorber introduction

The absorber ideally should serve the multifold purpose of neutron capture shielding, power peaking flattening, and mitigation of reactivity loss. While other materials like hafnium and europium are good absorbers in a fast neutron spectrum, they are not burnable as boron is. Employing 95% ^{10}B enriched B_4C, neutron moderation as well as absorber inventory is minimized. Figure 2 displays the absorption cross section of ^{10}B superimposed on the capture and fission cross sections of ^{241}Am. It is evident that an enriched boron carbide environment may suppress production rates of ^{242}Cm, while only affecting ^{241}Am fission rates to a minor extent.

Thus, boron carbide pins were introduced into fuel zones 3 and 4 in proportions yielding the flattest possible power distribution at BOL. Depleted uranium replaced the absorber in zone 1 and 2, in order to improve spallation neutron multiplication. Finally, technetium pins were positioned in zone 2, for transmutation purposes.

Table 4 shows a distribution (relative volume fraction) of transuranium nitride, uranium nitride and BA yielding a BOL radial power peaking equal to 1.2. The resulting radial power density along the symmetry axis of the core is displayed in Figure 3. Evidently, power peakings similar to those of critical reactor cores are feasible in subcritical systems.

The capture of slower neutrons in absorber rods placed in direct conjunction to fuel rods leads to suppression of the low energy part of the neutron spectrum in the fuel. By introducing the absorber pins directly in fuel assemblies instead of having them in separate fuel bundles (FBR approach), one avoids local flux suppression and is able to utilize the full reactivity worth of the absorber. Figure 4 exhibits the impact of the high boron carbide concentration in

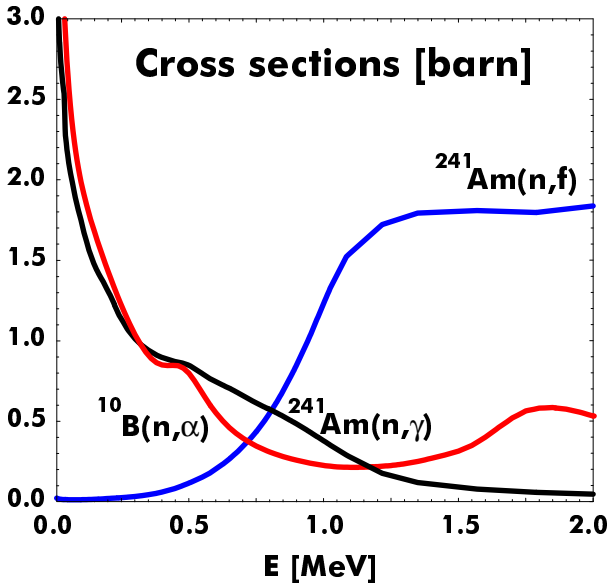

Figure 2: Absorption cross section of ^{10}B, compared to the capture and fission cross sections of ^{241}Am. For high ^{10}B concentrations in fuel bundles, neutron capture in ^{241}Am will be suppressed below 500 keV, without significant deterioration of ^{241}Am fission probabilities.

the outer fuel zones. While the magnitude of the neutron flux above the fast fission threshold ($E_n > 1$ MeV) is similar in zones one and three, a suppression factor larger than three is achieved in the resonance region ($E_n < 100$ keV).

The variation in neutron spectrum over the core is further characterized in Table 5, where median and flux weighted neutron energies are given for each fuel zone.

Comparing with the pin data given in Table 4 it is clear that a higher fraction of absorbing material, and a smaller fraction of diluent in the fuel (in our case ^{238}U) yields more energetic neutron spectra. Consequently, spectrum averaged cross sections for neutron capture in even neutron number nuclides become smaller in outer zones 3-4, and fission to absorption probabilities rise.

The spectrum averaged cross sections for capture and fission in relevant actinides at BOL are displayed in Tables 6 and 7. Note the significant decrease in capture cross sections as median neutron energies increase.

The probability of fission versus capture as a consequence of neutron absorption in a fuel nuclide is of signifi-

Property	zone 1	zone 2	zone 3	zone 4
Pitch/pin ratio	1.95	1.785	1.785	1.785
Fuel pins	331	317	251	319
Absorber pins	0	0	146	78
Technetium pins	0	80	0	0

Table 3: Fuel sub-assembly specification of the lead/bismuth, nitride fuelled Sing Sing Core.

Material	**TRUN**	**UN**	**B_4C**	**Tc**
Zone 1	0.33	0.67	0.00	0.00
Zone 2	0.38	0.42	0.00	0.20
Zone 3	0.63	0.00	0.37	0.00
Zone 4	0.80	0.00	0.20	0.00
Average	0.60	0.18	0.18	0.04

Table 4: Fuel/BA material distributions given as relative volume fractions in each fuel zone.

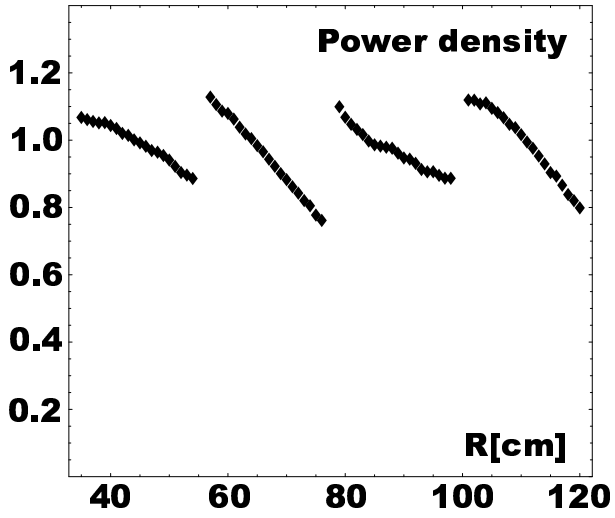

Figure 3: Fission power density at BOL in *fuel* rods along the symmetry axis of the Sing Sing Core. Values are given relative to the core averaged power density. Radial power peaking is seen to be less than 1.2 at a k-eigenvalue equal to 0.972.

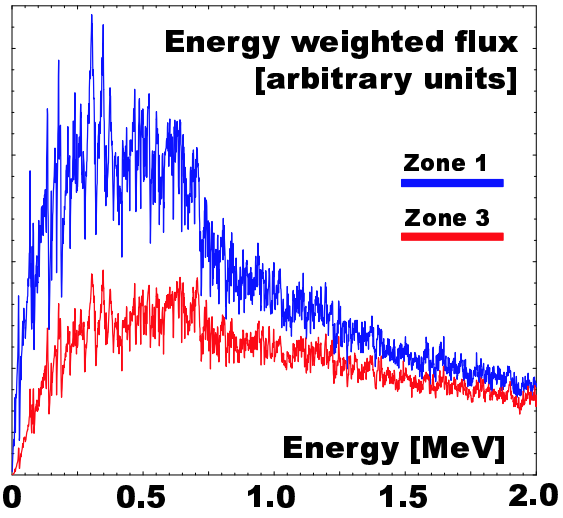

Figure 4: Energy weighted neutron flux spectrum in zone 1 (upper line) and zone 3 (lower line). Neutron capture by ^{10}B in the outer core zones leads to a suppression of flux levels by a factor of more than three in the low energy region ($E_n < 100$ keV).

cance not only for neutron economy, but also for the production of α-emitting nuclides. Formation of ^{242}Cm, having a half life of 163 days, will lead to problems with in-pile fuel swelling and pin pressurization as helium gas is accumulated. The appearance of ^{238}Pu and ^{244}Cm with half lives of 88 and 18 years, respectively, is likely to induce higher costs for reprocessing and fabrication. Thus one would like to maximize fission to absorption probability ratios for predecessors to the quickly decaying α-emitting isotopes. Table 8 displays this ratio for the Sing Sing Core and compares with corresponding values of CAPRA and Energy Amplifier designs [11, 9].

It is remarkable that the fission probability of the even neutron number nuclides is not only dependent on the presence of an absorber, but also the fraction of diluent material in the core appears to play a major role. In the CAPRA core, diluent steel and $^{11}B_4C$ moderator rods are introduced into the fuel assemblies to increase neutron leakage and moderation. In the Energy Amplifier, thorium ($\sim$ 75% volume fraction of fuel) is used to maintain reactivity. Evidently the concomitant neutron moderation through inelastic scattering on thorium eliminates the spectrum hardening benefit of metallic fuel.

Energy	Median	Flux weighted	E > 1 MeV	E > 20 MeV
Zone 1	194 keV	448 keV	10.6%	0.025%
Zone 2	246 keV	522 keV	13.8%	0.007%
Zone 3	356 keV	716 keV	21.8%	0.003%
Zone 4	354 keV	734 keV	22.6%	0.001%

Table 5: Characterization of BOL neutron energy spectrum in the fuel zones of the Sing Sing Core. Note that the contribution of high energy spallation neutrons ($E_n > 20$ MeV) to the total neutron flux at BOL is less than a promille even in the inner fuel zone.

Nuclide	zone 1	zone 2	zone 3	zone 4
^{238}U	0.239	0.193	0.144	0.156
^{237}Np	1.226	0.961	0.663	0.698
^{238}Pu	0.430	0.332	0.228	0.242
^{239}Pu	0.382	0.279	0.183	0.198
^{240}Pu	0.433	0.334	0.234	0.248
^{241}Pu	0.477	0.421	0.362	0.370
^{242}Pu	0.371	0.283	0.193	0.206
^{241}Am	1.604	1.332	1.000	1.029
^{243}Am	1.362	1.089	0.776	0.811
^{244}Cm	0.458	0.383	0.283	0.294
^{245}Cm	0.255	0.199	0.139	0.146

Table 6: One-group cross sections, in units of barn, for neutron capture in the Sing Sing Core fuel zones.

In particular, the increase in fission probability for ^{241}Am from 12% in CAPRA and EA core types to 33% in zone 3 of SSC, points towards a strategy where americium is to be burnt in strongly absorbing fast neutron environments, rather than in moderated targets or diluted cores.

Neutronics

The massive introduction of a non-resonant neutron absorber like boron carbide into a reactor core leads to degradation of reactivity coefficients. Coolant voiding, for instance, increases the probability for fission of even neutron number nuclides. Further, Doppler feedback vanishes, as hardly any neutrons ever reach the resonance region. Table 9 displays values of these important kinetic parameters

Nuclide	zone 1	zone 2	zone 3	zone 4
^{238}U	0.034	0.045	0.073	0.077
^{237}Np	0.346	0.419	0.591	0.600
^{238}Pu	1.133	1.187	1.349	1.359
^{239}Pu	1.714	1.658	1.646	1.663
^{240}Pu	0.400	0.468	0.636	0.646
^{241}Pu	2.236	2.026	1.824	1.859
^{242}Pu	0.282	0.345	0.493	0.501
^{241}Am	0.264	0.329	0.490	0.503
^{243}Am	0.204	0.258	0.392	0.403
^{244}Cm	0.455	0.543	0.753	0.763
^{245}Cm	2.367	2.148	1.962	2.003

Table 7: One-group cross sections, in units of barn, for fission in the Sing Sing Core fuel zones.

for the Pb/Bi cooled Sing Sing Core at BOL. The void worth was calculated by voiding the core (including gaps between sub-assemblies) and upper plena from coolant. The source mode value of the void worth obviously is the physically relevant, but we include the eigenmode void worth in order to enable comparison with deterministic codes. As seen, the advantage of comparatively small void worths (typically less than 1000 pcm, for optimal core designs even negative) of lead/bismuth is partially lost when boron carbide is abundant in the core. A positive value of about +3500 pcm for the present SSC design can be compared with +4500 pcm for JAERI:s sodium cooled ADS design [24].

The Doppler feedback was calculated by exchanging cross sections libraries processed at various temperatures in the core. It was checked that the cross sections used yielded correct temperature behaviour, with *k*-eigenvalue inversely proportional to temperature and Doppler constants in the range of -500 pcm for a simplified model of the CAPRA core [11]. In the very hard spectrum of the Sing Sing Core, however, resonance capture in fuel nuclides is a rare event, and only a small decrease in reactivity with temperature could be observed.

The fraction of delayed neutron emission, β, and the fraction of fissions induced by delayed neutrons, $\beta_{\rm eff}$, were

Nuclide	zone 1	zone 2	zone 3	zone 4	CAPRA	EA
^{237}Np	0.22	0.30	0.47	0.46	0.15	0.15
^{238}Pu	0.72	0.78	0.86	0.85	0.64	0.69
^{240}Pu	0.48	0.58	0.73	0.72	0.37	0.40
^{242}Pu	0.43	0.55	0.72	0.71	0.33	0.32
^{241}Am	0.14	0.20	0.33	0.33	0.12	0.12
^{243}Am	0.13	0.19	0.34	0.33	0.10	0.11
^{244}Cm	0.50	0.59	0.73	0.72	0.40	0.36

Table 8: Fission to absorption probability ratios for quickly decaying α-emitters and their predecessors in the Sing Sing Core fuel zones, compared to corresponding values of CAPRA and Energy Amplifier designs. The benefit of introducing neutron absorbers to reduce α activity and helium accumulation in fuel pins is clear.

Parameter	SSC	CAPRA (1)	CAPRA (2)
Void worth ($k_{\rm eff}$)	+3500 pcm	+1560 pcm	+2210 pcm
Void worth ($k_{\rm S}$)	+4400 pcm		
Doppler constant	-13 pcm	-450 pcm	-400 pcm
β	270 pcm		
$\beta_{\rm eff}$	160 pcm	320 pcm	300 pcm
Neutron life time	0.61 μs	0.84 μs	0.42 μs

Table 9: Kinetic parameters of the Sing Sing Core at BOL, compared to those of the reference CAPRA oxide core (1) and the high burnup CAPRA core featuring minor actinide targets in the reflector (2). Note the unusually small Doppler constant.

calculated by explicitly simulating delayed neutron transport with MCNP4C. The comparatively small value of $\beta_{\rm eff}/\beta \simeq 0.6$ in the Sing Sing Core is due to the low emission energies of delayed neutrons ($\overline{E_{\rm del}} \sim 0.5$ MeV), leading to large probability of absorption in ^{10}B.

A comparison with the kinetic parameters quoted for CAPRA designs [11, 25] shows that the Doppler feedback in case of coolant voiding is very unreliable in the Sing Sing Core, whence subcriticality appears to be a necessary requirement.

Thermal hydraulics

Several important aspects in the thermal hydraulic analysis of accelerator driven system cores differ from those of the classical FBR. Due to the different shape of the power distribution and especially its change over time, one has to be careful in calculating maximum temperatures. Further, with lead/bismuth as a coolant, the lower thermal conductivity will lead to higher temperature gradients within the coolant channel. The range of coolant flow speeds is also more limited for lead/bismuth than for sodium, as erosion of cladding protective oxide films may occur when maximum velocities exceed 3 m/s [18]. Having implemented the oxygen control and monitoring system developed for the russian lead/bismuth cooled submarine reactors [26], in conjunction with use of corrosion resistant, 12Cr-Si ferritic steels, maximum cladding temperatures should kept below 620 degrees C during extended operation [27].

Detailed three dimensional thermal hydraulics simulations of Sing Sing Core coolant flow were performed with StarCD [28], where the Navier-Stokes equation is solved by finite volume modelling employing $k-\varepsilon$ turbulence model. Due to the pronounced turbulent behaviour in near wall regions, wall functions are not applicable to describe the boundary condition between cladding and Pb/Bi coolant. The two-layer model used in the present simulations improves heat friction and heat transfer predictions within the boundary layer, a priori calculating distributions of velocities, temperatures, etc. Heat transfer is implemented through the chemico-thermal enthalpy conservation equations.

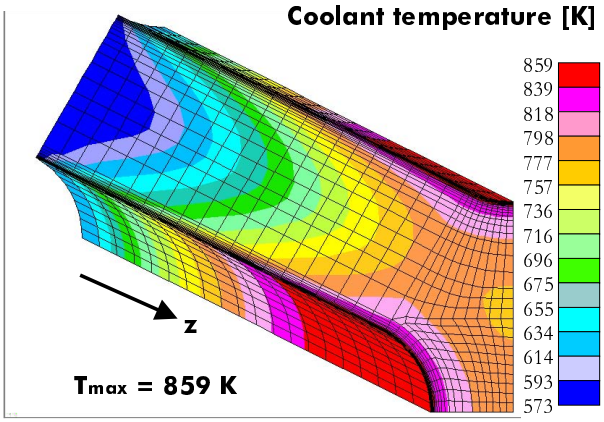

Figure 5: Temperature field in a zone 1 coolant channel, assuming 75 kW of fission power in each fuel pin. Out of this, 7 kW is directly deposited into the coolant by prompt and delayed gamma photons, and by neutrons. An inlet velocity $v = 2.65 m/s$ was adopted in order to keep maximum coolant velocities below $3.0 m/s$.

Pin by pin Monte Carlo simulations showed that the fraction of fission energy deposited directly in the coolant by prompt and delayed gamma photons and neutrons is about nine percent. This effect could be explicitly modelled in StarCD. Similarly, the impact of non-fissile absorber rod presence may be calculated. The resulting coolant temperature field for 75 kW of fission energy release per pin in zone 1 is displayed in Figure 5, for an inlet coolant velocity of 2.65 m/s. A maximum temperature in the interface between coolant and cladding equal to 586 degrees C is found, which is safely below the 620 degrees C limit. The axial temperature rise in the center of the channel is 270 K. The radial temperature gradient increases from about 50 K at the inlet to 120 K at z = 60 cm (where fuel temperatures are maximal). Note that the comparatively low thermal conductivity of lead/bismuth (a factor of six lower than for sodium) leads to higher radial temperature gradients than in typical FBR-channels for identical geometries and coolant velocities.

Thus limits to linear powers in the Sing Sing Core are set to 80 kW per pin in zone 1 and 65 kW in zones 2-4.

Knowing the linear power $\chi(z)$ and temperature profile $T_s(z)$ on the outer pellet surface, maximum fuel temperatures T_i on the inner surface of the pellet can be obtained from standard relations between fuel conductivity, linear power and geometry.

Using the thermal conductivities of actinide nitrides measured by Suzuki and coworkers [29] (The conductivity of AmN was assumed to be $\sim$ 75 % of PuN conductivity) we find that the expressions

$$T_i(z) \simeq T_s(z) + 3.95\chi(z) \text{ kW/(mK)} \quad (1)$$
$$T_i(z) \simeq T_s(z) + 4.61\chi(z) \text{ kW/(mK)} \quad (2)$$
$$T_i(z) \simeq T_s(z) + 5.41\chi(z) \text{ kW/(mK)} \quad (3)$$
$$T_i(z) \simeq T_s(z) + 5.41\chi(z) \text{ kW/(mK)} \quad (4)$$

are approximately valid, for the fuel compositions at BOL in zones 1 to 4, when $T_s < 1000$K and $\chi < 110$ kW/m.

Assuming that nitrogen bonding yields $\Delta T_{\text{gap}} = 1000$ K before gap closure [15], we find that the maximum fuel temperature at BOL is located at about 55 cm height in zone 4 pins closest to the spallation target, being 2100 K for an average core pin power of 44 kW.

In nitrogen atmosphere, decomposition can be suppressed up to T $\simeq$ 2800 K for NpN and PuN [14, 30]. This gives the present core configuration a margin to fuel failure of 700 degrees at BOL. Gap closure at about one percent burnup leads to a temperature decrease of 500 degrees in the pellet. Degradation of bonding conductivity due to release of gaseous fission products will be less severe than in helium bonded pins, especially taking into account that helium produced by α-decaying nuclides is also released in large amounts. Hence, temperature margins will remain larger than 600 degrees until EOL, in spite of the increase in power peaking as burnup proceeds.

Maximum power peaking, and hence maximum burnup is therefore limited by constraints to cladding temperatures, rather than fuel constraints (provided that radiation damage has not yet become unacceptable). The 620 degrees C limit then imposes irradiation to be interrupted before radial power peaking exceeds 1.40 in zone 2 pins, or 1.75 in zone 1 pins.

The issue of decay heat after shut down is less severe for the Sing Sing Core than for typical FBR cores. The larger pin pitches allows for accommodation of a larger heat deposition in the coolant in loss of flow scenarios. Shut down heat due to delayed neutron induced fission is also less by about one third, due to the high probability of delayed neutron absorption in the absorbers. The emission of decay heat was calculated with MCB to be about six percent of full core power at the instant of shut down, going down to one percent within three hours. In any case, cladding melt will occur before fuel temperatures reach the decomposition limit.

Burnup

Limited mainly by cladding temperature constraints a total core power of 1200 MW (including decay heat) was adopted for burnup simulations with MCB. Irradiation was continued without interruption for 300 days, with a 100 day time step where neutron fluxes, power distributions and transmutation rates were recalculated. In order to obtain a sufficient accuracy (one standard deviation less than four percent error in neutron multiplication), the histories of 40 000 neutrons emerging from the spallation target were sampled at each time step. 700 MHz Pentium III double processors running Linux were used for the calculation, yielding time step simulation times of the order of 24 hours. The resulting evolution of k-eigenvalues, required spallation target power, core flux, power peaking and other quantities of interest are summarized in Table 10.

Property	BOL	100 d	200 d	300 d
k-eigenvalue	0.972	0.955	0.936	0.916
ϕ_n^*	0.877	0.870	0.850	0.802
ϕ_f^*	0.875	0.867	0.847	0.797
Target power [MW]	20.5	36.9	54.9	75.1
Power peaking (zone 1)	1.08	1.29	1.49	1.70
Average flux $[10^{19}/(\mathrm{m}^2 \cdot s)]$	3.86	4.14	4.45	4.78
Flux peaking (zone 1)	1.97	2.27	2.57	2.88

Table 10: Evolution of important ADS parameters during 300 days of uninterrupted burnup, imposing a constant thermal power output of 1200 MW. Note that radial power peaking is considerably smaller than radial flux peaking, and stays below 1.75 even at a k-eigenvalue equal to 0.92!

The decrease in k-eigenvalue is 5600 pcm, accompanied by an increase in required spallation target power with a factor of 3.7. The growth in proton beam current is larger than what naively would be inferred from the loss in k-eigenvalue, due to the simultaneous decrease of the source neutron efficiency ϕ_i^*, defined as

$$\phi_i^* \equiv \frac{M_{\mathrm{ext}}^i - 1}{M_{\mathrm{fiss}} - 1} \tag{5}$$

where $M_{\mathrm{fiss}} = 1/(1 - k_{\mathrm{eff}})$ denotes the fundamental mode neutron multiplication. M_{ext}^i describes either the multiplication of the spallation source neutrons according to:

$$M_{\mathrm{ext}}^n = 1 + k_0 + k_0 \cdot k_1 + k_0 \cdot k_1 \cdot k_2 + \cdots \tag{6}$$

where k_0 is the external source neutron multiplication factor, and k_i (i>0) is the generation dependent multiplication factor, or the fission multiplication given by:

$$M_{\mathrm{ext}}^f = 1 + \bar{\nu} N_f \tag{7}$$

where $\bar{\nu}$ is the average number of neutrons released in a fission, and N_f is the number of fissions induced per spallation neutron.

The reasons for the source efficiency being smaller than unity are a larger probability of axial leakage out of the target for spallation neutrons and a relatively large moderation of neutrons within the spallation target, leading to a higher fraction of parasitic capture, than is the case for the average fission neutron. This is a price that is paid for achieving flat power power density, being inevitable if thermal striping of fuel assemblies is to be avoided.

Power peakings remain within the limits set by thermo-hydraulics as discussed above, with neutron fluxes not deviating much from typical FBR-values, except for pins and duct walls closest to the spallation target at EOL. Radiation damage in fuel cladding and ducts is thus not expected to be a problem, since the irradiation time is much shorter than in the typical FBR-cycle.

The transuranium density evolution is exemplified in Figure 6. The core averaged transuranium burnup at end of irradiation is 8.7%, with local burnups ranging from 7.3% in zone 4 to 11.5% in zone 1 and 2.

The higher actinide density is displayed separately in Figure 7. Note that the comparatively higher reduction of higher actinide density in zone 1 (12.2 %) to large extent is due to conversion of ^{241}Am into plutonium via neutron capture and α-decay of quickly decaying curium. As helium accumulation in fuel pins is likely to enhance fuel swelling rates, it would be preferable to burn americium by direct fission rather than by conversion into fissile plutonium. Figures 8 and 9 clearly show the higher densities of these troublesome nuclides appearing in the slower spectrum zones 1 and 2.

Consequently, a refined core design where americium is removed from fuel zones one and two would appear advantageous.

Regarding the reduced TRU transmutation efficiency imposed by the presence of depleted uranium in the inner fuel zones, we note that this is mainly an issue in zone 1, where the slow spectrum leads to a conversion of 5.5% of the present ^{238}U into ^{239}Pu. The corresponding figures for zone 2 is 3.4 % of initial uranium content. As can be seen from figure 6, TRU burnup in zone 1 still reaches 11.5%.

The burnability of ^{10}B is manifested in a 9.3% reduction in boron density in zone 3 and 7.8 % in zone 4. These numbers are larger than the transuranium burnups in each zone, and hence substantiates the proposed role of enriched boron carbide as an efficient burnable poison in a fast spectrum.

Several authors have proposed to use moderated neutron spectra for technetium transmutation [31, 9]. However, as self-shielding will significantly reduce the neutron flux in the center of technetium pins positioned in a thermal or epithermal spectrum [32], fast neutron spectra may perform

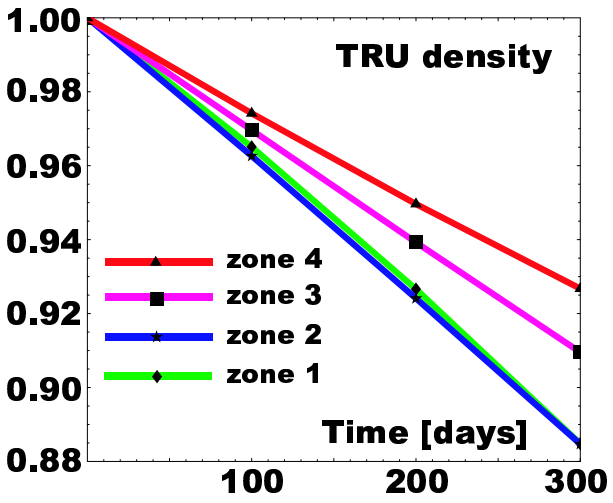

Figure 6: TRU density evolution in the Sing Sing Core operating at 1200 MW thermal power. Values are plotted as fractions of initial nuclide density in the individual fuel zones. A 8.7 % TRU burnup is achieved after 300 full power days.

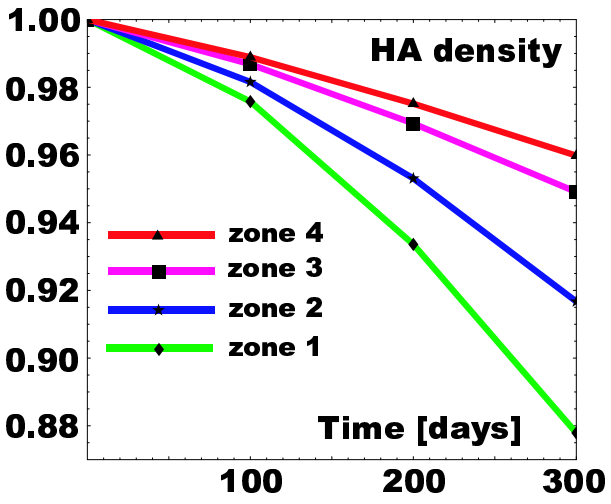

Figure 7: Evolution of higher actinide (americum + curium) density in the Sing Sing Core. The high reduction rate in zone 1 is mainly due to conversion into plutonium following neutron capture in ^{241}Am.

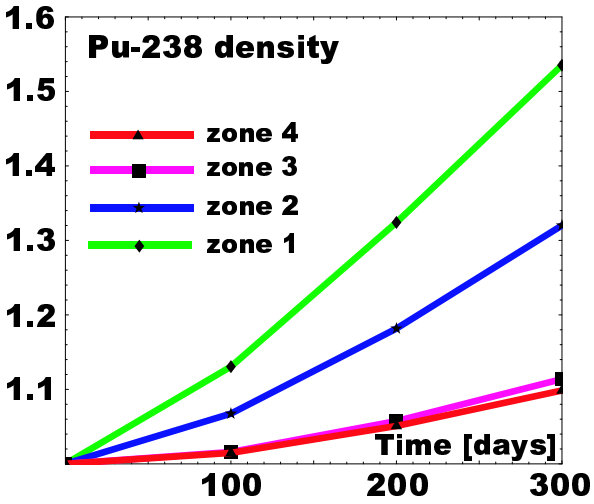

Figure 9: Evolution of ^{238}Pu density in the Sing Sing Core, relative to its initial concentration in each fuel zone. The high growth rate in zone 1 is due to larger capture to fission cross section ratios for neptunium and americium.

equally well. In the present configuration, 4.8% of the 300 kg technetium present in zone 2 is transmuted during the 300 day irradiation period, corresponding to an effective half life of 12 years. Comparing to the 15 year half life obtained in moderated fast reactor assemblies [31], we conclude that fast flux transmutation of ^{99}Tc is at least as efficient.

Conclusions

The introduction of burnable absorbers into sub-critical systems has been shown to have the multifold benefit of flattening power distributions, mitigating reactivity losses, increasing fission to absorption ratios in minor actinides, and lowering helium accumulation in fuel pins. Implementing a four zone differentiation in concentration of enriched boron carbide and depleted uranium we obtained a BOL radial power peaking equal to 1.2 at a *k*-eigenvalue equal to 0.972. Fission to absorption cross section ratios for ^{241}Am as high as 0.33 has been achieved in fuel assemblies where 37 % of the fuel pins had been replaced with absorber pins. Operating the core with a constant thermal power of 1200 MW for 300 days, a transuranium burnup of 8.7% for unrecycled TRU discharges from light water reactors was achieved. As a consequence of the boron introduction, helium accumulation in fuel pins due to formation and decay of ^{242}Cm could be significantly reduced, compared to absorber free core designs like CAPRA and the Energy Amplifier. The concomitant reactivity loss of 640 pcm per percent transuranium burnup in the present core configuration (19 pcm/day) is to be compared to 730 pcm per percent in absorber free cores burning similar TRU compositions. The EOL radial power peaking was 1.70 at a *k*-eigenvalue equal to 0.916, substantially lower than the corresponding flux peaking.

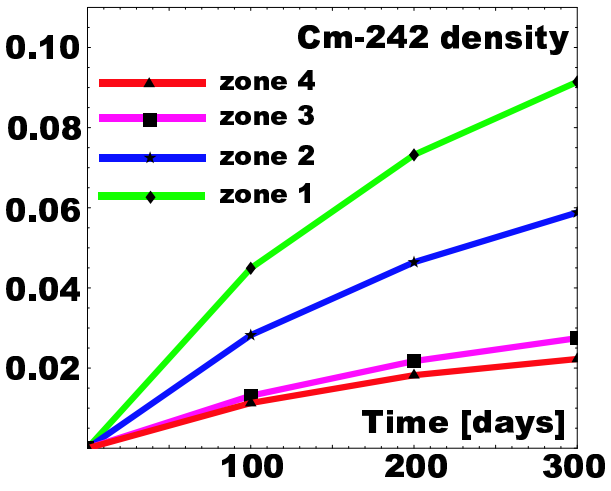

Figure 8: Concentration of ^{242}Cm in the Sing Sing Core, relative to initial ^{241}Am nuclide density in each fuel zone. The significantly lower accumulation rate in outer fuel zones is directly due to the introduction of enriched boron carbide pins in these parts of the core.

The introduction of nitrogen bonding of the fuel pins allows to maintain a margin to nitride decomposition of more than 1000 degrees as linear powers increase up to 77 kW/m in zone 1 at EOL. Measurements of americium nitride stability in nitrogen atmospheres need to be made, however, to verify the assumption made that AmN decomposes at the same temperature as NpN and PuN.

The obvious drawback following upon a massive absorber introduction is a positive void coefficient in conjunction with a minimal Doppler feedback. The choice of lead/bismuth as coolant instead of sodium somewhat mitigates this effect. Reactivity losses are still high enough for

the required spallation target power to rise by more than a factor of three. Such large availability of proton current margin may be a serious safety threat, if accidental insertion of full proton beam power at BOL should occur. These problems, will be addressed in more detailed studies to be performed on the Sing Sing Core in the near future.

Acknowledgements

This work was financially supported by SKB AB (Swedish Nuclear Fuel Ltd), EC (The European Commission), KTC (Centre for Nuclear Technology) and SI (Swedish Institute). The authors would like to thank C. Broeders, F. Venneri and W. Maschek for comments on the use of BA in accelerator driven systems.

References

[1] M. Delpech et al. The Am and Cm transmutation, physics and feasibility. In *International Conference on Future nuclear systems, GLOBAL 99*. ANS, 1999.

[2] S.L. Beaman. Actinide recycle in LMFBRs as a waste management alternative. In *First international conference on nuclear waste transmutation*, page 61. University of Texas, 1980.

[3] H. Murata and T. Mukaiyama. Fission reactor studies in view of reactor waste programs. *Atomkernenergie-Kerntechnik*, 45:23, 1984.

[4] D.G. Foster et al. Review of PNL study on transmutation processing of high level waste. Technical Report LA-UR-74-74, Los Alamos National Laboratory, 1974.

[5] T. Takizuka et al. Conceptual design of transmutation plant. In *Specialist meeting on accelerator driven transmutation technology for radwaste*, page 707. LA-12205-C, Los Alamos National Laboratory, 1991.

[6] M. Salvatores et al. Long-lived radioactive waste transmutation and the role of accelerator driven (hybrid) systems. *Nuclear Instruments and Methods A*, 414:5, 1997.

[7] B. Carluec and P. Anzieau. Proposal for a gas cooled ADS demonstrator. In *International conference on accelerator driven technologies and applications, ADTTA 99*, 1999.

[8] H. Takahashi et al. A fast breeder and incinerator assisted by a proton accelerator. In *Specialist meeting on accelerator driven transmutation technology for radwaste*, page 552. LA-12205-C, Los Alamos National Laboratory, 1991.

[9] C. Rubbia et al. Fast neutron incineration in the energy amplifier as alternative to geologic storage. Technical Report LHC/97-01 (EET), CERN, 1997.

[10] F. Venneri. Disposition of nuclear waste using subcritical accelerator driven systems. Technical Report LA-UR-98-985, Los Alamos National Laboratory, 1998.

[11] A. Languille et al. CAPRA core studies - the oxide reference option. In *International Conference on Future nuclear systems, GLOBAL 95*, page 874. ANS, 1995.

[12] G. Gastaldo, M. Rome, and J.C. Garnier. CAPRA core optimisation by use of $^{11}B_4C$. In *International Conference on Future nuclear systems, GLOBAL 95*, page 1324. ANS, 1995.

[13] H.M. Beaumont et al. CAPRA core studies, high burnup core - conceptual study. In *International Conference on Future nuclear systems, GLOBAL 97*, page 137. ANS, 1997.

[14] H. Matzke. *Science of Advanced LMFBR fuels*. North-Holland, 1986.

[15] M. Mignanelli, R. Thetford, and D. Williams. Fuel performance modelling of nitride fuels. In *International Conference on Future nuclear systems, GLOBAL 99*. ANS, 1999.

[16] H.W. Wiese. Actinide transmutation properties of thermal and fast fission reactors including multiple recycling. *J. Alloys and Compounds*, 271-273:522, 1998.

[17] M. Salvatores, I. Slessarev, and A. Tchistiakov. Analysis of nuclear power transmutation potential at equilibrium. *Nuclear Science and Engineering*, 124:280, 1996.

[18] N. Novikova, Y. Pashkin, and V. Chekunov. Some features of sub-critical blankets cooled with lead-bismuth. In *International conference on accelerator driven technologies and applications, ADTTA 99*, 1999.

[19] R.E. MacFarlane and D.W. Muir. *The NJOY nuclear data processing system, version 91*. LA-12740-M, Los Alamos National Laboratory, 1994.

[20] J.F. Briesmeister. *MCNP - A general Monte Carlo N-Particle transport code, version 4C*. LA-13709-M, Los Alamos National Laboratory, 2000.

[21] M.B. Chadwick et al. Cross section evaluations to 150 MeV for accelerator driven systems and implementation in MCNPX. *Nuclear Science and Engineering*, 131:293, 1999.

[22] J. Cetnar, J. Wallenius, and W. Gudowski. MCB - a continuous energy Monte Carlo Burnup code. In *Fifth international information exchange meeting*, page 523. OECD/NEA, 1998.

[23] J. Cetnar, W. Gudowski, and J. Wallenius. Transmutation calculations with Monte Carlo continuous energy burnup system MCB. In *International conference on accelerator driven technologies and applications, ADTTA 99*, 1999.

[24] T. Takizuka et al. Studies on accelerator driven transmutation systems. In *Fifth international information exchange meeting*, page 383. OECD/NEA, 1998.

[25] H.M. Beaumont et al. Heterogeneous minor actinide recycling in the CAPRA high burnup core with target sub-assemblies. In *International Conference on Future nuclear systems, GLOBAL 99*. ANS, 1999.

[26] B.F. Gromov et al. Use of lead-bismuth in nuclear reactors and accelerator driven systems. *Nuclear Engineering and Design*, 173:207, 1997.

[27] A.E. Rusanov et al. Developing and studying the cladding steels for the fuel elements of the NPIs with heavy coolant. In *Heavy liquid metal coolants in nuclear technology*. IPPE, 1998.

[28] Computational Dynamics Ltd. *Methodology Star-CD version 3.10*, 1999.

[29] Y. Suzuki and Y. Arai. Thermophysical and thermodynamic properties of actinide mononitrides and their solid solutions. *J. Alloys and Compounds*, 271-273:577, 1998.

[30] S. Pillon et al. Preliminary assessment of targets and fuels dedicated to the minor actinides transmutation in the frame of the CADRA program. In *International Conference on Future nuclear systems, GLOBAL 99*. ANS, 1999.

[31] J.L. Kloosterman and J.M. Li. Transmutation of Tc-99 and I-129 in fission reactors. Technical Report ECN-R-95-002, ECN, 1995.

[32] R.J.M. Konings et al. Transmutation of technetium in the Petten high flux reactor. *Nuclear Science and Engineering*, 128:70, 1998.

Paper IV

K. Tuček, J. Wallenius, and W. Gudowski
Optimal distribution of fuel, poisons and diluents in sub-critical cores dedicated to waste transmutation
In Proceedings of the International Conference on Emerging Nuclear Energy Systems, ICENES 00, Petten, NRG (2000)

Optimal distribution of fuel, poisons and diluents in sub-critical cores dedicated to waste transmutation

Kamil Tuček, Jan Wallenius, Waclaw Gudowski
Department of Nuclear & Reactor Physics
Royal Institute of Technology
100 44 Stockholm (Sweden)
kamil@neutron.kth.se

Keywords: accelerator driven systems, power peaking, helium production, source importance

Abstract

Introduction of accelerator driven systems (ADS) is believed to be of importance for efficient and safe transmutation of americium and curium. Among problems related to the use of ADS in this context are comparatively high power peakings and high helium accumulation rates in fuel pins. The present study shows that radial power peakings similar to those of critical configurations (~ 1.1) can be achieved in sub-critical cores by adequate distribution of fuel, burnable absorbers and diluents. The introduction of strong neutron absorbers in sub-assemblies containing americium increases fission to absorption ratios up to $\sim$0.50, which reduces helium production due to ^{242}Cm decay by a factor of two. In order to maintain a source importance reasonably close to unity, neutron poisons should be placed in the periphery of the core, and diluent materials with small cross sections for capture and inelastic scattering should be used in the vicinity of the spallation target.

1. Introduction

Introduction of diluent material in critical transmutation reactors has been proposed in order to cope with the high reactivity of plutonium (Languille et al., 1995; Gastaldo et al., 1995). In sub-critical systems dedicated to waste transmutation, a differentiated concentration of diluents in the core may serve the additional purpose of suppressing power peaking (Novikova et al., 1999), which may become as large as two in homogeneous configurations. However, using only diluents for this purpose, the ratio of fuel to diluent becomes very small. The consequence is an increased neutron moderation, and hence larger production rate of helium gas in fuel pins due to neutron capture in ^{241}Am followed by α-decay of ^{242}Cm.

Hence, a more sophisticated fuel zoning approach would be of great value. In sub-critical configurations, poison introduction into fast neutron cores may be feasible from a safety viewpoint. Consequently, a combination of fuel dilution and poisoning may enable the desired power profiling, without need for exceedingly low ratios of fuel to diluent concentrations close to the center of the core. In addition, the neutron absorber can be used to suppress neutron capture rates in the minor actinides.

A disadvantage of introducing absorbers into accelerator driven systems would be the larger probability for capture of spallation source neutrons, leading to a decrease in source importance. This problem may be addressed by placing the poison pins in peripheral parts of the core, together with all minor actinides. In the present paper, we have investigated properties of potential diluents and absorbers, in order to arrive at a distribution that maximizes both direct fission probabilities of minor actinides and source importance for minimum power peakings.

2. Modelling

The Monte Carlo code MCNPX (Waters, 1999) was used to model and calculate the creation and multiplication of target neutrons, while MCNP4C (Briesmeister, 2000) was used for eigenmode calculations.

3. Source importance

In contrast to critical systems, particular attention has to be paid to the economy of first generation neutrons, i.e. spallation neutrons. The multiplication of spallation neutrons exiting target can be evaluated either as:

$$M_{\mathrm{ext}}^{\mathrm{n}} = 1 + k_0 + k_0 \cdot k_1 + k_0 \cdot k_1 \cdot k_2 + \cdots \tag{1}$$

where k_0 is the external source neutron multiplication factor, and k_i ($i > 0$) is the generation dependent multiplication factor, or estimated in terms of fission multiplication as:

$$M_{\mathrm{ext}}^{\mathrm{f}} = 1 + \bar{\nu} N_{\mathrm{f}} \,, \tag{2}$$

where $\bar{\nu}$ is the average number of neutrons emitted per fission, and N_{f} is the number of fissions per spallation neutron. Spallation neutrons slow down or are absorbed in the target media before entering the core. Thus, for thick targets, the probability of spallation neutron induced fission is smaller than for the average fission neutron and $k_0 < k_i$. The resulting difference in neutron multiplication is then often parametrized in terms of the source neutron efficiency ϕ_{i}^*, defined as

$$\phi_{\mathrm{i}}^* \equiv \frac{M_{\mathrm{ext}}^{\mathrm{i}} - 1}{M_{\mathrm{fiss}} - 1} \,, \qquad \mathrm{i} = \mathrm{f}, \mathrm{n} \tag{3}$$

where $M_{\mathrm{fiss}} = 1/(1 - k_{\mathrm{eff}})$ denotes the fundamental mode neutron multiplication, k_{eff} is the k-eigenvalue of the neutron transport equation.

In order to clarify the influence of target and core geometry on the source importance, the external source neutron multiplication factor k_0 was calculated for different target sizes and pin pitch to diameter ratios in an infinite core lattice. A fixed fuel composition, given in Table 1, was assumed. Figure 1(a) shows how k_0 decreases with increasing target radius. The main reasons are increase in probability of parasitic absorption within the target, axial source neutron leakage from the system, and a decrease in fission to absorption probabilities in the core as inelastic collisions slow down the spallation neutrons before core entrance. The average energy of the neutrons exiting the target decreases by about 40 % when target radius is increased from R=20 cm to R=40 cm. Consequently, the fission to absorption ratio in the core drops by 25% for ^{240}Pu and by 4% for ^{239}Pu. Spallation neutron backscattering into the target is relevant especially for lead/bismuth, yielding further slowing down of neutrons and higher probability for parasitic absorption within the target. All together, the result is a strong dependence of k_0 on target dimensions, with values decreasing as much as 15% for a 10 cm increase of radius.

The dependence of k_0 on the volume fraction of coolant in the core is shown in Figure 1(b). Increasing pin pitches leads to a slower neutron spectrum and lower probability for fission. The probability for axial leakage is as high as 12% for the sodium cooled system at P/D=2.0, while only 6% leak out of the lead/bismuth cooled core.

Due to the high reactivity of plutonium, either an inert material or a neutron poison must be introduced in any reasonably sized core dedicated to waste transmutation. The choice of material will obviously

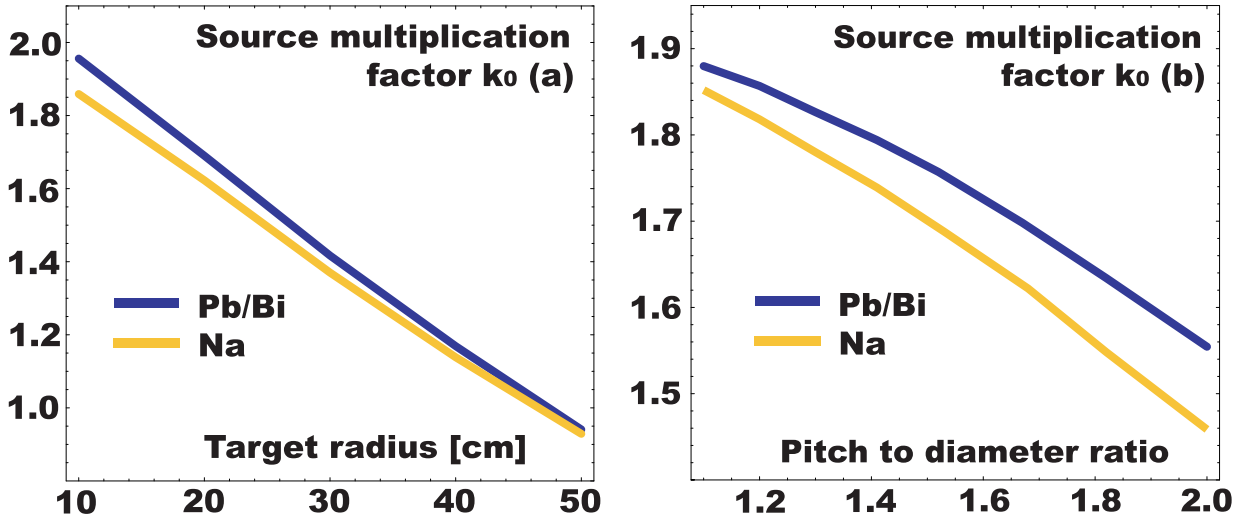

Figure 1: The external source multiplication factor k_0 as function of target radius (a) and pitch to diameter ratio (b) for diluent and poison free infinite lattices cooled by lead/bismuth and sodium. In (a) the pin pitch to diameter ratio was kept constant at 1.7, while in (b) the target had a radius of 20 cm.

have an impact on source importance. The effect of introducing the diluents ZrN, ^{238}UN, and the poison B_4C (95% ^{10}B enriched) on the external multiplication factor k_0 is displayed in Figure 2. ZrN provides a better multiplication of source neutrons as the macroscopic cross-section for absorption of spallation neutron in ZrN is only one eighth of that in UN. Boron carbide is as expected seen to absorb source neutrons very efficiently, and should thus be removed from the vicinity of the spallation target, if it is to be used in a sub-critical core.

4. Neutron absorbers

In most waste transmutation approaches, americium is supposed to be transmuted by neutron capture, followed by fission of daughter nuclides. This applies even to "fast" neutron concepts as JAERI:s sodium cooled ADS, Los Alamos ATW approach, and CERN:s Energy Amplifier (Takizuka et al., 1998; Venneri, 1998; Rubbia et al., 1997). The direct fission probability of ^{241}Am remains below 15% in all these proposals, due to the presence of diluent materials like zirconium and thorium,

Isotope	Mass fraction
^{237}Np	0.049
^{238}Pu	0.019
^{239}Pu	0.494
^{240}Pu	0.217
^{241}Pu	0.033
^{242}Pu	0.062
^{241}Am	0.110
^{243}Am	0.016

Table 1: TRU vector of the fuel used in the source importance and absorber studies. The composition represents the TRU discharge of an average PWR after a burnup of 40 GWd/t and 30 years of cooling.

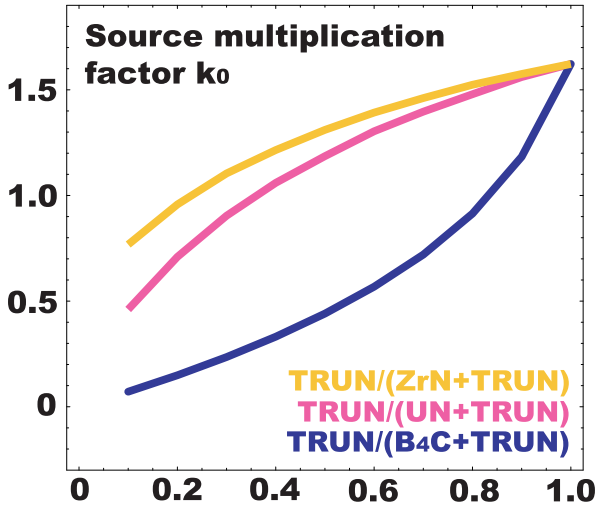

Figure 2: The external source multiplication factor k_0 as function of diluent and burnable absorber concentration in a sodium cooled core. A target radius of 20 cm and a pin pitch to diameter ratio of 1.7 was used. In the calculation, ^{238}UN, ZrN, and B_4C were each homogeneously mixed with transuranic nitride fuel.

that moderates neutrons down below the fast fission threshold by inelastic scattering. Consequently, about 80% of initial and produced ^{241}Am is converted into ^{242}Cm. The latter nuclide has a half-life of 162 days, and therefore to a large extent decays by α-emission within the fuel pins being under irradiation. The resulting helium accumulation leads to formation of gas bubbles that cause fuel swelling (Haas et al., 1999). The remedy usually suggested consists of fabricating porous fuels that would release all helium into pin plena, which then would have to be exceedingly large (Beaumont et al., 1999). A complementary approach, consisting of introducing strong neutron absorbers into sub-critical cores, was suggested by the present authors (Wallenius et al., 1999; Wallenius et al., 2000).

Figure 3 shows the neutron absorption cross section of ^{10}B, compared to the capture and fission cross sections of ^{241}Am. It is evident that the presence of ^{10}B enriched boron carbide pins in the sub-assemblies of a sub-critical core can suppress the rate of slow neutron capture in americium, while not seriously deteriorating the effective fast fission cross section.

The potential of the poison concept is investigated here in more detail, by calculating the probability for direct fission of ^{241}Am in an infinite lattice consisting of boron carbide pins dispersed among transuranium nitride pins immersed into liquid metal coolants. The high Pu fraction enables a large flux of fast fission neutrons to be maintained. Figure 4 (a) shows the fission probability as function of ^{10}B enrichment for equal fractions of B_4C and fuel pins, using the fuel composition of Table 1. It can be seen that already a modest ^{10}B enrichment of 50% yields fission probabilities above 50 percent! Very large absorber pin fractions would lead to vanishing neutron multiplication, but equal fractions of fuel and poison pins lead to a k_∞ of about 0.85, which is acceptable for a zone of sub-assemblies in a sub-critical core. The neutron deficit may be supplied by leakage neutrons from poison free, high multiplication assemblies.

The neutron spectrum in the poisoned sub-assembly is dependent on the macroscopic cross section of the coolant. Figure 4 (b) displays the dependence of the direct fission probability of ^{241}Am for equal proportions of fuel and poison pins, as function of pin pitch to diameter ratio. Note that sodium cooling gives rise to a harder spectrum, due to the smaller cross section for inelastic scattering for Na.

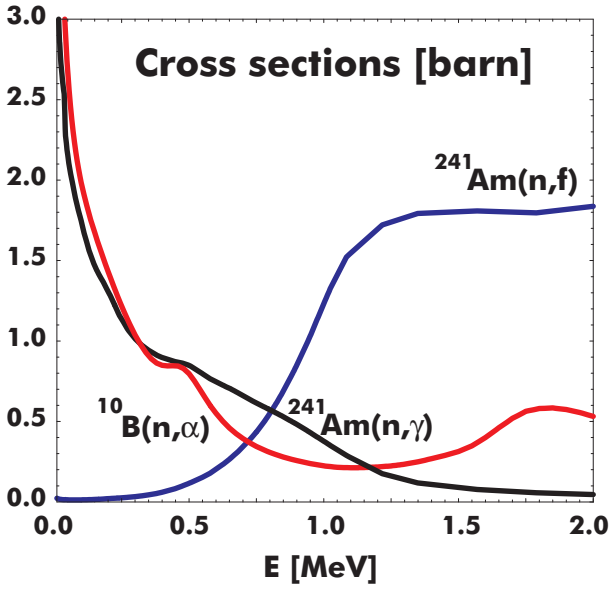

Figure 3: The cross section for neutron absorption in ^{10}B compared to the capture and fission cross sections of ^{241}Am.

The decrease of direct fission probability with increasing pin pitches is not very severe, and values above 50% are still feasible for the larger pitches required by lead/bismuth (Wallenius et al., 2000).

Considering what may be achieved in terms of direct ^{241}Am fissioning in a "real" sub-critical core, one may adopt a strategy where a heavily poisoned fuel zone containing the bulk of americium to be transmuted is folded in-between Pu-assemblies providing high multiplication of source neutrons. Taking into account that a strong absorption of slow neutrons is very degrading for the multiplication of spallation neutrons being moderated in a Pb/Bi target, these assemblies should be placed in the periphery of the core. Note that this approach is much different from the CAPRA strategy where, a moderated leakage flux in the core periphery is utilized for americium transmutation by capture.

In actual core configurations with flat power distribution and reasonable source importance, it is found that direct fission probabilities go down from 60-65 % to 40-50 %, as the leakage neutrons from adjacent assemblies already are somewhat moderated. Still, it appears that helium accumulation in fuel pins due to decay of ^{242}Cm may be cut by a factor of two, compared to non-poisoned designs, which alleviates the requirement of exceedingly large plena to accommodate helium release.

5. Distribution of fuel, diluents and poisons

With the above results in hand, the Sing Sing Core design presented in (Wallenius et al., 2000) could be improved as follows: The diameter of the spallation target was decreased to 18.4 cm, and the diluent uranium nitride in the two inner core zones was substituted with zirconium nitride, in order to improve source importance. The number of fuel zones was increased from four to five, enabling a finer differentiation in fuel and absorber pin concentrations. All minor actinides were removed from the inner core zones, to obtain highest possible probabilities for direct fission. A plutonium vector with higher concentration of thermally fissile nuclides was used in the inner core zones, to further increase source importance. A distribution of fuel and and absorber pins yielding a radial power peaking less than 1.2 is shown in Table 2, together with the concomitant probability for direct fission of ^{241}Am.

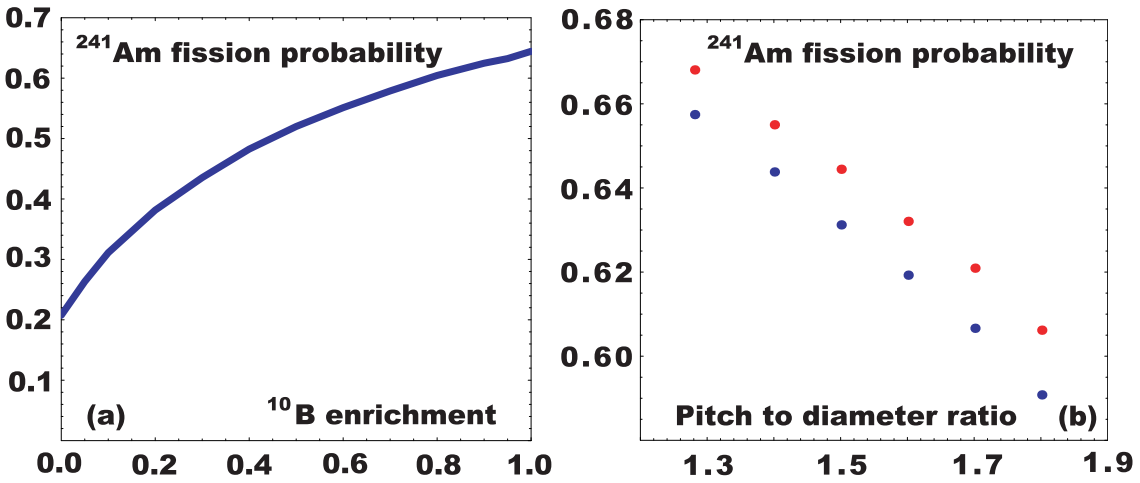

Figure 4: The probability of direct fission of ^{241}Am as function of (a) ^{10}B enrichment in B_4C pins and (b) pin pitch to diameter ratios. An infinite lattice with equal fractions of fuel and absorber pin was assumed. In (a) sodium cooling and a pin pitch to diameter ratio of 1.5 is assumed. In (b) 100% ^{10}B enrichment is assumed. Sodium cooling (red points) yields a slightly harder spectrum than lead/bismuth (blue points), and hence higher fission probabilities.

Property	zone 1	zone 2	zone 3	zone 4	zone 5
Pin pitch to diameter ratio	1.8	1.8	1.8	1.8	1.8
Fuel pins	217	217	84	147	184
Absorber pins	0	0	133	70	33
^{241}Am fission probability	-	-	0.41	0.47	0.42

Table 2: Number of fuel and absorber pins in sub-assemblies of the revised Sing Sing Core.

The molar fractions of ZrN in zones one and two are 77% and 62%, respectively. The k-eigenvalue of the configuration is 0.969, and the effective source neutron multiplication factor k_s equals 0.966, yielding a source importance of 0.91.

6. Conclusions

Combining diluents and poisons, power peaking factors smaller than 1.2 can be achieved in sub-critical systems at k-eigenvalues $\sim$0.97. Placing americium in peripheral fuel assemblies, featuring fractions of enriched boron carbide pins ranging from 15 to 60 percent, direct fission probabilities of americium larger than 0.4 can be achieved. Source importance decreases due to the presence of absorbers, but can be maintained at values close to 0.9 for small spallation targets, using ZrN as diluent in fuel zones close to the target.

Acknowledgements

This work was financially supported by SKB AB (Swedish Nuclear Fuel and Waste Management Ltd), KTC (Swedish Centre for Nuclear Technology) and SI (Swedish Institute).

References

Beaumont, H. et al., 1999. Heterogeneous minor actinide recycling in the CAPRA high burnup core with target sub-assemblies. In *International Conference on Future nuclear systems, GLOBAL 99*. ANS.

Briesmeister, J., 1997. *MCNP - A general Monte Carlo N-Particle transport code, version 4C*. LA-13709-M, Los Alamos National Laboratory.

Gastaldo, G., Rome, M., and Garnier, J., 1995. CAPRA core optimisation by use of $^{11}B_4C$. In *International Conference on Future nuclear systems, GLOBAL 95*, page 1324. ANS.

Haas, D. et al., 1999. The EFTTRA European collaboration for development of fuels and targets for transmutation: Status of recent developments. In *International Conference on Future nuclear systems, GLOBAL 99*. ANS.

Languille, A. et al., 1995. CAPRA core studies - the oxide reference option. In *International Conference on Future nuclear systems, GLOBAL 95*, page 874. ANS.

Novikova, N. et al., 1999. Some features of sub-critical blankets cooled with lead-bismuth. In *International conference on accelerator driven technologies and applications, ADTTA 99*.

Rubbia, C. et al., 1997. Fast neutron incineration in the energy amplifier as alternative to geologic storage. Technical Report LHC/97-01 (EET), CERN.

Takizuka, T. et al., 1998. Studies on accelerator driven transmutation systems. In *Fifth international information exchange meeting*, page 383. OECD/NEA.

Venneri, F., 1998. Disposition of nuclear waste using sub-critical accelerator driven systems. Technical Report LA-UR-98-985, Los Alamos National Laboratory.

Wallenius, J. et al., 1999. Neutronics of a sub-critical system burning non-recycled LWR waste. In *International conference on accelerator driven technologies and applications, ADTTA 99*.

Wallenius, J. et al., 2000. Application of burnable absorbers in an accelerator driven system. *Nuclear Science and Engineering*. Accepted for publication.

Waters, L., 1999. *MCNPX user's manual, version 2.1.5*. TPO-E83-G-UG-X-00001, Los Alamos National Laboratory.

Paper V

P. Seltborg, J. Wallenius, K. Tuček, and W. Gudowski
Definition and application of proton source efficiency in accelerator-driven systems
Nuclear Science and Engineering, **145**, 390 (2003)

Definition and Application of Proton Source Efficiency in Accelerator Driven Systems

Per Seltborg*, Jan Wallenius, Kamil Tuček, Waclaw Gudowski
Department of Nuclear and Reactor Physics
Royal Institute of Technology, Stockholm, Sweden

Abstract *– In order to study the beam power amplification of an accelerator driven system (ADS), a new parameter, the proton source efficiency (ψ^*) is introduced. ψ^* represents the average importance of the external proton source, relative to the average importance of the eigenmode production, and is closely related to the neutron source efficiency (φ^*), which is frequently used in the ADS field. φ^* is commonly used in the physics of sub-critical systems driven by any external source (spallation source, (d,d), (d,t), Cf-252 spontaneous fissions etc.). On the contrary, ψ^* has been defined in this paper exclusively for ADS studies, where the system is driven by a spallation source. The main advantage with using ψ^* instead of φ^* for ADS is that the way of defining the external source is unique and that it is proportional to the core power divided by the proton beam power, independently of the neutron source distribution.*

Numerical simulations have been performed with the Monte Carlo code MCNPX in order to study ψ^* as a function of different design parameters. It was found that, in order to maximize ψ^*, and therefore minimizing the proton current needs, a target radius as small as possible should be chosen. For target radii smaller than about 30 cm, lead-bismuth is a better choice of coolant material than sodium, regarding the proton source efficiency, while for larger target radii the two materials are equally good. The optimal axial proton beam impact was found to be located approximately 20 cm above the core center. Varying the proton energy, ψ^*/E_p was found to have a maximum for proton energies between 1200 and 1400 MeV. Increasing the americium content in the fuel decreases ψ^* considerably, in particular when the target radius is large.

* E-mail: per@neutron.kth.se

I. INTRODUCTION

Accelerator Driven Systems (ADS) [1, 2, 3, 4] are being investigated as a possible mean for reducing the long-term radiotoxicity of spent reactor fuel. In principle, the sub-criticality of ADS allows for dedicated cores with a much higher concentration of minor actinides than what is acceptable in critical reactors. Such dedicated cores enable multi-recycling of americium and curium, providing thus a potential for reducing the radio-toxicity by a factor of 50 to 100 [5].

In ADS, a high-power particle accelerator is used to accelerate protons to energies of the order of 1000 MeV. The protons impinge on a heavy metal target, generating a large number of neutrons via spallation. The spallation neutrons leak out from the target, after different kinds of interactions with the target nuclei, and are subsequently multiplied in the surrounding sub-critical blanket.

An important factor when designing an ADS is to optimize the beam power amplification, given that the reactor is operating at a certain sub-critical reactivity (with sufficient safety margins to criticality). Optimizing the source efficiency, and thereby minimizing the proton current needs, can have an important impact on the overall design of an ADS and on the economy of its operation. The neutron source efficiency parameter φ^* is commonly used to study this quantity, since it is related to the number of fissions produced in the core (which is closely related to the core power), by an average external source neutron.

However, calculating φ^* for an accelerator driven system introduces some complications, since the actual source particles are protons, and not neutrons. In order to determine φ^*, the external neutron source first has to be defined and then the efficiency of this neutron source can be determined. A drawback with using φ^* is that the neutron source can be defined in several different ways, and the results are directly dependent on the choice of definition. Therefore, completely different values of φ^* are often observed [6, 7, 8], due to different choices of external neutron source definition. Another complication associated to the neutron source efficiency is that, studying φ^* as a function of a certain system parameter might change the neutron source distribution and the number of neutrons produced per source proton. In this case, in order to represent the beam power amplification, φ^* needs to be weighted with the number of source neutrons produced per source proton.

With the motivation of simplifying the concept of source efficiency, we introduce in this paper a new parameter ψ^*, which refers to the number of fission neutrons produced in the system by each source **proton**. The advantages with using the proton source efficiency instead of the neutron source efficiency is that there is no ambiguity in how to define the external source, and that it is proportional to the beam power amplification, without the need of a weighting factor.

In this paper, ψ^* has been studied as a function of different system parameters, in order to find the optimal design conditions for maximum proton beam amplification, within the given safety constraints. For this purpose, a model of a nitride fuelled and lead-bismuth cooled ADS was used. First, the neutron source efficiency is defined and discussed (Section II) and then the proton source efficiency parameter is introduced (Section III). Section IV describes the reference model used in this study. In Section V.A, ψ^* and φ^* are studied as functions of the target radius and coolant material. In the following sections, ψ^* is studied as a function of the axial proton beam impact (V.B) and the proton beam energy (V.C). Finally, an americium based fuel has been compared with the plutonium based reference fuel (V.D).

II. NEUTRON SOURCE EFFICIENCY φ^*

II.A. *Definition of the Neutron Source Efficiency*

The neutron flux distribution ϕ_s in a sub-critical core is the solution to the inhomogeneous steady-state neutron transport equation

$$\boldsymbol{A}\phi_s = \boldsymbol{F}\phi_s + S_n \tag{1}$$

where **F** is the fission production operator, **A** is the net neutron loss operator and S_n is the external neutron source.

The neutron source efficiency [9, 10], usually denoted φ^*, represents the efficiency of the external source neutrons and can be expressed according to the following equation [11]:

$$\varphi^* = \left(\frac{1}{k_{eff}} - 1\right) \cdot \frac{< \boldsymbol{F}\phi_s >}{< S_n >} \tag{2}$$

which is valid in the range $0 < k_{eff} < 1$. $<\mathbf{F}\phi_s>$ is the total production of neutrons by fission and $<S_n>$ is the total production of neutrons by the external source. In the above formula, the brackets imply integration over space, angle and energy. Eq. (2) relates the total fission neutron production $<\mathbf{F}\phi_s>$ to the external neutron source, φ^* and the reactivity $(1 - 1/ k_{eff})$. It shows that, for given values of k_{eff} and $<S_n>$, the larger φ^* the larger the fission power produced in the system.

II.B. *Definition of the External Neutron Source*

Since the actual source particles in an accelerator driven system are protons and not neutrons, it is not obvious which

is the best way to define the neutron source. The procedure to calculate φ* is usually divided into two steps – the first generating the source neutrons, produced from the proton beam interacting with the target, and the second one determining the efficiency of these source neutrons. Different source definitions are possible and they will result in different values and meanings of φ*. A brief summary of four different definitions of the external neutron source that have been used in the ADS field is given in [12]. Among these, the two most frequently used definitions, the target neutron leakage source and the energy cut-off source, will be discussed in the two following sections. The other two definitions are the fission source, consisting of the first generation of fission neutrons, and the primary neutron source, which is the collection of neutrons that are created directly from proton induced spallation (primary spallation neutrons) [8].

II.B.1. The Target Neutron Leakage Source

This approach uses the neutrons that leak out radially from the target as source neutrons [6, 13]. The method consists of, in the first step, transporting the high-energy protons and the secondary particles that they produce in the target. The neutrons that leak out from the target are defined as the source, and their properties, in terms of position, direction and energy, are written to a source file. Only the target is present in the first simulation, so no once-leaked neutrons re-entering the target are included in the source definition. In the second step, the leakage neutrons are reemitted as fixed source neutrons in a separate run and the efficiency (φ*) of them is determined. Since the target neutron leakage spectrum includes a high-energy tail, both step 1 and 2 need to be simulated with a high-energy transport code (which can simulate neutrons with energy up to the incident proton energy).

Since the neutron source is generated by a proton beam/target simulation, the distribution of the source neutrons is dependent on the target properties and the proton beam properties. This might induce complications when trying to optimize φ* and the beam power amplification, by varying different system parameters. If a change in the studied system parameter changes the distribution of the source neutrons, φ* has to be weighted by the number of neutrons produced per source proton. With the target neutron leakage definition, examples of these parameters are the target dimension, the proton beam energy or the axial proton beam impact position. Other system parameters, such as the core coolant material, the fuel composition or the core dimensions, are independent of the target region and do not affect the neutron source.

II.B.2. The Energy Cut-off Neutron Source

The other way to define the neutron source is to collect the neutrons that fall below a certain cut-off energy (usually 20 or 150 MeV) [7, 14, 15]. In the first step, a high-energy code is used to transport the accelerated protons and the secondary high-energy particles. The neutrons that are produced are either killed if they are born below the cut-off energy or transported until they fall below this energy. The properties of the killed neutrons are written to a source file. In the second step, these neutrons are reemitted as fixed source neutrons in a separate run and φ* is determined.

An advantage of this approach is that the second step can be simulated with a low-energy transport code. The cut-off energy is set to the upper energy of the cross section library that will be used in the second step calculation. This is desirable since many reactor codes systems are limited to the upper energy limit of the cross-section data library (e.g. 20 or 150 MeV).

It has been shown in [7] that, in contrast to the target neutron leakage source, the neutron source distribution in this case is rather insensitive to changes in the target radius. However, substituting the coolant material or changing the fuel composition will affect the distribution of the neutron source.

III. PROTON SOURCE EFFICIENCY ψ*

III.A. *Introduction of the Proton Source Efficiency*

In order to simplify the concept of source efficiency, a new parameter, called "proton source efficiency" and denoted ψ*, which represents the product of φ* and the number of source neutrons generated per source proton (S_n/S_p), is introduced in this paper. We thus have the following relation between the ***proton*** source efficiency ψ* and the ***neutron*** source efficiency φ*:

$$\psi^* = \varphi^* \cdot \frac{< S_n >}{< S_p >} \tag{3}$$

This parameter could also, in analogy with φ*, be expressed in terms of k_{eff} and the total number of neutrons produced by fission in the core, for each source ***proton***. Inserting Eq. (2) in Eq. (3) it is expressed in the same way as φ*, only with the replacement of S_n by S_p,

$$\psi^* = \left(\frac{1}{k_{eff}} - 1 \right) \cdot \frac{< \boldsymbol{F}\phi_s >}{< S_p >} \tag{4}$$

$<\mathbf{F}\phi_s>/<S_p>$ is the total production of neutrons by fission over the total number of source protons.

Considering ψ* and φ* (according to the target neutron leakage definition) as functions of the target radius and of coolant material illustrates the discussion in the previous section about which design parameters that affect and do not affect the neutron source distribution. Changing the coolant material, S_n/S_p does not change, so ψ* and φ* vary in exactly the same way. When varying the target radius, on the other hand, S_n/S_p changes, so ψ* and φ* varies in different ways. Consequently, if one wants to use the neutron source efficiency parameter φ*, it needs to be weighted with S_n/S_p when it is studied as a function of the target radius, whereas this is not necessary when comparing different core coolant materials. However, with the introduction of the proton source efficiency and always referring to ψ*, none of this has to be considered, and the procedure is simplified.

III.B. *Relationship between ψ* and the Core Power*

The total power produced by fission in the core (P_f) can be expressed as the product of the total number of fission events and the average available energy released in a fission, according to the following relation;

$$P_f = \frac{< \boldsymbol{F}\phi_s >}{\bar{\nu}} \cdot \bar{E}_f \qquad (5)$$

Inserting Eq. (4) in Eq. (5), we obtain

$$\frac{P_f}{< S_p >} = \frac{\bar{E}_f}{\bar{\nu}} \cdot \frac{k_{eff}}{1-k_{eff}} \cdot \psi^* \qquad (6)$$

For a given fuel composition, $\bar{E}_f$ and $\bar{\nu}$ can, for the purpose of this study, be considered to be constant. Even though there are high-energy neutrons entering into the fuel (the neutron yield ν is not constant with respect to neutron energy), the fraction of fissions in the core that are induced by high-energy neutrons is very small. Therefore, a change in the neutron yield for these fission events will have very little impact on $\bar{\nu}$. The variations of $\bar{E}_f$ and $\bar{\nu}$ have been calculated for the series of different studies presented in this paper and were found to be much smaller than the statistical errors in the simulations (except in the case where the fuel composition was modified). When the fuel composition changes, $\bar{\nu}$ might also change, which should be kept in mind in Section V.D, where two different fuels are compared.

If we further make the approximation that the energy produced by fission is proportional to the total core power produced in the core, we find that ψ* is proportional to the total power divided by the source intensity (output/input power).

IV. SYSTEM MODELING

A homogenized model representing a nitride fuelled and lead-bismuth cooled ADS (maximum 800 MWth) has been studied. The height of the active core in the reference model (Fig. 1) is 100 cm and the outer radius is 70 cm. The inner radius is 20 cm, which is also the boundary of the lead-bismuth target. The accelerator tube has a radius of 15 cm and the axial position of the proton beam impact is 25 cm below the top of the core. The radius of the radially uniform 1000 MeV proton beam is 7.5 cm. Above and below the active zone of the core, plena for accommodation of gas release are included, having lengths of 100 and 50 cm, respectively. The radial reflector is assumed to consist of 90 % steel and 10 % lead-bismuth.

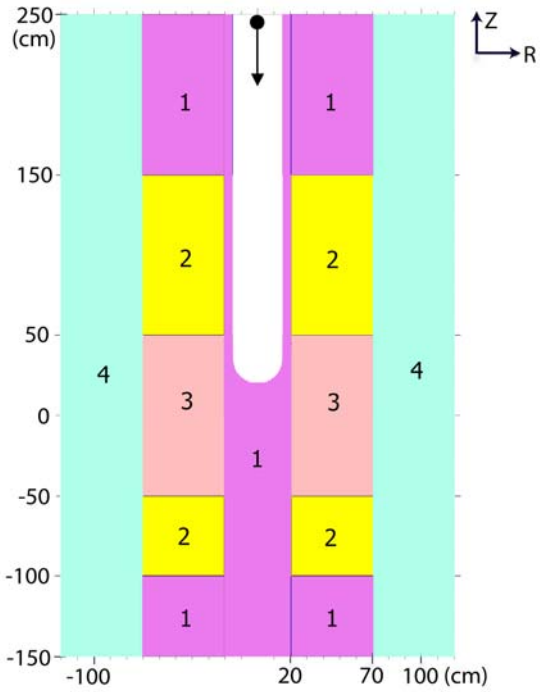

Fig. 1. RZ-view of the homogenised reference model. The 1000 MeV protons are guided through the accelerator tube and impinge on the Pb-Bi target. The different regions in the model are pure Pb-Bi (1), the plena (2), the active core (3) and the reflector (4).

The relative fraction of fuel, cladding and coolant material used in the homogenized model correspond to a pin radius of 2.5 mm and P/D = 1.72. The nitride actinide fuel is in solid solution with ZrN. The volume fraction of ZrN was adjusted to 83 %, in order to obtain a k_{eff} of about 0.95. The fuel consists of 80% plutonium and 20% americium (the actinide vectors are listed in Table I). The spallation target and the core coolant consist of lead-bismuth eutectic and the fuel pin cladding of 10% chromium and 90% iron.

TABLE I

Relative Fraction of Actinides in the Reference Fuel. The Pu vector corresponds to that of spent LWR MOX fuel after 7 years of cooling and the Am vector to a mixture of spent UOX and MOX fuel.

Plutonium	**80 %**	**Americium**	**20 %**
Pu-238	5 %	Am-241	67 %
Pu-239	38 %	Am-243	33 %
Pu-240	30 %		
Pu-241	13 %		
Pu-242	14 %		

The Monte Carlo code MCNPX [16] (Version 2.3.0), in coupled neutron and proton mode, was used for all simulations, relying on the evaluated nuclear data library ENDF/B-VI.8 (limited to 20 MeV). The Intranuclear Cascade model used by MCNPX was the Bertini package [17].

V. THE PROTON SOURCE EFFICIENCY AS A FUNCTION OF DIFFERENT SYSTEM PARAMETERS

The proton source efficiency ψ* has been studied as a function of a number of system parameters, such as the target radius, coolant material, axial proton beam impact position, proton beam energy and fuel composition. The starting point for each parameter study is the reference model. In each case when a parameter has been changed, the reactivity has been re-adjusted in order to keep k_{eff} constant at about 0.95.

V.A. *ψ* as function of Target Radius*

In this section, ψ* has been computed for different target radii, for the reference lead-bismuth cooled core and for a sodium cooled core. The neutron source efficiency φ*, using the target neutron leakage definition, has also been determined. k_{eff} was kept constant at 0.95 by adjusting the outer radius of the core.

Since changing the geometry of the core might affect the results, ψ* has also been studied as a function of the outer core radius, varying from 60 to 90 cm. It was found that an increase of the core radius leads to a slight increase of ψ*, on average 0.26% per cm. The explanation for this is that the radial neutron leakage into the reflectors decreases as the core radius increases. This dependence of ψ* (rather small but not automatically negligible) on the core radius should be kept in mind in the parameter studies where the core radius is varying.

V.A.1. The Lead-Bismuth Cooled Reference Model

ψ* was computed for the reference model for different target radii, both as the product of φ* and S_n/S_p (Eq. 3) and directly according to Eq. (4), in order to verify the consistency between the two different expressions. φ* was calculated using the target neutron leakage definition. The results are listed in Table II and we see that they are in good agreement with each other, the differences being within the statistical uncertainty. Hence, using a two-step simulation procedure, ψ* can be obtained according to Eq. (3), independently of the choice of neutron source definition. If MCNPX is used, ψ* can be obtained directly according to Eq. (4). ψ*, φ* and S_n/S_p are also plotted as functions of target radius later on in this section.

TABLE II

Computation of ψ* according to Eq. (3) and Eq. (4) (1σ-error ~ 0.75 %). For the 10 cm target radius, the radius of the accelerator tube was decreased to 10 cm. The results are also plotted below.

Target Radius	φ^*	$\frac{<S_n>}{<S_p>}$	$\varphi^* \cdot \frac{<S_n>}{<S_p>}$	ψ^*
10	1.81	21.9	39.8	39.6
20	1.35	26.8	36.3	35.9
30	1.13	29.0	32.9	32.4
40	0.99	30.0	29.6	29.5
50	0.89	30.2	26.7	27.0

Concerning the dependence on target radius, we see that ψ* decreases considerably when the radius increases. There are mainly two reasons for this behaviour. One of them is the softening of the radial neutron leakage spectrum from the target (the spectrum of the neutrons that enter into the fuel), when the target is enlarged. The probability to induce fission for the source neutrons strongly decreases with decreasing energy, especially when the core is loaded with even-neutron number actinides, as will be shown below. Lower neutron energy also inhibits other possible neutron multiplication reactions, such as (n,xn)-reactions and secondary spallation. The number weighted mean energy of the radial neutron leakage spectrum decreases by a factor of four when the target radius is increased from 20 cm to 50 cm and the fraction of neutrons above 20 MeV is only 0.5% for a radius of 50 cm, while 3.2% for a 20 cm radius. The radial neutron leakage spectra for different target radii are plotted in Fig. 2 and the fraction of leakage neutrons above some energy thresholds are listed in Table III.

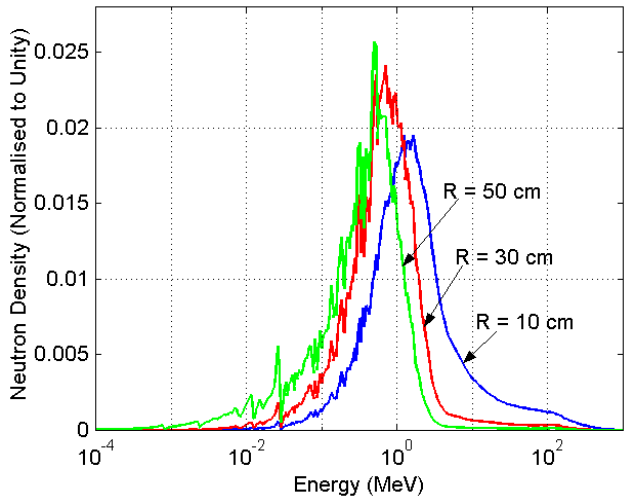

Fig. 2. Radial neutron leakage spectra from the target for different target radii.

TABLE III

Fraction of Neutrons Leaking out Radially from the Target that have Energies above 1, 7, 20 and 150 MeV.

Target Radius	>1 MeV	>7 MeV	>20 MeV	>150 MeV
10	62.4%	13.4%	6.9%	1.1%
20	45.2%	6.1%	3.2%	0.45%
30	31.0%	3.0%	1.7%	0.22%
40	20.7%	1.6%	0.9%	0.12%
50	13.5%	0.8%	0.5%	0.07%

The other reason for the decrease in ψ^* is that the axial target neutron leakage (the neutrons that leak out from the target axially and never enter the active core) increases significantly with increasing target radius. The fraction of axial target leakage neutrons relative to the total number of neutrons exiting the target is approximately 5 % for the 20 cm radius target while about 28 % for the 50 cm radius target. The major part of the axial leakage is in the backward direction, through the accelerator tube.

On the other hand, increasing the target radius increases the neutron multiplication inside the lead target, which leads to a higher number of neutrons created per source proton (S_n/S_p increases from 26.8 for r=20 cm to 30.2 for r=50 cm). The multiplicative effect of (n,xn)-reactions and secondary spallation in the lead target enhances the proton source efficiency. Consequently, with increasing target radius, there are more neutrons for each source proton that enter into the fuel, though the efficiency of these neutrons is strongly reduced. Accordingly, we see in Table II that ψ^* decreases less rapidly than φ^* with increasing target radius, due to the increase in S_n/S_p. These two competing factors in ψ^* are thus well represented by Eq. (3).

We conclude that, in order to optimize the proton source efficiency and the output/input power, a target radius as small as possible should be chosen (increasing the radius from 20 cm to 50 cm decreases ψ^* by about 25%). These results are in good agreement with other similar studies [7]. However, it has also been shown that, reducing the target radius has some undesirable effects, for instance higher fluence/burnup ratio (lower maximum burnup) and more severe high-energy damages. Moreover, for a large-scale ADS, the target must be sufficiently large to be able to remove the heat from the high-power accelerator beam. It is thus clear that, in order to optimally design a cost-efficient ADS with high fuel performances, a trade-off between several different aspects arises.

V.A.2. A Sodium Cooled Model

Replacing the lead-bismuth coolant with sodium reduces the reactivity by about 5000 pcm, so in order to maintain a k_{eff} of 0.95, the outer core radius was increased by 11 cm. As is shown in Fig. 3, the proton source efficiency for small target radii is lower for the sodium cooled core than with the lead-bismuth coolant (approximately 7% lower for r = 20 cm).

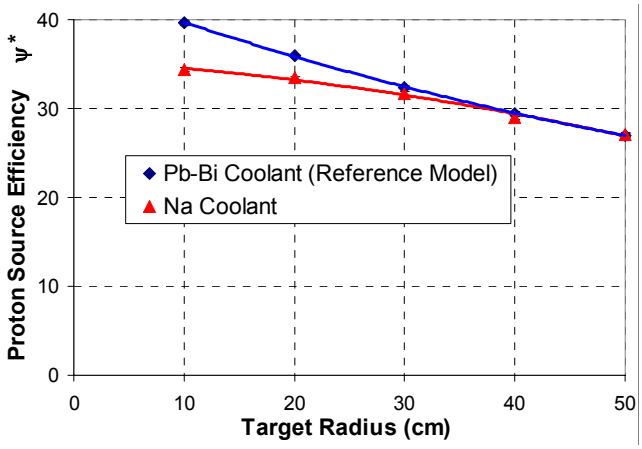

Fig. 3. Proton source efficiency ψ^* versus target radius for a Pb-Bi cooled and a Na cooled model (1σ-error ~ 0.75 %).

The main reason for this is that there is no neutron multiplication in the sodium coolant, in contrast to lead-bismuth. The differences between the two curves indicate that the contribution from (n,xn)-multiplication in the Pb-Bi coolant is significant for target radii smaller than about 30 cm. As long as there is a fraction of neutrons with energy higher than about 7 MeV (the (n,2n)-threshold in lead) there will be (n,xn)-neutron multiplication in lead. When the target radius is small, this high-energy fraction is rather high (6.1% have energies higher than 7 MeV for r=20 cm

compared to 0.8% for r=50 cm). When the target radius increases, the fraction of high-energy neutrons decreases, and at radii above 40 cm the ψ* values are essentially the same. Another difference between the two coolant materials is that lead-bismuth has better spallation-neutron production characteristics. This enhances ψ* for small target radii, in which cases there are still a significant fraction of very energetic neutrons leaking out into the fuel region. The difference between the Pb-Bi and the Na coolant are further illustrated in Fig. 4, where the neutron source efficiencies are depicted, together with the number of neutrons per source proton.

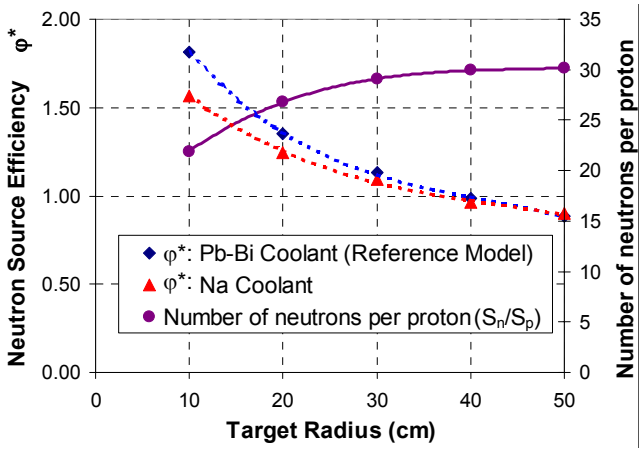

Fig. 4. Neutron source efficiency φ* (according to the target neutron leakage definition) and number of neutrons per source proton (S_n/S_p), versus target radius for the Pb-Bi cooled and the Na cooled model (1σ-error ~ 0.75 %).

V.B. *ψ* as function of Axial Beam Impact Position*

The proton source efficiency has been studied as a function of the axial beam impact position, varying from the center of the core (z = 0) to the top of the core (z = 50 cm). It is seen in Fig. 5 that, for the reference model (with an accelerator tube radius of 15 cm) the maximum in ψ* is obtained at about 20 cm above the core center. Moving away from the optimum impact position, ψ* decreases, due to increasing axial neutron leakage from the target.

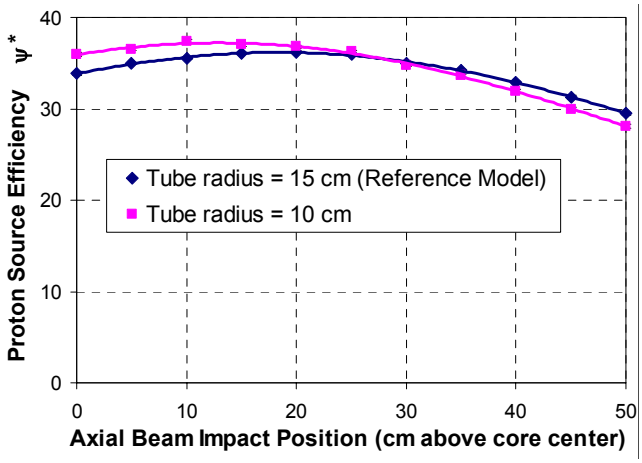

Fig. 5. Proton source efficiency ψ* versus axial beam impact position (cm above the core center) for a tube radius of 15 cm and of 10 cm (1σ-error ~ 0.50 %).

As is shown in Fig. 5, ψ* and its dependence of the axial beam impact is rather sensitive to the accelerator tube radius. For a tube radius of 10 cm, the beam impact position that maximizes ψ* is moved downwards in the core, with the optimum at about 13 cm above the core center. The maximum value of ψ* also increases somewhat (~ 3%) when the tube radius is changed from 15 cm to 10 cm.

When the tube radius decreases there are mainly two effects appearing. One is that the axial neutron leakage in the backward direction decreases (increasing ψ*) and the other one is that the energy spectrum of the neutrons entering into the fuel is softened (decreasing ψ*). When the beam impact is close to the core center, the impact of the leakage on the neutron balance is more pronounced than the softening of the neutron spectrum. On the contrary, when the beam impact is close to the top of the core, the softening effect is dominant and ψ* is lower for the 10 cm tube radius.

An accidental scenario that has been considered in an ADS is that the accelerator tube is filled (partially or fully) with the target material [18], which would increase k_{eff}. For the reference model, filling the tube from 20 cm above the core center till the top of the core, this increase is about 600 pcm. For an initial reactivity level of k_{eff} = 0.95, and not taking the variations in ψ* into account, this would increase the core power by 14 %. For the 10 cm tube radius, the change in k_{eff} is smaller and also the effect on the power. However, the rapid decrease in ψ* above z = 20 cm will tend to reduce the core power. Adding these two opposite effects together, according to Eq. (6), it is found that the core power decreases when the tube channel is filled with lead-bismuth coolant. Filling the tube from z = 20 cm to z = 50 cm decreases the core power by 7 % for the 15 cm tube radius and by 20 % for the 10 cm tube radius.

However, if the reactor is operating at a reactivity level closer to criticality, the effect on the core power from a reactivity insertion will be higher and might be more important than the decrease in ψ*. One way to increase the safety margins to prompt criticality, is to set the proton beam impact at the top of the core (z = 50 cm). However, the loss in proton source efficiency, by moving the impact from the optimal position to the top of the core would be large - about 18 % for the 15 cm tube radius and 24 % for the 10 cm tube radius.

V.C. *ψ* as function of Proton Beam Energy*

The proton source efficiency was calculated for different proton beam energies, varying from 400 MeV to 2.5 GeV, for a 20 cm and a 50 cm radius target. The ψ* values divided by the proton energy (ψ^*/E_p) are displayed in Fig. 6.

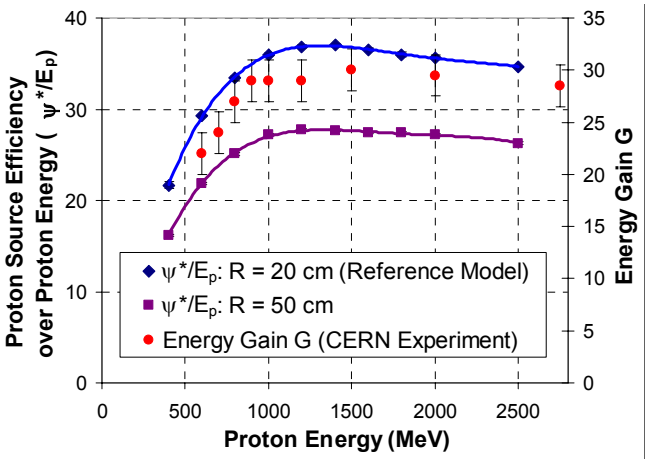

Fig. 6. Proton source efficiency divided by proton energy in GeV (ψ^*/E_p) versus proton beam energy, for target radii of 20 cm and 50 cm (1σ-error ~ 0.50 %). Energy gain G from CERN experiments [19] for a set-up configuration of $k_{eff} = 0.895$.

In coherence with Fig. 3, ψ* is higher for the 20 cm radius than for the 50 cm radius, for all proton energies. However, the shape of the two curves is very similar. ψ^*/E_p increases strongly with increasing proton energy up to about 1000 MeV. The maximum is reached at about 1200-1400 MeV. Above 1400 MeV the curves decrease slightly. The reason for this is that the range of the protons increases with increasing energy and a larger fraction of the spallation induced neutrons will be created far away from the center of the core (or even below the core). This increases the axial neutron leakage from the target in the downward direction. For instance, the range of 1 GeV protons impinging on a lead target is about 53 cm, while about 95 cm for 2 GeV protons [18]. The distance from the top of the target to the bottom of the core was 75 cm (Fig. 1).

The proton source efficiency divided by the proton energy (ψ^*/E_p) is closely related to the energy gain (beam power amplification) of a source driven sub-critical system. The energy gain (G), as defined in [19], represents the total power produced in the core over the accelerator power

$$G = \frac{P_{tot}}{P_{acc}} = \frac{G_0}{1 - k_{eff}} \tag{7}$$

where G_0 relates to the efficiency of the spallation regime. Similarly, using Eq. (6) and the fact that $P_{acc} = < S_p > \cdot E_p$, P_{tot}/P_{acc} can be expressed as

$$\frac{P_{tot}}{P_{acc}} = \frac{P_{tot}}{< S_p > E_p} \propto \frac{k_{eff}}{1 - k_{eff}} \cdot \left(\psi^* / E_p \right) \tag{8}$$

Hence, for given k_{eff}, ψ^*/E_p is proportional to the energy gain G. In the experiments performed at CERN [19], the energy gain was studied as function of the proton beam energy. The results are re-plotted in Fig. 6. We see in the figure that the MCNPX simulated values of ψ* have similar relative dependence on the proton energy, as the results from the CERN experiments. This comparison confirms that the ψ* parameter represents well the beam power amplification of an ADS.

The k_{eff} of the sub-critical assembly in the CERN experiments was 0.895. In order to obtain G for $k_{eff} = 0.95$, the values have to be multiplied by (1-0.895)/(1-0.95) = 2.1. For $E_p = 1000$ MeV the energy gain becomes 61.

V.D. *ψ* for an Americium Based Fuel*

Finally, ψ* has been studied for an americium based fuel (40% Pu and 60% Am), as a function of the target radius. The volume fraction of the ZrN matrix was re-adjusted to 63%, in order to keep a k_{eff} of about 0.95. The results are displayed, together with the results for the reference model, in Fig. 7. We see that the introduction of americium decreases the source efficiency significantly and makes it more sensitive to the target radius.

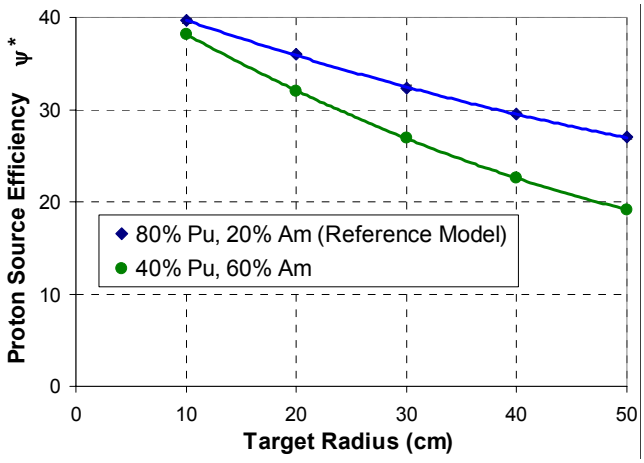

Fig. 7. Proton source efficiency ψ* versus target radius for an americium based fuel, compared with the plutonium based reference model (1σ error ~ 0.75 %).

This is expected, since the fission cross-section of Am-241 and Am-243 decreases rapidly for neutron energies below 1 MeV. Fig. 8, where the fission cross-section over the absorption cross section is plotted for Am-241 and Pu-239, shows that the fission probability of Am-241 is very sensitive to neutron energies between 0.1 and 1 MeV, whereas for Pu-239, it is high everywhere in this energy range. Above 1 MeV the fission probability for plutonium and americium are of the same order of magnitude. The other even-neutron number actinides, Pu-238, Pu-240, Pu-242 and Am-243, have similar cross-section dependence as Am-241, while the Pu-241 cross-section is similar to that of Pu-239.

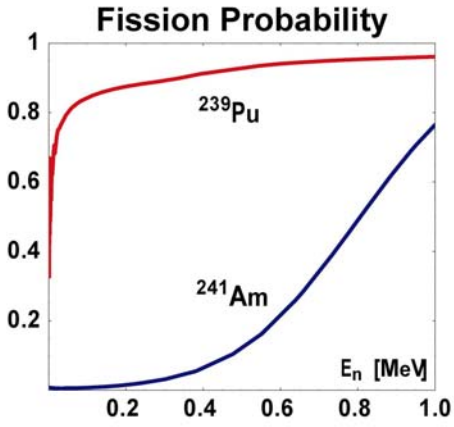

Fig. 8. Fission cross-section over absorption cross-section for Pu-239 and Am-241 (ENDF/B-VI).

Hence, the neutrons entering into the fuel with energy below 1 MeV will have less probability to induce fission in the fuel, when the core is loaded mainly with americium. As was shown in Fig. 2 and in Table III, the energy distribution of the radial target leakage neutrons is very sensitive to the target radius. For a 10 cm radius, only 38% of the leakage neutrons are below 1 MeV and ψ* is not so sensitive to the americium/plutonium ratio, which is also seen in Fig. 7. However, with increasing target radius, the fraction of neutrons above 1 MeV decreases rapidly, with a corresponding loss in proton source efficiency. Thus, increasing the americium concentration from 20% to 60%, reduces ψ* by 11% for the 20 cm target radius and by 29% for the 50 cm target radius.

In Section III.B, it was shown that, for a fixed fuel composition, ψ* is approximately proportional to the core power divided by the source intensity. However, increasing the fraction of americium in the fuel increases $\bar{\nu}$ by about 5 %. Therefore, normalising to the same core power, the difference between the two curves would be slightly larger (by 5%) than in Fig. 7.

VI. CONCLUSIONS

Instead of using the neutron source efficiency parameter φ*, in order to study the beam power amplification, a new parameter ψ*, representing the efficiency of the source protons, has been introduced. The proton source efficiency ψ* is related to the number of fissions produced in the system, which in its turn is approximately proportional to the total core power. By introducing ψ*, ambiguities in defining the external neutron source when calculating the source efficiency are avoided. Another advantages with ψ* over φ* is that it is proportional to the core power divided by the proton beam power, independently of the neutron source distribution. Maximizing the proton source efficiency minimizes the proton current needs and relaxes the constraints on the construction of the high-power accelerator. Studying ψ* when optimising different system parameters therefore becomes an important factor in the overall design of an ADS.

Studying the radius of the spallation target, it was found that ψ* decreases strongly with increasing target radius (by 25% when the radius is changed from 20 cm to 50 cm). The two main reasons for this behaviour is that, the axial neutron leakage from the target increases and that the energy spectrum of the neutrons that enter into the fuel is softened, when the target is enlarged. These effects are only partly compensated by the increased neutron multiplication inside the target. Hence, in order to maximize the beam power amplification, a target radius as small as possible should be chosen, without exceeding the limits determined by safety constraints and other target-core characteristics (e.g. high-energy particle fuel damages and beam power heat removal). Substituting the lead-bismuth coolant by sodium decreases ψ* for target radii smaller than 30 cm, whereas

for larger target radii, the two coolant options perform equally good.

The axial position of the proton beam impact that maximizes ψ^* was, for the reference model (tube radius = 15 cm), located approximately 20 cm above the core centre, but with relatively small variations between 0 and about 35 cm. However, the dependence of ψ^* on the impact position is sensitive to the accelerator tube radius, and for a tube radius of 10 cm, the maximum was found at about 13 cm above the core centre. Reducing the tube radius from 15 to 10 cm also increases the maximum of ψ^* by 3 %.

Investigating the proton source efficiency divided by the proton energy (ψ^*/E_p) as a function of the proton energy showed that a maximal accelerator power amplification is obtained for proton energies of about 1200 to 1400 MeV, but with rather small changes between 1000 and 2000 MeV. Finally, increasing the americium content in the fuel from 20% to 60%, decreases ψ^* considerably, especially for larger target radii. Due to the sharp decrease in fission cross-section below 1 MeV, americium is more sensitive than plutonium to the softening of the energy spectrum of the neutrons that enter into the fuel.

ACKNOWLEGDEMENTS

This work was financially supported by the Swedish Centre for Nuclear Technology, SKB AB (Swedish Nuclear Fuel and Waste Management Co) and the European Commission (Project MUSE: FIKW-CT-2000-00063). The authors would like to thank J. Cetnar, R. Klein Meulekamp and R. Jacqmin for useful discussions.

REFERENCES

1. M. SALVATORES et al., "Long-Lived Radioactive Waste Transmutation and the Role of Accelerator Driven (Hybrid) Systems," *Nucl. Instrum. Methods A*, **414**, 5 (1997).

2. D. G. FOSTER et al., "Review of PNL Study on Transmutation Processing of High Level Waste," LA-UR-74-74, Los Alamos National Laboratory (1974).

3. T. TAKIZUKA et al., "Conceptual Design of Transmutation Plant," Proc. Specialist Mtg. Accelerator Driven Transmutation Technology for Radwaste, LA-12205-C, p. 707, Los Alamos National Laboratory (1991).

4. D. G. CACUCI, "On Perturbation Theory and Reactor Kinetics: From Wigner's Pile Period to Accelerator Driven Systems," *Int. Meeting*, PHYSOR2002, Korea, Seoul (2002).

5. M. DELPECH et al., "The Am and Cm Transmutation – Physics and Feasability," *Proc. Int. Conf. Future Nuclear Systems, GLOBAL'99,* August 30-September 2, 1999, Jackson Hole, Wyoming, American Nuclear Society (1999).

6. J. WALLENIUS et al., Application of burnable absorbers in an accelerator driven system", Nuclear Science and Engineering, 96, 137 (2001)

7. W. S. YANG, L. MERCATALI et al., "Effects of Buffer Thickness on ATW Blanket Performances", *Int. Meeting Accelerator Applications/Accelerator Driven Transmutation Technology and Applications* ADTTA/AccApp'01*,* November 11-15, 2001, Reno, Nevada, USA (2001).

8. P. SELTBORG, R. JACQMIN, "Spallation Neutron Source Effects in a Sub-Critical System," *Int. Meeting Accelerator Applications/Accelerator Driven Transmutation Technology and Applications,* ADTTA/AccApp'01, November 11-15, 2001, Reno, Nevada, USA (2001).

9. M. SALVATORES et al., "The Potential of Accelerator-Driven Systems for Transmutation or Power Production Using Thorium or Uranium Fuel Cycles," *Nucl. Sci. Eng*., 126, 333 (1997).

10. R. SOULE, M. SALVATORES, R. JACQMIN, "Validation of Neutronic Methods Applied to the Analysis of Fast Sub-Critical Systems: The MUSE-2 Experiments," GLOBAL'97, page 639 (1997).

11. G. ALIBERTI et al., "Analysis of the MUSE-3 Subcritical Experiment", Int. Conf. Global 2001, France, Paris, September (2001).

12. R. KLEIN MEULEKAMP, A. Hogenbirk, "The Neutron Source in ADS applications", PDS-XADS D23 App. D, NRG report /I 20782 / 02.50727, Petten (2002).

13. K. TUCEK et al., "Source Efficiency in an Accelerator-Driven System with Burnable Absorbers,", *Int. Conf. on Back-End of the Fuel Cycle: From Research to Solutions, GLOBAL 2001*, Paris, France (2001).

14. S. ATZENI et al., "Statistical Fluctuations in Montecarlo Simulations of the Energy Amplifier," CERN/LHC/97-12 (EET), CERN (1997).

15. K. W. BURN, "A Decoupled Approach to the Neutronics of subcritical configurations: Evaluating the Neutron Source", RT/ERG/99/2, ENEA, Bologna, Italy (1999).

16. L. S. WATERS, "MCNPX™ User´s Manual – Version 2.1.5," Los Alamos National Laboratory, November 14, (1999).

17. H. W. BERTINI, Phys. Rev. 131, 1801, (1969).

18. L. MONSANT et al., "Proposed Sub-criticality level for an 80 MWth Lead-Bismuth Cooled ADS, 7th IEM, Jeju, Korea (2002).

19. S. ANDRIAMONJE et al., "Experimental determination of the energy generated in nuclear cascades by a high energy beam", Physics Letters B 348, 697-709 (1995).

20. S. BUONO, "Beam Target Design in Accelerator Driven Systems", Frederic Joliot/Otto Hahn Summer School '2002, August 21-30, 2002, Cadarache, France (2002).

APPENDIX 2

Per Seltborg, Janne Wallenius, Waclaw Gudowski, “Impact of Heterogeneous Cm-distribution on Proton Source Efficiency on Accelerator-driven Systems”, Int. Meeting Physor 2004, April 25-29, 2004, Chicago, Illinois, USA (2004).

PHYSOR 2004 -The Physics of Fuel Cycles and Advanced Nuclear Systems: Global Developments
Chicago, Illinois, April 25-29, 2004, on CD-ROM, American Nuclear Society, Lagrange Park, IL. (2004)

Impact of Heterogeneous Cm-distribution on Proton Source Efficiency in Accelerator-driven Systems

Per Seltborg*, Jan Wallenius, Waclaw Gudowski
Department of Nuclear and Reactor Physics
Royal Institute of Technology, Stockholm, Sweden

The proton source efficiency (ψ^*) was studied for homogeneous and heterogeneous distributions of minor actinides in a nitride-fuelled and lead-bismuth-cooled accelerator-driven system. The findings from the MCNPX simulations indicate that, compared to a homogeneous configuration, a gain in ψ^* by up to 16% can be obtained by distributing the minor actinides heterogeneously, Cm being placed in the inner zone of the active core and Am in the outer zone. The reason for this is the higher fission probability for neutrons for Cm than for Am in the energy range below 1.0 MeV.

Moreover, a comparative study of two different physics packages available in MCNPX, the Bertini and the CEM models, has been performed, focusing on the production of neutrons in the spallation target and on the proton source efficiency. The Bertini model was found to produce a higher number of neutrons in the low-energy range (below ~15 MeV) than the CEM model. Consequently, the Bertini model also over-estimates ψ^* by about 10%, compared to the CEM model.

KEYWORDS: Proton source efficiency, Spallation, ADS, Transmutation, MCNPX, CEM, Bertini, Curium

1 Introduction

In accelerator-driven systems (ADS) [1-3], a sub-critical core is coupled to a high-power proton accelerator. The high-energy protons impinge on a target of heavy metal, generating a large number of neutrons via spallation reactions. The produced spallation neutrons leak out from the target, thus providing the surrounding sub-critical core with a strong external neutron source.

One of the objectives when designing an ADS is to try to attain as high power as possible to be produced in the core (yielding high transmutation rates), using as low proton beam power as possible. Since the construction of a reliable high-power proton accelerator is a difficult technical task and its operation is very expensive, the optimization of the efficiency of the source protons could have an important impact on the overall design of a future ADS and on the economy of its operation. In order to study the beam power amplification (core power divided by proton beam power) of an ADS, a new parameter, the proton source efficiency (ψ^*), was introduced in a previous study [4]. ψ^* represents the average importance of the external proton source, relative to the average importance of the eigenmode neutron production. It is defined in analogy with the neutron source efficiency φ^*, but relates the core power to the source protons instead of to the source neutrons. φ^* is commonly used in the physics of sub-critical systems, driven by any external neutron source (spallation source,

* Corresponding author, Tel. +46-8 55 37 82 04, E-mail: per@neutron.kth.se

(d,d), (d,t), ^{252}Cf spontaneous fission etc.). ψ*, on the other hand, has been defined only for ADS studies, where the system is driven by a proton-induced spallation source. The main advantages with using ψ* instead of φ* are that the way of defining the external source is unique and that ψ* is proportional to the beam power amplification. It has been shown that the source efficiency can vary considerably for different reactor cores. Studying ψ* for various system parameters is therefore of interest when designing an ADS.

The proton source efficiency is equal to the product of φ* and the number of source neutrons generated per source proton (Z_{tot}). We thus have the following relation between the *proton* source efficiency ψ* and the *neutron* source efficiency φ*;

$$\psi^* = \varphi^* \cdot Z_{tot} \ . \qquad (1)$$

For a fixed system (constant Z_{tot}), it follows that ψ* is proportional to φ*. However, when studying a change in a system design, Z_{tot} might also change and only ψ* remains proportional to the beam power amplification. ψ* could also, in analogy with the definition of φ* [5], be expressed in terms of k_{eff} and the total number of neutrons produced by fission in the core, for each source proton;

$$\psi^* = \left(\frac{1}{k_{eff}} - 1 \right) \cdot \frac{< \boldsymbol{F}\phi_s >}{< S_p >} \ . \qquad (2)$$

$<\boldsymbol{F}\phi_s>/<S_p>$ is the total production of neutrons by fission over the total number of source protons. Since $<\boldsymbol{F}\phi_s>$ is approximately proportional to the total power produced in the core, ψ* thus relates the core power directly to the proton beam intensity.

In the present paper, the proton source efficiency has been investigated for two different core configurations, the first with the minor actinides homogeneously mixed with each other and the second with the fuel heterogeneously distributed, curium being moved to the inner part of the core and americium to the outer part. In Section 2, the model used in the simulations is described and in Section 3.1, these two configurations are studied and compared for different radii of the spallation target. Section 3.2 describes a comparative study of two different physics packages provided by MCNPX [6], the Bertini model [7] and the Cascade-Exciton Model (CEM) [8].

2 System Modeling

Numerical simulations have been performed with the high-energy Monte Carlo code MCNPX in order to study ψ* for two different double-zone core configurations. In the first configuration, americium and curium were distributed homogeneously together with plutonium over the entire core, while in the second one, all of the curium was concentrated to the inner zone and the americium to the outer zone. A homogenized model of a uranium-free nitride-fuelled and lead-bismuth-cooled ADS was used and the composition of actinides in the fuel is based on the indefinite recycling of plutonium (40%), americium (51%) and curium (9%) in the second stratum of the double-strata fuel cycle strategy [9]. The actinide vector used in the model is listed in Table 1.

The simulations were performed for different target radii, varying from 10 cm to 50 cm. In the model depicted in Fig. 1, the target radius is 20 cm, which is also the inner boundary of the active core. The outer radius of the active core is in this case 70 cm and the height of it

Table 1 Relative fraction of actinides in the fuel

Plutonium	40%	Americium	51%	Curium	9%
Pu-238	5 %	Am-241	67 %	Cm-244	90%
Pu-239	38 %	Am-243	33 %	Cm-245	10%
Pu-240	30 %				
Pu-241	13 %				
Pu-242	14 %				

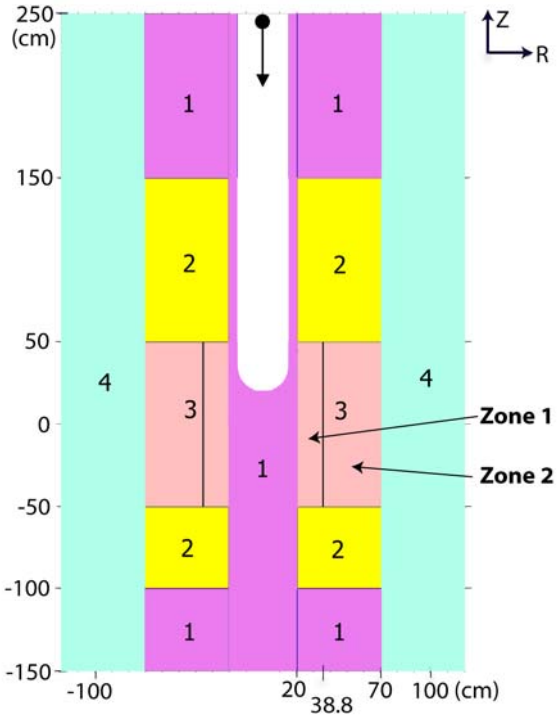

Fig. 1. RZ-view of the simulated model with target radius of 20 cm. The 1000 MeV protons are guided through the accelerator tube and impinge on the Pb-Bi spallation target. The different regions in the model are pure Pb-Bi (1), the plena (2), the active core (3) (zone 1 and zone 2) and the reflector (4).

100 cm. As the radius of the spallation target is varying, the outer radius of the core also needs to be changed, in order to maintain a constant reactivity and approximately the same volume of the core. The nitride fuel is mixed with an inert matrix of ZrN, and the fractions of inert matrix in the two zones were adjusted in order to obtain a k_{eff} of about 0.95 and to obtain the same maximum power density in the two zones, thereby yielding a flattening of the core power profile. In the heterogeneous configuration, the fraction of Pu was fixed to 40% in both zones, the fraction of Cm in zone 1 thus being 60%. The volume fractions of inert matrix in the different core zones are listed in Table 2. Due to the higher fission probability and fission neutron yield of Cm than of Am, the fraction of inert matrix in zone 1 is higher when Cm is concentrated to the inner zone of the core (75%), compared to when the minor actinides are mixed with each other (70%). The radius of the boundary between zone 1 and zone 2 was for each target radius determined by the matrix fractions and the total relative fractions of

actinides in the fuel. For the 20 cm target radius, the boundary was located at a radius of 38.8 cm.

Table 2 Volume fraction of inert matrix for the different core zones

Core configuration	Volume fraction of inert matrix	
	Zone 1	Zone 2
Homogeneous (Am and Cm mixed)	70%	66%
Heterogeneous (Am and Cm separated)	75%	64%

A 1000 MeV mono-energetic proton beam characterized by a Gaussian spatial distribution with a full width half maximum of 7.5 cm was used in the simulations. This proton source was guided through the vacuum beam tube of radius 15 cm towards the spallation target made of lead-bismuth eutectic. The Monte Carlo code MCNPX (version 2.3.0), in coupled neutron and proton mode, was used for all simulations, relying on the evaluated nuclear data library ENDF/B-VI.8. The high-energy physics package used by MCNPX was the Cascade-Exciton Model (CEM97).

3 Results and Discussion

3.1 Proton Source Efficiency for Homogeneous and Heterogeneous Cm Distribution

The main goal of this paper has been to investigate the impact on proton source efficiency of a heterogeneous distribution of Cm (zone 1) and Am (zone 2), compared to a homogeneous fuel distribution. From the results of the simulations, displayed in Fig. 2, we can draw the following conclusions. First, ψ^* decreases considerably when the radius of the spallation target increases. These results are in good agreement with our previous studies of the proton source efficiency [4, 10]. One reason for this behavior is the spectrum softening of the neutrons entering into the active core when the target is enlarged, since the probability to induce fission for neutrons strongly decreases with decreasing energy. The other main reason for the decrease in ψ^* is that the axial target neutron leakage increases with increasing target radius.

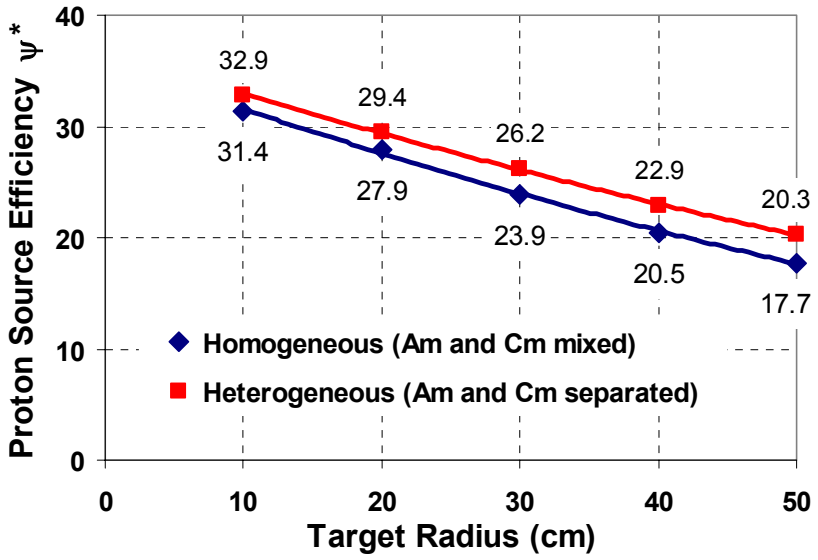

Fig. 2. Proton source efficiency ψ^* for different target radii of the homogeneous and the heterogeneous configurations (1σ-error ~0.50%).

Second, it is seen in Fig. 2 that, heterogenizing the fuel distribution by moving Cm to the inner zone and Am to the outer zone, increases ψ*, compared to when the two materials are homogeneously mixed with each other. The explanation for this is the higher fission probability for Cm than for Am, mainly in the energy range below 1 MeV, which is shown in Fig. 3. When the source neutrons leak out from the target and enter into the fuel, the first fission multiplication, normally occurring in the inner part of the core, is a determining factor for the magnitude of ψ*. Since a large fraction of the target leakage neutrons have energies below 1 MeV, the larger fission probability for Cm directly enhances the neutron multiplication and therefore increases ψ*. The gain in ψ* by concentrating Cm to zone 1 is further amplified for large target radii, as the spectrum of the neutrons entering into the fuel is softer in these cases. The fractions of target leakage neutrons below 1 MeV for the different target radii are listed in Table 3. The relative increase in ψ* by replacing the homogeneous fuel distribution by the heterogeneous distribution ranges from ~5% for the target radius of 10 cm to ~16% for the 50 cm target radius.

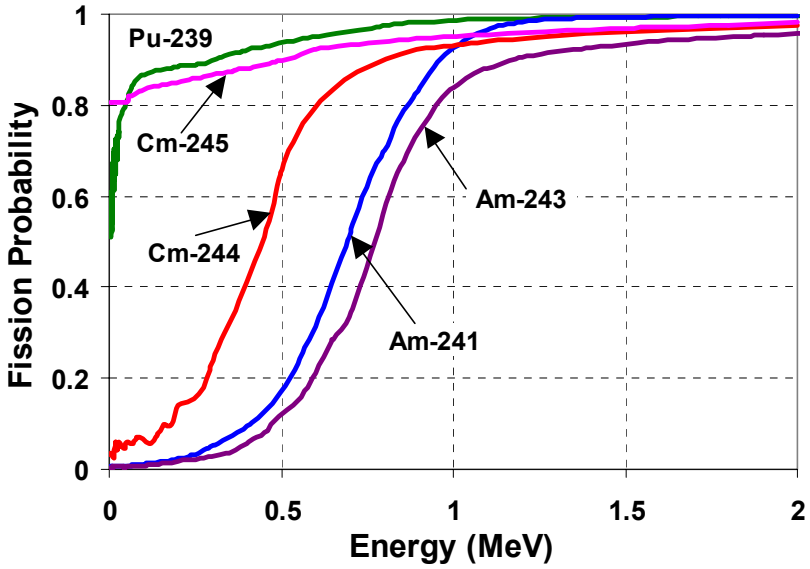

Fig. 3. Fission cross-section over absorption cross-section for ^{239}Pu, ^{241}Am, ^{243}Am, ^{244}Cm and ^{245}Cm (ENDF/B-VI.7) [11].

Table 3 Fraction of neutrons leaking out radially from the target that have energy below 1 MeV

Target Radius (cm)	E < 1 MeV (%)
10	38.4
20	55.2
30	69.1
40	79.3
50	86.4

3.2 Comparison of the CEM Model with the Bertini Model

In our previous studies of the proton source efficiency [4, 10], the physics models used in the MCNPX simulations was the Bertini package (default in MCNPX). However, the Bertini model has shown some disagreements with experimental results [12], the main deficiency of the model being that it over-predicts the low-energy neutron production resulting from high-energy protons impinging on different heavy-metal targets. With the purpose of improving the agreement with experiments [13], the Bertini package has in this study been replaced by the CEM package.

3.2.1 Primary Spallation Neutrons

In order to study the differences between the Bertini model and the CEM model, simulations determining the primary spallation neutron production, i.e. the number of neutrons produced in an average single spallation reaction, have been performed. The primary neutrons were defined as the neutrons created in a proton-induced spallation reaction and in order to record the collection of the these neutrons, the trajectory of a neutron was immediately terminated and its properties recorded at the moment it first appeared in the MCNPX transport simulation.

In Fig. 4, the energy spectrum of the primary spallation neutrons created using the Bertini model and the CEM model are plotted and the expected result that the Bertini model yields a higher number of neutrons in the low-energy range (below ~15 MeV) than the CEM model is clearly seen. In the energy range between about 15 and 80 MeV, the situation is slightly the opposite, while above this energy the neutron production is similar for the two models. Altogether, the number of primary spallation neutrons created for each proton (Z_{prim}) using the Bertini model was 15.0, while only 11.9 using the CEM model.

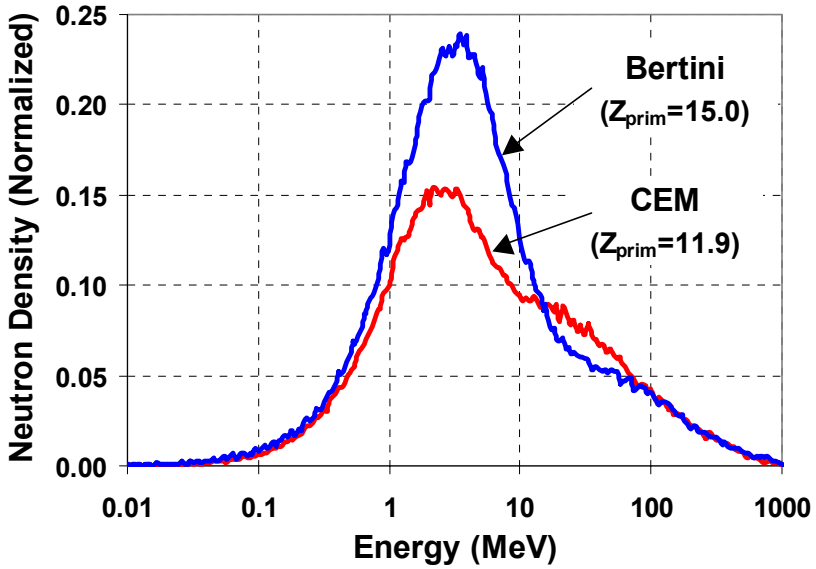

Fig. 4. Energy spectrum of the primary spallation neutrons (the neutrons created in an average spallation reaction) induced by 1000 MeV protons impinging on a Pb-Bi nucleus. Z_{prim} is the number of primary spallation neutrons created for each proton.

3.2.2 Target Leakage Neutrons

In the following study, the 1000 MeV protons were accelerated towards the spallation target of a radius varying from 10 to 50 cm, and the neutrons leaking out from the target were studied using the two different high-energy physics models. It is seen in Table 4 that the number of target leakage neutrons created for each source proton (Z_{tot}) increases for increasing target radius, which is due to the multiplication, by (n,xn)-reactions and secondary spallation reactions, of the primary spallation neutrons carrying very high energy. In column 3 and 5 in Table 4, the number of secondary neutrons (the neutrons created in reactions induced by the primary neutrons, $Z_{sec} = Z_{tot} - Z_{prim}$) is listed and it is seen that those numbers are more or less the same for all target radii, independently of which physics model that is used. This indicates that only the high-energy primary neutrons, which are approximately equal in number for the two different models, contribute to the production of secondary neutrons. This assumption can further be explained by the fact that (n,xn)-reactions in lead and bismuth have an energy threshold at about 7 MeV. The primary spallation neutrons with energy below 7 MeV (10.2 and 7.2 neutrons per proton, respectively, from using the Bertini and the CEM model) are thus transported through the target without inducing any multiplicative reactions. The primary neutrons with energy higher than this threshold (~4.7 for both physics models), on the other hand, are multiplied on their way out through the lead-bismuth and, consequently, the number of created secondary neutrons gradually increases with increasing target radius. However, as the target radius grows larger and reaches a value in the order of 40 cm, the fraction of neutrons above the threshold energy at 7 MeV is only about 1.5%, which is the reason why Z_{sec} (and Z_{tot}) changes only slightly when the radius increases from 40 to 50 cm.

Table 4 Number of primary neutrons (Z_{prim}), secondary neutrons (Z_{sec}) and total number of neutrons created in the target (Z_{tot}) for each incident 1000 MeV proton, calculated by MCNPX using the Bertini and the CEM physics packages.

	Bertini 15.0		CEM 11.9	
Z_{prim}				
Target Radius (cm)	Z_{tot}	Z_{sec}	Z_{tot}	Z_{sec}
10	21.9	6.9	18.7	6.8
20	26.8	11.8	23.6	11.7
30	29.1	14.1	25.9	14.0
40	30.1	15.1	27.0	15.1
50	30.3	15.3	27.3	15.4

Z_{prim} is the number of primary spallation neutrons per incident proton, i.e. the neutrons created in an average spallation interaction.
Z_{sec} is the number of secondary neutrons per incident proton, i.e. the neutrons created in reactions induced by the primary spallation neutrons.
Z_{tot} is the total number of neutrons created in the target per incident proton ($Z_{tot} = Z_{prim} + Z_{sec}$).

3.2.3 Proton Source Efficiency

The effect on the proton source efficiency by exchanging the two physics models in the MCNPX simulations is somewhat similar to that on the neutron production in the target. The results obtained show that replacing the Bertini model by the CEM model decreases ψ^* by approximately 11% to 9%, these numbers corresponding to the target radii of 10 cm and 50 cm, respectively. The reason why these relative differences are smaller than the corresponding

ones for Z_{tot} (15% to 10%) is that the high-energy parts of the target neutron leakage spectra, which has the strongest impact on ψ^*, are very similar for the two different models.

4 Conclusions

In order to study the optimization of the proton beam power amplification (core power divided by proton beam power) in an ADS, the proton source efficiency (ψ^*) has been investigated for a homogeneous and a heterogeneous distribution of Am and Cm. The results from the MCNPX simulations show that moving Cm to the inner part of the active core in the heterogeneous configuration increases ψ^*, compared to the homogeneous configuration, where the minor actinides are mixed with each other. This difference is due to the fact that Cm has higher fission probability than Am for neutrons below about 1.0 MeV, which enhances the multiplication of the neutrons entering into the fuel and thus increases ψ^*. The gain in choosing the heterogeneous Cm distribution is most important for large target radii, since the fraction of target leakage neutrons below 1 MeV is an increasing function of target radius. For the 10 cm target radius, the relative difference in ψ^* between the two configurations was found to be 5%, whereas as much as 16% for the 50 cm target radius.

Comparing the effects on neutron production in the target and on ψ^* by using two different physics packages provided by MCNPX, the Bertini model and the CEM model, the following findings were obtained. First, the Bertini model produces a larger number of primary spallation neutrons than does the CEM model (15.0 compared to 11.9), the major part of the difference being found in the low-energy part of the spectrum (below ~15 MeV). Consequently, the total number of neutrons produced in the target for each source proton is also higher for the Bertini model, the difference being about 3 neutrons for all target radii. The reason why the difference is constant and not dependant on target radius is that the production of high-energy primary spallation neutrons, that are responsible for the secondary neutron multiplication in the target, is about the same for the two models. Finally, concerning the proton source efficiency, the ψ^*-values obtained for the Bertini model were found to be larger by about 10% than those obtained for the CEM model.

Acknowledgements

This work was financially supported by the Swedish Centre for Nuclear Technology, SKB AB (Swedish Nuclear Fuel and Waste Management Co) and the European Commission (Project MUSE: FIKW-CT-2000-00063).

References

1 M. Salvatores et al., ”Long-Lived Radioactive Waste Transmutation and the Role of Accelerator Driven (Hybrid) Systems,” *Nucl. Instrum. Methods A*, **414**, 5 (1997).

2 D. G. Foster et al., ”Review of PNL Study on Transmutation Processing of High Level Waste,” LA-UR-74-74, Los Alamos National Laboratory (1974).

3 T. Takizuka et al., “Conceptual Design of Transmutation Plant,” Proc. Specialist Mtg. Accelerator Driven Transmutation Technology for Radwaste, LA-12205-C, p. 707, Los Alamos National Laboratory (1991).

4 P. Seltborg et al., “Definition and Application of Proton Source Efficiency in Accelerator Driven Systems,” *Nucl. Sci. Eng.*, **145**, 390 (2003).

5 G. ALIBERTI et al., "Analysis of the MUSE-3 Subcritical Experiment", Int. Conf. Global 2001, France, Paris, September (2001).

6 L. S. WATERS, "MCNPX™ User´s Manual – Version 2.1.5," Los Alamos National Laboratory, November 14, (1999).

7 H. W. BERTINI, Phys. Rev. **131**, 1801 (1969).

8 S. G. Mashnik and A. J. Sierk, "Improved cascade-exciton model of nuclear reactions," Proc. SARE4, September 14–16, 1998, Knoxville, TN, USA (ORNL, USA, 1999) pp. 29–51; Eprint nucl-th/9812069.

9 OECD Nuclear Energy Agency, "Accelerator-driven Systems (ADS) and Fast Reactors (FR) in Advanced Nuclear Fuel Cycles; A Comparative Study", Paris, France, (2002).

10 P. Seltborg and J. Wallenius, "Proton Source Efficiency for different Inert Matrix Fuels in Accelerator Driven Systems," Int. Meeting AccApp'03, June 1-5, 2003, San Diego, California, USA (2003).

11 NEA homepage, http://www.nea.fr/janis/

12 S. LERAY et al., "Spallation Neutron Production by 0.8, 1.2, and 1.6 GeV Protons on various Targets," *Phys. Rev*., **C65** (2002).

13 S. G. Mashnik and A. J. Sierk, "Recent Developments of the Cascade-Exciton Model of Nuclear Reactions", Int. Conf. on Nucl. Data for Science and Technology, October 7-12, 2001, Tsukuba, Japan, LA-UR-01-5390 (2001).

APPENDIX 3

P. Seltborg, A. Lopatkin, W. Gudowski, V. Shvetsov and A. Polanski, “Investigation of Radiation Fields outside the Sub-critical Assembly in Dubna”, International Conference on Radiation Shielding ICRS-10, May 9-14 2004, Funchal, Madeira Island, Portugal (2004).

Investigation of Radiation Fields outside the Sub-critical Assembly in Dubna

P. Seltborg[1], A. Lopatkin[2], W. Gudowski[1], V. Shvetsov[3], A. Polanski[3]

[1]*Department of Nuclear and Reactor Physics*
Albanova University Centre, Royal Institute of Technology
S-106 91 Stockholm, Sweden

[2]*Research and Development Institute of Power Engineering*
101 000, PB78, Moscow, Russia

[3]*Joint Institute for Nuclear Research*
141 980, Joliot-Curie 6, Dubna, Russia

The radiation fields outside the planned experimental Sub-critical Assembly in Dubna (SAD) have been studied in order to provide a basis for the design of the concrete shielding that cover the reactor core. The effective doses around the reactor, induced by leakage of neutrons and photons through the shielding, have been determined for a shielding thickness varying from 100 to 200 cm.

It was shown that the neutron flux and the effective dose is higher above the shielding than at the side of it, due to the higher fraction of high-energy spallation neutrons emitted in the direction of the incident beam protons. At the top, the effective dose was found to be ~150 μS/s for a concrete thickness of 100 cm, while ~2.5 μS/s for a concrete thickness of 200 cm. It was also shown that the high-energy neutrons (>10 MeV), which are created in the proton-induced spallation interactions in the target, contribute for the major part of the effective doses outside the reactor.

INTRODUCTION

Transmutation of plutonium and minor actinides in accelerator-driven systems (ADS) are being envisaged for the purpose of reducing the long-term radiotoxic inventory of spent nuclear reactor fuel [1-3]. Consequently, the physics of sub-critical systems are being studied in several different experimental programs across the world, one of the being the sub-critical assembly in Dubna (SAD) [4, 5]. In these experiments, a 660 MeV proton accelerator is coupled to a sub-critical core, loaded with fast reactor MOX (Mixed Oxide) fuel assemblies. The proton beam impinges on a target of lead, which generates a large number of neutrons via spallation reactions. The produced spallation neutrons leak out from the target, thus providing the sub-critical core with a strong external neutron source.

The SAD reactor core will be shielded by a thick layer of heavy concrete. In order to estimate the amount of shielding required for the experiments, the radiation fields outside the concrete shielding have been investigated with the high-energy Monte Carlo code MCNPX [6]. The studies have been quantified by first calculating the flux of particles leaking out through the shielding and then by converting the flux to effective dose. The effective dose is expressed in Sieverts (Sv) and relates the energy deposited in the human body to the medical hazards induced by the radiation. The effective doses have been obtained by using fluence-to-

effective dose conversion coefficients provided mainly by the International Commission for Radiological Protection (ICRP) [7] and the International Commission on Radiation Units (ICRU) [8].

In the present paper, a brief introduction to the conversion coefficients used for radiological protection against external radiation is first given, followed by a description of the SAD experiments and the MCNPX model used in the simulations. The results from the simulations determining the radiation fields and effective doses for varying thickness of the concrete shielding are then presented and analysed.

SYSTEM MODELLING

Fluence-to-effective Dose Conversion Coefficients

In order to calculate the effective dose induced by any particle fluence, the fluence-to-effective dose conversion coefficients for all energies of all particle types that may be present in the radiation field should be known. Using this set of conversion coefficients together with the specific particle flux that a person may be exposed of, the effective dose received by that person can be determined. The fluence-to-effective dose conversion coefficients have been determined by calculating the total effective dose in an anthropomorphic model representing the human body, for mono-energetic fields of all particles of interest. The resulting effective dose for each energy bin is then divided by the total fluence of each radiation. For the present study, the fluence-to-effective dose coefficients for neutrons from thermal neutrons up to 20 MeV are taken from the ICRU Report 57 [8]. For neutrons with energy from 20 up to 500 MeV, as well as for photons of all energies, the coefficients are taken from a study by V. Mares and H. Schraube [9].

The SAD Reactor

The SAD experimental reactor system is composed of the three main components characteristic of an accelerator-driven system; a proton accelerator, a target and a sub-critical core, which makes it the first small-scale prototype of an ADS in the world. The protons are generated by the JINR Phasotron proton accelerator, in which they reach an energy of 660 MeV. The maximum current of the accelerator is 3.2 μA ($2.0 \cdot 10^{13}$ protons/s). The protons are guided into the core from below, as depicted in Fig. 1, where they impinge on a target of heavy metal. The target is replaceable, with two available materials; Pb and W. In the present study, Pb was used as reference target material. The target consists of 19 hexagonal rods, each with a distance between two opposite sides of 3.6 cm, and the height of the target is 60 cm. However, in order to obtain a maximal neutron density in the centre of the core and therefore maximizing the proton source efficiency, the impact position of the proton beam is located 10 cm above the bottom of the active part of the fuel. The radius of the radially uniform proton beam is 1.5 cm.

Standard Russian fast reactor MOX fuel assemblies of the type BN-600 is used as fuel for the SAD assembly. The fuel contains about 30% PuO_2 and 70% UO_2, with the average fuel density of 10.4 g/cm^2. The fraction of ^{239}Pu in the plutonium vector is about 95%. The active part of the core consists of a number of hexagonal sub-assemblies adding up to a total core radius of about 25 cm. The height of the fuel sub-assemblies is 51 cm. The core is surrounded by a lead reflector, which is covered with a thick biological shielding of heavy concrete. The effective multiplication factor of the modelled SAD experimental set-up is about 0.95 and the nominal total core power is 20 kW.

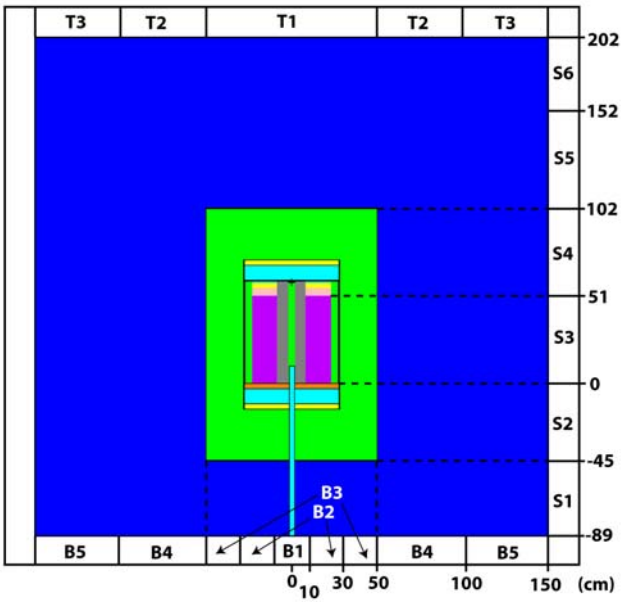

Fig. 1. Schematic RZ-view of the SAD reactor system for the model with a concrete thickness of 100 cm above and at the side of the core. T1-T3, S1-S6 and B1-B5 are the sections where the neutron and photon fluxes have been calculated.

Calculation Method

The Monte Carlo code MCNPX (Version 2.2.3) in coupled neutron, proton and photon mode, was used for all simulations, relying on the evaluated nuclear data library JEF2.2. The high-energy physics package used by MCNPX was the Cascade-Exciton Model (CEM) [10], which has proven to simulate the high-energy physics of proton-induced spallation reactions in better agreement with experiments [11] than, for instance, the Bertini model [12].

In order to obtain a total core power of 20 kW, at the given k_{eff} of 0.95, a proton current of 0.92 μA ($5.7 \cdot 10^{12}$ protons/s) is required, which corresponds to a proton beam power of 0.61 kW. The flux of the particles (neutrons and photons) induced by this proton beam, that leak out through the concrete shielding was calculated by MCNPX, with the energy spectrum divided into a number of energy bins. Knowing the flux, $\Phi_{E,P}$, and the fluence-to-effective dose conversion coefficients, $(E/\Phi)_{E,P}$, for each energy bin and each particle type, the total effective dose per unit time, E, can be determined as

$$E = \sum_{P} \left(\sum_{E} (E/\Phi)_{E,P} \cdot \Phi_{E,P} \right) . \qquad (1)$$

The summation is over all energy bins and all particles.

RESULTS AND DISCUSSION

Effective Doses Outside the SAD Reactor for Varying Thickness of the Shielding

Detailed Monte Carlo simulations determining the flux of neutrons and photons (no other particles contribute to the radiation hazards) outside the SAD reactor system have been performed. The thickness of the concrete shielding above and at the side of the core has been varied from 100 cm to 200 cm, while below the system, it was fixed to 54 cm. The reason for not extending the shielding thickness to more than 200 cm is that the computing time for

obtaining reliable statistics grows exceedingly long for larger dimensions. The surface of the shielding has been divided into different sections for the computational monitoring of the flux and the effective dose distributions around the core. Above the core, the sections are T1-T3, at the side S1-S6 and below B1-B5, as depicted in Fig. 1.

At the side, the maximum of the effective dose was found to be located in section S4, slightly above the level of the active part of the core, although that the neutron flux is maximal at S3. The reason for this is that a larger fraction of the high-energy neutrons released in the spallation interactions in the target are emitted in the forward direction, so the energy spectrum is a little harder in S4 than in S3. Since high-energy neutrons have higher fluence-to-effective dose conversion coefficients, the effective dose becomes higher in S4. Above and below the core, the maximal doses are found around the symmetry axis of the reactor (in section T1 and B1, respectively). In Table 1, the obtained fluxes and the calculated effective doses induced by neutrons and photons are displayed for the sections where the maximal doses are found at each side. The doses in T1 and S4 are also plotted as functions of shielding thickness in Fig. 2.

Table 1 Flux and effective dose above (T1), at the side (S4), and below (B1) the SAD system for varying thickness of the shielding. The relative errors account only for the statistical uncertainty in the MCNPX simulations.

Section	Thickness of shielding (cm)	Neutrons		Photons		All Particles	
		Flux ($10^3 \cdot cm^{-2}s^{-1}$)	E (μS/s)	Flux ($10^3 \cdot cm^{-2}s^{-1}$)	E (μS/s)	E (μS/s)	1σ-error (%)
Top (T1)	100	563	150	423	1.7	152	10
	120	246	68	182	0.8	68	15
	150	79	21	65	0.24	21	23
	200	8	2.5	12	0.03	2.5	57
Side (S4)	100	247	51	318	1.5	53	6
	120	100	20	123	0.6	21	8
	150	27	4.9	32	0.12	5.0	16
	200	6.1	0.9	5	0.03	1.0	29
Bottom (B1)	54	21 000	1 640	126 300	660	2 300	3

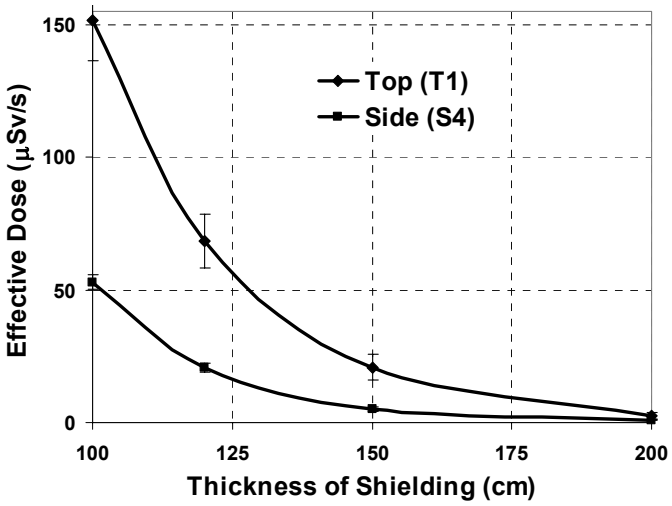

Fig. 2. Effective dose above (T1) and at the side (S4) of the core, for varying thickness of the concrete shielding.

It is seen in Table 1 that the highest doses are found below the reactor system (~2300 μS/s), which is expected since the thickness of the shielding is only 54 cm here. Moreover, a significant leakage of neutrons and photons occurs back through the accelerator tube. However, below the reactor is the ground and the radiological concerns are less important here, although some specific requirements have to be taken into account also in the area below the reactor. Therefore, the studies of this paper have focused on the fluxes and effective doses above the reactor (T1) and at the side of it (S4). It was also found that, above and at the side of the core, the neutrons contribute for almost the entire part of the total doses (95-100%), although the fluxes of photons are in the same order of magnitude as those of neutrons. The reason for the large difference in effective dose is that both the energy and the conversion coefficients are higher for the neutrons than for the photons. For this reason, the studies presented below have been performed only for neutrons.

Moreover, it is shown that the effective dose is significantly higher at the top of the core than at the side of it, ~150 μS/s compared to ~50 μS/s for a 100 cm thick shielding and ~2.5 μS/s compared to ~1 μS/s for a 200 cm thick shielding. It should be noted though, that increasing the concrete thickness to 200 cm, the limit of what is feasible with Monte Carlo methods, without using the more sophisticated variance reduction techniques, is approaching, and the corresponding values for the effective dose have relatively large statistical errors (57% at the top and 29% at the side). The explanation for the higher flux and effective dose at T1 than at S4 is that the neutrons released in the spallation reactions carrying very high energy are emitted mainly in the direction of the incident beam protons (towards the top of the core). Since these high-energy neutrons have longer range in the concrete and higher probability of inducing secondary neutron production than low-energy neutrons, the flux outside the shielding is higher in the direction where the emission density of high-energy neutrons is maximal.

According to radiation protection rules in Russia, the maximal allowed effective dose for civil personnel is 12 μS/h (3.3 nS/s), which is lower than the results obtained for the 200 cm thick shielding by more than two orders of magnitude. Consequently, access to the areas around the shielding of such thickness would be strictly prohibited during operation of the SAD reactor. In order to allow for the presence of workers nearby the reactor, a much thicker and/or modified shielding is required.

Energy Spectra of the Neutron Flux and the Effective Dose

The energy spectra of the neutron flux and the effective dose at the top (T1) and at the side (S4) of the core have been studied by decomposing the energy range into a number of energy bins. Since the computing time for obtaining reliable statistics is increasing rapidly with increasing shielding thickness, only the model with a 100 cm thick shielding has been used for this study. It is shown in Table 2 and Fig. 3 that the major parts of the neutron flux and effective dose are found in the high-energy part of the spectrum. At the top, 53% of the flux and ~83% of the effective dose come from the energy interval 10-660 MeV. Since only a very small fraction of the neutrons that leak out from the reflector and enter into the concrete are found in this high-energy interval (~0.1%), it appears that only these high-energy neutrons have high probability of reaching the edge of the shielding. It can moreover be assumed that these high-energy neutrons, originating from the proton-induced spallation interactions in the target, are responsible for the major part of neutron flux and the effective dose outside the SAD reactor. The neutrons created by fission in the active part of the core, on the other hand, seem to contribute only marginally to the effective dose.

Table 2 Neutron flux and effective dose in different energy intervals at the top (T1) and at the side (S4) of the reactor.

	Top (T1)				Side (S4)			
Energy intervals	Flux ($10^3 \cdot cm^{-2}s^{-1}$)		E (μS/s)		Flux ($10^3 \cdot cm^{-2}s^{-1}$)		E (μS/s)	
0-1	173	31%	5	3%	109	44%	3	5%
1-10	86	15%	21	14%	33	13%	7	14%
10-100	205	36%	78	52%	78	32%	29	57%
100-660	99	17%	46	31%	26	11%	12	24%
Total	563		150		247		51	

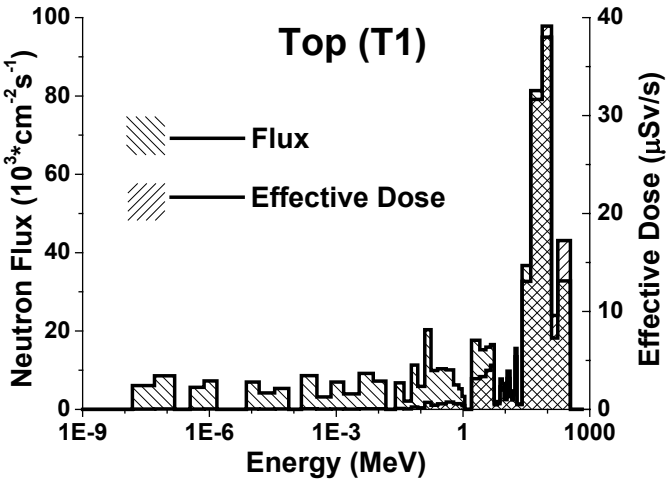

Fig. 3. Flux and effective dose for neutrons in the different energy bins at the top (T1) of the reactor.

CONCLUSIONS

The effective dose outside the accelerator-driven SAD reactor, induced by particles leaking out through the concrete shielding, has been studied using the high-energy Monte Carlo code MCNPX. It was shown that only neutrons and photons penetrate the shielding and contribute to the effective doses outside the reactor. At the top and at the side of the core, the neutrons contribute for the major part (95-100%) of the effective doses. Below the core is the ground and the radiological concerns are therefore more relaxed there.

The calculations have been performed for models with thickness of the concrete shielding varying from 100 cm to 200 cm. Not considering the bottom of the core, the highest fluxes and effective doses are found at the top of the reactor. For a 100 cm thick shielding, the maximal dose above the core is ~150 μSv/s, compared to ~50 μSv/s at the side of it, and for a shielding thickness of 200 cm in the order of 2.5, compared to 1 μSv/s, respectively. These values are a few orders of magnitude higher than the maximal allowed dose for civil personnel according to Russian radiation protection rules (12 μSv/h or 3.3 nSv/s). Hence, under these circumstances, access to the areas around the reactor will not be allowed during reactor operation. In order not to exceed the present dose limit regulations, a considerably thicker and/or modified shielding than the investigated two meters is needed.

The explanation for the higher fluxes and doses at the top of the reactor than at the side of it is that the neutrons emitted in the spallation process carrying very high energy (in the order of 100 MeV or more) and having long range in the concrete are emitted mainly in the direction of the incident beam protons (towards the top of the core). It was also shown that more than 80% of the effective dose comes from neutrons with energy higher than 10 MeV, which indicates that the high-energy neutrons created in the spallation target contribute for the dominant part of the effective dose outside the SAD reactor, while the neutrons created by fission contribute only marginally.

ACKNOWLEDGEMENTS

This work was partially supported by SKB AB (Swedish Nuclear Fuel and Waste Management Co) and the Swedish Centre for Nuclear Technology. The development of the SAD design is financed by ISTC.

REFERENCES

1 Salvatores, M., Slessarev, I., Ritter, G, Fougeras, P., Tchistiakov, A., Youinou, G. and Zaetta, A., "*Long-lived radioactive waste transmutation and the role of accelerator driven (hybrid) systems*," Nucl. Instrum. Methods A, **414**, 5 (1997).

2 Foster, D. G., "*Review of PNL study on transmutation processing of high level waste*," LA-UR-74-74, Los Alamos National Laboratory (1974).

3 Takizuka T., "*Conceptual design of transmutation plant*," Proc. Specialist Mtg. Accelerator Driven Transmutation Technology for Radwaste, LA-12205-C, p. 707, Los Alamos National Laboratory (1991).

4 Gudowski, W., Polanski, A., Puzynin, I. V., Schvetsov, V., ”*Monte Carlo modeling of a sub-critical assembly driven with the existing 660 MeV JINR Proton Accelerator*”, Int. Meeting AccApp'01, November 11-15, 2001, Reno, Nevada, USA (2001).

5 ISTC Project 2267. http://www.tech-db.ru/istc/db/projects.nsf/prjn/2267

6 Waters, L. S., “*MCNPX™ User´s Manual – Version 2.1.5*,” Los Alamos National Laboratory, November 14, (1999).

7 International Commission on Radiation Protection, “*Conversion coefficients for use in radiological protection against external radiation*,” ICRP Publication 74, Pergamon Press, Oxford (1997).

8 International Commission on Radiation Units and Measurements, “*Conversion coefficients for use in radiological protection against external radiation*,” ICRU Report 57, Bethesda, Maryland (1998).

9 Mares, V. and Schraube, H., “*The effect of the fluence to dose conversion coefficients upon the dose estimation to cosmic radiation*, ” Expert Group on Shielding Aspects of Accelerators, Targets and Irradiation Facilities (Sixth Meeting - SATIF-6), April 10-12, 2002, Menlo Park, USA (2002).

10 Mashnik, S. G. and Sierk, A. J., “*Improved cascade-exciton model of nuclear reactions*,” Proc. SARE4, September 14–16, 1998, Knoxville, TN, USA (ORNL, USA, 1999) pp. 29–51; Eprint nucl-th/9812069.

11 Mashnik, S. G. and Sierk, A. J., "*Recent Developments of the Cascade-Exciton Model of Nuclear Reactions*", Int. Conf. on Nucl. Data for Science and Technology, October 7-12, 2001, Tsukuba, Japan, LA-UR-01-5390 (2001).

12 Leray, S. et al. (31), ”Spallation Neutron Production by 0.8, 1.2, and 1.6 GeV Protons on various Targets,” Phys. Rev., **C65** (2002).

APPENDIX 4

Alberto Talamo, Waclaw Gudowski, Jerzy Cetnar and Francesco Venneri, Key physical parameters and temperature reactivity coefficients of the deep burn modular helium reactor fueled with LWRs waste, Annals of Nuclear Energy 31 (2004) 1913–1937

Available online at www.sciencedirect.com
SCIENCE DIRECT®
Annals of Nuclear Energy 31 (2004) 1913–1937
annals of NUCLEAR ENERGY
www.elsevier.com/locate/anucene

Key physical parameters and temperature reactivity coefficients of the deep burn modular helium reactor fueled with LWRs waste

Alberto Talamo [a,*], Waclaw Gudowski [b,1], Jerzy Cetnar [c], Francesco Venneri [d]

[a] *Department of Nuclear and Reactor Physics, Royal Institute of Technology, Roslagstullsbacken 21, S-10691, Stockholm, Sweden*
[b] *Department of Nuclear and Reactor Physics, Royal Institute of Technology, Roslagstullsbacken 21, S-10691, Stockholm, Sweden*
[c] *Faculty of Physics and Nuclear Techniques, University of Mining and Metallurgy, 30059 Cracow, Poland*
[d] *Los Alamos National Laboratory, USA*

Received 21 January 2004; accepted 10 May 2004
Available online 23 July 2004

Abstract

We investigated some important neutronic features of the deep burn modular helium reactor (DB-MHR) using the MCNP/MCB codes. Our attention was focused on the neutron flux and its spectrum, capture to fission ratio of ^{239}Pu and the temperature coefficient of fuel and moderator. The DB-MHR is a graphite-moderated helium-cooled reactor proposed by General Atomic to address the need for a fast and efficient incineration of plutonium for non-proliferation purposes as well as the management of light water reactors (LWRs) waste. In fact, recent studies have shown that the use of the DB-MHR coupled to ordinary LWRs would keep constant the world inventory of plutonium for a reactor fleet producing 400 TW_e/y. In the present studies, the DB-MHR is loaded with Np–Pu driver fuel (DF) with an isotopic composition corresponding to LWRs spent fuel waste. DF uses fissile isotopes (e.g. ^{239}Pu and

* Corresponding author. Fax: +46-8-5537-8465.
E-mail addresses: alby@neutron.kth.se (A. Talamo), wacek@neutron.kth.se (W. Gudowski), jerzy@neutron.kth.se (J. Cetnar), venneri@lanl.gov (F. Venneri).
[1] Fax: +46-8-5537-8465.

doi:10.1016/j.anucene.2004.05.006

^{241}Pu), previously generated in the LWRs, and maintains criticality conditions in the DB-MHR. After an irradiation of three years, the spent DF is reprocessed and its remaining actinides are manufactured into fresh transmutation fuel (TF). TF mainly contains non-fissile actinides which undergo neutron capture and transmutation during the subsequent three-year irradiation in the DB-MHR. At the same time, TF provides control and negative reactivity feedback to the reactor. After extraction of the spent TF, irradiated for three years, over 94% of ^{239}Pu and 53% of all actinides coming from LWRs waste will have been destroyed in the DB-MHR. In this paper we look at the operation conditions at equilibrium for the DB-MHR and evaluate fluxes and reactivity responses using state of the art 3-D Monte Carlo simulations.

1. Introduction

The deep burn modular helium reactor (DB-MHR) (Talamo et al., 2004; General Atomic, 2002; Rodriguez et al., 2003; Baxter and Fikani, 2002; Baxter and Rodriguez, 2001; Baxter et al., 2001; Plukiene and Ridikas, 2003; Kiryushin et al., 1997; Ohashi et al., 2000; Tsuchie, 2000; Wistrom and Simon, 1996) has been conceived by General Atomic (GA) as a new generation of nuclear power plants, graphite-moderated and helium-cooled, being able to face two major current problems of nuclear energy: proliferation and light water reactors (LWRs) waste handling. In fact, the DB-MHR concept has a unique flexibility concerning nuclear fuels that can be loaded into the core: it can run as well on military plutonium as on LWRs waste. In a scenario where the use of DB-MHRs would be coupled with further use of LWRs, the world plutonium inventory would be kept constant in coming decades for a nuclear reactor fleet producing 400 TW_e/y (Fig. 3 of Bonin and Greneche, 2002).

The current design of the DB-MHR consists of four modules, each of them with a thermal power of 600 MW_{th}. The reactor operates using two different types of fuel: driver fuel (DF) and transmutation fuel (TF). The fresh DF contains $NpPuO_{1.7}$ coming from LWRs spent fuel; whereas the fresh TF is made from spent DF, after it has been irradiated for three years in the DB-MHR, plus some set-aside Am–Cm, in the form $AmCmO_{1.7}$, coming directly from the reprocessing of the LWRs spent fuel. The DF depletes fissile isotopes and supplies the fission neutrons, mainly through fission of ^{239}Pu and ^{241}Pu. Whereas, the TF depletes non-fissile isotopes by neutron capture followed by natural decay or fission and it provides excess reactivity control. Because fissions in the DF are the main driver of the DB-MHR operations, and captures in the TF are control mechanism, the capture to fission ratio should be as low as possible for DF. After the three years irradiation of TF, transmutation of over 94% of ^{239}Pu and 53% of all actinides coming from LWRs waste (Talamo et al., 2004) is achieved. The spent TF constitutes the final waste of the DB-MHR. The high burnup capability of high temperature reactors has been also confirmed in pebble bed reactors (Kugeler et al., 1998); in addition, chemical analysis studies have shown good agreement with the predictions of numerical simulations (Werner, 1997).

A part from the deep burn of nuclear waste, the DB-MHR exhibits several benefits: a cost lower than an ordinary LWR (Labar and Simon, 1994), a clear passive safety mechanism (Fröhling, 1999; Kugeler and Phlippen, 1999; Kunitomi et al., 1996; Moore et al., 2002; Nakagawa et al., 1998, 2001; Schenk et al., 1994; Woaye-Hune and Ehster, 2002), a flexibility in the choice of fuel type, a high conversion energy efficiency, a well developed technology and an improvement of the barriers protecting the environment from the radiotoxicity of spent fuel. The DB-MHR fuel pins consist of a graphite matrix filled by a square lattice of triple isotropic coated particles (TRISO) (Baldwin and Kania, 1990; Chapelot et al., 2001; Fukuda et al., 1995; Golubev et al., 2002; Miller et al., 2001, 2002; Minato and Sawa, 2000; Minato et al., 1993; Nabielek et al., 1989; Nickel et al., 2002; Petti et al., 2002; Porta et al., 2001; Sawa and Tobita, 2003; Sawa et al., 2001; Sawa and Ueta, 2001), which are also an effective waste form with a reliable protective barrier. Each TRISO particle is made of a fuel kernel, a sphere with a radius of 150 μm for DF and 100 μm for TF, surrounded by a cladding of four layers: porous carbon, inner pyrolitic carbon, silicon carbide and outer pyrolitic carbon. The ratio between the width of the cladding and the radius of the kernel is 1.7 for DF and 2.6 for TF; by contrast, in ordinary LWRs the ratio between the width of zircaloy cladding and the radius of fuel pellets is only 0.14. Because of the large thickness of the cladding, TRISO particles can retain all fission products up to a temperature of 1600 °C. This limit can be higher, up to 1800 °C, if ZrC replaces SiC (Minato et al., 2000a,b; Minato et al., 1998; Minato et al., 1997). If the cooling of helium ceases, the passive heat removal guarantees that the temperature of the fuel never exceeds 1600 °C; in addition, the peak of power occurs after 72 h, a period long enough to allow the plant operators to activate all safety devices. Nevertheless, even if the TRISO particles resist a temperature of 1600 °C, a temperature excursion may trigger the oxidation of the TRISO graphite matrix, because at 1000 °C the graphite oxidation rate, as function of the surface temperature, increases to the asymptotic level (Fig. 2 of Moore et al., 2002).

The inner pyrocarbon layer usually is the first layer of a TRISO particle that fails, since it is subjected to counteracting mechanical stresses: swelling, due to the pressure of fission products gases, and shrinkage, due to the neutron irradiation. Therefore, the most usual failure is a radial crack on the internal side of the inner pyrocarbon layer (Fig. 3 of Miller et al., 2002), where the strains are stronger (Fig. 5 of Golubev et al., 2002). The strain of the mechanical stresses depends on: the fluence, the pyrocarbon density, the degree of anisotropy (the Bacon anisotropy factor) and the irradiation temperature. Recent studies have proven that the optimal width of the inner pyrocarbon layer of TRISO particles is about 15 μm, because, after this threshold, a greater thickness increases the probability of failure of the coating (Fig. 11 of Golubev et al., 2002). By contrast, a greater thickness of the porous carbon and SiC layers always reduces the probability of failure of the coating (Figs. 10 and 12 of Golubev et al., 2002).

Finally, the use of TRISO particles are useful also to reduce proliferation because it would be necessary to process 10^{10} coated particles to reach the critical mass of ^{239}Pu (Kugeler et al., 1998).

2. The DB-MHR – description and operation at the equilibrium of the fuel composition

The DB-MHR has been modeled in the numerical simulations as a cylinder, of 4 m radius and 10 m height, filled by a 13×13 matrix of fuel and graphite hexagonal blocks. The fuel blocks consist of three concentric rings of 36 hexagons as shown in Fig. 1. Each fuel block has a side of 20.8 cm and a height of 7.93 m; a graphite reflector covers further 1.035 m, both at top and at bottom, along the axial direction (Fig. 6 of Talamo et al., 2004). In each hexagonal block there are 108 cooling channels, with a diameter of 0.797 cm, 144 DF pins and 72 TF pins, both with a diameter of 0.622 cm (Fig. 1). The coolant channel surrounding the fuel pin has an external radius of 0.635 cm. Each fuel pin consists of graphite filled with a square lattice of TRISO particles, which are fuel oxide spheres (kernel) covered by a triple isotropic coated layer. The structure and properties of a TRISO particle are shown in Table 2 of Talamo et al. (2004) and Fig. 1. In order to decrease the capture to fission ratio of DF, and therefore of ^{239}Pu (Fig. 2, IANIS [2]), GA selected a higher radius for the DF kernel comparing to TF. For simplicity design, we kept for both fuels the same packing ratio (defined as the volume of fuel kernels over the total volume of fuel pin) (Talamo et al., 2004).

It takes about 12 years for DB-MHR to approach the equilibrium composition; therefore, all our studies have been focused on the 12th year. The in-core loading strategy is grounded on the following steps:

- At the beginning of the first year, we assumed that the reactor starts its life by loading the fresh DF into the inner ring.
- At the beginning of the second year, the spent DF is shuffled into the central ring and fresh DF takes its place.
- After two years, at the beginning of the third year, spent DF from the central ring is moved into the outer ring; the spent DF from the inner ring is shuffled in the central one; the inner ring is filled with fresh DF. No TF fuels the reactor during the first three years.
- At the end of the third year, the spent DF from the outer ring, which it has been irradiated a period of three years, is reprocessed, by fission products extraction, to build the fresh TF, which contains also some set-aside Am–Cm from the reprocessing of LWR spent fuel.
- At the beginning of the fourth year the inner ring contains both fresh DF and TF. In the following years, the shuffling policy is continued as in the first three years: moving both spent DF and TF outwardly at the end of each year.
- The reactor loads DF and TF in all three rings just at the beginning of the sixth year. After an irradiation of three years, the TF is extracted from the outer ring as waste.

In the approach to equilibrium, we simulated for a time being only the radial shuffling and we neglected the axial one. In the real project of GA, each hexagonal fuel block consists of 10 axial sub-blocks, which every year should shuffle from [0 1 2

[2] Version 1.0. Jef-2.2.

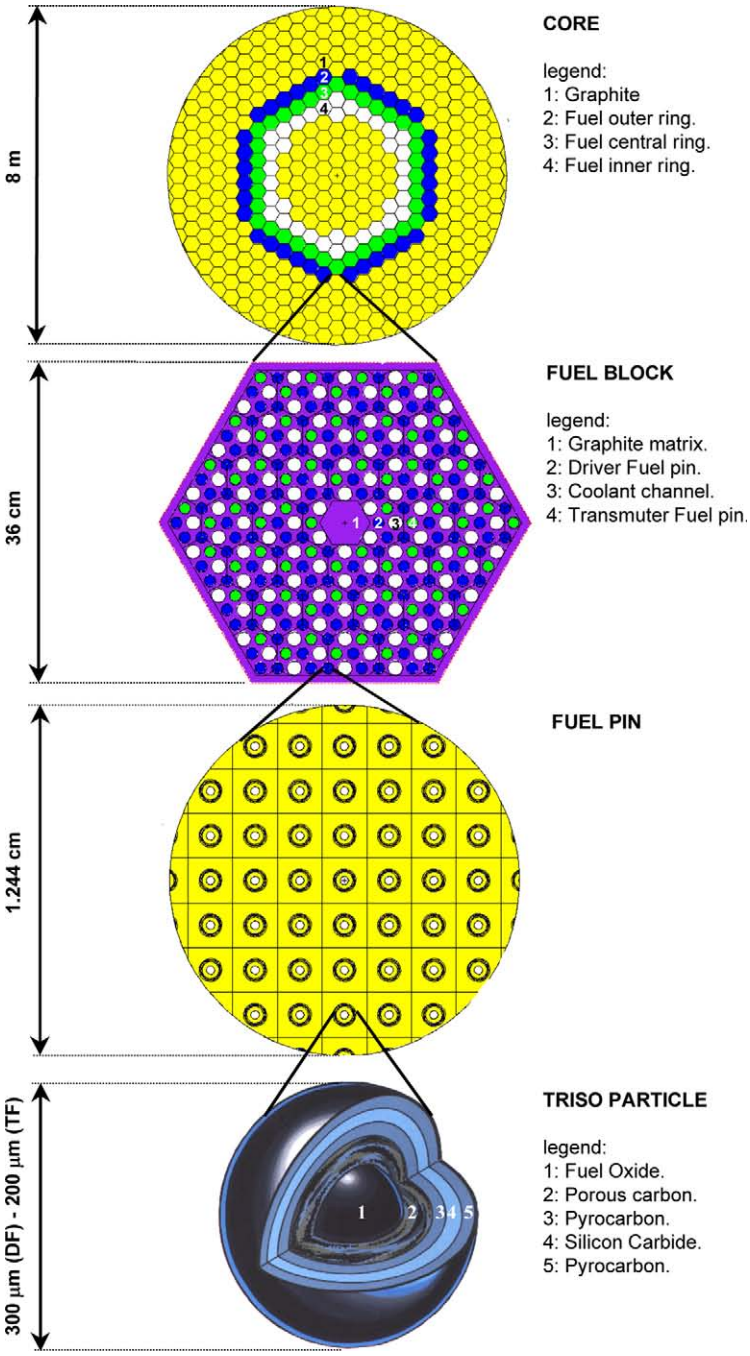

Fig. 1. The model of the DB-MHR used in simulations.

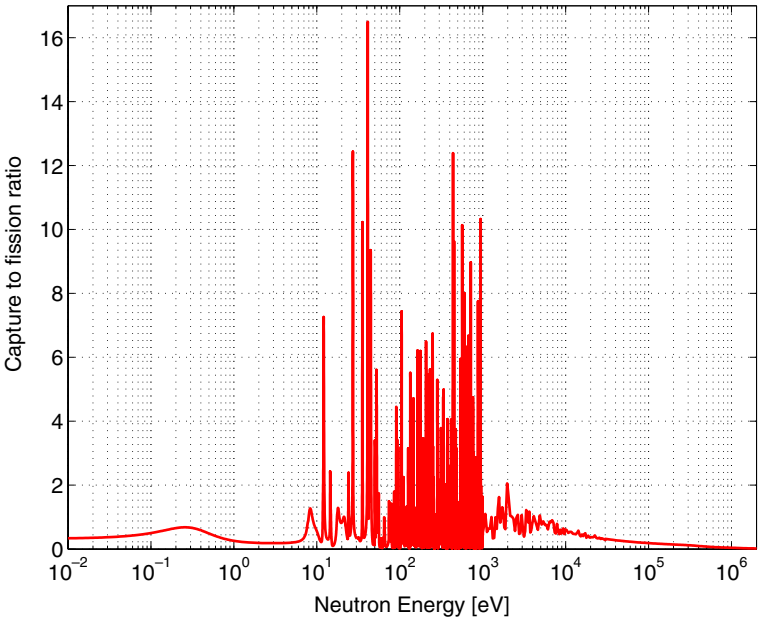

Fig. 2. Capture to fission ratio of ^{239}Pu.

3 4 5 6 7 8 9] to [4 3 2 1 0 9 8 7 6 5], where the first and last positions in the arrays indicate the top and bottom of the reactor. This axial shuffling optimization will be addressed in our further studies.

Our model of the DB-MHR lacks, at the moment, the representation of the control rods, but this approximation should not seriously affect burnup calculations since the value of k_{eff} is very close to criticality (Fig. 8 of Talamo et al., 2004).

We performed all time dependent simulations by the code MCB (Cetnar et al; Cetnar et al., 2001; Cetnar et al., 1999), an extension of MCNP (Briesmeister, 2002) with the burnup implementation; whereas, we used the MCNP code for the static calculations. Both numerical codes have been equipped with a cross-section library based on JEF-2.2 complemented with data from ENDF\B-6.8 and JENDL-3.2.

3. Neutron flux and spectrum at the equilibrium of the fuel composition

We investigated both the radial and the axial profile of the neutron flux in the DB-MHR core and in the fuel pins. We performed the calculations at the beginning of the 12th year and after 330 days of full power operation. In order to evaluate the radial flux profile in the core, we selected 11 hexagonal blocks, for the 12th block is cut by the edge of the reactor, disposed along the radial direction from the center of the reactor, which corresponds to the vertical direction of Fig. 1. At the same time, we divided each hexagonal block into 10 axial sub-blocks equally spaced along the z

axis in order to estimate the axial flux at different heights. It is important to highlight that the axial division into 10 sub-blocks reflects the real reactor, since all the hexagonal blocks are manufactured with this structure. Nevertheless, since the flux is symmetric along the z axis, we limited our studies only to the upper five axial sub-blocks. In this set of simulations we did not consider the flux in the two axial reflectors. Fig. 3 shows the radial profile of flux in the reactor sampled in the radial hexagonal blocks; each curve represents one of the five upper axial sub-blocks at the beginning of the 12th year. The neutron flux drops after the eighth block due to the increase of leakage in the outer blocks; the same effect plays a visible role in the last two axial sub-blocks, where, in addition, the flux becomes more flattened because neutrons with a higher energy escape the more. Nevertheless, leakage plays a little role in the economy of the reactor since only 3.2% of neutrons escape. We can observe in Fig. 3 that the peak of the neutron flux emerges in the fourth block, which consists of pure graphite and it is adjacent to the fuel block of the inner ring. This behavior is explained by the graphite moderation of neutrons coming from the inner fuel ring, which contains fresh fuel, and the circular shape of fuel, which reduces the leakage since half of the fission neutrons propagate towards the center of the reactor. Moreover, fuel blocks disposed in an annular shape flatten the flux in the center of the reactor.

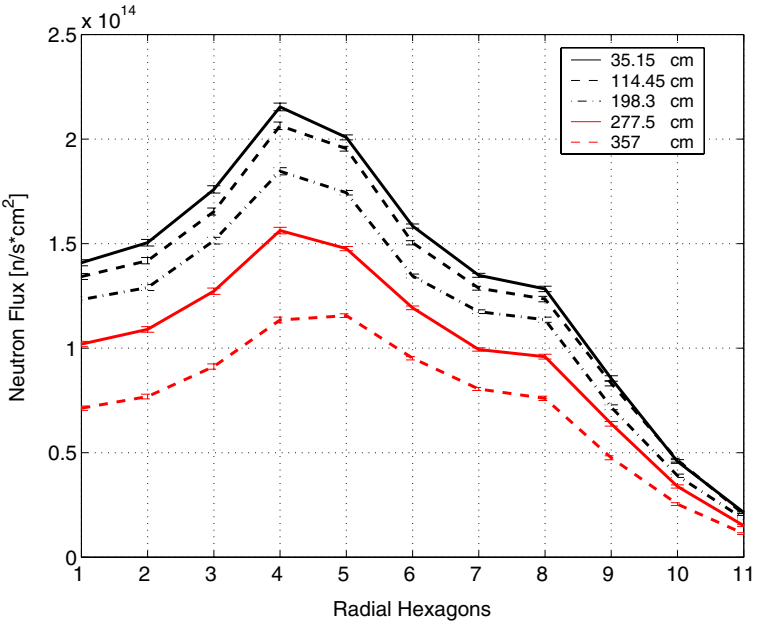

Fig. 3. Neutron flux profile at the beginning of the 12th year. Neutron flux has been averaged in 10 axial sub-blocks and 11 radial hexagonal blocks from the center of the reactor. Curves refer to the upper five axial sub-blocks. The fifth radial hexagonal block corresponds to the inner ring, the sixth to the central one and seventh to the outer one. Ticks on the curves represent the standard deviation.

In order to understand better the radial and axial flux behavior, we performed studies of the flux distribution inside of the DF and TF pins located at the center of a hexagonal block for each of the three rings of fuel. We analyzed a total of six pins: a pair of pins for the inner, central and outer rings. The six fuel pins have been separately divided, both along the radial and the z axes, into 10 equivolume regions. Fig. 4 shows the radial flux profile in the DF and TF pins located at the center of a hexagonal block for the inner, central and outer rings at the beginning of the 12th year. We can note that the flux in the inner ring is much higher because it contains fresh fuel. It is not surprising that the neutron flux is quite flat, because of the small radius of TRISO kernels (150 μm for DF and 100 μm for TF) compared to that one of the fuel pin (0.622 cm). Fig. 5 shows the axial flux profile for the same pins of Fig. 4; we can see that the flux drops about 50% along the height of the pins. By contrast, as Fig. 3 shows, the radial drop of the flux is significantly lower (about 25%). Therefore the axial shuffling of the fuel plays an important role for the optimization of the ^{239}Pu incineration.

Fig. 6 shows the same flux of Fig. 3 but referred to the end of the 12th year; we can note that the flux is a little higher (about 6%) than that one at the beginning of the year since the reactor operates at constant power and fuel depletes. Nevertheless, even if flux is a little higher, the values of flux in the 11th block, which is located close to the boundary of the reactor, remain unchanged at the end of the 12th year, since a higher flux increases neutron leakage. Let us note that the difference between the flux

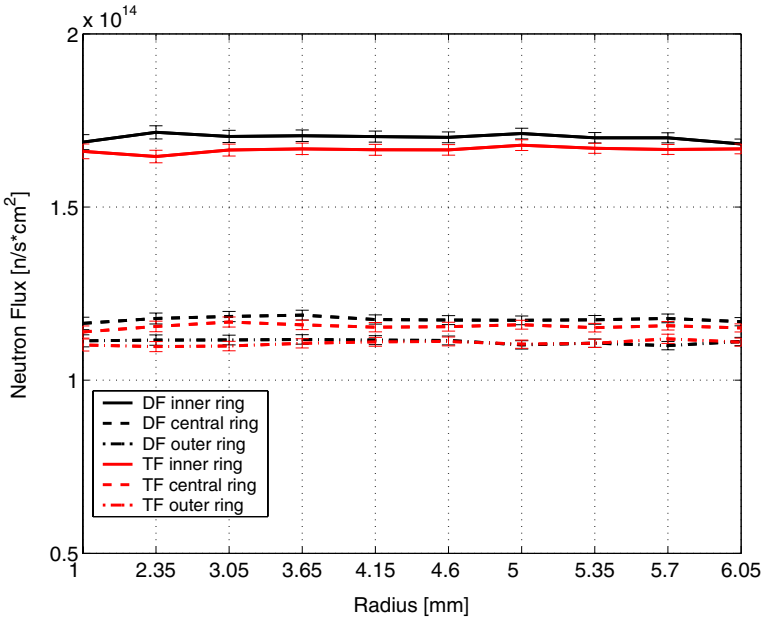

Fig. 4. Radial neutron flux at the beginning of the 12th year of DF and TF pins in the center of a hexagonal block in the inner, central and outer rings.

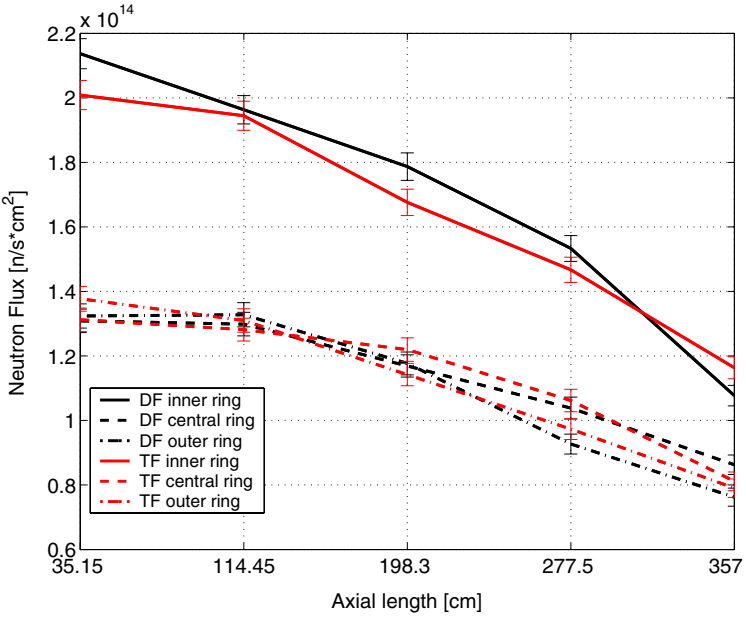

Fig. 5. Axial neutron flux at the beginning of the 12th year of DF and TF pins in the center of a hexagonal block in the inner, central and outer rings.

at the beginning of the year and that one at the end is not bound to the statistical error, since the relative standard deviation of flux is only 0.8%. For the numerical calculations of the neutron flux and spectra we increased, compared to the burnup numerical calculations, the MCNP precision from 30,000 neutrons in 150 cycles, including 40 inactive ones for the neutron source evaluation, to 10^5 neutrons. The two curves at top of Fig. 6 are closer than those ones in Fig. 3, because the fuel corresponding to the top curve of Fig. 3 experienced a higher burnup. Analogue considerations, about the difference between the flux at the beginning of the 12th year and that one at the end, may apply to Figs. 7 and 8 versus Figs. 4 and 5, respectively. Figs. 4 and 5 show that the flux in the DF is higher than in TF since DF contains an higher quantity of fissile actinides; nevertheless this effect if negligible at the end of the 12th year because of the burnup. Let us also remark that the choice of the cross-sections library between JEF, JENDL and ENDF/B may affect up to 6.5% the value obtained for neutron flux (Table 5 of Ridikas et al., 2002).

We calculated the neutron spectrum averaged over the whole reactor, including the two axial reflectors, over three hexagonal blocks located in different fuel rings and over the DF and TF kernels for each of the three fuel rings. All neutron spectra have been plotted using the energy binning corresponding to the 69 energetic groups of the WIMS cross-section library for thermal reactors; these groups are composed of 14 fast groups, 12 resonance groups, and 42 thermal groups (Kim et al., 1989; Taubman, 1975). Fig. 9, which shows the neutron spectrum at the beginning of the 12th year, clearly indicates the reactor operates in a thermal spectrum with a spectral

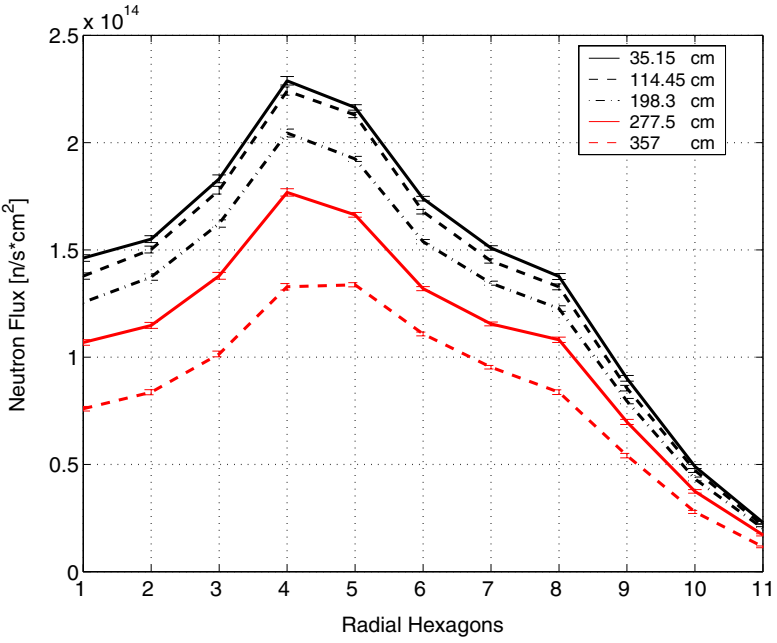

Fig. 6. Neutron flux profile at the end of the 12th year. Neutron flux has been averaged in 10 axial sub-blocks and 11 radial hexagonal blocks from the center of the reactor. Curves refer to the upper five axial sub-blocks. The fifth radial hexagonal block corresponds to the inner ring, the sixth to the central one and seventh to the outer one. Ticks on the curves represent the standard deviation.

peak located at the energy of 0.2 eV, which is in a very good agreement with the value calculated by Nakata et al. (1995).

The DB-MHR, as other power reactor types, requires a proper reactivity management in order to compensate for burnup of fissile isotopes without violating safety limits for reactivity excess available during operation. The ^{167}Er isotope can serve this purpose as a burnable poison enhancing simultaneously the Doppler temperature feedback. However, it is also possible to take advantage of the unique features of the TF, which contains isotopes having both a breeding potential which sustains reasonable reactivity margins and favorable neutron capture cross-sections contributing to the desired temperature feedbacks. Particularly, TF neutron capture cross-section is favorable in the energy region just behind the thermal peak of the spectrum (Fig. 2 of Talamo et al., 2004).

Fig. 10 compares in different fuel rings the neutron spectra of three hexagonal blocks; the inner ring, which contains fresh fuel, exhibits the highest value of flux. We can note how the presence of the surrounding moderator hexagonal blocks enhances the flux at thermal energies in the inner and the outer rings. In addition, the difference between the central and outer rings attenuates at higher energies since both of them contain irradiated fuel. We can note that in all spectra the distinct dip

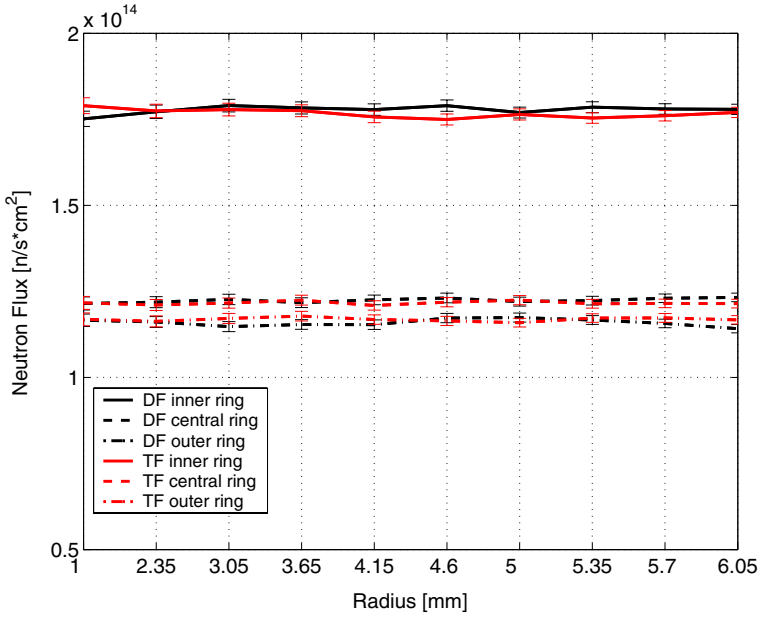

Fig. 7. Radial neutron flux at the end of the 12th year of DF and TF in the center of a hexagonal block in the inner, central and outer rings.

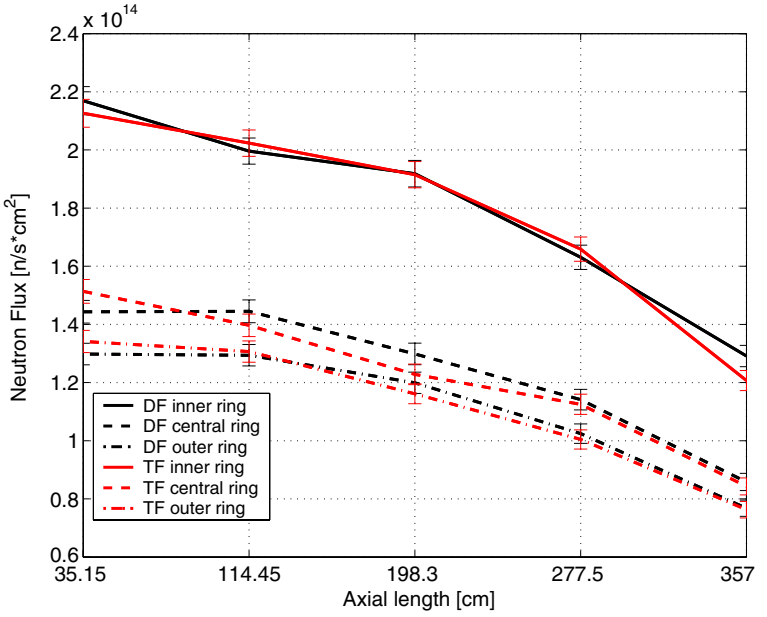

Fig. 8. Axial neutron flux at the end of the 12th year of DF and TF pins in the center of a hexagonal block in the inner, central and outer rings.

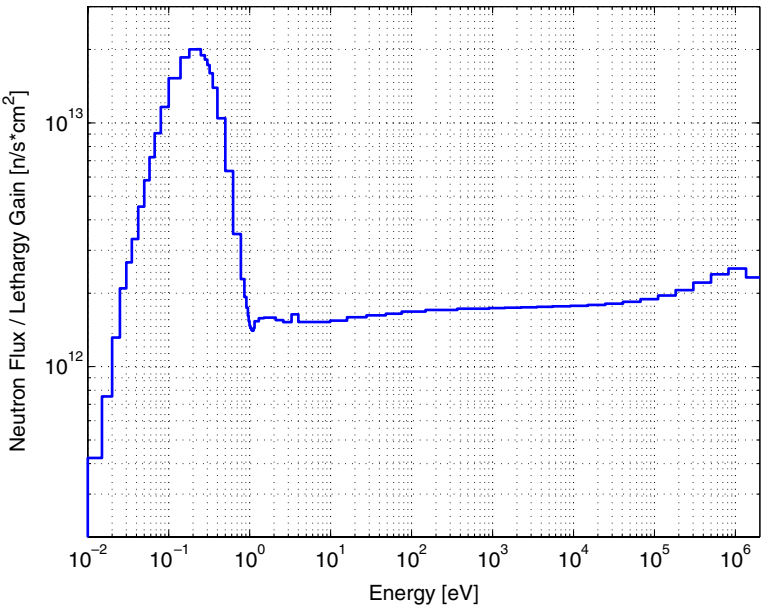

Fig. 9. Neutron spectrum at the beginning of the 12th year averaged in the whole reactor.

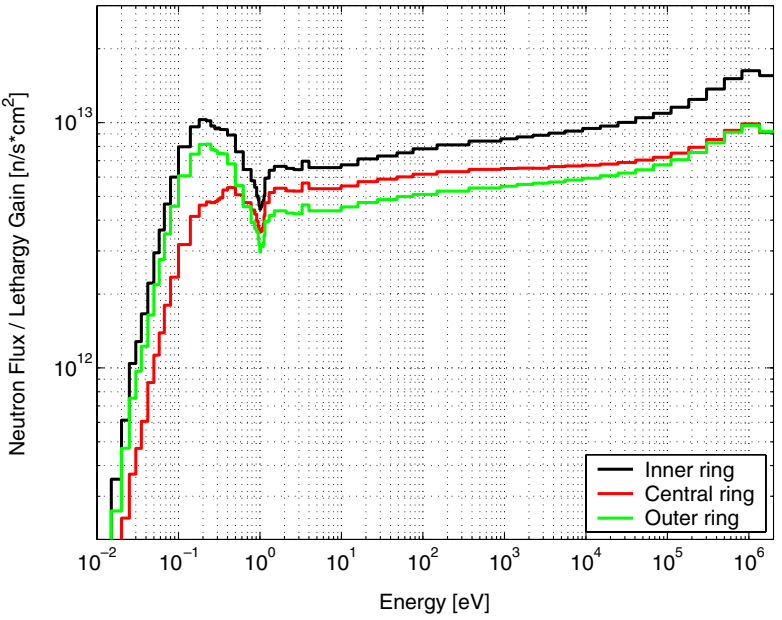

Fig. 10. Neutron spectrum at the beginning of the 12th year averaged in one hexagonal block.

located at 1 eV due to resonance capture of ^{240}Pu; the dip increases in the rings with a longer irradiation time since ^{240}Pu accumulates during the reactor operation.

The neutron spectra of DF and TF kernels, as showed on Figs. 11–16, exhibit a pattern reminding a fast spectrum. In fact, kernels as a bulk *see* mostly fast fission neutrons leaving; whereas, all thermalised neutrons entering back are immediately absorbed. We can note some fine differences on those neutron spectra. The central ring has hardest spectrum among the three fuel rings, since is not moderated by any adjacent block of graphite. Moreover, the inner ring has a harder spectrum than the outer one, because it is loaded with fresh fuel. In fact, ^{239}Pu, abundant in the fresh fuel, depresses significantly the low energy part of the spectrum on Fig. 12 in the energy range 0.25–0.3 eV due to its high capture to fission ratio (Fig. 1 of Talamo et al., 2004). During full power operation, the relative abundance of ^{239}Pu, both in DF and TF, decreases but abundance of ^{240}Pu increases. Consequently, the dip corresponding to ^{239}Pu resonance becomes more shallow while passing from the inner ring (Fig. 11), the central one (Fig. 12) to the outer one (Fig. 13). By contrast, resonance capture of ^{240}Pu responsible for the second dip has a somewhat opposite behavior due to the increased amount of ^{240}Pu in irradiated fuel: the dip corresponding to ^{240}Pu becomes deeper while passing from the inner ring (Fig. 11), the central one (Fig. 12) to the outer one (Fig. 13). The same phenomena can be observed by analyzing the spectra at the beginning of the 12th year and after 330 days of full power operation. In fact, the dip of ^{239}Pu decreases and that one of ^{240}Pu increases while

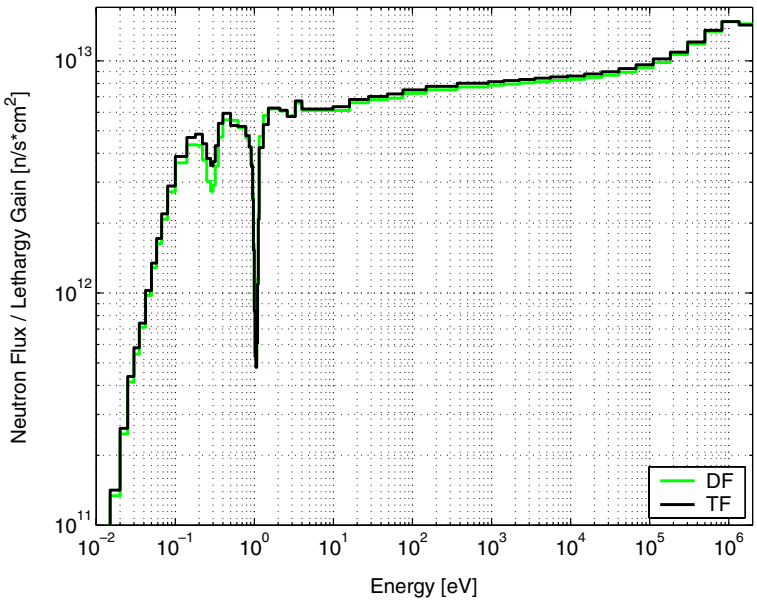

Fig. 11. Neutron spectrum at the beginning of the 12th year in the TRISO kernels of the hexagonal blocks in the inner ring.

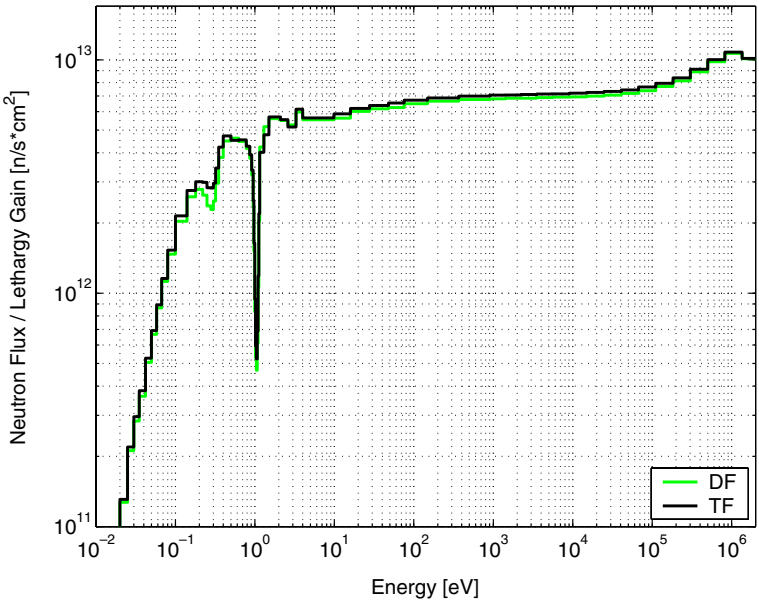

Fig. 12. Neutron spectrum at the beginning of the 12th year in the TRISO kernels of the hexagonal blocks in the central ring.

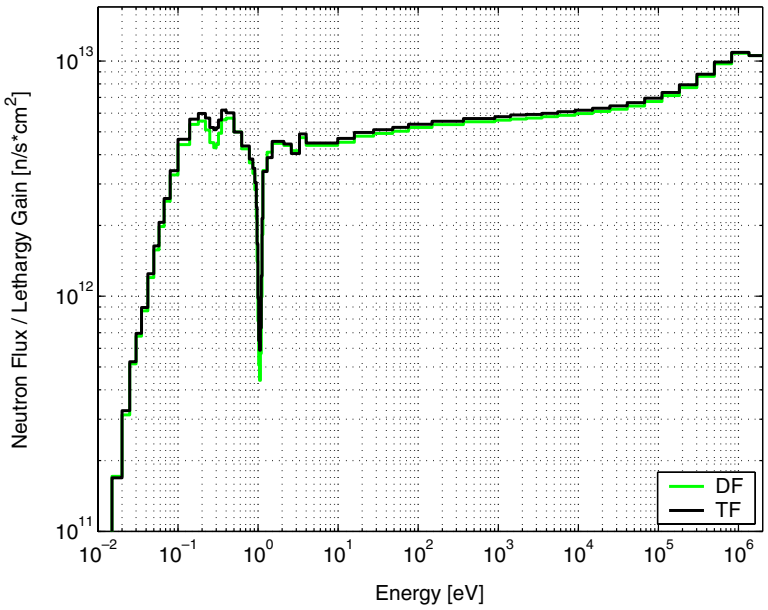

Fig. 13. Neutron spectrum at the beginning of the 12th year in the TRISO kernels of the hexagonal blocks in the outer ring.

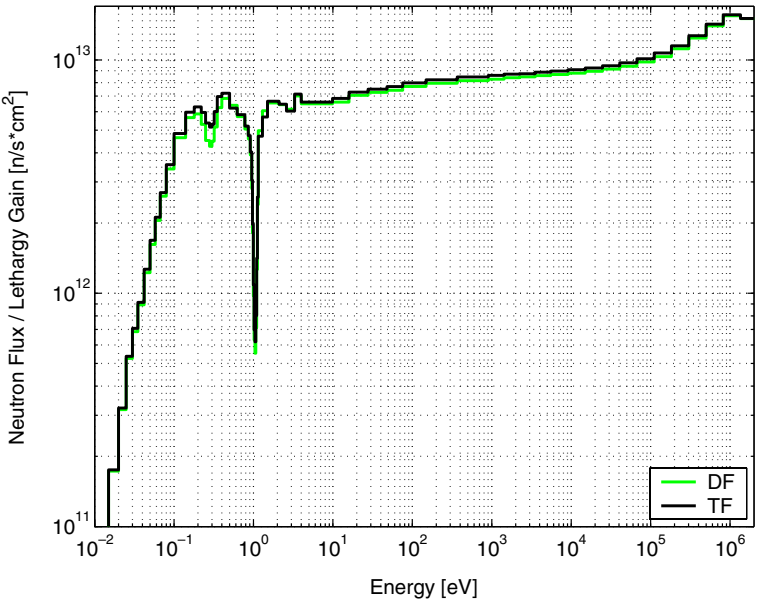

Fig. 14. Neutron spectrum at the end of the 12th year in the TRISO kernels of the hexagonal blocks in the inner ring.

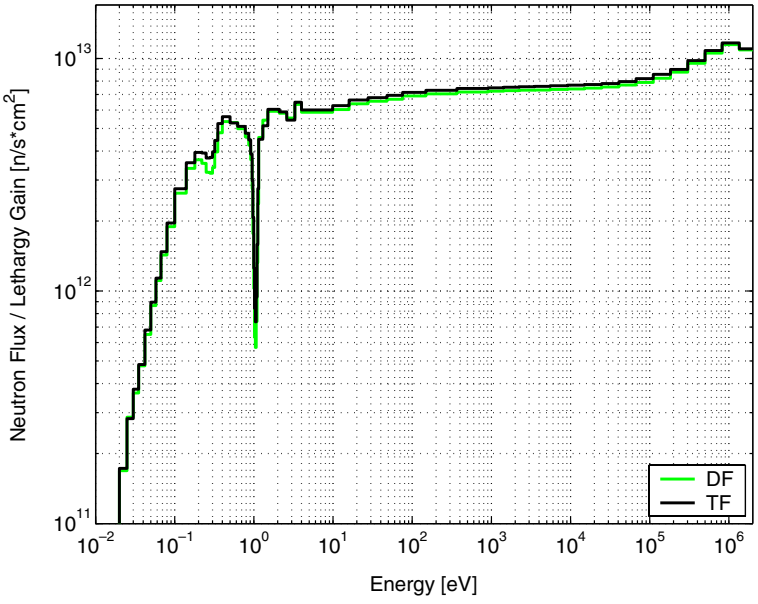

Fig. 15. Neutron spectrum at the end of the 12th year in the TRISO kernels of the hexagonal blocks in the central ring.

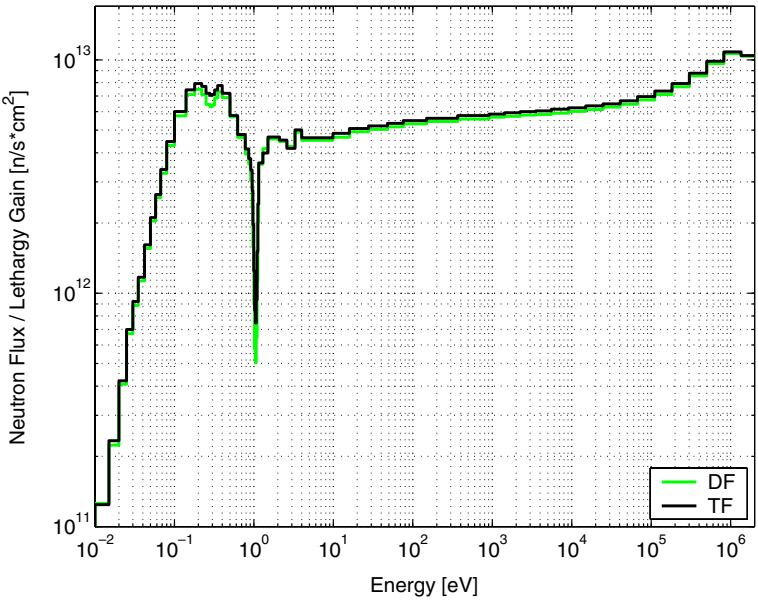

Fig. 16. Neutron spectrum at the end of the 12th year in the TRISO kernels of the hexagonal blocks in the outer ring.

comparing Fig. 14 with 11, Fig. 15 with 12 and Fig. 16 with 13. It is worth to note that at the end of the 12th year the ^{239}Pu dip in TF (Fig. 16) has almost disappeared because of ^{239}Pu depletion.

The spectrum averaged in the whole reactor at the end of the 12th year had as expected no significant differences with the corresponding one at the beginning of the year.

4. Effect of DF kernel volume to the capture to fission ratio

In order to optimize the rector performance, one would like to obtain the capture to fission ratio of fuel as low as possible for DF, since DF should be efficiently fissioned. Consequently, GA set the radius of the DF kernel of TRISO particles (150 μm) greater than that one of TF (100 μm). We tried to verify the benefits of this choice by studying the capture to fission ratio of ^{239}Pu, because this isotope is the most abundant one in DF and any change on its reaction rate strongly affects the behavior of the reactor. In order to analyze the effects of the kernel size in the capture to fission ratio of ^{239}Pu, we gradually changed, the radius of the DF kernel keeping constant its packing ratio. We used the set of values: 100, 150, 200, and 250 μm as radii of the DF kernel; whereas, we kept constant the radius and packing ratio of the TF kernel at their nominal values (Talamo et al., 2004). All calculations were performed at the beginning of the 12th year.

A greater radius of the kernel of TRISO particles induces a better thermalization of neutrons in the fuel volume and therefore a decrease in the capture to fission ratio, as Fig. 17 shows. In fact, the neutron spectrum in the fuel is fast and the major contribution to the capture to fission ratio comes from the resonances of the fast region (Fig. 2); therefore, better termalization of the spectrum results in a lower capture to fission ratio. Since the inner ring contains a larger quantity of ^{239}Pu, which determines a low flux (Fig. 11) in the slope of the capture to fission ratio between 0.25 and 0.3 eV (Fig. 2), it has a lower average capture to fission ratio than the outer one (Fig. 17). Whereas in the central ring, the hardest spectrum of all the three rings (Fig. 12) enhances the contribution of the energy dependent capture to fission ratio around the resonance peaks (Fig. 2) to its average value (Fig. 17). TF, as can be seen on Fig. 17, shows negligible changes, since the TF radius has been kept constant.

It can be concluded from Fig. 17 that there is no significant impact of the kernel size on the average capture to fission ratio, therefore it is possible to simplify the manufacture of fuel by setting the same size of DF and TF kernels.

Since ^{239}Pu is the most abundant isotope of DF, mostly responsible for sustaining the fission chain, a lower average capture to fission ratio of ^{239}Pu leads to a higher k_{eff} (Figs. 17 and 18).

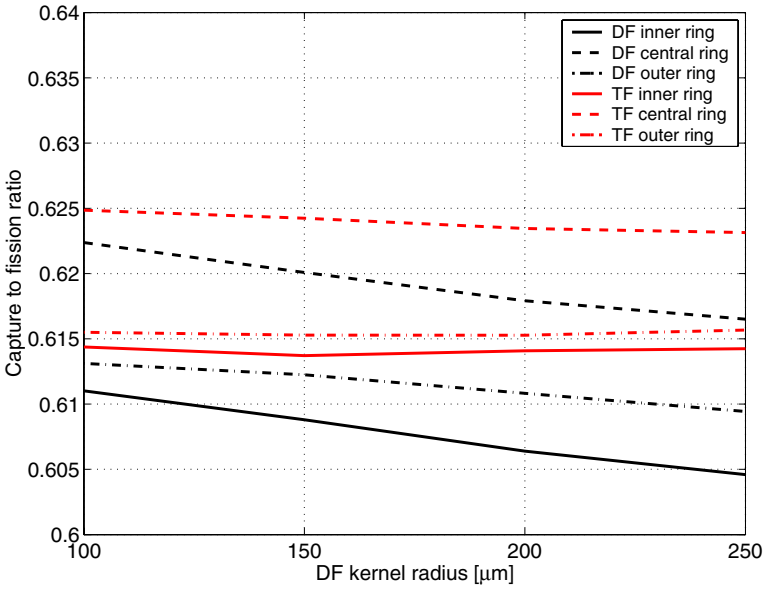

Fig. 17. Capture to fission ratio of ^{239}Pu at the beginning of the 12th year for different radii of the DF kernel. The TF radius has been kept constant to 100 μm.

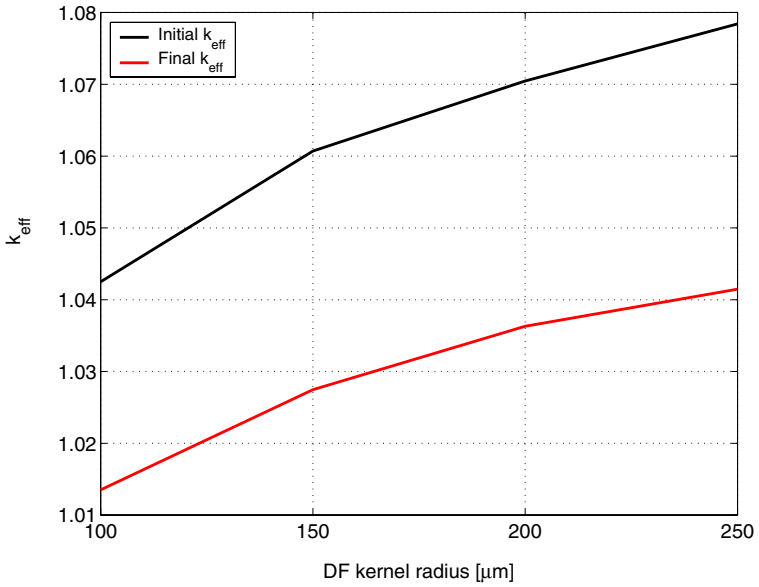

Fig. 18. k_{eff} for different radii of the DF kernel during the 12th year. Maximal standard deviation lower than 0.00041.

5. Reactivity temperature coefficients

5.1. Cross-section changes

We calculated the temperature coefficient (C_{T}) for a temperature excursion affecting only the cross-sections either of the fuel or of the moderator. Again, we focused our studies at the beginning of the 12th year.

Since the operational temperature of the DB-MHR fuel is about 1400 K and the coolant temperature is in the range of 758–1123 K, we assumed the reference temperatures of 1500 K for fuel and of 1200 K for graphite. Then, we varied separately the temperature of the fuel and the moderator from 1200 to 1500 K up to 1800 K. With this set of temperatures, we estimated the reactivity changes corresponding to the temperature variation, by the formula:

$$\Delta\rho = \rho(T) - \rho_{\text{reference}},$$

where $\rho(T)$ is the reactivity of the reactor for different fuel or moderator temperatures. $\rho_{\text{reference}}$ is the reactivity of the reactor for which both fuel and moderator are at the reference temperatures. Then, we calculated the temperature coefficient (C_{T}) by the formula:

$$C_{\text{T}} = \frac{\Delta\rho}{T - T_{\text{reference}}},$$

where $T_{reference}$ is 1500 K for the C_T of the fuel and 1200 K for the C_T of the moderator. Table 1 summarizes the results for the fuel temperature changes and Table 2 for the moderator ones. The DB-MHR exhibits negative reactivity temperature coefficients both for fuel and moderator cross-section variations. The reactivity changes corresponding to the 300 K temperature raise or drop are of the level of 420 pcm for the fuel and 4000–9000 pcm for the moderator. Consequently, the temperature coefficients for moderator are 10 times larger than those for the fuel. This huge difference may be explained by Fig. 19, because it shows that the peak of neutron spectrum, for a fuel temperature of 1800 K and a moderator one of 1500 K, shifts from 0.2 eV (at the reference temperatures, Fig. 9) to 0.3 eV, exactly where ^{239}Pu exhibits a peak in the capture to fission ratio (Fig. 2). Therefore, the shift of the spectrum generates a very strong feedback and it affects mainly the moderator C_T; in fact, the moderator C_T is mainly driven by the spectrum shift, whereas that one of fuel does by the broadening of capture resonances.

We performed also a set of simulations using different temperatures of the moderator to test the sensitivity of MCNP results on the $S(\alpha, \beta)$ thermal neutron treatment data, necessary for a proper simulation of the thermal neutron interactions with graphite (upscattering processes). Table 3, which shows the dependence of k_{eff} on the $S(\alpha, \beta)$ data, indicates that the thermal neutron scattering in graphite is responsible for almost the entire cross-section reactivity feedback from the moderator. Moreover, it should be noted that the $S(\alpha, \beta)$ reactivity feedback in the temperature interval 1200–1600 K is four times bigger than in the interval 800–1200 K. This behavior can be explained by the neutron spectral shift towards the peak at 0.3 eV of the ^{239}Pu capture to fission ratio.

Table 1
k_{eff}, reactivity ρ, differential reactivity ($\Delta\rho$) and temperature coefficient (C_T) for different temperatures of the cross-sections of the fuel at the beginning of the 12th year

Fuel temperature (K)	1200	1500	1800
k_{eff}	1.06511	1.06040	1.05550
ρ	0.06113	0.05696	0.05258
$\Delta\rho$	0.00417	0	−0.00438
C_T (pcm/K)	−1.39007	0	−1.45931

Maximal standard deviation of k_{eff} lower than 0.00023.

Table 2
k_{eff}, reactivity (ρ), differential reactivity ($\Delta\rho$) and coefficient of temperature (C_T) for different temperatures of the cross-sections of the moderator at the beginning of the 12th year

Moderator temperature (K)	1200	1500	1800
k_{eff}	1.06040	1.01883	0.96468
ρ	0.05696	0.01848	−0.03661
$\Delta\rho$	0	−0.03848	−0.09357
C_T (pcm/K)	0	−12.8259	−15.5955

Maximal standard deviation of k_{eff} lower than 0.00022.

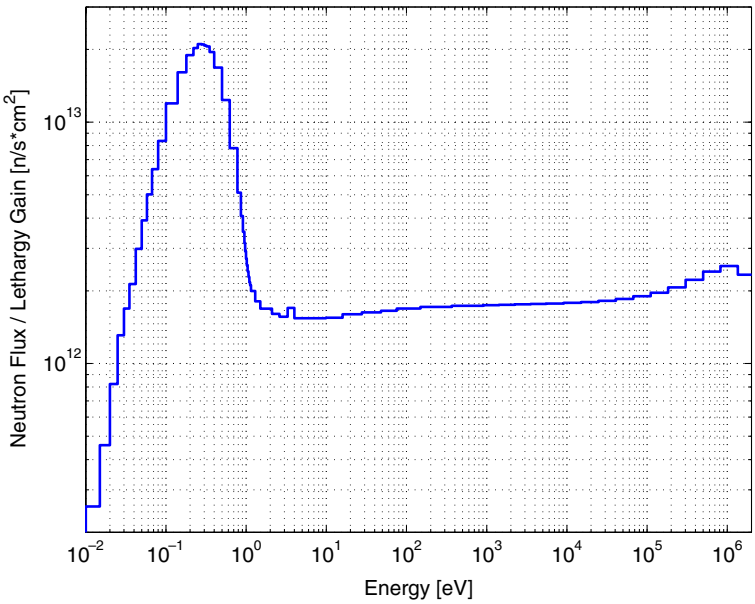

Fig. 19. Neutron spectrum at the beginning of the 12th year averaged in the whole reactor for fuel at 1800 K and graphite at 1500 K (with $S(\alpha,\beta)$ at 1600 K).

Table 3
k_{eff} at different temperatures of the moderator using a different thermal treatment

	$S(\alpha,\beta)$ 800 K	$S(\alpha,\beta)$ 1200 K	$S(\alpha,\beta)$ 1600 K
900 K	1.07090	1.06027	1.01895
1200 K	1.07083	1.06040	1.01890
1500 K	1.07095	1.06000	1.01883
1800 K	1.06847	1.05788	1.01671

In addition, we tested the sensitivity of k_{eff} on the temperature dependent free gas neutron treatment (TMP parameter of the cell cards of MCNP). As expected no significant impact has been found; in fact, the free gas treatment can be accounted as highest to only 70 pcm changes in k_{eff}, a value lightly higher than the standard deviation of our results (32 pcm).

5.2. Density and volume changes

Temperature dependent changes of density driven by the thermal volume expansion contribute also to the C_{T}. We simulated two different scenarios: increase of the fuel temperature (up to 1800 K) with a constant moderator temperature at the reference value of 1200 K; whereas, in the second scenario we increased also the temperature of moderator to the value of 1500 K.

In order to take into account the volume expansion of the fuel, the radius of the kernel of the TRISO particles at 1800 K (r_{1800}) has been increased according to the following formula (Thetford, 2000):

$$r_{1800} = r_{293} \cdot (a_0 + a_1 T + a_2 T^2 + a_3 T^3) \qquad T = 1800\ K.$$

The a_i are constants (given in Table 4) and r_{293} is the radius at the temperature of 293 K, which has been calculated by:

$$r_{293} = r_{\text{reference}} \cdot (a_0 + a_1 T + a_2 T^2 + a_3 T^3)^{-1} \qquad T = 1500\ K,$$

where $r_{\text{reference}}$ is the radius of the kernel during normal operation (150 μm for DF and 100 μm for TF at 1500 K). Then, we preserved the mass of fuel by decreasing its density according to the new volume.

In the second simulation we also modified the temperature of moderator, the H451 graphite. Irradiated graphite may tend to swell or shrink depending on the irradiation dose and the operational temperature (Marsden et al., 1998). However, in our model we neglected the irradiation effects on graphite volume, since we considered only the major fast contributes due to a temperature change: thermal expansion. We assumed the linear expansion coefficients of graphite (α_C) and silicon carbide (α_{SiC}) equal to 4.55×10^{-6} (Matsuo et al., 1986) and 4×10^{-6} K^{-1} (www.accuratus.com), respectively. Consequently, the density d_{1500} of all graphite zones at temperature of 1500 K and that one of silicon carbide in the layer of the TRISO particles have been recalculated according to the following formula:

$$d_{1500} = d_{\text{reference}} \cdot (1 + \alpha \Delta T)^{-3} \qquad \Delta T = 300\ K,$$

where α is the linear coefficient either of graphite or silicon carbide and $d_{\text{reference}}$ is the density during normal operation. In order to take into account the thermal expansion of graphite and silicon carbide, we increased all the geometric data regarding graphite and silicon carbide by the following equation:

$$x_{1500} = x_{\text{reference}} \cdot (1 + \alpha \Delta T) \qquad \Delta T = 300\ K$$

where x_{1500} and $x_{\text{reference}}$, respectively, are the geometric data at the temperature of 1500 and at 1200 K.

The temperature coefficients weakly depend on variation of the density and volume of materials comparing to the change of cross-sections temperature. In fact, the value of C_{T} reported in the first column of Table 5, which includes also the variation of density and volume, differs just 15% from the result calculated in the third column of Table 1, which includes only cross-sections variation. Moreover, Table 5 shows

Table 4
Fuel thermal expansion constants

a_0	0.99652
a_1	1.17876×10^{-5}
a_2	-2.42851×10^{-9}
a_3	1.21876×10^{-12}

Table 5
k_{eff}, reactivity ρ, differential reactivity ($\Delta\rho$) and temperature coefficient (C_T) at the beginning of the 12th year for different temperatures of fuel and moderator

	1800 fuel–1200 moderator	1800 K fuel–1500 K moderator
k_{eff}	1.05474	1.01387
ρ	0.05190	0.01368
$\Delta\rho$	−0.00506	−0.04328
C_T (pcm/K)	−1.68686	−14.4265

Maximal standard deviation of k_{eff} lower than 0.00024.

Table 6
Capture to fission ratio of ^{239} Pu at the beginning of the 12th for different temperatures of fuel and moderator

	Fuel at 1800 K–moderator at 1200 K	Fuel at 1800 K–moderator at 1500 K
Inner ring DF	0.609	0.616
Central ring DF	0.621	0.625
Outer ring DF	0.612	0.620
Inner ring TF	0.615	0.621
Central ring TF	0.624	0.628
Outer ring TF	0.615	0.623

that the addition of the variation of volume and density keeps unchanged the large difference (about an order of magnitude) between the moderator C_T and the fuel one.

Finally, by comparing the data reported in the second column of Table 6 with Fig. 17, we can see that an increase of temperature of the moderator, and consequently a faster neutron spectrum, increases the average value of the capture to fission ratio, because of the peak at 0.3 eV of the ^{239}Pu capture to fission ratio.

6. Conclusions

The disposition of fuel hexagonal blocks into three concentric rings and a corresponding radial shuffling strategy maintain a reasonably flat average neutron flux profile; in fact, the difference of the average flux amid the three rings of fuel is about 25%. The axial profile, however, exhibits larger variation than the radial one (up to 50% difference between central and peripheral regions); therefore, the axial shuffling in the simulation model is necessary and may better optimize the fuel utilization.

The peak of the radial neutron flux lies not in the inner ring of fuel blocks, which contains fresh fuel, but rather in the adjacent, toward the center of the reactor, graphite block. Leakage depresses the average neutron flux in the hexagonal blocks along the radial direction only in the last three blocks. The neutron flux level increases only of 6% during 330 full power operation days at the equilibrium of the fuel composition (12th year).

The spectral peak of neutron flux is at 0.2 eV, which ensures that the DB-MHR operates in a thermal region.

The neutron spectrum in the fuel exhibits two dips in the thermal region due to resonance captures of ^{239}Pu and ^{240}Pu. The depth of the dips varies according to both the location of fuel pin (different rings experienced a different level of fluence due to the radial shuffling) and the irradiation time during operation.

No clear benefit has been observed from the choice of GA to set a radius of the DF kernel greater than the TF one.

The temperature reactivity coefficients for fuel and moderator are negative; the temperature coefficient of moderator is very large (about 4000–9000 pcm) and it is one order of magnitude higher than the fuel temperature coefficient. The temperature reactivity coefficients of the DB-MHR ensure a safe operation of this reactor through the negative temperature reactivity feedback. This effect is mainly due to the spectral shift of the neutron flux towards a favorable cross-section region, with a peak in the capture to fission ratio of ^{239}Pu. Simulations show that this process is driven by temperature dependence of the $S(\alpha, \beta)$ data. The introduction of the volume thermal expansion contributes only to about 15% of the reactivity changes.

Finally, it can be concluded that the physical characteristics of ^{239}Pu determine largely the parameters of DB-MHR fueled by LWRs waste.

References

Baldwin, C.A., Kania, M.J., 1990. Fission product retention in TRISO coated UO2 particle fuels subjected to HTR simulate core heating tests. In: IAEA Proceedings of the Conference on Gas-Cooled Reactors, Oak Ridge, USA, IWGGCR-25, pp. 132–138.

Baxter, A., Fikani, M. 2002. Reactor-based transmutation-physics studies of the gas-cooled graphite-moderated deep burn reactor, General Atomic, GA-501-0-TRT-000140.

Baxter, A., Rodriguez, C., 2001. The application of gas-cooled reactor technologies to the transmutation of nuclear waste. Progress in Nuclear Energy 38, 81–105.

Baxter, A., Rodriguez, C., Venneri F. 2001. Deep burn MHR, a Based Transmutation of Nuclear Waste, Framatom presentation, Paris, France.

Bonin, B., Greneche, D., 2002. Prospective studies of HTR fuel cycles involving plutonium. In: IAEA Proceedings of the Conference on High Temperature Reactors, Petten, Holland.

Briesmeister, J.F. 2002. A General Monte Carlo N-Particle Transport Code–version 4c, LANL LA-13709-M.

Cetnar, J., Gudowski, W., Wallenius, J. 1999. MCB: a Continuous Energy Monte Carlo Burnup Simulation Code, in Actinide and Fission Product Partitioning and Transmutation, EUR 18898 EN, OECD/NEA 523.

Cetnar, J., Gudowski, W., Wallenius, J., Monte Carlo continuous energy burnup MCB1C–the description, methods and benchmarks. Nuclear Science and Engineering, in preparation.

Cetnar, J., Gudowski, W., Wallenius, J., Tucek, K., 2001. Simulation of nuclide transmutation with Monte-Carlo Continuous Energy Burnup Code (MCB1C). In: Proceedings of the Accelerator application 2001 and ADTTA 2001 Nuclear Application in the New Millennium, Reno, USA. ANS.

Chapelot, P. et al., 2001. Requirements for high temperature reactor fuel particle design assessment. Progress in Nuclear Energy, 38.

Fröhling, W., 1999. Courses and limitations of damage with air ingress accidents in HTR modules. In: OECD Proceedings of the Conference on Survey on Basic Studies in the Field of High Temperature Engineering, Paris, France, pp. 173–181.

Fukuda, K., Kashimura, S., Tobita, T., Kikuchi, T., 1995. Irradiation behavior of HTGR coated particle fuel at abnormally high temperature. Nuclear Engineering and Design 157, 221–230.

General Atomic, 2002. GT-MHR conceptual design description report. GA/NRC-337-02.
Golubev, I., Kadarmetov, I., Makarov, V., 2002. Mathematical model and computer code for coated particles performance at normal operating conditions. In: IAEA Proceedings of the Conference on High Temperature Reactors, Petten, Holland.
Kim, J.J., Lee, J.T., Kim, H.R., 1989. Generation Benchmarking of a 69 Group Cross-Section Library for Thermal Reactor Applications. Journal of Korean Nuclear Society 21, 245.
Kiryushin, A.I., Kodochigov, N.G., Kouzavkov, N.G., et al., 1997. Project of the GT-MHR high temperature helium reactor with gas turbine. Nuclear Engineering and Design 173, 119–129.
Kugeler, K., Phlippen, P.W., 1999. Aspects of inherent safety of future high temperature reactors. In: OECD Proceedings of the Conference on Survey on Basic Studies in the Field of High Temperature Engineering, Paris, France, pp. 29–39.
Kugeler, K., von Lensa, W., Haag, G., Rtten, H.J. Use of plutonium in pebble bed HTGRs. In: IAEA International Working Group on Gas-Cooled Reactors Meeting, Beijing, China, 1998, IAEA-TECDOC-1210, pp. 229–236.
Kunitomi, K., Nakagawa, S., Shinozachi, M., 1996. Passive heat removal by vessel cooling system of HTTR during no forced cooling accidents. Nuclear Engineering and Design, 166.
Labar, M.P., Simon, W.A. 1994. Comparative economics of the GT-MHR and power generation alternatives, General Atomics, GA-A-21722.
Marsden, B.J., Hall, G.N., Smart, J. 1998. Nuclear graphite ageing and turnaround. In: IAEA International Working Group on Gas-Cooled Reactors Meeting, Beijing, China, IAEA-TECDOC-1210, pp. 133–153.
Matsuo, H., Nomura, S., Imai, H., Oku, T. 1986. Effects of high temperature neutron irradiation on the physical, chemical and mechanical properties of fine-grained isotropic graphite. In: JAERI Specialists Meeting on Graphite Component Structural Design, Tokai, Japan.
Miller, G.K., Petti, D.A., Varacalle, D.J., Maki, J.T., 2001. Consideration of the effects on fuel particle behavior from shrinkage cracks in the inner pyrocarbon layer. Journal of Nuclear Materials 295, 205–212.
Miller, G.K., Petti, D.A., Maki, J.T., 2002. Development of an integrated performance model for TRISO-Coated gas reactor particle fuel. In: IAEA Proceedings of the Conference on High Temperature Reactors, Petten, Holland.
Minato, K., Sawa, K., et al., 2000. Fission product release behavior of individual coated fuel particles for HTGR. Nuclear Technology, 131.
Minato, K., Ogawa, T., et al., 1993. Release behavior of metallic fission products from HTGR fuel particles at 1600 and 1900 °C. Journal of Nuclear Materials 202, 47–53.
Minato, K., Ogawa, T., Fukuda, K., Sekino, H., Kitagawa, I., Mita, N., 1997. Fission product release from Zr-coated fuel particles during post-irradiation heating at 1800 and 2000 °C. Journal of Nuclear Materials 249, 142–149.
Minato, K., Fukuda, K., Sekino, H., et al., 1998. Deterioration of ZrC-coated fuel particle caused by failure of pyrolitic carbon layer. Journal of Nuclear Materials 252, 13–21.
Minato, K., Ogawa, T., Koya, T., et al., 2000a. Retention of fission product cesium in ZrC-coated fuel particles for high-temperature gas-cooled reactors. Journal of Nuclear Materials 279, 181–188.
Minato, K., Ogawa, T., Sawa, K., et al., 2000b. Irradiation experiment on ZrC-coated particles for high temperature gas cooled reactors. Nuclear Technology, 130.
Moore, R.L., Oh, C.H., Merrill, B.J., Petti, D.A., 2002. Studies of air ingress for pebble bed reactors. In: IAEA Proceedings of the Conference on High Temperature Reactors, Petten, Holland.
Nabielek, H., Schenk, W., Heit, W., Mehner, A.W., Goodin, D.T., 1989. The performance of HTR fuel particles at extreme temperatures. Nuclear Technology 84, 62–81.
Nakagawa, S., Saikusa, A., Kunitomi, K. 1998. Safety evaluation during a depressurization accident of the SFHTR. In: IAEA International Working Group on Gas-Cooled Reactors Meeting, Beijing, China, pp. 77–84, IAEA-TECDOC-1210.
Nakagawa, S., Saikusa, A., Kunitomi, K., 2001. Development of a simulation model and safety evaluation for a depressurization accident without reactor scram in an advanced HTGR. Journal of Nuclear Technology, 133.

Nakata, T., Matsuki, Y., Mouri, T., 1995. Plutonium burning with high temperature gas-cooled reactor. Progress in Nuclear Energy 29, 209–215.

Nickel, H., Nabielek, H., et al., 2002. Long time experience with the development of HTR fuel elements in Germany. Nuclear Engineering and Design 217, 141–151.

Ohashi, K., Okamoto, F., Hayakawa, H., 2000. Modular High temperature reactor contributing the global environmental protection. Progress in Nuclear Energy 37, 307–312.

Petti, D.A., Buongiorno, J., Maki, J.T., Miller, G.K., 2002. Key differences in the fabrication of US and German TRISO-coated particle fuel, and their implications on fuel performances. In: IAEA Proceedings of the Conference on High Temperature Reactors, Petten, Holland.

Plukiene, R., Ridikas, D., 2003. Modelling of HTRs with Monte Carlo: from a homogeneous to an exact heterogeneous core with microparticles. Annals of Nuclear Energy 30, 1573–1585.

Porta, J., Lo Pinto, P., Bonnet, M., Kugeler, K., et al., 2001. Coated particle fuel to improve safety, design, and economics in water-cooled and gas-cooled reactors. Progress in Nuclear Energy 38, 407–410.

Ridikas, D., Bletzacker, L., et al., 2002. Comparative analysis of ENDF, JEF and JENDL data libraries by modeling high temperature reactors and plutonium based fuel cycles. Journal of Nuclear Science and Technology supplement 2, 1167–1170.

Rodriguez, C., Baxter, A., et al., 2003. Deep-Burn: making nuclear waste transmutation practical. Nuclear Engineering and Design 222, 299–317.

Sawa, K., Tobita, T., 2003. Investigation of irradiation behavior of SiC-Coated fuel particle at extended burnup. Nuclear Technology, 142.

Sawa, K., Suzuki, S., Shiozawa, S., 2001. Safety criteria and quality control of HTTR fuel. Nuclear Engineering and Design 208, 305–313.

Sawa, K., Ueta, S., et al., 2001. Prediction of fuel performance and fission gas release behavior during normal operation of the high temperature engineering test reactor by JAERI and FZJ modeling approach. Journal of Nuclear Science and Technology, 411–419.

Schenk, W., Fr, R., Moormann, R., Nabielek, H. 1994. Simulation of air ingress with irradiated fuel samples. In: JAERI Meeting on Validation of Predictive Methods for Fuel and Fission Product Behavior in Gas-Cooled Reactors, Tokai, Japan.

Talamo, A., Gudowski, W., Venneri, F., 2004. The burnup capabilities of the Deep Burn Modular Helium Reactor analyzed by the Monte Carlo Continuous Energy Code MCB. Annals of Nuclear Energy 31/2, 173–196.

Taubman, C.J., 1975. The WIMS 69-Group Library Tape 166259. Report AEEW-M1324, U.K. Atomic Energy Authority, Winfrith, Great Britain.

Thetford, R., 2000. Physical properties of minor actinides and diluents in oxide fuels. AEA technology report ARMM/P(00)15.

Tsuchie, Y., 2000. Desirability of small reactors, HTGR in particular. Progress in Nuclear Energy 37, 253–258.

Werner, H., 1997. Build up of plutonium isotopes in HTR fuel elements, a comparison between computed predictions and chemical analysis. Nuclear Engineering and Design 170, 147–164.

Wistrom, J.D., Simon, W.A., 1996. Where does the GT-MHR go from here? Nuclear Engineering and Design, 41.

Woaye-Hune, A., Ehster, S., 2002. Calculation of the decay heat removal transient by passive means for a direct cycle modular HTR. In: IAEA Proceedings of the Conference on High Temperature Reactors, Petten, Holland. Available from: www.accuratus.com/silicar.html.

APPENDIX 5

Alberto Talamo, Waclaw Gudowski and Francesco Venneri, The burnup capabilities of the Deep Burn Modular Helium Reactor analyzed by the Monte Carlo Continuous Energy Code MCB, Annals of Nuclear Energy 31 (2004) 173–196

Available online at www.sciencedirect.com
SCIENCE DIRECT®
PERGAMON
Annals of Nuclear Energy 31 (2004) 173–196
annals of NUCLEAR ENERGY
www.elsevier.com/locate/anucene

The burnup capabilities of the Deep Burn Modular Helium Reactor analyzed by the Monte Carlo Continuous Energy Code MCB

Alberto Talamo[a,*], Waclaw Gudowski, Francesco Venneri[b]

[a]*Department of Nuclear and Reactor Physics, Royal Institute of Technology, Roslagstullsbacken 21, S-10691, Stockholm, Sweden*
[b]*Los Alamos National Laboratory, USA*

Received 17 March 2003; accepted 19 June 2003

Abstract

We have investigated the waste actinide burnup capabilities of a Gas Turbine Modular Helium Reactor (GT-MHR, similar to the reactor being designed by General Atomics and Minatom for surplus weapons plutonium destruction) with the Monte Carlo Continuous Energy Burnup Code MCB, an extension of MCNP developed at the Royal Institute of Technology in Stockholm and University of Mining and Metallurgy in Krakow. The GT-MHR is a gas-cooled, graphite-moderated reactor, which can be powered with a wide variety of fuels, like thorium, uranium or plutonium. In the present work, the GT-MHR is fueled with the transuranic actinides contained in Light Water Reactors (LWRs) spent fuel for the purpose of destroying them as completely as possible with minimum reliance on multiple reprocessing steps. After uranium extraction from the LWR spent fuel (UREX), the remaining waste actinides, including plutonium are partitioned into two distinct types of fuel for use in the GT-MHR: Driver Fuel (DF) and Transmutation Fuel (TF). The DF supplies the neutrons to maintain the fission chain reaction, whereas the TF emphasizes neutron capture to induce a deep burn transmutation and provide reactivity control by a negative feedback. When used in this mode, the GT-MHR is called Deep Burn Modular Helium Reactor (DB-MHR). Both fuels are contained in a structure of triple isotropic coated layers, TRISO coating, which has been proven to retain fission products up to 1600 °C and is expected to remain intact for hundreds of thousands of years after irradiation. Other benefits of this reactor consist of: a well-developed technology, both for the graphite-moderated core and the TRISO structure, a high energy conversion efficiency (about 50%), well established passive safety mechanism and a competitive cost. The destruction of more than 94% of ^{239}Pu and the

* Corresponding author. Fax: +46-8-5537-8465.
E-mail addresses: alby@neutron.kth.se (A. Talamo), wacek@neutron.kth.se (W. Gudowski), venneri@lanl.gov (F. Venneri).

0306-4549/$ - see front matter
doi:10.1016/S0306-4549(03)00213-5

other geologically problematic actinide species makes this reactor a valid proposal for the reduction of nuclear waste and the prevention of proliferation.

1. Introduction

One of the major problems of the once-through nuclear fuel cycle applied in Light Water Reactors (LWRs) is the significant amount of generated nuclear waste that will require geological repositories lasting for hundreds of thousands of years (US Nuclear Waste Technical Review Board, 1999). Moreover, the amount of weapons-usable Pu in this waste is a serious proliferation risk, since the radioactivity of spent fuel is lowered by 90% after 100 years (Richards, 1996) and the isotopic fraction of ^{239}Pu increases with time, opening the possibility of mining the repository for its weapons-usable contents (US National Academy of Sciences, 1995a). The aim of our research is to verify the high burnup performance of the Deep Burn Modular Helium Reactor (DB-MHR) (Baxter et al., 2001; Baxter and Fikani, 2002; Ohashi et al., 2000; Kiryushin et al., 1997; Baxter and Rodriguez, 2001; Richards, 1995; Chudin, 1999) to address these problems. A possible plant layout of a DB-MHR nuclear facility uses four modules of 600 MW (Baxter and Rodriguez, 2001) to destroy Pu from LWRs and, at the same time, to produce electricity or generate high temperature process heat for the production of hydrogen or other purposes. Each module consists of a gas-cooled graphite-moderated DB-MHR. The modular arrangement and small size are aimed at reducing the core power density, so that the complication of the security devices decreases, as well as the power excursion during an accident. The attractive features of the DB-MHR are:

- Cost lower than an ordinary LWR (Labar and Simon, 1994).
- Clear passive safety mechanism.
- High conversion energy efficiency (about 50%), which also reduces the thermal impact on the natural environment.
- Well-developed nuclear technology both for the core and the fuel structure.
- Improvement of the barriers protecting the environment from dispersion of residual waste.
- High burnup, up to 700 000 MWd/t, with better than 90% destruction of selected actinides (including ^{239}Pu).
- Great flexibility in the choice of the fuel type: fertile and non-fertile cores (e.g. Th, U or Pu).

Several factors contribute in the passive safety mechanism of the DB-MHR: negative temperature coefficient of reactivity, helium coolant (which is inert, operates in a gas single phase and it is almost transparent to neutrons), H451 graphite core (which provides high heat capacity and structural stability), low power density over the whole reactor core—about 2.1 MW/m^3 (the average power density in the power generating rings is 6.23 MW/m^3), triple isotropic (TRISO) coated fuel particles (which retain fission products even under a severe accident scenario), opera-

tional temperature of graphite above 270 °C (which facilitates the reallocation of interstitial atoms and lacunas in the lattice and avoids the Wigner effect). The low power density of the DB-MHR is a benefit from the security point of view but also a drawback concerning electricity production. The H451 nuclear-grade graphite used in the DB-MHR is a special type of graphite that differs from normal graphite in several aspects (Richards, 1995): it inhibits exothermic oxidation reactions (graphite fires), it contains a low concentration of impurities (which catalyze the oxidation reaction), it has a high density (which reduces porosity and inhibits oxidation), it has a high thermal conductivity and specific heat, it creates (while burning) neither an external porous ash layer (which would allow oxygen to pass through) nor methane (which would react exothermically with air).

The main objective of the DB-MHR design has been the extended destruction of ^{239}Pu, one of the major contributors to long lasting radiotoxicity and the major proliferation concern. Because of the radiological importance of several minor actinides in the geologic repository (Baxter and Rodriguez, 2001), we have also focused our attention also on the transmutation of Minor Actinides (MA).

Before fueling the DB-MHR, LWRs waste is reprocessed by uranium and fission products extraction (UREX). The final products of the LWRs spent fuel reprocessing are $NpPuO_{1.7}$ and $AmCmO_{1.7}$; the first material constitutes the Driver Fuel (DF). The DF is the primary nuclear fuel for the DB-MHR and it sustains the fission chain reaction, mainly by ^{239}Pu. Spent DF is mixed after discharge from the reactor core with the $AmCmO_{1.7}$, which was set-aside after UREX, to build fresh Transmutation Fuel (TF). After irradiation, spent TF is sent into the repository. ^{239}Pu plays a key role in the operation of the DB-MHR, because it is the most abundant fissile isotope in LWR spent fuel after UREX, and therefore provides most of the reactivity of the DF. We can note in Fig. 1 (IANIS) that ^{239}Pu exhibits a particularly undesirable neutronic behavior in the neutron energy range of 0.25–1 eV, where resonances of fission and capture cross sections of ^{239}Pu set a positive temperature reactivity feedback, since the capture to fission cross section ratio, so called alpha parameter, decreases with the increase of temperature. Also production of xenon contributes in the positive reactivity feedback because of the low ^{239}Pu Doppler coefficient (Nakagawa et al., 2001). Usually, the undesired behavior of ^{239}Pu in the neutron energy range above 0.25 eV is mitigated by adding ^{167}Er as burnable poison (Fig. 2) (Baxter et al., 2001). Nevertheless, in graphite moderated reactors, ^{167}Er might be replaced by ^{241}Am, ^{237}Np and ^{240}Pu (Fig. 2), which are abundant in the TF. These actinide isotopes have resonances in the right energy range to compensate for the increased reactivity of ^{239}Pu; they need to be transmuted and are also fertile. Therefore in the DB-MHR, they can replace the parasitic rare earth burnable poisons to great advantage. The graphite-moderated DB-MHR is well suited to use some of the MA in this way, because graphite exhibits a gradual slowing down of the fission neutrons (compared to water for instance, Fig. 3) (Baxter et al., 2001): in fact, the neutron average energy lost per collision is 14.6% for graphite and 60.1% for water. Therefore, graphite allows the effective use of the resonance absorption for ^{241}Am, ^{237}Np and ^{240}Pu to counteract the reactivity feedback of ^{239}Pu, since the neutron samples the energy space with much smaller steps.

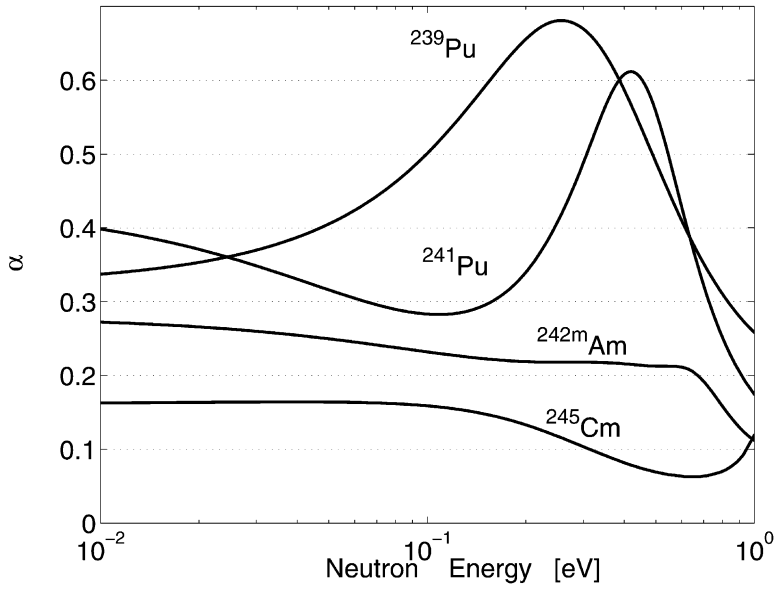

Fig. 1. Capture to fission ratio of fissile Actinides.

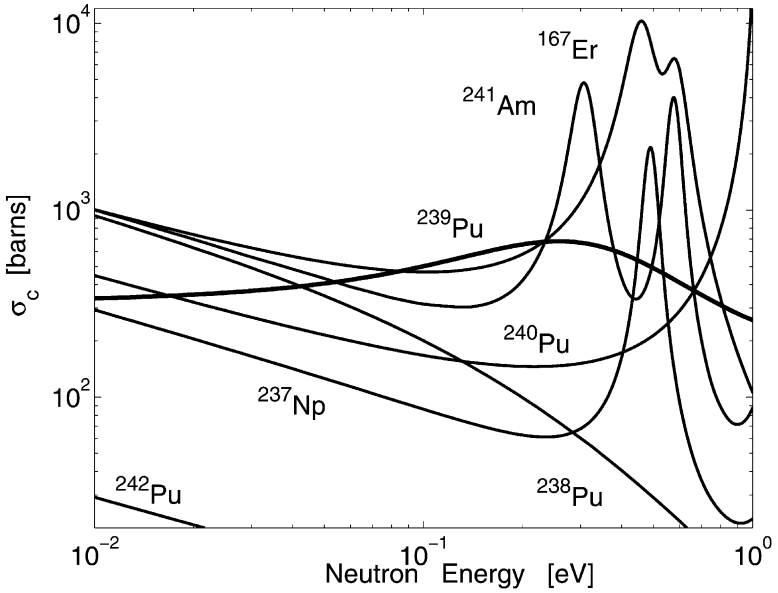

Fig. 2. Capture cross section of non-fissile Actinides and capture to fission ratio of ^{239}Pu.

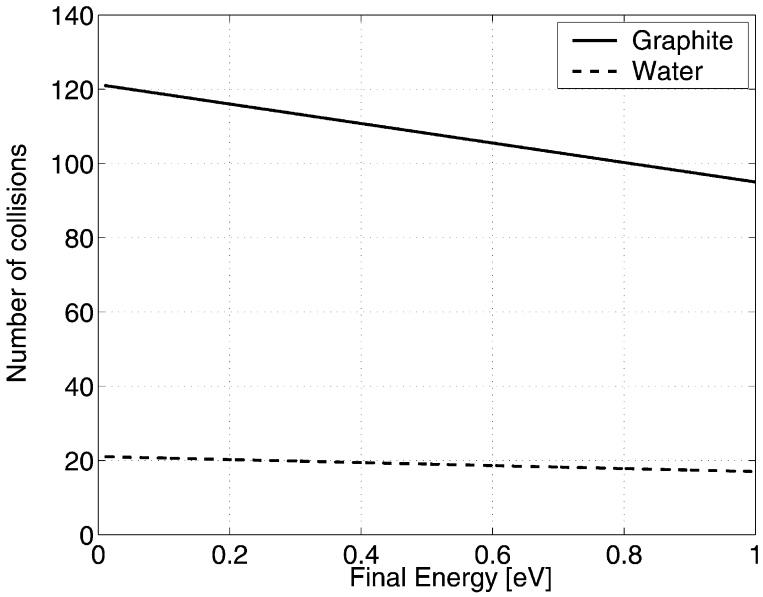

Fig. 3. Number of collisions to slowdown a fission neutron (Baxter et al., 2001).

2. The DB-MHR description

Fig. 4 (Baxter and Fikani, 2002) describes the General Atomic-Minatom DB-MHR. The core is composed by a matrix of hexagonal blocks, which contain: the inner replaceable reflectors, the outer replaceable reflectors and three rings of fuel. The space between two hexagonal blocks is 0.1016 cm. The reactor has 48 operational control rods, which are filled with boron carbide spheres. 18 control rods are located in the fuel blocks and 30 control rods in the outer replaceable reflectors. The fuel blocks are equipped with further 18 reserve shutdown control rods (RSC). The matrix of hexagonal blocks of the core is surrounded by a permanent reflector, which, on the outer border, is filled with borated steel pins. Nevertheless, in the model we used for numerical simulations, we neglected the presence of control rods and the space between two blocks of graphite. Since we estimated a low variation of k_{eff} during the operation at equilibrium, we retain the neglecting of control rods a valid approximation.

The DB-MHR has been modeled in numerical calculations as a cylinder, with a radius of 4 m and a height of 10 m, filled by hexagonal blocks of graphite (density 1.74 g/cm^3) and fuel. Namely, the fuel is disposed along three concentric rings each of 36 hexagonal blocks (Fig. 5). Fuel covers just 7.93 m of the height of a hexagonal block; the remaining 2.07 m, 1.035 m at top and at bottom, are filled with graphite, which acts as blanket (Fig. 6).

The side of the hexagonal blocks is 20.8 cm. In each fuel block there are 108 cooling helium channels, 144 DF pins and 72 TF pins (Fig. 5); therefore, the ratio between DF pins and TF ones, as well as their volume ratio, is 2:1. The cooling

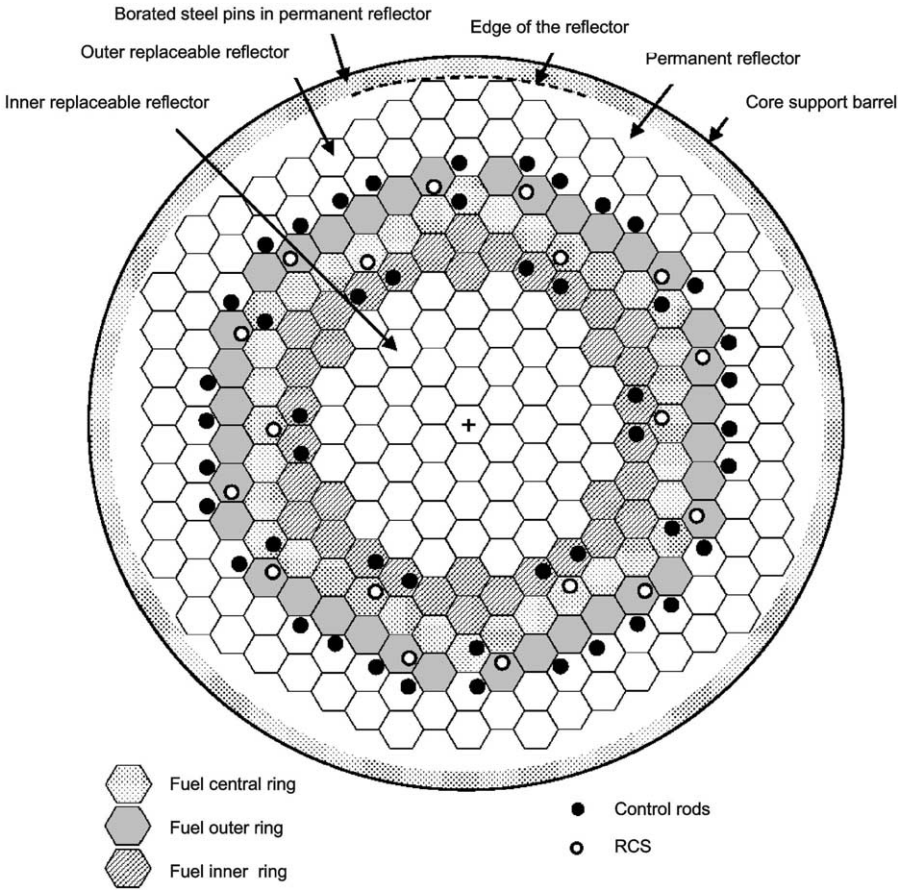

Fig. 4. Horizontal section of the core of the General Atomic-Minatom DB-MHR.

channels have a radius of 0.797 cm, whereas the driver and transmutation pins have a radius of 0.622 cm. A further cooling channel, with an external radius of 0.635 cm, surrounds each driver and transmutation pin. Helium enters the cooling channels from the bottom of the reactor at 490 °C, with a pressure of 7 MPa, and it exits at the top with a temperature of 850 °C. Table 1 shows the design parameters of the model used in numerical simulations to represent the DB-MHR.

Both the driver and transmutation pins consist of a graphite matrix (fuel compact) filled with triple isotropic (TRISO) coated layers fuel particles (Fig. 5). We set the packing ratio (the fraction of the TRISO particles volume over the total volume of the fuel pin) to 14.41% for DF and to 32.92% for TF. Whereas the packing ratio of the fuel central sphere (kernel) (the fraction of the fuel volume over the total volume of the fuel pin) of TRISO particles is 0.7% both for driver and transmutation fuel; therefore, the volume ratio between DF and TF is 2:1, since the number of DF pins is twice as that one of TF.

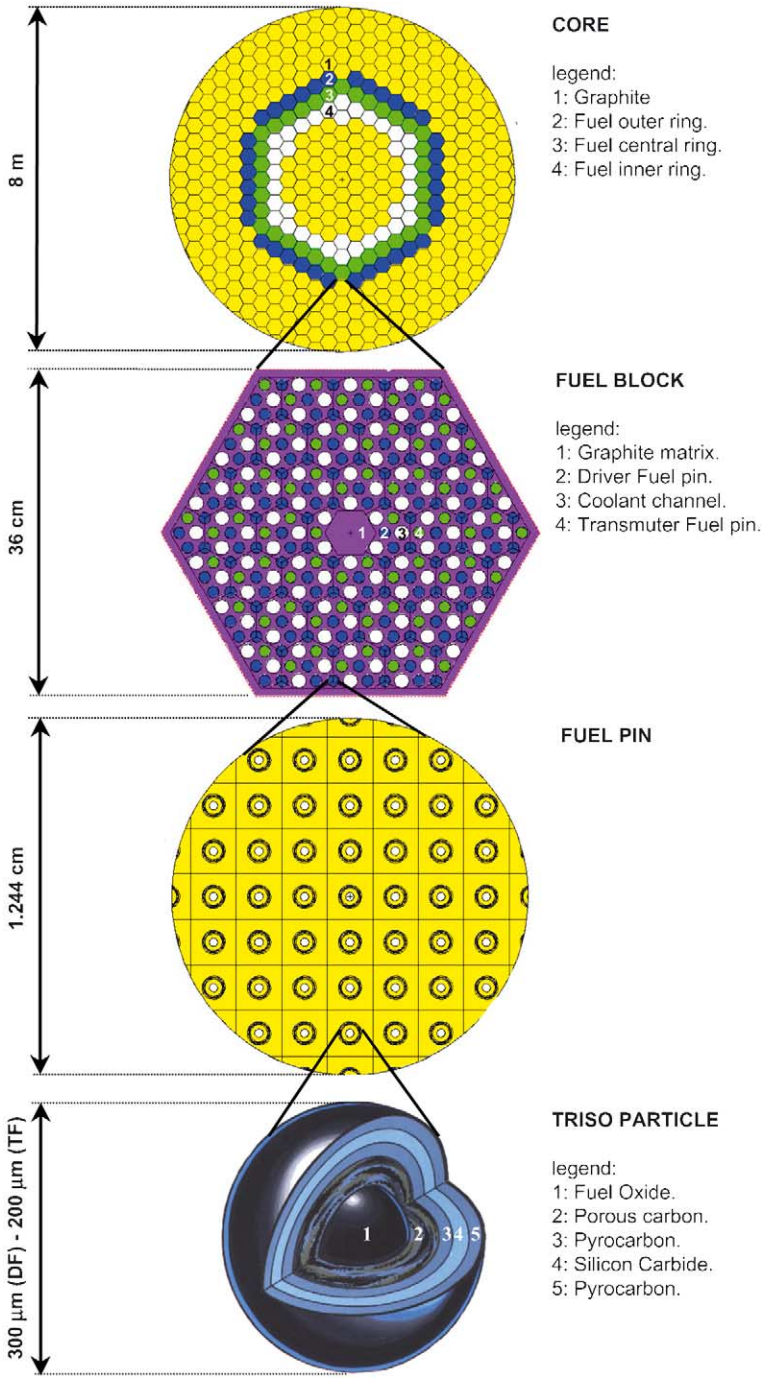

Fig. 5. The model of the DB-MHR used in simulations.

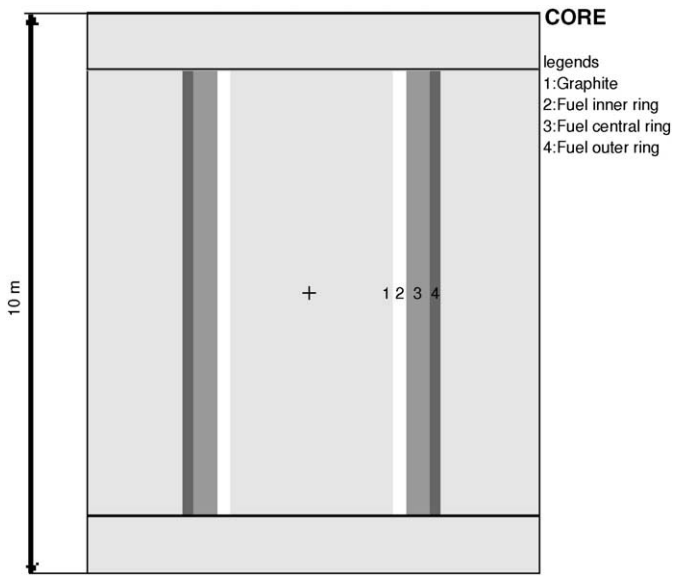

Fig. 6. Vertical section of the core of the DB-MHR used in simulations.

Table 1
Core design parameters for the numerical simulations of the DB-MHR (for TRISO particles description see Table 2)

Core Power (MW_t)	600
Core radius (cm)	400
Core height (cm)	1000
Side of an hexagonal block	20.8
Fuel blocks	36×3
DF pins in a fuel block	144
TF pins in a fuel block	72
Coolant channels in a fuel block	108
Radius of a fuel pin (cm)	0.622
Height of a fuel pin (cm)	793
Radius of coolant channel surrounding a fuel pin (cm)	0.635
Radius of a coolant channel (cm)	0.797
Distance between DF TRISO particles in the fuel pin (cm)	0.0794138
Distance between TF TRISO particles in the fuel pin (cm)	0.0529425

The kernel of a TRISO particle consists of fuel oxide, whereas the three surrounding concentric spherical layers are made by (Table 2 and Fig. 5) (Baxter et al., 2001):

- Porous carbon, which provides the volume for the expansion of fission gases and attenuates fission recoils.
- Pyrocarbon (inner layer), which sets the substrate for the SiC layer.

Table 2
Structure of a TRISO particle[a]

Material	External radius [μm]	Initial density [g/cm^3]
DF-(TF_4; TF_{12})	150–100	10.2–(10.5; 15.7)
Porous carbon layer	300–250	1
Pyrocarbon	335–285	1.85
Silicon carbide	370–320	3.2
Pyrocarbon	410–360	1.85

[a] The values of density for TF refer to the inner ring at the beginning of the 4th and 12th years.

- SiC, which retains the gas and metal fission products and provides the mechanical resistance.
- Pyrocarbon (outer layer), which sets a bonding surface for compacting and acts as fission products barrier in particles with defective SiC.

Since the mean free path of neutrons, in the resonance region 0.2–0.4 eV (Fig. 2), is 10–100 μm (Baxter et al., 2001), General Atomic fixed a radius of 150 μm for the DF and of 100 μm for the TF. In order to enhance the resonance capture, and therefore the transmutation of the non-fissile actinides, the radius of a TF particle is smaller than that one of a DF particle. The greater radius of DF decreases the effective capture-to-fission ratio for ^{239}Pu (averaged on the whole kernel), therefore improving the fission performance of the DF and reducing the buildup of higher actinides.

TRISO particles have proven to retain fission products up to 1600 °C (Nabielek et al., 1989; Nickel et al., 2002; Fukuda et al., 1995; Minato et al., 1993, 2000b). After this threshold, several factors can degrade their integrity: manufacture defects, internal pressure of the gas fission products, failure of the Pyrocarbon layer due to neutron-induced enbrittlement, Amoeba effect (which is the migration of the kernel into the surrounding layers), failure of SiC due to chemical interaction with fission products and dissociation of SiC, which occurs at 2000 °C. During manufacture, a more isotropic and porous pyrocarbon layer can improve by a factor 1000 the gas release under irradiation (Petti et al., 2002; Miller et al., 2001). Recent studies have suggested that replacing SiC with ZrC improves the performance of TRISO fuel, since ZrC TRISO particles show no failure up to 1800 °C (Minato et al., 1997, 1998, 2000b). We have not considered ZrC coatings in our models.

In the case of an accident, TRISO particles can stay intact for 3 h at 1500 °C (Fröhling, 1999). During this interval of time the reactor will most probably be depressurized (10 bar/min) (Kugeler and Phlippen, 1999) and air may penetrate the vessel. When the air enters the reactor, TRISO particles loose integrity because of the gasification of the fuel graphite matrix by the oxidation of the pyrocarbon (Fröhling, 1999; Kugeler and Phlippen, 1999; Schenk et al., 1994). In this scenario, the DB-MHR exhibits a passive security mechanism because heat conduction (in graphite), thermal radiation and natural convection (from graphite to air), coupled to a low power density (2.1 MW/m^3), can keep the temperature excursion of fuel lower than 1600 °C (Kugeler and Phlippen, 1999; Nakagawa et al., 2001). In fact,

the nuclear-grade graphite H451 is not subjected to the *red glow*, which occurs when the heat removed by air convention is smaller than heat produced by exothermic reaction of graphite with oxygen (Richards, 1995).

In a repository environment, spent TRISO particles should maintain their integrity for millions of years, even if they would permanently be flooded with groundwater (Gray, 1982; Knobloch and Nachmilner, 1994). By contrast, the American National Academy of Sciences (NAS) estimated that, in the Yucca Mountain repository of the, Zircaloy cladding of ordinary spent fuel would retain the radiotoxic nuclides for only a few thousand years at best (US National Academy of Sciences, 1995b).

The initial composition of the DF is showed in Table 3, where the relative abundance of the Actinides reflects the inventory of LWRs spent fuel.

3. The MCB numerical simulations

The numerical simulations have been performed at the Nuclear and Reactor Physics Department of the Royal Institute of Technology of Stockholm (KTH) by the Monte Carlo Continuous Energy Burnup Code, MCB, version 1C (Cetnar et al., in preparation, 1999, 2001), which is an extension of the MCNP code (Briesmeister, 2002).

The strategy of MCB is to divide the analyzed burnup time interval into several steps: at each step it calculates the decay probability of all nuclides in the initial fuel composition, afterwards it updates densities and cross sections by a MCNP run, as shown in Fig. 7. Then, MCB generates all the transmutation chains from the initial nuclides until the probability of a transmutation branch is below the default threshold value of 10^{-10}. Version 1C of MCB describes all known decay schemes, using over 2400 different isotopes. Within a time step, the MCNP track length estimator of neutron flux scores, for each neutron collision, the contribution to the reaction rates of burnable materials (Fig. 7). The user can define the size of each time step; otherwise, it is automatically adjusted by the code, according to the change of k_{eff} or power density between two consecutive time steps. By default, all isotopes with a decay half-life shorter than 1000 s are treated as prompt; of course this threshold can be modified at the expense of computing time. In order to save computing time, MCB performs a quick run before starting to score results, to esti-

Table 3
Initial composition of the fresh DF

Isotope	Atomic percentage	Mass (kg)
^{237}Np	1.91	16.49
^{238}Pu	0.56	4.849
^{239}Pu	21.11	184
^{240}Pu	8.5	74.36
^{241}Pu	3.09	27.16
^{242}Pu	1.87	16.49
^{16}O	62.96	36.70

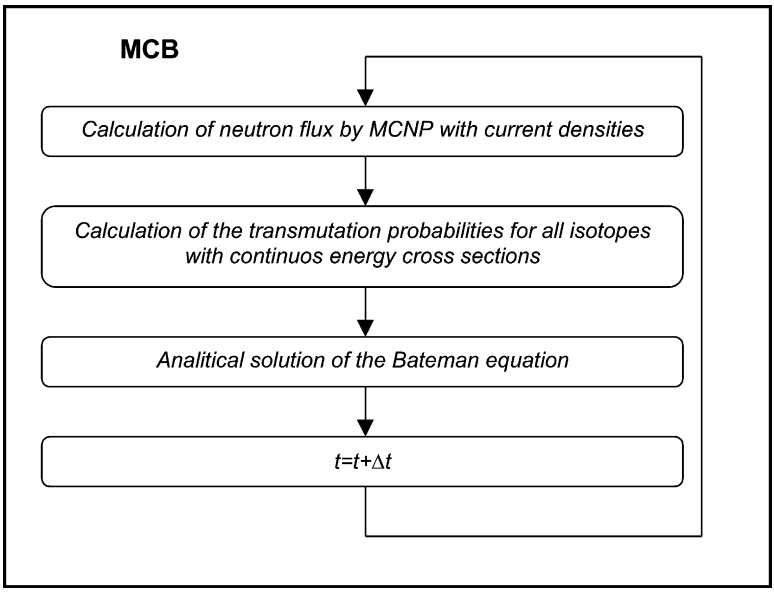

Fig. 7. Simplified flow-chart of the MCB code.

mate the generated nuclides, so that most of the cross sections are transferred into the RAM memory (the number of cycles of the quick run is 10 times smaller than the 4th entry of the KCODE card of MCNP). MCB can work either in k-code mode, when the reactor is close to criticality and it is normalized by the total thermal power, or in fixed-source mode, when the reactor is subcritical and it is normalized by the strength of an external neutron source. The heating of the system is calculated using the KERMA factor of cross sections libraries, which includes neutron and gamma heating, as well as the decay heat.

The MCB code has been verified (but not yet validated versus experimental data) by several numerical benchmarks, which showed an excellent agreement with other burnup codes (Cetnar et al., 1999). The main differences of MCB versus other modeling tools, such as Monteburns (Trellue and Poston, 1999) are: application of linear chain method solution of the Bateman equation (whereas Munteburns uses the matrix method), integration of the transport module and the burnup module in the same code (which simplify the system description to the user), it automatically forms the set of transmutation chains that cover every meaningful transmutation transition depending on the physical condition and data set, transmutation chains that cover every isotope and reaction are available at any time, continuous energy cross sections (with temperature dependence) are fully applied for all the processes of transmutation including the yield of fission products and isomer nuclides (e.g. ^{242m}Am).

Version 1C of MCB can provide: burnup and buildup reaction rates, decay probabilities, neutron flux, fission product distributions, radiation heating, decay heating, transmutation transitions, density evolution, radiotoxicity (dose in case of ingestion according to the EURATOM Directive).

In the present work, MCB used the nuclear cross section library JEF-2.2. Cross sections temperature was 1200 K for core graphite and 1500 K for fuel (both DF and TF). The cross section of graphite has been corrected by the S(α,β) treatment to take into account the upscattering of thermal neutrons.

During burnup, the recalculation of neutron flux with the updated densities was performed two times: after 165 days and immediately after the shutdown of the reactor, which occurred after 330 days. The total amount of ^{239}Pu, left in the reactor after 330 days, changed 2.4% when the recalculation of neutron flux after 165 days was not performed. At each recalculation of neutron flux, MCB executed a total of 150 cycles, with 40 inactive ones (cycles which do not contribute in the final score of the results), each of them simulating 30000 neutrons. MCB inputs, to describe the DB-MHR, required about 150 MB of RAM memory for each CPU task, tough this value depends on the type of the cross section library, and 30 computing hours for each year of simulated operations. The computing time has been distributed over 10 processors of 1900 MHz by the Parallel Virtual Machine (PVM) version 3.

The MCB code does not supply information about the statistical error on its burnup predictions; nevertheless we performed a sensitivity test by modifying the starting pseudorandom number (the first value of the DBCN card of the MCNP code) in a set of ten runs. The result of this test was a standard deviation of the remaining mass of ^{239}Pu (after 330 days operation) close to the standard deviation of k_{eff}. By contrast the value for the mass of ^{244}Cm was two orders of magnitudes higher, as Table 4 shows.

4. Fuel shuffling strategy

The Deep Burn concept is based on the use of Driver Fuel, rich in fissile actinides (^{239}Pu) and Transmutation Fuel, rich in non-fissile actinides. The DF provides the excess reactivity to drive the power production and sustain large effective transmutation rates. The TF provides burnable poison and reactivity control.

In the DB-MHR, the hexagonal fuel blocks are disposed along three rings; in addition, each fuel block is divided into 10 sub-blocks along the z-axis. The shuffling strategy moves hexagonal fuel blocks both radially and axially. Namely, the fresher fuel is loaded in the internal rings and it is shuffled outwardly in the radial direction after 330 days, at the same time the 10 axial subblocks of fuel are shuffled from [1 2 3

Table 4
Sensitivity test of MCB on a set of 10 simulations with different values of the starting pseudorandom number

	Standard Deviation
^{239}Pu	0.00052
^{244}Cm	0.01989
k_{eff}	0.00050
k_{eff} (MCNP value)	0.00039

4 5 6 7 8 9 10] into [5 4 3 2 1 10 9 8 7 6]. Nevertheless, in the present studies, we considered only the radial shuffling. While the fresh DF is fixed in composition, the fresh TF is in part made of irradiated (spent) DF; therefore, the TF composition changes with time and it reaches the equilibrium according to the specific reactor refueling strategy. From a starting point with only DF, in order to arrive at equilibrium conditions with representative mass flows for both driver and transmutation fuels, we adopted a 12-year "fuel strategy" consisting of periodic refueling and shuffling. At the end of the 12th year the reactor is at equilibrium and meaningful mass flow balances can be calculated.

At the startup of operations (1st year), the fresh DF is loaded into the inner ring of 36 hexagonal fuel blocks (white ring in Fig. 5). Each block is loaded with 10 kg of DF, in the form of $NpPuO_{1.7}$; therefore, the total initial mass of DF is 360 kg. As a consequence of the isotopic ratios in LWRs spent fuel, the set-aside amount of $AmCmO_{1.7}$ after UREX is 40 kg; Table 5 reports the isotopic composition of the set-aside $AmCmO_{1.7}$.

During the first year, the reactor operates just by the inner ring (white ring in Fig. 5). After the first year, the DF is shuffled into the central ring (gray ring in Fig. 5) and fresh DF is loaded again into the inner one. During the 2nd year the reactor operates with the two inner rings loaded with DF. After the second year, the DF from central ring is moved into the outer ring (dark-gray ring in Fig. 5) and the fuel from inner ring takes its place; fresh DF is loaded into the inner ring. Finally, during the 3rd year, the DF fills all the three rings. Each year consists of 330 days of full power operation (600 MW) and 35 days of outage at 0 power, in order to allow the necessary time for refueling and shuffling. At the end of the 3rd year, the spent DF from the outer ring is reprocessed (Pu and MA extraction) and mixed with the set-aside $AmCmO_{1.7}$ from the initial UREX process to build the fresh TF. At the beginning of the fourth year, both fresh Driver and Transmutation Fuel fill the inner ring, with the ratio of two DF pins for each TF pin; the DF, irradiated in the inner ring during the previous year, fills now the central ring; the DF, previously irradiated in the central ring, moves into the outer ring. Therefore, during the 4th year, the DF is present in all the three rings and the TF just in the inner one. The remaining 2 years follow the radial shuffling policy of 2nd and 3rd year for both for DF and TF, with the constraint of loading the inner ring with fresh DF and TF.

After the initial 6 years, DF and TF fill all the three rings and the shuffling/refueling scheme is continued, with DF irradiated for 3 years and reprocessed to produce fresh TF, which ends its life after three years of irradiation. In the present work we limited our studies to the first 12 years since at the 12th year fuel composition reaches the equilibrium.

5. Approach to equilibrium

During approach to equilibrium, the reactor satisfies the constraints for k_{eff} for most of the time and the equilibrium operation has sufficient reactivity margins (Fig. 8). The 5th and 6th year show a slight reactivity deficit at the end of the

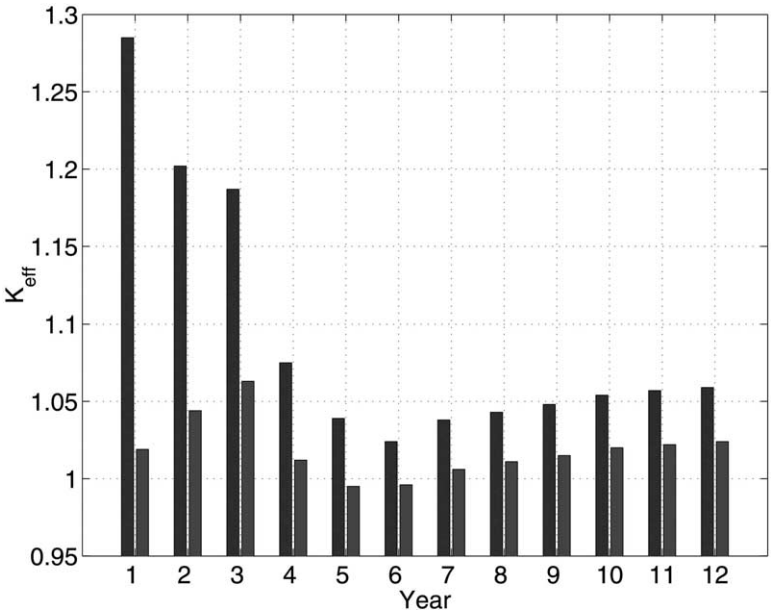

Fig. 8. Values of k_{eff} at beginning (left columns) and at the end (right columns) of each year. All values have a RSD smaller than 0.04%.

refueling cycle. This can be easily overcome with modifications of the fuel feed or altered refueling strategy.

The sharp decrease of the initial k_{eff}, during the first 6 years is due to the net increase of the total amount of capturing isotopes (e.g. fission products, ^{240}Pu, ^{242}Pu and ^{241}Am), since the total amount of irradiated fuel accumulates in the core. At beginning of the 4th year, the initial k_{eff} drops further because TF starts to fuel the reactor.

During the first 3 years, the loading and shuffling policy explains the increase of the k_{eff} final values. The reactor operates at a constant power, 600 MW; therefore, the power density and flux intensity are very high during the first 2 years (during the 1st year all power is generated only in one ring, and during the 2nd year in two rings, which leads to high fluxes). The flux decreases year by year as more rings are fuelled and generate power, therefore decreasing the fuel pin power density. As a consequence of the higher flux, during the first 3 years we can observe a higher consumption of ^{239}Pu in the DF (Figs. 9, 11 and 13). This effect decreases when DF fills all the three rings.

Between the 4th and the 6th year, the initial and final values for k_{eff} reach a minimum. The depression in k_{eff} is due to the fact that the TF fed to the reactor during these years is very poor in fissile material (^{239}Pu) because the original DF feed was overtransmuted due to the higher flux in the first years of operation.

After the 6th year, the values of k_{eff} increase towards the final equilibrium conditions, reached around the 12th year, when fuel reached its equilibrium composition.

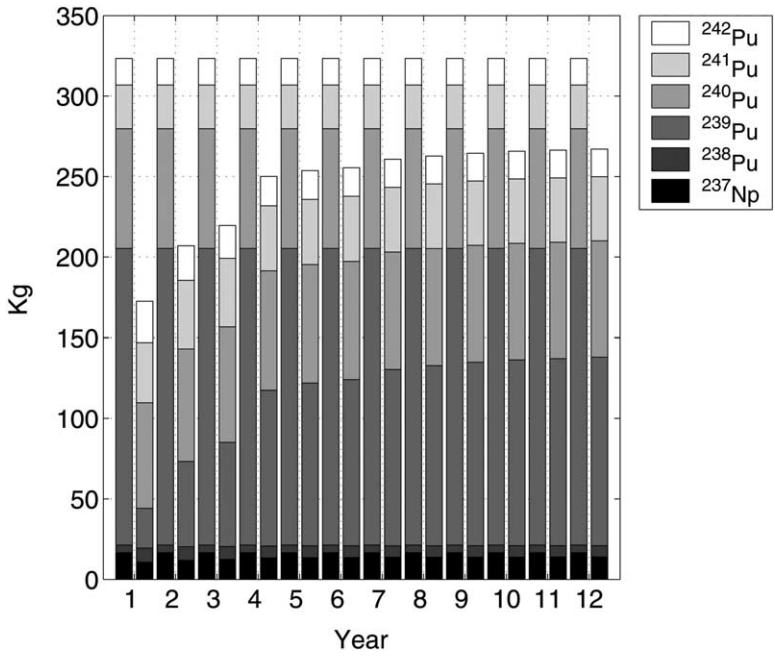

Fig. 9. Initial (left columns) and final (right columns) mass of Actinides of DF in the inner ring.

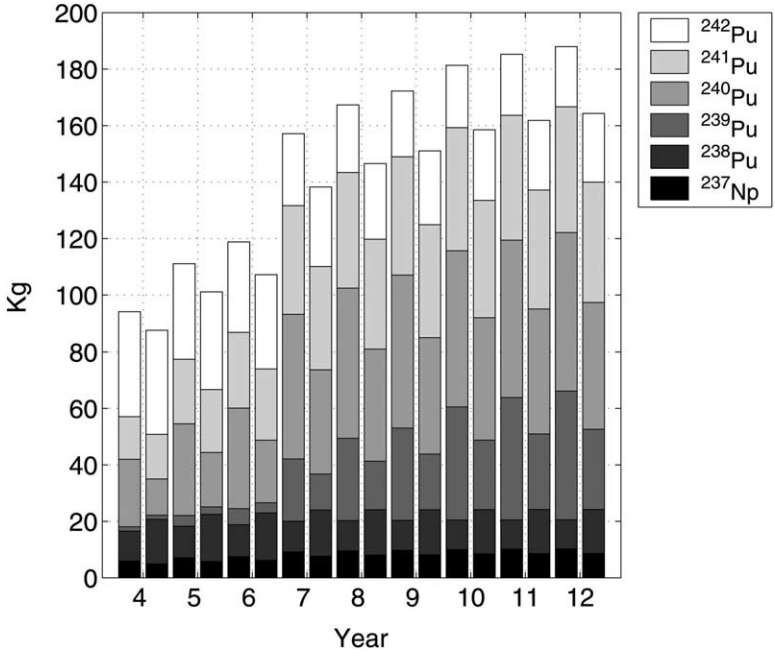

Fig. 10. Initial (left columns) and final (right columns) mass of Actinides of TF in the inner ring.

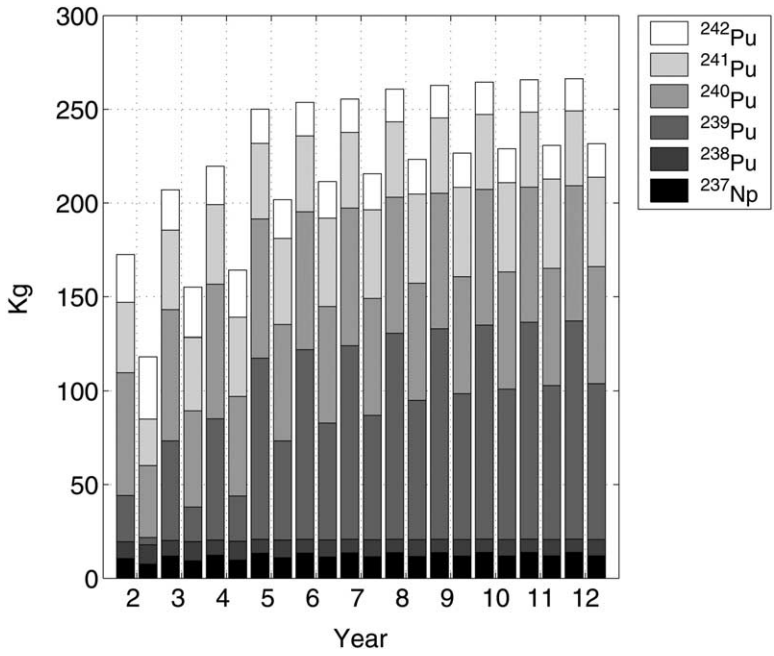

Fig. 11. Initial (left columns) and final (right columns) mass of Actinides of DF in the central ring.

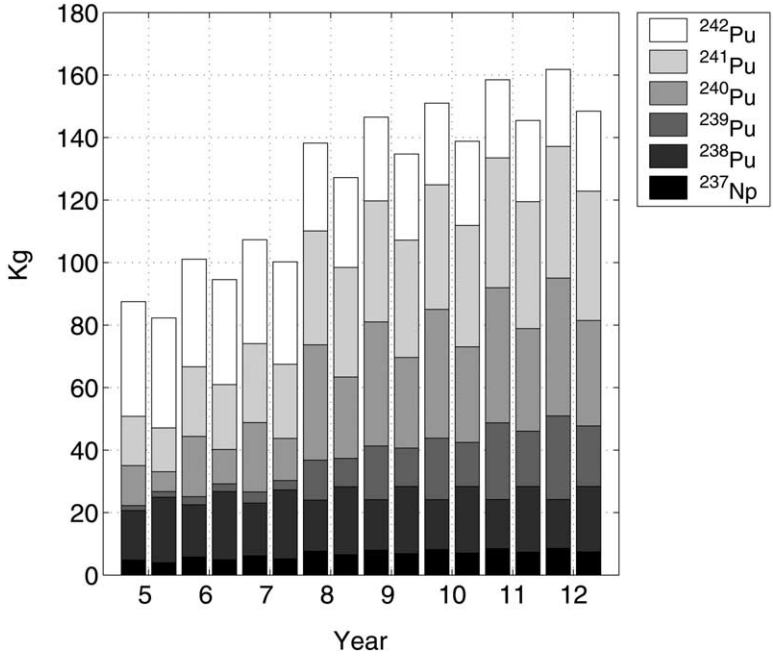

Fig. 12. Initial (left columns) and final (right columns) mass of Actinides of TF in the central ring.

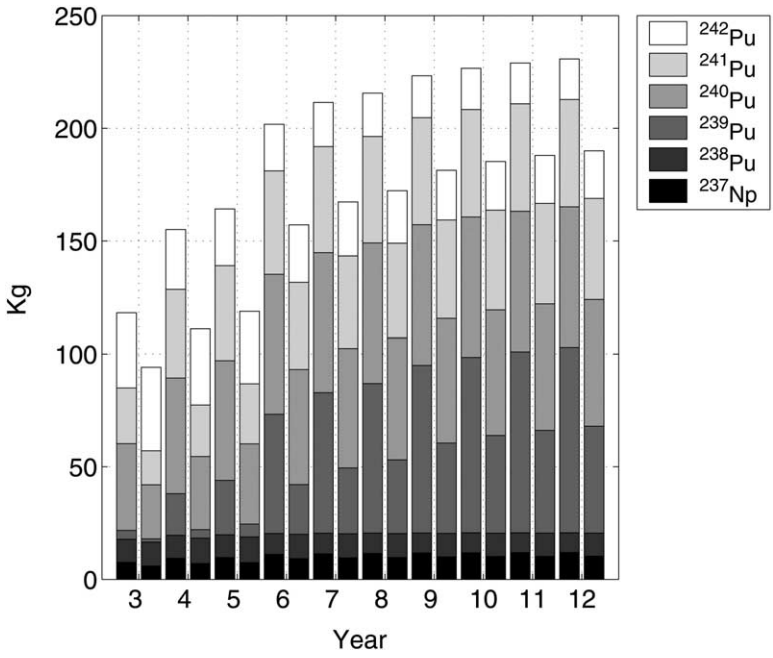

Fig. 13. Initial (left columns) and final (right columns) mass of Actinides of DF in the outer ring.

In addition, the difference between the initial and final values of k_{eff} becomes smaller, since ^{237}Np, ^{238}Pu, ^{240}Pu, ^{241}Am and ^{242}Cm (abundant in the TF), contribute to the breeding of fissile isotopes (Figs. 10, 12 and 14).

Fig. 9 shows the evolution of DF concentration in the inner ring, Fig. 10 shows the simultaneous evolution of the TF in the same ring. Similarly, Figs. 11 and 12 illustrate the evolution of driver and transmutation fuel in the central ring, and Figs. 13 and 14 in the outer ring. By comparing Figs. 10 and 11 we see how DF approaches equilibrium at the 6th year whereas the TF does it at the 10th year. For the central ring the equilibrium occurs at the 8th year for DF and at the 11th year for TF, whereas the outer ring does at the 10th year for DF. At the end of the 12th year TF composition is not exactly at equilibrium but is quite close. The inner ring approaches faster the equilibrium because its initial composition is constant during all the 12 years, whereas the central and outer rings reach equilibrium at a later stage. The TF is introduced in the reactor only after the 3rd year and it is produced from the spent DF, so it reaches equilibrium with considerable delay comparing to the DF.

^{239}Pu is the most abundant isotope of DF just in the inner ring and in the central ring (Figs. 9 and 11), because in the outer ring ^{240}Pu dominates (Fig. 13). This remark suggests moving the spent DF first into the outer ring (for 1 year) and then into the central ring (whereas the policy of the present work moves spent DF first into the central ring and then in the outer one). In fact, with this new policy the

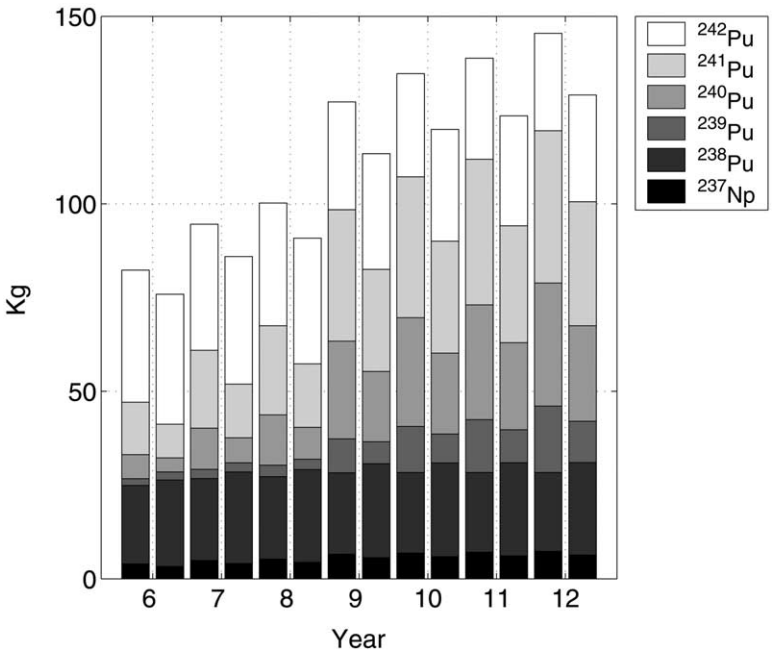

Fig. 14. Initial (left columns) and final (right columns) mass of Actinides of TF in the outer ring.

neutron flux would be more flatten, since ^{239}Pu would be distributed more homogeneously in the reactor; in fact, at the beginning of the third year the two rings more rich in ^{239}Pu would not be adjacent.

A real approach to equilibrium may differ from our studies because of three factors. First, we neglected the representation of the control rods, which may affect the shape of the axial and radial flux profiles as well as the flux spectrum. Second, at the beginning of the 12th year, the TF initial density reached the value of 15.7 g/cm^3 which is much higher than the value for DF (10.2 g/cm^3) Third, we neglected the axial shuffling, which may jeopardize the curvature of neutron flux along the axial direction.

6. Operation at equilibrium

During equilibrium operation, the yearly balance mass involves: the mass of fresh DF in the inner ring at the beginning of the year, the set-aside Am-Cm after UREX, the mass of fresh TF in the inner ring at the beginning of the year, the mass of spent DF in the outer ring at the end of the year (after 3 years of irradiation), the mass of spent TF in the outer ring at the end of the year (after 3 years of irradiation) and the mass of fission products extracted from processing of spent DF and TF.

Fig. 15, which has been obtained bt MCB code, describes the ^{239}Pu transmutation chain at the 12th year when fuel composition is at equilibrium: all the reaction

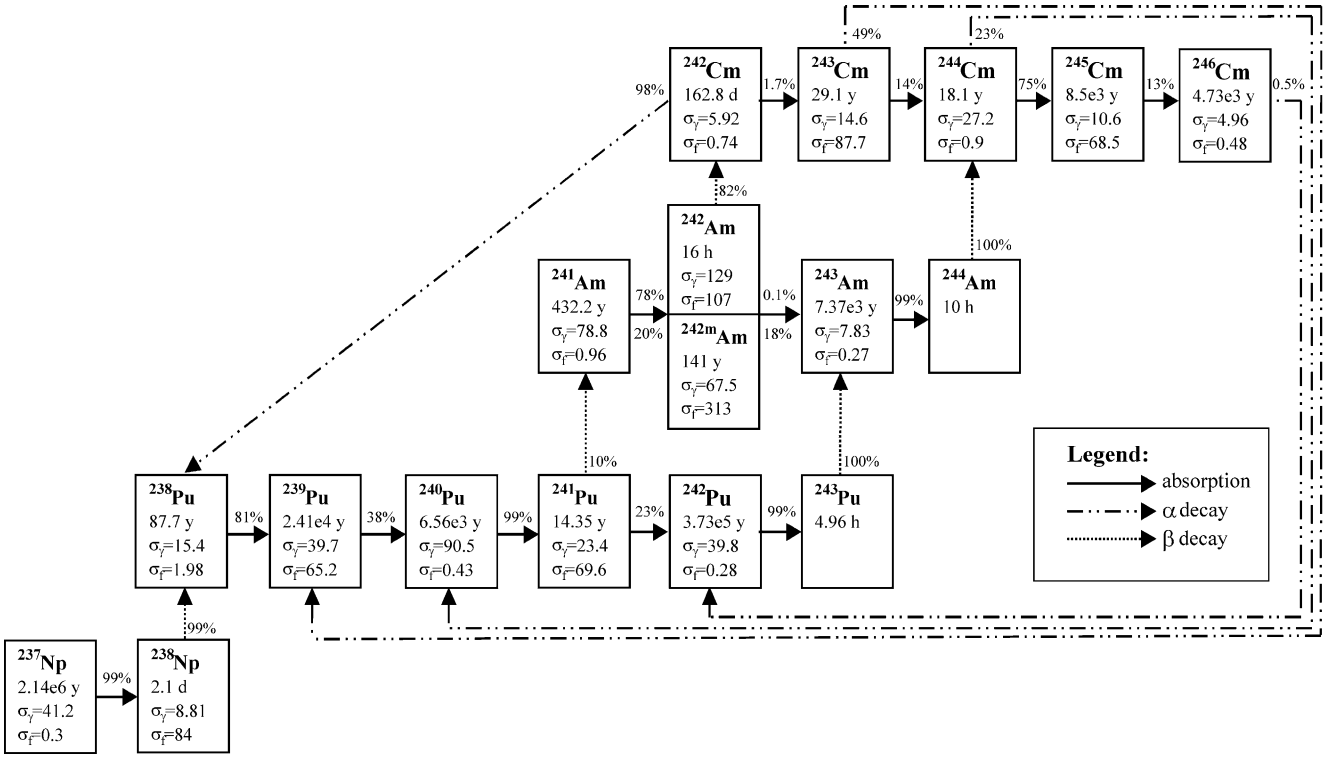

Fig. 15. ^{239}Pu transmutation chain. The second row of the boxes reports the half-life constant. The third and fourth rows report the one group effective cross sections for the neutron capture and fission calculated at the 12th year. The percentages are the relative reaction rates and sum up to 100% with fission probability and negligible reaction channels.

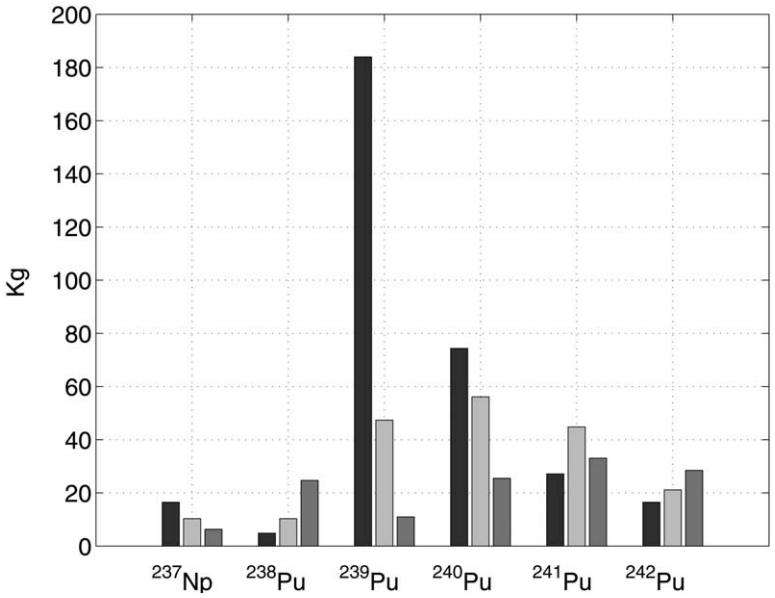

Fig. 16. Mass of the Actinides in the fresh DF in the inner ring at the beginning of the 12th year (left columns), in the spent DF in the outer ring at the end of the 11th year (middle columns) and residual mass in the spent TF in the outer ring at the end of the 12th year (right columns).

branches below 0.05% have been neglected as well as the α decay of ^{241}Am (0.5% branch producing ^{237}Np), which was not drawn just to simplify the scheme.

If we focus our attention to the 12th year, when fuel composition has reached the equilibrium in all the three rings, 74% of ^{239}Pu and 41% of all Pu in the input feed (fresh DF) have been destroyed (fissioned) in the DF irradiation. In the subsequent irradiation of the TF (produced from spent DF) destruction levels are pushed to 94% for ^{239}Pu and 61% for all Pu isotopes. These results are in line with expectations: Chudin (1999) calculated, from the experimental data of the DRAGON project, a value of 90% for the transmuted ^{239}Pu; in addition, Baxter and Rodriguez (2001) estimated, by the Monteburns code, a value of 57% for the destroyed Pu. Results compare very favorably also with the performance of pure Pu fueled LWRs, which can transmute 93% of ^{239}Pu in 4 years (Paratte and Chawla, 1995).

Fig. 16 illustrates the destruction of the Pu isotopes at equilibrium. The three columns for each isotope describe respectively the amount of the isotopes in fresh DF (input to the reactor), in the spent DF or equivalently in the fresh TF, and in the spent TF, the final residual waste discharged from the reactor. The effective destruction performance at equilibrium is therefore proportional to the ratio of the third to the first column for each isotope. The behavior of ^{241}Pu in Fig. 16 is anomalous, since it accumulates in DF whereas it is burned in TF. In fact, ^{241}Pu of fresh TF is three year old and it starts decaying since it has a half life of 14.3 years (Fig. 15). We can note in Fig. 16 that ^{238}Pu and ^{242}Pu accumulate instead of decreasing; in fact, these are low cross section isotopes produced according to the

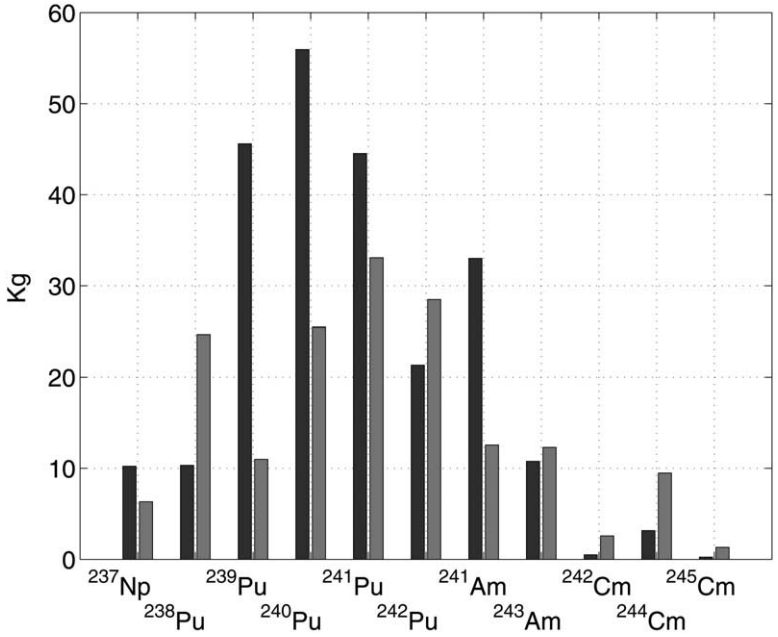

Fig. 17. Mass of the Actinides in the fresh TF in the inner ring at the beginning of the 12th year (left columns) and residual mass in the spent TF in the outer ring at the end of the 12th year (right columns).

schemes shown in Fig. 15. However ^{241}Pu and ^{238}Pu are "short lived" ($T_{1/2} = 14.3$ and 87.7 years, resp.) from the perspective of long term performance of the geological repository.

Fig. 17 describes the mass balance of TF and shows that the concentration of Cm increases. In fact, fresh TF contains 2.7 kg of Cm, whereas the spent TF contains 13.5 kg. ^{244}Cm accumulates due to double absorption of neutrons into ^{242}Pu (Fig. 15). None of the Cm isotopes has long-half life and therefore they do not pose risk to the geological repository performance especially if they are immobilized in the TRISO-particle fuel. However, Cm may pose problems with reprocessing of spent Driver Fuel and the manufacturing of TF.

The values of the middle columns in Fig. 16 correspond to the left columns of Fig. 17, since the spent DF in the outer ring at the end of the 11th year is processed to build fresh TF in the inner ring at the beginning of the 12th year.

Fig. 18 graphically illustrates the overall equilibrium mass balance. From 359 kg of Actinides loaded as fresh DF and set aside Am-Cm, we obtain 180 kg of fission products and 169 kg of Actinides (53% destruction rate), including only 11 kg of ^{239}Pu, mixed with other Pu-isotopes in a composition unusable for nuclear weapons purposes.

The value of the initial mass of fresh TF in Fig. 18 it is 236 kg; this value is 2 kg lower than the sum of the mass of spent DF in the outer ring at the end of the 12th year (202 kg, Fig. 18) and the set aside Am-Cm (36 kg, Fig. 18). This discrepancy is explained by the fact that fresh TF in the inner ring at the beginning of the 12th year

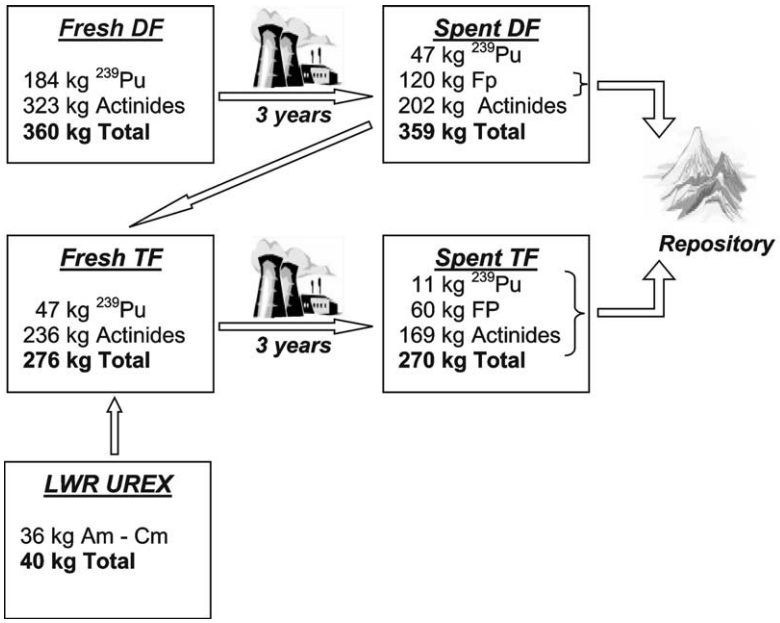

Fig. 18. Yearly mass flow of one module of the DB-MHR during the 12th year. The total mass takes into

Table 5
Composition of the 40 kg of set-aside $AmCmO_{1.7}$ from UREX that are added to spent DF in the manufacture of the fresh TF

Isotope	Atomic percentage
^{241}Am	30.35
^{242}Am	0.11
^{243}Am	5.45
^{244}Cm	1.06
^{245}Cm	0.07
^{16}O	62.96

comes from spent DF in the outer ring at the end of the 11th year (which is 2 kg lower than the mass of spent TF in the outer ring at the end of the 12th year). In fact, Fig. 13 shows that the mass of spent DF in the outer ring at the end of the 11th year is lower than that one at the 12th year.

7. Conclusions

A detailed simulation of the Deep Burn-Modular Helium Reactor has been performed using 3D Monte Carlo techniques with advanced burnup capabilities. The

operation of this reactor was modeled for deep burn of nuclear fuel manufactured from the LWR waste. Deep burn operation requires the use of driver and transmutation fuels. Starting with a fresh reactor core loaded with Actinides coming from the LWR waste, a strategy of reactor refueling and shuffling was simulated until equilibrium was established. We analyzed in detail the approach to equilibrium and equilibrium operation, which sets after 12 years.

The results of the analysis confirm the viability of the Deep Burn concept for effective destruction of LWRs wastes. k_{eff} evolution with 1 year refueling intervals should guarantee reactor operation with sufficient reactivity margins. Years 5 and 6 indicate a temporary slight shortage of reactivity that can easily be overcome with external means (e.g. slight modification of feed fuel—TF or DF). Equilibrium destruction rates for ^{239}Pu, overall Pu and all Actinides are respectively: 94%, 61% and 53%. The residual waste contains Pu in isotopic composition that does not raise proliferation concerns. Moreover, Am and Np content is significantly reduced by more than 50%. This performance depends on the chosen refueling intervals, and can be significantly improved, if desired. Buildup of ^{238}Pu and ^{244}Cm was observed, which requires further studies to investigate if it is necessary an intermediate storage of the spent TF. These are short-lived isotopes that do not contribute to degradation of repository performance and are effectively immobilized within the TRISO-particle residual waste.

References

A. Baxter and M. Fikani, 2002. Reactor-based transmutation—physics studies of the gas-cooled graphite-moderated deep burn reactor (GA-501-0-TRT-000140). General Atomics.

Baxter, A., Rodriguez, C., 2001. The application of gas-cooled reactor technologies to the transmutation of nuclear waste. Progress in Nuclear Energy 38, 81–105.

Baxter, A., Rodriguez, C., Venneri, F., 2001. Deep Burn MHR/A-based Transmutation of Nuclear Waste. Framatom presentation, Paris.

Briesmeister, J.F., 2002. A General Monte Carlo N-Particle Transport Code—version 4c (LA-13709-M, LANL).

Cetnar, J., Gudowski, W., Wallenius, J. Monte Carlo continuous energy burnup MCB1C—The description, methods and benchmarks. Nuclear Science and Engineering (in preparation).

Cetnar, J., Gudowski, W., Wallenius, J., 1999. MCB: A Continuous Energy Monte Carlo Burnup Simulation Code, in Actinide and Fission Product Partitioning and Transmutation (EUR 18898 EN, OECD/NEA 523).

Cetnar, J., Gudowski, W., Wallenius, J., Tucek, K., 2001. Simulation of nuclide transmutation with Monte-Carlo continuous energy burnup code (MCB1C). In: ANS Proc. on Accelerator Application and ADTTA 2001 Nuclear Application in the New Millennium, Reno.

Chudin, A., 1999. Potential for power utilization of weapons-grade plutonium in GT-MHR nuclear reactors. In: OECD Proceedings of the Conference on Survey on Basic Studies in the Field of High Temperature Engineering, Paris, pp. 79–88.

Fröhling, W., 1999. Courses and limitations of damage with air ingress accidents in HTR modules. In: OECD Proceedings of the Conference on Survey on Basic Studies in the Field of High Temperature Engineering, Paris, pp. 173–181.

Fukuda, K., Kashimura, S., Tobita, T., Kikuchi, T., 1995. Irradiation behavior of HTGR coated particle fuel at abnormally high temperature. Nuclear Engineering and Design 157, 221–230.

Gray, W.J., 1982. Radioactive Waste Management and the Nuclear Fuel Cycle 3, 137.

IANIS version 1.0 (Jef-2.2).

Kiryushin, A.I., Kodochigov, N.G., Kouzavkov, et al., 1997. Project of the GT-MHR high temperature helium reactor with gas turbine. Nuclear Engineering and Design 173, 119–129.

Knobloch, V., Nachmilner, L., 1994. High Level Radioactive Waste Management. In: Annual Conference of the ANS.

Kugeler, K. and Phlippen, P.W., 1999. Aspects of inherent safety of future high temperature reactors. In: OECD Proceedings of the Conference on Survey on Basic Studies in the Field of High Temperature Engineering, Paris, pp. 29–39.

Labar, M.P., Simon, W.A., 1994. Comparative Economics of the GT-MHR and Power Generation Alternatives (GA-A 21722), General Atomics.

Miller, G.K., Petti, D.A., Varacalle, D.J., Maki, J.T., 2001. Consideration of the effects on fuel particle behavior from shrinkage cracks in the inner pyrocarbon layer. Journal of Nuclear Materials 295, 205–212.

Minato, K., Fukuda, K., Sekino, H., et al., 1998. Deterioration of ZrC-coated fuel particle caused by failure of pyrolitic carbon layer. Journal of Nuclear Materials 252, 13–21.

Minato, K., Ogawa, T., et al., 1993. Release behavior of metallic fission products from HTGR fuel particles at 1600 and 1900 °C. Journal of Nuclear Materials 202, 47–53.

Minato, K., Ogawa, T., Fukuda, K., Sekino, H., Kitagawa, I., Mita, N., 1997. Fission product release from Zr-coated fuel particles during post-irradiation heating at 1800 and 2000 °C. Journal of Nuclear Materials 249, 142–149.

Minato, K., Ogawa, T., Sawa, K., et al., 2000a. Irradiation experiment on ZrC-coated particles for high temperature gas cooled reactors. Nuclear Technology 130.

Minato, K., Sawa, K., et al., 2000b. Fission product release behavior of individual coated fuel particles for HTGR. Nuclear Technology 131.

Nabielek, H., Schenk, W., Heit, W., Mehner, A.W., Goodin, D.T., 1989. The performance of HTR fuel particles at extreme temperatures. Nuclear Technology 84, 62–81.

Nakagawa, S., Saikusa, A., Kunitomi, K., 2001. Development of a simulation model and safety evaluation for a depressurization accident without reactor scram in an advanced HTGR. Nuclear Technology 133.

Nickel, H., Nabielek, H., et al., 2002. Long time experience with the development of HTR fuel elements in Germany. Nuclear Engineering and Design 217, 141–151.

Ohashi, K., Okamoto, F., Hayakawa, H., 2000. Modular High temperature reactor contributing the global environmental protection. Progress in Nuclear Energy 37, 307–312.

Paratte, J.M., Chawla, R., 1995. On the feasibility of LWR plutonium fuels without uranium. Annals of Nuclear Energy 22, 471–481.

Petti, D.A., Buongiorno, J., Maki, J.T., Miller, G.K., 2002. Key differences in the fabrication of US and German TRISO-coated particle fuel, and their implications on fuel performances. In: IAEA Proceedings of the Conference on High Temperature Reactors, Petten, Netherlands.

Richards, M.B., 1996. Disposition of spent fuel using the modular Helium reactor. Energy 21, 333–341.

Richards, M.B., 1995. A preferred RAPD-based strategy for permanent disposal of commercial LWR spent nuclear fuel. Energy 20, 811–822.

Schenk, W., Fröhling, W., Moormann, R., Nabielek, H., 1994. Simulation of Air Ingress with Irradiated Fuel Samples. In: Meeting on Validation of Predictive Methods for Fuel and Fission Product Behavior in Gas-cooled Reactors. JAERI, Tokai.

Trellue, Poston, 1999. User's Manual Version 2.0 for Monteburns, version 5B (LA-UR-99-4999, LANL).

US National Academy of Sciences, 1995a. Management Disposition of Excess Weapons Plutonium, Reactor-related Options. National Academy Press, Washington, DC.

US National Academy of Sciences, 1995b. Technical Basis for Yucca Mountain Standards. National Academy Press, Washington, DC.

US Nuclear Waste Technical Review Board, 1999. Report to the US Congress and the Secretary of Energy.

APPENDIX 6

Alberto Talamo and Waclaw Gudowski Studies of a Deep Burn Fuel Cycle for the Incineration of Military Plutonium in the GT-MHR using the Monte-Carlo Burnup Code, Int. ANS Conference PHYSOR 2004,Chicago, Illinois, April 25-29, 2004

PHYSOR 2004 – The Physics of Fuel Cycles and Advanced Nuclear Systems: Global Developments
Chicago, Illinois, April 25-29, 2004, on CD-ROM, American Nuclear Society, Lagrange Park, IL. (2004)

Studies of a Deep Burn Fuel Cycle for the Incineration of Military Plutonium in the GT-MHR using the Monte-Carlo Burnup Code

Alberto Talamo[♣] and Waclaw Gudowski
Department of Nuclear and Reactor Physics
Royal Institute of Technology,10044 Stockholm, Sweden

Abstract

The graphite moderated and helium cooled reactors may play an important role in the future development of nuclear energy because of their unbeatable benefits: passive safety mechanism, low cost, flexibility in the choice of fuel, high conversion energy efficiency, high burnup, more resistant fuel cladding (because of the TRISO particles) and low power density. General Atomic possesses a long time experience with this type of reactors and it has recently developed a design in which this type of reactor is structured into 4 modules of 600 MW_{th}: the Gas Turbine – Modular Helium Reactor (GT-MHR). Since the GT-MHR offers a rather large flexibility in the choice of fuel type, Th, U, and Pu may be used in the manufacture of fuel with a quite ample degree of freedom. As a consequence, the GT-MHR may operate for very different purposes: e.g. the reduction of waste production trough fuel cycles based on thorium, which is quite attractive proposal for countries which approach for the first time the market of nuclear energy, the transmutation of LWRs waste or military Pu.
In the previous studies we analyzed the behavior of the GT-MHR with a fuel built on LWRs waste; whereas, in the present studies we tried to focus on the incineration of military Pu. This choice of fuel requires a detailed numerical modeling of the reactor, since the pretty high value of k_{eff} at the beginning of the fuel cycle does not allow to neglect the control rods and burnable poison in the computing simulations. By contrast, when the reactor is fueled with LWRs waste the breeding of fissile isotopes, at the equilibrium of the fuel composition, keeps almost constant and close to the criticality the value of k_{eff}.

Keywords: GT-MHR, TRISO, military plutonium, MCNP, MCB, Deep Burn

[♣] Corresponding author, Tel. +46-8-55378204, E-mail: alby@neutron.kth.se

1. Introduction

In our previous [1-2] studies we demonstrated the capacity of the Gas Turbine Modular - Helium Reactor (GT-MHR) [3] to operate on a fuel cycle based on Light Water Reactors (LWRs) waste. It has been found that this reactor reaches the equilibrium of the fuel composition after 12 years of operation and the reduction of ^{239}Pu, Pu and all actinides reaches 94%, 61% and 53%, respectively. This good performance is a result of the *Deep Burn* fuel cycle strategy. This strategy is based on use of two types of fuels: a Driver Fuel (DF) and a Transmutation Fuel (TF). DF is maintaining the criticality of the reactor by the fission of fissile isotopes. TF "controls" reactivity of the reactor by the neutron capture of non-fissile actinide isotopes followed by fission or natural decay. In this scenario, the negative reactivity feedback offered by the TF allows the reactor to operate without burnable poisons. The outstanding capacity of TRISO particles to allow an irradiation time of over three years, because of a burnup limit of 700000 MWd, enables a fuel management strategy with 3 year fuel residency time. Initially, the reactor is loaded with the DF consisting of $NpPuO_{1.7}$, in an isotopic composition coming from the reprocessed LWRs waste. Then the TF consisting of irradiated DF plus some set-aside $AmCmO_{1.7}$, coming from the separation of the LWRs waste is loaded into the core. After 6 years of operation, the GT-MH Reactor is close to equilibrium and the reactivity margin is small enough [1, fig. 8] to neglect modeling of control rods in the numerical simulations.

2. Adapting the Deep Burn strategy to a military plutonium fuel cycle

In the present studies we tried to adopt the *Deep Burn* strategy to a fuel cycle based on military plutonium with 96% of ^{239}Pu. In this case, the irradiated DF is so rich in fissile isotopes that the TF cannot garantuee a negative reactivity feedback, and the presence of erbium as burnable poison is absolutely necessary for the reactivity safety reasons. At beginning of life (BoL) the fuel is composed of DF, consisting of fresh military plutonium; after an irradiation period of three years the fuel is reprocessed into Post Driver Fuel (PDF), with isotopic composition of the spent DF. To be compatible with our previous papers and with an established convention, we refer herewith to the TF as PDF and we assume that PDF actinide isotopic composition corresponds to the three year irradiated DF. However, the reactor requires the presence of erbium as burnable poison because the PDF is still a very "reactive" fuel due to the high residual ^{239}Pu content. Moreover, to ensure a proper reactivity management in this reactor core we introduced in the numerical calculations modeling of control rods.

3. The Gas Turbine – Modular Helium Reactor concept

In the GT-MHR, the fuel is disposed into 3 concentric rings of hexagonal blocks. The reactor is equipped with 12 startup control rods, 18 shutdown ones and 36 operational ones; we modeled all of them, but we used only the operational in the approach to the equilibrium of the fuel composition (fig. 1).

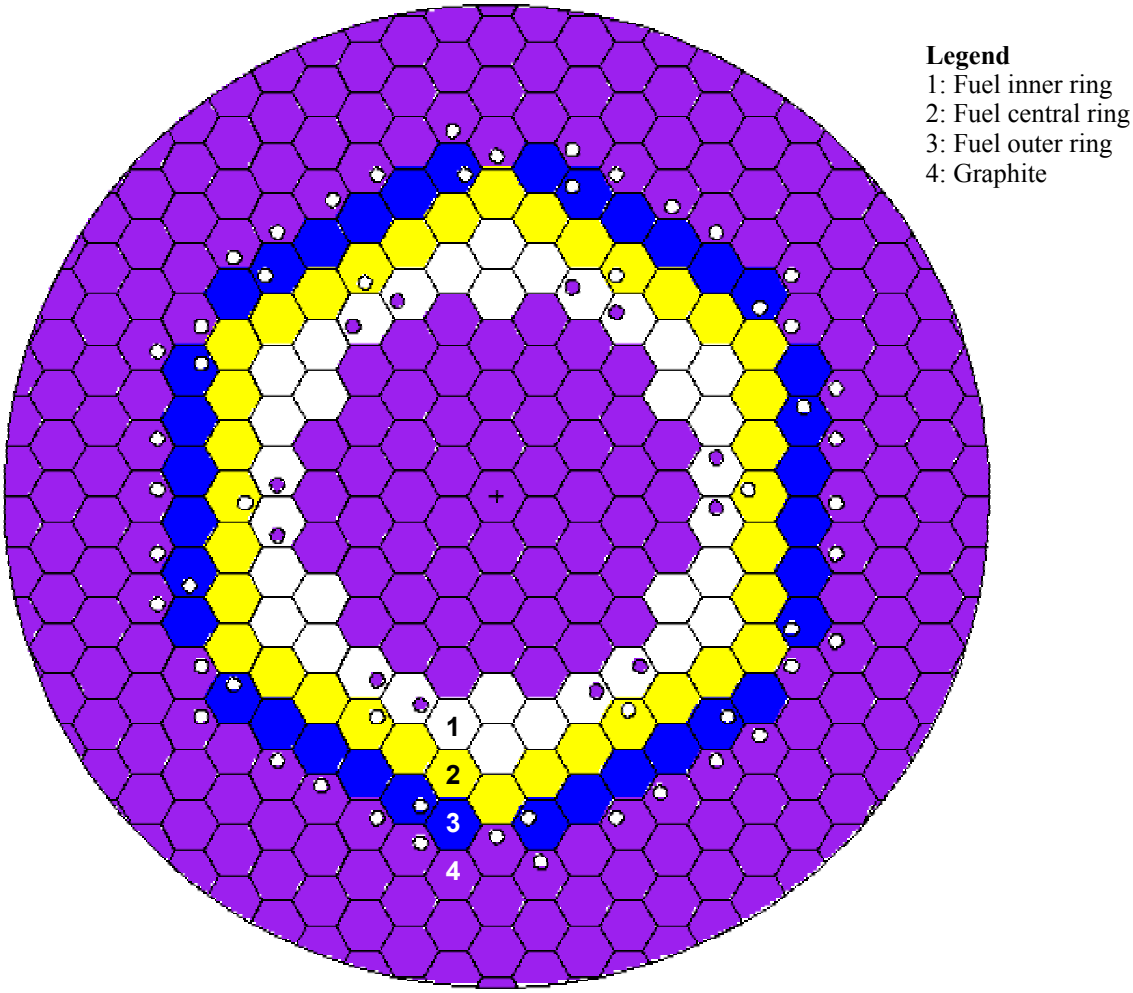

Figure 1: *GT-MHR core design. The inner ring of fuel (white) contains 12 startup control rods, the central (yellow) and outer ring (blue) respectively do 6 and 12 shutdown control rods, the outer graphite reflector ring does 36 operational control rods.*

Each control rod consists of a graphite matrix filled by TRISO particles of boron carbide. The burnable poison consists of 6 rods per hexagonal fuel block of erbium TRISO particles dispersed in a graphite matrix (fig 2). Each hexagonal fuel block of the GT-MHR contains 144 DF and 72 PDF pins in the case it is not equipped with control rods, otherwise it does 124 DF and 64 PDF pins.

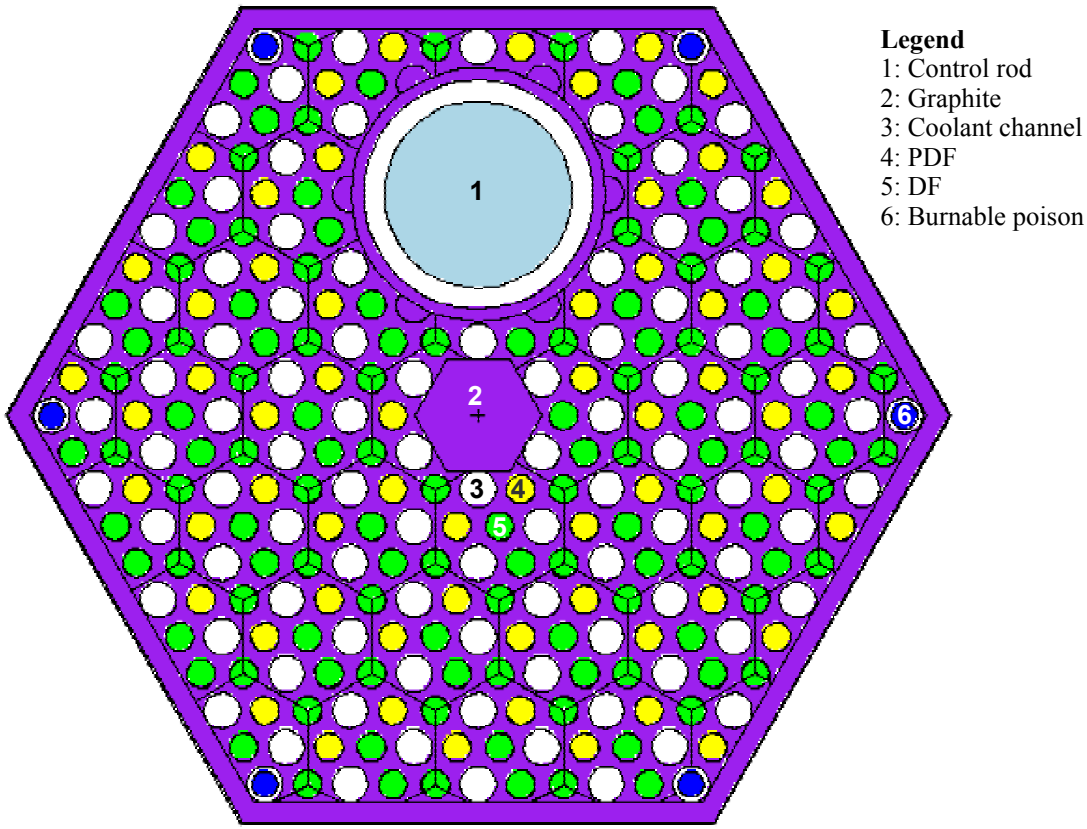

Figure 2: *Hexagonal fuel block. The graphite matrix contains 95 coolant channels (white), 124 DF pins (green), 62 DF pins (yellow), 6 burnable poison pins (blue) and 1 (startup/shutdown) control rod (light blue).*

The GT-MHR has been modeled with the MCNP/MCB codes [4-5] based on an original design of General Atomic (GA) [3]. Some important core parameters have been altered in order to optimize reactor performance. The radius and packing ratio of TRISO kernels for DF and PDF have been set equal, since we observed that this parameter does not affect significantly the averaged capture-to-fission ratio of fuel [2]. Moreover, we substituted the silicon carbide of TRISO particles with zirconium carbide (ZrC), since ZrC coated fuel resists higher temperatures in the case of accidental conditions. Finally, we replaced boron with erbium as burnable poison .
The geometry and material data of the GT-MHR are respectively shown in table I and II.

Table I: *Geometry data of the GT-MHR.*

Core – radius [cm]	350
Core – height [cm]	1000
Control rods – startup (inner ring)	12
Control rods – operational (outer moderator reflector ring)	36
Control rods – shutdown (central ring/outer ring)	6/12
Control rods – internal radius (startup/operational/shutdown) [cm]	0/2.64/0
Control rods – external radius [cm]	4.13
Control rods – hole radius [cm]	5.05
Control rods – distance from the center of the hexagon [cm]	9.75614
Control rods – height at bol (startup/operational/shutdown) [cm]	0/647/0
Hexagonal fuel blocks – number	36x3
Hexagonal fuel blocks – side [cm]	17.99844
Hexagonal fuel blocks – height [cm]	793
Hexagonal blocks – interstitial gap [cm]	0.1
Fuel blocks – DF pins (with control rod/without control rod)	140/124
Fuel blocks – PDF pins (with control rod/without control rod)	70/62
Fuel blocks – burnable poison pins	6
Fuel blocks – coolant channels (with control rod/without control rod)	108/95
Pins – radius (fuel/burnable poison) [cm]	0.6223/0.5715
Pins – distance between pins [cm]	3.25628
Pins – hole radius (fuel/coolant channel/burnable poison) [cm]	0.635/0.795/0.795
Pins – height [cm]	793
TRISO particles – kernel radius (DF/burnable poison) [cm]	0.015/0.035
TRISO particles – width porous carbon layer (DF/burnable poison) [cm]	0.015/0.0025
TRISO particles – width inner pyrocarbon layer (DF/ burnable poison) [cm]	0.0035/0.0035
TRISO particles – width ZrC layer (DF) [cm]	0.0035
TRISO particles – width outer pyrocarbon layer (DF) [cm]	0.0040
TRISO particles – distance between particles [cm]	0.0794138

Table II: *Material data of the GT-MHR.*

Material	***Atomic percentage***	***Density at BoL [g/cm^3]***
TRISO $PuO_{1.7}$	^{239}Pu (34.83%) ; ^{240}Pu (2.21%) ; ^{16}O (62.96%)	10.2
TRISO porous graphite	C (100%)	1
TRISO pyrocarbon	C (100%)	1.85
TRISO ZrC	Zr (50%) ; C (50%)	6.56
Graphite	C (100%)	1.74
Control rods (B_4C)	^{10}B (72%) ; ^{11}B (8%) ; ^{16}O (20%)	2.47
Burnable poison (Er_2O_3)	^{166}Er (23.77%) ; ^{167}Er (16.23%) ; ^{16}O (60%)	4.89

4. The approach to equilibrium

The fuel cycle adopted for this reactor concept has a residency time of 3 years, with a refueling and shuffling period of one year. At BoL and after each refueling of the reactor, the central ring is loaded with fresh DF. At the beginning of the 2nd year, the one year irradiated DF is moved from the central ring into the inner one. At the beginning of the 3rd year, the one year irradiated fuel of the central ring is shuffled into the outer ring and this operation repeats in the following years; the inner ring retains its DF. At the beginning of the 4th year, the 3 year irradiated DF of the inner ring becomes PDF and fills the central ring together with fresh DF; the two years irradiated DF from the outer ring moves into the inner one and this operation repeats in the following years. At the beginning of the 5th year the inner ring is filled with PDF from its 3 year irradiated DF; the central ring retains its PDF. At the beginning of the 6th year, the inner ring keeps its PDF; the central ring also keeps its PDF; the outer ring loads with the PDF from the three years irradiated DF of the inner ring. In the following years the reactor operates with the same configuration of the 6th year; therefore, after the 6th year the shuffling policy assumes the following permutations:

- DF inner ring $\Rightarrow$ DF outer ring.
- DF central ring $\Rightarrow$ Fresh fuel
- DF outer ring $\Rightarrow$ DF central ring
- PDF inner ring $\Rightarrow$ PDF outer ring
- PDF central ring $\Rightarrow$ PDF inner ring
- PDF outer ring $\Rightarrow$ DF inner ring

The detailed description of the refueling and shuffling strategy during the first 6 years is shown in fig. 3.

Concerning the management of control materials, we applied a residency time of 6 years for the control rods and 1 year for the burnable poison.

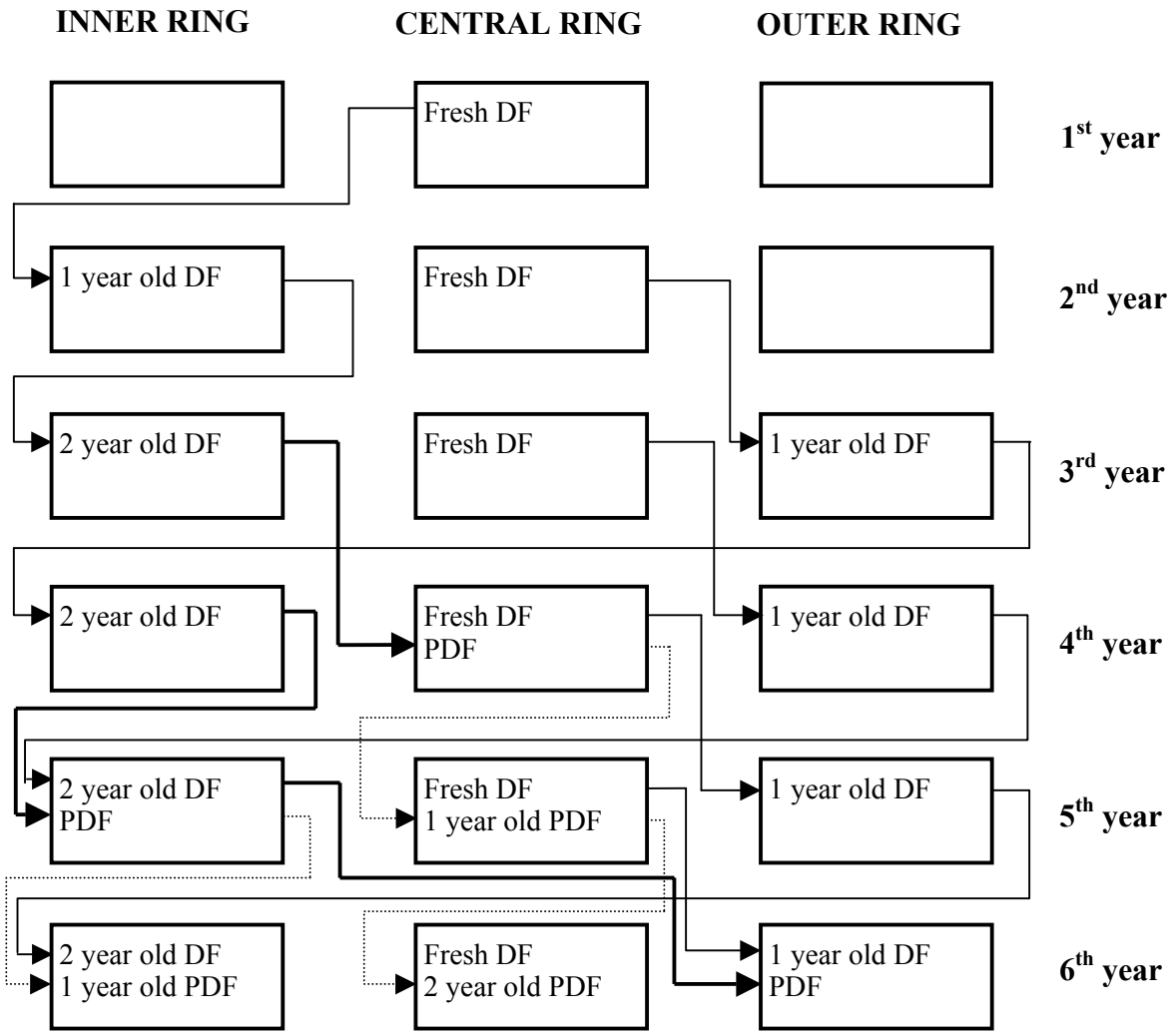

Figure 3: *Refueling and shuffling schedule during the first 6 years.*

5. The incineration of military plutonium

Fig. 4 shows the values of k_{eff} starting from the BoL up to the equilibrium 12th year. Blue color indicates the beginning of each year, read color does its corresponding end. During the first 2 years not all 3 rings are loaded with fuel, therefore the total amount of burnable

poison is lower and consequently k_{eff} of "reactive" load is higher. The initial k_{eff} value at the first year is lower than that one at the second because fuel is loaded only in one ring. At third year, k_{eff} drops down as a combined effect of burnup and burnable poison content. Since the third year of operation, the k_{eff} values smoothly increases to the asymptotic value as a result of the fuel management strategy. The subcritical value of k_{eff} at the end of the 3rd year can be easily adjusted by the withdrawn of the operational control rods, which cover only 647 cm of the available 793 cm.

During all simulation steps control rods were kept at the constant position in the reactor (see Table I) core leaving the sufficient margins for reactivity compensations, particularly at 3rd year of operation.

After an irradiation of three years, the GT-MHR transmutes about 66% of the ^{239}Pu mass of the DF (fig. 5); at the same time, the fraction of ^{240}Pu accumulates and a small quantity of ^{241}Pu builds up; whereas, the production of ^{242}Pu and ^{241}Am remains limited to a few kilograms.

Since 50% of the mass of the irradiated DF becomes PDF the right columns of fig. 6 are equal to the left ones of fig. 5 divided by 2. In the irradiation of PDF the concentration of ^{239}Pu and ^{240}Pu respectively diminishes 75% and 53%. Among the isotopes of the spent PDF, ^{238}Pu and ^{241}Pu decay within few hundreds of years and therefore they do not pose any risk for the safety of the geological repository. In addition, the residual quantities of Am and Cm isotopes are so small that they do not arise particular problems in the managing of the spent PDF comparing to that one of LWRs waste; also ^{242}Pu production is quite moderated (about 5 kg).

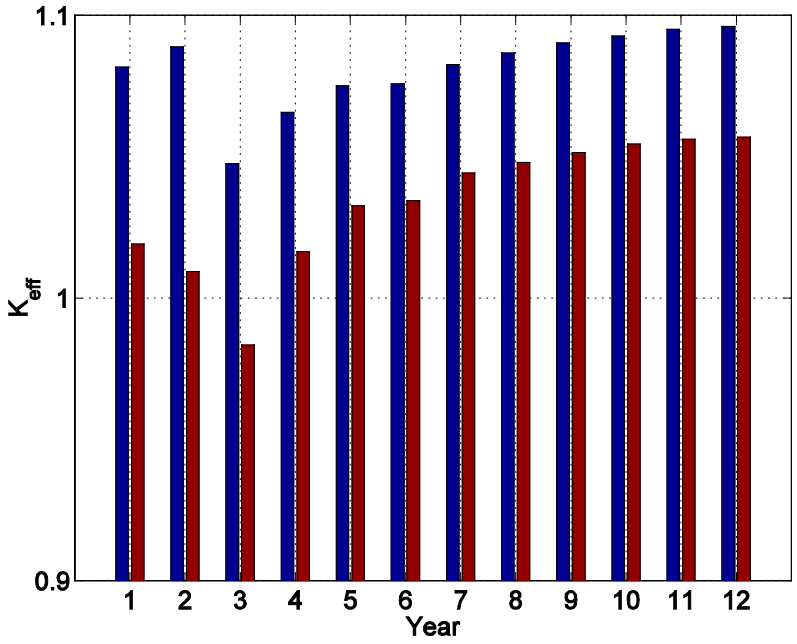

Figure 4: *Evolution of k_{eff} during the first 12 years. All values have a relative standard deviation lower than 0.06%.*

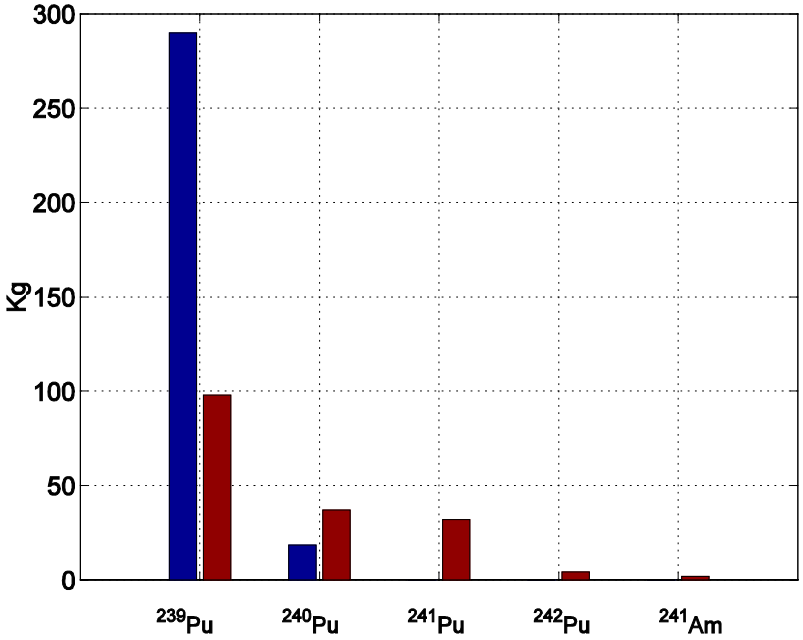

Figure 5: *Mass of the most abundant actinides of the fresh DF (central ring at beginning of the 12th year) and after three years irradiation (inner ring at the end of the 12th year).*

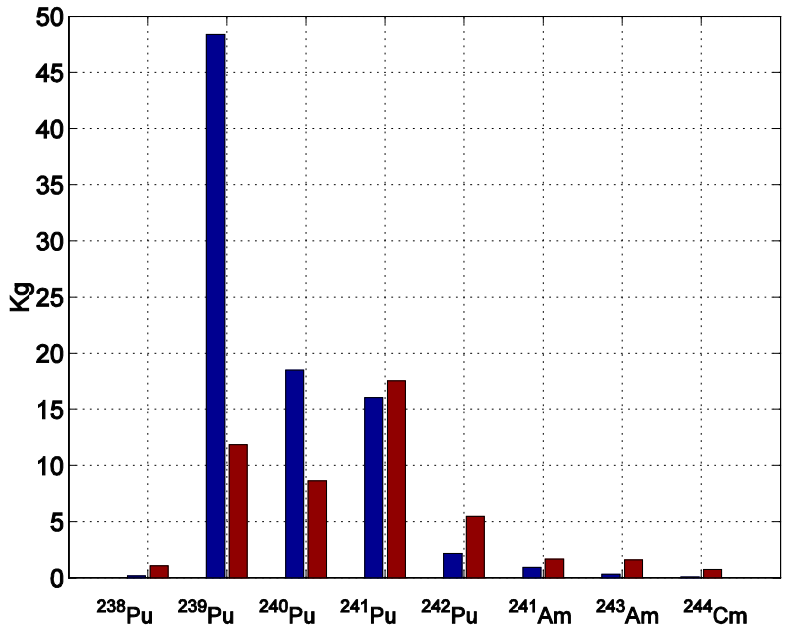

Figure 6: *Mass of the most abundant actinides of the fresh PDF (outer ring at beginning of the 12th year) and after three years irradiation (central ring at the end of the 12th year).*

6. Conclusions

The adapting of the Deep Burn strategy to a fuel cycle based on military plutonium forces to use erbium as burnable poison; in addition, the numerical simulations must include the modeling of control rods because of the high initial reactivity of the reactor.
The GT-MHR loaded with military plutonium has proved to satisfy the k_{eff} constraints during the approach to equilibrium.
The mass flow of the GT-MHR fueled by military plutonium at the equilibrium of the fuel composition shows that 66% of ^{239}Pu is burned in three years and 92% in six years. The radiotoxicity of the fission products equals the level of natural uranium after few hundreds of years leaving in the long run the ^{239}Pu as the major contributor to the radiotoxicity PDF waste. Nevertheless, the ^{239}Pu extraction from the spent PDF for military purposes poses some technological problems since it would be necessary to process over 10^{10} TRISO particles to reach the critical mass of ^{239}Pu. Finally, the spent PDF constitutes a safe form of waste because the TRISO particles have proven to keep intact for hundreds of thousands years, even if they would permanently be flooded with groundwater.

REFERENCES

[1] A. Talamo, W. Gudowski et al., *The burnup capabilities of the Deep Burn Modular Helium Reactor analyzed by the Monte Carlo Continuous Energy Code MCB*. Annals of Nuclear Energy 31/2 pp. 173-196, 2004.

[2] A. Talamo, W. Gudowski, J. Cetnar and F. Venneri. *Neutron flux, spectrum, capture to fission ratio and temperature coefficients of the Beep Burn Modular Helium Reactor fed by LWRs waste.* Submitted for publication in the Annals of Nuclear Energy.

[3] General Atomic. *GT-MHR conceptual design description report*, US Nuclear Regulatory Commission, GA/NRC-337-02, 2002.

[4] J. Cetnar, W. Gudowski, J. Wallenius and K. Tucek. *Simulation of nuclide transmutation with Monte-Carlo Continuous Energy Burnup Code (MCB1C)*. Proc. Accelerator application 2001 and ADTTA 2001 Nuclear application in the new millennium, Reno, U.S.A. (2001).

[5] J. Cetnar, W. Gudowski and J. Wallenius. *MCB : a continuous energy Monte Carlo burnup simulation code, in actinide and fission product partitioning and transmutation*. EUR 18898 EN, OECD/NEA 523 (1999).

APPENDIX 7

M. Jolkkonen, M. Streit and J. Wallenius, “Thermo-chemical modelling of uranium-free nitride fuels. “, J. Nucl. Sci. Technol. 41 (4), p.457-465 (April 2004)

Journal of NUCLEAR SCIENCE and TECHNOLOGY, Vol. 41, No. 4, p. 457–465 (April 2004)

ORIGINAL PAPER

Thermo-chemical Modelling of Uranium-free Nitride Fuels

Mikael JOLKKONEN[1,*,†], Marco STREIT[2] and Janne WALLENIUS[1]

[1]*Royal Institute of Technology, Department of Nuclear and Reactor Physics, 106 91 Stockholm, Sweden*
[2]*Paul-Scherrer-Institut, 5232 Villigen PSI, Switzerland*

(Received October 10, 2003 and accepted December 22, 2003)

A production process for americium-bearing, uranium-free nitride fuels was modelled using the newly developed ALCHYMY thermochemical database. The results suggested that the practical difficulties with yield and purity are of a kinetic rather than a thermodynamical nature. We predict that the immediate product of the typical decarburisation step is not methane, but hydrogen cyanide. HCN may then undergo further reactions upon cooling, explaining the difficulty in observing any carbophoric molecules in the gaseous off stream. The thermal stability of nitride fuels in different environments was also estimated. We show that sintering of nitride compounds containing americium should be performed under nitrogen atmosphere in order to the avoid the excessive losses of americium reported from sintering under inert gas. Addition of nitrogen in small amounts to fuel pin filling gas also appears to significantly improve the in-pile stability of transuranium nitride fuels.

KEYWORDS: thermo-chemical modelling, minor actinides, uranium-free nitride fuels, carbothermic nitridation, decarburisation, thermal stability, accelerator-driven systems

I. Introduction

Several fuel types have been suggested for the reduction of nuclear waste by transmutation of plutonium and minor actinides. One of the most promising is a mixture of transuranium mononitrides and zirconium mononitride, forming a homogenous solid solution over a wide range of temperatures and compositions. The main advantage of this fuel is its good thermal conductivity combined with a high melting temperature, yielding high power to melt. The dissolution of spent uranium-free nitride fuel in nitric acid is also much easier than for the corresponding oxides. There have, however, been some safety concerns regarding the possible decomposition of nitride into metal and nitrogen gas at elevated temperatures.[1,2] Furthermore, a cost penalty is imposed by the need to use ^{15}N for fabrication of the fuel, in order to avoid excessive in-pile production of ^{14}C.[3]

Fabrication of uranium-free nitride fuels has been done only on a small scale and experience in this field is limited. Only a few laboratories are equipped to handle americium in gram amounts, and the conversion process from metal or oxide feed streams sets further constraints on what can be performed in these facilities. In particular, loss of americium during carbothermic reduction of oxides has been shown to occur at temperatures typical for the fabrication process.[4–6] Considering that americium-bearing nitride fuels are planned to be irradiated in the Advanced Test Reactor in Idaho, as well as in Phenix, there is a need for optimisation of the fabrication process.[7] Consequently, we have developed a computer model for the evaluation of production processes and identification of suitable conditions for the thermochemical reactions involved. In the present report, we describe the findings from modelling of carbothermic nitridation of oxides as well as the stability of the resulting nitrides at conditions relevant for sintering and irradiation. The thermochemical database ALCHYMY was developed for this particular task, and was applied in calculations using the Thermo–Calc package. The approach we have used is generic, and we expect that the database can be applied to modelling of oxide and carbide fuels as well.

In this paper we give a brief introduction to Thermo–Calc and to the approach used when building ALCHYMY. The methods for simulating nitride fuel production and behaviour are described in some detail. Then we present an evaluation of and some recommendations for the carbothermic nitridation process. Finally we show how the high temperature stability of PuN and AmN can be improved by adjusting the composition of the gas used for sintering and/or pin filling.

II. Software

1. The Thermo–Calc Package

Thermo–Calc is a well-established commercial software package for the calculation of chemical equilibria, diffusion and phase diagrams.[8] Using a database, wherein the thermochemical properties of selected elements, compounds and phases are expressed in mathematical form, the code can calculate the state that yields the lowest global Gibbs energy by, figuratively speaking, reducing the system to its constituent atoms and finding the energetically most favourable way of putting them together again. Although there are some ''universal'' databases for general chemistry, the more advanced databases focus on a selection of substances relevant for a particular field in research or industry. Such databases exist also for nuclear materials, but they contain no data on the minor actinides. We have therefore built our own database, ALCHYMY, especially adapted for uranium-free fuels. ALCHYMY covers the essential metal phases, oxides, nitrides and carbides of Pu, Am, Np and Zr, as far as these

*Corresponding author: Tel. +46-08-5537 8792, Fax: +46-08-5537 8465, E-mail: jolkkonen@neutron.kth.se
†Present address: *Department of Nuclear and Reactor Physics, KTH, SE-106 91 Stockholm, Sweden*

are known. There is also data on the elemental forms and many common compounds of H, C, N and O, and He for use as inert gas.

2. The ALCHYMY Database

All thermochemical data used in ALCHYMY was collected from freely available sources such as printed scientific tables, monographs, journal articles and electronically published public databases. All references are listed in the ALCHYMY database itself. The polynomials contained in ALCHYMY share certain basic features, such as using only integer powers and natural logarithms of the temperature variable, a form resulting from the integration of Maier–Kelley-type polynomial expressions for the temperature dependence of heat capacity. Some of the used sources already express the Gibbs energy as a function of temperature. More often the starting point was the heat capacity expressed as some variant of the Maier–Kelley polynomial. This was combined with values for the enthalpy and entropy to construct the Gibbs energy function. For instance, all expressions for americium oxides were built in this way from values published in printed form, and those for compounds of neptunium from data available at the OECD/NEA Thermochemical Data Base (TDB) Project.[9,10] In cases where experimental determinations of the heat capacity were tabulated with sufficient accuracy, corresponding polynomial functions were constructed in Mathematica and critically compared and evaluated. In yet other cases, it was possible to use combinations of functions and/or tabulated values to arrive at the desired function. When using such combinatory methods, efforts were made to avoid mixing data from different sources. When necessary, the required thermodynamical quantities were constructed from the thermodynamical parameters of formation by adding the corresponding values for the constituent elements. This method admittedly involves combining data from different sources, but since there is nearly universal agreement on the thermodynamical properties of the elements it should not increase the uncertainty of the result. This method was for instance used with AmN, where the ΔG_f function had been experimentally estimated from the vapour pressure over a dilute solid solution of AmN in PuN, and for Am_2C_3, where estimated ΔG_f values had been published in tabulated form.[4,11] Special attention was given to avoid any discontinuities where the Gibbs energy is expressed with a series of overlapping functions for different temperature intervals.

In a few cases where it proved impossible to get trustworthy data for a substance of phase we chose to exclude it from the database rather than to risk that it is erroneously reported to appear in a reaction. Examples of such substances are molten actinide carbides and the gaseous forms of many metal oxides. For this reason, some substances may remain in solid (or liquid) form at temperatures above their melting (boiling) points. This was not deemed a serious problem at temperatures typical for fuel production. Solid plutonium monoxide, for which data is reported in many thermochemical works, was excluded on the grounds that it probably does not exist at all.[9,12] Other, empirically established compounds that represent gradually interchanging hypo- and hyperstoichiometric forms resulting from disproportionation or the preferential loss of one element, are for practical reasons represented by the stoichiometric compounds or a fixed non-stoichiometric composition.

The ALCHYMY database will be distributed free of charge through KTH, NEA and Thermo–Calc Software AB.

3. Model Design

We have performed two main types of simulations, a single-equilibrium setup corresponding to a closed vessel and a multi-segment setup mimicking a gas-flow furnace. The single-equilibrium setup is simple, with a fixed content and no gas-exchange but unrestricted heat-exchange with the surroundings (the system remains at a pre-defined temperature). It is especially suitable for modelling of closed systems such as sealed crucibles or welded fuel pins, but an open system can be simulated by making the gas phase very large, leading to a high degree of dilution of gaseous reaction products and near constant composition of the gas phase. With this setup it is easy to follow the mass balance of the reaction, since all material is retained. One deviation from most ''real'' cases is that the pressure is assumed to be constant, as if the volume of the system would accommodate to the production or consumption of gas.

The multi-segment setup, which utilises the REACTOR module included in the Thermo–Calc package, is a more complicated, iterative model where the ''system'' is carried through a number of discrete segments with optional addition and/or removal of heat and gasses (**Fig. 1**). A new ther-

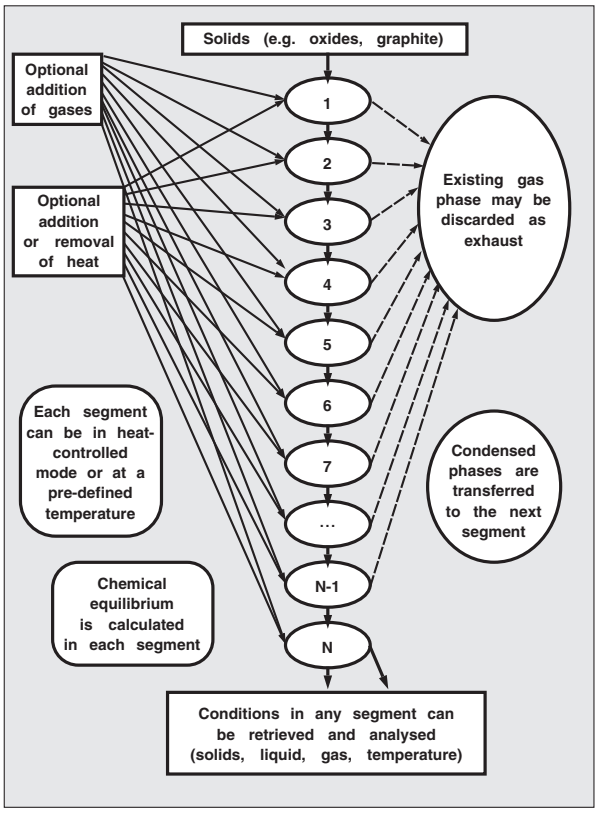

Fig. 1 Schematic representation of a generic multi-stage model for use with the REACTOR module of Thermo–Calc

mochemical equilibrium is calculated in each segment, whereupon the products move on to the next segment, with or without exchange of the gas phase. This rather well emulates the conditions when a flow of gas or liquid is passed through an stationary solid phase, and can be adapted to many different processes by creative designation of ''solid'' and ''gas'' phases.

4. Limitations

The ALCHYMY/Thermo–Calc model predicts the thermodynamical equilibrium in an idealised and abstract system without a time or length scale. Consequently kinetic factors, such as reaction barriers or diffusion rates, and spatial factors, such as distances, particle sizes, interfaces, mixing *etc.* are not taken into consideration. The model presently does not correct for concentration-dependent changes in stability and chemical potential in solid solutions, but treats all the components as pure substances.

Hence, one can expect a certain discrepancy between the model and experimental findings especially in the case of solid reactant mixtures, where inter-particle contact and diffusion rates may be severely limiting factors. Also reactions reported during cooling must be critically evaluated, since the reaction rates may be effectively zero at low temperatures. The same will be true for metastable phases at higher temperatures.

III. Modelling of Nitride Fuels

1. Production of Mixed Nitride: Methods

A model for the production of (Am,Np,Pu,Zr)N fuel was constructed, largely based on the combined nitridation-decarburisation procedure used at PSI for the production of (Pu,Zr)N pellets by a conventional powder-pressing route.[13] Briefly, the corresponding oxides are reduced with graphite and simultaneously reacted with a stream of N_2 at a temperature between 1,500 and 2,000 K, following the overall reaction formula

$$2\ MeO_2 + 4\ C + N_2 \rightarrow 2\ MeN + 4\ CO, \qquad (1)$$

where MeO_2 represents ZrO_2 in mixture with any or all of the oxides AmO_2, NpO_2 and PuO_2.

Experience has shown that using equimolar amounts of carbon and oxygen results in incomplete reduction of the oxide as well as some residual carbon in the form of carbonitride.[5,14] It is therefore customary to use an excess of graphite to eliminate as much of the oxygen as possible, and add a subsequent decarburisation step in which surplus carbon is removed.[15] For this purpose the gas stream is, after about 24 h, changed from pure N_2 to 7% H_2 in either N_2 or argon. The residual graphite and carbonitride then react with the hydrogen gas forming volatile compounds by one or several paths which will be discussed in detail in Chap. V of this paper.

The model consists of 20 consecutive segments, or separate calculations of equilibrium, having different, pre-determined temperatures and independently defined gas feed. The solids resulting from the nitridation part (first 10 segments) were fed directly into the decarburisation part (last 10 segments). In this study the proportions of reactants were kept fixed while variations in the temperature profile of the process were simulated.

The starting material included one mole of dioxides in the proportions ($Am_{0.20}Np_{0.04}Pu_{0.16}Zr_{0.60}$), which is representative for JAERI's minor actinide burner concept, *i.e.* including 40% Pu in the actinide vector in order to minimise the reactivity swing.[16] Two point three moles of graphite was present as reducing agent, which represents a 0.3 mol excess over oxygen. The total amount of gas passed through the materials was 200 moles, evenly divided over the 20 segments, and is on the same scale with the amount used at PSI. Consequently at each nitridation segment there was 10 moles of pure N_2, which represents a 20 times excess of nitrogen over metal in reaction (1).

The effects of different blanket gas during decarburisation were compared, using 7% H_2 in N_2 as well as 7% H_2 in inert gas, here represented by helium.

The model discards the gas phase after each segment and adds new gas in the following one. This setup mimics the gas-flow furnaces used in production: it prevents the back-reaction of previously formed carbon oxides to form metal carbides, it illustrates the losses through evaporation of volatile actinides like americium, and it keeps the gas phase at nominal composition.

To further emulate the production methods in use, segment 1 was designed to represent the warming-up stage (1,000 K), segment 20 was reserved for cooling of the product (typically to 1,200 or 300 K), and the temperature profile during nitridation always included a 200 K increase in temperature after segment 6. Thus there were three independent temperature variables determining the nitridation, decarburisation and cooling conditions (**Fig. 2**). The composition reported at segments 10 and 19 were plotted as representing the resulting product from nitridation and decarburisation, respectively. Furthermore, information on the gaseous products of decarburisation was obtained from segment 11. 25 to 35 process temperatures were simulated for each series of data.

2. Thermal Stability: Methods

After pressing of nitride powder or microspheres, ''green

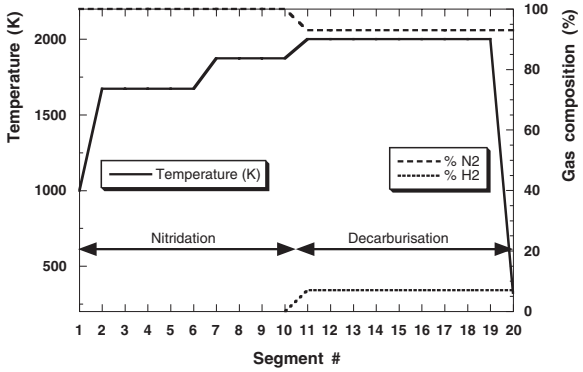

Fig. 2 Variables and breakpoints for modelling of the nitridation-decarburisation process. This sample profile shows conditions leading to high yield and purity of the product in our model

pellets'' with a density of 65 to 75% of the theoretical density is usually obtained. Sintering is performed at high temperature ($T > 2,000$ K) in order to achieve the 15–20% porosity recommended for nitride fuels.[17] However, metal nitrides tend to dissociate at the temperatures used, and volatile elements may evaporate:

$$2\ \mathrm{MeN}\ (\mathrm{s}) \rightarrow \mathrm{N_2}\ (\mathrm{g}) + 2\ \mathrm{Me}\ (\mathrm{l,g}). \quad (2)$$

Keeping Guldberg–Waage's law in mind, it is obvious that this process is counteracted by increasing the concentrations of N_2 and metal vapour. To increase the stability of *e.g.* AmN, one may thus use a nitrogen atmosphere during sintering. Any liquid americium metal formed will then not be thermodynamically stable (unless at very high temperatures) and will immediately revert to nitride. Similarly, there will always be a small partial pressure of Am vapour above the AmN surface. If this vapour is transported away, more nitride will dissociate. From this point of view the gas exchange should be kept at a minimum. Yet the importance of the gas phase has not always been properly appreciated. There are many reports of sintering under noble gas, and unsurprisingly these often describe serious problems with material loss. This practice probably originated as a precaution against the formation of higher nitrides during cooling down (K. Chidester, private communication), a phenomenon seen with uranium nitrides but not relevant for the uranium-free fuels discussed here.[18,19]

We set out to investigate how the vaporisation of AmN and PuN depends on the temperature and gas environment. For this purpose we used a single-equilibrium setup with a large amount of gas, to simulate a moderately ventilated sintering furnace in an atmosphere of pure inert gas (represented by helium) or pure nitrogen. The modelled system contained 100 moles of gas and 1 mole nitride of the composition $(Am_{0.24}Pu_{0.16}Zr_{0.60})N$, which corresponds to the nitride fuel suggested for dedicated minor actinide burners in Europe.[20] Twenty-three separate equilibria were determined between 1,000 and 2,350 K for each series of data.

The heat stability of nitride fuels, and especially fuels containing americium, is of central importance also in the reactor core. The conclusions drawn above, namely that the stability of the nitride is enhanced in a nitrogen environment, should also be applicable in the fuel pin, with some modifications due to the reversed proportions of the nitride and the gas phase.

In fast reactor fuel pins the plenum is dimensioned to accomodate fission gases that are released from the fuel. The volume of the bonding gas (He) is similar to that of the nitride fuel pellets, but since the standard molar volume of a gas is about three orders of magnitude larger than that of a simple solid, the amount of gas is very small compared to that of nitride.

Uranium-free fuels intended for use in accelerator-driven systems feature special safety issues, since Doppler feedback is not sufficient to counteract events like Unprotected Loss of Flow (ULOF) and Accelerator Transient Over Power (ATOP). Therefore the failure margin needs to be greater than for FBR fuels.

It has been suggested that nitride fuel in nitrogen-bonded fuel pins might exhibit improved heat tolerance.[21] It would, however, be unrealistic to fill fuel pins with pure nitrogen, which has six times lower thermal conductivity than helium, but a minute admixture of nitrogen could stabilise the fuel without noticeably impairing heat transfer.

To investigate this idea, we again modelled the heating of 1 mole of the $(Am_{0.24}Pu_{0.16}Zr_{0.60})N$ fuel, this time with only 0.001 moles of gas, in a single-equilibrium setup and compared the behaviour in pure helium with that in a mixture of 1% nitrogen in helium. This is a much simplified model of a fuel pin, as it assumes constant pressure, uniform fuel temperature and no condensation on cold surfaces such as the inside of the cladding. While the results obviously should not be taken too literally, the general trends should be rather reliable. 21 separate equilibria were determined between 1,000 and 2,000 K for each series.

IV. Results

1. Production of Mixed Nitride: Observations

A separate study of the nitridation step was performed to determine a suitable temperature for the initial step, the conversion of oxides to nitrides. Following the earlier described temperature profile, our model reports the best results, virtually quantitative conversion and yield, to occur with final temperatures of 1,800 to 1,950 K (**Fig. 3**). In other words, the method used at PSI (end temperature 1,873 K) appears nearly optimal in this respect, even when the material contains not only zirconium and plutonium but also neptunium and americium, whose compounds all have different formation and dissociation temperatures.

Hence this part of the temperature profile was fixed (Segment 1: 1,000 K, 2–6: 1,673 K, 7–10: 1,873 K) while the decarburisation temperature (segment 11–19) was varied between 1,300 and 3,000 K. Decarburisation was modelled in two different atmospheres: 93% inert gas (He) with 7% H_2, and 93% N_2 with 7% H_2.

In a nitrogen environment, graphite did not react with the other solids and at temperatures above 1,800 K it was elim-

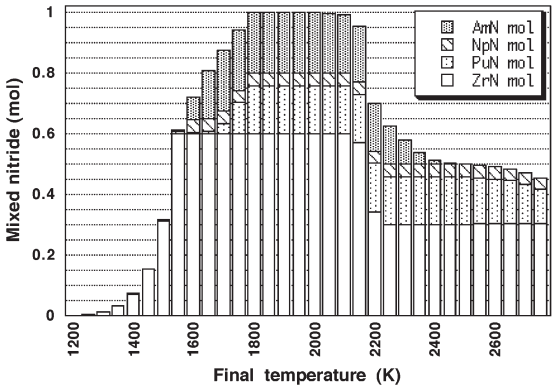

Fig. 3 Outcome of carbothermic nitridation at different temperatures

The graph shows the conditions at the last of ten reaction segments with the respective temperatures: Seg. 1, 1,000 K; Seg. 2–6, 200 K below final temperature; Seg. 7–10, final temperature.

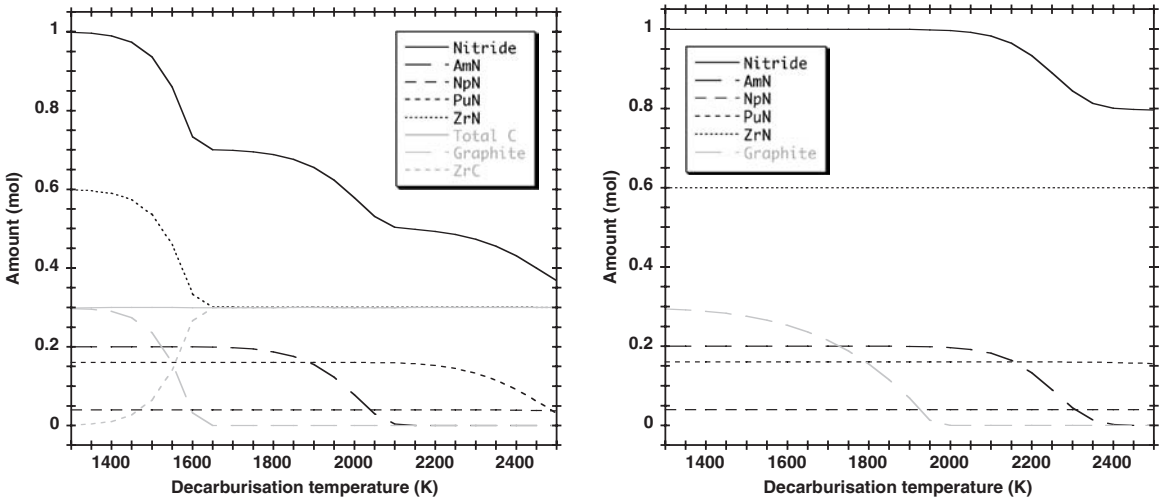

Fig. 4 Solid products from decarburisation at constant temperature in 93% He, 7% H_2 (left) and in 93% N_2, 7% H_2 (right)

The output from carbothermic nitridation at optimal temperature, performed as in legend to Fig. 3, constitutes the starting material: that is, essentially 1.0 mol of $(Am_{0.20}Np_{0.04}Pu_{0.16}Zr_{0.60})N$ and 0.30 mol of graphite. The conditions at the ninth decarburisation segment (Seg. 19) are shown.

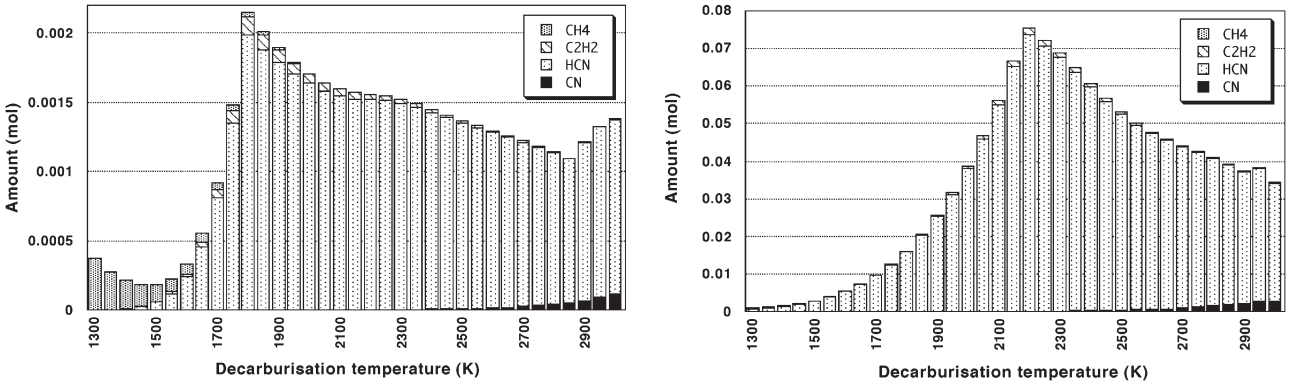

Fig. 5 Gaseous products from decarburisation in 93% He, 7% H_2 (left) and in 93% N_2, 7% H_2 (right)

Here are shown the conditions at Segment 11, representing the initial stage of decarburisation, before graphite has been eliminated (in N_2) or converted to ZrC (in He).

inated at an appreciable rate, that is, a significant fraction was removed in each segment. The efficiency of the reaction increased up to 2,000 K, which may be the practical limit due to premature sintering of the product, something we would not see in the computer model. Also above 2,000 K the model starts to report a tendency towards evaporation of the AmN component (**Fig. 4**).

In inert gas the ZrN component lost N_2 and combined with graphite to form ZrC at temperatures above 1,500 K. The carbide did not show much tendency to react with H_2, and the remaining nitride, already depleted in ZrN, showed a strong tendency towards decomposition above 1,900 K. Consequently, in our model, decarburisation in inert gas results in failure.

Contrary to expectations, the gaseous products from decarburisation at 1,500–2,000 K contained very little methane. On closer consideration, this is quite in accordance with earlier results showing that gasification of graphite by the methane process is three orders of magnitude slower than for coal or charcoal and that the equilibrium constant of the reaction is very unfavourable above 1,500 K.[22,23]

Instead of methane, the model reported a large production of HCN, together with small quantities of acetylene (**Fig. 5**). This was the case both in nitrogen and in inert gas, although the overall levels of gaseous products were much lower in inert gas due to the lower efficiency of the decarburisation process. Decarburisation reactions including HCN as an intermediate or a product have also been suggested in earlier studies.[24,25]

When decarburisation was modelled in a He–H_2 environment below 1,300 K, or in N_2-H_2 at still lower temperatures (not shown), the predominant gaseous product was indeed reported to be methane. While this reaction is thermodynamically more advantageous the lower the temperature, real-world reaction kinetics place a lower limit on what temperatures can be used.

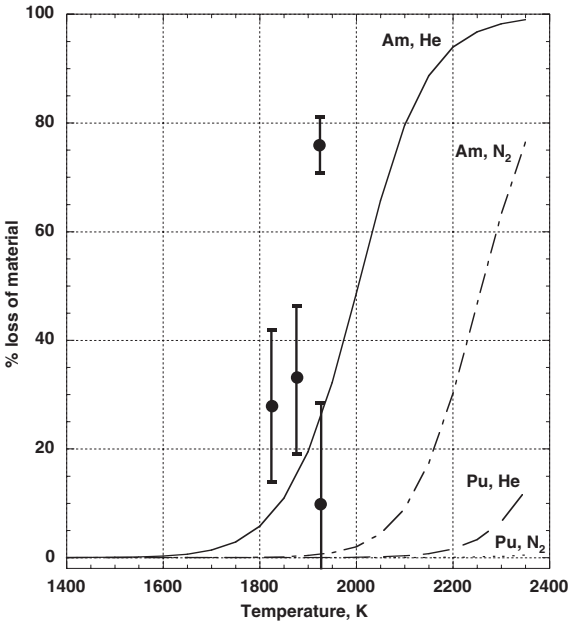

Fig. 6 Modelled evaporation of metals from $(Am_{0.24}Pu_{0.16}Zr_{0.60})N$ in a large amount of He or N_2, illustrating material loss during sintering of fuel pellets

Dots and error bars show the Am losses experienced during sintering in Ar at LANL.

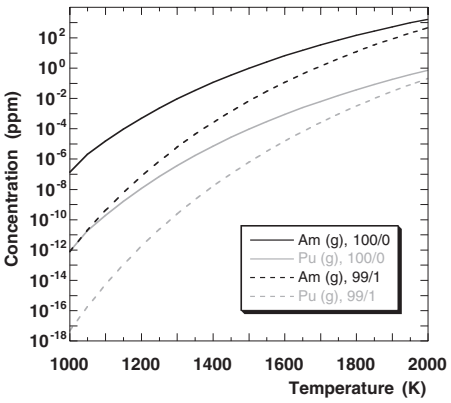

Fig. 7 Modelled evaporation of metals from $(Am_{0.24}Pu_{0.16}Zr_{0.60})N$ in a small amount of He (solid lines) or 99% He, 1% N_2 (dotted lines), illustrating the actinide mobility in gas-bonded fuel pins

The levels of metal vapour in the total amount of gas, calculated in molar units of Am, Pu, He and N_2, are plotted as parts per million.

2. Thermal Stability: Observations

The simulated heating of PuN and AmN under atmospheric pressure, as is done during pellet sintering, results in losses of solid material as expected. However, as can be seen from **Fig. 6**, the losses of americium are predicted to occur at about 250 degrees higher temperature in a nitrogen atmosphere than in inert gas. This holds true in the entire interval from onset to near completion of the AmN decomposition. Losses of plutonium were similarly suppressed. Experimentally determined losses of Am during sintering of (Pu,Am,Zr) nitrides in argon are marked in the figure for comparison.[6)]

Simulated heating of PuN and AmN in a small sealed compartment such as a fuel pin has a different outcome. The onset of decomposition is delayed by introduction of nitrogen in the bonding gas, but in contrast to the ''sintering'' model described above, there is no substantial effect in the later stages of the process (**Fig. 7**). The explanation lies in the initial proportions between nitride and gas. In the ''sintering'' case the dissociation of the nitride had little effect on the overall composition of the gas phase, but when thermal decomposition of nitride in a fuel pin starts to produce any larger quantities of N_2, then it makes little difference whether some small amount of N_2 was present from the start.

Thus we find that the addition of 1% nitrogen to the bonding gas lowers the partial pressure of actinide vapours by five orders of magnitude at 1,000 K, that it still suppresses dissociation of the nitrides by 99% at 1,500 K, but that it in no way counteracts the extensive decomposition above 2,000 K (not shown). No liquid phase and no solid phase other than mixed nitride was reported within the shown temperature range.

The conclusion is that at the lower end of the temperature scale, the suggested nitrogen admixture may dramatically reduce actinide migration and would in principle allow us to increase the temperature by 200 K while remaining within safety limits as far as nitride stability is concerned. This is in accordance with results from other studies.[26)]

V. Discussion

We have chosen to emulate actual production methods including the use of excess graphite as described in Sec. III-1. It should be mentioned that if the starting material contains equimolar amounts of carbon and oxygen (2 mol graphite per mol oxides), the model will still report virtually quantitative nitridation. Thus, strictly from the modelling viewpoint, nothing is gained by using graphite in excess. An excess of a pure, solid reactant does not shift the thermodynamical equilibrium. The effect nevertheless observed in real production depends on kinetic and spatial factors outside the scope of our model. It is of interest that there seems to exist a reasonably wide temperature region where pure nitrides could in theory be obtained with over 99.9% yield and 100% purity of the product (Fig. 3). In practice the solid reactants in the carboreduction step, graphite and metal dioxide, will be in direct contact only along a fraction of their surface, while reaction in the bulk will depend on diffusion of the reactants themselves or gaseous intermediates. These limitations can be only partially overcome by using more finely milled powders, improved mixing or longer reaction times. It is therefore not surprising that we find deviations between the ideal and the real case.

The use of argon as a blanket gas during heat-treatment of nitrides has been attributed to the risk of producing higher nitrides during cooling down after *e.g.* sintering in nitrogen, but we believe that this is both unnecessary and counterproductive. It is highly questionable whether the suggested higher nitrides Zr_2N_3, Zr_3N_8 and Pu_2N_3 exist at all.[27–30)] The compound Zr_3N_4 does exist, but is considered unstable

with respect to the mononitride in 1 atm N_2 and spontaneously decomposes to the mononitride at approximately 1,100 K.[27,31,32] PuN_2 has been produced only with great effort and in trace amounts.[33] Nor are any stable higher nitrides of neptunium, americium or other transuranium elements known to exist.[34]

It is a not uncommon assumption that the main product of the decarburisation is methane. This reaction would decrease the entropy of the system, since two molecules of gas combine with a solid to form one gas molecule:

$$\begin{aligned} &C + 2\ H_2 \rightarrow CH_4, \\ &\Delta S^{\circ}_{1,800\,K} = -112.0\,J{\cdot}mol^{-1}{\cdot}K^{-1}. \end{aligned} \tag{3}$$

It can therefore be expected that it is thermodynamically disadvantageous at high temperatures.

The formation of HCN in a He–H_2 environment uses the nitride as its source of nitrogen, and according to our model the ZrN component is converted to carbide in the process. This reaction leads to an increase in gas volume and can be summarised as

$$\begin{aligned} &4\ C + H_2 + 2\ ZrN \rightarrow 2\ HCN + 2\ ZrC, \\ &\Delta S^{\circ}_{1,800\,K} = 206.0\,J{\cdot}mol^{-1}{\cdot}K^{-1}. \end{aligned} \tag{4}$$

In a N_2–H_2 environment the model reports no decrease in nitride, meaning that the nitrogen component comes only from N_2. Thus there is no net change in gas amount:

$$\begin{aligned} &2\ C + H_2 + N_2 \rightarrow 2\ HCN, \\ &\Delta S^{\circ}_{1,800\,K} = 61.1\,J{\cdot}mol^{-1}{\cdot}K^{-1}. \end{aligned} \tag{5}$$

Although the numerical values must not be directly compared due to differences in stoichiometry, the difference in sign shows that from the thermodynamical viewpoint, the production of HCN will be more and that of CH_4 less advantageous the higher the temperature.

Neither CH_4 nor HCN was detected in the exhaust gases from actual production of nitride fuel [M. Streit, 2003, personal communication; R. Konings, 2003, personal communication]. HCN has a tendency to decompose into the elements at 1,000 to 1,400 K, but whether this is part of the explanation remains to be seen.[35,36] The formation of HCN during decarburisation has been confirmed in the production of (U,Pu)N fuel.[25] The reaction (5) has also been experimentally confirmed in other context, and acetylene was detected as a minor component, much as in our model.[37]

The possible addition of small amounts of nitrogen to the bonding gas of fuel pins raises the question whether this might cause nitridation of the cladding. Some N_2 will be present even in strictly He-bonded pins, initially only the minute traces resulting from the equilibrium (2), but at higher burnup the partial pressure is expected to increase with the ratio of nitrogen to metal. This has not yet been observed to cause any significant deterioration of the cladding material, but further testing would be needed to rule out the risk of corrosion in (He,N_2) bonded pins.[38]

Many experimental determinations of the limits of PuN stability have been made, and the nitride may decompose by ''melting'' as well as by evaporation. The ''melting'' point should be regarded as the appearance not of liquid nitride but of a liquid phase of plutonium metal, possibly saturated to a high extent with nitrogen, and the ''melting'' or evaporation temperature is strongly dependent on the properties of the gas phase.[39,40]

Literature values of the decomposition temperature for PuN in 1 bar N_2 range from 2,857 to 3,103 K, while decomposition occurs as early as 2,200 K in helium and 1,923 K in near vacuum.[40–43]

The dissociation depends on both the N_2 and the Pu activity in the gas phase. Therefore the evaporisation temperature observed when heating PuN in what is nominally pure N_2 at 1 bar will change with the experimental setup and with the size and proportions of the system. There is a measurable partial pressure of Pu(g) over PuN already at 1,600 K, and the nitride will decompose until the equilibrium pressure is reached.[44] The same goes for dissociation in pure He, where both Pu(g) and N_2 will build up until their equilibrium pressure is reached.

For comparison, we estimated the dissociation temperatures for PuN in different environments using the ALCHYMY database and the COMPUTE_TRANSITION command of Thermo–Calc's POLY module. Only the solid state of PuN is included in the database, since the ''melting'' of PuN is, as noted above, a poorly defined phenomenon on which little thermochemical data seems to exist, and the gas phase over hot PuN is assumed to contain very little if any PuN at normal pressures.[26,28]

In a small quantity of N_2, *e.g.* 0.001 moles N_2 per mole PuN, the simulation shows complete nitride disappearance at 3,249 K. At this point the gas phase is N_2 saturated with Pu vapour. In a 1,000 times molar excess of N_2, 1 mole of PuN evaporates already at 2,619 K due to the lower partial pressure of Pu(g), and in He at a 1,000 times molar excess, the PuN phase disappears at 2,313 K, due to the low partial pressures of both N_2 and Pu(g). The total pressure is in all cases constant at 1 bar.

We have not found any direct experimental determination of the melting or decomposition temperature of macroscopic amounts of pure AmN. It is known to be stable at least up to 1,573 K,[5] and the decomposition temperature is expected to be lower than for PuN. The experimental results used for comparison in Fig. 6 are among the few controlled observations that have been made of AmN evaporation.[6] In analogy with the modelling of PuN above, and at a constant total pressure of 1 bar, ALCHYMY reports that in 0.001 moles N_2 per mole AmN, the nitride has completely evaporated at 2,607 K; in a 1,000 times molar excess of N_2, AmN volatilises already at 2,102 K due to the lower partial pressure of Am(g); and in a 1,000 times molar excess of He, AmN disappears at 1,876 K, due to the low partial pressures of both N_2 and Am(g).

VI. Conclusions

Modelling uranium free nitride fuel fabrication processes with the newly developed thermo-chemical database ALCHYMY, we found that temperatures between 1,800 and 2,000 K seem the most suitable for the production of mixed nitride fuels by carbo-thermic nitridation. This is in accordance with practical experience. Our results suggest that with

certain, now implemented modifications of the decarburisation step, the protocol used for production of (Pu,Zr)N should work also for fuels containing minor actinides.

We predict that at temperatures above 1,500 K, the immediate gaseous product of the decarburisation step is not methane, but rather hydrogen cyanide. We further predict that compared to the use of hydrogen in inert gas, a H_2–N_2 mixture will result in more efficient decarburisation, prevent the loss of material by evaporation, and suppress the formation of metal carbides. We also recommend that sintering of Am-containing nitrides be performed in a nitrogen atmosphere, instead of in inert gas. Finally, we suggest that addition of small amounts of nitrogen to the bonding gas may significantly delay the onset of nitride decomposition during in-pile transients and counteract migration of material.

Acknowledgements

The authors wish to thank Prof. Bo Sundman at the Division of Thermodynamic Modelling, Dept. of Material Science and Engineering, KTH, Stockholm, for his invaluable and patient assistance with understanding the intricacies of Thermo–Calc and the database syntax. This work was supported by the European Commission as a part of the 5th Framework Program CONFIRM project.

References

1) J. L. Faugère, M. Pelletier, J. Rousseau, *et al.*, ''The CEA helium-bonded nitride fuel design,'' *Proc. Int. Conf. on Design and Safety of Advanced Nuclear Power Plants (ANP'92)*, Tokyo, Japan, Oct. 25–29, 1992, p. 28.1-1 (1992).
2) T. Umeoka, M. Akimura, H. Matsumiya, *et al.*, ''Study of CDA driven by ULOF for the nitride fuel core,'' *Proc. Int. Conf. Future Nuclear Systems (GLOBAL 99)*, Jackson Hole, Wyoming, Aug. 29–Sep. 3, 1999, (1999). (CD. ISBN 0-89448-641-1).
3) J. Wallenius, S. Pillon, ''N-15 Requirement for 2nd Stratum ADS Nitride Fuels,'' *2001 ANS Topical Meeting Proceedings (AccApp/ADTTA'01)*, Reno, Nevada, U.S.A., Nov. 11–15, 2001, (2002). (CD. ISBN 0-89448-666-7).
4) T. Ogawa, T. Ohmichi, A. Maeda, *et al.*, ''Vaporization behaviour of (Pu,Am)N,'' *J. Alloys Compounds*, **224**, 55 (1995).
5) M. Takano, A. Itoh, M. Akabori, *et al.*, ''Synthesis of americium mononitride by carbothermic reduction methods,'' *Proc. Int. Conf. Future Nuclear Systems (GLOBAL 99)*, Jackson Hole, Wyoming, Aug. 29–Sep. 3, 1999, (1999). (CD. ISBN 0-89448-641-1).
6) R. Margevicius, *AFC Fuels Development Update: 2003 Semi-Annual Meeting*, LANL document LA-UR-03-0415, Los Alamos National Laboratory (LANL), (2003).
7) *AFC/AAA Quarterly Report Jul–Sept 2002*, LANL document LA-UR-02-7220, Los Alamos National Laboratory (LANL), (2002).
8) J.-O. Andersson, T. Helander, L. Höglund *et al.*, ''Thermo–Calc and DICTRA, computational tools for materials science,'' *Calphad*, **26**, 273 (2002).
9) E. H. P. Cordfunke, R. J. M. Konings (Eds.), *Thermochemical Data for Reactor Materials and Fission Products*, North-Holland/Elsevier, Amsterdam, (1990).
10) H. Wanner, ''The NEA Thermochemical Data Base Project,'' *Radiochim. Acta*, **44/45**, 325 (1988).
11) C. E. Holley, M. H. Rand, E. K. Storms (Eds.), *The Chemical Thermodynamics of Actinide Elements and Compounds Part 6: The Actinide Carbides*, IAEA, Vienna, (1984).
12) L. B. Pankratz, *Thermodynamic Properties of Elements and Oxides*, Bulletin 672, U.S. Bureau of Mines, (1982).
13) M. Streit, F. Ingold, M. Pouchon, *et al.*, ''Zirconium nitride as inert matrix for fast systems,'' *J. Nucl. Mater.*, **319**, 51 (2003).
14) M. Streit, F. Ingold, L. J. Gauckler, J.-P. Ottaviani, ''(Pu,Zr)N annular fuel pellets shaped by direct coagulation casting,'' *J. Nucl. Sci. Technol.*, **Supplement 3**, 741 (2002).
15) W. O. Greenhalgh, ''Kinetic measurements for the carbothermic synthesis of UN, PuN, and (U,Pu)N,'' *J. Am. Ceram. Soc.*, **56**[11], 553 (1973).
16) T. Takizuka, T. Sasa, K. Tsujimoto, H. Takano, *Proc. 5th Int. Information Exchange Meeting on Actinide and Fission Product Partitioning and Transmutation*, Mol, Belgium Nov. 25–27 1998, OECD/NEA, Paris, 383 (1999).
17) H. Blank, ''Nonoxide ceramic nuclear fuels,'' *Materials Science and Technology, Volume 10A, Nuclear Materials*, B. R. T. Frost (Ed.), John Wiley & Sons, 191 (1994).
18) J. Wallenius (Ed.), *CONFIRM Progress Report 1*, Department of Nuclear and Reactor Physics, KTH, (2002).
19) Y. Arai, S. Fukushima, K. Shiozawa, M. Handa, ''Fabrication of uranium-plutonium mixed nitride and thermally stable carbide fuels,'' *Technical Committee Meeting on Advanced Fuel for Fast Breeder Reactors: Fabrication and properties and their optimization*, Nov 3–5, 1987, Vienna, Austria, 25 (1988).
20) J. Wallenius, To be published in *Report of The Fuels and Materials Subgroup of the NEA Working Party on Partitioning and Transmutation*, OECD/NEA.
21) J. Wallenius, K. Tuček, J. Carlsson, W. Gudowski, ''Application of burnable absorbers in an accelerator-driven system,'' *Nucl. Sci. Eng.*, **137**, 96 (2001).
22) J. D. Blackwood, ''Application of burnable absorbers in an accelerator-driven system,'' *Aust. J. Appl. Sci.*, **13**, 206 (1962).
23) D. D. Wagman, J. E. Kilpatrick, W. J. Taylor, *et al.*, ''Heats, free energies, and equilibrium constants of some reactions involving O_2, H_2, H_2O, C, CO, CO_2, and CH_4,'' *J. Res. Nat. Bur. Stand.*, **34**, 143 (1945).
24) T. Ogawa, Y. Shirasu, K. Minato, *et al.*, ''Thermodynamics of carbothermic synthesis of actinide mononitrides,'' *J. Nucl. Mater.*, **247**, 151 (1997).
25) C. Prunier, P. Bardelle, J. P. Pages, *et al.*, ''European collaboration on mixed nitride fuel,'' *Proc. Int. Conf. Fast Reactors and Related Fuel Cycles (FR'91)*, Kyoto, Japan, Oct. 28–Nov. 1, 1991, paper 15-9, (1991).
26) M. A. Mignanelli, R. Thetford, D. A. Williams, ''Fuel performance modelling of nitride fuels,'' *Proc. Int. Conf. Future Nuclear Systems (GLOBAL 99)*, Jackson Hole, Wyoming, Aug. 29–Sep. 3, 1999, (1999). (CD. ISBN 0-89448-641-1).
27) M. Hansen, *Constitution of Binary Alloys*, 2nd ed., McGraw-Hill, New York, (1958).
28) T. B. Massalski (Ed.), *Binary Alloys Phase Diagrams*, 2nd ed., ASM International, (1990).
29) J. M. Matthews, ''The preparation of zirconium nitrides,'' *J. Am. Chem. Soc.*, **20**, 843 (1898).
30) J. M. Blocher, Jr., ''Nitrides,'' *High-temperature Technology*, I. E. Campbell (Ed.), John Wiley & Sons, New York, p. 171 (1956).
31) M. Lerch, E. Füglein, J. Wrba, ''Synthesis, crystal structure, and high temperature behavior of Zr_3N_4,'' *Z. anorg. allg. Chem.*, **622**, 367 (1996).
32) M. Lerch, ''Phase relationships in the ZrO_2–Zr_3N_4 system,'' *J.*

Mater. Sci. Lett., **17**, 441 (1998).
33) D. W. Green, G. T Reedy, ''Infrared spectra of matrix-isolated plutonium nitrides,'' *J. Chem. Phys.*, **69**, 552 (1978).
34) T. Ogawa, To be published in Draft report of the The Fuels and Materials Subgroup of the NEA Working Party on Partitioning and Transmutation, OECD/NEA.
35) G. A. Voerkelius, ''Über die Entstehung der Blausäure aus Ammoniak und Holzkohle, sowie aus Di- und Trimethylamin,'' *Chem.-Ztg.*, 1078 (1909), [in German].
36) T. K. Sherwood, E. R. Gilliland, S. W. Ing, ''Hydrogen cyanide. Synthesis from its elements and from ammonia and carbon,'' *Ind. Eng. Chem.*, **52**, 601 (1960).
37) H. von Wartenberg, ''Über das Cyan, Cyanwasserstoff- und Acetylengleichgewicht,'' *Z. Anorg. Chem.*, **52**, 299 (1907), [in German].
38) R. Thetford, M. Mignanelli, ''The chemistry and physics of modelling nitride fuels for transmutation,'' *J. Nucl. Mater.*, **320**, 44 (2003).
39) M. H. Rand, O. Kubaschewski (Ed.), Plutonium: Physico-chemical Properties of Its Compounds and Alloys, Atomic energy review, Special issue 1, Vienna, p. 36 (1966).
40) K. Richter, C. Sari, ''Investigation of the operational limits of uranium-plutonium nitride fuels,'' *J. Nucl. Mater.*, **184**, 167 (1991).
41) F. Anselin, ''Etude des nitrures d'uranium, de plutonium et de leurs solutions solides,'' *J. Nucl. Mater.*, **10**, 301 (1963), [in French].
42) W. M. Olson, R. N. R. Mulford, ''The decomposition pressure of plutonium nitride,'' *J. Phys. Chem.*, **68**, 1048 (1964).
43) TAPP v.2.2 chemical database, ES Microware, Inc., 2234 Wade Court, Hamilton, OH 45013, USA.
44) T. Matsui, R. W. Ohse, ''Thermodynamic properties of uranium nitride, plutonium nitride and uranium-plutonium mixed nitride,'' *High Temp.-High Pressures*, **19**, 1 (1987).

APPENDIX 8

D. Terentyev, C. Lagerstedt, P. Olsson, K. Nordlund, J. Wallenius, and L. Malerba, "Effect of the interatomic potential on the features of displacement cascades in .-Fe: a molecular dynamics study", submitted for the Proceedings of the Symposium on Microstructural Processes in Irradiated Materials San Francisco, CA, 13-17 February 2005 (Annual TMS meeting)
To be published as special issue of the Journal of Nuclear Materials

Paper submitted for the Proceedings of the
Symposium on Microstructural Processes in Irradiated Materials
San Francisco, CA, 13-17 February 2005
(Annual TMS meeting)

To be published as special issue of the Journal of Nuclear Materials

Effect of the interatomic potential on the features of displacement cascades in α-Fe: a molecular dynamics study

D. Terentyev[1], C. Lagerstedt[2], P. Olsson[3], K. Nordlund[4], J. Wallenius[2] and L. Malerba[1,*]

[1]*SCK•CEN, the Belgian Nuclear Research Centre – Boeretang 200, B-2400 Mol, Belgium*

[2]*Dept. of Nuclear and Reactor Physics, Royal Institute of Technology*
Roslagstullsbacken 21, SE-106 91 Stockholm, Sweden

[3]*Dept. of Neutron Research, Ångstrom Laboratory, Uppsala University*
Box 525, SE-751 20 Uppsala, Sweden

[4]*Accelerator Laboratory, University of Helsinki, POB 43 (Pietari Kalmin katu 2) FIN-00014, Finland*

Abstract

Depending on the interatomic potential used for molecular dynamics (MD) simulation of displacement cascades, primary states of damage characterised by different spatial distributions of point-defects (clustered fractions in particular) are obtained. These differences may influence the microstructural evolution predicted in damage accumulation modelling using the input from MD cascade simulations. In this work, a number of displacement cascades initiated by recoils of energy ranging from 5 to 40 keV have been simulated in the same way using four different interatomic potentials for α-Fe, each providing, among other things, different descriptions for the self-interstitial atoms (SIA) in this metal. The behaviour of the cascades in correspondence with their different phases and the final surviving defect population have been studied using the same criteria for cascade analysis and compared. The outcome is discussed trying to identify the characteristics of the potential that mostly influence the predicted primary state of damage.

* Corresponding author, Phone #: +32-14-333090, Fax #: +32-14-321216, e-mail: lmalerba@sckcen.be

1. Introduction

Displacement cascades are the fundamental process of radiation damage production under neutron and ion irradiation. Their study by means of numerical simulation based on the use of an interatomic potential dates back to the 60s [Gibson60, Erginsoy64, Erginsoy65, Beeler66]. In this old, pioneering work the choice of the potential and the study of how the result of the simulation may depend on it were felt as a priority issue [Gibson60]. On the contrary, during the last fifteen years, which have experienced a real boom of displacement cascade simulation using many-body potentials [English92, Bacon94, Bacon95, Bacon97, Averback98, Bacon00, Bacon03], relatively little attention has been paid to this problem, with only few exceptions [Becquart00]. Nonetheless, as demonstrated in a review of existing results for α-Fe, also proposed in these proceedings [Malerba06], in spite of the difficulty of performing a fully consistent comparison between data available from the literature, different potentials do appear to produce cascades with different features. Therefore, the question of determining which characteristics of the interatomic potential are mostly responsible for the result of the simulation arises as an important one. This paper strives to address this question, by comparing the characteristics of cascades simulated by molecular dynamics (MD) using four recently fitted potentials for α-Fe, each providing different descriptions of point-defects and featuring different threshold displacement energies and stiffness. The comparison is particularly significant because all cascades were simulated following exactly the same procedure and analysed using the same criteria, so that differences in the results can only be ascribed to the inherent features of the potential used.

2. Simulation technique

2.1 Interatomic potentials

Four potentials for α-Fe were used for the MD simulations herein reported, namely: (i) the short-range Finnis-Sinclair-type potential proposed by Ackland et al. as part of an Fe-Cu potential [Ackland97], henceforth denoted as ABC; (ii) the long-range embedded-atom method (EAM) potential fitted by Chakarova et al. as part of an Fe-Cr potential [Chakarova02], henceforth denoted as CWP; (iii) the long-range EAM potential recently developed as part of an Fe-P potential by Ackland et al. [Ackland04], denoted as AMS; and (iv) a version of the long-range EAM potential recently developed as part of an Fe-Cr potential by Wallenius et al. [Wallenius04], denoted as WOL. These potentials were selected for being relatively recent and for providing significantly different descriptions of, in particular, self-interstitial atoms (SIA). While CWP incorrectly predicts the ⟨111⟩ crowdion to be the most stable configurations, ABC, AMS and WOL all feature the correct stability of the ⟨110⟩ dumbbell configuration. However, the energy difference between the two mentioned configurations is very small according to ABC (which adopts a cutoff distance

between 2nd and 3rd nearest neighbour) and increasingly larger according to WOL and AMS (both characterised by a cutoff beyond 3rd nearest neighbour distance). AMS belongs to a family of potentials for α-Fe which has been shown to reproduce fairly closely the behaviour of the SIA as described by *ab initio* calculations [Willaime04]. WOL, on the other hand, predicts too large formation energies for all SIA configurations. These different descriptions of the SIA are expected to influence the mobility of SIA and SIA clusters predicted by each of these potentials [Osetsky00, TerentyevSIA]. In particular, the mobility of the SIA will be lower according to AMS, because rotation to, and glide along, the ⟨111⟩ direction are unfavoured compared to other potentials [TerentyevSIA]. The selected potentials also exhibit partially different threshold displacement energies (TDE) and different range (R) and stiffness (S), defined as, respectively, the interatomic distance where the interaction energy equals 30 eV and the gradient of the potential in correspondence with the same distance. The latter magnitudes have been shown to correlate with the number of replacement collision sequences (RCS) and density of the cascade [Becquart02]. Table 1 summarises the main properties of the four potentials.

2.2 Cascade simulation

All simulations were performed using the MD code Dymoka [Becquart00], working - as is common practice to do [Becquart00, Vascon00, Soneda98] - in the microcanonical statistical ensemble, with periodic boundary conditions. Temperature was not controlled because this parameter has been shown to have negligible effect on the cascade simulation results [Gao97, Stoller00]. At any rate, the average temperature of the box never rose by more than 100-200 K. A block of atoms was initially equilibrated for 1 ps at 100 K. The cascade was initiated by imparting the desired kinetic energy to a primary knock-on atom (PKA, or recoil). The PKA was chosen to be at the centre of the cubic box and to move along ⟨135⟩ directions, in order to avoid channelling [Stoller00, Calder93]. The PKA energies ranged between 5 and 40 keV and at least 10 cascades per potential and recoil-energy were produced. The size of the box was increased for increasing PKA energies and the same box-size was used for simulations of the same recoil energy with all four potentials, as summarized in Table 2. This decision prevented 40 keV cascades from being simulated with WOL, as a consequence of the particularly large volume of cascades according to this potential (see below). The cascade evolution was monitored visually during the collisional and post-collisional stages, to make sure that there was no self-interaction when boundary crossing occurred. In order to ensure that the finite difference method used in the MD code to integrate the equations of motion does not produce uncontrolled errors, the time-step, Δt, was adapted to the cascade phase, as summarised in Table 3. During the ballistic phase, when some atoms possess very high kinetic energy and undergo long displacements in very short times, $\Delta t \sim 10^{-17}$ s, while during the post-collisional phase $\Delta t \sim 10^{-16}$ s. After the recombination phase of the cascade, the evolution was

followed for ~23 ps using, for the last 10 ps, a larger time step (Δt~10^{-15} s), until the block of atoms ended up close to thermal equilibrium.

2.3 Cascade analysis

Point-defects were located and counted in two ways: (1) using the Wigner-Seitz (WS) cell method, and (2) using displacement analysis. The former requires WS cells to be defined around each perfect lattice position: an empty cell means a vacancy, while two (or more) atoms in the same cell mean an interstitial configuration. The latter corresponds to using spheres instead of WS cells and essentially corresponds to checking the distance between the perfect lattice position and the displaced atom, using appropriate cutoff radii to decide whether displacement occurred or not and identify the type of defect [Calder93]. This second method was mostly used for comparison purposes, to make sure that the criterion used to identify point-defects did not influence the result of the analyses, particularly when verifying the absence of cascade self-interaction through periodic boundary conditions. Either way, the evolution in time of the number of defects can be monitored, so as to identify (i) the peak stage, in terms of time since cascade initiation, in correspondence with the maximum number of defects, (ii) the recombination, or relaxation, phase and (iii) the number of surviving Frenkel pairs (FP). As an indication of the duration of the recombination phase, roughly coincident with the thermal spike, the characteristic relaxation time, τ_r, was also determined. Following Calder and Bacon [Calder93], this parameter was estimated using an exponential decay approximation from peak time (t_{peak}) for the number of FP (ν_{FP}) versus time: $\{\nu_{FP}-\nu_{FP}^{end}\}(t-t_{peak}) = A\exp[-(t-t_{peak})/\tau_r]$, where ν_{FP}^{end} is the number of FP surviving recombination, counted when the cascade reached the final steady state. The defect analysis allowed also the defect positions to be recorded, thereby enabling the cascade evolution to be visualised, with the aid of appropriate tools.

The cascade volume and density at peak stage were evaluated using the component analysis procedure described in [Hou85, Souidi01]. The volume of the cascade is associated to an ellipsoid, whose axes are defined based on the variance of the spatial point-defect distribution. The major axis has the direction maximising the variance, the second one maximises the variance of the distribution projected onto a plane perpendicular to the first one, and the third one has the direction minimising this variance. These directions are parallel to the directions of the eigenvectors of the covariance matrix of the point-defect distributions and the associated eigenvalues are the variances of the distribution projected onto the directions of the eigenvectors. Thus, the problem is reduced to the diagonalisation of a 3×3 symmetrical, real and positive matrix, which is a straightforward operation. This method may not be completely justified when subcascade formation becomes important, but provides nevertheless a good reference.

The number of defects in clusters and clusters produced during the evolution of the cascade were determined using an automated procedure, whereby point-

defects located at a distance below a certain cutoff were associated to the same cluster. However, the situation at the end of the cascade was further analysed by visual inspection. Different criteria (cutoff distances) for the automated procedure were used: vacancy clusters were defined using both 2nd and 4th nearest neighbour (nn) criteria [Stoller00] and SIA clusters using both 1st [Vascon97, Becquart00] and 3rd nn [Soneda01] criteria. The visual inspection was used in addition because it has been observed that automated procedures tend to provide somewhat smaller fractions of SIA in clusters [Terentyev05].

3. Results

3.1 Peak stage and recombination phase

The main features characterising the cascade peak stage are: time elapsed from the initiation of the cascade (peak time), maximum number of defects, cascade volume and cascade density, all of them as a function of recoil energy.
Number of defects and cascade density at peak time are shown in Figure 1 for the four potentials used in this work. Clearly, WOL provides significantly less defects at peak time than any other potentials and the cascade density, as a consequence of both this fact and a larger average cascade volume (figure not shown), is the smallest. At the other extreme, AMS produces the largest number of defects at peak time (a factor from 2 to 5 compared to WOL) and exhibits the highest cascade density. The other two potentials lie in-between, with ABC density closer to AMS and CWP density closer to WOL. Figure 2 shows the relaxation time versus recoil energy for the four potentials and it appears that the potential ranking according to this parameter is the same as for the cascade density. This fact will be discussed below.

3.2 Primary state of damage

3.2.1 Defect production efficiency

Figure 4 presents the defect production efficiency, $\eta = \nu_{FP}^{end} / \nu_{NRT}$, versus recoil energy, for the four potentials considered in this work. Here $\nu_{NRT}=0.8E_D/2E_d$ is the standard number of NRT displacements [NRT74], where E_D is the damage energy, coincident with the recoil energy in the MD simulation, and E_d is an average TDE which, following common practice [Phythian95, Stoller00, ASTM], has been taken equal to 40 eV. However surprising it may seem, potentials with different TDE (Table 1), as well as different number of defects and density at peak time (Figure 1) produce, at the end, roughly the same amount of defects, with the only partial exception of WOL, which stands out for a slightly higher η (note that at peak time this potential produced the *lowest* number of defects). At any rate, efficiencies between 0.2 and 0.4 are in line with results available from the literature obtained with other potentials and in agreement with experimental assessments [Malerba06]. AMS seems to exhibit a minimum efficiency at 10 and 20 keV, the latter value being in agreement

with the behaviour observed by Stoller and attributed to onset of sub-cascade splitting above this value [Stoller00]. However, CWP displays a minimum at 5 keV, which is hardly ascribable to sub-cascade formation above this value, and ABC presents an η steadily decreasing with increasing recoil energy, so most likely oscillations should be attributed to lack of sufficient statistics. The main observation is that little or no difference is found in the amount of surviving FP going from one potential to another, for the same PKA energy.

3.2.2 Defect clustered fractions

The amount of point-defects found in clusters, as well as their size distribution, is considered a fundamental information that has to be provided from displacement cascade studies as input for damage accumulation modelling [Zinkle93]. In Figure 5 the point-defect clustered fraction, f_t^{cl} (t = V or SIA) is given as a function of recoil energy for the four potentials: the f_{SIA}^{cl} was determined by visual inspection, while f_V^{cl} is the result of an automated analysis using a 2nd nn criterion. These magnitudes, when plotted versus recoil energy, are affected by even larger oscillations than others and in no case is a completely smooth, monotonous behaviour obtained [Becquart00, Stoller00]. In broad agreement with observations made in previous work [Bacon95, Bacon97, Bacon00, Bacon03, Stoller00], the SIA clustered fraction tends to increase with increasing PKA energy. This increase is particularly steep according to CWP; much less according to the other potentials. AMS produces a tendentially smaller fraction of SIA in clusters than the other potentials. The vacancy clustered fraction, with the exception of a few outlying points, remains globally rather constant for all PKA energies. Its value stays around 0.2-0.3 for three of the four potentials, but AMS stands out for a particularly high value (f_V^{cl}~0.4-0.5), which broadly equals the fraction of SIA in clusters according to the same potential.

4. Discussion

It is almost surprising that potentials which: (i) give different descriptions of point-defects, (ii) predict different TDE and (iii) provide largely different amounts of defects and cascade densities at peak time, end up producing essentially the same number of surviving FP. Clearly, there must be features of the potentials that induce opposite results, which compensate each other. Figures 1 and 2 suggest that the mutually offsetting results may be higher cascade density at peak time, followed by longer relaxation times.
Work of comparison of potentials performed in the binary collision approximation (BCA) has shown that the cascade density may correlate with the stiffness of the potential, which can be indicatively quantified through the parameters R and S of Table 1 [Becquart02]. Stiffer and shorter-ranged potentials (i.e. characterised by a high S/R ratio) favour the process of energy transfer during the binary collision, thereby favouring the production of more and longer RCS. Long and numerous RCS may correlate with more extended

cascades, more dilute damage and, possibly, reduced recombination during cascade relaxation, leading to a higher number of surviving FP. It has been demonstrated, always through BCA studies, that, although long RCS are not a frequent phenomenon in cascades, short RCS are necessary to explain a large part of in-cascade production of FP [Hou02]. The visual inspection of the cascades produced with the potentials used in this work by sufficiently high energy recoils does not generally show formation of long RCS, except in the case of WOL (Figure 5), whose cascades exhibit indeed the smallest density, with the shortest relaxation time, and a slightly higher number of surviving defects. With the other three potentials the "cascade regime", characterised by shock-induced collective effects, whereby whole regions of the crystal are displaced along close-packed directions, as observed by Calder and Bacon [Calder93], seems to be easily reached and in the case of AMS very dense cascades, followed by very long thermal spikes, are produced (Figure 5). Now, the S/R ratio is the largest for WOL ($|S/R|\sim183$) and the smallest for AMS ($|S/R|\sim50$), i.e. with the former RCS formation is favoured, while it is highly unlikely with the latter. Even more than this, the order of the curves in Figures 1 and 2 can be anticipated from the S/R ratio, if density and relaxation time are assumed to be both inversely proportional to it (CWP: $|S/R|\sim101$; ABC: $|S/R|\sim73$). The HA-VD potential of Ref. [Malerba06] has $|S/R|\sim267$, i.e. the highest of all, and indeed this potential produces very dilute cascades, with also an abnormally high number of surviving FP [Becquart00, Malerba06]. It may therefore be put forward that too high a stiffness prevents the attainement of a full cascade regime, which is in turn favoured when the potential is soft. A full cascade regime involves the production of a state close to a melt [Calder93]. How close to to a melt will also depend on the melting point predicted by the potential. But the more deeply this type of regime is gone into, the longer the thermal spike (whose duration can be estimated through the relaxation time) will be and the larger the probability of recombination during relaxation becomes. However, since softer potentials, such as AMS, produce at peak time a much higher number of atomic displacements, through collective motion, the two phenomena (large number of defects at peak time and long relaxation time) offset each other, eventually leading to a similar, in all cases, number of surviving FP. Nonetheless, stiff potentials eventually may produce higher number of surviving defects, because relaxation is not assisted by thermal effects, or only marginally, and the larger dilution of damage reduces the probability of spontaneous recombination between SIA and vacancies. This effect is visible in WOL, but reaches an extreme manifestation in the case of the HA-VD potential of Ref. [Malerba06]. Potential stiffness and range appear therefore to offer a means to rationalise some of the cascade features that appear to vary from one potential to another, although most likely also the prediction that the potential gives of the melting point of the metal plays a role. On the contrary, however astonishing, no correlation is found between the number of defects, both at peak time and at the end, and the TDE values. This is surprising in particular for the number of defects at peak time, which should be in principle the result of purely ballistic

effects. Yet, clearly, the potential with the largest average TDE (CWP) *does not* produce, ever, the smallest number of defects.

While the stiffness of the potential is of use to explain, at least tentatively, the differences concerning defect production, it is not as much useful when it comes to rationalise differences in defect clustered fraction. In this case the potential exhibiting the most peculiar behaviour is AMS, for which it is easy to see (Figure 4) that the production bias [Woo92], $PB=f_{SIA}^{cl}-f_{V}^{cl}$, is very close to zero in most cases. The other potentials display more uniform behaviour, although the steep increase of f_{SIA}^{cl} with CWP stands out as a peculiarity, too. In order to try to understand the reasons of the differences between AMS and the other potentials, the evolution of the clustered fraction for 23 ps after peak time has been monitored, using automated procedures for both vacancies (using a 2nd nn criterion) and SIA (using a 3rd nn criterion). An example, for the 15 keV cascades, is given in Figure 6. According to Bacon et al [Bacon97], two mechanisms of SIA cluster in-cascade formation can be devised: partly they form at the end of the thermal spike, as a consequence of collective atomic motion in conditions of highly enhanced defect diffusion, due to high local temperature, and partly by later local defect re-organization, driven by elastic interaction among neighbouring SIA and SIA clusters. The upper graph in Figure 6 reveals that indeed both mechanisms may occur, but their respective weight is different going from one potential to another. According to both AMS and ABC essentially all SIA are in clusters at peak time, which is a way of saying that collective atomic displacements are taking place. However, during relaxation the clustered fraction drops by about 50%. WOL, on the other hand, produces only a relatively small fraction of SIA in clusters at peak time, a sign that little or no collective displacement of atoms occurs, in agreement with the above discussion, and the drop is limited to about 10%. After relaxation, WOL and ABC exhibit similar behaviour: SIA rearrange themselves into an increasing fraction of defects in cluster, via (maybe thermally enhanced) diffusion. On the contrary, the fraction of SIA in clusters remains unchanged according to AMS. This may be the effect of the different SIA mobility predicted by the two classes of potentials: according to AMS, glide along the close-packed direction is unlikely and migration is fully tridimensional, with a migration energy ~0.3 eV, while according to the other two potentials glide is possible and the effective SIA migration energy is much lower [Osetsky00, TerentyevSIA]. Concerning vacancies, because of their much slower diffusivity compared to SIA, very similarly described by all potentials (Table 1), clustering is only expected to occur during the ballistic phase (unless collapse, so unusual in α-Fe, occurs [Soneda01]). The lower graph of Figure 6, however, shows that this is not always the case. The peak and relaxation time behaviour is, with the three potentials, symmetrical to the SIA case. But later, three different evolutions are possible. According to WOL, the vacancy clustered fraction experiences a slow decrease, most likely because of further, diffusion-driven recombination with fastly migrating SIA. According to ABC the clustered fraction remains essentially unchanged. But according to AMS a clear increase is seen to occur. This is difficult to explain, because vacancy diffusion

should be negligible on a picosecond scale. Different factors may combine to produce this post-relaxation clustering. The density of the cascade may be so high that a very small number of vacancy jumps may be sufficient to drive further clustering. Alternatively, or simultaneously, the actual temperature in the cascade region during this phase may represent, in AMS's case, a larger fraction of the melting point, thereby allowing enhanced vacancy diffusion compared to the other potentials. Further studies are necessary to clarify the origin of this behaviour. It is however clear that the clustered fraction predicted by a certain potential is determined by a complicated combination of interplaying factors, related partly to the equilibrium point-defect description, partly to the description that the potential gives of the cascade regime (so, possibly influenced by its stiffness) and partly to other properties, such as the melting point.

5. Conclusions

The main goal of the present paper was to produce a set of cascade simulations using different potentials, to be analysed in exactly the same manner, in order to find out whether different potentials do provide or not the same result and which, among the potential features, are mostly responsible for the possible differences in the final primary state of damage. It can be concluded that:

- The number of Frenkel pairs produced in a cascade during the whole displacement process does not correlate with the threshold displacement energies predicted by the potential.
- A correlation is found with the stiffness and range of the potential in the region of tens of eV interaction. With too stiff potentials damage production cannot reach a full cascade regime, characterised by collective atomic displacements and pronounced thermal spike, typical of soft potentials. On the contrary, with stiff potentials replacement collision sequences become more frequent and longer and determine an average larger distance between SIA and their vacancies, thereby decreasing the cascade density and partially preventing SIA-vacancy recombination during relaxation. The role of the thermal spike in this process may depend among other things also on the melting point predicted by the potential.
- Nonetheless, with the exception of especially pathological cases, all potentials predict the same final amount of surviving Frenkel pairs. This is likely to be the effect of two mutually offsetting effects of the same cause: namely larger number of defects at peak time, accompanied by longer relaxation time.
- Vacancy and SIA in-cascade clustering are potential dependent, but in a more involved way: differences are the result of a complicated interplay between different features of the potential, from the description of the mobility of point-defects, to the density of the cascade, possibly related to the stiffness, and the extent of the thermal spike, which may depend also on the melting point predicted by the potential.

The most worrying conclusion is that the result of cascade simulations using a given potential may be greatly influenced by the partially arbitrary choices made when stiffening it, the TDE being of essentially no use to guide in this operation. For example, would cascades simulated with the AMS potential, probably the best one available right now for α-Fe, still predict the same large amount of vacancies in clusters after harder stiffening? For the moment, there is no asnwer to this question.

Acknowledgements

This work required a fairly large amount of CPU time to be performed and the simultaneous use of different computing facilities was necessary. Four PC clusters, located respectively at SCK•CEN, KTH, U. Uppsala and ULB (how to refer to Marc's cluster?) were used for the task. This work, supported by the European Commission under the contract of Association between Euratom and the Belgian, Swedish and Finnish States, was carried out within the framework of the European Fusion Development Agreement (EFDA), task TTMS-007. The views and opinions expressed herein do not necessarily reflect those of the European Commission.

References

Tables

Table 1 – Summary of the main properties of the four interatomic potentials used in this work for cascade simulations. Legend: a_0 (lattice parameter); E_{coh} (cohesive energy); $\Delta E_{fcc\text{-}bcc}$ (energy difference between the two phases); E_V^f and E_V^m (vacancy formation and migration energy);

Q^{SD} (self-diffusion activation energy); $E^f_{\langle 110\rangle}$ and $E^f_{\langle 111\rangle}$ (SIA configuration formation energy); $\Delta E_{\langle 111\rangle\text{-}\langle 110\rangle}$ (relative stability of SIA configurations); TDE along the three main directions and in average, including median value[Nordlund]; S (stiffness) and R (range), (see text).

Equilibrium properties	**ABC**	**CWP**	**AMS**	**WOL**	**Exp.**	**Ab initio**
a_0 [Å] (0 K)	2.867	2.866	2.855	2.860	2.86[a]	2.85-2.86[b]
E_{coh} [eV]	-4.316	-4.28	-4.013	-4.28	-4.28[c]	
$\Delta E_{fcc\text{-}bcc}$ [meV]	54	50	?	47	50[d]	35[e]
Point-defect energies [eV]	**ABC**	**CWP**	**AMS**	**WOL**	**Exp.**	**Ab initio[b]**
E_V^f	1.70	1.54	1.71	2.08	2.0±0.2[f],1.5[g], 1.6±0.10[h], ~1.6-1.75[i]	1.93-2.09
E_V^m	0.78	0.73	0.63	0.81	0.55[j], 0.57±0.14[k];(1.3)[l,±]	0.59-0.67
$Q^{SD} = E_V^f + E_V^m$	2.48	2.27	2.34	2.89	2.48[m]-3.13[n,*]	*2.52-2.76*
$E^f_{\langle 110\rangle}$	4.87	4.15	3.59	6.45	Stable config is ⟨110⟩ db; E^f=4.7-5[o]	3.64
$E^f_{\langle 111\rangle}$	5.00	4.02	4.03	6.87		4.34
$\Delta E_{\langle 111\rangle\text{-}\langle 110\rangle}$	0.13	-0.13	0.44	0.42		0.70

TDE [eV]	**ABC**	**CWP**	**AMS**	**WOL**	**Exp.**
⟨100⟩	18	20	18	22	17[p]
⟨110⟩	32	48	34	28	>30[p]
⟨111⟩	36	30	34	32	20[p]
Mean (Median)	45.8±0.4 (42)	54.5±0.5 (54)	40±0.3 (36)	41.8±0.3 (38)	(40)[q] (recomm. value)

Stiffness	**ABC**	**CWP**	**AMS**	**WOL**
R [Å]	1.30	1.23	1.29	1.11
S [eV/Å]	-95	-124	-65	-203

[a]Ref [Simmons&Wang]
[b]Ref [Fu04]
[c]Ref [Kittel]
[d]Ref [Bendick82]
[e]Ref [Moroni97]
[f]Ref [DeSchepper83]
[g]Ref [Maier78]
[h]Ref [Schaefer77, Matter79]
[i]Ref [Fürderer87,Seeger98]
[j]Ref [Cuddy68]
[k]Ref [Tabata83]
[l]Ref [Woo83, Philipp87]
[m]Ref [Buffington61]
[n]Ref [Amonenko64]
[o]Ref [Wollenberger96]
[p]Ref [Maury76]
[p]Ref [ASTM,Broeders04]

[±] The value 1.3 seems to be the result of not high enough purity of Fe [Tabata83]

* About 15 experimental measurements reported, giving values within this range, see e.g. website: http://diffusion.nims.go.jp/index_eng.html

Table 2 – Summary of recoil energies, simulation box size and number of simulated cascades in this work.

PKA energy [keV]	Box size [number of atoms]	Number of cascades			
		ABC	**CWP**	**AMS**	**WOL**
5	250000	*10*	*10*	*10*	*10*
10	250000	*10*	*10*	*10*	*10*
15	432000	*10*	*10*	*10*	*10*
20	432000	*10*	*10*	*10*	*10*
30	~750000 (?)	*10*	*10*	*10*	*10*
40	800000	*10*	*10*	*10*	*10*

PKA energy [keV]	Box size [number of atoms]	Number of cascades (per potential)
5	250000	10
10	250000	10
15	432000	10
20	432000	10
30	~750000 (?)	10
40	800000	10*

* In the case of WOL no 40 keV cascades could be simulated (see text)

Table 3 – Time-step scheme used for cascade simulations in this work.

Cascade phase	Duration	Adopted time-step
Ballistic	0 – 0.5 ps	0.01 fs
Post-collisional	0.5 – 3.0 ps	0.05 fs
Recombination	3.0 – 13.0 ps	0.1 fs
Short-term defect evolution	13.0 – 23.0 ps	0.5 fs

Figure captions

Figure 1 – Number of defects (above) and cascade density (below) at peak time versus recoil energy according to the four potentials used in this work. Lines are guides for the eyes.

Figure 2 – Relaxation time versus recoil energy according to the four potentials used in this work. Lines are linear interpolations.

Figure 3 – Defect production efficiency compared to NRT displacements (see text) according to the four potentials used in this work.

Figure 4 – Fraction of SIA (above) and vacancies (below) in cluster according to the four potentials used in this work. The SIA clustered fraction was determined by visual inspection, while for the vacancies an automated procedure with 2nd nn distance criterion was applied.

Figure 5 *– Appearance at peak time of a typical cascade simulated with WOL (above) and with AMS (below). The two potentials predict opposite cascade behaviour and the former is the softest, while the latter is the stiffest..*

Figure 6 – Evolution in time of the fraction of SIA (above) and vacancies (below) in cluster in 15 keV cascades, according to potentials AMS, ABC and WOL (CWP provides results extremely similar to ABC and the relevant curves are therefore not shown). SIA and V clusters are defined, respectively, using a 3rd nn and a 2nd nn criterion.

Figure 1

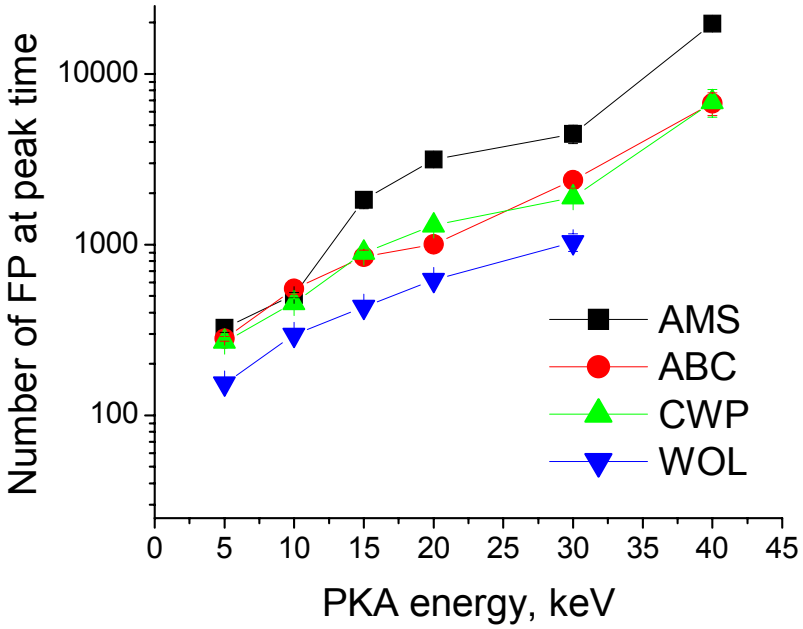
Number of FP at peak time
10000
1000
100
0
5
10
15
20
25
30
35
40
45
PKA energy, keV
AMS
ABC
CWP
WOL

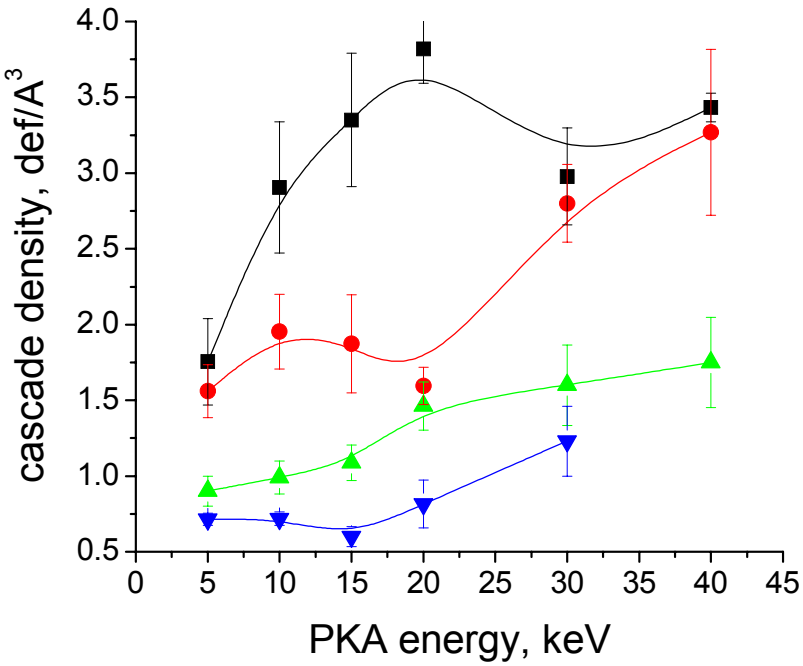
cascade density, def/A^3
4.0
3.5
3.0
2.5
2.0
1.5
1.0
0.5
0
5
10
15
20
25
30
35
40
45
PKA energy, keV

Figure 2

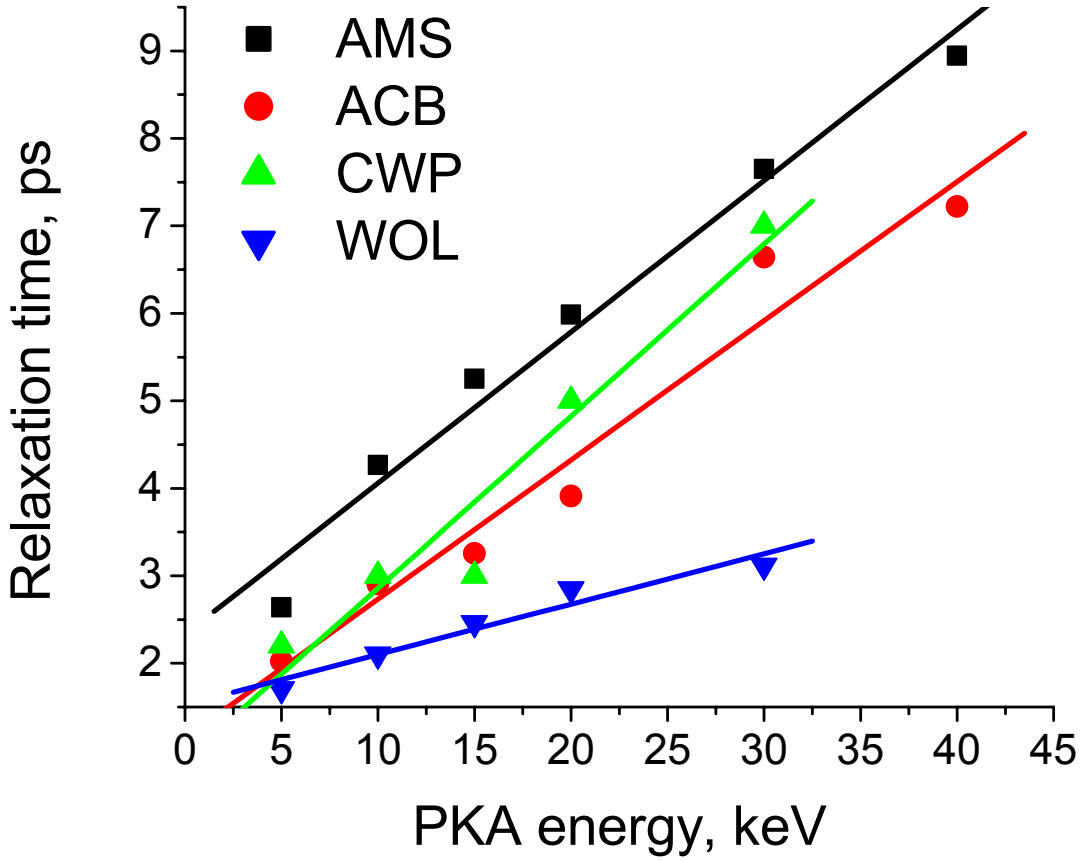
AMS
ACB
CWP
WOL
Relaxation time, ps
PKA energy, keV
0
5
10
15
20
25
30
35
40
45
2
3
4
5
6
7
8
9

Figure 3

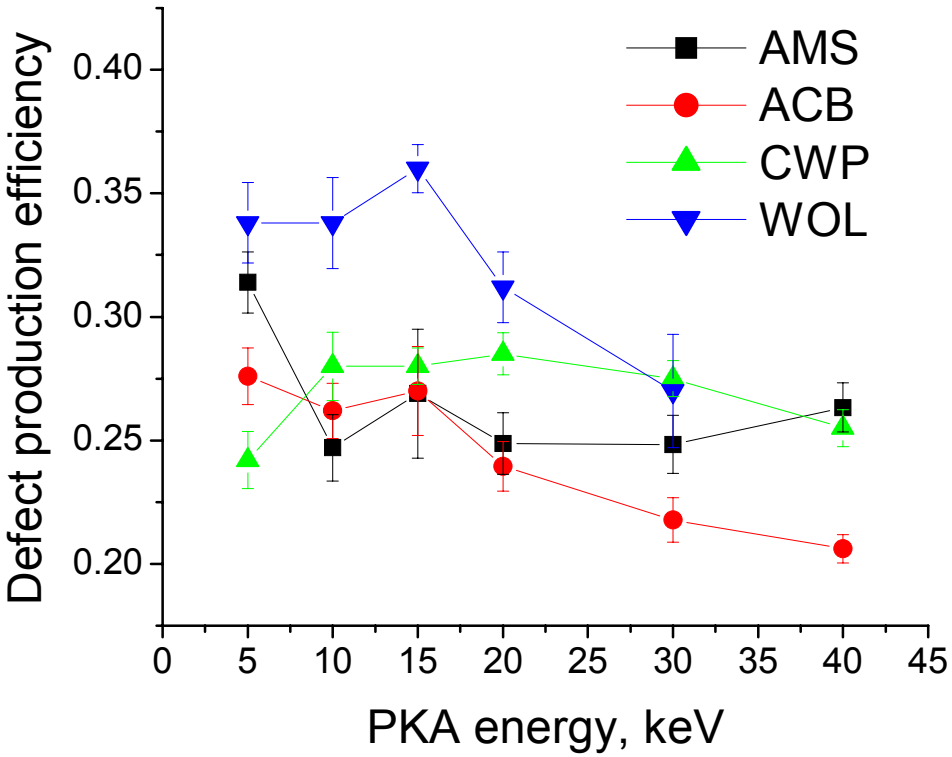
Defect production efficiency
0.40
0.35
0.30
0.25
0.20
0
5
10
15
20
25
30
35
40
45
PKA energy, keV
AMS
ACB
CWP
WOL

Figure 4

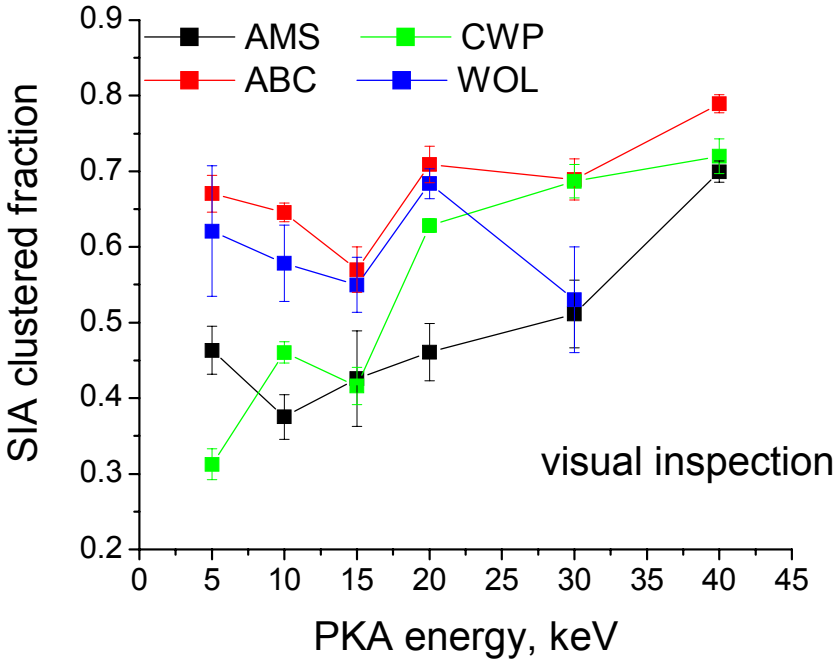
AMS
CWP
ABC
WOL
SIA clustered fraction
visual inspection
PKA energy, keV

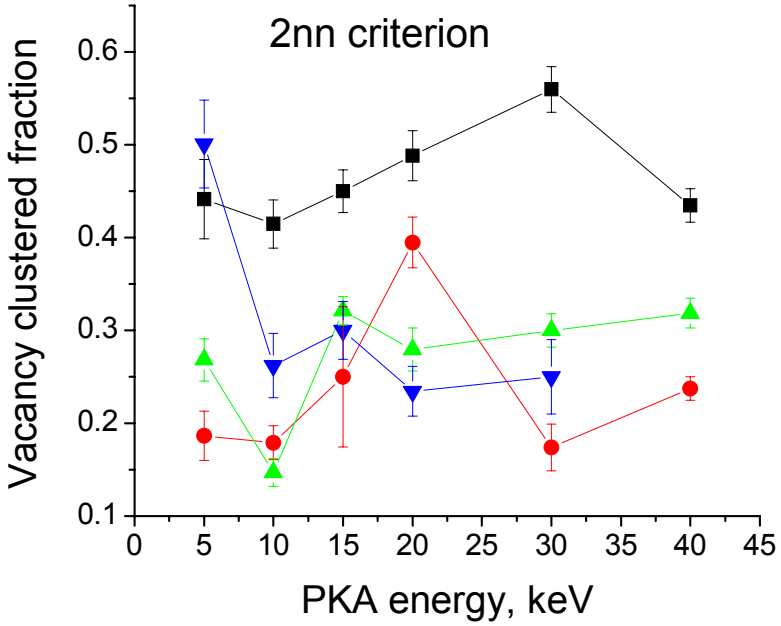
2nn criterion
Vacancy clustered fraction
PKA energy, keV

Figure 5

Figure 6

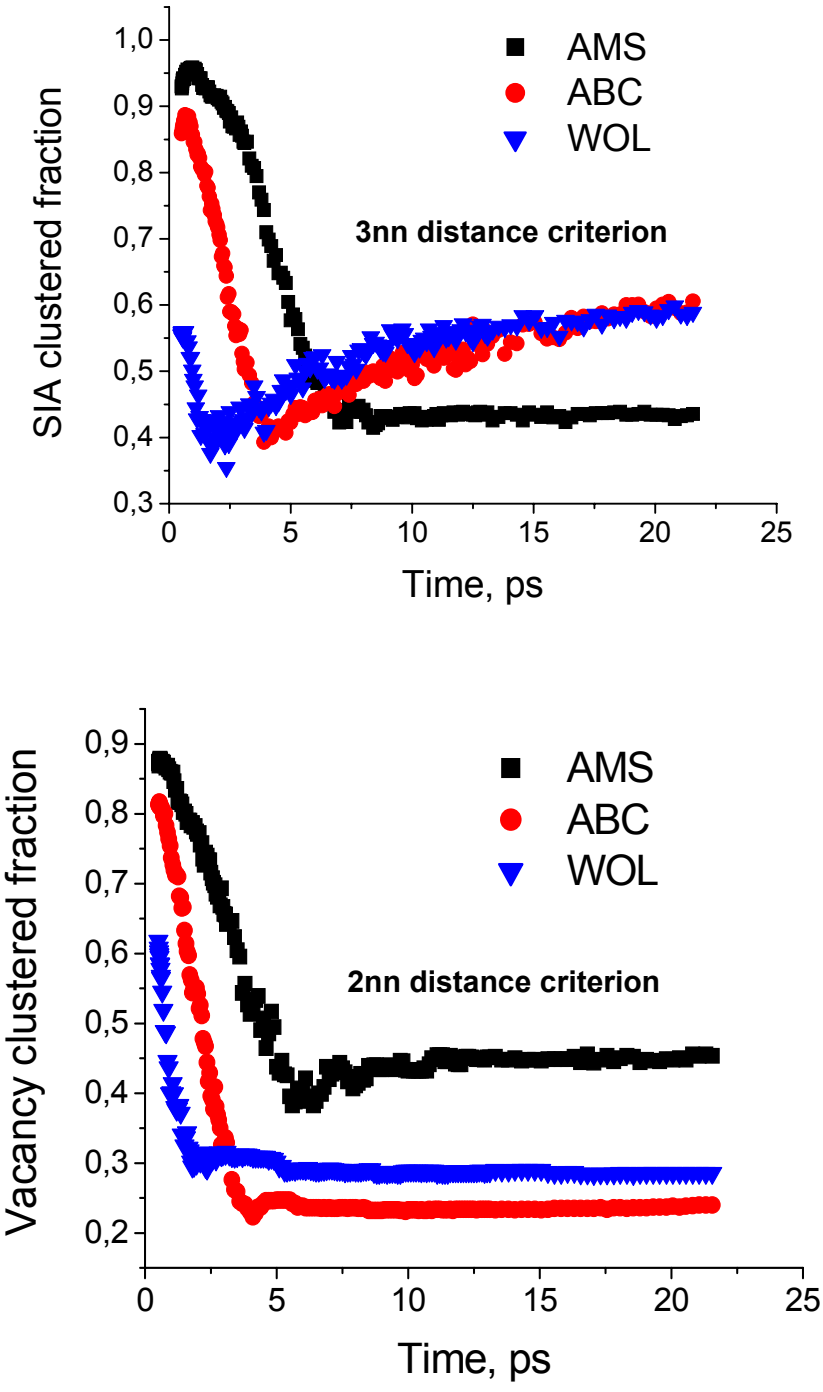
SIA clustered fraction
Time, ps
AMS
ABC
WOL
3nn distance criterion
Vacancy clustered fraction
Time, ps
AMS
ABC
WOL
2nn distance criterion

APPENDIX 9

J. Wallenius P. Olsson, C. Lagerstedt, N. Sandberg, R. Chakarova and V. Pontikis, Modelling of Chromium precipitation in Fe-Cr alloys, Phys. Rev. B 69, 094103 (2004)

Modelling of Chromium precipitation in Fe-Cr alloys

J. Wallenius[1,2], P. Olsson[2], C. Lagerstedt[1], N. Sandberg[1], R. Chakarova[1] and V. Pontikis[3]
[1] *Department of Nuclear and Reactor Physics, Royal Institute of Technology, Stockholm, Sweden*
[2] *Department of Neutron Research, Uppsala University, Uppsala, Sweden*
[3] *CNRS-CECM, Paris, France*
(Dated: November 4, 2003)

We have implemented a set of Embedded Atom Method (EAM) potentials for simulation of Fe-Cr alloys. The functions for the pure elements were fitted to the respective elastic constants, vacancy formation energy and thermal expansion coefficients. For Cr, properties of the paramagnetic state were applied, providing a positive Cauchy pressure and hence applicability of the EAM. By relaxing the requirement of reproducing the pressure-volume relation at short interaction distances, stability of the $\langle 110 \rangle$ self-interstitial could be obtained. Our Fe-potential gives $E^f_{\langle 110 \rangle} - E^f_{\langle 111 \rangle} = -0.22\ eV$. Mixed Fe-Cr pair potentials were fitted to the calculated mixing enthalpy of ferromagnetic Fe-Cr, which is negative for Cr concentrations below 6%. Simulation of thermal ageing in Fe-Cr alloys using a potential fitted to the mixing enthalpy of Fe-20Cr exhibited pronounced Cr-precipitation for temperatures below 900 K, in agreement with the phase diagram. No such ordering was observed at any temperature using a potential fitted to the mixing enthalpy of Fe-5Cr. Applied to recoil cascade simulations the new potentials predict a smaller number of surviving defects than potentials found in the literature. We obtain a cascade efficiency of 0.135 NRT for damage energies inbetween 10 and 20 keV. An enhanced probability for Cr atoms to end up in defect structures is observed.

PACS numbers: 61.66.Dk,61.80.Hg,61.82.Bg

INTRODUCTION

An improved understanding of the radiation effects in ferritic steels is of importance for development of new reactors and maintenance of already operating systems. Neutron and proton irradiation cause hardening, embrittlement and dimensional instability of the construction components. The material response is complicated with a strong dependence on the particular composition. Experiments on irradiation of Fe-Cr alloys at doses below 15 DPA, where impact of He generation is possible to neglect, show that adding 2-6 percent of Cr leads to a decrease in swelling as compared to pure Fe [1, 2]. There is a general trend towards a minimum in ductile to brittle transition temperatures at about nine percent Cr content. Formation of the Cr rich α' phase above Cr concentrations of 10% is a major cause of hardening, indicating that chromium plays a main role in the qualitative understanding of Fe-Cr properties in- and out of pile [3–7].

The Molecular Dynamics (MD) method is widely used as a basic theoretical tool, providing physical insight into kinetic processes and interactions leading to the formation of defect clusters, dislocation loops etc. The validity of the conclusions is directly related to the validity of the interaction potential adopted. A binary alloy potential is usually constructed on the basis of the potentials of the elements constituting the alloy [8, 9]. Thus the quality of the potential is determined by the extent to which the pure element - and the alloy properties are reproduced.

Two different types of many-body potentials have been used in MD studies of bcc-iron reported in the literature, namely Finnis-Sinclair potentials, relying on a second moment approximation to the tight binding theory [10–12], and Embedded Atom Method (EAM) potentials [13–18], having their roots in Density Functional Theory.

Fe-Cr alloy potentials have also been constructed using the Finnis-Sinclair approach [19] as well as the EAM [20]. These are fitted to measurements of mixing enthalpy and to the lattice parameter of the alloy. The experimental values of the heat of mixing used in those works are however valid only for for the paramagnetic state of the material (above the Curie temperature). Further, properties of anti-ferromagnetic (AFM) Cr were used in fitting of the Cr potential used by these authors, in spite of the negative Cauchy pressure of the AFM state.

The objective of the present work is to construct a set of Fe-Cr potentials that can reproduce essential properties of the alloy, such as the mixing enthalpy of the ferromagnetic (FM) state. The potentials should be applicable to simulations of the primary defect formation induced by high energy recoils, as well as to modelling of the subsequent defect evolution. It has to be noted that experimental data describing basic Fe-Cr alloy characteristics of use to the potential fitting, are not always available. In our case, there are experimental data for the bulk modulus of Fe-Cr alloys with different Cr contents. However, no measurements are reported for the mixing enthalpy of ferromagnetic Fe-Cr. Therefore, our modelling approach integrates Ab Initio calculations of Fe-Cr alloy properties, design of an EAM potential fitted to these data and usage of the potential in MD cascade simulations.

In what follows, we will describe our approach to obtain physically consistent EAM-potentials for ferromagnetic iron, paramagnetic (PM) chromium, and ferromagnetic alloys of these elements. The applicability of our potentials is corroborated by kinetic Monte Carlo simulation of thermal ageing of alloys with varying concentrations of chromium. We then account for results from recoil cascade calculations, pointing out significant differences in defect production in the alloy, as compared to pure iron. Finally we discuss the impact of our results on the general understanding of Fe-Cr properties in- and out of pile.

CONSTRUCTION OF THE EAM POTENTIAL

Within the EAM formalism, the total energy of the system of n atoms is written as a sum over atomic energies [13]:

$$E_{\mathrm{tot}} = \sum_{i=1}^{n} E_i = \sum_{i=1}^{n} \left[\frac{1}{2} \sum_{j=1}^{n} \Phi(r_{ij}) + F(\rho_i) \right], \quad (1)$$

where $\Phi(r_{ij})$ is the pairwise (electrostatic) interaction between atoms i and j; the function $\rho_i = \sum_{j \neq i} \rho(r_{ij})$ represents the electron density of the host system with atom i removed and r_{ij} is the scalar distance between atoms i and j. $F(\rho_i)$ is the many body term, i.e. the quantum mechanical energy required to embed atom i into a homogeneous electron gas of density ρ_i . Because the electron density depends only on scalar distances to neighbouring atoms, the many body term here has no angular dependence. The curvature of F may be interpreted in terms of the traditional chemical bonding concept, where a new bond increases the total bonding energy but decreases the average energy per bond. In this context, ρ_i becomes a measure of the total bond order and $\rho(r)$ is a bond sensor. The weakening of successive bonds corresponds to a positive curvature of F:

$$\frac{\partial^2 F}{\partial \rho^2} > 0. \quad (2)$$

The complete EAM energy expression in the case of binary Fe-Cr alloys involves definitions for the pair potentials $\Phi_{\mathrm{Fe}}(r), \Phi_{\mathrm{Cr}}(r)$ of pure Fe and Cr, the mixed pair potential $\Phi_{\mathrm{FeCr}}(r)$, the electronic density functions $\rho_{\mathrm{Fe}}(r), \rho_{\mathrm{Cr}}(r)$ and the embedding functions $F_{\mathrm{Fe}}(\rho)$ and $F_{\mathrm{Cr}}(\rho)$:

$$\begin{aligned} E_{\mathrm{tot}} &= \sum_{i_{\mathrm{Fe}}} F_{\mathrm{Fe}}(\rho_i) + \sum_{i_{\mathrm{Cr}}} F_{\mathrm{Cr}}(\rho_i) \\ &+ \frac{1}{2} \sum_{i_{\mathrm{Fe}}, j_{\mathrm{Fe}}} \Phi_{\mathrm{Fe}}(r_{ij}) + \frac{1}{2} \sum_{i_{\mathrm{Fe}}, j_{\mathrm{Cr}}} \Phi_{\mathrm{FeCr}}(r_{ij}) \quad (3) \\ &+ \frac{1}{2} \sum_{i_{\mathrm{Cr}}, j_{\mathrm{Cr}}} \Phi_{\mathrm{Cr}}(r_{ij}) + \frac{1}{2} \sum_{i_{\mathrm{Cr}}, j_{\mathrm{Fe}}} \Phi_{\mathrm{FeCr}}(r_{ij}) \end{aligned}$$

It is seen from equation 3 that the potentials of the pure elements potentials are part of the alloy potential.

The following parametric form of the pair interaction terms is assumed [12, 15]:

$$\Phi(r) = \sum_{i=1}^{5} a_i (r - r_i)^3 H(r_i - r) \quad (4)$$

Here, r_i are knot points of the cubic splines used to represent the potential, H is the Heaviside step function, and a_i are spline coefficients. The atom electron density is approximated by the Thomas-Fermi screening function suggested in reference [15].

The Fe and Cr embedding functions are calculated by fitting the cohesive energy to the Rose expression, which gives the equation of state of a perfect crystal as a function of the reduced lattice parameter $\overline{a}$ [21]:

$$E_{\mathrm{Rose}}(\overline{a}) = -E_{\mathrm{coh}}(1 + \overline{a}) e^{-\overline{a}} \quad (5)$$

with

$$\overline{a} = \sqrt{\frac{9\Omega B}{E_{\mathrm{coh}}}} \left(\frac{R_1}{R_{1e}} - 1 \right) \quad (6)$$

where R_{1e} is the equilibrium value of the distance to the nearest neighbour. Ω is the atomic volume and B denotes the bulk modulus. Note that the alloy bulk modulus is not involved in expression 6, but only the bulk modulus of the pure elements. Since the range of the interactions needs to be finite, a cut-off is introduced in the electron density, with a corresponding modification of the Rose expression for large lattice parameters [9, 22].

Potentials for Fe and Cr

The fitting procedure has been perfomed in several steps. Three of the spline coefficients for ferromagnetic iron, corresponding to knot points larger than R_{1e}, were obtained by fitting to the lattice parameter, cohesive energy, vacancy formation energy and elastic constants as measured at zero Kelvin. A modified version of the Merlin code package was written for this step of the procedure. The package is based on elastic theory of deformation, including multi-parametric optimization with options for different algorithms [23, 24]. The conditions of equilibrium are expressed as a requirement of no stresses in a perfect crystal. Stresses are evaluated by expanding the energy to the first order with respect to an infinitesimal homogeneous strain applied to the system. The second order elastic constants are evaluated by expanding the energy of the system to the second order with respect to an infinitesimal homogeneous stress. For example,

$$C_{44} = \frac{\partial^2 E_{tot}}{\partial \gamma^2} \quad (7)$$

with γ being the angle of distortion by shear deformation imposed on the crystal when keeping the volume constant. In the case of compression in one direction and expansion in the other, the amplitude of deformation for a constant volume is denoted by ϵ, and the corresponding elastic constant is

$$C' = \frac{1}{2}(C_{11} - C_{12}) = \frac{1}{4}\frac{\partial^2 E_{tot}}{\partial \epsilon^2} \quad (8)$$

The bulk modulus is obtained by simulating isotropic compression:

$$B = \frac{1}{9}\frac{\partial^2 E_{tot}}{\partial \epsilon^2}. \quad (9)$$

The embedding function of iron was then calculated using these three spline coefficients for the pair potential. After thus fixing the embedding function, the fourth spline coefficient was determined by fitting to the lattice parameter of iron at room temperature. The position of the corresponding knot point was adjusted to mimic the temperature dependence of the thermal expansion coefficient in the temperature range $0 - 600\ K$. The molecular dynamics code XMD was used for this purpose, in which the condition of constant pressure is imposed by the *pressure clamp* command [25]. The final spline coefficient was set to ensure a smooth transition of the pair potential into the universal screened Coulomb function of Biersack et al [11, 12, 26].

A similar procedure was implemented to obtain the potential for pure chromium. Previous attempts to fit a central many-body potential to the elastic constants of anti-ferromagnetic chromium have failed, as may be expected from the negative value of the Cauchy pressure at zero Kelvin:

$$\frac{1}{2}(C_{12} - C_{44}) \simeq -13\ GPa. \quad (10)$$

We note however, that at temperatures relevant for reactor operation ($T > 450\ K$), chromium is paramagnetic, featuring a positive Cauchy pressure [27]. Further, it is sufficient to add a few percent of iron or vanadium to obtain an alloy that is paramagnetic at room temperature [28, 29]. We therefore fit our Cr potential to the elastic constants of paramagnetic chromium, linearly extrapolated down to zero Kelvin. Stiffening of the pair potential is made by fitting to thermal expansion coefficients measured for paramagnetic Cr-5V, being equal to the expansion coefficient of pure Cr when $T > 600\ K$ [29]. Considering that the Cr precipitates observed in real Fe-Cr alloys contain about 15 percent iron, we believe that our potential for paramagnetic Cr should be valid for describing Cr-Cr interactions in the present context.

In Table I we list the resulting spline coefficients and knot points for Fe and Cr. In Figure 1 the pair-potentials are plotted as function of r. Note the slightly larger depth of the potential for paramagnetic Cr, reflecting the larger vacancy formation energy predicted for Cr.

TABLE I: Knot points and spline coefficients for the pair potentials of Fe and Cr obtained in the present work. The knot points are given in units of nearest neighbour distance.

	Fe	$(a_0 = 0.2860\ nm)$	Cr	$(a_0 = 0.2875\ nm)$
i	r_i	a_i	r_i	a_i
1	0.945	2633	0.945	310
2	0.967	-2500	0.972	-603
3	1.030	10.75857	1.150	50.28020
4	1.320	-24.28842	1.280	-61.24700
5	1.540	7.078864	1.470	14.66964

We note that by stiffening the pair potentials inside the equilibrium nearest neighbour distance, *after having fixed* the embedding function, we violate the pressure-volume relation given by the Rose expression (5). The reason for doing so, is that we otherwise were un-able to simultaneously fit experimental values for $E_{\rm bcc} - E_{\rm fcc}$, $E^f_{<110>} - E^f_{<111>}$ and the thermal expansion coefficient. Our potentials are hence not applicable to simulation of isotropic compression under high pressure. However, the presence of high electron densities in recoil cascades as well as in defect configurations are of local character, which may be difficult to characterise through an equation of state like the Rose expression.

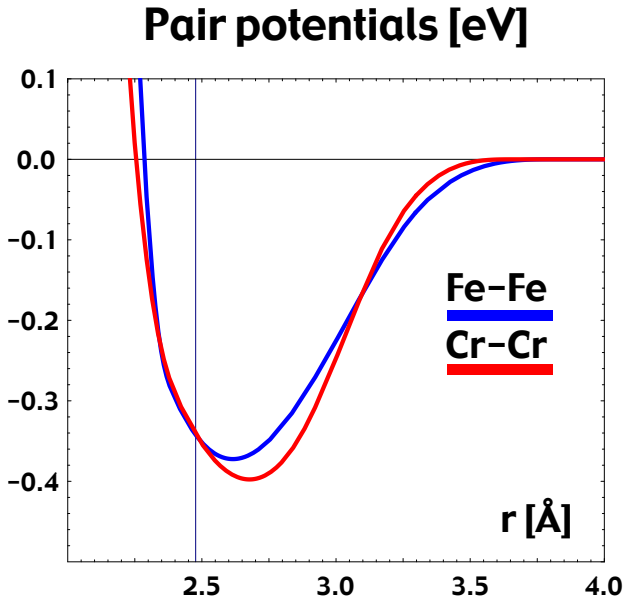

FIG. 1: Pair potentials for ferromagnetic Fe (blue line) and paramagnetic Cr (red line) obtained in the present work.

Mixed Fe-Cr pair potentials

The potentials obtained for the pure elements have been further used in equation 3 to calculate the parameters a_i for the mixed Fe-Cr pair potential, fitting them to the mixing enthalpy of the ferromagnetic alloy. Table II displays the formation energy of ferromagnetic Fe-Cr calculated with the EMTO method [31].

Previous attempts to construct mixed pair potentials for Fe-Cr [18, 20] relied on fitting to the formation energy of the paramagnetic state of the alloy, which is strictly positive. A single pair-potential for the Fe-Cr interaction would however not be able to reproduce the change in sign of the formation energy of the relevant magnetic state. Therefore, a set of potentials have to be created, providing the correct total energy of the random ferromagnetic alloy. In the present paper, we have performed the fitting for Cr-concentrations of 5% and 20%. The lower concentration should yield a potential with small but negative mixing entalphy, thus ensuring phase stability at all temperatures. The larger concentration was selected to study a region where the predicted mixing enthalpy is positive, and Cr precipitation (formation of the α' phase) is observed in real materials [3, 5].

The parameters obtained for the Fe-Cr mixed pair potentials are given in Table III. The sharp dip in the measured bulk modulus at Cr concentrations about five percent [30] lead us to assume a longer range for the corresponding pair potential. Due to the lack of thermal expansion data for the alloy, stiffening of the potentials at short distances was made in a rather arbitrary fashion, simply requiring a smooth transition to the universal Coulomb screening function at $r \simeq 1.7$ Å.

TABLE III: Knot points and spline coefficients for the mixed Fe-Cr pair potentials obtained in the present work. The knot points are given in units of nearest neighbour distance.

	Fe-5Cr	($a_0 = 0.2861\ nm$)	Fe-20Cr	($a_0 = 0.2863\ nm$)
i	r_i	a_i	r_i	a_i
1	0.945	2239	0.945	2624
2	0.967	-2199	0.967	-2476
3	1.030	0.000	1.030	10.000
4	1.400	-12.737	1.320	-24.500
5	1.650	4.210	1.53	7.620

VERIFICATION OF THE POTENTIALS

The quality of the potential has been inspected by calculations of elastic constants, structural stability and formation energies of various defect configurations. The results are shown in Tables IV, V and Table VII. Comparing with experimental data and values obtained by other authors, one may note the following: The potential here presented reproduces more closely the experimental elastic characteristics and structural stability of pure iron than the EAM-potentials published by Simonelli et al. Our relaxed vacancy formation energy (2.04 eV) was fitted to the resistivity measurements by De Schepper et al [34], indicating a significantly higher value for $E^f_{\rm vac}$ than earlier measurements in less pure materials [40]. The potential *predicts* an activation energy for self diffusion equal to 2.91 eV, in very good agreement with data obtained at temperatures sufficiently low for the influence of paramagnetism to be safely neglected [35, 36].

Our fit to thermal expansion data was made using a single spline coefficient, and can thus not be expected to reproduce measured data over the whole temperature range. One may note however that potentials not fitted to thermal expansion underestimates the expansion by a factor of two or more.

In comparison with the Finnis-Sinclair potential developed by Ackland and co-workers, our potential yields a stability of the $\langle 110 \rangle$ interstitial with respect to the $\langle 111 \rangle$ configuration that is in better agreement with measured

TABLE II: Formation energies ΔH_f of random ferromagnetic Fe-Cr alloys, calculated with the Exact Muffin Tin Orbital Ab Initio method [31].

Cr-fraction	ΔH_f [meV]
0.02	-1.8
0.04	-1.3
0.06	+0.6
0.08	+5.1
0.10	+10.4
0.15	+27.9
0.20	+45.3

TABLE IV: Properties of pure iron obtained with the potential for ferromagnetic Fe here presented. Elastic constants are given in units of GPa, energies in eV and thermal expansion coefficients in units of 10^{-6}. Comparison is made with experimental data and values calculated using the potentials of Simonelli [15] and Ackland [12].

Fe property	This work	Exp	Sim A	Sim B	Ackland
B	172	173[a]	146	146	178
C'	56.7	52.5[a]	48.0	48.0	49.0
C_{44}	135	122[a]	115	115	116
$E_{\rm coh}$	4.28	4.28	4.28	4.28	4.316
$E_{\rm bcc} - E_{\rm fcc}$	-0.047	-0.050[b]	-0.03	-0.007	-0.054
E^f_{vac}	2.04	2.0 ± 0.2[c]	1.63	1.56	1.62
$E^{\rm SD}_{\rm vac}$	2.91	2.91 ± 0.04[d]	2.32	2.29	2.48
$E^f_{<110>}$	7.72	3-12[e]	3.66	4.11	4.87
$E^f_{<110>}$-$E^f_{<111>}$	-0.23	-0.30[f]	+0.12	-0.19	-0.13
$\alpha\ (T = 300K)$	12.8	11.7[g]	5.8	3.4	7.4
$\alpha\ (T = 600K)$	14.2	15.8[g]	7.9	4.9	7.2

a) Ref. [32] b) Ref. [33] c) Ref. [34] d) Ref. [35, 36] e) Ref [37, 38] f) Ref [38] g) Ref. [39]

data. The predicted absolute formation energy of the Fe self-interstitial is higher than what results from using any other potential found in literature. We note that the experimental values are derived from measurements of stored energy release per resistivity recovery ($dQ/d\rho$) in samples irradiated at low temperature [38, 41]. The enthalpy for formation of a Frenkel pair is obtained by multiplying $dQ/d\rho$ with an assumed resistivity $\rho_{\rm F}$ for a single Frenkel pair. Estimates of $\rho_{\rm F}$ vary from 0.20 to 0.30 $m\Omega \times cm$ [42, 43]. Selecting the higher value, Wollenberger arrives at a formation energy $E_F^f = 6.6\ eV$ for a Frenkel pair in electron irradiated α-Fe, and $E_F^f = 13.6\ eV$ for a neutron irradiated sample [41]. Subtracting a vacancy formation energy of 2.0 eV would then give $E^f_{<110>} = 4.6\ eV$ in the former case, and 11.6 eV in the latter. The uncertainty of these values is obviously large, since just by assuming $\rho_{\rm F} = 0.20\ m\Omega \times cm$, one could obtain $E^f_{<110>} = 7.7\ eV$ for the neutron irradiated sample. Note that results from the electron irradiation not necessarily are more accurate, since experimental boundary conditions are more difficult to control in stages $I_{\rm A}$ to $I_{\rm C}$ (absent in neutron irradiation) than in stage $I_{\rm D}$.

The SIA formation energy in iron havs recently been calculated with the Ab Initio package VASP as $E^f_{<110>} \simeq 3.4\ eV$ [46]. This result is compatible with data from electron irradiations. However, since the calculation did not take into account possible effects of non-colinear magnetism, the discrepancy with data from neutron irradiated samples remains an open question. As will be seen later, the magnitude of the interstitial formation energy has a significant impact on defect recombination in recoil cascades, and we will argue that a high value is consistent with defect distributions actually observed.

TABLE V: Properties of paramagnetic Cr calculated with the potential here presented. Comparison is made with experimental data for Cr in AFM and PM states, as well as values calculated using the potential of Farkas [20]. PM elastic constants were obtained by extrapolation to zero Kelvin of high temperature data [27]. The paramagnetic thermal expansion coefficient at $T = 300\ K$ refers to measurements on Cr-5V [29].

Cr property	This work	Exp (AFM)	Exp (PM)	Farkas
B	207	195^a	207^a	148
C'	153	153^a	155^a	42.5
C_{44}	105	104^a	105^a	-
$E_{\rm coh}$	4.10	4.10	4.10	4.10
$E_{\rm bcc} - E_{\rm fcc}$	-0.025	-	-	-0.053
$E^f_{\rm vac}$	2.14	-	2.0 ± 0.2^b	1.12
$E^{\rm SD}_{\rm vac}$	2.93	-	2.95^c	2.30
$E^f_{<110>}$	5.16	-	-	3.03
$E^f_{<110>}$-$E^f_{<111>}$	-0.62	-	-	0.19
$\alpha\ (T = 300K)$	7.5	4.4^d	7.9^d	5.2
$\alpha\ (T = 600K)$	9.8	-	9.6^d	9.5

a) Ref [27] b) Ref.[44] c) Ref.[45] d) Ref.[29]

TABLE VI: Comparison of Fe-Cr mixing enthalpy obtained with the potentials here presented, the Exact Muffin Tin Orbital calculation of Olsson et al [31] and values calculated using the potential of Farkas et al [20].

Property	Data	Fe-5Cr	Fe-20Cr
$H^f_{\rm FeCr}$ [meV]	This work	-0.04	+45
	EMTO	-0.05	+45
	Farkas	+24	+86

Concerning the properties of chromium predicted by the potential here presented, we emphasize that the fit was made to elastic constants of *paramagnetic* chromium, extrapolated to zero Kelvin. Hence we are able to retain a positive Cauchy pressure at all temperatures. The relaxed vacancy formation energy is compatible with experimental data, in contrast to the prediction of the potential by Farkas et al [20], for which an apparently incorrectly quoted value of $E^f_{\rm vac}$ has been used in the fit. We further note that the activation energy for vacancy diffusion predicted by the potential is in excellent agreement with measured data [45].

As seen in Table VI, the alloy potentials well reproduce the mixing enthalpies of Fe-5Cr and Fe-20Cr calculated with the EMTO method. The heat of mixing obtained with Farkas' potential should be considered to represent the paramagnetic state of the alloy, and is hence not applicable for MD or KMC simulations below the Curie temperature.

Table VII displays formation and binding energies of a single mixed $\langle 110 \rangle$ Fe-Cr dumbbell in an iron matrix. We find that the mixed $\langle 110 \rangle$ Fe-Cr dumbbell is more stable than the $\langle 110 \rangle$ Fe-Fe dumbbell in the case of local Cr concentrations less than 20%. The Cr-Cr dumbbell is even more stable, with a binding energy exceeding 0.3 eV. Hence one may expect that Cr will tend to accumulate in defect structures created in collision cascades.

The sparse experimental data for the elastic constants of the alloy are unfortunately not fully consistent [30, 48]. Below the solubility limit of Cr though, there is a clear tendency for a decrease in bulk modulus, which is sup-

TABLE VII: Formation and binding energies of a single mixed $\langle 110 \rangle$ Fe-Cr dumbbell in an iron matrix with lattice parameter $a_0 = 2.860$ Å. Predictions of the alloy potentials are compared to VASP Ab Initio data [47] and values calculated with Farkas' potential [20]. $-E^b_{<110>} = E^{\rm Cr}_{<110>} - E^{\rm Fe}_{<110>} - E^s_{\rm Cr}$ is calculated relative to the energy of an Fe-Fe dumbbell, subtracting the substitution energy $E^s_{\rm Cr}$ of a single Cr atom.

Property	$E^f_{<110>}$	$E^s_{\rm Cr}$	$E^b_{<110>}$	$E^f_{<110>}$-$E^f_{<111>}$
Fe-5Cr	7.63	+0.18	+0.27	-0.03
Fe-20Cr	8.19	+0.46	-0.01	-0.20
VASP	3.06	-0.35	-0.00	+0.36
Farkas	4.31	+0.70	+0.05	+0.07

ported by Ab Initio calculations. The range of the Fe-5Cr potential was therefore enlarged, in order to obtain a smaller bulk modulus. This procedure must however be considered as arbitrary, and better experimental data for the alloy, including thermal expansion, is of necessity to enable construction of fully consistent mixed pair potentials.

Due to the non-monotonous behaviour of the bulk modulus and the formation energy, a potential for a given Cr-concentration can in general not be used for predicting alloy properties at a different concentration. Proper simulation of non-equilibrium behaviour of the alloy would require use of different potentials for different local concentrations of chromium.

APPLICATION OF THE FE-CR POTENTIAL IN SIMULATION OF THERMAL AGEING

It is well known that precipitation of Cr occurs under thermal ageing at $T < 900\ K$ in FeCr alloys with Cr content ranging from 10 to 90% [3, 5]. The formation of the so-called α' phase is responsible for hardening of the binary alloy [49, 50]. The magnitude of the miscibility gap for low Cr-concentrations could be theoretically explained only recently, when Ab Initio calculations showed that the mixing enthalpy of Fe-Cr is negative for the *ferromagnetic* state of the random alloy, if the Cr concentration is below six percent [31]. Above this limit, the formation energy is positive, providing a driving force for phase separation. In order to obtain the temperature dependence of the solubility, one needs to perform molecular dynamics, or rather Kinetic Monte Carlo (KMC) simulations. We have performed such simulations of thermal ageing at a range of temperatures, using several different techniques implemented in the DYMOKA code, developed by Electricite de France (EDF) and University of Lille [51].

The out- of pile process of segregation is assumed to be driven purely by vacancy assisted migration. According to classical diffusion theory, the frequency for a lattice atom to exchange lattice position with a neighbouring vacancy is

$$\Gamma(T) = \nu C_{\mathrm{vac}}(T) e^{-\frac{E_m}{k_{\mathrm{B}}T}} \tag{11}$$

where ν is the attempt frequency of the jump and C_{vac} is the equilibrium concentration of vacancies. The vacancy concentration as function of temperature is given by

$$C_{\mathrm{vac}}(T) = e^{-\frac{G_f}{k_{\mathrm{B}}T}}. \tag{12}$$

Here, $G_f = E^f_{\mathrm{vac}} - TS^f_{\mathrm{vac}}$ is the Gibbs energy of vacancy *formation*. The entropy of formation may be calculated from the following formula [52]:

$$S^f_{\mathrm{vac}} = k_{\mathrm{B}} \left(\sum_n^{3(N-1)} \ln \omega_n^{\mathrm{vac}} - \frac{(N-1)}{N} \sum_n^{3N} \ln \omega_n^{\mathrm{bulk}} \right) \tag{13}$$

where ω_n are eigen frequencies of the force-constant matrices with an without a vacancy in the system, respectively. MD simulations using our potential for ferromagnetic iron gives $S^f_{\mathrm{vac}} = 1.78\ k_{\mathrm{B}}$ for a relaxed system of $N = 432$ atoms.

Similarly, the attempt frequency ν may be calculated from [53]

$$\nu = \frac{k_{\mathrm{B}}}{2\pi} \frac{\prod_{n=1}^{3N} \omega_n^{\mathrm{vac}}}{\prod_{n=1}^{3N-1} \omega_n^{\mathrm{TST}}} \tag{14}$$

where ω^{TST} are the eigenfrequencies evaluated at the transition state of the vacancy jump. For the present potential we obtain $\nu = 9.15 \times 10^{13}\ s^{-1}$ which gives us a prefactor for self-diffusion in ferromagnetic iron: $D_0 = 2.13 \times 10^{-5} m^2/s$. This value, valid in the harmonic approximation, is very close to the one observed in experiments [36].

In general, the probability of all possible vacancy jumps in an alloy (8 first nearest neighbours in a bcc structure) should be computed for every Monte Carlo step, selecting one of them to be performed, weighted with that probablity. Time is then introduced as the inverse of the system averaged jump frequencies. In our case, the vacancy assisted migration energy for Fe and Cr atoms are close to each other; 0.87 eV and 0.84 eV, respectively. We hence make a concentration weighted average for our system and calculate an average timestep as

$$\Delta\tau = \frac{1}{8\Gamma(T)}. \tag{15}$$

We performed simulations of vacancy migration assuming a single vacancy in a box with 16 000 atoms. It was checked that the rate of energy loss in the Fe-20Cr alloy did not change significantly when increasing the box sixe.

In order to arrive at a fully segregated final state, we used a Metropolis Monte Carlo algorithm, together with the vacancy KMC. The metropolis algorithm exchanges all atoms of differing type if it is energetically favorable. If an exchange increases the energy it is accepted with a weight $\exp(-E/kT)$ where E is the potential energy of the system. The Metropolis MC method is much faster, but provides no explicit time-scale. However, it was found that a time-step could be assigned to each Metropolis MC step by fitting energy losses to the explicit vacancy KMC simulation.

In Figure 2, the total energy of an initially random Fe-20Cr alloy is plotted as function of time and temperature. Since the mixing enthalpy of the random alloy is positive,

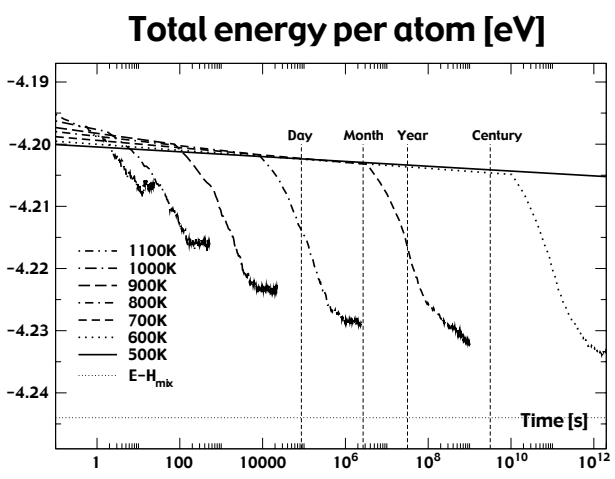

FIG. 2: Total energy of an initially random Fe-20Cr alloy, as function of time and temperature.

a loss in energy is a sign of segregation. For infinite segregation, the energy loss would equal the formation energy $\Delta H^f_{Fe-20Cr} = 45\ meV$. In a finite box, however, there will alway remain a surface to bulk factor. The surface atoms of a Cr cluster will all have Fe neighbours and thus a higher energy. In our most segregated case (T = 500 K) we arrive at 84% of the mixing enthalpy. This may be understood from the fact that a single Cr cluster of spherical shape in our simulation box has a surface to bulk ratio of Cr atoms equal to about 30%. On the cluster surface, half of the neighbours to Cr atoms are Fe atoms, and hence the surface energy of final Cr cluster provides the missing 16%.

We note that for 700 K, the time needed to obtain a significant energy loss is of the order of months, which is consistent with the experimental time threshold for observation of hardening in Fe-45Cr alloys aged at 673 K [50]. For 800 K we have segregation occurs in a matter of days, while for 900 K, the energy loss saturates within a few hours, before complete phase separation has taken place. At 1000 K, less than half the energy loss is achieved, which corresponds to a limited ordering of the system, without actual phase separation.

The process of segregation is illustrated in Figure 3, where the distribution of Cr atoms is shown before and after ageing during 30 years at 700 K. This simulation was done with an initial Cr content equal to 12%, using the Fe-20Cr potential. The final Cr-precipitate appearing during the simulation is free of Fe atoms, due to the fact that our potential incorrectly predicts a positive mixing enthalpy even for Cr concentrations in the vicinity of 90%.

In order to quantify the temperature dependence of the phase separation, we define the degree of segregation

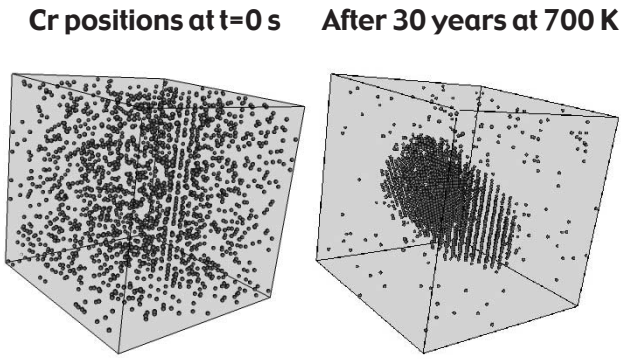

FIG. 3: Distribution of Cr atoms in a box with 16 000 atoms, before and after thermal ageing at 700 K. A crystal clear segregation is observed, with formation of a single cluster.

ξ as

$$\xi = \frac{1}{\xi_{\max}} \frac{N_{Cr}^{\mathrm{Emb}}}{N_{Cr}^{\mathrm{Tot}}}. \tag{16}$$

Here, N_{Cr}^{Tot} is the number of Cr atoms in the system, N_{Cr}^{Emb} is the number of Cr atoms that only have Cr first nearest neighbours amd $\xi_{\max}$ is the theoretical maximum number of Cr atoms that may have Cr first nearest neighbours, accounting for the surface layer of a spherical cluster.

The degree of segregation produced by the Fe-20Cr potential after the energy loss has reached its asymptotic value is shown in Figure 4. If an arbitrary limit of $\xi > 0.5$ is set to distinguish the α' phase from α, we find that this corresponds to $T < 900\ K$. Considering that the range of temperature where the phase transition takes place is uncertain, quoted as 750±125 K in reference [7], our results may be considered to be in reasonable agreement with the phase diagram. Performing the same type of

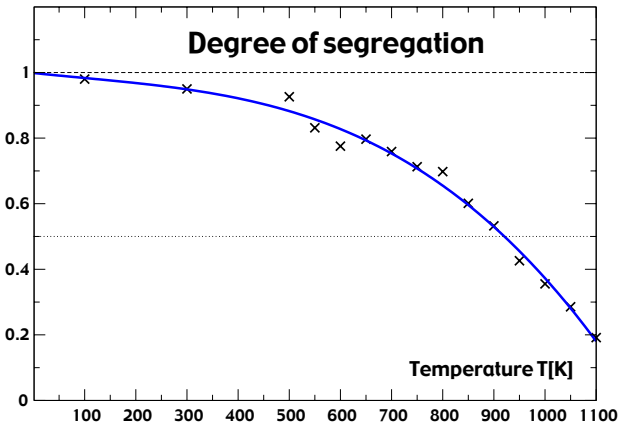

FIG. 4: Degree of segregation ξ as a function of temperature. The line is a cubic fit to asymptotic averages obtained with the Metropolis Monte Carlo procedure.

simulations using the potential fitted to the mixing enthalpy of Fe-5Cr, no significant energy loss is found at any temperature, which means that the alloy remains random. We may thus conclude that our potentials reproduce the out-of pile state of ferromagnetic Fe-Cr as function of temperature and time at Cr concentrations of zero, five and twenty percent.

It is important to note that in reality, the driving force for the decomposition would be lost when the local concentration of Cr becomes too high or too low. Hence, in order to obtain the physically observed final states with an iron content in the α' precipitates ranging from 10 to 20%, we would have to switch potentials during the simulation according to the local density of Cr, a feature not yet implemented in the codes we have used. Therefore the size of the clusters we observe at infinite times cannot be expected to agree with the measured size distribution, being of the order of 2-4 nm [50].

APPLICATION OF THE FE-CR POTENTIAL IN CASCADE SIMULATIONS

The potentials here presented were applied in molecular dynamics simulations of collision cascades initiated by recoils having energies up to 20 keV. Periodic boundary conditions were used, and the sizes of the MD boxes were adjusted to make sure that the cascade did not interact with its periodic image. For 10 keV cascades, it was found that 128000 atoms (40x40x40 lattice units) was sufficient for recoils in the $\langle 135 \rangle$ direction, while 250 000 atoms had to be used when launching in the $\langle 111 \rangle$ direction. The initial atom velocities were sampled from a Maxwellian distribution for a particular temperature, set to $T = 100$ K in the present study. The block is equilibrated for about a pico-second before launching an energetic recoil in the central region. The time step was varied from 0.02 fs (when the recoil is generated) up to 0.5 fs at the end of the simulation period, (10 ps). The first thing to be noted is that the new potentials predict a much smaller number of surviving defects than potentials found in the literature [11, 54]. This is a direct result of the higher interstitial formation energy, leading to larger probability for recombination of Frenkel pairs during cooling down of the cascade. Table VIII shows the average number of surviving defects in Fe and Fe-20Cr, for a set of representative recoil energies in the $\langle 135 \rangle$ direction.

As seen the difference between the alloy and pure iron is statistically insignificant. For recoil energies between 10 and 20 keV, we arrive at a cascade efficiency of 0.135 ± 0.005 NRT, which may be compared to a value of 0.3 NRT in pure Fe obtained at $T = 100$ K with a Finnis-Sinclair potential yielding an SIA formation energy of 4.9 eV [54].

The main impact of introducing chromium is found in the relative population of the elements in the defects produced by the cascade. In Fe-5Cr, where the Fe-Cr dumbbell is more stable than the pure Fe-Fe dumbbell, the fraction of chromium atoms in the surviving interstitial defects is as large as 19%, fairly independent of recoil energy. The mixed dumbbells are less mobile than pure Fe interstitials, and will thus act as obstacles for migration of Fe interstitial clusters. In Fe-20Cr, where the mixed Fe-Cr and pure Fe-Fe dumbbells have about the same energy, chromium atoms constitute roughly 30% of the interstitial atoms.

TABLE VIII: Average number of surviving Frenkel pairs as function of recoil damage energy. The quoted uncertainty corresponds to one standard deviation.

E_{dam}	5 keV	10 keV	20 keV
Fe	7.4 ± 0.7	13.4 ± 0.9	27.0 ± 1.0
Fe-5Cr	8.9 ± 0.7	14.0 ± 0.8	28.7 ± 1.6
Fe-20Cr	8.5 ± 0.6	13.6 ± 0.7	27.0 ± 1.3

CONCLUSIONS

The set of EAM potentials for Fe-Cr alloys implemented in the present work yield activation energies for vacancy migration in the pure elements that are in very good agreement with experimental data. The predicted SIA formation energies arising from fitting to thermal expansion coefficients are higher than values obtained by other authors using both EAM and Ab Initio methods. While electron irradiation data seems to support lower numbers, the stored energy release measured in neutron irradiated samples is compatible with our results. Our potentials further correctly predict the $\langle 110 \rangle$ interstitial to be the stable form in both the pure elements as well as in the alloy.

Applied to simulation of thermal ageing, there is no sign of precipitation taking place when using the potential fitted to the negative formation energy previously calculated for ferromagnetic Fe-5Cr. KMC simulations using the potential fitted to the mixing enthalpy of Fe-20Cr yield formation of Cr clusters on a time and temperature scale that is in good agreement with measurements of hardening in high Cr binary alloys.

We predict that the $\langle 110 \rangle$ Fe-Cr and Cr-Cr dumbbells are more stable than the corresponding defect in pure iron. Consequently, Cr will tend to end up in defect structures forming during cooling down of recoil cascades, and we register that 19% of the interstitial atoms in Fe-5Cr are chromium atoms.

The total number of defects surviving after recoil cascades is smaller than predicted by Fe-potentials from the literature. This fact is directly related to the higher SIA formation energy. For damage energies between 10 and 20 keV, we obtain a cascade efficiency of 0.135 ± 0.005

NRT at $T = 100\ K$, which in part may explain the long standing mystery of the small number of freely migrating defects observed in experiments [55].

ACKNOWLEDGEMENTS

The authors would like to thank I. Abrikosov, A. Almazousi, L. Malerba, B. Singh, D. Bacon and Y. Osetski for inspiring discussions. This work was supported in part by the EU 5th FP project SPIRE (R.C.), Svensk Kärnbränslehantering AB (J.W.) and Svenskt Kärntekniskt Centrum (C.L.).

[1] E. Little and D. Stow, J. Nucl. Mat. **87**, 25 (1979).
[2] F. Garner, M. Toloczko, and B. Sencer, J. Nucl. Mat. **276**, 123 (2000).
[3] R. Fischer, E. Dulis, and K. Carroll, Trans. AIME **197**, 690 (1953).
[4] E. Little and L. Stoter, in *Effect of Radiation on Materials, ASTM STP* (1982), vol. 782, p. 207.
[5] H. Kuwano, Trans. JIM **26**, 473 (1985).
[6] M. Miller, J. Hyde, A. Cerezo, and G. Smith, Appl. Surf. Sci. **87/88**, 323 (1995).
[7] M. Mathon, Y. Carlan, G. Geoffrey, X. Averty, A. Alamo, and C. de Novion, J. Nucl. Mat. **312**, 236 (2003).
[8] R. Johnson, Phys. Rev. B **39**, 12554 (1985).
[9] A. Voter, in *Intermetallic Compounds, Principles*, edited by J.H.Westbrook and R.L.Fleischer (John Wiley and Sons, 1995), vol. 1.
[10] M. Finnis and J. Sinclair, Phil. Mag A **50**, 45 (1984).
[11] A. Calder and D. Bacon, J. Nucl. Mat. **207**, 25 (1993).
[12] G. Ackland, D. Bacon, A. Calder, and T. Harry, Phil. Mag A **75**, 713 (1997).
[13] M. Daw and M. Baskes, Phys. Rev. B **29**, 6443 (1984).
[14] R. Pasianot, D. Farkas, and E. Savino, Phys. Rev. B **43**, 6952 (1991), erratum Phys. Rev. B 47 (1993) 4149.
[15] G. Simonelli, R. Pasianot, and E. Savino, in *Mat. Res. Soc. Symp.* (1993), vol. 291, p. 567.
[16] G. Simonelli, R. Pasianot, and E. Savino, Phys. Rev. B **50**, 727 (1994).
[17] G. Simonelli, R. Pasianot, and E. Savino, Phys. Stat. Sol. **217**, 747 (2000).
[18] O. Yifang, Z. Bangwei, L. Shuzhi, and J. Zhanpeng, Z. Phys. B **101**, 161 (1996).
[19] T. Konishi, K. Ohsawa, H. Abe, and E. Kuramoto, Comput. Mat. Sci. **14**, 108 (1999).
[20] D. Farkas, C. Schon, M. de Lima, and H. Goldstein, Acta Mater. **44**, 409 (1996).
[21] J. Rose, J. Smith, and J. Ferrante, Phys. Rev. B **28**, 1835 (1983).
[22] J. Adams and S. Foiles, Phys. Rev. B **41**, 3316 (1990).
[23] P. Legrand, Ph.D. thesis, University of Paris (1993).
[24] G. Evangelakis, J. Rizos, I. Lagaris, and I. Demetropoulos, *Merlin, a portable system for multidimensional minimization*, University of Ioannina (1986).
[25] J. Rifkin, *XMD*, Center for Materials Simulation, University of Connecticut (1999).
[26] J. Biersack and J. Siegler, J. Nuc. Inst. Meth. **141**, 93 (1982).
[27] K. Katahara, M. Nimalendran, M. Manghnani, and E. Fischer, J. Phys. F **9**, 2167 (1979).
[28] S. Burke, R. Cywinski, J. Davis, and B. Rainford, J. Phys. F **13**, 451 (1983).
[29] G. White, R. Roberts, and E. Fawcett, J. Phys. F **16**, 449 (1986).
[30] G. Speich, A. Schwoeble, and W. Leslie, Metallurgical Transactions **3**, 2031 (1972).
[31] P. Olsson, I. Abrikosov, L. Vitos, and J. Wallenius, J. Nucl. Mat. **321**, 84 (2003).
[32] J. Rayne and B. Chandrasekar, Phys. Rev. **122**, 1714 (1961).
[33] W. Bendick and W. Pepperhof, Acta Metallurgica **30**, 679 (1982).
[34] L. D. Schepper, D. Segers, L. Dorikens-Vanpraet, M. Dorikens, G. Knuyt, L. Stals, and P. Moser, Phys. Rev. B **27**, 5257 (1983).
[35] M. Lübbehusen and H. Mehrer, Acta Metall. Mater. **38**, 283 (1990).
[36] A. Seeger, Pys. Stat. Sol. A **167**, 289 (1998).
[37] P. Moser, Mem. Sci. Rev. Metall. **63**, 431 (1966).
[38] H. Bilger, V. Hivert, J. Verdone, J. Leveque, and J. Soulie, in *Int. Conf. on vacancies and interstitials in metals* (Kernforshungsanlage Jülich, 1968), p. 751.
[39] F. Nix and D. MacNair, Phys. Rev. **60**, 597 (1941).
[40] H. Schaefer, K. Maier, M. Weller, D. Herlach, A. Seeger, and J. Diehl, Scripta Metall. **11**, 803 (1977).
[41] H. Wollenberger, in *Physical Metallurgy*, edited by R. Cahn and P. Haasen (North-Holland, 1996), vol. 2.
[42] P. Vadja, Rev. Mod. Phys. **49**, 481 (1977).
[43] P. Erhart, in *Mat. Res. Soc. Symp.* (1985), vol. 41, p. 13.
[44] G. Loper, L. Smedskjaer, M. Chason, and R. Siegel, in *Positron Annihilation*, edited by P. Jain, R. Singru, and K. Gopinathan (World Scientific, 1985), p. 461.
[45] H. Schultz, Mater. Sci. Eng. A **141**, 149 (1991).
[46] C. Domain and C. Becquart, Phys. Rev. B **65**, 024103 (2002).
[47] C. Domain (2002), private communication, quoted in Olsson et al, SCK-CEN-BLG-950.
[48] H. Maxumoto and M. Kikuchi, in *Trans. JIM* (1975), vol. 12, p. 90.
[49] S. Brenner, M. Miller, and W. Soffa, Scripta Metallurgica. **16**, 831 (1982).
[50] J. Hyde, M. Miller, A. Cerezo, and G. Smith, Appl. Surf. Sci. **87/88**, 311 (1995).
[51] C. Domain and C. Becquart, *DYMOKA User's Guide*, 6th ed. (2002).
[52] G. Grimvall, *Thermodynamic Properties of Materials* (Elsevier, 1999).
[53] G. Vineyard, J. Phys. Chem. Solids **3**, 121 (1957).
[54] R. Stoller, G. Odette, and B. Wirth, J. Nucl. Mat. **251**, 49 (1997).
[55] L. Rehn, J. Nucl. Mat. **174**, 144 (1990).

APPENDIX 10

J. Wallenius et al., Development of an EAM potential for simulation of radiation damage in Fe–Cr alloys, Journal of Nuclear Materials 329–333 (2004) 1175–1179

Available online at www.sciencedirect.com
SCIENCE DIRECT®
Journal of Nuclear Materials 329–333 (2004) 1175–1179
journal of nuclear materials
www.elsevier.com/locate/jnucmat

Development of an EAM potential for simulation of radiation damage in Fe–Cr alloys

J. Wallenius [a], I.A. Abrikosov [b,1], R. Chakarova [a], C. Lagerstedt [a,*], L. Malerba [c], P. Olsson [b], V. Pontikis [d], N. Sandberg [a,2], D. Terentyev [c]

[a] *Department of Nuclear and Reactor Physics, Royal Institute of Technology, Alba Nova University Centre, SE-106 91 Stockholm, Sweden*
[b] *Department of Neutron Research, Angstrom Laboratory, Uppsala University, Box 525, SE-751 20 Uppsala, Sweden*
[c] *SCK-CEN, Reactor Materials Research Unit, Boeretang 200, 2400 Mol, Belgium*
[d] *Centre d'Etudes de Chimie Metallurgique, CNRS-UPR2801, 15 rue Georges Urbain, F-94407 Vitry-sur-Seine, France*

Abstract

We have developed a set of EAM potentials for simulation of Fe–Cr alloys. By relaxing the requirement of reproducing the pressure–volume relation at short distances and by fitting to the thermal expansion coefficients of Fe and Cr, stability of the ⟨1 1 0⟩ self-interstitial could be obtained. For Cr, properties of the paramagnetic state were applied, providing a positive Cauchy pressure. Mixed Fe–Cr pair potentials were fitted to the calculated mixing enthalpy of ferromagnetic Fe–Cr. Simulation of thermal ageing in Fe–Cr alloys using the Fe–20Cr potential exhibited pronounced Cr-precipitation for temperatures below 900 K, a feature not observed at any temperature using a potential fitted to the mixing enthalpy of Fe–5Cr.

1. Introduction

An improved understanding of the radiation effects in ferritic steels is of importance for development of new reactors and maintenance of already operating systems. In order to study defect production and evolution on a short time scale molecular dynamics may be applied. This requires development of adequate many-body potentials. Until recently it was thought that Cr could not be described by ordinary EAM or FS-potentials without angular terms. The present authors have however demonstrated [1] that the elastic constants of paramagnetic chromium, having a positive Cauchy pressure, may be reproduced by a central potential. Further, the mixing enthalpy of the alloy, which was measured to be strictly positive in the paramagnetic regime, has been shown to be negative for the ferromagnetic state when the Cr concentration is below 6% [2]. In the present contribution, we will dwell on some of the details in the procedure to obtain physically consistent EAM potentials for Fe–Cr that have not previously been published [1]. First, we discuss peculiarities of the thermal expansion data for Cr used for the fit. Then we illustrate the method for obtaining the EAM embedding functions. Finally we describe results from simulation of thermal ageing.

2. Construction of the potentials

The embedded atom method (EAM) formalism [3,4] was used to obtain the potentials [1]. The fitting procedure was performed in several steps. The pair potentials

* Corresponding author. Address: Department of Nuclear and Reactor Physics, SCFAB, KTH, SE-106 91 Stockholm, Sweden. Tel.: +46-8 5537 8193; fax: +46-8 5537 8465.
E-mail address: christina@neutron.kth.se (C. Lagerstedt).
[1] Present address: NTNU, Institutt for fysikk, 7491 Trondheim, Norway.
[2] Present address: Linköpings Universitet, SE-581 83 Linköping, Sweden.

0022-3115/$ - see front matter © 2004 Elsevier B.V. All rights reserved.
doi:10.1016/j.jnucmat.2004.04.317

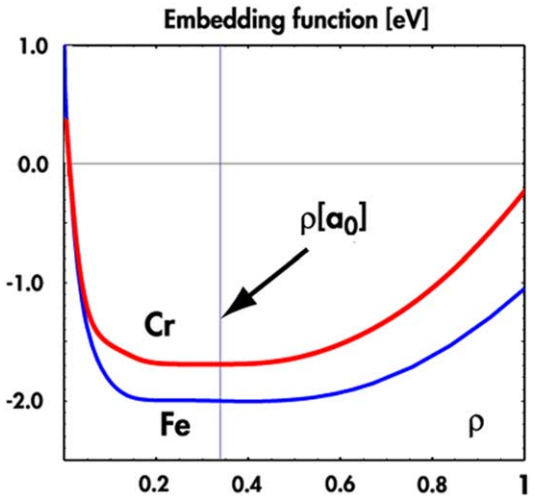

Fig. 1. Embedding functions for Fe and paramagnetic Cr obtained by introducing a cut-off in the Rose expression [5].

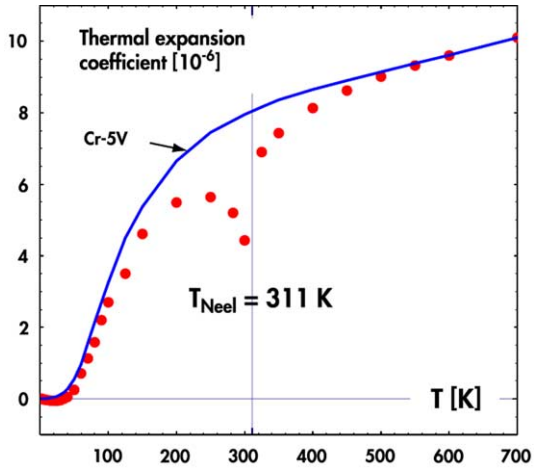

Fig. 2. Thermal expansion coefficients of Cr and paramagnetic Cr–5V, adapted from [7]. Note the cusp for pure Cr at the Néel temperature.

of the pure elements for $R > 2.4$ Å was obtained by fitting to the lattice parameter, cohesive energy, vacancy formation energy and elastic constants as measured at zero Kelvin. In the case of Cr, the elastic constants of paramagnetic Cr at $T > 600$ K were linearly extrapolated to zero Kelvin. The embedding functions shown in Fig. 1 were then calculated using this pair potential. We emphasize that a cut-off in the Rose expression [5] had to be introduced to obtain an acceptable second derivative of the embedding functions. The cut-off was made according to the procedure described by Voter [4].

After fixing the embedding function, the pair potential for 2.0 Å $< R <$ 2.4 Å was determined by fitting to temperature dependent lattice parameters of Fe and artificial Cr data, identical to that of paramagnetic Cr–5V [6,7]. In Fig. 2 we display the temperature dependence of the thermal expansion coefficients of Cr and Cr–5V, adapted from [7]. Note that it is sufficient to add a few percent of iron or vanadium to make a Cr based alloy paramagnetic even at room temperature [7,8]. For the short range of the pair potentials, a smooth transition to the universal Coulomb function of Biersack was made [9]. Details of the pair potentials, including range parameters and spline coefficients can be found in Ref. [1].

The cross potentials for the alloy were obtained by fitting to the mixing enthalpy of ferromagnetic Fe–Cr calculated with the EMTO method [2]. Previous attempts to construct mixed pair potentials for Fe–Cr [10,11] relied on fitting to the mixing enthalpy of the paramagnetic state of the alloy, which is strictly positive. A single pair-potential for the Fe–Cr interaction would not easily reproduce the change in sign of the formation energy of the relevant magnetic state. Therefore, a set of potentials has been created, providing the correct total energy of the random ferromagnetic alloy.

3. Verification and discussion

3.1. Thermodynamic properties and point defects

The first test any new potential should be subjected to is if it reproduces experimental thermodynamical properties. The second test is the properties of point defects. We have used the molecular dynamics (MD) code DYMOKA [12] to calculate formation, binding, migration, activation and substitutional energies of different objects. The results are presented in Table 1 together with values calculated using potentials from literature as well as experimental data.

The iron potential of Ackland et al. has been considered as state-of-the-art. Comparing with properties calculated using our potential we note that they yield similar structural properties, but that the thermal expansion predicted by Ackland appears to be unphysical. The largest experimental uncertainty is seen to be in the formation energies of vacancies and interstitials and this is also where our potential diverges the most from the other potentials. For the formation energy of a vacancy we have quoted the latest experiments [20] for high purity iron. We further note that very recent ab initio calculations yield a vacancy formation energy differing by less than 0.05 eV from our value [21]. The predicted value of 7.72 eV for the formation energy of interstitials in Fe is quite different from the 4.9 eV fitted by Ackland. Experimentally the situation is unclear since there is such a large discrepancy between electron

Table 1
Properties of the new potential

Fe	This work	Exp.	Ackland	
B	172	173[a]	178	
C'	56.7	52.5[a]	49.0	
C_{44}	135	122[a]	116	
E_{coh}	4.28	4.28	4.316	
$E_{bcc} - E_{fcc}$	−0.047	−0.050[b]	−0.054	
E^{SD}_{vac}	2.91	2.91[c]	2.48	
E^{f}_{vac}	2.04	2.0 ± 0.2[d]	1.62	
$E^{f}_{\langle 1\,1\,0\rangle}$	7.72	3-12[e]	4.87	
$E^{f}_{\langle 1\,1\,0\rangle} - E^{f}_{\langle 1\,1\,1\rangle}$	−0.23	−0.30[f]	−0.12	
α ($T = 300$ K)	12.8	11.7[g]	7.4	
α ($T = 600$ K)	14.2	15.8[g]	7.2	
Cr	This work	Exp. (AFM)	Exp. (PM)	Farkas
B	207	195[h]	207[h]	148
C'	153	153[h]	155[h]	42.5
C_{44}	105	104[h]	105[h]	–
E_{coh}	4.10	4.10	4.10	4.10
$E_{bcc} - E_{fcc}$	−0.025	–	–	−0.053
E^{SD}_{vac}	2.93	–	2.95[i]	2.30
E^{f}_{vac}	2.14	–	2.0 ± 0.2[j]	1.12
$E^{f}_{\langle 1\,1\,0\rangle}$	5.16	–	–	3.03
$E^{f}_{\langle 1\,1\,0\rangle} - E^{f}_{\langle 1\,1\,1\rangle}$	−0.62	–	–	0.19
α ($T = 300$ K)	7.5	4.4[k]	7.9[k]	5.2
α ($T = 600$ K)	9.8	–	9.6[k]	9.5
Fe–Cr	Fe–5Cr	Fe–20Cr	VASP	Farkas
$E^{f}_{\langle 1\,1\,0\rangle}$	7.63	8.19	3.99[l]	4.31
E^{s}_{Cr}	+0.18	+0.46	−0.03[l]	+0.70
$E^{b}_{\langle 1\,1\,0\rangle}$	+0.27	−0.01	−0.43[l]	+0.05
$E^{f}_{\langle 1\,1\,0\rangle} - E^{f}_{\langle 1\,1\,1\rangle}$	−0.03	−0.20	−0.11[l]	+0.07

Comparison is made with experimental data, VASP ab initio data [13,14] and other potentials. For Fe we have compared with the potential of Ackland [15]. For Cr there are experiments on both the anti-ferromagnetic (AFM) phase at room temperature as well as the paramagnetic (PM) phase at higher temperatures. The Farkas potential [10] is used as a comparison for pure Cr and the Fe–Cr alloy. For the alloy we have the two new potentials, Fe–5Cr and Fe–20Cr, fitted to different mixing enthalpies.

[a] Ref. [16].
[b] Ref. [17].
[c] Refs. [18,19].
[d] Ref. [20].
[e] Ref. [22,23].
[f] Ref. [23].
[g] Ref. [5].
[h] Ref. [27].
[i] Ref. [28].
[j] Ref. [29].
[k] Ref. [6].
[l] Ref. [14].

and neutron irradiation experiments. The experimental values are derived from measurements of stored energy release per resistivity recovery ($dQ/d\rho$) in samples irradiated at low temperature [23,24]. The enthalpy for formation of a Frenkel pair is obtained by multiplying $dQ/d\rho$ with an assumed resistivity Ω_F for a single Frenkel pair. Estimates of Ω_F vary from 0.20 to 0.30 mΩ cm [25,26]. Selecting the higher value, Wollenberger arrives at a formation energy $E^{f}_{\langle 1\,1\,0\rangle} = 6.6$ eV for a Frenkel pair in electron irradiated α-Fe, and $E^{f}_{\langle 1\,1\,0\rangle} = 13.6$ eV for a neutron irradiated sample [24]. Subtracting a vacancy formation energy of 2.0 eV would

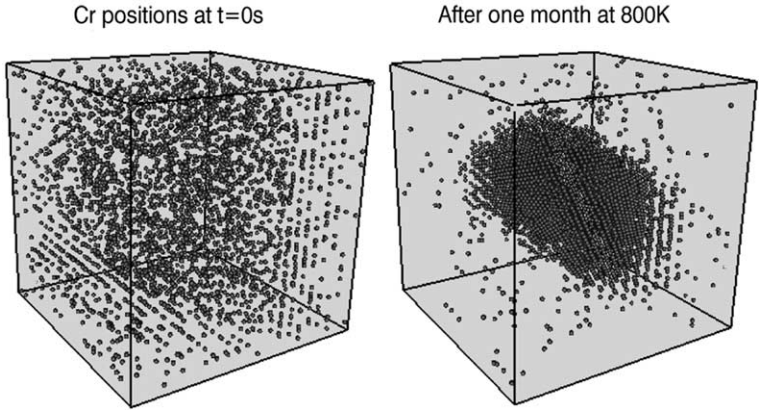

Fig. 3. The distribution of Cr atoms in a box with 16 000 atoms, before and after thermal ageing at 800 K. In total there are 20% Cr atoms in the box. A crystal clear segregation is observed, with the formation of a single cluster.

then give $E^{f}_{\langle 1\,1\,0\rangle} = 4.6$ eV in the former case, and 11.6 eV in the latter. The uncertainty of these values is obviously large, since just by assuming $\Omega_F = 0.20$ mΩ cm, one could obtain $E^{f}_{\langle 1\,1\,0\rangle} = 7.7$ eV for the neutron irradiated sample. Note that results from the electron irradiation are not necessarily more accurate, since experimental boundary conditions are more difficult to control in stages I_A to I_C (absent in neutron irradiation) than in stage I_D.

The SIA formation energy in iron has recently been calculated using ab initio codes as $E^{f}_{\langle 1\,1\,0\rangle} = 3.4$ eV [14,21]. This result is compatible with data from electron irradiations. However, since the calculation did not take into account possible effects of non-colinear magnetism, the discrepancy with data from neutron irradiated samples remains an open question.

3.2. Chromium precipitation

The well-known 475 °C embrittlement of high-Cr Fe–Cr alloys is due to nano-segregation of chromium. A potential that aims at a correct description of a material should be able to predict such a phase separation. The ranges in which we have this effect are Cr content between 10% and 90% and temperatures between 750 and 900 K [30,31]. We have simulated thermal ageing by introducing a vacancy in the system and letting it exchange places with its neighbours in a kinetic Monte Carlo (KMC) scheme. The frequency for a lattice atom to exchange position with a neighbouring vacancy is

$$\Gamma(T) = \nu C_{\mathrm{vac}}(T) \exp(-E_m/k_B T), \quad (1)$$

where ν is the attempt frequency of the jump, C_{vac} is the concentration of vacancies and E_m is the vacancy migration energy. The average time step is then equal to the inverse of 8Γ, where eight is the number of nearest neighbours.

This vacancy-assisted migration is assumed to be the driving force for thermal ageing out-of-pile. One measure of the degree of segregation is the loss of energy as time evolves. For the Fe–20Cr potential we see an energy loss in the system corresponding to 85% of the mixing enthalpy. This is perfectly consistent with the surface to bulk relation of 30% in this system considering that half the neighbours of the surface atoms are Fe atoms. For the Fe–5Cr we should not see any energy loss at all since the potential predicts a negative mixing enthalpy. As can be seen in Fig. 3 we have a clear segregation of Cr atoms in a system of 20% Cr after a simulated month at 800 K. The time scale is in very good agreement with experiments on 45% Cr at 770 K [32].

4. Summary and Conclusions

The set of EAM potentials for Fe–Cr alloys under development yield activation energies for vacancy migration in the pure elements that are in very good agreement with experimental data. The predicted SIA formation energies arising from fitting to thermal expansion coefficients are higher than values obtained by other authors using both EAM and ab initio methods. While electron irradiation data seems to support lower numbers, the stored energy release measured in neutron-irradiated samples is compatible with our results.

Applied to simulation of thermal ageing, there is no sign of precipitation taking place when using the potential fitted to the negative formation energy previously calculated for ferromagnetic Fe–5Cr. KMC simulations using the potential fitted to the mixing enthalpy of Fe–20Cr yield formation of Cr clusters on a time and temperature scale that is in good agreement with measurements of hardening in high Cr binary alloys.

We predict that the ⟨1 1 0⟩ Fe–Cr and Cr–Cr dumbbells are more stable than the corresponding defect in pure iron. Consequently, Cr would tend to end up in defect structures forming during the cooling down of recoil cascades.

Acknowledgements

The authors would like to thank B. Singh, D. Bacon and Y. Osetsky for inspiring discussions and the following institutions for financial support: The Swedish Research council (P.O, I.A.A), the EU 5th FP project SPIRE (R.C.), Svensk Kärnbränslehantering AB (J.W.) and Svenskt Kärntekniskt Centrum (C.L.).

References

[1] J. Wallenius, P. Olsson, C. Lagerstedt, N. Sandberg, R. Chakarova, V. Pontikis, Phys. Rev. B 69 (2004) 094103.
[2] P. Olsson, I.A. Abrikosov, L. Vitos, J. Wallenius, J. Nucl. Mater. 321 (2003) 84.
[3] M.S. Daw, M.I. Baskes, Phys. Rev. B 29 (1984) 6440.
[4] A.F. Voter, Principles, in: J.H. Westbrook, R.L. Fleischer (Eds.), Intermetallic Compounds, vol. 1, Wiley, 1995.
[5] J. Rose, J. Smith, J. Ferrante, Phys. Rev. B 28 (1983) 1835.
[6] F. Nix, D. MacNair, Phys. Rev. 60 (1941) 597.
[7] G. White, R. Roberts, E. Fawcett, J. Phys. F 16 (1986) 449.
[8] S. Burke, R. Cywinski, J. Davies, B. Rainford, J. Phys. F 13 (1983) 451.
[9] J.P. Biersack, J.F. Siegler, Nucl. Instrum. and Meth. 141 (1982) 93.
[10] D. Farkas, C.G. Schon, M.S.F. de Lima, H. Goldstein, Acta Mater. 44 (1996) 409.
[11] O. Yifang, Zh. Bangwei, L. Shuzhi, J. Zhanpeng, Z. Phys. B 101 (1996) 161.
[12] C.S. Becquart, C. Domain, A. Legris, J.-C. van Duysen, J. Nucl. Mater. 280 (2000) 73.
[13] P. Olsson, L. Malerba, A. Almazouzi, SCKCEN Report, BLG-950, June 2003.
[14] C. Domain, private communication, 2004.
[15] G. Ackland, D.J. Bacon, A.F. Calder, T. Harry, Philos. Mag. A 75 (1997) 713.
[16] J.A. Rayne, B.S. Chandrasekar, Phys. Rev. 122 (1961) 1714.
[17] W. Bendick, W. Pepperhof, Acta Metall. 30 (1982) 679.
[18] M. Lübbehusen, H. Mehrer, Acta Metall. Mater. 38 (1990) 283.
[19] A. Seeger, Phys. Stat. Sol. A 167 (1998) 289.
[20] L. De Schepper, D. Segers, L. Dorikens-Vanpraet, M. Dorikens,, G. Knuyt, L.M. Stals, P. Moser, Phys. Rev. B 27 (1983) 5257.
[21] C.C. Fu, Proceedings of ITEM Technical Workshop WP2, 2003.
[22] P. Moser, Mem. Sci. Rev. Metall. 63 (1966) 431.
[23] H. Bilger, V. Hivert, J. Verdone, J.L. Leveque, J.C. Soulie, Int. Conf. on Vacancies and Interstitials in Metals, Kernforschungsanlage Jülich, 1968, p. 751.
[24] H. Wollenberger, in: R. Chan, P. Haasen (Eds.), Physical Metallurgy, vol. 2, North-Holland, 1996.
[25] P. Vadja, Rev. Mod. Phys. 49 (1977) 481.
[26] P. Erhart, Mater. Res. Soc. Symp. 41 (1985) 13.
[27] K.W. Katahara, M. Nimalendran, M.H. Manghnani, E.S. Fischer, J. Phys. F 9 (1979) 2167.
[28] H. Schultz, Mater. Sci. Eng. A 141 (1991) 149.
[29] G.D. Loper, L.C. Smedskjaer, M.K. Chason, R.W. Siegel, in: P. Jain, R. Singru, K. Gopinathan (Eds.), Positron Annihilation, World Scientific, 1985, p. 461.
[30] R. Fischer, E. Dulis, K. Carrol, Trans. AIME 197 (1953) 690.
[31] H. Kuwano, Trans. JIM 26 (1985) 473.
[32] J. Hyde, M. Miller, A. Cerezo, G. Smith, Appl. Surf. Sci. 87&88 (1995) 311.

APPENDIX 11

L. Malerba , D. Terentyev, P. Olsson, R. Chakarova, J. Wallenius Molecular dynamics simulation of displacement cascades in Fe–Cr alloys, Journal of Nuclear Materials 329–333 (2004) 1156–1160

Available online at www.sciencedirect.com
SCIENCE DIRECT®
Journal of Nuclear Materials 329–333 (2004) 1156–1160
journal of nuclear materials
www.elsevier.com/locate/jnucmat

Molecular dynamics simulation of displacement cascades in Fe–Cr alloys

L. Malerba [a,*], D. Terentyev [a], P. Olsson [b], R. Chakarova [c], J. Wallenius [c]

[a] SCK•CEN, Reactor Materials Research Unit, Boeretang 200, B2400 Mol, Belgium
[b] Department of Neutron Research, Ångström Laboratory, Uppsala University, Box 525, SE75120 Uppsala, Sweden
[c] Department of Nuclear and Reactor Physics, Royal Institute of Technology, AlbaNova University Centre, SE10691 Stockholm, Sweden

Abstract

An embedded atom method (EAM) empirical potential recently fitted and validated for Fe–Cr systems is used to simulate displacement cascades up to 15 keV in Fe and Fe–10%Cr. The evolution of these cascades up to thermalisation of the primary damage state is followed and quantitatively analysed. Particular attention is devoted to assessing the effect of Cr atoms on the defect distribution versus pure Fe. Using the Wigner–Seitz cell criterion to identify point defects, first results show that the main effect of the presence of Cr in the system is the preferential formation of mixed Fe–Cr dumbbells and mixed interstitial clusters, with expected lower mobility than in pure Fe.

1. Introduction

The development of models to assess the mechanical stability under intense neutron irradiation of high-Cr reduced-activation ferritic/martensitic (RAFM) steels is an important part of fusion reactor materials research. The starting point for any neutron-irradiation-damage modelling effort is the study of the primary damage state produced by displacement cascades in the relevant material. Molecular dynamics (MD) is well known to be the simulation tool 'par excellence' for the study of displacement cascades, provided that a valid and adequately stiffened many-body interatomic potential is available for the system of interest [1]. In the past, much work has been done on MD simulation of displacement cascades, using pure Fe as model alloy for steels, described by a variety of interatomic potentials [2–6]. However, to take a step forward toward modelling real engineering materials, the assessment of the effect of Cr, the main alloying elements, in RAFM steels, on the primary damage state is of critical importance. Thus, this paper reports a first set of results on displacement cascades initiated by Fe recoils up to 15 keV in Fe–10%Cr. The simulations have been performed using a recently fitted and validated many-body potential for the Fe–Cr system [7,8]. For comparison, cascades in pure Fe were simulated as well, using the same potential. The objective of the reported work is (i) to further validate this potential by comparing the obtained results with earlier work for pure Fe, (ii) to analyse and discuss the main effects of the presence of Cr in terms of primary defect population.

2. Simulation method

The details of the fitting procedure and validation of the embedded atom method (EAM) [9] interatomic potential for Fe–Cr used in this work can be found elsewhere [7,8]. Briefly, the Fe–Fe potential was fitted following the approach described in Ref. [10] and stiffened using the same method as in Ref. [2]. The Cr–Cr potential was taken from the literature [11]. The Fe–Cr crossed pair contribution was fitted, using the procedure

* Corresponding author. Tel.: +32-14 333090; fax: +32-14 321216.
E-mail address: lmalerba@sckcen.be (L. Malerba).

0022-3115/$ - see front matter © 2004 Elsevier B.V. All rights reserved.
doi:10.1016/j.jnucmat.2004.04.270

described in [12], to the experimental values of bulk modulus (1544 kbar), cohesive energy (−4.262 eV) and lattice parameter (2.866 Å) of the Fe–10%Cr alloy, as well as to the mixing enthalpy for the same alloy (5.16 meV), calculated by ab initio methods to take into account the effect of ferromagnetism [13]. This potential has proven to provide a reasonably good description of the interaction between Cr atoms and point defects in a ferritic matrix compared to ab initio results obtained with the VASP code [8,14,15]. In particular, the stability of the Fe–Cr and Cr–Cr dumbbells is correctly reproduced, as well as the negligible binding energy of Cr atoms with vacancies [8]. In addition, the description of Cr diffusivity in Fe is also in good agreement with experimental results [16,17]. The main limitation is that this potential should not be used in the range of compositions where α'-phase nano-segregation is expected.

The potential was implemented in the classical MD code Dymoka, which is suitable for the simulation of displacement cascades [6]. Prior to initiating the cascade, a block was equilibrated for 1 ps at 300 K. This atom block was then used as starting point for the cascade simulation and defect detection. The cascade was started by imparting a kinetic energy E_{MD} to the selected primary knock-on atom (PKA) along a high-index direction $\langle 1\,3\,5\rangle$, in order to avoid channelling [2,5]. Cubic box size, simulated time and number of cascades versus E_{MD} are summarised in Table 1. Following common practice [1–3,5,6], no rigorous attempt was made to control the temperature of the system and all presented results were obtained working in the NVE microcanonical ensemble with periodic boundary conditions [3,4,6]. Only in the case of high recoil energy (10 and 15 keV) were the boundary atoms damped using the rescaling velocity algorithm, to partially extract heat. It is anyhow accepted that the simulation temperature scarcely influences the defect population produced in displacement cascades in Fe [18,5]. The evolution of the cascades was monitored using appropriate visualisation tools. The final atomic configuration was then analysed to detect and count defects, using a Wigner–Seitz cell method: an empty cell corresponds to a vacancy, two atoms in the same cell correspond to an interstitial configuration. Replacements were also accounted for and the number of displaced atoms was defined as the sum of replaced and interstitial atoms. Clusters were defined using a third nearest neighbour (nn) criterion for interstitials and second nn for vacancies.

3. Results and discussion

3.1. Defect number

In Fig. 1(a) the average number of surviving Frenkel pairs at the end of the cascade (N_{FP}) in both pure Fe and Fe–10%Cr resulting from the MD simulations is plotted as a function of E_{MD}. The points have been interpolated using the empirical power law proposed by Bacon et al., $N_{FP} = A \cdot E_{MD}^{m}$ [1], whose validity has been determined to cover the range from about 1 to 20 keV [5]. Prefactors and exponents obtained in a least-square fit are in close agreement with previous work on Fe [1,5].

Traditionally, to estimate the number of Frenkel pairs produced per cascade the NRT formula is used [19,20]: $N_{NRT} = 0.8E_D/2E_d$, where E_d is the average displacement energy for all crystallographic directions and E_D is the damage energy. E_D is the fraction of recoil energy that goes into displacive damage, after subtracting the portion dissipated for electron excitation. Since in the present MD simulations the interaction between ions and electrons is not included, it is assumed that $E_D = E_{MD}$, as is customarily done [1]. The defect production efficiency is defined as the ratio of the MD surviving Frenkel pairs to the number of NRT displacements ($N_{FP}N_{NRT}$). For the sake of simplicity and following Ref. [20], we took $E_d = 40$ eV to estimate the number of defects with the NRT formula for both pure Fe and Fe–10%Cr. In both cases (Fe and Fe–Cr) the defect production efficiency decreases with recoil energy down to a more or less asymptotic value of about

Table 1
Summary of number of cascades, simulation time and box size versus E_{MD}

E_{MD} (keV)	No. of cascades		Other parameters	
	Fe	Fe–10%Cr	Time (ps)	Box size (atoms)
0.5	10	10	10	54 000
0.7	10	10	10	54 000
1	10	10	10	54 000
2	10	10	10	128 000
5	10	10	20	128 000
8	10	10	20	250 000
10	10	10	30	432 000
15	5	10	30	432 000

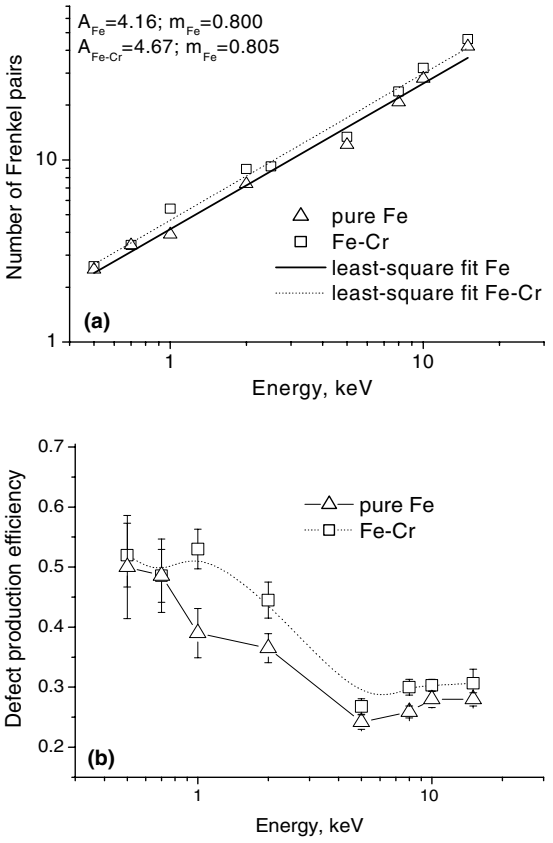

Fig. 1. Number of surviving Frenkel pairs (a) and defect production efficiency compared to NRT (b) at the end of the cascade versus recoil energy, in Fe and Fe–10%Cr. In (a) the power law proposed by Bacon et al., $N_{FP} = A \cdot E_{MD}^{m}$ [1] has been used for interpolation.

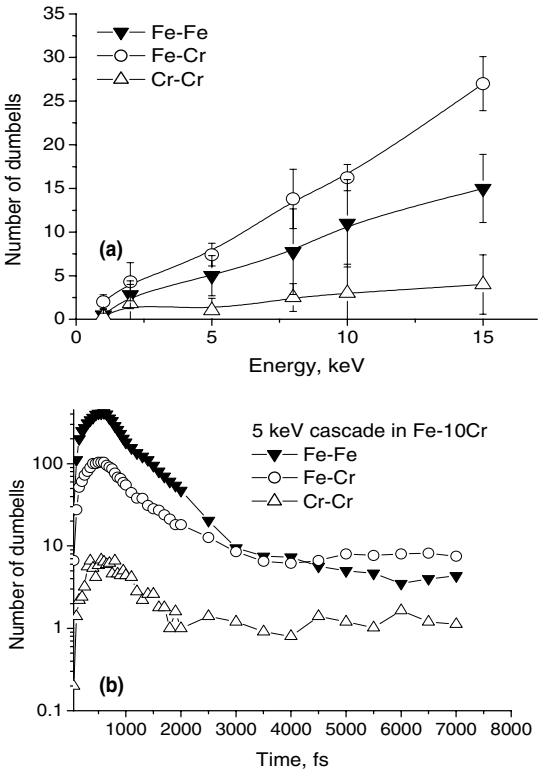

Fig. 2. Number of Fe–Fe, Fe–Cr and Cr–Cr dumbbells in Fe–10%Cr cascades versus (a) recoil energy and (b) time in 5 keV cascades (average evolution of 10 cascades).

0.3 (0.28 in Fe and 0.31 in Fe–Cr), in agreement with previous work [1,5,6] (see Fig. 1(b)).

A close inspection of Fig. 1 reveals a slightly higher defect production when Cr is present. A study of the threshold displacement energies of a Cr atom in a ferritic matrix along the three main crystallographic directions showed that only in one direction, $\langle 1\,1\,0 \rangle$, the threshold is 5 eV lower than for Fe atoms, independently of the Cr concentration [21]. Thus, the resulting slightly lower average threshold energy for Cr atoms cannot alone explain the somewhat higher defect production efficiency in Fe–10%Cr. It is more likely that the higher production results from stable Fe–Cr and Cr–Cr dumbbell formation during cascade cooling, which limits recombination. Indeed, in agreement with ab initio calculations [8] the present potential predicts a positive binding energy for Fe–Cr and Cr–Cr dumbbells (larger than 0.3 eV). This feature leads to the formation of a number of mixed dumbells that is remarkably higher than the number of Fe–Fe dumbells at the end of the cascade, as is shown in Fig. 2(a). Independently of the recoil energy, 67% (±6% of standard deviation) of the final dumbbells contain Cr atoms, to be compared with the 10% Cr concentration of the alloy. Fig. 2(b) shows clearly, in the case of 5 keV cascades, that the formation of mixed dumbbells is a post-collisional-phase phenomenon. Initially, as is to be expected, more Fe atoms than Cr atoms are displaced and counted as interstitials. However, during the cooling stage most of these Fe–Fe dumbbells, possibly assisted by the still high temperature, glide till they become trapped at the closest Cr atoms, thereby determining a cross-over of the curves of the number of mixed and self-interstitial dumbbells versus time in Fig. 2(b). The same process has been seen to occur for all cascade energies investigated in this work.

In summary: Cr atoms do not appear to significantly affect the collisional stage of the cascade, as may be expected, considering the negligible difference in mass between Fe and Cr atoms. Yet, the presence of Cr determines a redistribution of dumbbell species during the post-collisional stage, where most of the dumbbells end up containing Cr atoms, in percentage far higher than the Cr concentration in the alloy. The thermal stability of these dumbbells is likely to be responsible for

the somewhat reduced recombination observed during the cooling phase of Fe–10%Cr cascades, as compared to pure Fe.

3.2. Cluster formation

All previous papers on displacement cascades in Fe agree on that very little in-cascade vacancy clustering occurs in this material, while sizeable interstitial clusters are found to form [1,2,5,6]. Our results agree with these findings, as is shown in Fig. 3(a) and (b), where the fraction of, respectively, surviving vacancies and interstitials in clusters (containing at least two elements) is plotted versus E_{MD} for both Fe and Fe–10%Cr. We find that the average fraction of clustered vacancies hardly exceeds 30%, the mean cluster size being rather small (2–3 vacancies). Conversely, up to 50% of the interstitials are found in clusters, of sizes up to 11. These results, allowing for the large scatter, are in broad agreement with most previous work [1,2,4–6], provided that the same criterion is used for the definition of clusters (second nn for vacancies, third nn for interstitials).

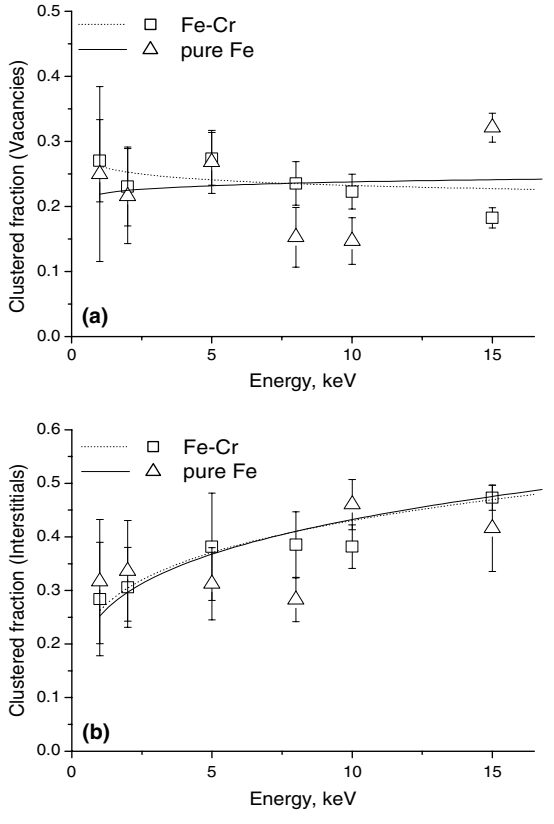

Fig. 3. Fraction of defects in cluster at the end of the cascade, in both Fe and Fe–10%Cr, versus recoil energy: (a) vacancies (2 nn criterion); (b) interstitials (3 nn criterion). The lines represent trend power.

The presence of Cr does not seem to influence the fraction of defects in clusters. Also the cluster size distribution is comparable in both materials. No detailed analysis was conducted to detect a possible preferential association of vacancies and vacancy clusters to Cr atoms, but this is not likely to be a large effect, due to the very low Cr–V binding energy. On the contrary, a large portion of the interstitials in cluster in Fe–10%Cr are Cr atoms. Although further investigation is required, the promotion of the formation of mixed interstitial loops, stabilised by the presence of Cr, will have a large impact on the subsequent evolution of radiation damage if, as one should expect, their mobility is lower than in pure Fe. A first simulation study of single interstitial diffusivity in Fe and Fe–Cr has shown a decrease of the interstitial diffusion prefactor by about one order of magnitude, due to the presence of Cr atoms [16]. The experimental observation of slowing down of interstitial loop motion in Fe due to the presence of Cr is also reported in these proceedings [22]. Moreover, Okada et al. observed, in neutron and electron irradiation experiments performed between 200 and 500 °C, that the addition of even small percentages (0.1 at.%) of Cr to ultra-pure Fe induces more frequent nucleation of small loops of interstitial nature than in ultra-pure Fe [23]. These experimental findings seem to be correctly reflected by the results of our simulations.

4. Summary and conclusions

Displacement cascades up to 15 keV recoil energy were simulated by molecular dynamics in Fe and Fe–10%Cr, using a recently fitted and validated EAM many-body potential. The different phases of the cascades were monitored and analysed using ad hoc post-processing tools. In this paper, results concerning the number of surviving defects and their distribution in clusters have been reported. In the case of pure Fe, our results are consistent with previous ones. The presence of 10% Cr atoms does not seem to affect the collisional stage of the cascade, but it does determine a redistribution of dumbbell species during the post-collisional stage. Most interstitial atoms are Cr, in percentage far higher than the concentration in the alloy. This effect seems to reduce recombination, thereby leading to a slightly higher defect production in the alloy compared to pure Fe. No substantial difference is detected between Fe and Fe–10%Cr in the fraction of clustered defects. However, interstitial clusters contain a large percentage of Cr atoms which stabilise them. This feature may drastically reduce the mobility of interstitial loops in Fe–Cr compared to pure Fe, as confirmed by recent experiments, with significant impact on the subsequent evolution of radiation induced defects in the alloy.

Acknowledgements

This work was performed in the framework of the European Fusion Technology Programme and partially funded by EFDA, task TW3-TTMS-007.

References

[1] D.J. Bacon, A.F. Calder, F. Gao, V.G. Kapinos, S.J. Wooding, Nucl. Instrum. and Meth. B 102 (1995) 37.
[2] A.F. Calder, D.J. Bacon, J. Nucl. Mater. 207 (1993) 25.
[3] R. Vascon, N.V. Doan, Radiat. Eff. Def. Solids 141 (1997) 375.
[4] N. Soneda, T. Díaz de la Rubia, Philos. Mag. A 78 (5) (1998) 995.
[5] R.E. Stoller, J. Nucl. Mater. 276 (2000) 22.
[6] C.S. Becquart, C. Domain, A. Legris, J.-C. van Duysen, J. Nucl. Mater. 280 (2000) 73.
[7] R. Chakarova, V. Pontikis, J. Wallenius, Development of Fe(bcc)–Cr many body potential and cohesion model, Delivery report WP6, SPIRE project, EC contract no. FIKW-CT-2000-00058, June 2002, available at www.neutron.kth.se/publications.
[8] P. Olsson, L. Malerba, A. Almazouzi, A first step towards a multiscale modelling of Fe–Cr alloys, SCKCEN Report, BLG-950, June 2003.
[9] M.S. Daw, M.I. Baskes, Phys. Rev. B 29 (1984) 6440.
[10] G. Simonelli, R. Pasianot, E.J. Savino, Mater. Res. Soc. Symp. Proc. 291 (1993) 567.
[11] D. Farkas, C.G. Schon, M.S.F. de Lima, H. Goldstein, Acta Mater. 44 (1996) 409.
[12] A.F. Voter, in: J.H. Westbrook, R.L. Fleischer (Eds.), Principles, Intermetallic Compounds, vol. 1, John Wiley, 1995.
[13] P. Olsson, I.A. Abrikosov, L. Vitos, J. Wallenius, J. Nucl. Mater. 321 (2003) 84.
[14] G. Kresse, J. Hafner, Phys. Rev. B 47 (1993) 558; G. Kresse, J. Hafner, Phys. Rev. B 65 (1993) 14251.
[15] C. Domain, C.S. Becquart, Phys. Rev. B 65 (2002) 024103.
[16] D. Terentyev, L. Malerba, this Proceedings.
[17] D. Terentyev, L. Malerba, A.I. Melker (Eds.), in: Proceedings of the 7th International Workshop on Nondestructive Testing and Computer Simulations in Science and Engineering NDTCS-7, St. Petersburg, Russia, 9–15 June 2003, to be published as SPIE Proceedings, 2003.
[18] F. Gao, D.J. Bacon, P.E.J. Flewitt, T.A. Lewis, J. Nucl. Mater. 249 (1997) 77.
[19] M.J. Norgett, M.T. Robinson, I.M. Torrens, Nucl. Eng. Design 33 (1975) 50.
[20] ASTM Standard E693-94, Annual Book of ASTM Standards, vol. 12.02, 1994.
[21] D. Terentyev, L. Malerba, to be published.
[22] K. Arakawa, M. Hatanaka, H. Mori, K. Ono, these Proceedings.
[23] A. Okada, H. Maeda, K. Hamada, I. Ishida, J. Nucl. Mater. 256 (1999) 247.

APPENDIX 12

M. Eriksson, J. Wallenius, M. Jolkkonen and J. E. Cahalan, “Inherent Safety of Fuels for Accelerator-Driven Systems”, Nuclear Technology, October 2004 (submitted).

INHERENT SAFETY OF FUELS FOR ACCELERATOR-DRIVEN SYSTEMS

M. ERIKSSON*, J. WALLENIUS, M. JOLKKONEN
Royal Institute of Technology (KTH), AlbaNova University Center, Dep. Nuclear & Reactor Physics, 10691 Stockholm, Sweden.

J. E. CAHALAN
Argonne National Laboratory, Nuclear Engineering Division, 9700 South Cass Ave., IL 60439, USA.

Submitted *Nuclear Technology* (Oct, 2004)
Accepted (Jan, 2005)

Transient safety characteristics of accelerator-driven systems (ADS) using advanced minor actinide fuels have been investigated. Results for a molybdenum-based Ceramic-Metal (CerMet) fuel, a magnesia-based Ceramic-Ceramic (CerCer) fuel, and a zirconium-nitride based fuel are reported. The focus is on the inherent safety aspects of core design. Accident analyses are carried out for the response to unprotected loss-of-flow and accelerator beam-overpower transients, and coolant voiding scenarios. An attempt is made to establish basic design limits for the fuel and cladding. Maximum temperatures during transients are determined and compared with design limits. Reactivity effects associated with coolant void, fuel- and structural-expansion, and cladding relocation are investigated. Design studies encompass variations in lattice pitch and pin diameter. Critical mass studies are performed. The studies indicate favorable inherent safety features of the CerMet fuel. Major consideration is given to the potential threat of coolant voiding in accelerator-driven design proposals. Results for a transient test case study of a postulated steam generator tube rupture event leading to extensive cooling voiding are presented. The study underlines the importance of a having a low coolant void reactivity value in a lead-bismuth system, despite the high boiling temperature of the coolant. It was found that the power rise following a voiding transient increases dramatically near the critical state. The studies suggest that a reactivity margin of a few dollars in the voided state is sufficient to permit significant reactivity insertions.

I. INTRODUCTION

Accelerator-driven systems (ADS) have been proposed for reducing the long-term hazards of spent nuclear fuel disposition [1,2]. The primary objective is to minimize the inventory of americium and curium that, besides plutonium, are responsible for the majority of the long-term radiotoxicity in nuclear waste. If successful, the technology could enable a reduction of the mass and radioactivity of the spent nuclear fuel by a factor of 100, and reduce the required storage time from ~100 000 years to ~1000 years.

Studies of ADS neutronics and thermal hydraulics have been accomplished, leading to the selection of LBE as main choice for the coolant [3,4]. Concerning the selection of a suitable fuel material, investigations are made in connection with the joint European research programs [5,6]. While some of the originally suggested fuels did not fulfill basic safety and/or design criteria, three fuels have been selected for detailed examination, namely: two composite oxide fuels and one solid solution nitride fuel. The detailed motivation for selecting these fuels has been outlined in a recent article [7]. In this paper, attention is directed to their inherent safety characteristics and performance during reactor transient conditions. Various accident events of interest in accelerator-driven systems are considered. Reactivity sources are examined with regard to their influence on reactor safety.

*Email: marcus@neutron.kth.se

II. INHERENT SAFETY

The term "inherent safety" is in widespread use, particularly in discussions of advanced nuclear reactors. Generally, it is used without further definition and sometimes with inconsistent meaning. In most cases, it is meant to denote an applied design approach or to describe a particular system feature and often to indicate a possible safety advantage. According to the IAEA [8], an inherent safety characteristic is a "fundamental property of a design concept that results from the basic choices in the materials used or in other aspects of the design which assures that a particular potential hazard can not become a safety concern in any way". The potential hazards include the radioactive materials, decay heat, excess reactivity, high temperatures, high pressures, and energetic

chemical reactions. An "inherently safe" reactor would require all these hazards to be eliminated, which is impossible for all practical reactor purposes. Nevertheless, a reactor may possess inherent safety characteristics with respect to a particular eliminated hazard and for specific events. To avoid the potential of being misleading, this does not imply absolute safety for all possible situations.

In the following studies, we seek to investigate the inherent safety characteristics of an ADS with respect to specific accident-initiating events. Inherent safety characteristics associated with reactor transients translates into reactor performance when the protective shutdown devices do not perform their function. Studying this specific class of transients is of considerable importance since they describe the fundamental response of the reactor in the absence of safety system intervention. These so-called "unprotected" transients are potentially of the worst kind. Despite their extremely low probability of occurrence, reactor designs must still be protected against such events to assure the health and safety of the general public. Lessons learned from commercial nuclear power operation and reactor accidents recognize that safety should not rest solely on proper operation of the control and safety systems, or even on ideal performance of plant operators. Every mechanical system, electric power supply, instrumentation system, etc., has a non-vanishing probability of failure, and humans make mistakes. Hence, the reactor should be designed such that there is no undue risk for the environment outside the reactor building even in the hypothetical situation that the shutdown system should fail when needed. That implies that the energy releases, reactivities, pressures, and temperatures for critical reactor elements be kept within safe limits under all conditions.

III. FUEL SELECTION PROCESS

The overall mission of the ADS is to maximize the destruction rate of transuranic elements, primarily americium (Am) and curium (Cm). While plutonium is recyclable in fast reactors and to some extent in commercial light water reactors, the amount of Am that can be charged into a critical reactor is limited by safety concerns. The Doppler feedback coefficient and effective delayed neutron fractions decline when americium is added to the fuel [7] and the reactivity effect associated with loss-of-coolant becomes more positive. The ADS is a nuclear reactor operating in a subcritical mode, which provides for the added safety margin to allow for high concentration of Am. With ADS, transmutation of the minor actinides (Am, Cm, and Np) may be confined to a single process, which will improve the operation of critical reactors and ease the burden on recycling in the overall process. Different fuel cycle strategies could be foreseen. The Japan Atomic Energy Research Institute (JAERI) has proposed the double-strata concept [9], utilizing both commercial light-water reactors and fast reactors for plutonium recycling and energy production and ADS's for MA consumption.

The MA based ADS fuel does not require $^{238}U/^{232}Th$ for normal operation, but a certain amount of plutonium is necessary for reactivity management. A support material is needed to reduce the power density, and in some cases, improve thermal properties. The support material constitutes an "inert matrix" in which the fuel particles are embedded ("inert" in this context refers to an inactive material with a high transparency to neutrons). These fuels are then referred to as "inert matrix fuels". The inert matrix fuel may be of homogeneous (solid solution) and heterogeneous (composite) type and the fuel may be a Ceramic-Ceramic (CerCer) mixture or a combined Ceramic-Metal (CerMet) mixture. CerCer fuels of interest utilize a metal oxide matrix such as magnesia (MgO), spinel ($MgAl_2O_4$), and alumina (Al_2O_3). CerMet fuels are attractive because of high thermal conductivity. The refractory metals such as molybdenum, chromium, tungsten, and vanadium are of particular interest because of their high melting point. During a pre-selection phase [3], a number of inert matrices have been considered and examined. Among them, the magnesia (MgO) and molybdenum (^{92}Mo) matrices were singled out as potential materials for use with oxide fuels and these are studied in the some more detail in the current paper. The major reason for this selection is a combination of good thermal properties, acceptable neutronics, and solubility in nitric acid. For a detailed account, see ref. [3,7].

Nitride fuel is an alternative to oxide fuels, yet the knowledge on nitride fuels is limited compared to the extensive experience available on oxide fuel. Nitride fuels offer relatively high thermal conductivity and dissolution rate in nitric acid, which makes it compatible with the PUREX reprocessing technique. The nitride fuels of potential use are of the solid solution type; composite nitride fuels are of little interest. Previous studies [10] have indicated that there are a limited number of inert matrices suitable for nitride fuels. So far, the diluents that have been considered are zirconium nitride (ZrN), hafnium nitride (HfN), and yttrium nitride (YN). At this stage of development, ZrN is the primary choice. HfN has high neutron absorption cross-section, and YN is difficult to handle, as it reacts chemically with air and water. ZrN offers relatively high thermal conductivity and high melting point [11]. It forms a solid solution with plutonium nitride [12], has a stabilizing effect on americium nitride [13] and is itself stable in air. Furthermore, it has a high transparency to neutrons, good chemical compatibility with steel, and is soluble in nitric acid. A disadvantage of the nitride fuel is the need for using nitrogen enriched in ^{15}N [14], in order to minimize the production of radioactive ^{14}C during neutron irradiation [by (n, p) reaction in ^{14}N].

In summary, two oxide fuels, one MgO-CerCer and one Mo-CerMet, and one solid solution ZrN-nitride fuel are examined in this article. The materials are listed in TABLE I.

TABLE I.
Minor actinide fuels investigated in this study.

Fuel*	Composition	Form
AnO_{2-x}-MgO	Oxide	CerCer
AnO_{2-x}Mo	Oxide	CerMet
(An,Zr)N	Nitride	Solid solution

*"An" denotes a mixture of actinides (Pu, Am, and Cm). The oxide fuels are hypostoichiometric and the chemical formula is referred to as AnO_{2-x}, where x is the deviation from stoichiometry.

IV. FUEL MATERIAL PROPERTIES

Material property data for the minor actinide fuels is limited, particularly at high temperature. Thermophysical properties of minor actinide oxide fuel [15] and nitride fuel [16] were recently reviewed by Thetford and Mignanelli. We have applied their recommendations with minor modification. It is assumed that the correlations depend on temperature, matrix fraction, and porosity. In the case of oxide fuels, the influence of stoichiometry is considered. These are the most important variables. While other parameters also have an effect, these are not reliably established yet. Correlations are based on unirradiated properties (see section IV.B for discussion on irradiation effects). Selected physical properties are presented in TABLE II. Material properties for standard MOX-fuel are included for reference purposes. The values are given at 1000°C and for the fully dense and fresh material. Fuel and matrix proportions correspond to an average fuel pin in the core, as explained later. The fuels contain 40% plutonium, 50% americium, and 10% curium. A more detailed account on this composition is given in later sections. It is seen that the CerCer has considerably lower thermal conductivity, lower density, and much higher specific heat than the nitride and CerMet fuels. It also has a higher coefficient of thermal expansion, which tends to increase the negative reactivity feedback associated with fuel expansion, but may also increase the risk for fuel-cladding mechanical interaction, thermal stresses, and cracking.

TABLE II.
Selected fuel material properties at 1000ºC.

Fuel	Properties at 1000ºC (100% TD)			α^*
	ϱ g/cm^3	k W/mK	c_p kJ/kgK	1e+6/K
CerCer[a]	6.6	4.7	0.90	14.0
CerMet[b]	10.6	51.2	0.33	9.2
Nitride[c]	9.3	17.0	0.43	9.0
MOX[d]	10.7	2.8	0.33	12.1

*Mean linear coefficient of thermal expansion (300 to 2100 K).
[a] $0.42(Pu_{0.4},Am_{0.5},Cm_{0.1})O_{1.9}+0.58MgO$
[b] $0.51(Pu_{0.4},Am_{0.5},Cm_{0.1})O_{1.9}+0.49Mo$
[c] $(Pu_{0.13},Am_{0.17},Cm_{0.03},Zr_{0.67})N$
[d] Standard MOX, $U_{0.8}Pu_{0.2}$, 95% TD, O/M=2.0.

IV.A. Effect of diluent and porosity

The effect of the diluent on the material properties is approximated using Vegard's law, i.e., sum of the properties of the fissile fuel and diluent phases weighted by their respective atomic fractions. This is a rather crude approximation, but one which we need to accept in the absence of experimental data. Consequently, the fuel thermal conductivity becomes a linear and increasing function of the matrix content. The effect of fuel porosity on the thermal conductivity is modeled with the classical Maxwell-Eucken formula. For oxides and nitrides a pore shape factor of $\beta=2$ has been recommended and is used in our analyses. However, it is noted that the pore geometry depends on the fabrication process and different correction models are in use. The CerCer fuel has a bulk density of 95% of the theoretical value. Hence, the correction factor for the thermal conductivity is 0.86. For the CerMet fuel, the as-fabricated porosity of the oxide inclusions has a limited effect on the overall conductivity since it is mainly determined by the metallic component, which is fully dense. The porosity has a significant effect on the conductivity of the low-density nitride fuel. The effective thermal conductivity of the nitride fuel is reduced to 65% of the fully dense material. Fig 1 shows the effective thermal conductivity of the investigated fuels as function of temperature. Values are given for the porous material. The CerMet fuel has excellent thermal conductivity. The thermal conductivity of the nitride fuel is quite high, about 4-6 times higher than classical MOX-fuel in the typical reactor operating temperature range. The CerCer fuel has the lowest thermal conductivity of the fuels, however, it is still higher than the standard MOX-fuel (between 1.5 to 3 times higher). The thermal conductivity of the CerCer fuel has a minimum around 1500 K.

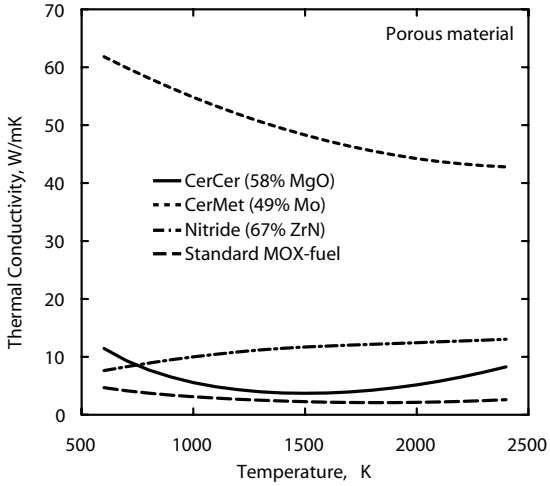

Fig. 1. Effective thermal conductivity of the examined fuels.

IV.B. Effect of irradiation

Fuel properties change during irradiation as a result of restructuring, cracking, chemical redistribution, and introduction of fission products. Such differences play an important role in establishing safety margins as function of temperature and burnup history – both for steady-state operation and during thermal upset conditions. Restructuring (grain growth and pore migration) affects thermal conductivity, void formation, density, volumetric heat generation levels, and hence operating temperatures. An analysis of all the governing processes is beyond the scope of this article. Suffice it to say that restructuring and development of thermal stresses (cracking) depend strongly upon thermal gradients and operating temperatures and is usually small for high-thermal conductivity fuels [17], which suggest limited thermal restructuring for the CerMet and nitride fuels, whereas significant changes may occur in the CerCer fuel. Cracking is further aggravated by a high coefficient of thermal expansion, which suggests more severe cracking for the CerCer fuel. For oxide fuel, decrease in the thermal conductivity due to the introduction of fission products is small in comparison with the larger effects of restructuring. The development of a central void in typical fast reactor mixed-oxide fuel and densification of the restructured regions tend to reduce the maximum fuel

temperature with irradiation time even though the local linear power is constant [18]. Yet, very little in-pile data is available upon which to judge the irradiation behavior for the minor actinide dispersal fuels. Studies have been performed on a UO_2+64%Mo composite fuel irradiated to a burnup of 5 atom% [19]. Post-irradiation examination revealed little or no signs of restructuring, which indicates that molybdenum is a potentially stable matrix material. The reduction of the thermal conductivity with burnup is probably larger for the CerMet fuel because of higher fission gas retention and less pore migration, but it is expected that the net effect of irradiation is to reduce maximum fuel temperatures because of fuel-cladding gap closure early in life. We presume that such a displacement of the fuel surface act to reduce centre line temperatures in the nitride case too, but to a lesser extent as compared to the CerMet fuel. Fission gas (xenon and krypton) mixture effects on the fill gas (helium) conductivity are largely offset by reduced fuel-cladding gap thickness and higher gas pressure. Although restructuring and swelling phenomena may improve fuel thermal performance, for reasons explained above, it is possible that higher burnup negatively affects fuel melting temperatures, fuel-pin mechanical performance as well as power peaking factors. It is apparent that an assessment of the variation of safety margins (power-to-melt, thermo-mechanical limits, etc.) as function of irradiation time would require examination of a wide range of phenomena, each suffering from large uncertainties and, consequently, we find it speculative to extract such limits at this stage.

V. DESIGN LIMITS

We attempt to establish design limits for the fuel and cladding. The fuel failure limit is prescribed by accident conditions and has little constraints on normal operation, whereas the cladding failure limits are defined for steady-state and transient conditions. It should be noted that the design studies are yet in a pre-conceptual stage and it is not meant to imply that the indicated limits are complete. The objective at this point is to describe the analysis methodology involved and to provide a framework for guiding further design work, not to spell out elaborate details on the design criteria or particular failure processes. Inevitably, there are many uncertainties regarding potential failure mechanisms (e.g. mechanical and chemical interactions between fuel components, fission products, and cladding constituents), and, as discussed in Chapter IV.B, further research is required to establish reliable design limits based on in-pile experimental data.

To this end, we have selected Si-modified 15-15Ti austenitic stainless steel as reference cladding material. This class of alloy has demonstrated favourable performance up to 150 dpa [20] and has good high temperature mechanical properties [21].

V.A. Oxide melting

Complications arise in describing the melting behavior of the present oxide fuels. Due to a low solid solubility of the oxide fuel particles in the diluents (MgO and Mo), the two constituents will melt at different temperatures. In addition, eutectic melting may appear at temperatures below the melting points of the individual materials. The melting point of the mixed actinide oxide, $AnO_{1.9}$, is estimated to 2640 K, based on the melting points of PuO_{2-x} [22], AmO_{2-x} and CmO_{2-x} [23], and applying Vegard's law. We have assumed a melting point dependence on the oxygen content similar to the recommendations for $(U,Pu)O_{2-x}$ [24]. It appears that no eutectic reaction occurs between molybdenum and UO_2 [25] If a similar behavior is assumed for $AnO_{1.9}$-Mo, then the first sign of melting will occur in the oxide phase (the melting point of pure Mo is 2900 K). The oxygen content may affect the potential for eutectic formation and oxidization of Mo into MoO_2, however, these effects are not sufficiently known to be taken into account. For the CerCer fuel, complication arises due to the possibility for eutectic reaction below the melting points of AnO_2 and pure MgO (T_m=3100 K). Laboratory measurements [26] found no eutectic reaction up to ~1923 K, while theoretical calculations [27] predicted that an eutectic may start to form at temperatures as low as 1930 K for low oxygen contents. The same study also estimated that the melting point stabilizes around 2300 K for oxygen-to-metal ratios above 1.62. Keeping low oxygen content, however, is desirable because it reduces corrosion of the cladding. The melting point of PuO_{2-x}-MgO [28] ranges from 2341 to 2503 K when the oxygen content changes from 1.61 to 2. Following these results, we estimate the failure limit of the $AnO_{1.9}$-MgO fuel somewhere in the range 2200-2300 K.

V.B. Nitride dissociation

The main concern about nitrides is the dissociation of AmN into metal and nitrogen gas at temperatures around 1600 K [29], which is too low to meet safety requirements under overpower conditions. To investigate this problem, thermo-chemical modeling has been performed on minor actinide nitride compounds in various environments. In this study, an updated version of the ALCHYMY database [30] for Thermo-Calc [31] was used to model the dissociation of AmN in $(Pu_{0.2}Am_{0.3}Zr_{0.5})N$ heated in a constant-volume system mimicking the dimensions and materials proportions of an actual fuel pin with and without a stabilising addition of 1% N_2 to the filling gas. The assumed pin pressure is that of the bonding gas at the corresponding temperature plus 1.5 times that of americium vapour (AmN -> Am(g) + 0.5 N_2). Up to 2400 K, the contribution from dissociation of PuN is smaller by three orders of magnitude and can be ignored. In the same range, the increase in pressure arising from AmN dissociation is only a few percent of the total pressure and should not be an issue from a purely mechanical point of view. The depletion of Am from the fuel is in itself very small during uniform heating, below 0.01% even in pure helium. Based on these results, we estimate the failure point for the nitride fuel at 2400 K. This failure criteria should be considered applicable only during rapid overpower excursion. For slow transients, one may expect transport effects, with nitride continuously dissociating in hot zones and reforming on colder surfaces, if the overheating would persist for longer time. As the model contains several other simplifications (congruent vaporisation of AmN at stoichiometric composition, ideal solid solution of nitrides) and considering that thermodynamical parameters for AmN are based on

some reasonable but unverified assumptions [32], the results must not be interpreted too literally.

V.C. Cladding transient burst limit

Thermal limits relevant for cladding during thermal upset conditions were established based on transient burst test data. These tests, called Fuel Cladding Transient Test (FCTT), duplicate reactor transient conditions in which the cladding (irradiated or unirradiated) is heated (out-of-pile) until failure occurs. The failure temperature is recorded as function of hoop stress and often related to a particular thermal ramp rate. The FCTT tests are typically carried out for relatively fast ramp rates, in the range 0.5-100 K/s. In our estimates, we have assumed an internal pin pressure of 14 MPa (equivalent to a membrane stress of 100 MPa) and a thermal ramp rate of 5 K/s. This thermal ramp rate was selected because it is similar to the heating rates involved in loss-of-flow conditions. Temperature limits for 15-15Ti are estimated using data for unirradiated D9 pin cladding [33]. The D9 alloy is a titanium modified 316 austenitic stainless steel, which has similar composition as 15-15Ti steel. Tension tests [21] show that the mechanical properties of irradiated 15-15Ti is better than Ti-stabilized 316, indicating that transient/mechanical properties should be no worse than for D9. The failure temperature of irradiated cladding specimens is comparable to the unirradiated cladding [34], as the fuel adjacency effect (FAE) [35] may be negligible in the actual fuel pin environment [36]. Based on these studies, we estimate a failure temperature for 15-15Ti cladding equal to 1330 K.

V.D. Cladding creep rupture limit

For long-term operation, nominal temperatures are limited by thermo-mechanical creep rates. Stress rupture data is scarce for 15-15Ti steels. However, a reasonable amount of data is available for D9. The better tensile properties of 15-15Ti suggest that the thermal creep performance of CW 15-15Ti could be comparable or better than D9. Ongoing studies show that silicon modified CW 15-15Ti stainless steel posses even better tensile properties, indicating that further improvement might be possible. Tests conducted on 20% CW D9 cladding [37], showed that the in-pile rupture lifetime is lower compared to out-of pile data, indicating that the pin cladding might fail sooner than predictions based on out-of-core test results. The maximum operating temperature for the CW 15-15Ti cladding, with respect to thermal creep, was estimated to be 920 K (maximum midwall temperature). This limit was determined for a constant plenum pressure loading of 10 MPa (equivalent to a hoop stress of 74 MPa) and an expected in-pile service of 3 years (exposure time 30,000 h).

V.E. Cladding corrosion limit

Corrosive attack by the coolant imposes additional constraints. The effect of LBE corrosion is manifest as wall thinning, as structural material dissolves in the coolant, and higher stresses, which altogether leads to reduced cladding lifetime. The corrosion rate shows a strong dependence on temperature and some correlation with fluid velocity. It has been demonstrated that, for non-protected stainless steels, nominal temperatures must not exceed 670 K for austenitic steels and 720 K for ferritic steels [38]. In an oxygen-controlled environment, however, a protective oxide film may form on the surface of the structure, which may slow down the dissolution rate. The protective film is formed by oxidation reactions between the oxygen dissolved in the coolant and steel alloy elements (Fe, Cr, Si, and others with high affinity to O_2). Using this technique, operating temperature can be raised by 150-200 degrees. In Russia, where most corrosion studies with Pb/Bi have been carried out, the results indicate that the ferritic/martensitic steels offer the best performance. This appears to be due to the low nickel content of the ferritic steels compared to the austenitic steels [38]. Nickel shows high solubility in Pb/Bi alloy, which has an impairing effect on the stability of the oxide film and increases the corrosion rate. At this stage of development, long-term operation (≥30.000 hours) at temperatures above 890 K appears to be difficult [38], even for the most promising corrosion resistant steel, i.e., Russian type silicon-alloyed ferritic-martensitic steel (EP823). With reference to austenitic 15-15Ti steels, we assume that the operating clad temperature is to be kept below 840 K (surface temperature).
TABLE III summarizes the current estimates of the design limits for the investigated fuels and cladding materials. It is cautioned that these limits are preliminary estimates and may change in the light of further testing.

TABLE III.
Summary of thermal limits for fuel and cladding.

Component	Failure temp. (K)	Failure mechanism
Fuel		
CerCer	2200-2300	Eutectic melt
CerMet	2640	Oxide melting
Nitride	2400	AmN dissociation
Cladding (type 15-15Ti)		
Surface (steady-state)	840	Corrosive thinning
Midwall (steady-state)	920	Creep rupture
Midwall (transient)	1330	Mech. burst limit

VI. COMPUTATIONAL METHODS

The continuous energy Monte Carlo code MCNP4C [39] together with the JEF2.2 nuclear data library is used for neutronic calculations. A three-dimensional pin-by-pin model is employed. The MCNP code is used to calculate neutronics input data required for transient modeling (kinetics parameters, reactivity coefficients, power distributions, and gamma heating).

The SAS4A/SASSYS-1 computer code [40] is used for thermal- and hydraulic calculations at steady-state and transient conditions. The SASSYS-1 code is an integrated safety analysis computer code for the analysis of reactor plant transients in liquid-metal cooled reactors. A detailed description of the SAS code is outside the scope of this paper. The code has been adapted to enable the analysis of heavy liquid-metal cooled reactor designs and accelerator-driven systems. The calculational model used in this study employs two thermal-hydraulic channels. One channel represents an average pin within the core and a second channel represents the hottest pin in the core (with a power peaking factor of 1.3). The primary system includes models of the core, primary pumps, shell side of the steam generators, connecting piping,

and compressible pool volumes with cover-gas surfaces. The fuel-cladding gap conductance model accounts for gas conduction, radiative heat-transfer, surface roughness, and differential thermal expansion of fuel and cladding during transient conditions. Reactivity feedbacks are calculated for coolant expansion, fuel elongation, radial core expansion, and Doppler effect. Changes in power level are computed with point kinetics theory. The performance of the point kinetics approximation for transient analysis of ADS's was considered in a previous assessment [41] and found adequate for similar problems.

VII. CORE MODEL

A reference core was constructed largely based on previous parametric studies. The core model pertains to a LBE-cooled accelerator-driven system with a thermal rating of 800 MW. The core consists of a central lead-bismuth spallation target surrounded by a fuel region. The active core is 1 m high with a diameter of 1.6 to 2.2 m, depending on the core configuration. The core is surrounded by axial and radial reflectors 0.5 m thick. The reflectors consist of subassemblies filled with coolant and empty cladding tubes. The pitch-to-diameter (P/D) ratio and the pin diameter are design parameters. The reference configuration uses a P/D equal 1.50 and a pin diameter of 5.72 mm. In a second configuration, the P/D value is increased to 1.75 by changing the pin pitch. In a third modification, the pin diameter is increased to 6.8 mm while holding the P/D ratio at 1.50. In all the cases the flat-to-flat distance is fixed while the number pins per subassembly is either 91 or 127. A summary of design parameters is given in TABLE IV.

TABLE IV.
Core lattice configurations

SA pitch	10.2 cm
FTF outer	10.0 cm
FTF inner	9.6 cm
P/D	1.50/1.75
Pins per SA (1.50/1.75)	127/91
Volume fractions	27/16/52 % (P/D=1.50)
(fuel/steel/coolant)	19/14/63 % (P/D=1.75)
Cladding o.d.	5.7/6.8
Cladding i.d.	5.0/6.0
Active core height	1.0 m
Core diameter	~1.6-2.2 m
Spallation target diameter	0.4 m
Gas plenum height	1.50 m

The core is partitioned into three regions of different matrix fractions. The purpose is to level out the radial power distribution. Matrix fractions are adjusted to obtain an initial k_{eff} equal 0.97 and a radial peak-to-average power ratio factor of 1.3. Matrix contents drop towards the edges, as shown in TABLE V. The poorer neutron economy of the oxides result in matrix contents lower compared to the nitride, which has an adverse effect on the fuel performance. A high volume fraction of diluents is favorable from the viewpoint of thermal performance, stability, and fuel fabrication. Increasing the P/D ratio requires lower concentration of diluents while increasing the pin diameter enables a slightly larger fraction of matrix to be used. The plutonium fraction is fixed at 40%, which is similar to the initial Pu loading in the double-strata cycle studied by JAERI. It was shown that this plutonium content provides minimal burnup reactivity swing over a large number of irradiation cycles [42]. The fuel has total americium content of 50% and 10% curium. Neptunium is not considered because it is not an important contributor to the long-term radiotoxicity. The americium vector consists of two thirds ^{241}Am and one third of ^{243}Am. Curium is composed of 87% ^{244}Cm and 13% ^{245}Cm. The isotopic vector of plutonium (5% ^{238}Pu, 38% ^{239}Pu, 30% ^{240}Pu, 13% ^{241}Pu, and 14% ^{241}Pu) corresponds to discharged MOX fuel from LWRs after 7 years cooling. The isotopic composition of americium and curium derives from a mixture of spent UOX and MOX fuel. Burnup reactivity losses are compensated by increasing the proton beam current by a factor of 1.5 at end-of-life. Delayed neutron parameters and prompt neutron generation times are shown in TABLE VI. Clearly, there is a large difference between the effective delayed neutron fraction (β_{eff}) and the actual delayed neutron fraction (β). The β_{eff} is around 180 pcm, while the corresponding β value is in the range of 230-280 pcm. The reason for this variation is that delayed neutrons are emitted with much smaller average energy (~0.5 MeV) and thus with lower chance of causing fission in the even neutron numbered nuclei (^{241}Am, ^{243}Am, ^{240}Pu, and ^{242}Pu) than prompt neutrons. The prompt neutron generation time (Λ) varies between 0.5-0.8 μs and increases for higher P/D.

TABLE V.
Inert matrix volume fractions.

Fuel	D_{clad}	P/D	Zone 1	Zone 2	Zone 3
CerCer	5.7	1.50	0.65	0.58	0.42
	5.7	1.75	0.56	0.51	0.41
	6.8	1.50	0.68	0.62	0.52
CerMet	5.7	1.50	0.54	0.48	0.37
	5.7	1.75	0.47	0.41	0.31
	6.8	1.50	0.60	0.54	0.45
Nitride	5.7	1.50	0.73	0.67	0.54
	5.7	1.75	0.66	0.61	0.50
	6.8	1.50	0.76	0.71	0.60

TABLE VI.
Delayed neutron fractions (β and β_{eff}) and neutron generation times (Λ).

Fuel	D_{clad}	P/D	β (pcm)	β_{eff} (pcm)	Λ (μs)
CerCer	5.7	1.50	250	180	0.65
	5.7	1.75	250	190	0.81
	6.8	1.50	250	190	0.76
CerMet	5.7	1.50	240	170	0.50
	5.7	1.75	230	180	0.67
	6.8	1.50	270	190	0.60
Nitride	5.7	1.50	280	180	0.55
	5.7	1.75	240	180	0.71
	6.8	1.50	260	170	0.67

Additional fuel pin specifications are given in TABLE VII. Because of lower thermal conductivity, the CerCer fuel is required to operate at lower linear powers; 25 kW/m compared to 35 kW/m for the CerMet and the nitride fuel.

The initial gap thickness is chosen so that direct solid-to-solid contact is prevented during transients (assuming unirradiated geometry). As oxide fuels have a high plasticity and low swelling characteristics, pellet cladding mechanical interactions (PCMI) are less acute, and hence a rather small pre-fabricated porosity is sufficient. In the case of the nitride and the CerMet, PCMI cannot be tolerated, and hence a larger porosity of the nitride and a larger fuel-cladding gap of the CerMet have been adopted. The smear density for the CerCer, CerMet, and the nitride fuels are 91%, 88%, and 82%, respectively.

TABLE VII.
Fuel pin description (at operating condition).

Fuel	CerCer	CerMet	Nitride
Average linear power, kW/m	25	35	35
Smeared density (%)	91	88	82
Fuel-clad gap width, μm	50	100	50

VII.A. Temperature profile

The temperature distribution in structural components and fuel elements depend on the surface heat transfer conditions. Following recommendations by the IPPE (Obninsk), the heat-transfer coefficient between element and lead-bismuth coolant is determined using the following Lyon-Martinelli correlation [43]:

$$Nu = 5 + 0.025 Pe^{0.8}$$

In Fig. 2, the steady-state temperature profile in the fuel rod is shown. The plot reproduces the profile for the hottest pin at core midplane and for the configuration using a pin diameter of 5.7 mm. Because of the low thermal conductivity, the CerCer fuel suffers from a steep temperature gradient (more than 300 K/mm). Despite that the CerCer fuel is operating with a lower specific power, it is the hottest of the three fuels. The CerMet fuel remains relatively cold, reaching a maximum temperature of 1690 K. The margin to melting is 950 K. The larger gap size for the CerMet eliminates some of the advantage of its high conductivity. Use of a liquid-metal bonding material could reduce fuel surface temperatures further, but at the risk of introducing additional problems, e.g., compatibility issues with fuel and cladding, bond vaporization, practical problems associated with manufacturing and reprocessing. Considering the small temperature gradient in the CerMet fuel (approaching 50 K/mm) suggests lower tendency for thermal restructuring and cracking, and the relatively low operating temperature implies lower fission gas release rates. Peak fuel and cladding temperatures as function of P/D and pin diameter are tabulated in TABLE VIII. It is seen that the reference case, with a tight pin lattice and thin pin diameter, is not consistent with a permissible cladding surface temperature of 840 K as dictated by long-term cladding corrosion damage. Cladding temperatures reported in TABLE VIII refer to the cladding midpoint. The surface temperature, which is of interest for the corrosion rate, is approximately 10-20 degrees lower. Maximum cladding temperatures occur at the outlet where coolant temperatures are highest. To maintain the cladding temperature within the given limit, a higher coolant mass flow rate is desirable. This may be achieved by increasing the P/D ratio. The reason the steady-state temperatures are lower for the cases with larger pin diameter is twofold: coolant temperatures are lower because the coolant flow area is larger and the thermal conductivity of the fuel is better because matrix fractions are generally higher.

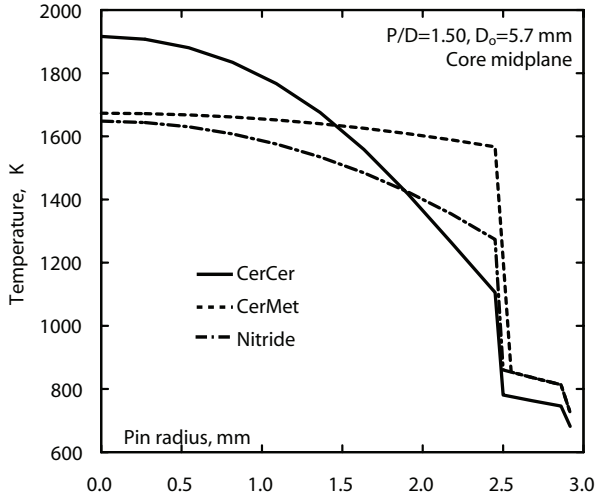

Fig. 2 Steady-state temperature profile at core midplane.

TABLE VIII.
Peak fuel and cladding (midpoint) temperatures in the hottest channel at normal operating conditions.

Fuel	P/D=1.50, D_o=5.7 mm		P/D=1.75, D_o=5.7 mm		P/D=1.50, D_o=6.8 mm	
	Fuel	Clad	Fuel	Clad	Fuel	Clad
CerCer	1920	840	1920	770	1740	770
CerMet	1690	940	1690	840	1530	850
Nitride	1660	940	1650	840	1540	850

VIII. REACTOR PLANT SYSTEM

TABLE IX contains major specifications of the lead-bismuth cooled ADS plant. The primary system is of pool type design. Due to high corrosion activity, coolant temperatures and velocities are limited. The coolant flow velocity in the pin bundle is limited to 2.5 m/s and the reactor inlet temperature is set at 573 K. LBE is chemically inert with water/steam. Hence, a two-circuit system is utilized, with the steam generator located in the primary system, which simplifies the overall plant design and reduces the cost. The primary system includes four centrifugal pumps (two for each loop) and four steam generators (two for each loop). Based on a seismic analysis, as discussed in the next section, a vessel height of 10 m is selected. The elevation difference between the core midplane and the thermal center of the steam generators should be as large as possible to increase natural circulation contribution. To allow room for cover gas and bottom support, however, the separation distance is limited to 5.5 m. The pump design includes flywheels to prolong the coast-down time in the event of a loss-of-flow accident. The size of the flywheel was optimized to provide a smooth transition to natural circulation. A pump inertia (pump, motor, and flywheel) equal to 400 kg·m^2 was found appropriate. As a

comparison, the FFTF reactor, which is a sodium-cooled 400 MWth reactor, had a primary pump inertia of 700 kg·m² [44].

VIII.A. Seismic analysis

A tall vessel is desirable to promote natural circulation. On the other hand, a large vessel increases the cost and decreases seismic stability. The vessel thickness increases with the vessel size and weight of the contained liquid. According to one report [45], wall thickness for type 316SS is limited to 130 mm by manufacturing capability. Thus, to ensure acceptable stress levels under a seismic event, it is necessary to limit the size of the vessel. A rough estimate of the allowable vessel height was calculated based on a seismic model suggested by Buongiorno [46]. We assume that the vessel has an outer diameter of 6 m and contains lead-bismuth with an average density of 10.2 g/cm3. The vessel is made of grade 316 stainless steel with a steady-state operating temperature of 693 K. Following Buongiorno's example, the vessel is subject to an earthquake with a peak ground acceleration of 0.5g (horizontal motion). This criterion is adequate for licensing purposes of most sites in the U.S. The calculated peak stress intensity is compared with limits specified by the ASME code for 316SS. The analysis suggests an allowable vessel height in the range 10-12 m. It should be noted that this estimate is based on a tentative maximum wall thickness of 130 mm for a vessel made of 316SS, as compared to thicknesses around 200-250 mm for PWR systems (utilizing carbon steels). It is found that, a wall thickness of 250 mm should admit a vessel height around 15-16 m, which indicates a rather high sensitivity of the stress level on the vessel height. The dependence on the vessel diameter is not strong, however. The study also depends on seismic load conditions, which are site dependent. Use of bottom horizontal structure support and/or base isolation could enhance seismic performance. The effect of seismic isolation is a reduction of the natural frequency of the structure, which may lead to significant reduction of building accelerations in an earthquake. This was recently shown in the application to an ADS plant [47].

TABLE IX.
Plant specification

General	
Type of plant	Pool type
Reactor power	800 MWth
Coolant	LBE (44.5%Pb+55.5%Bi)
Reactor inlet temperature	573 K
Coolant inlet velocity	2.5 m/s
Reactor vessel	
Height	10 m
Diameter	6 m
Wall thickness	13 cm
Weight (incl. coolant)	~2500 ton
Primary system	
Steam generators	4 (integrated)
No. of pumps	4
Pump mass of inertia	400 kg·m²
Distance between thermal centers of core and SG's	5.5 m

VIII.B. Thermal- and hydraulics analysis

Plant thermal-hydraulics data are presented in TABLE X. Because of different linear power ratings, the exit temperature for the CerCer core is lower than the CerMet and nitride cores. It is noted that the coolant mass flow rate is higher and the exit temperatures are lower for the configurations using a pin diameter of 6.8 mm, which is a geometrical effect of maintaining a constant P/D ratio while the pin diameter is increased. Friction factors for the calculation of the pressure drop in the rod bundle are determined from the Blasius relation for turbulent flow:

$$f = 0.316\,\mathrm{Re}^{-0.25}$$

The pressure drop through the core depends on the pitch-to-diameter ratio and on the cladding diameter. It is found that for P/D=1.50 it accounts for 90% of the total system pressure loss at normal forced flow operation; at P/D=1.75 it is responsible for about 60% of the pressure loss.

TABLE X
Thermal-hydraulics data during steady-state.

Fuel	D_{clad}	P/D	CerCer	CerMet	Nitride
Coolant exit	5.7	1.50	740	810	810
temp. (K)	5.7	1.75	680	720	720
	6.8	1.50	690	740	740
Hot channel	5.7	1.50	790	880	880
exit temp. (K)	5.7	1.75	710	760	760
	6.8	1.50	730	790	790
Mass flow rate	5.7	1.50	0.96	0.96	0.96
(kg/s)	5.7	1.75	1.61	1.61	1.61
	6.8	1.50	1.33	1.33	1.33
SA friction,	5.7	1.50	$2.8 \cdot 10^5$	$2.8 \cdot 10^5$	$2.8 \cdot 10^5$
Δp (Pa)	5.7	1.75	$1.6 \cdot 10^5$	$1.6 \cdot 10^5$	$1.6 \cdot 10^5$
	6.8	1.50	$2.4 \cdot 10^5$	$2.4 \cdot 10^5$	$2.4 \cdot 10^5$
Primary loop,	5.7	1.50	$3.1 \cdot 10^5$	$3.1 \cdot 10^5$	$3.1 \cdot 10^5$
Δp (Pa)	5.7	1.75	$2.5 \cdot 10^5$	$2.5 \cdot 10^5$	$2.5 \cdot 10^5$
	6.8	1.50	$3.0 \cdot 10^5$	$3.0 \cdot 10^5$	$3.0 \cdot 10^5$

IX. REACTIVITY SOURCES

Identification of potential reactivity sources is an important element influencing the inherent safety characteristics of the reactor. These sources may come into play because of temperature changes during normal operation or as a result of displacement of core materials under accident conditions. Because of the built-in subcritical margin, reactivity feedbacks involving only temperature changes have a limited role in ADS's [48]. We have chosen to include them in the discussion for completeness.

IX.A. Temperature coefficients

The main reactivity feedback mechanisms and their numerical values are shown in TABLE XI. These coefficients are whole core values and reflect the effect of changes in temperature about the normal operating point. The reactivity coefficients are calculated through two successive eigenvalue calculations, one for the initial state, and one for a perturbed state (involving a certain change in density, temperature, or geometric configuration around the operating point). The coefficient for thermal expansion of the associated material (fuel, coolant, steel) is used to define the appropriate relationship with the temperature coefficient of reactivity. The radial expansion reactivity is calculated by expanding the core grid in the horizontal direction. The fuel expansion reactivity effect is determined based on elongation of the fuel column; any contact between the fuel and the cladding is ignored. It is seen that the coolant density coefficient is somewhat stronger in the CerCer core than in the CerMet and nitride cases. Literature values for the typical sodium-cooled and MOX-fueled fast breeder reactor (FBR) are included for comparison. It is noteworthy that the positive reactivity effect due to sodium expansion in the FBR is about twice the LBE-expansion coefficient in the investigated cores. The Doppler coefficient is around 0.05 pcm/K for the studies cores, which is an order of magnitude smaller than in the FBR. The integrated effect (up to fuel failure) due to Doppler feedback is in the range –0.2-0.3$, which is unimportant for transients in ADS's. Reactivity feedback due to axial expansion is approximately 5 times the Doppler coefficient, but usually it has a small effect. It may be compared with subcriticality levels around 16-18 dollars for the examined cores. All cores feature a net negative temperature coefficient, assuming isothermal heatup. Radial core expansion is by far the most important feedback effect in this respect. However, radial core expansion effect is determined by temperature changes of the grid support structure and heating of the duct walls at the above-core load pads, so the overall effect depends on the heating rate and local temperature distribution.

TABLE XI.
Whole-core temperature reactivity coefficients for reference core P/D=1.5, D=5.7 mm (as calculated around the operating point).

Reactivity coefficients	$\Delta k/\Delta T \cdot 10^5$ (pcm)			
	CerCer	CerMet	Nitride	FBR
Coolant expansion	+0.43	+0.32	+0.35	+0.80[a]
Axial fuel expansion	-0.28	-0.18	-0.25	-0.18[b]
Radial core expansion	-0.94	-0.97	-1.01	-1.10[a]
Doppler effect	-0.05	-0.05	-0.05	-0.40[a]
Net (isothermal heatup)	-0.84	-0.88	-0.96	-0.88

[a]Super-Phénix, sodium cooled, UO_2-PuO_2 fuel.
[b]FFTF, sodium cooled, UO_2-PuO_2 fuel.

IX.B. Coolant void

Considerable attention is given to the reduction of the coolant void worth in current ADS designs. It has been shown that coolant voiding could introduce reactivities that may override the subcritical reactivity for certain combinations of fuel and liquid-metal coolant [3,4,49]. A parametric study of the effect of americium content on the void worth was made by Tucek, et al. [50]. It was found that the void reactivity effect increases with the americium content. LBE yields lower void worths than sodium for a wide range of fuel types and core sizes [3,51]. The low void worth and high boiling point in comparison with sodium are principal advantages that favour the selection of LBE. The higher sodium void worth is partly due to its higher moderating power, which causes a larger spectrum shift during voiding. The void worths associated with the present fuels were calculated in a previous paper [7]. For convenience, these results are listed in TABLE XII. The effect of changing the core size and pin diameter is shown. The negative leakage component tends to decrease with increasing reactor size, while the spectrum hardening effect increases for higher coolant volume fractions. The net effect is that the void effect becomes more positive when the core size increases. The calculations indicate an increase in void worth for larger pin diameters. The effect of separately voiding the core region and plenum region was investigated. The spectral contribution to the void reactivity is usually more positive near the center of the core, while the leakage component is more negative near the edges where the flux gradient is stronger. As a result, expulsion of coolant from the central region results in a positive reactivity gain. However, if the plenum region is voided simultaneously, the reactivity effect may decrease considerably. Evidently, the CerMet fuel offers low void worths. For tight lattice configurations with this fuel, even central voiding can be accommodated. The void worth of the CerCer core is considerably higher than the

CerMet and nitride. The reason is the larger core size (more fuel pins) of the CerCer core, which is an effect of the lower linear rating requirement of this fuel. It is noted, however, that all three fuels provide acceptable void values when the core and plenum is voided simultaneously.

TABLE XII.
Coolant void reactivity worth (in pcm) computed for the examined fuels in various lattice configurations.

Fuel	P/D=1.50, D_o=5.7 mm		P/D=1.75, D_o=5.7 mm		P/D=1.50, D_o=6.8 mm	
	Core	Core+ plenum	Core	Core+ plenum	Core	Core+ plenum
CerCer	4060	1790	5300	2300	4570	2250
CerMet	2460	220	3580	470	2990	520
Nitride	2960	680	4150	880	3610	1080

IX.C. Cladding relocation

Theoretically, molten cladding could be ejected into the coolant and swept upwards with a consequent positive reactivity effect. Such a scenario has been suggested by Maschek, et al. [52] in a previous paper. The effect is important if the cladding leaves the core ahead of the fuel. For transient events, it is likely to be associated with coolant overheating, e.g., due to a reduction in flow. On a longer timescale, positive reactivity could be inserted because of dissolution of structural materials in the coolant. In this study, we calculated the reactivity effect assuming all cladding is removed from core, which enables a rough estimate of the reactivity values involved. The results are presented in TABLE XIII. It can be seen that cladding removal leads to a net positive reactivity insertion around 3000 pcm. Note that this value is more or less the same for all fuels. It is further seen that the cladding reactivity worth is largely insensitive to the size of the pin, but decreases for larger pitches as the volume fraction of cladding is lower. Evidently, a larger core size may reduce the cladding worth, but at the cost of a higher void worth. Use of a thinner cladding could further reduce the positive reactivity effect, but it would also degrade mechanical strength.

TABLE XIII.
Reactivity changes (in pcm) following removal of the cladding from the core.

Fuel	P/D=1.50, D_o=5.7 mm	P/D=1.75, D_o=5.7 mm	P/D=1.50, D_o=6.8 mm
CerCer	3170	2610	3190
CerMet	3360	2750	3310
Nitride	3350	2790	3400

IX.D. Fuel relocation

Reactivity might be introduced in a fast reactor if the fuel would collect in a denser configuration. This is a fundamental distinction between reactors operating on a fast neutron spectrum and thermal systems. The latter is arranged in nearly an optimum configuration to maximize neutron multiplication and any change to the configuration is likely to shut down the chain reaction. By comparison, if the fuel in an ADS melts or the structure collapses, it is possible that criticality would occur. Neutronic calculations have been performed to determine critical fuel geometries. TABLE XIV shows critical mass, critical volume, and theoretical number of critical assemblies available. The critical mass is sensitive to the material composition (additions of steel, neutron absorbing materials, reflective conditions, etc.) and the fuel geometry. The calculations were carried out for a cylinder containing pure fuel material (fresh fuel) at its normal density. The height-to-diameter (H/D) ratio of the cylinder is 1. It was further assumed that the cylinder is surrounded by LBE on all surfaces. Of course, the assumed critical geometry is an idealized form of the actual configuration of a hypothetical core melt. Calculations for standard fast reactor fuel ($U_{0.8}Pu_{0.2}O_2$ surrounded by Na) were also performed to enable comparison. It is seen that the critical mass of the minor actinide fuels is quite small in comparison with standard fast reactor fuel, however, variations occur. The nitride fuel has the smallest critical mass (70 kg), which is approximately 20 times smaller than classical MOX-fuel surrounded by sodium. This corresponds to the fuel mass contained in three subassemblies (127-pin bundles). The critical mass of the CerMet fuel is 340 kg, which is a factor of 5 larger than the nitride fuel. The critical mass of the CerCer fuel is somewhat smaller than for the CerMet. Clearly, an ADS core contains sufficient fuel to assemble several critical masses. About 69 critical masses were calculated for the nitride core while the oxide cores contain 18 critical masses each. By comparison, Super-Phénix held about 17 critical masses. Given that the total fuel mass in the French reactor is about 4 times larger than for the present ADS cores, a direct comparison is not appropriate. Based solely on the critical mass, it would seem desirable to use a neutron absorbing matrix material, such as molybdenum or magnesia. However, the recriticality question is complex and in comparison with fast reactors, the behavior of an ADS under these conditions is not well known. The critical size of the fuel is merely one element affecting the recriticality potential.

TABLE XIV.
Critical mass studies.

Fuel	Critical mass* (kg)	Critical volume (dm^3)	Reactor total (critical masses)
CerCer	290	47	18
CerMet	340	33	18
Nitride	70	9	69
Super-Phénix	1370	130	17**

*Cylindrical volume element (H/D=1) surrounded by LBE.
**Based on $(U_{0.8}Pu_{0.2})O_2$, 3000 MWth (23 tons of fuel).

X. UNPROTECTED LOSS-OF-FLOW

This section presents results for a flow coastdown transient. It is assumed that all primary pumps are tripped in conjunction with failure of the shutdown system, i.e., the proton beam remains on. It is further assumed that the heat rejection system maintains core inlet temperature at the pre-transient value. This is a reasonable assumption, since negligible changes in the inlet temperature typically occur during a loss-of-flow event. During the transition to natural circulation condition, the flow rate is determined by the inertia of the pump and the thermal buoyant drive, which is

counterbalanced by the system pressure losses. It was mentioned earlier that the pump moment of inertia was optimized to soften the cladding-heating rate following pump trip. The cladding-heating rate gradually decreases for longer flow coast-down time, which implies longer grace periods with ever increasing pump inertia. There are, however, operational problems associated with high inertia pumps that impose an upper limit on the pump mass. Besides mechanical problems on the pump shaft, an adverse negative effect is sluggish speed control. In a controlled shutdown event, it is desirable to match the flow and power to avoid thermal cold shock in reactor components (mainly in upper internal structures and heat exchangers). In that case, a large rotating mass is a drawback. Multiple shutdown events may result in thermal fatigue [53], which can cause premature failure. This problem is of particular concern for ADS's because of the possibility for frequent beam interruptions [54]. Therefore, a balance must be struck in the selection of the flywheel size.

X.A. Transient results

Examination of Fig. 3, which shows the coolant flow rate in the average channel for the case with P/D=1.75, reveals that the natural circulation flow reaches a quasi-steady value of 23-27% of initial flow at 50-60 seconds after the pump trip. From this data plus the thermal response for the cladding shown later, it is apparent that the transition to natural circulation is smooth. Because the CerCer system operates with a lower coolant ΔT, the fluid density difference between the hot leg and the cold leg is smaller, which provides for a lower circuit buoyant head. As a result, the natural circulation flow level is lower in the CerCer reactor. Fig. 3 shows the power history. All three cores feature overall negative temperature-induced reactivity feedbacks. The power decreases steadily during the entire transition to natural circulation conditions. The overall effect of the reactivity feedbacks is not great, however. The power falls to approximately 95% of the initial value of 800 MWth when equilibrium is reached. The power response behavior is similar among the cores.

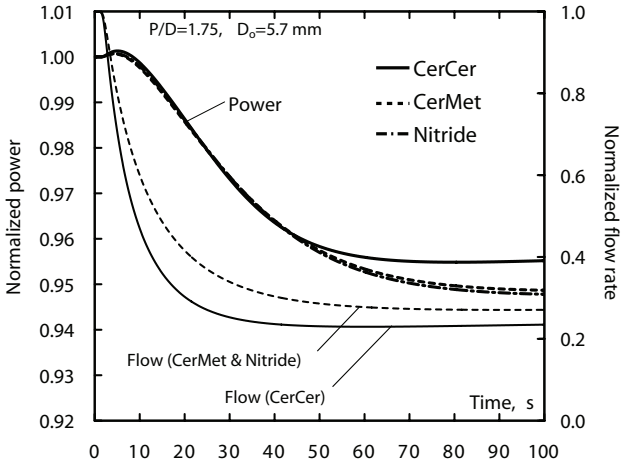

Fig. 3. Transient power and flow conditions for unprotected loss-of-flow transient.

Reactivity feedbacks are illustrated in Fig. 4. For simplicity only the case with CerCer fuel and P/D=1.75 is shown. Reactivity feedback from radial expansion of the core is the dominant negative feedback mechanism – it contributes about minus one dollar at equilibrium conditions. A brief description on the radial expansion reactivity model is in place. The radial growth of the core is determined by the expansion of the grid support structure and by the expansion of the hexcan duct walls and the above-core load pads. The model does not explicitly account for subassembly bowing or for subassembly clearance at the upper load pads. Since the coolant inlet temperature is constant during the transient, the reactivity feedback is determined solely by the temperature rise of duct walls and the structure in the upper load pad region. Axial fuel expansion reactivity differs somewhat between the fuels, where the coefficient of thermal expansion for the CerCer fuel is larger by a factor 1.6 in comparison with the CerMet and nitride. The smaller axial expansion reactivity coefficient for the CerMet fuel tends to reduce the reactivity effect associated with this feedback. As the coolant temperature increases it produces a positive reactivity effect. The resulting reactivity increment due to coolant expansion amounts to +0.5$ for the CerCer core and +0.4$ for the nitride. The coolant reactivity is however exceeded by the reactivity losses due to radial expansion and fuel elongation. The positive coolant expansion effect is largely compensated by the negative feedback from fuel elongation. The Doppler effect is insignificant.

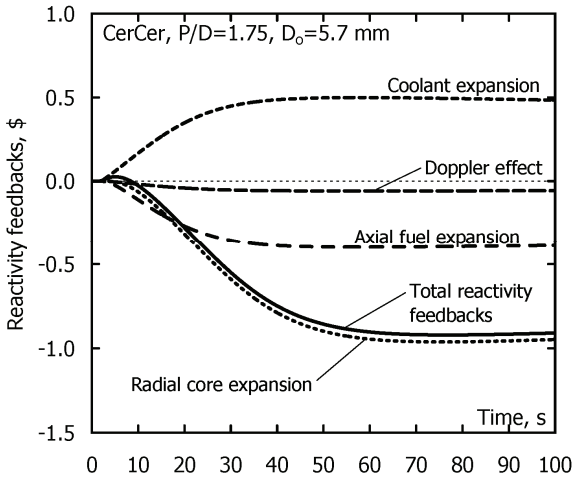

Fig. 4. Reactivity feedback contributions plotted for unprotected loss-of-flow transient.

The immediate effect of the flow reduction is a temperature rise in the coolant, and this in turn leads to higher cladding and fuel temperatures. Coolant boilout is not an issue with lead/bismuth. The major concern is whether the cladding exceeds design limits. Lower cladding temperatures are promoted by higher coolant volume fractions. Larger distance between the fuel pins reduces the core pressure drop and in turn increases contribution from natural circulation. As a result, less forced flow is lost in a pump failure event. Cladding temperature is highest for the CerMet and nitride cores because of their higher power rating. A comparison of cladding temperatures for these cores corresponding to P/D=1.50 and P/D=1.75 is shown in Fig. 5. The burst temperature for the cladding is 1330 K, as discussed previously. Thus, for the smaller pitch design, the cladding exceeds the failure point within 30-40 seconds after pump

failure, which leaves small safety margins. On the other hand, increasing the P/D ratio to 1.75 reduces cladding temperatures by more than 200 degrees. In that case, early cladding failure can be avoided. It is noted however, that a safe state cannot be assured indefinitely. The burst limit is applicable in transients in which the cladding is heated, without interruption, until failure. Thermal creep rates increase rapidly at high temperatures. Based on creep rupture data for D9 alloy [37], the lifetime at 1280 K is in the minute-scale. Thus, damage prevention will eventually require the need for shutdown and restored cooling capability.

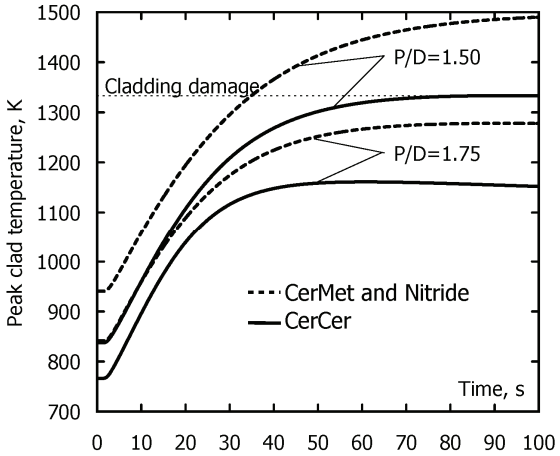

Fig. 5. Peak cladding temperatures for unprotected loss-of-flow transient. Effect of P/D is illustrated.

Maximum fuel and cladding temperatures as function of pitch-to-diameter ratio and pin diameter are presented in TABLE XV. Since the fuel temperature increases along with the coolant temperature, the potential for fuel damage must also be considered. The CerCer temperature reaches close to the damage limit for the cases of the smaller pins. Increasing the pin diameter should be considered in this case.

TABLE XV.
Peak fuel and cladding temperatures at a time t=100 seconds during unprotected loss-of-flow transient as function of P/D and pin diameter.

Fuel	P/D=1.50 D_o=5.7 mm		P/D=1.75 D_o=5.7 mm		P/D=1.50 D_o=6.8 mm	
	Fuel	Clad	Fuel	Clad	Fuel	Clad
CerCer	2160	1330	2130	1160	1970	1200
CerMet	2120	1490	2030	1280	1920	1340
Nitride	2080	1490	1980	1280	1920	1340

XI. BEAM OVERPOWER

In accelerator-driven system designs, fission reactions are maintained through multiplication of neutrons from a spallation neutron source, which is driven by a proton accelerator. In such systems, the neutron source is the controller of the chain reaction [55]. Thus, it is appropriate to consider transients in which the source intensity suddenly changes. This could for example happen due to a control system failure, accelerator malfunction, or operator error. In the study, it is assumed that the source intensity increases by a factor of 1.5 times the initial strength, which corresponds to the beam output capability at end-of-cycle. The ramp is initiated at t=1 second and halted at 1.001 seconds. The source is held constant thereafter. It is noted that the source strength in an ADS may change rapidly while transients in a traditional reactor are limited by mechanical speeds. Since the prompt adjustment time in an ADS is very short (tens of Λ), the power will instantaneously respond to any source variation, which permits accidents with very short initial ramp times in comparison with transients in critical reactors. No safety system can act instantaneously; there are always time delays involved. For a traditional safety rod based shutdown system, there is typically a 200 ms delay from detection to control rod motion [56], and then an insertion time of the order of a second. This is fast enough to detect all accident initiators identified for fast reactors [17], which always appear as gradual changes. A beam overpower accident, however, can produce a considerable power change before the malfunction has been detected. Hence, failure prevention should be precluded by the design, and not simply rely on proper control system action.

XI.A. Transient results

Power variation and fuel hot-channel temperatures are illustrated in Fig. 6. It shows the case with a pin diameter of D=6.8 mm. Beam overpower transients are characterized by higher fuel temperatures and the primary concern is fuel melting. As indicated in TABLE XVI, the configuration with the smaller P/D and smaller pin diameter is unacceptable for the CerCer fuel. The melting point is reached at 3 seconds after the beam insertion, which leaves little room for control action. Transient temperatures drop when a larger pin diameter is used because steady-state temperatures are lower with this configuration, for reasons discussed previously. It seems that the CerCer fuel needs to employ a larger pin diameter to avoid premature fuel failure. The temperature of the CerMet fuel reaches 2130 K for the same configuration, which corresponds to a margin to melting of 500 degrees. The nitride fuel, which has lower thermal conductivity than the CerMet fuel but smaller gap size, is slightly colder (2080 K) leaving a margin to dissociation of 320 degrees. As seen in TABLE XVI, the cladding remains well below the damage limit for all three fuel-systems and core configurations.

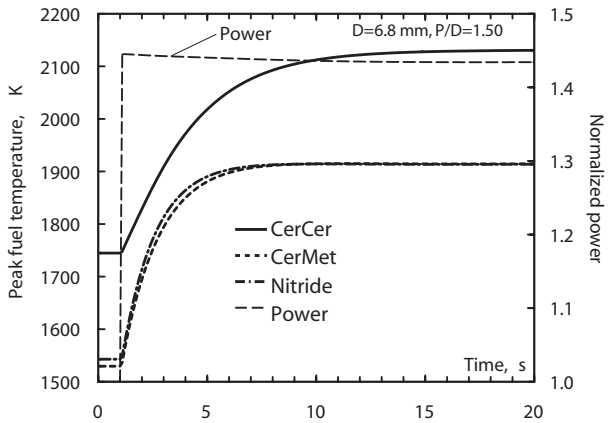

Fig. 6. Transient power and fuel temperatures for beam overpower transient.

TABLE XVI.
Peak fuel and cladding temperatures at a time t=20 seconds during beam overpower accident.

Fuel	P/D=1.50 D_o=5.7 mm		P/D=1.75 D_o=5.7 mm		P/D=1.50 D_o=6.8 mm	
	Fuel	Clad	Fuel	Clad	Fuel	Clad
CerCer	2290	950	2300	850	2130	860
CerMet	2130	1090	2130	950	1920	970
Nitride	2080	1090	2070	950	1910	970

XII. COOLANT VOIDING

The purpose is to investigate transient response associated with coolant voiding. Extensive voiding in a liquid-metal reactor (LMR) may, for example, be caused by a leak in the primary system, sudden release of fission gases, failure in the heat-transport system that causes gas bubbles to enter the coolant, or coolant overheating and vaporization. Usually, LMR plant designs are arranged with backup protection to mitigate the impact of vessel leakage or rupture, to the degree that large-scale loss-of-coolant accidents (LOCA) are extremely unlikely. Pool systems typically have a second guard vessel, and loop systems are normally double pipe and tank designs. Since the liquid-metal coolant is not pressurized under normal operation, a leak in the primary system will not automatically result in coolant boiling, as opposed to the situation in LWR's. In a sodium-cooled reactor, voiding may arise due to boiling out of coolant. This is prevented in a LBE system. In order for the LBE to get hot enough to boil (T_b=1940 K), temperatures have to be above the melting point of steel (T_m=1700 K). In that case, much larger reactivity changes may become available due to fuel or cladding relocation. Coolant can be expelled by the rapid escape of fission gases from ruptured fuel pins. Such an accident has been analyzed by Maschek in a previous study [57]. Fission gas release is of concern for unvented and high burnup ADS fuels. Significant amounts of helium are produced due to production of ^{242}Cm through neutron capture in ^{241}Am, and its subsequent alpha-decay into ^{238}Pu. Another possible mechanism for coolant voiding, without the precondition of steel melting, is the possibility of entrainment of air into the core from the cover gas region or steam/water during a failure in the steam generator, i.e., a so-called steam generator tube rupture (SGTR) event. In sodium plants, intermediate sodium-loops are introduced as a second physical barrier to minimize the consequences of SGTRs and to avoid violent chemical reactions between water and sodium in the primary system. Because lead/bismuth is chemically inert with water/steam, two-circuit designs are suggested, with the steam generators located in the primary system. In such designs, there will only be one barrier to fail in order to get high-pressure steam into the primary system. It is noted that the pressure on the steam side can be as high as 100-150 bars and low pressure on the metal side, about 1 bar. Thus, a significant head is available to push steam into the primary system or cause overpressurization in the circuit, which could open further leakage paths. Normally, steam generator tube failures have a high enough probability occurrence to be considered in the licensing procedure. It is noteworthy that a steam-generator failure was the cause of a LOCA and radioactive contamination in a Russian LBE-cooled nuclear submarine in 1982 [58].

XII.A. Modeling approach

The steam transfer in the circuit and the rate of coolant removal depends on the hydraulic design of the reactor and the size of leak (i.e. number of ruptured steam generator tubes). In this study, we have assumed that that the coolant is swept upwards through the core, beginning at the lower cold-leg region, and that the void front moves at the average coolant velocity through the core (2.5 m/s). Since the total height of the core plus plenum regions is 2.5 m, the passage occurs in 1 second. The transient calculation uses a reactivity history based on progressive axial voiding of the core. It is assumed that the void spreads axially and simultaneously in all subassemblies. The reactivity effect, as function of axial void level, is pre-calculated using the MCNP code. The results are illustrated in Fig. 7. Based on this information, a time pattern for the reactivity change is constructed, which is applied in the transient calculation. The configuration employing P/D=1.75 is investigated, which posses the largest positive void reactivity effect. Note that the reactivity effect is strongest for the CerCer fuel and most positive when the core has been voided up to slightly below the top of the active fuel region. The reactivity insertion rate is highest at core midlevel. As a coincidence, the maximum reactivity insertion due to coolant void corresponded to the initial subcritical reactivity of the CerCer core.

The model is intended for scoping evaluations on a shorter time scale. It is noted that the coolant could not be removed from the channel in a physical sense; only the associated reactivity effect is reproduced. As a result, the insulating effect of the gas is neglected. This will affect fuel pin temperatures. The cladding will be subject to the largest uncertainty since it has the shortest time response to changes in convective conditions. The effect on the fuel is expected to be limited during the time frame studied. Power estimates are not affected since all thermal feedback effects are small in comparison with the void reactivity.

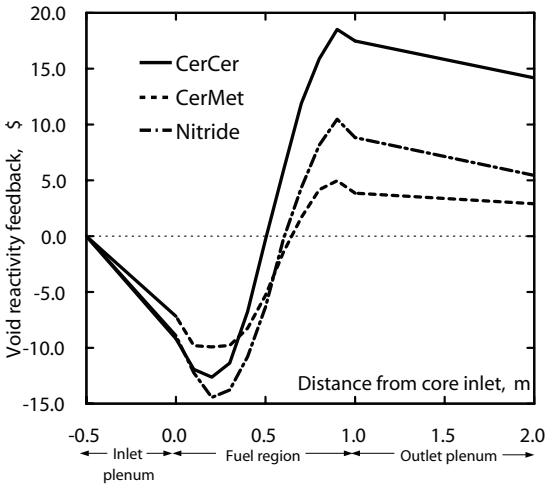

Fig. 7. Reactivity effect ($) following progressive axial voiding of coolant beginning at the lower plenum.

XII.B. Transient results

The resulting power history is presented in Fig. 8. It is assumed that the steam bubble reaches the lower plenum at 1 second after the steam generator failure. Initially, the bubble passage produces a negative reactivity effect due to increased neutron leakage, as the lower plenum is voided first. The power will find its peak as the reactivity reaches its maximum. The reactivity at peak power, is –0.2$, -12.3$, and –6.8$, respectively for the CerCer, CerMet, and nitride cores, the corresponding peak power is 15.3, 1.3, and 2.1, times the initial power. The power rise in the nitride and CerMet fueled cores is quite modest. The CerCer core, on the other hand, suffers from a sharp power peak. Except from coolant void, axial fuel expansion is the only feedback effect that has some impact on the transient. At peak conditions, the contribution from axial expansion provided an extra reactivity margin, which was sufficient to maintain the reactor in the subcritical state, thereby limiting the magnitude of the peak. Radial core expansion is too slow to be of any significance. It was found that the flux shape in the voided state was similar to the initial shape, and power peaking factors were even lower. The power rise is halted when the void has extended to the top of the core and begins to void the upper plenum region. Judging from Fig. 8, voiding of the upper plenum plays a vital role in reversing the accident. It is assumed that the beam is shutdown after 2 seconds. After shutdown, heat is generated by fissions produced by delayed neutrons plus the reactor decay heat. The delayed neutron source dies away in about 80 seconds (which is the mean life of the longest living precursor ^{87}Br).

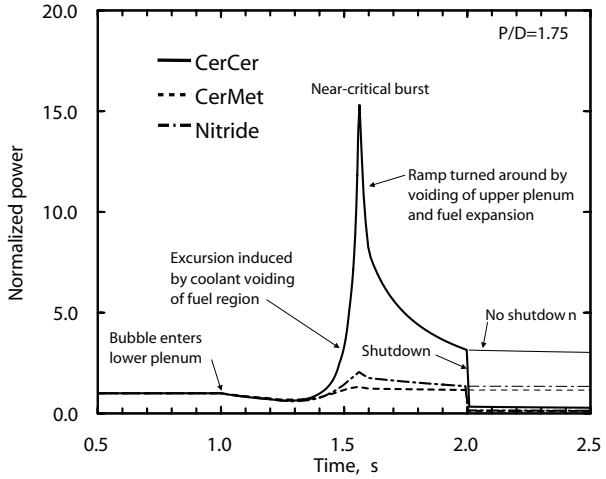

Fig. 8. Transient power for coolant voiding transient.

It is interesting to see that the power in the CerMet and nitride cases is only slightly affected, despite that the reactivity input is of the order of 5-10 dollars. This is a consequence of the fact that these two systems maintain a considerable margin to criticality during the entire transient. The power following a reactivity insertion in a subcritical reactor is inversely proportional to the reactivity in the perturbed state, which tends to zero as the reactor approaches the critical state. Thus, in the presence of an external source, the power approaches infinity as the reactor approaches critical conditions (a $1/\varrho$ approach). As a result, the majority of the power rise will occur near the critical state. The analysis shows that it can be extremely productive to adjust the initial multiplication constant even by a relatively small amount. For example, if the CerCer core would be designed with an initial k_{eff}=0.96 instead of k_{eff}=0.97, then the same voiding scenario (subject to an equivalent reactivity input) would cause a mild peak of approximately 3 times the initial value, instead of 15.

Fig. 9 illustrates the maximum fuel temperature during the accident. The temperature of the CerCer fuel rises considerably; reaching over 2500 K at the time when the reactor is shutdown (the thicker curve represents the temperature evolution after shutdown takes place). The temperature exceeds the assumed melting point of 2200 K at 1.6 seconds. Unless shutdown is initiated, fuel temperatures would continue to rise according to the thinner curve depicted in Fig 9. The temperature of the CerMet and nitride fuels is well below their failure limits. In these systems, the main effect of the coolant expulsion is the loss in heat removal capability on the surface, which presents greatest hazard to the cladding. The temperature rise in the CerCer fuel is overshadowed by the power rise caused by the positive void reactivity insertion. When the power falls during the shutdown phase, the temperature profile tends to level out across the fuel rod. Thus, fuel centerline temperatures decrease, according to Fig 9. Nevertheless, the average temperature of the core continues to rise even after the reactor has been shutdown since the core is deprived of cooling (assuming no coolant reentry). Beam shutdown alone does not prevent the reactor from reaching a failure point, as it would require restored cooling capability. Because of the limited power rise in the nitride and CerMet cores, it is predicted that cladding failure will occur prior to fuel failure.

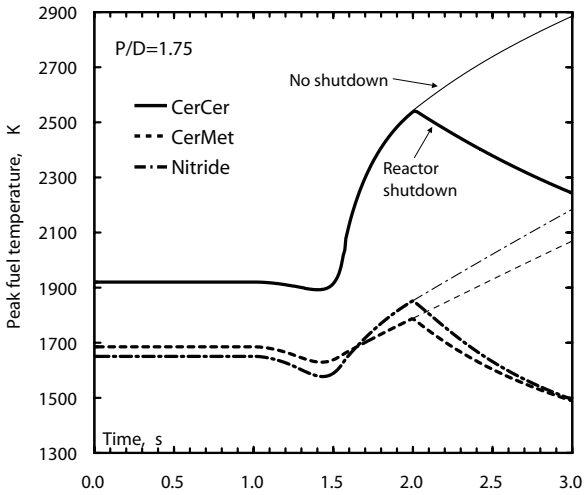

Fig. 9. Peak fuel temperatures for coolant voiding transient.

XIII. CONCLUSIONS

The objective was to study transient safety characteristics of lead-bismuth cooled accelerator-driven systems (ADS) with CerCer-, CerMet-, or nitride-fueled cores. Major consideration was given to the inherent safety aspects of core design. Analyses were carried out for the short-term transient response to unprotected loss-of-flow and accelerator beam-overpower accidents, and a coolant voiding scenario. The

effect of design changes involving variations in the lattice pitch and pin diameter was investigated. Design limits for the fuel and selected cladding materials were compiled. Fuel thermophysical properties were updated according to recently published review articles. Maximum temperatures were determined and compared with design limits. Reactivity effects associated with the relocation of core materials were investigated.

In summary, the better thermal conductivity, higher melting point, and lower coolant void worth of the CerMet fuel combine to contribute to better inherent safety features. In none of the studied transients was the CerMet fuel close to melting. The swelling behavior and hardness of the molybdenum metal raise safety concerns regarding fuel-cladding mechanical interactions. The approach so far has been to increase the initial fuel-cladding gap to accommodate fuel swelling. Although, the results indicate favorable safety performance of the CerMet fuel, many questions still need to be answered and irradiation performance remains to be demonstrated. The CerCer fuel suffers from low thermal conductivity and uncertain melting behavior, which limits both the achievable power density and predicted performance during overpower conditions. Even though the fuel is set to operate at a lower linear power, hot channel fuel temperatures are fairly high, leaving a limited margin to melting. This margin is easily exceeded in an overpower accident and the fuel reaches close to melting during unprotected loss-of-flow conditions. Further measures must be taken to lower the fuel temperature, e.g., increasing the coolant flow area. Increasing the pin diameter will enable lower operating temperature as it allows larger matrix fractions to be used. In addition, the reactivity void worth of this fuel is relatively high in comparison with the other fuels, which is a safety dilemma. It is noted that the specific power density has a critical impact on the achievable burnup level, recycling requirements, overall transmutation efficiency, etc., and, thus, has a strong influence on the economics of the entire fuel cycle. The lower power rating capability of the CerCer fuel leads to obvious performance penalties. The principal problem with the nitride fuel, with regards to the safety performance, is its tendency to dissociate at low temperatures. However, recent studies have shown that decomposition could be suppressed in a nitrogen atmosphere. Whether this is an effective solution under accident conditions, is subject to further investigation. Efforts to increase the understanding of nitride dissociation phenomena are underway. The cladding reactivity worth was essentially the same for all fuels and comparable to the maximum void reactivity available. The study showed that the fuels posses smaller critical masses in comparison with classical fast reactor fuel, but significant variations were observed. The studies point to a particular small critical mass for the low absorbing nitride fuel, about 70 kg, which corresponds to the fuel inventory contained in three individual subassemblies. The critical mass is much larger for the oxide fuel versions, by a factor of ~5. The higher melting point of the CerMet fuel in combination with its larger critical mass is favorable characteristics from the recriticality point of view.

Standard type 316 stainless steel is excluded as potential cladding material because of unacceptable radiation swelling. HT-9 cladding, which has excellent irradiation performance, is rejected because of unsatisfactory high-temperature mechanical performance. At this point, type 15-15Ti austenitic stainless steel is the suggested cladding material. While previous studies indicate high reliability for this material, experimental confirmation of corrosion stability and transient mechanical performance is necessary. For a lead/bismuth-cooled reactor, cladding corrosion leading to wall thinning is a major life-limiting factor. The corrosion rate is strongly dependent on temperature. Cladding temperatures during normal operation are essentially determined by the coolant outlet temperature, which is given by the linear power and the coolant mass flow rate. For a given geometrical arrangement, the coolant mass flow rate is the same for all three fuels; only the linear power rating varies. It was found that the higher rated CerMet and nitride fuels required a higher coolant mass flow rate in order to achieve acceptable cladding temperatures for normal operation. This suggests the use of a higher pin pitch. A higher lattice pitch is also necessary to avoid mechanical failure during unprotected loss-of-flow.

Finally, a steam generator tube rupture event was identified as a potential threat, which could lead to extensive voiding in current accelerator-driven design proposals. A preliminary transient test case study was performed. Due to the strong positive reactivity effect, the CerCer system was subject to a sharp power peak, while the power rise in the nitride and CerMet fueled cores was quite modest, which simply confirms the importance of a having a low coolant void reactivity value in a lead/bismuth system, despite of its high boiling temperatures.

REFERENCES

1. D. G. FOSTER, et al., "Review of PNL Study on Transmutation Processing of High Level Waste," LA-UR-74-74, Los Alamos Scientific Laboratory (1974).

2. T. TAKIZUKA, et al., Proc. 5th Int. Conf. Emerging Nuclear Energy Systems 1989, ICENES '89, Karlsruhe, July 3-6 (1989).

3. J. WALLENIUS, "Neutronic aspects of inert matrix fuels for application in ADS," J. Nucl. Mater. **320** (2003) 142-146.

4. M. ERIKSSON, J. WALLENIUS, J. E. CAHALAN, K. TUCEK, and W. GUDOWSKI, "Safety analysis of Na and Pb-Bi coolants in response to beam instabilities," Proc. 3rd International Workshop on Utilisation and Reliability of High Power Proton Accelerators, Santa Fe, May 12-16, NEA/OECD (2002).

5. J. WALLENIUS, "CONFIRM: Collaboration on Nitride Fuel Irradiation and Modelling," Proc. of the AccApp/ADTTA 2001 Meeting, Reno, November 11-15, American Nuclear Society (2001).

6. S. PILLION and J. WALLENIUS, "Oxide and nitride TRU-fuels: lessons drawn from the CONFIRM and FUTURE projects of the 5th European framework

programme," Nucl. Sci. Eng., Accepted for publication (2004).

7. J. WALLENIUS and M. ERIKSSON, "Neutronic design of minor actinide burning accelerator driven systems," Nucl. Technol., Submitted (2004).

8. "Safety related terms for advanced nuclear plants," IAEA-TECDOC-626, September (1991).

9. H. MURATA and T. MUKAIYAMA, "Fission reactor studies in view of reactor waste programmes," Atomkernenergie – Kerntechnik, **45** (1984) 23-29.

10. H. KLEYKAMP, "Selection of materials as diluents for burning of plutonium fuels in nuclear reactors," J. Nucl. Mater. **275** (1999) 1-11.

11. M. BURGHARTZ, G. LEDERGERBER, H. HEIN, R. R. VAN DER LAAN, and R. J. M. KONINGS, "Some aspects of the use of ZrN as an inert matrix for actinide fuels," J. Nucl. Mater. **288** (2001) 233-236.

12. K. MINATO, M. AKABORI, M. TAKANO, Y. ARAI, K. NAKAJIMA, A. ITOH, and T. OGAWA, "Fabrication of nitride fuels for transmutation of minor actinides," J. Nucl. Mater. **320** (2003) 18-24.

13. M. TAKANO, "Study on The Stability of AmN and (Am,Zr)N," Proc. GLOBAL 2003, New Orleans, Louisiana, November 16-20 (2003).

14. J. WALLENIUS and S. PILLON, "N-15 Requirement for 2nd Stratum ADS Nitride Fuels," Proc. of the AccApp/ADTTA 2001 Meeting, Reno, November 11-15, American Nuclear Society (2001).

15. M. A. MIGNANELLI and R. THETFORD in Proc. on Advanced Reactors with Innovative Fuels, ARWIF-2001, Chester, October 22-24 (2001).

16. R. THETFORD and M. MIGNANELLI, "The chemistry and physics of modeling nitride fuels for transmutation," J. Nucl. Mater. **320** (2003) 44-53.

17. A. E. WALTAR and A. B. REYNOLDS, Fast Breeder Reactors, p. 260 and 540, Pergamon Press, New York (1981).

18. D. R. OLANDER, Fundamental Aspects of Nuclear Reactor Elements, p. 131-135, Published by Technical Information Center, Office of Public Affairs, Energy Research and Development Administration, Springfield, VA (1976).

19. Ph. DEHAUDT, A. MOCELLIN, G. EMINET, L. CAILLOT, G. DELETTE, M. BAUER, and I. VIALLARD, "Composite Fuel Behaviour Under and After Irradiation," IAEA Technical Committee Meeting on Research of Fuel Aimed at Low Fission Gas Release, Moscow, October 1-4 (1996).

20. J. L. SÉRAN, V. LÉVY, P. DUBUISSON, D. GILBON, A. MAILLARD, A. FISSOLO, H. TOURON, R. CAUVIN, A. CHALONY, and A. LE BOULBIN, "Behavior under Neutron irradiation of the 15-15Ti and EM10 Steels Used as Standard Materials of the Phénix Fuel Subassembly," Effects of Radiation on Materials: 15th Int. Symposium, ASTM STP 1125, R. E. Stoller, A. S. Kumar, and D. S. Gelles, Eds., American Society for Testing and Materials, p. 1209-1233, Philadelphia (1992).

21. A. FISSOLO, V. LÈVY, J. L. SÈRAN, A. MAILLARD, J. ROYER, and O. ARBOUILLE, "Tensile Properties of Neutron Irradiated 316Ti and 15-15Ti Steels," Effects of Radiation on Materials: 16th Int. Symposium, ASTM STP 1175, A. S. Kumar, D. S. Gelles, R. K. Nanstad, and E. A. Little, Eds., American Society for Testing and Materials, p. 646-663, Philadelphia (1993).

22. E. H. P. CORDFUNKE and R. J. M. KONINGS, Thermochemical Data for Reactor Materials and Fission Products, North-Holland, Amsterdam (1990).

23. J. J. KATZ, G. T. SEOBORG, and L. R. MOSS, The chemistry of the actinide elements, 2nd ed., Vols. 1 and 2, Chapman and Hall, London (1986).

24. J. EDWARDS, et al., "Fast Reactor Manual," Fast Reactor European Collaboration report (1990).

25. R. KONINGS, Personal Communication (January, 2004).

26. S. CASALTA, HJ. MATZKE, and C. PRUNIER, Proc. Int. Conf. On Evaluation of Emerging Nuclear Fuel Cycle Systems, GLOBAL'95, Versailles, September 11-14, p. **1725** (1995).

27. H. ZHANG, R. J. M. KONINGS, M. E. HUNTELAAR, and E. H. P. CORDFUNKE, "Melting behaviour of oxide systems for heterogeneous transmutation of actinides. III. The system Am-Mg-O," J. Nucl. Mater. **250** (1997) 88-95.

28. H. ZHANG, R. J. M. KONINGS, M. E. HUNTELAAR, and E. H. P. CORDFUNKE, "Melting behaviour of oxide systems for heterogeneous transmutation of actinides. I. The systems Pu-Al-O and Pu-Mg-O," J. Nucl. Mater. **249** (1997) 223-230.

29. M. TAKANO, A. ITOH, M. AKABORI, et al., "Synthesis of americium mononitride by carbothermic reduction method," Proc. Int. Conf. On Future Nuclear Energy Systems, GLOBAL'99, Jackson Hole, Wyoming, Aug. 29 – Sep. 33, p. 110, American Nuclear Society (1999).

30. M. JOLKKONEN, M. STREIT, and J. WALLENIUS, "Thermo-chemical modelling of uranium-free nitride fuels," J. Nucl. Sci. Technol. **41**(4), 457 (2004).

31. J.-O. ANDERSSON, et al., "Thermo-Calc and DICTRA, computational tools for materials science," Calphad **26**, 273 (2002).

32. T. OGAWA, T. OHMICHI, A. MAEDA, et al., "Vaporization behaviour of (Pu,Am)N," J. Alloys and Compounds, **224**, 55 (1995).

33. N. S. CANNON, F. R. HUANG, and M. L. HAMILTON, "Transient and Static Mechanical Properties of D9 Fuel Pin Cladding and Duct Material Irradiated to High Fluence," Effects of Radiation on Materials: 15th Int.

APPENDIX 13

K.Tuček J. Wallenius, W. Gudowski Coolant void worth in fast breeder reactors and accelerator-driven transuranium and minor-actinide burners, Annals of Nuclear Energy 31 (2004) 1783–1801

Available online at www.sciencedirect.com
SCIENCE DIRECT®
Annals of Nuclear Energy 31 (2004) 1783–1801
annals of NUCLEAR ENERGY
www.elsevier.com/locate/anucene

Technical note

Coolant void worth in fast breeder reactors and accelerator-driven transuranium and minor-actinide burners

K. Tuček *, J. Wallenius, W. Gudowski

Department of Nuclear and Reactor Physics, Royal Institute of Technology, SE-106 91 Stockholm, Sweden

Received 24 December 2003; accepted 8 May 2004
Available online 26 June 2004

Abstract

Liquid metal coolant void worth have been calculated as a function of fuel composition and core geometry for several model fast breeder reactors and accelerator-driven systems (ADSs). The Monte Carlo transport code MCNP with continuous energy cross-section libraries was used for this study. With respect to the core void worth, lead/bismuth cooled FBRs appear to be inferior to those employing sodium for pitch-to-diameter ratios exceeding 1.4. It is shown that in reactor systems cooled by lead/bismuth eutectic radial steel pin reflector significantly lowers the void worth. The void worth proves to be a strong function of the fuel composition, reactor cores with high content of minor actinides in fuel exhibiting larger void reactivities than systems with plutonium based fuel. Enlarging the lattice pitch in ADS burners operating on Pu rich fuel decreases the void worth while the opposite fact is true for ADSs employing americium based fuels.

1. Introduction

A number of innovative reactor systems for transmutation of plutonium and minor actinides were proposed in last decades (Takizuka et al., 1991; Conti et al., 1995). Fuels utilised in these reactors have low uranium content or are completely U-free, and the

* Corresponding author. Tel.: +46-8-5537-8197; fax: +46-8-5537-8465.
E-mail address: kamil@neutron.kth.se (K. Tuček).

0306-4549/$ - see front matter © 2004 Elsevier Ltd. All rights reserved.
doi:10.1016/j.anucene.2004.05.005

systems are usually conceived to operate on fast neutron spectrum. The presence of americium leads to a decrease in Doppler reactivity coefficient and delayed neutron fractions, raising significant safety concerns (Wallenius and Eriksson, submitted). It was therefore suggested that sub-critical reactor systems should be implemented in fuel cycles involving recycling of minor actinides. For this purpose, accelerator-spallation (Foster et al., 1974; Murata and Mukaiyama, 1984) and deuterium–tritium fusion neutron sources (Rose et al., 1977; Cheng et al., 1995; Stacey et al., 2002) were both envisioned. Additional reactivity margin is hence provided in sub-critical systems, limiting the influence of reactivity coefficients and allowing steady-state operation of the system. However, it has appeared that such MA-fuelled ADS have a potential for rapid reactivity excursions following loss of coolant from the core, which may lead to fuel failure and core disruption (Maschek et al., 2000; Eriksson et al., 2002).

Therefore, it is necessary to provide a fuel and core design that minimises conceivable reactivity insertions in the standard set of design basis accidents. In this parametric study, we investigate coolant void worth for series of fast breeder and accelerator-driven system (ADS) configurations with aim to identify suitable core and fuel design parameters.

First, we discuss physical mechanisms involved in coolant voiding. Then, we perform scoping studies of Δk_∞ in two-dimensional pin lattices for several fuel compositions and wide range of pitches. Finally, we investigate the coolant void worth in various types of model critical and ADS transmutation systems, employing nitride and oxide fuel, different types of inert matrices and two types of coolants – lead/bismuth and sodium. Void reactivity is studied as a function of core geometry parameters as e.g. reactor lattice pin pitch and fuel pin design. The optimal pin pitch is then identified for each configuration. Finally, we discuss the implications of our results for ADS core design in general.

2. Voiding mechanism

The occurrence of void in the core can be a result of following events:

- fuel pin rupture, releasing fission gases and helium into the core,
- blow-down of steam from ruptured steam generator,
- coolant boiling,
- blow-down of bubbles from gas injection system (Cinotti and Gherardi, 2002).

We note, that in sodium cooled systems undercooling can result in coolant boiling prior any significant damage to the fuel, clad, or structural material is inflicted. On the other hand, due to the high boiling temperatures of lead and lead/bismuth (Pb: $T_b = 2023$ K; Pb/Bi: $T_b = 1943$ K), coolant boiling in these systems occurs first *after* the integrity of reactor core is lost, rendering such events to the realm of beyond-design basis accident analyses.

The void worth and void reactivity coefficient are the major safety parameters, determining permissive maximum criticality level of the system (k_{eff}).

2.1. Phenomena occurring during the voiding

The physical effects associated with coolant voiding are

- reduction of neutron moderation (spectral hardening), increasing fission probabilities of even neutron number actinides,
- reduction of neutron capture in fuel, coolant, and cladding.

The coolant void worth is the difference in the k-eigenvalue between the flooded and voided state

$$W = \Delta k_{\text{eff}} = k_{\text{eff}}^{\text{void}} - k_{\text{eff}}^{\text{flood}} \tag{1}$$

$$= \overline{\nu}_{\text{void}} L_{\text{f}}^{\text{void}} - \overline{\nu}_{\text{flood}} L_{\text{f}}^{\text{flood}}. \tag{2}$$

where L_{f} is neutron loss to fission in one neutron generation for respective core state – flooded or voided.

In fast neutron systems, the average fission neutron yield can be considered as constant ($\overline{\nu} \equiv \overline{\nu}_{\text{flood}} \simeq \overline{\nu}_{\text{void}}$). Then,

$$W = \overline{\nu}(L_{\text{f}}^{\text{void}} - L_{\text{f}}^{\text{flood}}), \tag{3}$$

from which follows that $W = \overline{\nu}\Delta L_{\text{f}}$.

The neutron balance equation for *one neutron fission generation* in an eigen-state can be written as

$$1 + C_{\text{x}} = L_{\text{c}} + L_{\text{e}} + L_{\text{f}} + L_{\text{x}}, \tag{4}$$

where L_{x} denotes the neutron loss rate in non-fission multiplication reactions, $C_{\text{x}} = \overline{\nu_{\text{x}}} L_{\text{x}}$ is the neutron creation rate in non-fission multiplication reactions, $\overline{\nu_{\text{x}}}$ is the average neutron yield in non-fission multiplication reactions ($\overline{\nu_{\text{x}}} \simeq 2$), L_{e} denotes the loss rate to leakage, L_{c} the loss rate to capture reactions, and L_{f} is the loss rate to fission.

Upon coolant voiding, $\Delta C_{\text{x}} \leqslant 10^{-3}$ in most of the cases yielding $\Delta L_{\text{f}} + \Delta L_{\text{c}} + \Delta L_{\text{e}} \sim 0$. In the infinite pin lattice 2-D model ($L_{\text{e}} = 0$), the coolant void worth can be subsequently decomposed as

$$W = \overline{\nu} \cdot \Delta L_{\text{f}} = -\overline{\nu}(\Delta L_{\text{c,fuel}} + \Delta L_{\text{c,coolant}} + \Delta L_{\text{c,clad}}). \tag{5}$$

where $L_{\text{c,fuel}}$, $L_{\text{c,coolant}}$, and $L_{\text{c,clad}}$ is neutron capture rates to fuel, coolant, and cladding, respectively.

In realistic three dimensional core configurations, the void worth is given by

$$W = -\overline{\nu}(\Delta L_{\text{c,fuel}} + \Delta L_{\text{c,coolant}} + \Delta L_{\text{c,clad}} + \Delta L_{\text{e}} - \Delta G_{\text{x}}), \tag{6}$$

where L_{e} quantifies a rate of neutron leakage from the system, and $G_{\text{x}} = C_{\text{x}} - L_{\text{x}}$ is the neutron gain from non-fission multiplication reactions. The neutron balance equation is evaluated for the whole geometry inclusive reflectors and plena.

2.2. Cross-sections

In order to apprehend the nature of neutron slowing-down process in coolant due to the elastic and inelastic scattering, we define the energy-loss cross-section as

$$\overline{\Sigma_{\Delta E}} \equiv \frac{\Sigma_{\mathrm{el}}\overline{\Delta E_{\mathrm{el}}} + \Sigma_{\mathrm{inel}}\overline{\Delta E_{\mathrm{inel}}}}{E}, \tag{7}$$

where

$$\overline{\Delta E_{\mathrm{el}}} = \frac{1}{2}(1-\alpha)E_{\mathrm{n}}, \quad \alpha = \left(\frac{A-1}{A+1}\right)^2 \tag{8}$$

and

$$\overline{\Delta E_{\mathrm{inel}}} = E_{\mathrm{n}} - \left(\frac{A}{A+1}\right)^2\left[E_{\mathrm{n}} - Q\frac{A+1}{A}\right] \tag{9}$$

is the average energy loss in elastic scattering and inelastic scattering, respectively; Q denotes the excited energy levels of the target nuclei, E_{n} is the neutron energy, and A is the target nucleus mass number.

The energy-loss cross-section for sodium decomposed into the contributions from elastic and inelastic scattering is displayed in Fig. 1. We observe that for the energy region below 500 keV, neutron slowing down is dominated by elastic collisions, while in-between 0.7 and 2 MeV inelastic scattering becomes about equally effective.

In Fig. 2, the same comparison is made for natural lead. We note that energy-loss cross-section due to the elastic scattering is significantly smaller than for sodium in whole energy range investigated. However, due to the presence of several thresholds for inelastic scattering in the energy interval from 0.57 to 2 MeV, the energy loss in inelastic scattering is notably larger than for sodium. The neutron spectrum of lead and lead/bismuth cooled reactors will be thus somewhat suppressed for energies above 1 MeV comparing with Na-cooled systems having the same geometry, see Fig. 3. For sodium, the magnitude of neutron spectrum relative to lead/bismuth is

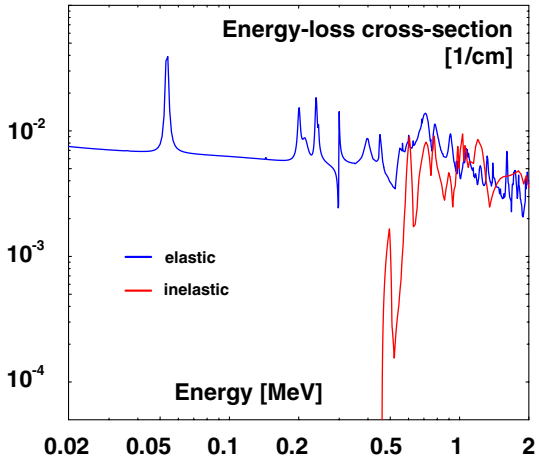

Fig. 1. Energy-loss cross-section for ^{23}Na. Data from JEF2.2 library were used. Macroscopic scattering cross-sections were taken at $T = 600$ K.

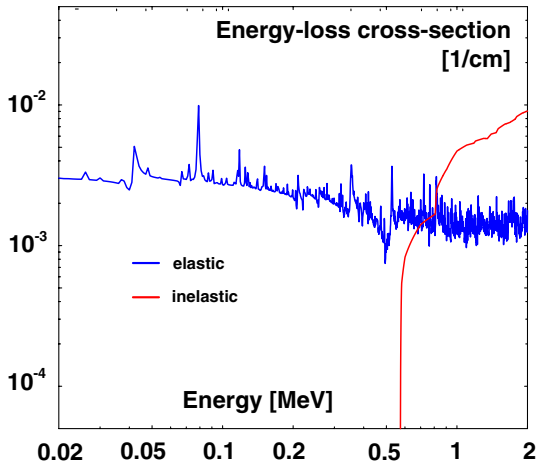

Fig. 2. Energy-loss cross-section for natural lead. Cross-section data were taken from ENDFB/VI-8 cross-section library. Σ_{el} and Σ_{inel} at $T = 600$ K were used.

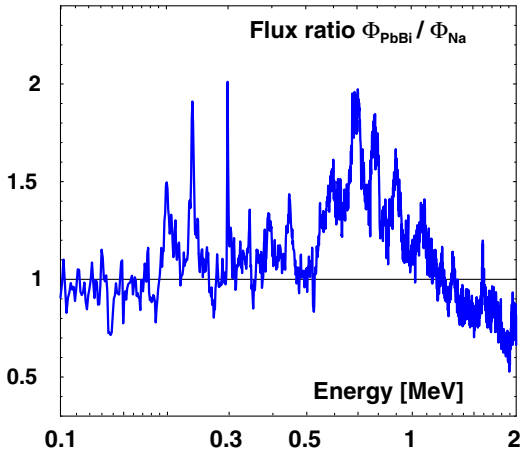

Fig. 3. The neutron spectrum of lead–bismuth cooled system relative to that cooled by sodium with the same geometry and fuel composition.

suppressed in the energy region of 0.7–1.5 MeV where contributions to the neutron slowing down from elastic and inelastic scattering reactions merely equal.

We further note that within the range of energies considered the ^{206}Pb features a number of threshold levels, while the threshold for inelastic scattering of the doubly magic isotope ^{208}Pb is well above 2 MeV, see Table 1.

One could therefore theoretically consider to enrich lead in ^{208}Pb. With energy-loss cross-section remaining below 0.003 cm^{-1}, a very hard neutron spectrum can be attained. As also the capture cross-section of ^{208}Pb is low in comparison to other

Table 1
Threshold energies for inelastic scattering of heavy metal coolants used in the study

Nuclide	Abundance	Threshold energies (keV)		
		1st	2nd	3rd
^{23}Na	100%	459.1	2166	2495
^{206}Pb	24.1%	806.9	1171	1347
^{207}Pb	22.1%	572.5	902.1	1641
^{208}Pb	52.4%	2628	3213	3492
^{209}Bi	100%	900.6	1617	2455

^{206}Pb has further five excited energy levels yielding threshold energies below or close to 2 MeV limit: 1474, 1692, 1713, 1793, and 2008 keV.

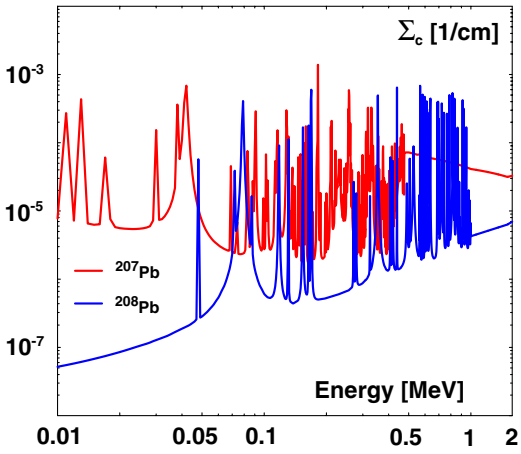

Fig. 4. Macroscopic capture cross-section of ^{207}Pb and ^{208}Pb. ENDFB/VI-8 cross-section library data were used.

isotopes, see Fig. 4, such a coolant would yield a very small void worth (Shmelev et al., 1992).

2.3. Calculation methodology

Our study of void reactivity is performed as a function of core geometry: reactor lattice pin pitch and fuel pin design parameters. Two types of fuel actinide isotopic compositions have been studied: corresponding to an immediate (four years of cooling), and somewhat delayed (30 years of cooling) use of spent LWR UOX fuel. The plutonium and americium vectors applied in our studies are presented in Table 2.

The void worth is typically a relatively small difference between two large terms, critically depending on a correct description of geometry as well as transport slowing-down and capture cross-sections properly adjusted for change in self-shielding. Hence, we used the Monte Carlo code MCNP, version 4C3 (Briesmeister,

Table 2
Pu and Am vectors used in the investigations

Isotope	Cooling time	
	4 years	30 years
^{238}Pu	0.024	0.020
^{239}Pu	0.520	0.521
^{240}Pu	0.226	0.229
^{241}Pu	0.119	0.035
^{242}Pu	0.065	0.064
^{241}Am	0.030	0.114
^{243}Am	0.016	0.017

The compositions correspond to those found in spent LWR UOX fuel with an averaged burnup of 41.2 GWd/tHM; fuel cooling time is 4 and 30 years, respectively.

2000), for the present study. The estimation of neutron creation and loss rates is performed exclusively in the eigen-state as modelled by MCNP KCODE mode. A temperature adjusted version of the JEF2.2 cross-section library is applied.

We start by evaluating the void worth in an infinite triangular fuel pin lattice for three heavy metal coolant candidates – sodium, lead, and lead/bismuth eutectic. Fuels with different fractions of plutonium and minor actinide, relevant for use in ADSs, are analysed. The impact of fast fission threshold for even neutron number nuclides is thus assessed.

In the 3-D reactor model, we further evaluate the effect of neutron leakage from the core on the void worth. The reactor core, axial plena, and bottom plenum spacer regions are modelled pin-by-pin, while materials were smeared in axial and radial reflectors, as well as in ADS target region. For simplicity, a ductless fuel assembly design is assumed. The target region consists of Pb/Bi eutectic, steel structures contain 90 at% iron and 10 at% chromium. For individual components of the het-

Table 3
Reference system, pin, and pellet design specifications

Pellet density (% TD)	0.85
Pellet outer radius R_{fuel} (mm)	2.4
Clad inner radius R_{gap} (mm)	2.5
Clad outer radius R_{pin} (mm)	3.0
Active pin length (cm)	100
Length of upper fission gas plenum (cm)	150
Length of lower fission gas plenum (cm)	10
Length of bottom plenum spacer (cm)	10
Length of radial reflector S/As (cm)	140
Thickness of radial reflector (cm)	150
Length of upper reflector (cm)	200
Length of lower reflector (cm)	230
ADS target radius (cm)	20
Radius of accelerator beam tube (cm)	15
Distance of target window from centreplane (cm)	20

A triangular pin lattice is adopted.

erogeneous design, average stead-state temperatures are assumed: 1500 K for fuel, 900 K for pin clad in the core, and 600 K for coolant and steel structures of plena, spacer, target, and reflectors.

The model parameters as used in the calculations are summarised in Table 3. The total core power was set to 800 MW_{th}. The assumed linear power of 30 kW/m then corresponds to cores with ~26,700 fuel pins.

A homogeneous, single zone core configuration is assumed in all cases. In this context, we note that core heterogeneity significantly alters the coolant void reactivity (Khalil and Hill, 1991). The results of this study should be thus considered rather as qualitative, in terms of a relative intercomparison of the void worths in-between different design options.

3. Results

Three types of fuel are used for our analyses: standard FBR fuel $(U,Pu)O_2$, a plutoniurn based – TRU mononitride fuel (TRU,Zr)N, and minor actinide based fuel (MA,Zr)N, relevant for ADS minor actinide burners operating in double-strata incineration scheme. An inert matrix has to be added to the fuel in order to compensate for high fuel reactivity and achieve a reasonably good stability at high temperature. In our studies we have chosen ZrN as a representative inert matrix material. In order to reduce production of ^{14}C, the use of nitride fuel with 99% ^{15}N enrichment is foreseen.

3.1. Elementary cell analysis

The void worth was analysed in an infinite pin lattice geometry, examining changes in neutron capture upon coolant voiding. The relative fractions of metals in the fuel is given in Table 4. In Fig. 5, the void worth for three types of fuel is displayed as a function of pitch-to-diameter ratio. We note that, as expected, the void worth increases with increasing fraction of higher actinides in the fuel; the difference being most significant for high pin pitches. Results of pin lattice sodium void worth decomposed into individual components are displayed in Table 5. The values given in the table corresponds to $P/D = 2.0$, in order to emphasise any effect of reduced capture in the coolant, should it be significant.

Table 4
Atomic fractions of metallic elements in fuels investigated in the elementary cell analyses

Element	$(U,Pu)O_2$	(TRU,Zr)N	(MA,Zr)N
U	0.750	–	–
Pu	0.250	0.165	0.133
Am	–	0.035	0.267
Zr	–	0.800	0.600

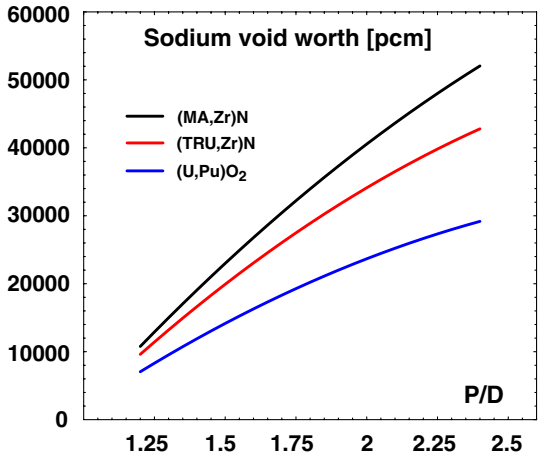

Fig. 5. Sodium void worth in an infinite pin lattice with a pin diameter of 6 mm.

Table 5
Infinite pin lattice void worth analyses

Fuel	ΔL_f	$\Delta L_{c,fuel}$	$\Delta L_{c,cool}$	$\Delta L_{c,clad}$	$-\Delta L_{c,fuel}/\Delta L_f$	$\left(\frac{\sigma_f}{\sigma_a}\right)_{voided}/\left(\frac{\sigma_f}{\sigma_a}\right)_{flooded}$
$(U,Pu)O_2$	+0.078	−0.059	−0.012	−0.007	0.76	1.20
(TRU,Zr)N	+0.108	−0.090	−0.011	−0.007	0.83	1.22
(MA,Zr)N	+0.119	−0.111	−0.005	−0.003	0.93	1.33

Sodium void worth was decomposed into the individual constituents. Pitch-to-diameter ratio is 2.0. The neutron loss rates are normalised per one fission neutron generation.

We observe that the main contribution to the void worth is a reduction in fuel capture rate, with concurrent increase of fission probability of even neutron number actinides, see Fig. 6. While capture reduction in the fuel provides about 76% of the void worth in (TRU, Zr)N fuel, it is more then 93% for the fuel containing 60% of minor actinides. We further note that the spectral gradient accompanying removal of the coolant from a lattice is strongest for (MA,Zr)N fuel. The capture rate in the cladding is less significant and constitutes less than 10% of the void worth.

In Table 6, we illustrate the effect of increasing the pin pitch on the void worth. Comparing with Table 5, one may note that the contribution of the coolant capture reduction to the void worth is significantly higher for Pb/Bi than for sodium, for same P/D. With increasing P/D ratio, understandably, the relative contribution of coolant capture rate reduction to the void worth increases. Even for P/D = 1.2, 41% of the LBE void worth constitutes of $\Delta L_{c,cool}$.

The void worth of lead is very similar to that of lead/bismuth for the whole range of pitches investigated, see Fig. 7. Both heavy metals – lead and lead/bismuth – feature very similar neutronic characteristics and we therefore further focus in our studies only on systems cooled by sodium and lead/bismuth eutectic.

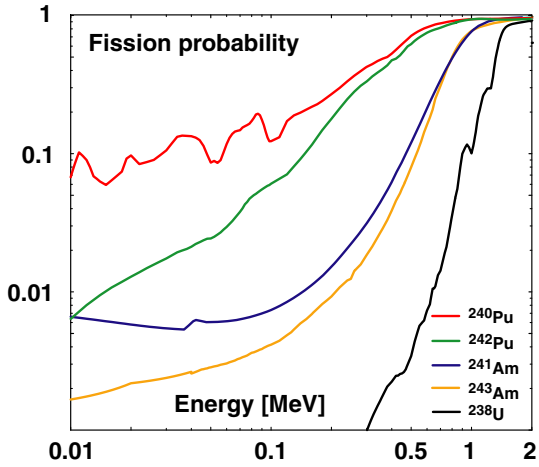

Fig. 6. Fission probability σ_f/σ_a of even neutron number actinides.

Table 6
Void worth analyses in an infinite pin lattice employing lead/bismuth coolant, and (TRU,Zr)N fuel; Pu/Am fraction was kept at 4/1

P/D	ΔL_f	$\Delta L_{c,fuel}$	$\Delta L_{c,cool}$	$\Delta L_{c,clad}$	$-\Delta L_{c,fuel}/\Delta L_f$	$-\Delta L_{c,cool}/\Delta L_f$
1.2	+0.022	−0.012	−0.009	−0.001	0.55	0.41
1.6	+0.057	−0.027	−0.028	−0.002	0.47	0.49
2.0	+0.090	−0.039	−0.048	−0.003	0.43	0.53
2.4	+0.121	−0.047	−0.070	−0.004	0.39	0.59

The neutron loss rates are normalised per one fission neutron generation.

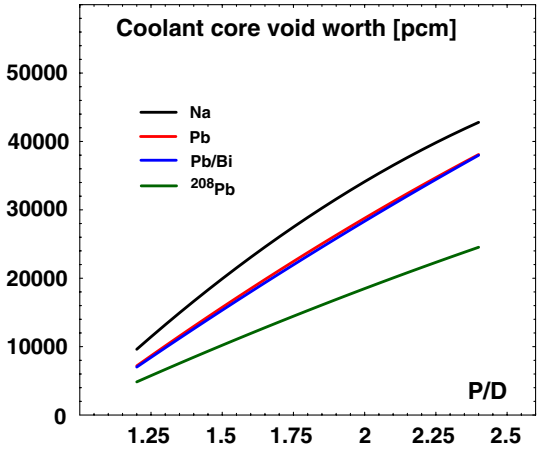

Fig. 7. Void worth in an infinite pin lattice of a system employing (TRU,Zr)N fuel. Four types of coolant were investigated – sodium, lead/bismuth, lead, and ^{208}Pb. ENDFB/VI-8 cross-section library data were used for ^{208}Pb.

Due to its low moderating power, lead enriched in double-magic isotope ^{208}Pb displays very low void worths. We note, however, that lead enrichment process is not realistically feasible.

3.2. Critical 3-D systems

The importance of enhanced leakage becomes apparent when observing the void worth in realistic system configurations, see Fig. 8. In Table 7 and Fig. 9, we display the coolant void worth as a function of pitch-to-diameter ratio for a model critical fast reactor employing $(U,Pu)O_2$ fuel cooled by sodium and lead/bismuth. In the case of the Pb/Bi-cooled core, we investigate two different radial reflector configurations

(a) similar to the one used for sodium cooled system, i.e. consisting of steel pins, immersed in the coolant; coolant volume ratio being 20 vol%,
(b) with the whole radial reflector region filled by lead/bismuth eutectic only. Such radial reflector configurations have been proposed in a number of studies (Rubbia et al., 1997).

In contrast to the standard notion of the leakage term (Waltar and Reynolds, 1981), L_e in our case denotes those neutrons leaking out of the *whole reactor system* to the surrounding shielding. We note that the probability of these neutrons to enter the core and induce fission is rather remote and these neutrons can be effectively perceived as captured in clad and capture material of reflector. The reason why we list the leakage component separately in our study is thus merely phenomenological.

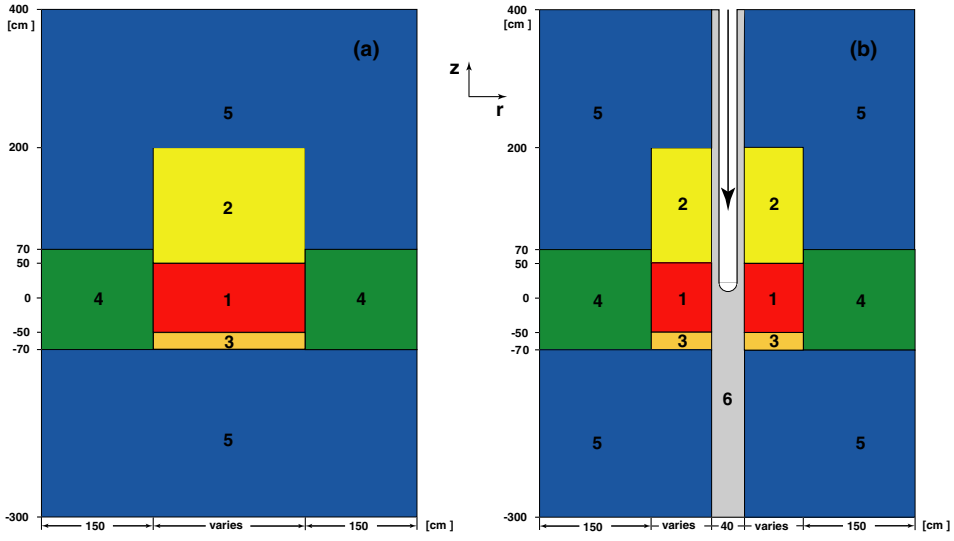

Fig. 8. *R–z* view of critical (a) and sub-critical (b) reactor model configurations. The regions are 1 – core, 2 – upper fission gas plenum, 3 – lower fission gas plenum and bottom plenum spacer, 4 – radial reflector, 5 – axial reflector, and 6 – target. Axial reflector and bottom plenum spacer regions are filled by their respective core's coolant. The spallation target consists of lead/bismuth eutectic.

Table 7
Void worth analyses in a model fast-breeder reactor, for sodium and lead/bismuth coolant with $(U,Pu)O_2$ fuel

Coolant	P/D	Atomic fraction Pu/(U+Pu)	ΔL_f	$\Delta L_{c,fuel}$	$\Delta L_{c,cool}$	$\Delta L_{c,clad}$	ΔL_e	ΔG_x
Na								
Core void worth								
	1.2	17%	+0.0076	−0.0281	+0.0063	+0.0123	+0.0037	+0.0002
	1.6	22%	+0.0096	−0.0689	+0.0181	+0.0316	+0.0105	+0.0001
	2.0	27.5%	+0.0071	−0.0908	+0.0265	+0.0428	+0.0156	+0.0006
	2.4	33%	+0.0035	−0.1048	+0.0323	+0.0487	+0.0197	+0.0006
Core and upper plenum void worth								
	2.0	27.5%	−0.0166	−0.1282	+0.0471	+0.0397	+0.0598	+0.0006
Pb/Bi								
Core void worth, radial reflector with steel pins								
	1.2	16%	+0.0058	−0.0247	−0.0036	+0.0211	+0.0008	−0.0003
	1.6	19%	+0.0107	−0.0506	−0.0088	+0.0471	+0.0023	−0.0006
	2.0	22.5%	+0.0114	−0.0709	−0.0129	+0.0677	+0.0039	+0.0006
	2.4	26%	+0.0112	−0.0804	−0.0172	+0.0819	+0.0053	−0.0008
Core void worth, Pb/Bi radial reflector								
	2.0	22%	+0.0216	−0.0555	+0.0124	+0.0060	+0.0163	−0.0006

$\Delta L_{c,clad}$ includes capture in the structural material of the reflectors. Note that $\Delta G_x = \Delta C_x - \Delta L_x < 10^{-3}$.

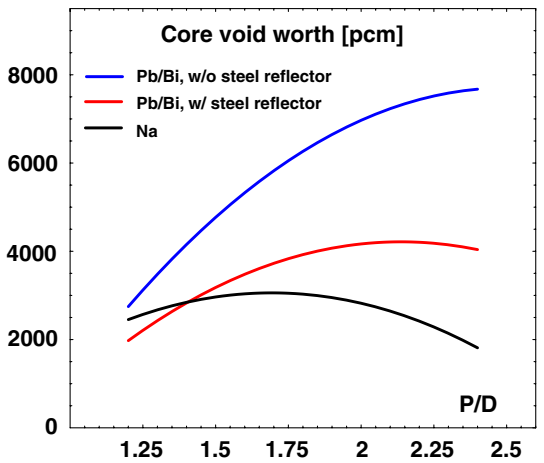

Fig. 9. Coolant void worth in a critical FBR employing $(U,Pu)O_2$ fuel. The Pu/(U+Pu) ratio was varied with P/D in order obtain $k_{eff} \sim 1$, for Na in the range between 17% and 33%, for Pb/Bi without steel pin reflector between 16% and 26%, and in the case of Pb/Bi with steel reflector between 17% and 27%.

In our model, the effect of the enhanced neutron leakage *from the core* upon coolant voiding is thus exhibited as a change in the capture of neutrons in coolant and structural material of plena and reflectors. Hence, in contrast to the infinite pin

lattice analyses the changes in the capture probability in clad introduces a *negative* reactivity upon coolant voiding.

We note that the spectrum hardening responsible for reduction of neutron parasitic capture in fuel is the only source inserting positive reactivity into the system in the case of sodium. With increasing pitches we observe both reduction of the neutron capture probability in the fuel as well as its gradual increase in coolant and clad material of plena and reflectors. The probability of neutrons to leak out the reactor system increases consequently with increasing pitches too, though not as strongly as the coolant capture term. For P/D > 1.6, the coolant and clad capture and leakage terms together increase faster than the neutron capture probability in fuel is reduced, leading to a subsequent decrease of the void worth.

In comparison to sodium cooled system, the reduction of neutron capture in Pb/Bi during coolant voiding for the core with radial steel pin reflector introduces positive reactivity to the system. The negative reactivity feedback is then supplied mainly due to the increase of neutron capture in the *structural material of reflector.* However, this negative feedback is not able to compensate for the total reduction in fuel and coolant capture rates. Adding smaller leakage, in comparison to sodium, Pb/Bi-cooled FBRs thus yield higher void worths than systems cooled by sodium, for P/D larger than 1.4!

When the steel pin reflector is replaced by Pb/Bi, the only significant effect introducing negative reactivity to the systems is the increased neutron capture in coolant and surrounding reactor shielding material (manifested in our study as an increased leakage term L_e). This results in excessive void worths even for large pitch-to-diameter ratios.

One could therefore supply an absorbing material into the core reflector in order to increase the neutron capture upon coolant voiding and consequently reduce void worth.

The leakage effect itself becomes significantly pronounced when the upper plenum is voided together with the reactor core, providing more than 40% of the negative reactivity upon coolant voiding.

3.3. ADS

The void worth was further studied in realistic models of ADSs for fuel compositions relevant for transmutation purposes.

Fig. 10 shows coolant void worth for TRU fuels having a fixed inert matrix fraction, a condition which might be imposed by reasons of high temperature stability or fabricability of fuel (Wallenius and Eriksson, submitted). In order to keep k_{eff} constant, the Pu/Am ratio is hence varied as a function of P/D. We note that the absolute value of the core void worth is a factor of 2–3 higher than for FBRs utilising $(U,Pu)O_2$ fuel. However, on the contrary to the situation in the FBR, lead/bismuth yields *lower* core void worth than sodium for pitch-to-diameter ratios less than 2.3!

A dramatic change in core void worth behaviour with respect to increasing P/D is observed when the Pu/Am ratio in fuel is kept constant at Pu/Am = 2/3, corresponding to the equilibrium fraction of fuel in MA-ADS burner in double-strata

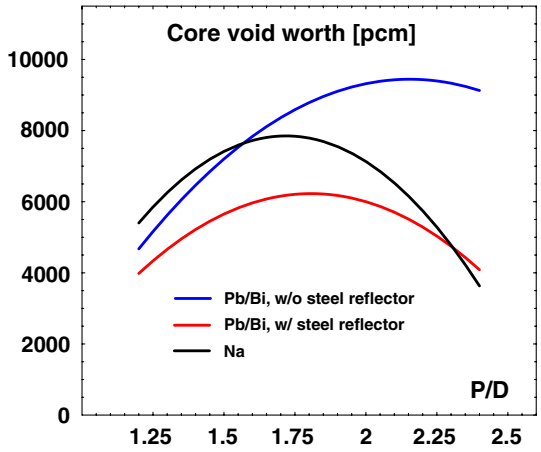

Fig. 10. Core void worth in ADSs cooled by sodium and lead/bismuth. The inert matrix fraction is kept constant at 50 vol%, and Pu/(Pu+Am) ratio is adjusted to obtain $k_{\text{eff}} \sim 0.96$, for Na in the range between 23% and 67%, for Pb/Bi without steel pin reflector between 20% and 49%, and in the case of Pb/Bi with steel reflector between 21% and 51%. The Pu and Am vectors are those of spent LWR UOX fuel after 30 years of cooling.

scheme (Takizuka et al., 1998). In this case, the enhanced neutron leakage and capture in structural material are not able to compensate for reduction of neutron capture rate in the fuel and coolant, causing core void reactivity to grow with P/D, see Fig. 11. A similar behaviour was also observed for solid solution oxide fuels (Wallenius, 2003).

In Fig. 12, the change in reactivity while voiding both core and upper plenum is compared to the core void worth. In this case, neutron leakage is enhanced proportionally to P/D, reducing the void worth by several thousands of pcm (for standard size pitch-to-diameter ratio equal to 1.6, by more than 2000 pcm). W however remains positive, even for $P/D = 2.4$.

Fig. 13 displays results of the void worth calculations in a TRU-ADS burner cooled by lead/bismuth eutectics for two pin diameters, 6 and 8 mm. The ratio of Pu/Am is kept at 4/1, corresponding to a case when all Pu from the LWRs is directed to the ADS, a so called two component scenario. The relative fraction of MA in fuel is small and the increase in neutron fission-to-capture ratio upon coolant voiding is thus not as dramatic as in MA-based ADSs, leaving the reduction of neutron capture probability in fuel to be the only significant factor introducing positive reactivity to the system. Generally, the void worth is now found to be decreasing with growing pitch due to increasing neutron leakage.

In order to illustrate an effect of the fissile isotope content in the Pu-vector on the void worth, the same calculation was also made for "fresh", high quality, plutoniurn, coming from LWR UOX spent fuel after 4 years of cooling. In this case, the minor actinide content in fuel is further decreased, lowering consequently also the void worths.

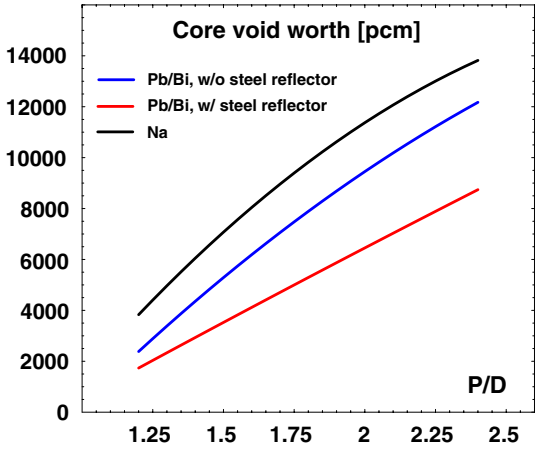

Fig. 11. Core void worth in ADSs cooled by sodium and lead/bismuth. The Pu/Am ratio was kept constant at 2/3, and actinide fraction (AcN) in fuel was adjusted to obtain $k_{\text{eff}} \sim 0.96$, for Na in the range between 35 and 85 vol%, for Pb/Bi without steel reflector between 31 and 59 vol%, and in the case of Pb/Bi with steel pin reflector between 33 vol%. and 63 vol%. The Pu and Am vectors are those of spent LWR UOX fuel after 30 years of cooling.

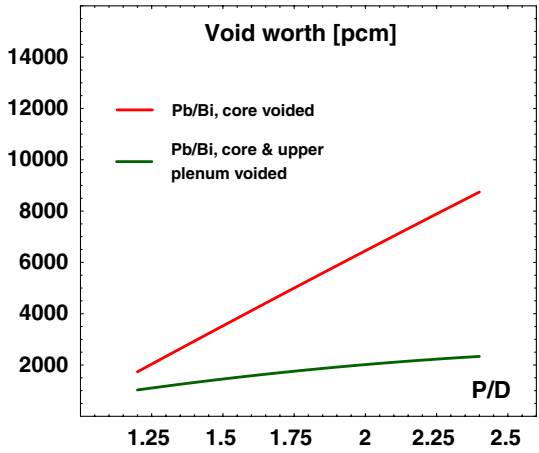

Fig. 12. Core and plenum void worths in ADS employing Pb/Bi coolant and steel pin radial reflector. Pu/Am fraction was kept at 2/3, AcN fraction was varied to obtain $k_{\text{eff}} \sim 0.96$. The Pu and Am vectors are those of spent LWR UOX fuel after 30 years of cooling.

Fuel pins with smaller pin diameter appeared to be more favourable with respect to the void worth, the difference being most pronounced for larger-pitches.

Exchanging ZrN for an absorbing matrix, in our case HfN, increases the void worth, but in the case of TRU-based fuel, W remains at acceptable levels, see Fig. 14. While the core void worth becomes slightly positive, the coupled core and upper plenum void is still strongly negative for all pitches.

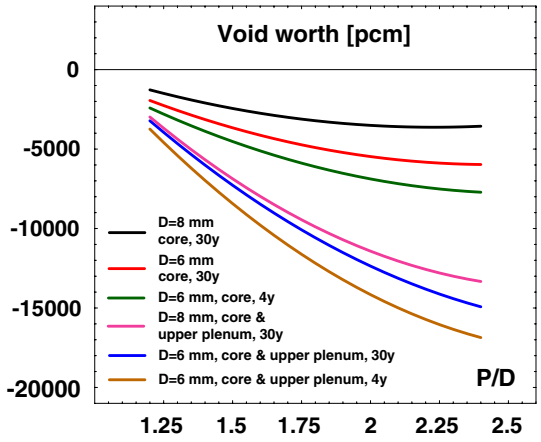

Fig. 13. Coolant void worth in ADS employing (TRU,Zr)N fuel, Pb/Bi coolant and steel pin radial reflector. Pu/Am ratio is 4/1, AcN fraction is varied with P/D to obtain $k_{\text{eff}} \sim 0.96$, for pins with a radius of 3 mm in the range between 13 and 25 vol% (when applying 30-y actinide vector) and between 12% and 23% (for 4-y actinide vector). For 4-mm-radii pins, AcN volume fraction was adjusted in the range between 10% and 19%.

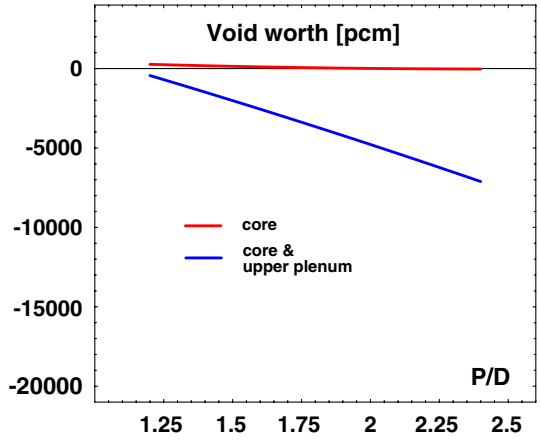

Fig. 14. Coolant void worth in Pb/Bi-cooled ADS employing TRU fuel with an absorbing matrix – (TRU,Hf)N. The steel pin reflector is used. Pu/Am fraction is kept at 4/1, AcN fraction in fuel is varied between 28 and 41 vol% to obtain $k_{\text{eff}} \sim 0.96$. Pin diameter is 6 mm, the Pu and Am vectors are those of spent LWR UOX fuel after 30 years of cooling.

In Table 8, we display the coolant void worth for different types of mononitride fuels employed in a model ADS burner with lattice pitch-to-diameter ratio equal to two and decomposed into the individual terms with respect to capture in fuel, clad, coolant, and with regards to neutron leakage. We note that the statistical error of calculations is of the same order of magnitude as ΔG_x, which we therefore do not list.

Table 8
Breakdown of coolant void worth into individual components shown for different types of mononitride fuels employed in a model ADS with sodium or lead/bismuth coolant; pitch-to-diameter ratio is 2.0

Coolant	Atomic fraction Pu/(Pu+Am)	Volume fraction AcN/(AcN+inert matrix)	R_{pin}	ΔL_f	$\Delta L_{c,fuel}$	$\Delta L_{c,cool}$	$\Delta L_{c,clad}$	ΔL_e
Core void worth								
Na	80%	29.5%	3 mm	−0.0102	−0.0839	+0.0205	+0.0524	+0.0214
	55%	50%	3 mm	+0.0164	−0.0910	+0.0171	+0.0409	+0.0172
	40%	66%	3 mm	+0.0296	−0.0948	+0.0148	+0.0361	+0.0150
Core void worth, radial reflector with steel pins								
Pb/Bi	80%	20%	3 mm	−0.0226	−0.0650	−0.0104	+0.0903	+0.0060
	80%	15.5%	4 mm	−0.0156	−0.0690	−0.0138	+0.0908	+0.0059
	42%	50%	3 mm	+0.0109	−0.0794	−0.0019	+0.0649	+0.0048
	40%	52%	3 mm	+0.0127	−0.0803	−0.0019	+0.0646	+0.0046

Similarly to the results obtained for the pin lattice model, the amount of positive reactivity introduced upon coolant voiding by reduction of capture in fuel increases with growing MA fraction in the fuel. Evidently, this is due to the pronounced increase of fuel fission-to-capture ratio. As a common characteristics for all fuels studied, the positive reactivity introduced by the reduction of capture in fuel is lower in sodium cooled systems than for lead/bismuth. We also observe that the reactivity being introduced by a change in coolant capture is lower for high MA content fuel than for fuels dominated by plutonium.

4. Conclusions

We found that reactor cores with high minor actinide content fuel exhibit generally higher void worths than cores fuelled primarily with plutonium. A disadvantage of sodium versus Pb/Bi in terms of larger positive coolant void worth is apparent for all transmutation type fuels investigated.

For an FBR with $(U,Pu)O_2$ fuel, on the contrary, Pb/Bi yields larger void worth than sodium when $P/D \gtrsim 1.4$, which is in contradiction with the results obtained by Yiftah and Okrent (1960). While in sodium cooled FBRs the negative reactivity is introduced upon coolant voiding by both increase of neutron capture in structural material and coolant (in the reflectors and plena), in Pb/Bi-cooled reactors the reactivity contribution is negative only from the former.

In lead/bismuth-cooled systems, a radial steel pin reflector has to be applied, if coolant void worth is to be significantly reduced.

Enlarging the pitch-to-diameter ratio lowers the coolant void worth in ADS burners operating in two-component scenario, while ADS reactors with MA based fuel should be designed with minimum allowable P/D.

Wallenius, J., Eriksson, M. Neutronic design of sub-critical minor actinide burners. Nuclear Technology (submitted).

Waltar, A., Reynolds, A., 1981. Fast Breeder Reactors. Pergamon Press, New York.

Yiftah, S., Okrent, D., 1960. Some physical calculations on the performance of large fast breeder power reactors. Tech. Rep. ANL-6212, Argonne National Laboratory, USA.

Symposium, ASTM STP 1125, R. E. Stoller, A. S. Kumar, and D. S. Gelles, Eds., American Society for Testing and Materials, p. 1071-1082, Philadelphia (1992).

34. I. SHIBAHARA, T. OMORI, Y. SATO, S. ONOSE, and S. NOMURA, "Mechanical Property Degradation of Fast Reactor Fuel Cladding During Thermal Transients," Effects of Radiation on Materials: 16th Int. Symposium, ASTM STP 1175, A. S. Kumar, D. S. Gelles, R. Nanstad, and E. A. Little, Eds., American Society for Testing and Materials, p. 664-678, Philadelphia (1994).

35. M. G. ADAMSON, E. A. AITKEN, and S. VAIDYANATHAN, "Synergistic tellurium-caesium embrittlement of Type 316 stainless steel", Nature, **295**, 49 (1982).

36. S. TANI, S. NOMURA, and I. SHIBAHARA, "Fuel Cladding Mechanical Property Degradation Mechanisms and Fuel Reliability Under Transient Conditions," Int. Conf. on Reliable Fuels for Liquid Metal Reactors, Sep. 7-11, Tucson (1986).

37. R. J. PUIGH and M. L. HAMILTON, Influence of Radiation on Materials Properties: 13th Int. Symposium (Part II), ASTM STP 956, F. A. Garner, C. H. Henager, N. Igata, Eds., American Society for Testing Materials, p. 22-29 (1987).

38. G. S. YACHMENYOV, A. YE. RUSANOV, B. F. GROMOV, YU. S. BELOMYTSEV, N. S. SKVORTSOV, and A. P. DEMISHONKOV, "Problems of structural materials' corrosion in lead-bismuth coolant," Proc. Heavy Liquid Metal Coolants in Nuclear Technology, Vol. 1, Obninsk, October 5-9, p. 133-140, State Scientific Center of Russian Federation Institute for Physics and Power Engineering (1998).

39. J. F. BRIESMEISTER, "MCNP - A general Monte Carlo N-Particle transport code," LA-13709-M, Los Alamos National Laboratory (2000).

40. J. E. CAHALAN, A. M. TENTNER, and E. E. MORRIS, "Advanced LMR Safety Anlaysis Capabilities in the SASSYS-1 and SAS4A Computer Codes," Proc. of the International Topical Meeting on Advanced Reactors Safety, Pittsburgh, April 17-21 (1994).

41. M. ERIKSSON, J. E. CAHALAN, and W. S. YANG, "On the Performance of Point Kinetics for the Analysis of Accelerator Driven Systems," Accepted for publication in the March Issue of Nucl. Sci. Eng. (2005).

42. K. TSUJIMOTO, T. SASA, K. NISHIHARA, H. OIGAWA, and H. TAKANO, "Neutronics Design for Lead-Bismuth Cooled Accelerator-Driven System for Transmutation of Minor Actinides," J. Nucl. Sci. & Technology, **41** (2004) 21.

43. P. A. USHAKOV, "Hydrodynamics and Heat Transfer in Reactor Cooled by Lead-Bismuth Alloy," Proc. Heavy Liquid Metal Coolants in Nuclear Technology, Vol. 2, Obninsk, October 5-9, p. 612-626, State Scientific Center of Russian Federation Institute for Physics and Power Engineering (1998).

44. F. E. DUNN and D. J. MALLOY, "LMR Centrifugal Pump Coastdowns," Proc. Anticipated and Abnormal Transients In Nuclear Power Plants, Vol. 1, American Nuclear Society Topical Meeting, Atlanta, Georgia, April 12-15 (1987).

45. H. TAKANO, et al., "A Design for Inherent Safety Core, Aseismicity and Heat Transport System in Lead-Cooled Nitride-Fuel Fast Reactor," Proc. Int. Topical Meeting on Advanced Reactor Safety, Pittsburgh, April 17-21 (1994).

46. J. BUONGIORNO and B.D. HAWKES, "Seismic analysis of heavy-liquid-metal-cooled reactor vessels", Nuclear Engineering and Design **228** (2004) 305–317.

47. I. MICHELI, S. CARDINI, A. COLAIUDA, P. TURRONI, "Investigation upon the dynamic structural response of a nuclear plant on aseismic isolating devices," Nuclear Engineering and Design **228** (2004) 319–343.

48. M. ERIKSSON and J. E CAHALAN, "Inherent shutdown capabilities in accelerator-driven systems," Annals of Nuclear Energy, vol. 29/14 pp 1689-1706, (2002).

49. W. MASCHEK, et al., "Safety Improvements for ADS Transmuters with dedicated Fuel," Proc. of the AccApp/ADTTA 2001 Meeting, Reno, November 11-15, American Nuclear Society (2001).

50. K. TUCEK, J. WALLENIUS, and W. GUDOWSKI "Coolant void worths in fast breeder reactors and accelerator driven transuranium and minor actinide burners," Annals of Nuclear Energy, accepted for publication (2004).

51. J. WALLENIUS, K. TUCEK, and W. GUDOWSKI, "Safety analysis of nitride fuels in cores dedicated to waste transmutation," Proc. 6th Information Exchange Meeting on Actinide and Fission Product Partitioning and Transmutation, Madrid, December 11-13, OECD/NEA (2000).

52. W. MASCHEK, T. SUZUKI, X. CHEN, MG. MORI, C. M. BOCCACCINI, M. FLAD, K. MORITA, "Behavior of Transmuter Fuels of Accelerator Driven Systems under Severe Accident Conditions," GENES4/ANP2003, Kyoto, September 15-19 (2003).

53. F. E. DUNN and D.C. WADE, "Estimates of Thermal Fatigue Due to Beam Interruptions for an ALMR-Type ATW," Proc. 2nd International Workshop on Utilisation and Reliability of High Power Proton Accelerators, Aix-en-Provence, November 22-24, NEA/OECD (1999).

54. M. ERIKSSON, "Reliability Assessment of the LANSCE Accelerator System," M.Sc. Thesis, Royal Institute of Technology, Dep. Nuclear and Reactor Physics (Nov. 1998).

55. J. E. CAHALAN and M. ERIKSSON, "Active and Passive Safety Control Performance in Sub-critical, Accelerator-Driven Nuclear Reactors," Proc. 3rd International Workshop on Utilisation and Reliability of High Power Proton Accelerators, Santa Fe, May, NEA/OECD (2002).

56. Y. S. TANG, R. D. COFFIELD, and R. A. MARKLEY, Thermal Analysis of Liquid Metal Fats Breeder Reactors, p.

Pins with small diameters and non-absorbing fuel matrices are preferable with regard to obtain low coolant void worth. However, even an application of strongly absorbing matrix (HfN), does not have to deteriorate the void worth critically; large amount of negative reactivity still being introduced into the reactor upon voiding both core and upper plenum, as e.g. in the case of TRU-fuelled ADS.

Acknowledgements

Financial support of the Swedish Nuclear Fuel and Waste Management Co (SKB AB) is acknowledged.

References

Briesmeister, J., 2000. MCNP – A general Monte Carlo N-Particle transport code, version 4C. Tech. Rep. LA 13709- M, Los Alamos National Laboratory, USA.

Cheng, E., et al., 1995. Actinide transmutation with small tokamak fusion reactors. In: Proceedings of the International Conference on Evaluation of Emerging Nuclear Fuel Cycle Systems, GLOBAL'95. Versailles, France, p. 1428.

Cinotti, L., Gherardi, G., 2002. The Pb-Bi cooled XADS status of development. Journal of Nuclear Materials 301 (1), 8.

Conti, A., et al., 1995. CAPRA exploratory studies of U-free fast Pu burner cores. In: Proceedings of the International Conference on Evaluation of Emerging Nuclear Fuel Cycle Systems, GLOBAL'95. Versailles, France, p. 1316.

Eriksson, M., et al., 2002. Safety analysis of Na and Pb–Bi coolants in response to beam instabilities. In: Proceedings of the Third International Workshop on Utilisation and Reliability of High Power Proton Accelerators, Santa Fe, USA.

Foster, D., et al, 1974. Review of PNL study on transmutation processing of high level waste. Tech. Rep. LA-UR-74-74, Los Alamos National Laboratory, USA.

Khalil, H., Hill, R., 1991. Evaluation of liquid-metal reactor design options for reduction of sodium void worth. Nuclear Science and Engineering 109, 221.

Maschek, W., et al., 2000. Safety analyses for ADS cores with dedicted fuel and proposals for safety improvements. In: Proceedings of the IAEA TCM Meeting. Argonne National Laboratory, USA.

Murata, H., Mukaiyama, T., 1984. Fission reactor studies in view of reactor waste programs. Atomkernenergie-Kerntechnik 45, 23.

Rose, R., et al., 1977. Fusion-driven actinide burner design study. Tech. Rep., Electric Power Research Institute, EPRI ER-451, USA.

Rubbia, C., et al., 1997. Fast neutron incineration in the energy amplifier as alternative to geologic storage: The case of Spain. Tech. Rep. CERN/LHC/97-01(EET).

Shmelev, A. et al., 1992. Safety of reactor burning long-lived actinides from radioactive waste. Bezopasnost' bystrogo reaktora-vyzhigatelya dolgo-zhivushchikh aktinoidov, izvlechennykh iz radio-aktivnykh otkhodov. Atomnaya Ehnergiya 73 (6), 450.

Stacey, W. et al., 2002. A fusion transmutation of waste reactor. Fusion Science and Technology 41, 116.

Takizuka, T., et al., 1991. Conceptual design of transmutation plant. In: Proceedings of the Specialist Meeting on Accelerator Driven Transmutation Technology for Radwaste. LA-12205-C, Los Alamos National Laboratory, USA, p. 707.

Takizuka, T., et al., 1998. Studies on accelerator driven transmutation systems. In: Proceedings of the Fifth International Information Exchange Meeting. OECD/NEA, Mol, Belgium, p. 383.

Wallenius, J., 2003. Neutronic aspects of inert matrix fuels for application in ADS. Journal of Nuclear Materials 320, 142.

277, American Nuclear Society, LaGrange Park, Illinois (1978).

57. W. MASCHEK, et al., "Safety Analyses for ADS Cores with Dedicated Fuel and Proposals for Safety Improvements," IAEA-TECDOC-1356, IAEA (2000).

58. B. F. GROMOV, O. G. GRIGORIEV, A. V. DEDOUL, G. I. TOSHINSKY, V. S. STEPANOV, "The Analysis of Operating Experience of Reactor Installations Using Lead-Bismuth Coolant and Accidents Happened," Proc. Heavy Liquid Metal Coolants in Nuclear Technology, Vol. 1, Obninsk, October 5-9, p. 60-66, State Scientific Center of Russian Federation Institute for Physics and Power Engineering (1998).

APPENDIX 14

W. Gudowski, “Nuclear waste management. Status, prospects and hopes”, INPC2004,

Nuclear waste management.

Status, prospects and hopes

W. Gudowski,
Kungliga Tekniska Högskolan
100 44 Stockholm, Sverige
wacek@neutron.kth.se

Introduction

Developing reliable and sustainable energy systems for Europe is the general strategic goal of the European energy research. In addition, the aim is to contribute to a more **sustainable development,** worldwide. This strategy should lead to an increased security and diversity of energy supply and will provide Europe with:

- high-quality, low-cost energy services
- improved industrial competitiveness
- reduced environmental impact, and
- a better quality of life for all Europeans

Nuclear energy currently provides about 35% of electrical power in the European Union (EU) and some 15% of primary energy without using fossil resources and without producing CO_2. Thus, it is an important element of a sustainable European energy system together with other renewable energy sources. The low cost of nuclear energy may even allow an increased deployment and share of – still more expensive - CO_2-free alternatives in an energy mix.

Nevertheless, nuclear energy presently suffers from a lack of public and political acceptance in many European countries leading – in some instances - to moratoria and phase-out decisions. This is mainly caused by safety concerns, continued accumulation of nuclear waste and a general lack of consensus on the implementation of waste disposal strategies such as disposal in geological repositories though excellent technical progress has been made in this regard. The main concern in the disposal of radioactive waste is related to long-lived radionuclides—some of them will remain hazardous for tens of thousands of years.

Management of nuclear waste generated by commercial nuclear power plants world over has been in a focus of public attention since 1970's and contributed largely to a growing criticism against nuclear power. While most of the nuclear power countries consider geological repository of nuclear waste as the only option, the research and development on methods for partitioning and transmutation (P&T) of long-lived radionuclides in spent nuclear fuel has attracted considerable interest during the last decade. The main objective of P&T is just to eliminate or at least substantially reduce the amount of such long-lived radionuclides that has to go to a repository for final disposal. The radionuclides of main concern are those of the transuranium elements and a few fission products that are also of some interest for transmutation.

For a nuclear physicist it is very logical that the long-lived radionuclides, products of the nuclear processes in a reactor should be coped with nuclear physics methods, the only method

that can reduce life time and radiotoxicity of radionuclides. In theory and in laboratory scale several such processes are possible, but in practice so far only transmutation by irradiation with neutrons can be achieved in macroscopic scale with a reasonable energy balance. Transmutation on large scale of the transuranium elements from spent nuclear fuel must be done in a device similar to a nuclear reactor.

A prerequisite for transmutation by irradiation with neutrons is that the nuclides to be transmuted are separated (partitioned) from the other nuclides in the spent fuel. The objective of current research on partitioning is to find and develop processes suitable for separation of the heavier actinides (and possibly some long-lived fission products) on an industrial scale.

The objective of current research on transmutation is to define, investigate and develop facilities that may be suitable for transmutation of the aforementioned long-lived radionuclides.

The processes and facilities that could be implemented as results of such developments must meet very high standards of safety and radiation protection as well as have low environmental impact. They shall be economically viable and have good proliferation resistance. The large amount of energy released in the transmutation process should be used in a proper way. In other words the processes and facilities must be acceptable to society.

Quantifying the Nuclear Waste Problems

Figure 1 shows the relative radiotoxic inventory of the Light Water Reactor (LWR) discharged spent fuel as a function of time. From this figure it can be seen that the main problem of the longlived nuclear waste is limited to few isotopes: plutonium, which constitutes about 90 % of the transuranium elements in spent fuel dominates radiotoxic inventory for about $2*10^6$ years, ^{241}Am in the time interval of 50-400 years.

It is worth to mention that the radiotoxic inventory due to the presence of ^{237}Np is less than that of uranium in nature.

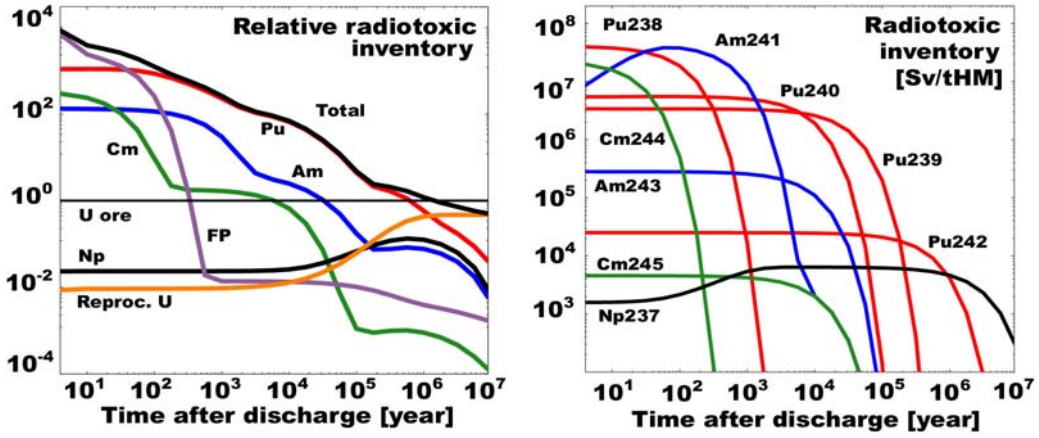

Figure 1. Relative radiotoxic inventory (element and isotopic dependent, from left to right) of the discharged Light Water Reactor spent fuel. FP – fission products, Reproc. U – reprocessed Uranium, tHM – ton of Heavy Metal.

Nuclear Waste generated today by reactors are determined mainly by the technical choices of reactor types (LWR) and a ONCE-THROUGH (see Figure 2) fuel cycle together with

neutronics (neutron physics) of reactor cores, in particular a complicated physics of neutron transport driven by energy dependent neutron cross sections and safety issues and requirements that the self-sustained chain reaction must be under a strict control.

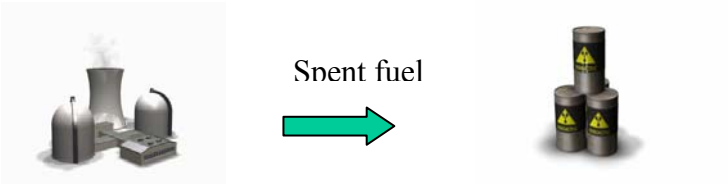

Figure 2. Once-through fuel cycle. Reactor fuel after its single residence period in a nuclear reactor is treated as nuclear waste.

A prerequisite for transmutation by irradiation with neutrons is that the nuclides to be transmuted are separated (partitioned) from the other nuclides in the spent fuel. In particular the remaining uranium must be taken away unless you want to produce more plutonium and other transuranium elements. Separation of the various elements can at least in principle be achieved by mechanical and chemical processes. Currently there exist some large scale facilities for separation of uranium and plutonium from the spent fuel – reprocessing plants. These, however, do not separate, mainly of economical reasons, the minor actinides – neptunium, americium and curium – from the high level waste that goes to a repository.

Systems for partitioning and transmutation – international landscape

A number of system studies on P&T have been published in the last few years. These studies give a good overview of the extensive work required for implementing P&T, of the relative large and complex system of facilities that are needed as well as of those problems that must be solved and the issues that must be addressed before such a system can be deployed. A very extensive summary of those studies is given in report [1].

OECD/NEA has published few reports on transmutation system prepared by the expert groups [2]-[4] concluding:

- While P&T will not replace the need for appropriate geological disposal of high-level waste, the study has confirmed that different transmutation strategies could significantly reduce, i.e. a hundred-fold, the long-term radiotoxicity of the waste and thus improve the environmental friendliness of the nuclear energy option. *In that respect, P&T could contribute to a sustainable nuclear energy system.*
- Very effective fuel cycle strategies, including both fast spectrum transmutation systems (FR and/or ADS) and multiple recycling with very low losses, would be required to achieve this objective.
- Multiple recycle technologies that manage Pu and MA either together or separately could achieve equivalent reduction factors in the radiotoxicity of wastes to be disposed.
- The study shows that pyrochemical reprocessing techniques are essential for those cycles employing ADS and FRs where very high MA-content fuels are used.

- In strategies where Pu and MA are managed separately, ADS can provide additional flexibility by enabling Pu-consumption in conventional reactors and minimising the fraction of dedicated fast reactors in the nuclear system, see Figure 3.

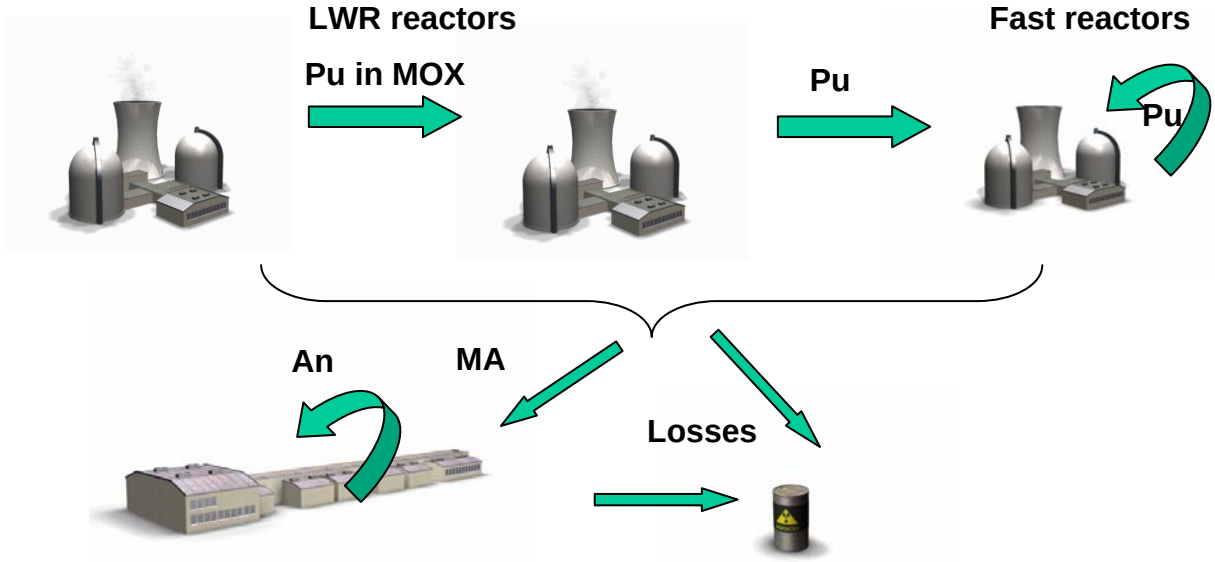

Figure 3. An advanced strategy of separately managed Pu and Minor Actinides.

- In strategies where Pu and MAs are managed together, the waste radiotoxicity reduction potential by use of FRs and ADS is similar and the system selection would need to be made based on economic, safety and other considerations.
- Further R&D on fuels, recycle, reactor and accelerator technologies would be needed to deploy P&T. The incorporation of transmutation systems would probably occur incrementally and differently according to national situations and policies.
- Fully closed fuel cycles may be achieved with a relatively limited increase in electricity cost of **about 10 to 20 %, compared with the LWR once-through fuel cycle**.
- The deployment of these transmutation schemes need long lead-times for the development of the necessary technology as well as making these technologies more cost-effective.
- To achieve the goal of reducing the amount of long-lived radionuclides in the waste by a factor of 100 or more the losses in each partitioning cycle must be less than 0.1 %.
- Transmutation of plutonium alone will decrease the long-term radiotoxicity by only a factor of five compared to spent fuel.
- Transmutation can be achieved either by fast reactors or by different combinations of light water reactors, fast reactors and accelerator-driven systems.
- Physical limitations imply that very long time is needed to pursue a “complete” transmutation. This means that the indicated objectives can only be reached if the technology is used for at least 100 years.

- The use of pyrochemical methods implies new potential chemical and radiological risks that must be mastered.
- All transmutation strategies for light water reactors give considerable amounts of depleted and irradiated uranium that have to be managed. If this uranium not is considered as a resource for future fast reactors, the long-term radiological effects when radium, radon and its daughters grow in must be accounted for.
- Transmutation of long-lived fission products involves many technical and practical difficulties. At present ^{99}Tc and possibly ^{129}I seem to be the major or only candidates.
- Experimental research on transuranium fuel is a highly prioritised subject. A bottle-neck for such research is the availability of facilities with high fast neutron flux.
- The basic research and development on fast reactors as well as accelerator-driven systems should be simpler if an international accord was obtained on the advantages and disadvantages of different coolants for such systems.

In the USA a certain interest arouse for transmutation using accelerator-driven systems in the early 1990ies. The centre of this interest was Los Alamos National Laboratory (LANL) that introduced the concept ATW – Accelerator-driven Transmutation of nuclear Waste. This gradually led to a broad study of ATW by the US Department of Energy at the request of US Congress. The study, published in the autumn of 1999 [5], proposed a research programme for ATW that could be the start of a large scale concentration on such systems.

In 2003 USA announced the so-called Advanced Fuel Cycle Initiative (ACFI), which aims at a broad study of fuel cycles for future nuclear power reactors – also named Generation IV reactors [6]. This initiative is planned to be pursued in three phases – phase 1 basic evaluation; phase 2 – proof of principles; phase 3 – proof of performance. The programme is broadly laid out and includes review of all current reactor concepts and systems (LWR, HTR, ADS, FR, aqueous based reprocessing and pyrochemical reprocessing, etc.).

Upon initiative from the research ministers in France, Italy and Spain a European technical working group – TWG –was formed in 1999. This working group proposed a plan for development of an accelerator-driven system (ADS) in Europe [7]. The ambition from the group was that the plan should form the base for continued EU-financed research work on ADS. In the plan the construction of a small experimental plant at 100 MW thermal power is proposed. The plant is envisaged to start operation in 2015. The cost for the first twelve years R&D-programme is estimated to M€ 980. In addition another M€ 180 are proposed for R&D on nuclear fuels especially suited to ADS. This first phase would then be followed by a second where a prototype for a full scale ADS is developed and constructed. After successful operation of this prototype industrial plants may be deployed starting around 2040. This study agrees fairly well concerning required times with the USDOE study. In details, however, the two studies have considerable differences. The US study has much more specified selections of systems for partitioning (pyrochemical process) as well as for transmutation (ATW cooled by liquid lead-bismuth eutectic) than the European one. The latter is delimited to transmutation with ADS, but keeps several parts of the ADS open for later choice of design – accelerator, coolant, etc.

Transmutation

The radionuclides of primary interest for transmutation - the transuranium elements (TRU) are most suitably transmuted by neutron fission. Several of the nuclides are, however, only fissionable by fast neutrons. Two different types of facilities are considered to obtain a sufficiently high fast neutron flux – fast reactors with a self-sustaining chain reaction and an accelerator-driven subcritical system (ADS). In the period 1950-1985 a number of fast reactors were constructed in several countries. The majority of them had liquid sodium as coolant. The largest was the French Superphenix with 1200 MW_e power. Only a few of these fast breeder reactors are still in operation.

During the 1990ies the interest for accelerator-driven systems increased substantially and currently there are considerable interests for studies of such systems.

An ADS consists of the following main components (see Figure 4):

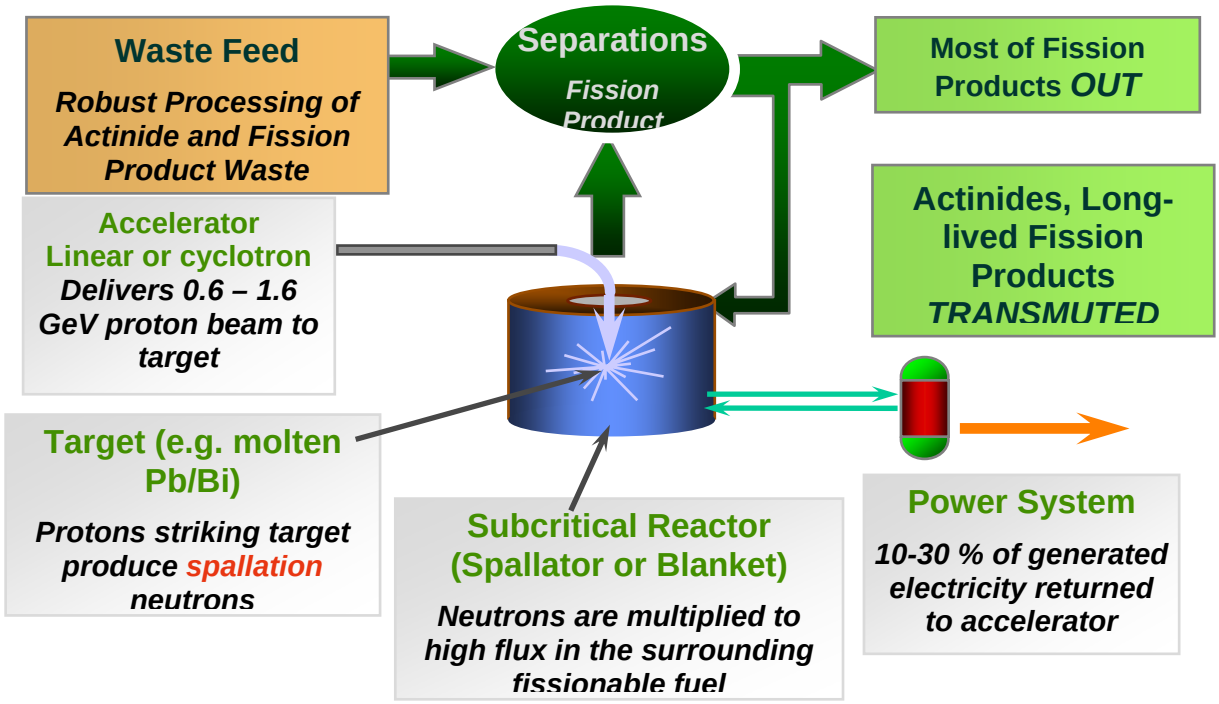

Figure 4. Main components of the Accelerator Driven System

- A proton accelerator to give a current of protons at about 1 GeV/proton energy.
- A spallation source that is hit by the proton current and where spallation reactions with heavy nuclides (lead, bismuth, tungsten, etc.) create a neutron flux of several tens of neutrons per proton.
- A subcritical nuclear reactor with fuel that contains the long-lived radionuclides to be transmuted by the neutrons from the spallation source. Due to the fission of these nuclides new neutrons are formed and for each incoming neutron from the source about 20 new neutrons are released and cause additional fission reactions. The design of the reactor shall be such that a self-sustaining chain reaction cannot occur.
- Balance of plant systems to take care of the energy released by the fission processes and by radioactive decay and to supply electricity to the accelerator.
- Equipment to control and monitor the entire process with its safety systems.

Proton accelerators exist in two different principal designs – a linear accelerator (linac) or a cyclotron (with near circular particle tracks). Cyclotrons have some technical limitations concerning proton energy, beam current and flexibility. This has caused the interest to focus more and more on linacs. A linac for the required proton energy will be very long – several hundred metres – and puts high demands on several different technical parts as well as on radiation protection. Up to recently accelerators have mainly been built for pure research purposes where the requirements on availability have been modest. A plant for transmutation does, however, include large systems with high temperatures and built in inertia for changes in the system operating conditions. This in addition to requirements of efficiency and reasonable economy puts strongly increased demands on the availability of accelerators for ADS.

The spallation source is a central component in an ADS situated between the accelerator and the subcritical reactor. It is placed in a demanding environment with high level of radiation, high temperature, strongly varying pressure and requires very effective cooling. Different heavy materials may in principle be used for the source (tantalum, tungsten, bismuth, lead, etc.) but considering the cooling requirements and other factors the current main candidate is a eutectic mixture of lead and bismuth. An important issue is the design of the "window" between the source and the vacuum tube that brings the proton beam from the accelerator to the lead-bismuth target. The alternatives are a hot "window" close to the target or "windowless" design (meaning a cold "window" away from the hot target metal). The latter design puts high demands on maintaining sufficiently good vacuum in the access tube to avoid beam energy losses. A hot "window" on the other hand puts very high demands on strength and irradiation resistance of the metal in the "window" in order to limit replacements to once per year. Currently two spallation sources with liquid lead-bismuth are built or planned in Europe. One is MEGAPIE at PSI in Switzerland where a hot "window" design has been selected [8]. The other one is for the MYRRHA-project in Belgium where a "windowless" design will be tested [9].

Different designs are being considered for the subcritical reactor. Fuel as well as coolant are still open choices. Water is not a possible coolant for a fast flux reactor. Possible options are gas (particularly helium) or liquid metal. Gas-cooling requires high pressure and is therefore often turned down due to the risk of loss of cooling. Earlier fast reactor programmes have accumulated considerable experiences on liquid sodium. The problems then encountered are obviously currently discouraging and the interest is more and more focusing on liquid lead-bismuth. This eutectic mixture has a relatively low melting point and a high boiling point and is also the main candidate for the spallation source. The latter simplifies of course the design of the systems. Experiences from reactors cooled with liquid lead-bismuth have only been obtained in Russia where seven submarine reactors have been built with this coolant. Their total operating time is about 70 reactoryears.

The research on fuel for ADS follows several parallel lines. Nitrides and alloys with inert metals, e.g. zirconium, attract considerable interest. The requirements on the fuel are i.a good heat conductivity to allow high power density, good irradiation resistance and ability to achieve high burnup – tens of percent compared to a few percent in current light water reactor fuel.

Fast reactors can, as already mentioned, be used for transmutation. During the 1990ies the research has i.a. been focused on burning plutonium in sodium cooled fast reactors. Specific types of fuel have been studied in France. In recent years the interest has also been directed towards fast gas-cooled reactors. The fast reactor may also be used for transmutation of other transuranium elements. This requires however special designs in order to prevent serious deterioration of the dynamic and safety properties of the reactor. If the fast reactor is designed

as a breeder reactor it may be possible to achieve very high energy extraction from the mined uranium as well as an effective transmutation of all transuranium elements.

In Russia there is also an interest for civil applications of fast reactors cooled with liquid lead-bismuth. Furthermore some work is done on ADS mainly financed through the so-called ISTC-programme (International Science and Technology Centre).

As already mentioned a system with high fast neutron flux is of main interest for an almost complete transmutation of all transuranium elements. For transmutation of only plutonium also other systems may be used. French studies show that by using specially designed fuel assemblies the amount of plutonium generated by a light water reactor park can be limited and stabilised. Studies by General Atomics in USA and others have shown that it may be feasible to develop fuel for a high temperature gas cooled reactor that admits burnup up to 700 MWd/kg and burning of more than 90 % of the actinide content including ^{239}Pu.

Conclusions

There is no unanimous view on the objectives for partitioning and transmutation. Many see it as a way to achieve broad acceptance for nuclear power at large and make nuclear power a sustainable option for the future. Others promote it as a way to get out of the impasse for a deep repository in several countries. Others again put a strong emphasise on the proliferation aspects of a growing stock of plutonium from light water reactors, from other reactor fuels and from dismantling of nuclear weapons.

There are some possible missions for ADS:

- burning of all transuranium nuclides from the present enriched uranium fuelled light water reactors;

or

- a supplement particularly suitable for burning minor actinides (americium, curium and neptunium), whereas the major part of the plutonium should be burned in light water reactors (or in fast reactors)

The construction of a small ADS experimental plant is a necessary step to develop and demonstrate the concept. This experimental plant should then be followed by a demonstration plant in almost full scale.

The interest for P&T is mainly concentrated to the national research laboratories in USA, Europe, Japan and some other countries. The universities in many countries including Sweden also show a strong interest. P&T-research attracts considerable interest among students in nuclear science. Several important research programmes are going on at universities and research laboratories in several countries.

The nuclear industry, however, has shown only a limited interest in the development and is mainly visible in France and a few other countries with large nuclear programmes. The long-term interest in industry is much more focused on new types of reactors – often called Generation IV.

The national and industrial efforts on spent fuel and high level waste management in almost all countries are primarily focused on the resolution of the deep repository issues. Despite all the delays and all the setbacks in many countries the prospects of reaching this goal are much better and much closer in time than the very long-term and costly goal of implementing and operating any P&T-system.

A successful development of P&T will not make a deep geological disposal obsolete. The complex processes will inevitably generate some wastes containing small amounts of long-lived radionuclides. These wastes will require a deep geological repository. A successful development may, however, decrease the requirements on the engineered barriers in the deep repository and also decrease the volumes needed for disposal of wastes.

P&T at an industrial scale requires large nuclear facilities that must be accepted by society.

The costs for P&T are not possible to determine with any good accuracy before the systems have been better defined and tested. The estimates that have been made indicate an electricity production cost that is between 10 % and 50 % above the costs from modern light water reactor designs with once-through fuel cycle [11]. The investments needed in R&D and in new nuclear facilities are large. They are, however, spread over long time and the major part should be looked upon as investments for energy production. It is not economically defensible to implement P&T without effectively using the energy released. This is particularly the case with transmutation of plutonium. Some experts have the opinion that it might be feasible to construct small ADS-plants specifically for burning americium and curium.

The introduction of a P&T-system for effective reduction of the amount of long-lived radioactive nuclides that must be disposed of in a deep geological repository thus requires a commitment to nuclear energy for a very long time. It may, however, on the other hand be looked upon as a long-term strategy for recycling and recovering energy from materials that otherwise are seen as very troublesome wastes.

References

[1] P-E Ahlström, S. Andersson, Ch. Ekberg, J-O Liljenzin, M. Nilsson, G. Skarnemark, J. Blomgren, M. Eriksson, W. Gudowski, P. Seltborg, J. Wallenius and B-R Sehgal, ”Partitioning and transmutation Current developments - 2004. A report from the Swedish reference group on P&T-research”, SKB TR-04-15, 2004

[2] Actinide and Fission Product Separation and Transmutation, Status and Assessment Report (Synthèse des travaux). OECD/NEA report (1999)

[3] Accelerator-driven Systems (ADS) and Fast Reactors (FR) in Advanced Nuclear Fuel Cycles. A Comparative Study. OECD/NEA report 2002.

[4] NEA 03 Plutonium management in the medium term. A report by the OECD/NEA working party on the physics of plutonium fuels and innovative fuel cycles (WPPR). OECD/NEA 2003. ISBN 92-64-02151-5.

[5] DOE/RW-0519. A Roadmap for Developing Accelerator Transmutation of Waste (ATW) Technology. A Report to Congress. October 1999.

[6] Report to Congress on Advanced Fuel Cycle Initiative: The Future Path for Advanced Spent Fuel Treatment and Transmutation Research. U.S. Department of Energy Office of Nuclear Energy, Science, and Technology January 2003, http://www.ne.doe.gov/reports/AFCI_CongRpt2003.pdf .

[7] A European Roadmap for Developing Accelerator Driven Systems (ADS) for Nuclear Waste Incineration. April 2001. Report prepared by European Technical Working Group of Experts on ADS. ENEA, April, 2001

[8] C. Fazio, R. Stieglitz et al, The Megapie-Test Project. Proceedings of International Workshop on P&T and ADS Development (INWOR) October 6-8, 2003 SCK·CEN, Mol, Belgium.

[9] P. Benoit, D.Maes, et al., Small-scale LBE-cooled ADS: MYRRHA – engineering design description, International Workshop on P&T and ADS Development, SCK·CEN, Mol, Belgium, October 6-8, 2003

[10] International Science and Technology Centre – http://www.istc.ru

[11] D. Westlén, A cost benefit analysis of an accelerator driven transmutation system, Diploma thesis, KTH 2001.